Medical Imaging for Health Professionals

Technologies and Clinical Applications

Edited by
Raymond M. Reilly, Ph.D

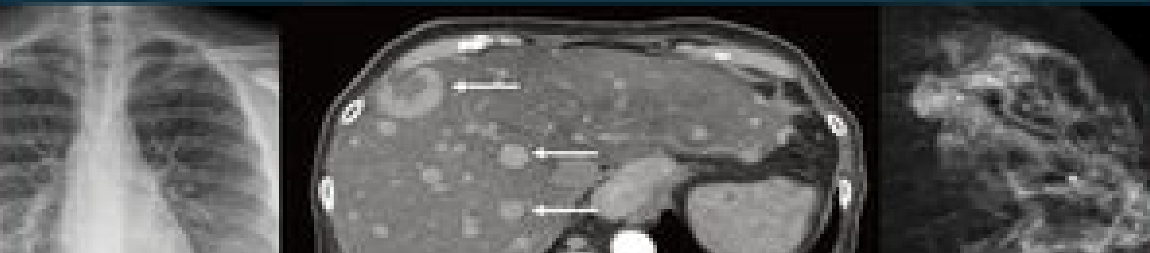

WILEY

Medical Imaging for Health Professionals

Medical Imaging for Health Professionals

Technologies and Clinical Applications

Edited by

Raymond M. Reilly, PhD
University of Toronto
Toronto, Ontario, Canada

WILEY

This edition first published 2019
© 2019 John Wiley & Sons, Inc.

All rights reserved. No part of this publication may be reproduced, stored in a retrieval system, or transmitted, in any form or by any means, electronic, mechanical, photocopying, recording or otherwise, except as permitted by law. Advice on how to obtain permission to reuse material from this title is available at http://www.wiley.com/go/permissions.

The right of Raymond M. Reilly to be identified as the editor of this work has been asserted in accordance with law.

Registered Office
John Wiley & Sons, Inc., 111 River Street, Hoboken, NJ 07030, USA

Editorial Office
111 River Street, Hoboken, NJ 07030, USA

For details of our global editorial offices, customer services, and more information about Wiley products visit us at www.wiley.com.

Wiley also publishes its books in a variety of electronic formats and by print-on-demand. Some content that appears in standard print versions of this book may not be available in other formats.

Limit of Liability/Disclaimer of Warranty
In view of ongoing research, equipment modifications, changes in governmental regulations, and the constant flow of information relating to the use of experimental reagents, equipment, and devices, the reader is urged to review and evaluate the information provided in the package insert or instructions for each chemical, piece of equipment, reagent, or device for, among other things, any changes in the instructions or indication of usage and for added warnings and precautions. While the publisher and authors have used their best efforts in preparing this work, they make no representations or warranties with respect to the accuracy or completeness of the contents of this work and specifically disclaim all warranties, including without limitation any implied warranties of merchantability or fitness for a particular purpose. No warranty may be created or extended by sales representatives, written sales materials or promotional statements for this work. The fact that an organization, website, or product is referred to in this work as a citation and/or potential source of further information does not mean that the publisher and authors endorse the information or services the organization, website, or product may provide or recommendations it may make. This work is sold with the understanding that the publisher is not engaged in rendering professional services. The advice and strategies contained herein may not be suitable for your situation. You should consult with a specialist where appropriate. Further, readers should be aware that websites listed in this work may have changed or disappeared between when this work was written and when it is read. Neither the publisher nor authors shall be liable for any loss of profit or any other commercial damages, including but not limited to special, incidental, consequential, or other damages.

Library of Congress Cataloging-in-Publication Data

Names: Reilly, Raymond, editor.
Title: Medical imaging for health professionals : technologies and clinical
applications / edited by Raymond M. Reilly.
Description: First edition. | Hoboken, NJ : John Wiley & Sons, Inc., 2019. |
Includes bibliographical references and index. |
Identifiers: LCCN 2018036244 (print) | LCCN 2018037499 (ebook) | ISBN
9781119120292 (Adobe PDF) | ISBN 9781119120322 (ePub) | ISBN 9781119120285
(hardback)
Subjects: | MESH: Diagnostic Imaging–methods
Classification: LCC RC78.7.D53 (ebook) | LCC RC78.7.D53 (print) | NLM WN 180 |
DDC 616.07/54–dc23
LC record available at https://lccn.loc.gov/2018036244

Cover design by Noor Al-saden
Cover image: (Left) Courtesy of Anastasia Oikonomou, (Middle) Courtesy of Chirag Patel,
(Right) Courtesy of Hemi Dua

Set in 10/12pt Warnock by SPi Global, Pondicherry, India

Printed in the United States of America

10 9 8 7 6 5 4 3 2 1

To my students who provided the inspiration for this book. There is no more joyful aspect of being a professor than to teach young people to better understand the world.

Contents

Contributors *xix*
Preface *xxi*
Acknowledgments *xxiii*

1 Introduction to Medical Imaging *2*
Raymond M. Reilly
1.1 Medical Imaging Procedures *2*
1.1.1 Procedures Involving Ionizing vs. Nonionizing Radiation *3*
1.2 Radiation Doses from Medical Imaging Procedures *4*
1.2.1 Estimating Radiation Doses from Medical Imaging *5*
1.2.2 Radiation Doses and Increased Use of Medical Imaging *8*
1.3 Summary *8*
References *9*

2 X-Ray, CT, and Mammography Technology *11*
Raymond M. Reilly
2.1 Introduction *11*
2.2 X-Rays *11*
2.2.1 X-Ray Tube *13*
2.2.2 X-Ray Machine *14*
2.3 Radiography *15*
2.4 Computed Tomography *16*
2.4.1 Image Acquisition *18*
2.4.2 Image Reconstruction *20*
2.4.3 CT Contrast Agents *21*
2.5 Mammography *23*
2.5.1 Mammography System *23*
2.5.2 Tomosynthesis *25*
2.6 Summary *25*
References *26*
Additional Reading *26*

3 Nuclear Medicine Imaging Technology *27*
Raymond M. Reilly
3.1 Introduction *27*
3.2 Scintillation Detectors *28*
3.2.1 Conversion of Light to an Electronic Signal *30*
3.2.2 Amplification and Analysis of the Electronic Signal *30*
3.3 The Gamma Camera *31*
3.3.1 Collimator Designs *34*
3.3.2 Image Acquisition, Display, and Analysis *34*
3.4 Single Photon Emission Computed Tomography *37*
3.5 Positron Emission Tomography *38*
3.5.1 Design of the PET Tomograph *40*
3.5.2 Time-of-Flight PET *40*
3.6 Multimodality Imaging – SPECT/CT, PET/CT, and PET/MR *41*
3.7 Summary *42*
References *42*

4 Radionuclide Production and Radiopharmaceuticals *46*
Noor Al-saden and Raymond M. Reilly
4.1 Introduction *46*
4.2 Production of Radionuclides *47*
4.2.1 Reactor Production *48*
4.2.2 Cyclotron Production *50*
4.2.3 Generator Production *52*
4.2.3.1 ^{99}Mo/^{99m}Tc Generator *54*
4.2.3.2 ^{68}Ge/^{68}Ga and ^{82}Sr/^{82}Rb Generators *56*
4.3 Radiopharmaceutical Preparation and Supply *57*
4.4 Radiopharmaceuticals for Cardiac Imaging *58*
4.4.1 ^{99m}Tc-Sestamibi *60*
4.4.2 ^{99m}Tc-Tetrofosmin *60*
4.4.3 ^{201}Tl Thallous Chloride *61*
4.4.4 ^{82}Rb Rubidium Chloride *62*
4.4.5 ^{15}O Water ($H_2{}^{15}O$) *62*
4.4.6 ^{13}N Ammonia ($^{13}NH_3$) *62*
4.4.7 ^{99m}Tc Red Blood Cells *62*
4.4.8 ^{18}F-2-Fluorodeoxyglucose (^{18}F-FDG) *63*
4.4.9 ^{123}I-Metaiodobenzylguanidine (^{123}I-MIBG) *63*
4.5 Radiopharmaceuticals for Tumor Imaging *63*
4.5.1 ^{18}F-Fluoro-L-Thymidine (^{18}F-FLT) *64*
4.5.2 ^{18}F-Fluorodeoxyglucose (^{18}F-FDG) *64*
4.5.3 ^{18}F- and ^{11}C-Choline *67*
4.5.4 ^{18}F-FAZA *67*

4.5.5 ^{18}F-Fluoroethyltyrosine (^{18}F-FET) *67*
4.5.6 ^{111}In-Pentetreotide and ^{68}Ga-DOTATOC/DOTATATE *67*
4.5.7 ^{123}I-Metaiodobenzylguanidine (^{123}I-MIBG) *68*
4.5.8 ^{123}I and ^{131}I Sodium Iodide *68*
4.5.9 ^{67}Ga Gallium Citrate *69*
4.5.10 ^{111}In-Ibritumomab Tiuxetan *69*
4.5.11 ^{111}In-Capromab Pendetide *69*
4.6 Radiopharmaceuticals for Brain/CNS Imaging *70*
4.6.1 ^{18}F-Fluorodeoxyglucose (^{18}F-FDG) *70*
4.6.2 ^{99m}Tc-HMPAO (^{99m}Tc-Exametazime) *70*
4.6.3 ^{99m}Tc-ECD (^{99m}Tc-Bicisate) *72*
4.6.4 ^{15}O Water ($H_2{}^{15}O$) and ^{13}N Ammonia ($^{13}NH_3$) *72*
4.6.5 ^{123}I-Iodobenzamide (^{123}I-IBZM) and ^{11}C-Raclopride *72*
4.6.6 ^{11}C-Methylspiperone *73*
4.6.7 ^{18}F-Fluorodopa (^{18}F-FDOPA) *73*
4.6.8 ^{11}C-Flumazenil and ^{123}I-Iomazenil *74*
4.6.9 ^{111}In-Diethylenetriaminepentaacetic Acid (^{111}In-DTPA) *74*
4.7 Radiopharmaceuticals for Renal Imaging *74*
4.7.1 ^{99m}Tc-Diethylenetriaminepentaacetic Acid (^{99m}Tc-DTPA) *74*
4.7.2 ^{99m}Tc-MAG$_3$ (^{99m}Tc-Mertiatide) *76*
4.7.3 ^{99m}Tc-Glucoheptonate *76*
4.7.4 ^{99m}Tc-DMSA (^{99m}Tc-Succimer) *76*
4.8 Radiopharmaceuticals for Hepatobiliary Imaging *76*
4.8.1 ^{99m}Tc Sulfur Colloid *77*
4.8.2 ^{99m}Tc-Iminodiacetic Acid Derivatives *77*
4.9 Radiopharmaceuticals for Bone Imaging *77*
4.9.1 ^{99m}Tc-Bisphosphonates *78*
4.9.2 ^{18}F-Sodium Fluoride (Na^{18}F) *79*
4.10 Radiopharmaceuticals for Lung Imaging *79*
4.10.1 ^{99m}Tc-Macroaggregated Albumin (^{99m}Tc-MAA) *79*
4.10.2 ^{99m}Tc-Aerosols *80*
4.11 Radiopharmaceuticals for Thyroid/Parathyroid Imaging *80*
4.11.1 ^{123}I- and ^{131}I Sodium Iodide (Na^{123}I and Na^{131}I) *81*
4.11.2 ^{99m}Tc Sodium Pertechnetate ($^{99m}TcO_4^-$) *82*
4.11.3 Other Thyroid Imaging Agents *82*
4.11.4 Parathyroid Gland Imaging Agents *82*
4.12 Radiopharmaceuticals for Imaging Infection/Inflammation *83*
4.12.1 ^{67}Ga Gallium Citrate *83*
4.12.2 ^{111}In- or ^{99m}Tc-Labeled Leukocytes (^{111}In- or ^{99m}Tc-WBC) *83*
4.12.3 ^{99m}Tc-Sulesomab Fab’ *84*
4.13 Therapeutic Radiopharmaceuticals *84*
4.14 Summary *85*
Reference *85*
Additional Reading *85*

5 Magnetic Resonance Imaging (MRI) Technology *87*
Raymond M. Reilly
5.1 Introduction *87*
5.2 Principles of MRI *87*
5.2.1 Precession *88*
5.2.2 Resonance and Phase *90*
5.2.3 The Magnetic Resonance Signal *91*
5.2.4 RF Pulse Sequences *92*
5.2.5 T1- and T2-Times *94*
5.2.6 T1- and T2-Weighted MRI *94*
5.2.7 Signal Encoding Using Magnetic Gradients *95*
5.2.8 *K*-Space and Image Formation *97*
5.3 Components of the MRI System *98*
5.3.1 Superconducting Magnet *99*
5.3.2 Gradient Coils *99*
5.3.3 RF Coils *100*
5.3.4 Computer and Image Storage System *100*
5.4 MRI Safety Considerations *100*
5.5 MRI Contrast Agents *102*
5.6 Summary *104*
References *105*
Additional Reading *105*

6 Ultrasound Imaging Technology *107*
Raymond M. Reilly
6.1 Principles of Ultrasound Imaging *107*
6.1.1 US Transducer *109*
6.1.2 Image Acquisition and Display Modes *110*
6.2 Doppler US *111*
6.3 US Contrast Agents *112*
6.4 Summary *113*
References *113*
Additional Reading *113*

7 Cardiac Imaging *117*
Laura Jimenez-Juan, Shaheeda Ahmed, and Katherine Zukotynski
7.1 Introduction *117*
7.2 Cardiovascular Magnetic Resonance Imaging (CMR) *117*
7.3 Cardiovascular MRI Techniques *118*
7.3.1 Cardiac Anatomy *118*
7.3.2 Cardiac Function *118*
7.3.3 Myocardial Tissue Characterization *119*
7.3.4 Clinical Importance of the Assessment of Myocardial Viability *124*

7.3.5 Prognostic Value of LGE Imaging After Myocardial Infarction *125*
7.3.6 Other Imaging Modalities for Assessment of Myocardial Viability *126*
7.4 Echocardiography *129*
7.4.1 Clinical Applications of Echocardiography *130*
7.4.1.1 The Cardiac Chambers *130*
7.4.1.2 Cardiac Valves *133*
7.4.1.3 Pericardial Disease and the Great Vessels *133*
7.5 Nuclear Cardiology *133*
7.5.1 Myocardial Perfusion Imaging *134*
7.5.2 PET Myocardial Viability Imaging *136*
7.5.3 MUGA Scans *139*
7.6 Summary *140*
References *140*

8 Lung Imaging *146*
Anastasia Oikonomou
8.1 Introduction *146*
8.2 Chest Radiograph – Projections *146*
8.3 Normal Findings in a Chest X-Ray *148*
8.3.1 Airways – Pulmonary Lobes and Segments *148*
8.3.2 Pulmonary Arteries and Veins *151*
8.3.2.1 Pulmonary Hila *151*
8.3.2.2 Radiographic Density and Pulmonary Markings *153*
8.3.3 Pleura – Fissures *153*
8.3.4 Mediastinum *154*
8.3.5 Heart *154*
8.3.6 Diaphragm *155*
8.3.7 Chest Wall *155*
8.4 Normal Findings in a Chest CT *155*
8.5 Pneumonia *158*
8.6 Tuberculosis *159*
8.7 Chronic Obstructive Pulmonary Disease *163*
8.7.1 Emphysema *163*
8.7.2 Chronic Bronchitis *164*
8.7.3 Bronchiectasis *165*
8.7.4 Asthma *166*
8.8 Pleural Effusion *167*
8.9 Pneumothorax *169*
8.10 Pulmonary Embolism *170*
8.11 Solitary Pulmonary Nodule *172*
8.12 Lung Cancer *176*
8.13 Summary *178*
References *180*

9 Breast Imaging *186*
Hemi Dua and Jagbir Khinda
9.1 Introduction *186*
9.2 Risk Factors for Breast Cancer *186*
9.3 Guidelines for Breast Cancer Screening *187*
9.3.1 Screening in Average Risk Women *188*
9.3.2 High-risk Screening *188*
9.4 Breast Anatomy *189*
9.5 Imaging Techniques *191*
9.6 Mammography *191*
9.6.1 Mammography System *191*
9.6.2 Image Review and Mammography Views *192*
9.6.2.1 Craniocaudal (CC) View *193*
9.6.2.2 Mediolateral Oblique (MLO) View *193*
9.6.3 Normal Mammogram *193*
9.6.4 Screening vs. Diagnostic Mammogram *195*
9.6.5 Mammographic BI-RADS Lexicon *196*
9.6.6 Breast Tomosynthesis *197*
9.7 Ultrasound Imaging *197*
9.7.1 Ultrasound Technique *198*
9.7.2 Ultrasound BI-RADS Lexicon *198*
9.8 Breast MRI *198*
9.8.1 Indications *200*
9.8.2 Enhancement Kinetics *201*
9.8.3 Breast MRI BI-RADS *201*
9.9 PEM and Breast-Specific Gamma Camera Imaging *202*
9.10 Contrast-Enhanced Spectral Mammography *202*
9.11 The ABCs of Breast Imaging – Image Interpretation *203*
9.11.1 Benign vs. Malignant Imaging Features *203*
9.11.2 Breast Masses *203*
9.11.2.1 Fat-containing Breast Masses *203*
9.11.2.2 Circumscribed Solid Masses *203*
9.11.2.3 Cystic Breast Masses *207*
9.11.2.4 Malignant Masses *207*
9.11.2.5 Axillary Masses *207*
9.11.2.6 Breast Calcifications *207*
9.11.2.7 Breast Asymmetries *207*
9.12 BI-RADS Assessment Categories *209*
9.13 Image-Guided Breast Intervention *209*
9.13.1 Ultrasound-Guided Core Needle Biopsy *216*
9.13.2 Ultrasound-Guided Needle Aspiration *216*
9.13.3 Stereotactic-Vacuum-Assisted Core Needle Biopsy *217*
9.13.4 MR-Guided Vacuum-Assisted Core Biopsy *218*

9.13.5 Radiopaque Markers *218*
9.13.6 Pre-Operative Image-Guided Wire Localization and Specimen Imaging *218*
9.14 Extramammary Staging *219*
9.15 Breast Lymphoscintigraphy *220*
9.16 Summary *220*
References *220*

10 Endocrine Gland Imaging *225*
Katerina Mastrocostas, Kim May Lam, Shereen Ezzat, and Sangeet Ghai
10.1 Introduction *225*
10.2 The Thyroid Gland *225*
10.3 Thyroid Hormone Diseases *227*
10.3.1 Increased Production of Thyroid Hormones *227*
10.3.2 Graves Disease *229*
10.3.3 Hyperfunctional "Toxic" Thyroid Adenoma *230*
10.3.4 Hyperfunctional "Toxic" Multinodular Goiter *232*
10.3.5 Granulomatous (de Quervain) Thyroiditis *234*
10.3.6 Subacute Lymphocytic Thyroiditis *234*
10.3.7 Struma Ovarii *235*
10.3.8 Radioactive Iodine Treatment of Hyperthyroidism *236*
10.3.9 Decreased Production of Thyroid Hormones *237*
10.3.10 Primary Hypothyroidism *237*
10.3.11 Secondary Hypothyroidism *238*
10.3.12 Use of Iodinated Contrast in Thyroid Disease *239*
10.3.13 Mass Lesions in the Thyroid Gland *239*
10.4 Thyroid Cancer *240*
10.4.1 Thyroid Cancer Metastasis *241*
10.4.2 Imaging Thyroid Cancer Metastases *243*
10.4.3 Radioactive Iodine Treatment of Thyroid Cancer *243*
10.5 The Parathyroid Glands *244*
10.5.1 Altered Production of PTH *244*
10.5.2 Primary Hyperparathyroidism *245*
10.5.3 Parathyroid Adenoma *246*
10.5.4 Parathyroid Hyperplasia *247*
10.5.5 Parathyroid Carcinoma *248*
10.5.6 Parathyroid 4D CT Imaging *248*
10.5.7 Secondary and Tertiary Hyperparathyroidism *248*
10.6 The Adrenal Glands *249*
10.7 Mass Lesions of the Adrenal Cortex *250*
10.7.1 Adrenocortical Adenoma *250*
10.7.2 Adrenocortical Carcinoma *252*
10.7.3 Adrenal Myelolipoma *253*

10.8 Mass Lesions of the Adrenal Medulla *253*
10.8.1 Pheochromocytoma and Extra-adrenal Paraganglioma *253*
10.9 Other Neuroendocrine Diseases *255*
10.9.1 Pancreatic Neuroendocrine Tumors (PanNET) *255*
10.9.2 Carcinoid Tumor *258*
10.10 Summary *259*
Additional Reading *260*

11 Abdominal Imaging *264*
Vivek Singh and Chirag Patel
11.1 Introduction *264*
11.2 Surgical Sieve *265*
11.3 Peritoneum/Mesentery *265*
11.4 Acute Peritoneal Pathologies *266*
11.4.1 Pneumoperitoneum *266*
11.4.2 Hemoperitoneum *267*
11.4.3 Ascites *268*
11.4.4 Peritoneal Carcinomatosis *269*
11.5 Gastrointestinal Tract *270*
11.5.1 Bowel Obstruction *271*
11.5.2 Diverticulitis *274*
11.5.3 Appendicitis *277*
11.6 Inflammatory Bowel Disease *279*
11.6.1 Crohn’s Disease *279*
11.6.2 Ulcerative Colitis *280*
11.7 Colorectal Adenocarcinoma *282*
11.7.1 Screening *282*
11.7.2 Imaging *285*
11.8 Hepatic System *287*
11.9 Diffuse Hepatic Disease *289*
11.9.1 Fatty Infiltration *289*
11.9.2 Hepatic Cirrhosis *290*
11.10 Focal Hepatic Disease *292*
11.10.1 Hepatic Abscess *292*
11.10.2 Cavernous Hemangioma *293*
11.10.3 Cysts *294*
11.10.4 Focal Nodular Hyperplasia *295*
11.10.5 Hepatic Metastases *296*
11.10.6 Hepatocellular Carcinoma *299*
11.11 Biliary Tract *300*
11.12 Gallbladder *301*
11.12.1 Cholelithiasis *301*
11.12.2 Acute Cholecystitis *302*

11.12.3 Neoplasms *302*
11.13 Bile Ducts *304*
11.13.1 Biliary Dilation *304*
11.13.2 Neoplasms *305*
11.14 Pancreas *306*
11.14.1 Acute Pancreatitis *306*
11.14.2 Pancreatic Trauma *309*
11.14.3 Chronic Pancreatitis *310*
11.14.4 Pancreatic Neoplasms *310*
11.14.5 Pancreatic Ductal Adenocarcinoma *311*
11.15 Spleen/Lymph Nodes *313*
11.15.1 Splenic Trauma *315*
11.15.2 Splenomegaly/Splenic Masses *316*
11.15.3 Lymphadenopathy *316*
11.16 Summary *316*
Reference *317*
Additional Reading *317*

12 Genitourinary Tract Imaging *320*
Sarah Johnson
12.1 Introduction *320*
12.2 GU System Imaging Modalities *321*
12.2.1 Ultrasound *321*
12.2.2 Computed Tomography *326*
12.2.3 Magnetic Resonance Imaging *326*
12.2.4 Nuclear Scintigraphy *326*
12.3 Evaluation of the Kidneys and Collecting Systems *328*
12.3.1 Urinary Tract Calculi (Nephroureterolithiasis) *328*
12.3.2 Renal Infection and Inflammation *329*
12.3.3 Renal Vascular Anomalies *332*
12.3.4 Renal Lesions *333*
12.3.5 Renal Transplants *336*
12.3.6 Renal Function and Dysfunction *337*
12.3.7 Ureteric Neoplasms *339*
12.4 Bladder and Urethra *343*
12.4.1 Bladder Cancer *343*
12.4.2 Lower Urinary Tract Trauma *343*
12.5 Testicles *345*
12.5.1 Testicular Cancer *345*
12.5.2 Testicular Pain *346*
12.6 Prostate *348*
12.7 Female Genitourinary Tract *350*
12.7.1 Abnormal Vaginal Bleeding *350*

12.7.2 Endometrial Cancer *351*
12.7.3 Cervical Cancer *353*
12.7.4 Adnexal Masses and Ovarian Cancer *354*
12.7.5 Acute Pelvic Pain *355*
12.7.6 Pregnancy – First Trimester *356*
12.7.7 Obstetrical Evaluation *357*
12.7.8 Pregnancy – Second and Third Trimester *358*
12.8 Pediatric Genitourinary Tract *360*
12.8.1 Congenital Anomalies *360*
12.8.2 Cystic Renal Disease *361*
12.8.3 Renal Masses *361*
12.8.4 Urinary Tract Infections *362*
12.8.5 Assessing Pediatric Genitalia *363*
12.9 Summary *364*
References *364*

13 Imaging of the Head, Neck, Spine, and Brain *371*
Laila Alshafai, Eugene Yu, and Sylvain Houle
13.1 Introduction *371*
13.2 Imaging the Skull and Brain *372*
13.2.1 Trauma *372*
13.2.2 Vascular Imaging *372*
13.2.3 Tumor Imaging *378*
13.2.4 Infection Imaging *379*
13.2.5 Imaging Inflammatory/Metabolic Lesions *382*
13.2.6 Imaging Dementia *382*
13.3 Imaging the Spine *383*
13.3.1 Trauma *383*
13.3.2 Vascular Imaging *385*
13.3.3 Tumor Imaging *385*
13.3.4 Infection Imaging *385*
13.3.5 Imaging Inflammatory/Metabolic Conditions *387*
13.4 Imaging the Head and Neck *390*
13.4.1 Trauma *390*
13.4.2 Vascular Imaging *393*
13.4.3 Tumor Imaging *394*
13.4.4 Infection Imaging *395*
13.4.5 Imaging Inflammatory Conditions *395*
13.5 PET and SPECT Neuroimaging *396*
13.6 Summary *401*
References *401*

14 Musculoskeletal Imaging *404*
Rakesh Mohankumar and Ali Naraghi
14.1 Introduction *404*
14.2 Plain Radiography (X-rays) *404*
14.3 Computed Tomography *408*
14.4 Magnetic Resonance Imaging *411*
14.5 Ultrasound *413*
14.6 Applications of Musculoskeletal Imaging *415*
14.6.1 Trauma *415*
14.6.2 Infection *417*
14.6.3 Arthritis *420*
14.6.4 Musculoskeletal Tumors *427*
14.7 Summary *435*
Additional Reading *435*

15 Molecular Imaging with Positron Emission Tomography *439*
Ur Metser, Noam Tau, and Amit Singnurkar
15.1 Introduction *439*
15.2 PET Probes Including ^{18}F-FDG *440*
15.2.1 ^{18}F-FDG PET/CT Protocol *440*
15.2.2 Technical Considerations in Performing and Interpreting PET *440*
15.3 ^{18}F-FDG PET in Oncology *442*
15.3.1 ^{18}F-FDG-PET/CT in the Management of Lung Cancer *442*
15.3.2 Role of ^{18}F-FDG PET in Lymphoma *445*
15.3.2.1 Staging *445*
15.3.2.2 Therapy Response Assessment *446*
15.3.3 ^{18}F-FDG PET/CT in Gastrointestinal Malignancies *448*
15.3.3.1 ^{18}F-FDG-PET/CT in Esophageal Cancer *448*
15.3.3.2 ^{18}F-FDG-PET/CT in Colorectal Cancer *450*
15.3.4 ^{18}F-FDG-PET/CT in Head and Neck Cancers *452*
15.4 ^{18}F-FDG PET in Non-Oncology Indications *453*
15.4.1 Cardiac PET *453*
15.4.2 Neurological Applications of PET *455*
15.4.3 ^{18}F-FDG-PET in Infectious and Inflammatory Disorders *457*
15.4.3.1 Sarcoidosis *457*
15.4.3.2 Fever of Unknown Origin *458*
15.4.3.3 Infected Implanted Medical Devices *459*
15.5 Overview of Other PET Radiopharmaceuticals *460*
15.5.1 Other PET Agents for Myocardial Perfusion Imaging *461*
15.5.2 Agents for Imaging Tumor Proliferation *461*
15.5.3 Agents for Tumor Receptor Imaging *463*
15.5.3.1 ^{68}Ga-DOTATATE *463*

15.5.3.2 Imaging PSMA in Prostate Cancer *465*
15.5.4 Imaging Tumor Hypoxia *466*
15.6 Multimodal Imaging – PET/CT Versus PET/MR *468*
15.6.1 Technical Challenges in PET/MR *468*
15.6.2 Current Status of Clinical PET/MRI *469*
15.7 Summary *470*
References *470*

Index *485*

Contributors

Shaheeda Ahmed
Department of Medical Imaging
Sunnybrook Health Sciences Centre
University of Toronto
Toronto, Ontario
Canada

Noor Al-saden
Leslie Dan Faculty of Pharmacy
University of Toronto
Toronto, Ontario
Canada

Laila Alshafai
Joint Department of Medical
Imaging, University of Toronto
Toronto, Ontario
Canada

Hemi Dua
Joint Department of Medical
Imaging, University of Toronto
Toronto, Ontario
Canada

Shereen Ezzat
Departments of Medicine and
Oncology, Endocrine Oncology Site
Group at the Princess Margaret
Cancer Centre, University Health
Network, University of Toronto
Toronto, Ontario
Canada

Sangeet Ghai
Joint Department of Medical
Imaging, University of Toronto
Toronto, Ontario
Canada

Sylvain Houle
Centre for Addiction and Mental
Health, Research Imaging Centre and
Department of Psychiatry
University of Toronto
Toronto, Ontario
Canada

Laura Jimenez-Juan
Department of Medical Imaging
Sunnybrook Health Sciences
Centre, University of Toronto
Toronto, Ontario
Canada

Sarah Johnson
Joint Department of Medical
Imaging, University of Toronto
Toronto, Ontario
Canada

Jagbir Khinda
Department of Medical Imaging
University of Toronto
Toronto, Ontario
Canada

Katerina Mastrocostas
Department of Medical Imaging
Concord Repatriation General Hospital
University of Sydney
Concord, NSW
Australia

Kim May Lam
Department of Medical Imaging
University of Toronto
Toronto, Ontario
Canada

Ur Metser
Joint Department of Medical Imaging, University of Toronto
Toronto, Ontario
Canada

Rakesh Mohankumar
Joint Department of Medical Imaging, University of Toronto
Toronto, Ontario
Canada

Ali Naraghi
Joint Department of Medical Imaging
University of Toronto
Toronto, Ontario
Canada

Anastasia Oikonomou
Department of Medical Imaging
Sunnybrook Health Sciences Centre
University of Toronto
Toronto, Ontario
Canada

Chirag Patel
Department of Medical Imaging
Sunnybrook Health Sciences Centre
University of Toronto
Toronto, Ontario
Canada

Raymond M. Reilly
Leslie Dan Faculty of Pharmacy
University of Toronto
Toronto, Ontario
Canada

Vivek Singh
Department of Medical Imaging
Quinte Health Care
Belleville, Ontario
Canada

Amit Singnurkar
Division of Nuclear Medicine
Department of Radiology
Hamilton General Hospital and St. Joseph's Health Care
McMaster University
Hamilton, Ontario
Canada

Noam Tau
Joint Department of Medical Imaging, University of Toronto
Toronto, Ontario
Canada

Eugene Yu
Departments of Medical Imaging and Otolaryngology – Head and Neck Surgery
University of Toronto
Toronto, Ontario
Canada

Katherine Zukotynski
Departments of Medicine and Radiology, McMaster University
Hamilton, Ontario
Canada

Preface

Patient care is interdisciplinary and requires a health-care team approach to be most effective. The health-care team includes pharmacists, nurses, physiotherapists, medical technologists, and other allied health-care professionals who interact on a daily basis with physicians who have a wide range of specialties. Appropriate treatment relies on an accurate diagnosis, thus diagnostics and therapeutics are the two pillars of an optimal patient-care plan. Medical imaging is a critical tool in diagnosing disease and in assessing the effectiveness of treatment. Radiologists and nuclear medicine physicians are the experts in medical imaging on the health-care team and treatment decisions rely on their judgement. Non-radiologist professionals on the health-care team need to understand medical imaging in order to appreciate the results of these tests that are communicated by the radiologists and nuclear medicine physicians. This book aims to educate the non-radiologist health professional about medical imaging, including the principles of the imaging technologies as well as the most common clinical applications of medical imaging. The terminology in the book has been carefully edited to make it suitable for a broader health professional readership. The motivation for this book arises from an elective course that I teach on Medical Imaging for Pharmacists, at the University of Toronto. This course has proven to be very popular among the undergraduate pharmacy students. Practicing pharmacists have similarly expressed a strong interest in learning more about medical imaging, and therefore, I hope that this book will provide an important learning tool for students in the health professions as well as practicing health professionals.

Raymond M. Reilly, PhD
Toronto, Ontario
Canada

Acknowledgments

The editor greatly appreciates the contributions of the radiologists to this book in writing the clinical chapters and their understanding of the need to communicate the important role of medical imaging in terminology that is understood by most health professionals. Most of all, the editor thanks all of the contributors for their great patience in awaiting completion of the book. The editor hopes that all authors and readers will be pleased with the book, which is one of the few aimed at a wide range of health professionals who recognize the importance of medical imaging in patient care.

Raymond M. Reilly

Raymond Reilly is a Full Professor and Director of the Centre for Pharmaceutical Oncology at the Leslie Dan Faculty of Pharmacy, University of Toronto. He is a pharmacist, who obtained his BScPhm and MScPhm degrees in pharmacy and a PhD in Medical Biophysics from the University of Toronto. Dr. Reilly practiced as a nuclear pharmacist in nuclear medicine at the University Health Network in Toronto prior to his academic position. He teaches undergraduate courses in the PharmD program in the areas of clinical laboratory medicine and medical imaging, and teaches a graduate course on radiopharmaceuticals. Dr. Reilly's research is focused on the development of molecular imaging and radioimmunotherapeutic agents for cancer. He has trained 15 PhD and 12 MSc students. His research is supported by the Canadian Institutes of Health Research, the Canadian Breast Cancer Foundation, the Canadian Cancer Society Research Institute and the Ontario Institute for Cancer Research.

Medical Imaging for Health Professionals: Technologies and Clinical Applications, First Edition.
Edited by Raymond M. Reilly.
© 2019 John Wiley & Sons, Inc. Published 2019 by John Wiley & Sons, Inc.

1

Introduction to Medical Imaging

Raymond M. Reilly

1.1 Medical Imaging Procedures

Medical imaging is widely used in patient care to diagnose disease, to plan treatment, and to monitor response to treatment. Medical imaging includes radiological technologies such as X-ray, computed tomography (CT), mammography, ultrasound (US), and magnetic resonance imaging (MRI) as well as nuclear medicine imaging, which includes single photon computed tomography (SPECT) and positron emission tomography (PET). In the United States (U.S.), there were almost 400 million radiological imaging procedures performed in 2006 (most recent data) including 18 million nuclear medicine studies, a 10-fold increase since 1950 [1]. Worldwide, there were more than 3.6 billion medical imaging procedures performed annually from 1997 to 2007 and 36 million nuclear medicine tests [1]. More recent data from Canada in 2015 show that nine million imaging tests are performed each year, including 1.5 million SPECT/CT studies and almost 80 000 PET procedures (Table 1.1). Statistics in the U.S. are likely more than 10-fold higher, due to the population size differences between Canada and the U.S. PET has been more widely adopted in the U.S. and it is estimated that there are more than 1.5 million PET scans performed in that country each year [2]. Medical imaging procedures are used to diagnose a wide range of disease conditions including infections, cancer, myocardial perfusion and function, abdominal masses, thyroid disorders, renal dysfunction, liver and biliary tract diseases, Alzheimer's and Parkinson's disease, muscle and bone abnormalities, and many others. Chapters 2–6 in this book present the basic principles of medical imaging technologies while Chapters 7–15 discuss the clinical applications of medical imaging. In this chapter, the general considerations of different medical imaging technologies will be discussed.

Medical Imaging for Health Professionals: Technologies and Clinical Applications, First Edition.
Edited by Raymond M. Reilly.
© 2019 John Wiley & Sons, Inc. Published 2019 by John Wiley & Sons, Inc.

Table 1.1 Number of medical imaging procedures in Canada each year.

Technology	Number of imaging systems	Number of procedures each year (million)
CT	538	5.28
MRI	340	1.95
SPECT and SPECT/CT	478	1.48
PET	47	0.077

Source: Data from https://www.cadth.ca/canadian-medical-imaging-inventory-2015.

1.1.1 Procedures Involving Ionizing vs. Nonionizing Radiation

Some medical imaging procedures (X-ray, CT, mammography, SPECT, and PET) employ radiation that has sufficient energy to ionize biological molecules, while other procedures (MRI and US) do not cause such ionizations. Since the body is composed mostly of water molecules, most ionizations result in formation of hydroxyl free radicals (HO•) and hydronium ions (H_3O^+). These species have the potential to cause DNA strand breaks that could increase the long-term risk for cancer (see Section 1.2). The minimum energy required to ionize molecules is >5–100 electron volts (eV). An electron volt is defined as the energy acquired by an electron when accelerated across a potential difference of 1 V. The energy of different forms of electromagnetic radiation in electron volts is shown in Table 1.2. X-ray, CT, and mammography, which utilize X-rays for imaging, and SPECT and PET, which employ γ-rays emitted by radiopharmaceuticals, cause ionizations in biological molecules. In contrast, MRI employs radiofrequency (RF) energy, which has insufficient energy to cause ionizations. US imaging employs high-frequency sound waves that have extremely low energy in eV ($8–40 \times 10^{-9}$ eV), which is not able to cause ionizations. Thus, sometimes a technology that is nonionizing (e.g. MRI or US) may be preferred over one that is ionizing (e.g. CT, SPECT, or PET) to minimize the risk for long-term effects such as cancer, especially if these technologies are available and provide equivalent diagnostic information. When imaging technologies that use ionizing radiation are required, the radiation dose to the

Table 1.2 Energy of different forms of radiation in electron volts (eV).

Type of radiation	Imaging procedure	Energy (eV)
Ultrasound waves	US	<0.000 000 04
Radiofrequency	MRI	<0.001
X-rays	X-ray and CT	1000–10 000
γ-Rays	SPECT and PET	100 000–500 000

patient is kept as low as possible to minimize long-term risks (As Low as Reasonably Achievable [ALARA] principle). Nonetheless, these risks from medical imaging procedures are very low (see Section 1.2).

1.2 Radiation Doses from Medical Imaging Procedures

The energy deposited per unit mass of tissue by radiation is known as the *radiation dose*. The SI unit of radiation dose is the Gray, which is defined as 1 Joule per kg ($\mathrm{J\,kg^{-1}}$). An older unit still in use in the United States is the rad, which is defined as $100\,\mathrm{ergs\,g^{-1}}$ of tissue ($0.01\,\mathrm{J\,kg^{-1}}$). Since different types of radiations exhibit different abilities to cause biological damage, this is further incorporated into the term *equivalent dose*, which has units of Sievert (Sv) or rem. The Sv or rem is the Gy or rad multiplied by a radiation weighting factor (w_R). The w_R for X-rays and γ-rays is 1, thus in medical imaging, 1 Sv = 1 Gy and 1 rem = 1 rad. Once radiation doses are estimated, a further refinement takes into account the relative radiation sensitivity of tissues by multiplying the dose estimates by a tissue sensitivity factor (w_T) to provide the *effective dose*. The units of effective dose remain the Sv or rem. Estimates of radiation doses from medical imaging procedures inform on possible acute effects as well as long-term risks such as the development of cancer. The radiation doses from most medical imaging procedures range from 1 to 14 mSv (Table 1.3) [3].

Table 1.3 Radiation doses from common medical imaging procedures.[a]

Imaging procedure	Modality	Radiation dose (mSv)
Chest	X-ray	0.02–0.04
Lumbar spine	X-ray	0.7
Mammogram	X-ray	0.7
Abdomen	CT	10.0
Coronary angiogram	CT	4.6–15.8
Bone scan (^{99m}Tc-MDP)	SPECT	4.2
V/Q lung scan (^{99m}Tc-MAA/^{99m}Tc aerosol)	SPECT	2.0
Renal scan (^{99m}Tc-MAG$_3$)	SPECT	3.6–5.2
Myocardial perfusion scan (^{99m}Tc-sestamibi/^{99m}Tc-tetrofosmin)	SPECT	11.2
Whole body scan (^{18}FDG)	PET	14.0

[a] Whole-body dose.

Source: Data from https://hps.org/documents/meddiagimaging.pdf.

A mSv is 1/1000th of a Sv. To put these doses in perspective, a whole-body PET scan is associated with a radiation dose of 14 mSv (Table 1.3), which is more than 130-times lower than the minimum dose of radiation required to cause significant toxicity to the bone marrow (2 Sv), one of the most radiation sensitive tissues in the body. A single chest X-ray deposits 1 000 000 times less radiation dose than that required to cause bone marrow toxicity. Harmful radiation doses to the liver or kidneys are 15–20 Sv and 20–30 Sv, respectively [4]. A whole-body PET scan deposits doses of radiation that are 1000–2000 times less than the radiation doses required to cause toxicity to the liver or kidneys. These dose-related acute effects of radiation are termed *non-stochastic effects*. These effects are not considered clinically significant at the radiation doses associated with medical imaging procedures. *Stochastic effects* of radiation are not necessarily related to radiation dose and include the long-term risk for development of cancer. However, back-extrapolation of data from the atomic bomb blasts in Japan suggests that the risk of cancer from radiation is not significantly increased above that in the general population at doses <100 mSv [5]. As mentioned, radiation exposure from medical imaging procedures is <10–15 mSv (Table 1.3).

1.2.1 Estimating Radiation Doses from Medical Imaging

Radiation doses from radiological imaging procedures (X-ray, CT) are estimated using "phantoms," which are models of the body or regions of the body (e.g. chest or abdomen) filled with water which approximates the density of tissues, into which are placed dose-measuring devices called dosimeters (Figure 1.1). These phantoms are imaged and the dose deposited in simulated organs in the phantom is measured by the dosimeter. Radiation doses from nuclear medicine procedures that employ radiopharmaceuticals (see Chapters 3 and 4) are more complex to estimate, since they depend on the properties of the radionuclide, pharmacokinetics of the radiopharmaceutical, and the geometry of organs in a phantom model of the body (Figure 1.2). The method of estimating radiation doses from radiopharmaceuticals is called the Medical Internal Radiation Dose (MIRD) formalism [7]. The MIRD formalism incorporates a source organ (S) into which radioactivity accumulates and a target organ (T) that receives radiation dose from radioactivity in the source organs. In some cases, the source and target organs may be the same, e.g. radioactivity in the liver irradiating and depositing dose in the liver. In other cases, the source and target organs are different, e.g. radioactivity in the liver irradiating and depositing dose in the lungs.

The equation for radiation dose deposited into a target organ is:

$$D_{\mathrm{T}\leftarrow\mathrm{S}} = \tilde{A}_{\mathrm{S}} \times S$$

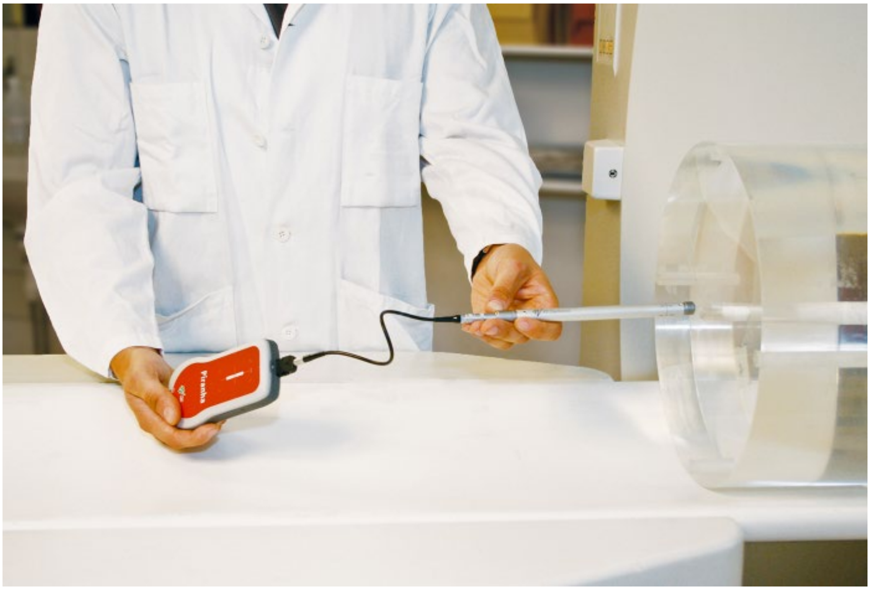

Figure 1.1 Estimating radiation doses from radiological procedures (e.g. CT) by imaging a phantom model of a region of the body with a dosimeter to measure radiation exposure. *Source:* From info@rtigroup.com.

where $D_{T \leftarrow S}$ is the dose (Gy Bq^{-1} × seconds) deposited in a target organ (T) per unit cumulative radioactivity in a source organ (S), $\tilde{A}_S$ is the cumulative radioactivity in the source organ (Bq × seconds), and S is the Snyder factor.

The cumulative radioactivity in the source organ ($\tilde{A}_S$) is determined by quantitative imaging in patients administered the radiopharmaceutical in a clinical trial by integrating the radioactivity vs. time curve for the organ (Figure 1.3). The Snyder factor (S) takes into account the properties of the radionuclide (physical half-life [$t_{1/2p}$] and the type, energy, and abundance of all emissions) as well as the geometry of organs (size and distance between organs) in the phantom (Figure 1.2). The total radiation dose to a target organ is the sum of the individual doses deposited from radioactivity in all source organs. An interesting aspect of radiation doses from radiopharmaceuticals is that the total body dose is *not* the sum of all of the doses to individual organs. Rather, the total body is considered as a separate target organ in the MIRD formalism. Moreover, since radiation dose is the amount of energy deposited per kg of tissue and the body is a large target organ (50–70 kg in an adult), the radiation dose to the whole body can often be lower than the dose to any individual organ in the body (Table 1.4). Computer software (OLINDA/EXM) has been introduced to facilitate estimation of radiation doses from radiopharmaceuticals [9].

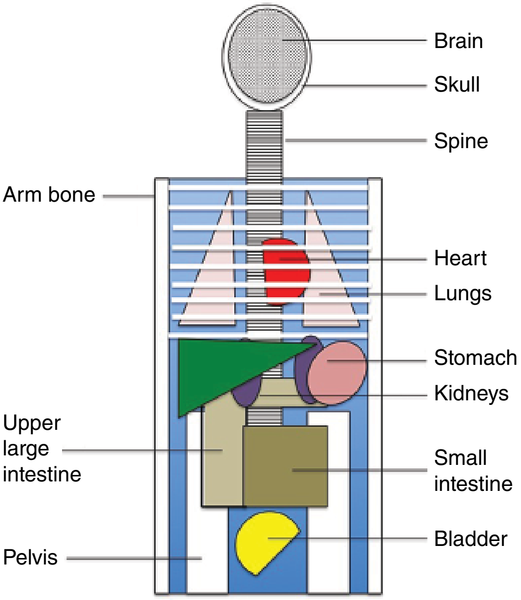
Brain
Skull
Spine
Arm bone
Heart
Lungs
Stomach
Kidneys
Upper large intestine
Small intestine
Bladder
Pelvis

Figure 1.2 The MIRD adult phantom used to estimate radiation doses to organs from radiopharmaceuticals (not all organs are shown). Other phantoms are available for newborns through 15-year-old children as well as for a pregnant female adult, and dynamic phantoms that take into account excretion of radioactivity from the bladder. *Source:* Adapted from Snyder et al. [6].

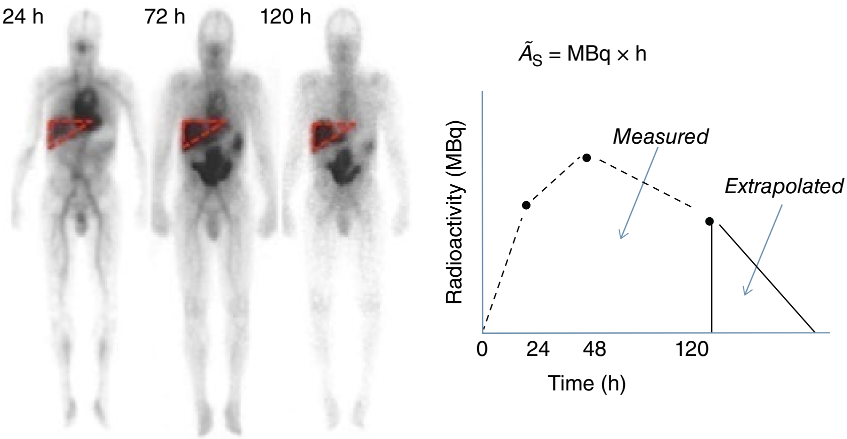
24 h
72 h
120 h
$\tilde{A}_S$ = MBq × h
Measured
Extrapolated
Radioactivity (MBq)
0
24
48
120
Time (h)

Figure 1.3 Estimation of cumulative radioactivity ($\tilde{A}_S$) in a source organ (i.e. liver; broken triangle on image) from administration of a radiopharmaceutical by quantitative gamma camera imaging and region-of-interest (ROI) analysis (left panel). The cumulative radioactivity from the last time point for which there is a measurement is estimated by extrapolation. The total $\tilde{A}_S$ (right panel) is used to estimate radiation doses from radiopharmaceuticals using the MIRD formalism. Source: From Wiseman et al. [8]. Reproduced with permission from Society of Nuclear Medicine and Molecular Imaging (SNMMI) publication.

Table 1.4 Radiation doses from a nuclear medicine bone scan using ^{99m}Tc-MDP.

Organ	Radiation dose (mSv MBq^{-1})	Dose for 740 MBq[a] (mSv)
Bone	0.0630	46.6
Brain	0.0017	1.3
Heart	0.0012	0.9
Kidneys	0.0073	5.4
Liver	0.0012	0.9
Lungs	0.0013	1.0
Spleen	0.0014	1.0
Whole body	0.0057	4.2

[a] Usual administered dose of radioactivity.

1.2.2 Radiation Doses and Increased Use of Medical Imaging

Natural radiation exposure mainly from radon gas present in the environment is responsible for most of the radiation dose exposure of the general population, accounting for an annual dose of about 3 mSv. However, since 1980, there has been a rapid increase in the use of medical imaging procedures in the United States, such that the dose from medical imaging now accounts for an additional 3 mSv per year, representing about half of the total radiation dose to individuals [10]. In 1980, medical imaging only accounted for one quarter of the total radiation dose to individuals. The increased utilization of medical imaging is due to major advances in imaging technology, which allow more applications (e.g. CT colonography, PET scans, myocardial perfusion imaging, and others). Nonetheless, it has been suggested that there may be overutilization of medical imaging, since in some cases, imaging procedures have not yielded additional information that changed patient management [11]. The most rational approach is to judiciously use imaging whenever it will yield diagnostic information that significantly improves patient care.

1.3 Summary

Medical imaging technologies include X-ray, CT, mammography, SPECT and PET, MRI, and US. Billions of imaging procedures are performed annually around the world to diagnose a wide range of diseases and health conditions, as well as monitor response to treatment. Only MRI and US do not use ionizing radiation. However, the risk of cancer development from medical imaging procedures is very low. Radiation doses from radiological procedures that employ X-rays are measured using phantoms of the body and dosimeters. Radiation doses from nuclear medicine procedures need to take into account the decay properties of the radionuclide, the pharmacokinetics of the radiopharmaceutical, and the geometry of organs in the body. Increased utilization of medical imaging due to advancements in technology has increased the annual radiation exposure of the population over the past 40 years. Judicial use of imaging to maximize impact on patient care is warranted to minimize radiation doses.

References

1. Mettler, F.A. Jr., Bhargavan, M., Faulkner, K. et al. (2009). Radiologic and nuclear medicine studies in the United States and worldwide: frequency, radiation dose, and comparison with other radiation sources – 1950–2007. *Radiology* 253: 520–531.
2. Delbeke, D. and Segall, G.M. (2011). Status of and trends in nuclear medicine in the United States. *J. Nucl. Med.* 52 (Suppl 2): 24S–28S.
3. Mettler, F.A. Jr., Huda, W., Yoshizumi, T.T., and Mahesh, M. (2008). Effective doses in radiology and diagnostic nuclear medicine: a catalog. *Radiology* 248: 254–263.
4. Emami, B., Lyman, J., Brown, A., et al. (1991). Tolerance of normal tissue to therapeutic radiation. *Int. J. Radiat. Oncol. Biol. Phys.* 21: 109–122.
5. Hendee, W.R. and O'Connor, M.K. (2012). Radiation risks of medical imaging: separating fact from fantasy. *Radiology* 264: 312–321.
6. Snyder, W.S., Ford, M.R., and Warner, G.G. (1978). *Revision of MIRD Pamphlet No. 5 – Estimates of Absorbed Fractions for Monoenergetic Photon Sources Uniformly Distributed in Various Organs of a Heterogeneous Phantom*. Reston, VA: Society of Nuclear Medicine.
7. Loevinger, R., Budinger, T.F., and Watson, E.E. (1988). *MIRD Primer for Absorbed Dose Calculations*. New York: Society of Nuclear Medicine.
8. Wiseman, G.A., Kornmehl, E., Leigh, B. et al. (2003). Radiation dosimetry results and safety correlations from 90Y-ibritumomab tiuxetan radioimmunotherapy for relapsed or refractory non-Hodgkin's lymphoma: combined data from 4 clinical trials. *J. Nucl. Med.* 44: 465–474.
9. Stabin, M.G., Sparks, R.B., and Crowe, E. (2005). OLINDA/EXM: the second-generation personal computer software for internal dose assessment in nuclear medicine. *J. Nucl. Med.* 46: 1023–1027.
10. Einstein, A.J. (2009). Medical imaging: the radiation issue. *Nat. Rev. Cardiol.* 6: 436–438.
11. Hendee, W.R., Becker, G.J., Borgstede, J.P. et al. (2010). Addressing overutilization in medical imaging. *Radiology* 257: 240–245.

2

X-Ray, CT, and Mammography Technology

Raymond M. Reilly

2.1 Introduction

X-rays were discovered by Wilhelm Conrad Roentgen in 1895, who subsequently received the Nobel Prize for his discovery in 1901 (https://www.nobelprize.org/nobel_prizes/physics/laureates/1901/rontgen-bio.html). Roentgen found that if he passed an electric current through a container with a gas at very low pressure and the container was surrounded by black material to prevent light from escaping, that a plate covered with barium platinocyanide (a type of photographic plate) would turn dark, due to the emission of an unknown form of "rays." Roentgen called these rays, "X"-rays in reference to mathematical formulae, which aim to solve for an unknown, "x." He took the first X-ray of his wife's hand (Figure 2.1), which showed the bones, soft tissue, and her wedding ring. The X-rays discovered by Roentgen are now the basis for medical X-rays, computed tomography (CT), and mammography.

2.2 X-Rays

An X-ray is a form of electromagnetic radiation that originates from the interaction of a high-energy electron accelerated towards a target element, with the nucleus or orbital electrons of the target element (Figure 2.2) [1]. Most commonly, the electron interacts with the nucleus resulting in deflection of its path, deceleration, and partial loss of its energy. The X-rays produced by this process are called *Bremsstrahlung* X-rays, a term based on the German word for braking [2]. Since the amount of energy that is lost by the electron through this process may be variable, the spectrum of X-rays produced in this way has a broad range of energies (Figure 2.3). Alternatively, the electron may collide

Medical Imaging for Health Professionals: Technologies and Clinical Applications, First Edition.
Edited by Raymond M. Reilly.
© 2019 John Wiley & Sons, Inc. Published 2019 by John Wiley & Sons, Inc.

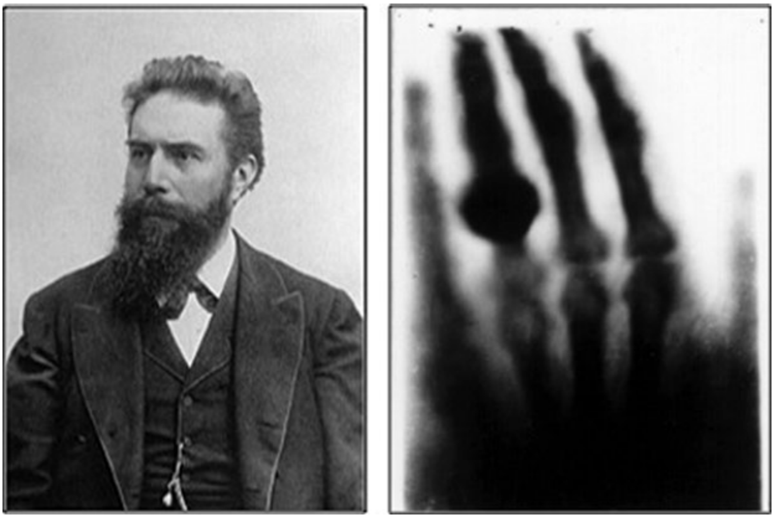

Figure 2.1 Wilhelm Conrad Roentgen received the Nobel Prize in 1901 for his discovery of X-rays. He took the first X-ray of his wife's hand (Anna Bertha Ludwig), which showed her wedding ring and the bones of her fingers and some soft tissues. *Source:* Image adapted from https://en.wikipedia.org/wiki/Wilhelm_Röntgen.

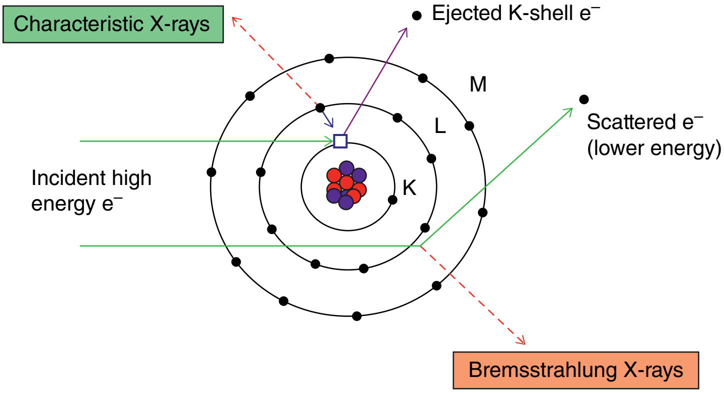

Figure 2.2 An X-ray is produced by the interaction of a high-energy incident electron with an orbital shell electron in a target element. If the incident electron impacts the orbital electron, the orbital electron may be ejected resulting in a vacancy in the shell. Decay of an electron from a higher shell to fill the vacancy results in the emission of electromagnetic energy in the form of X-rays. Since the energy released is dependent on the energy difference held by an electron in the higher shell versus the lower shell, these X-rays have discrete energies and are called *characteristic* X-rays. If the incident electron does not impact the orbital electron, but is instead deflected in its path by the orbital electron, there is a loss of energy by the incident electron. This loss of energy is released as X-rays of varying energy, depending on the extent of deflection of the path of the incident electron. These X-rays are called Bremsstrahlung X-rays.

Figure 2.3 Spectrum of X-rays produced by the interaction of a high-energy incident electron with the orbital electrons of a tungsten target. Characteristic X-rays have discrete energies due to the transitions between different orbital shells and are evident by sharp peaks on the spectrum. Bremsstrahlung X-rays have variable energies and are evident on the spectrum by the broad band of energies.

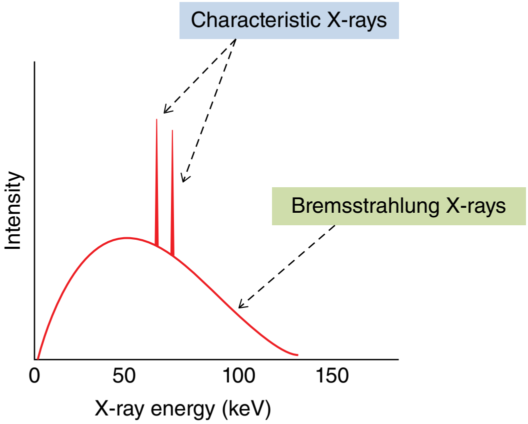

with an orbital electron in the target element, causing ejection of the orbital electron. The vacancy created is quickly filled by the decay of an electron from a higher shell. The binding energy of an orbital electron depends on the distance from the nucleus, i.e. an M-shell electron has a lower binding energy than an L-shell electron, which has lower energy than a K-shell electron. The difference in energies of the electron that is ejected, and that of the higher shell electron that decays to fill the vacancy, is released as an X-ray. The energies of orbital electrons are given in kilo-electron volts (keV). One electron volt is the energy acquired by an electron when accelerated across a potential difference of one volt. For example, the K-shell orbital electron energy of tungsten, a target element often used to produce X-rays, is 69.5 keV, while the L-shell electron energy is 10.2 keV. Thus, ejection of a K-shell electron and decay of an L-shell electron to fill the vacancy will result in emission of an X-ray with energy, $E = 69.5 - 10.2 = 59.3$ keV [1,2]. Since these X-rays have a defined energy dependent on the difference in electron energies between two orbital shells, they are known as *characteristic* X-rays [1,2]. Only about 5–10% of X-rays produced by interaction of a high-energy electron with a target element are released as characteristic X-rays [2]. These X-rays appear as well-defined energy "spikes" superimposed on the Bremsstrahlung X-ray spectrum (Figure 2.3).

2.2.1 X-Ray Tube

The X-ray tube (Figure 2.4) consists of a tungsten filament cathode that is heated to produce and release electrons that are then accelerated across a large potential difference to impact the anode target element, which may be tungsten, molybdenum, or rhodium [2]. The voltage applied is 40 000–150 000 V (40–150 kV) for most diagnostic X-ray procedures, but is lower (25–40 kV) for mammography [2]. Interaction of high-energy electrons with the target element results mainly in heat generation, with only a small amount of X-rays produced.

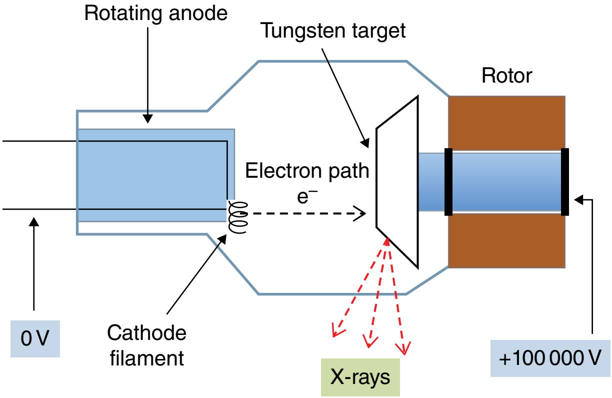

Figure 2.4 An X-ray tube consists of a cathode filament that is heated to release electrons that are accelerated across a potential difference of 100 000 V through a vacuum towards an anode most often constructed from tungsten. The anode is rotated to dissipate the heat caused by interaction of the high-energy incident electrons with the tungsten target. Interaction of the incident electrons with orbital electrons in the tungsten target results in the production of X-rays.

Thus, tungsten is often used to form the anode since it has a high melting point and is a high atomic number element ($Z = 74$), which increases the likelihood of X-ray production due to interaction with the electrons [2]. Molybdenum and rhodium are used as anode target elements in mammography since these generate characteristic X-rays with lower energies more useful for imaging the breast than the higher energy X-rays produced by tungsten targets [2]. The anode is rotated to more efficiently dissipate heat and maximize X-ray production. The X-ray tube incorporates a vacuum tube across which the high-energy electrons traverse from the cathode to the anode. Vacuum conditions prevent interaction of the electrons with gas molecules prior to impacting with the anode.

2.2.2 X-Ray Machine

The X-ray tube is surrounded by lead shielding except for the X-ray port in an X-ray machine (Figure 2.5) [2]. Oil circulating around the anode housing provides efficient cooling. X-rays passing through the port are collimated by two vertical and horizontal lead shutters that can be opened or closed to permit focusing of the X-ray beam on a particular region of the body [2]. A light system aligned with the X-ray port aids in positioning of the patient for the X-ray procedure. The X-ray beam may also be filtered by an aluminum insert placed between the beam and the patient to remove very low-energy X-rays (<15 keV) [2]. These low-energy X-rays do not have sufficient energy to penetrate the body and would be

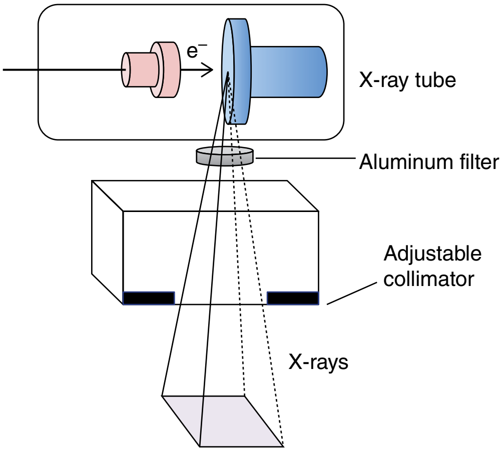

Figure 2.5 An X-ray machine consists of the X-ray tube, an aluminum filter to remove low-energy X-rays, and a lead collimator to focus the X-ray beam on the field of view in the patient.

absorbed by surface tissues, depositing unnecessary radiation dose in the patient that does not contribute to forming the image. Thin filters made of molybdenum, rhodium, or silver are employed in mammography systems to select X-rays with low-intermediate energies of 15–25 keV [2]. Transformers convert low voltage power available in hospitals to the high voltage required to generate X-rays.

2.3 Radiography

Radiography is the application of X-rays to produce a two-dimensional image of an anatomical region of a patient such as a chest X-ray (Figure 2.6b) [3]. The image is formed based on the attenuation of the X-rays by tissues as they pass through the body. Dense tissues such as bone attenuate the X-rays more and appear “white” on the X-ray image, while low-density tissues such as the lungs, which contain mostly air, permit the X-rays to pass through without significant attenuation, and appear “black” on the image (Figure 2.6a). Historically, X-ray images were obtained by screen-film technology, but digital radiography is now most commonly used [3]. A screen-film cassette is composed of an intensifying screen employing a gadolinium sulfide (Gd_2O_2S) scintillator, which converts the X-rays into light directly in contact with a photographic emulsion film composed of silver bromide/iodide crystals [4]. The screen-film is two-sided and may be inverted to obtain additional X-ray images. The exposed film is developed to produce the image analogous to conventional photographic film. A limitation with screen-film technology is that the film is only linear to light exposure over a defined range, and thus too low or too high exposure will not result in an accurate depiction of the X-ray attenuation by the body [3].

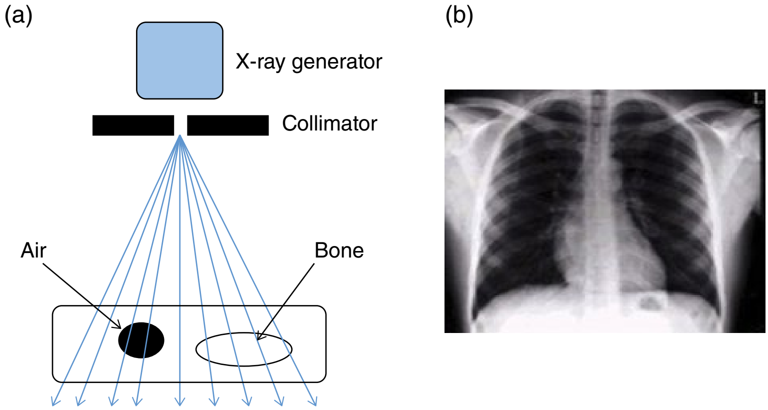

Figure 2.6 (a) X-rays are attenuated more by dense tissues (e.g. bone) than by non-dense tissues (e.g. air in lungs). (b) In a chest X-ray, the lungs appear dark since there is little attenuation of the X-rays whereas the ribs appear white due to attenuation of the X-rays, as they pass through the patient.

In addition, if the X-ray exposure of the screen-film is not adequate with respect to intensity and contrast, the X-ray needs to be repeated, resulting in unnecessary radiation exposure to the patient. There is no method of changing the intensity or contrast on the image post X-ray acquisition. Thus, more recently, digital radiography has been widely introduced in which X-rays interact with a Gd_2O_2S scintillator screen to generate light photons that are then reflected by a mirror into an array of charge-coupled devices (CCD), similar to those used by a digital camera [4]. The CCD array converts the light photons into electrons to form the computed image. A major advantage of digital X-ray images is that the image intensity and contrast may be adjusted as needed by the radiologist after the X-ray acquisition.

2.4 Computed Tomography

Attenuation by overlying tissues may obscure organ or lesion visualization using an X-ray. Also, a planar, i.e. 2-dimensional X-ray does not provide information on the positional location in 3-dimensions of an organ or lesion within the body [5,6]. In order to obtain depth information, planar X-rays can be obtained at different orientations around the body. For example, a chest X-ray is often obtained in the posteroanterior and lateral views to discern the depth position of a lesion (see Chapter 8). CT (Figure 2.7a) is a three-dimensional imaging technique that rapidly measures the attenuation of an X-ray beam by tissues in multiple dimensions by rotating the X-ray source and detector 360° around the body, storing these measurements on a computer, and then reconstructing the attenuation

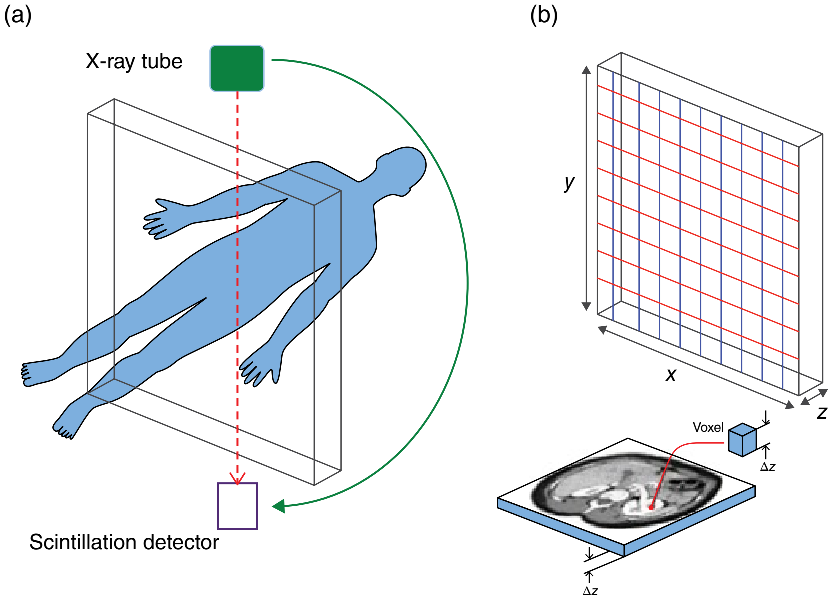

Figure 2.7 (a) In CT, the X-ray beam and scintillation detector are rotated 360° around the patient and attenuation measurements are taken at many different angles. (b) The attenuation measurements are reconstructed to form a three-dimensional image of the patient, which can then be "sliced" at any location and direction (axial, sagittal, and coronal) in the body to obtain a tomographic image. The tomographic image is composed of voxels that are typically 0.5 mm × 0.5 mm × 13 mm in the *x*, *y*, and *z*-directions. *Source:* Figure adapted from Bushberg et al. [5]. Reproduced with permission of Wolters Kluwer.

data to form a three-dimensional image of the body. A section (slice) through the body may then be visualized at any selected depth (Figure 2.7b). Allan Cormack and Godfrey Hounsfield received the Nobel Prize for their invention of CT in 1979. Many technological advances have been made in CT technology over the past four decades, but the basic principle of imaging remains unchanged from the first CT scanner. In the first design, a single X-ray beam and a single detector were moved in parallel across the area to be imaged and X-ray attenuation measurements were obtained [5,6]. This permitted reconstruction of a single tomographic CT slice. To acquire a subsequent slice, the bed on which the patient was positioned was moved slightly in the *Z*-axis direction, and the process was repeated. This was very time-consuming since at least five minutes were needed to obtain a single CT slice [5]. An improvement in this design was *fan beam* CT in which the X-ray source was rotated 360° around the patient and the X-ray beam after passing through the patient, interacts with an array of detectors formed in an arc shape [5]. However, this design still yielded a single thin CT slice. A major improvement was *cone beam* CT (Figure 2.8a) in which the X-ray beam interacts with an array of detectors that have a defined width in

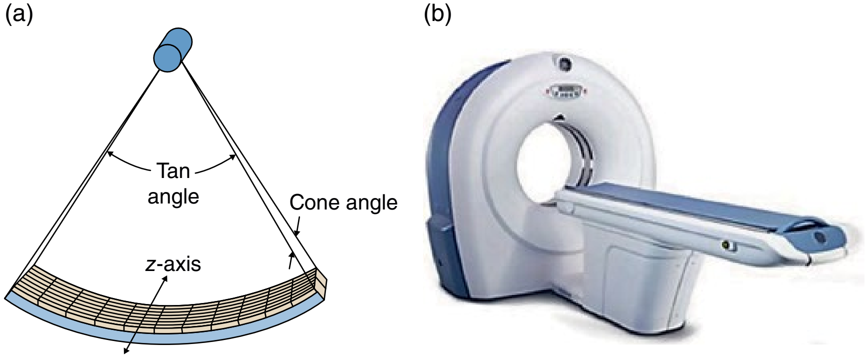

Figure 2.8 (a) Cone beam CT rotates the X-ray beam and an array of scintillation detectors 360° around the patient to rapidly acquire attenuation measurements to form the CT image. *Source:* Bushberg et al. [5]. Reproduced with permission of Wolters Kluwer. (b) Clinical CT scanners now employ cone beam CT technology to obtain a tomographic slice through the body in only 0.3 second.

the *Z*-axis direction, permitting several neighboring CT sections to be simultaneously acquired. Modern cone beam CT scanners (Figure 2.8b) require only 0.3 second to acquire a single image slice through the body. Multiple slices are acquired in only a few minutes and these are combined and reconstructed to form a three-dimensional image of the body. A radiologist may then select and view a particular slice through the body.

2.4.1 Image Acquisition

The X-ray tube in CT operates at 80–120 kV and provides continuous X-ray production during image acquisition [5]. The X-ray tube is attached to the circular gantry of the CT scanner and rotates simultaneously with an array of detectors 360° placed around the patient. Collimators are used to set the width of the X-ray beam [5]. X-ray attenuation measurements are expressed in Hounsfield Units (HU), named after Godfrey Hounsfield, and are depicted on the images by a gray intensity scale. HU values describe the linear attenuation of the X-ray (μ_{voxel}) compared to that in water (μ_{water}) in a voxel (unit of volume) of tissue. HU are calculated from the attenuation measurements as follows [6]:

$$\text{HU} = \frac{1000\left(\mu_{\text{voxel}} - \mu_{\text{water}}\right)}{\mu_{\text{water}}}$$

For a voxel composed entirely of water, HU = 0, since $\mu_{\text{voxel}} - \mu_{\text{water}} = 0$. In a voxel of air, in which there is almost no attenuation of the X-ray, i.e. $\mu_{\text{voxel}} = 0$, HU = −1000. HU values usually range from −100 (adipose tissue) to +20 to +50

Figure 2.9 Attenuation measurements in CT are reported as Hounsfield Units (HU), which describes the attenuation of the X-ray by a tissue compared to the attenuation by water. HU range from +1000 to −1000, but most tissues in the body have HU of +100 to −100. The highest HU are depicted as white while the lowest are shown as black, and tissues with intermediate HU are shown in a gray scale on the image.

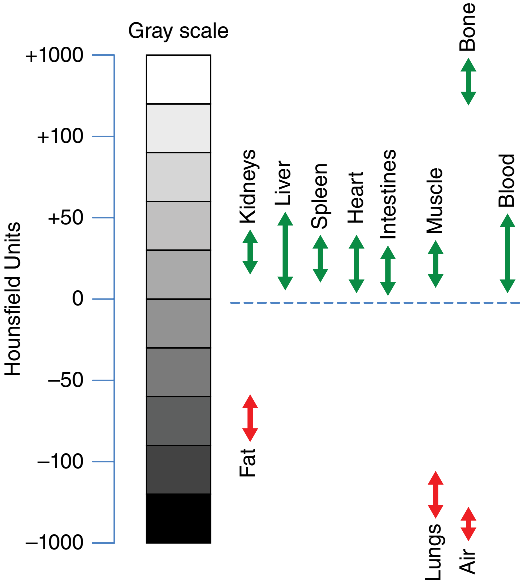

for soft tissues (Figure 2.9) while bone, which is much more dense, has a HU value of +1000 [6]. The HU values are displayed in CT images in slices through the body with each voxel used to form the image having x, y, and z dimensions of 0.5 mm × 0.5 mm × 13 mm (Figure 2.7b). The z-dimension of the voxel may vary depending on the design of the CT scanner [5].

The detectors used in CT are scintillation crystals composed of gadolinium oxysulfide (Gd_2O_2S) that generate small flashes of light (scintillations) when the X-ray interacts with the crystals. A typical detector may have 64 × 64 individual crystal elements. The crystal array is interfaced with a photodiode that converts light scintillations into an electronic signal, which is then amplified. Scintillation detectors are also used in nuclear medicine imaging (see Chapter 3). In older CT systems, the slice width through the body was controlled by the X-ray beam width and detector width, but in modern multiple detector CT (MDCT) systems, the slice width for image reconstruction may be set by the operator [5]. For example, for a 64-slice MDCT, the width of the slices may be reconstructed to form slices of 64 × 0.5 mm, 32 × 1 mm, 16 × 2 mm, or 8 × 4 mm, etc [5].

CT images of a patient are obtained by gradually moving the patient bed through the scanner in the axial direction. In sequential axial acquisition mode, one complete CT slice is obtained, then the bed is moved in the axial direction, and a subsequent CT slice is obtained. This is very time consuming, and thus, more recently other acquisition modes such as helical (spiral) and cone beam CT have been introduced [5]. In helical mode, the bed moves at a constant rate while the CT scanner rotates around the patient, providing a series of CT slices in a spiral fashion around the patient. In cone beam CT, a limited area of the body may be imaged without moving the bed due to the ability to obtain a series of slices through the body using a cone-shaped X-ray beam and array of detectors [5]. Cone beam CT is useful for imaging the heart and is used for CT angiography.

2.4.2 Image Reconstruction

The mathematics of image reconstruction in CT are complex and beyond the scope of this chapter, but the essential concept is presented by a simplified example illustrated in Ref. 5 (Figure 2.10a). The example shows X-rays passing through an array of nine voxels in a hypothetical region of the body from four different directions. The attenuation by each voxel (μ_{voxel}) in each direction is summed by the detectors. This provides the total attenuation of the X-ray beam resulting from interaction with all the voxels in a particular direction, which is called the projected value. However, the projected value does not provide any information on the attenuation of the X-rays by the individual voxels, which is necessary to form the image. In order to solve for the individual voxel attenuation values, the projected values from each direction are back-projected, and

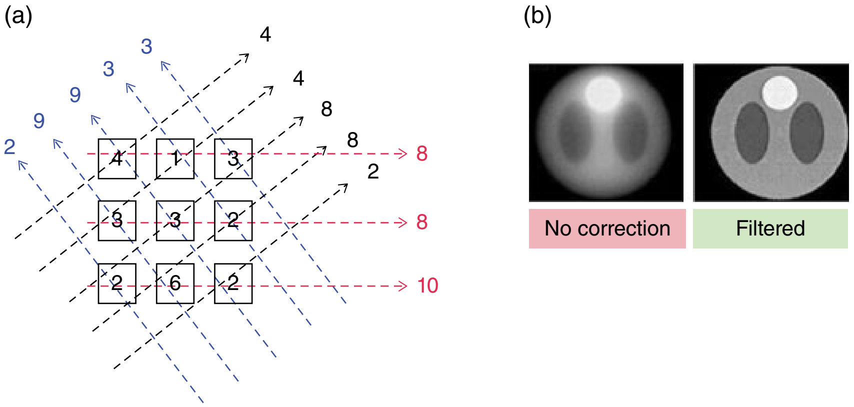

Figure 2.10 (a) Attenuation of X-rays is measured from different angles in CT. In this very simple example of nine voxels that have the different attenuation values shown, the attenuation of the X-ray from three different angles is depicted. The attenuation by the individual voxels in the path of the X-ray from different directions is summed (shown). By a process called backprojection that takes into account the sums of the attenuation measurements from different angles, the attenuation values in individual voxels can be deduced, analogous to solving a Sudoku puzzle. The deduced attenuation values in all of the voxels are used to reconstruct the image. (b) Images reconstructed by a process of backprojection have blurred edges, which are then corrected by applying a mathematical filter to create the final image. *Source:* (a) Bushberg et al. [5]. Reproduced with permission of Wolters Kluwer. (b) Goldman et al. [6].

mathematically deconvolved to deduce the values in each of the voxels. As described in Ref. 5, this is analogous to solving a Sudoku puzzle, but since actual CT data incorporates not nine voxels, but 262 144 voxels in a 528 × 528 matrix, the problem is far more complex and requires reconstruction algorithms and a powerful computer to solve. Back-projection causes some resolution artifacts, particularly at the edges of imaged objects, and reconstruction algorithms additionally incorporate mathematical "filtering" corrections (filtered back-projection) to accurately depict the object on an image (Figure 2.10b).

2.4.3 CT Contrast Agents

Contrast agents (CA) are administered to patients to improve the contrast between two tissues that attenuate X-rays similarly (i.e. similar HU values) [7]. CA may be administered intravenously (e.g. iodinated CA) or may be taken orally (e.g. barium sulfate). High doses of intravenously injected CA that yield millimolar concentrations in the blood and tissues are required to improve CT image contrast, raising toxicity concerns, especially for patients who have poor renal function and are not able to adequately clear these agents. Iodinated CA are commonly used because iodine has a high atomic number (*Z* = 53), which increases the attenuation of X-rays. There are two classes of iodinated CA (Figure 2.11): high osmolality ionic and low-osmolality nonionic CA. Ionic

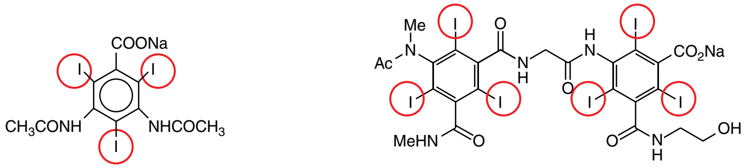

Diatrizoate (Hypaque)

Ioxaglate (Hexabrix)

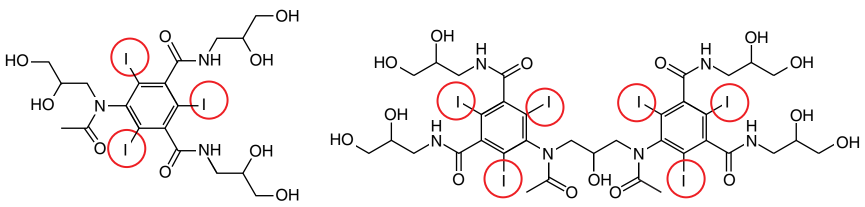

Iohexol (Ominipaque)

Iodixanol (Visipaque)

Figure 2.11 Intravenous contrast agents used in CT imaging. Diatrizoate (Hypaque) and ioxaglate (Hexabrix) are ionic agents, while iohexol (Omnipaque) and iodixanol (Visipaque) are nonionic. Contrast agents contain multiple iodine atoms in their structures, which increase the attenuation of X-rays by tissues. Differential localization of contrast agents in tissues provides the contrast enhancement on CT images.

agents include ioxaglate (Hexabrix) and diatrizoate (Hypaque) while iodohexol (Omnipaque) or iodixanol (Visipaque) are non-ionic. Ionic agents are associated with a greater risk for adverse reactions including renal toxicity causing nephrosis, vasodilation, bradycardia, and pulmonary hypertension [7]. Pain and a sensation of heat at the injection site and metallic taste may also be experienced. About 5% of patients will have an adverse reaction to CA. Allergic reactions are most commonly manifested by pruritus and urticaria, but severe reactions including anaphylaxis may occur in <0.2% of patients. Previous allergic reaction to CA greatly increases the likelihood of a subsequent severe allergic reaction. Asthma or a history of allergy to iodine or shellfish increases the risk for allergic reaction to iodinated CA. The risk for kidney damage from CA is higher in patients with poor renal function, diabetes, dehydration, congestive heart failure, or age >70 years. Proper hydration minimizes the risk of kidney toxicity, and if needed, patients at risk for allergy to CA may receive premedication with corticosteroids. Examples of ionic-iodinated CA include diatrizoate (Hypaque), metrizoate (Isopaque), iothalamate (Conray), and ioxaglate (Hexabrix; Mallinckrodt). Examples of nonionic CA are iohexol (Omnipaque; GE Healthcare), iopromide (Ultravist; Bayer Healthcare), iodixanol (Visipaque; GE Healthcare), and iopamidol (Isovue; Bracco Imaging). Nonionic CA are safer to use than ionic CA.

In addition to intravenously administered iodinated CA, patients undergoing CT imaging of the gastrointestinal (GI) tract may receive barium sulfate taken orally or instilled rectally (barium enema) to visualize the bowel (Figure 2.12) [7]. Barium has a high atomic number ($Z = 56$), which increases the

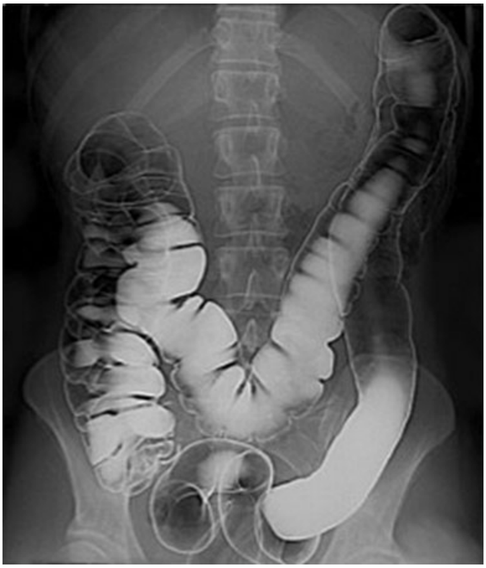

Figure 2.12 Barium ($Z = 56$) sulfate is administered orally as a positive contrast agent for imaging the bowel while air is used as a negative contrast agent since it attenuates X-rays much less than soft tissues. *Source:* Image obtained from https://en.wikipedia.org/wiki/Double-contrast_barium_enema.

attenuation of X-rays. Air insufflation of the bowel provides a “negative” contrast, i.e. lower attenuation of X-rays than the surrounding tissues. These agents may cause some GI side effects such as stomach cramps, diarrhea, nausea, vomiting, and constipation. Minor allergic reactions may occur infrequently.

2.5 Mammography

Mammography is a specialized form of X-ray imaging of the breast used to screen women at risk for breast cancer and to aid in the diagnosis of breast cancer in symptomatic patients. Many advances have been made over several decades to improve the quality of mammograms from historically-used screen-film technology through the introduction of digital mammography, and most recently, digital *tomosynthesis* [8]. Tomosynthesis is tomographic X-ray imaging of the breast that acquires a series of images around the breast, which are then reconstructed into a three-dimensional image, which may be sliced as needed through a particular region of the breast.

2.5.1 Mammography System

The design of a mammography system is shown in Figure 2.13 [8]. The components include an X-ray tube, a filter to select the desired X-ray energies, a collimator to focus the X-rays on the breast, a compression paddle to compress the breast, and an X-ray detector, which measures the attenuation of the transmitted X-rays to form the image. A major difference between mammography and other forms of radiographic imaging is that intermediate energy X-rays are used (15–25 keV) [8]. These X-ray energies provide the highest contrast between the normal breast and cancerous lesions. However, a limitation of X-rays with these intermediate energies is high absorption by breast tissue, resulting in higher radiation doses than those occurring for higher energy X-rays. Molybdenum (Mo) and rhodium (Rh) are commonly used target materials in the X-ray tubes, because their low K-shell energies (17.5 and 19.6 keV for Mo and 20.2 and 22.7 keV for Rh) yield characteristic X-rays in the desired energy range [8]. Tungsten (W) targets may also be used due to the higher proportion of Bremsstrahlung X-rays, but these generate more low-energy X-rays (8–12 keV) that need to be removed by filtration. Filters made of Mo, Rh, silver (Ag), or aluminum (Al) are inserted between the X-ray tube and the collimator to remove these low-energy X-rays (<15 keV) that increase the radiation dose to the breast without contributing to the image, and higher energy X-rays (>25 keV), which decrease image contrast. The X-ray beam is focused on the breast using collimators equipped with a light system to align the field-of-view for imaging [8]. Breast

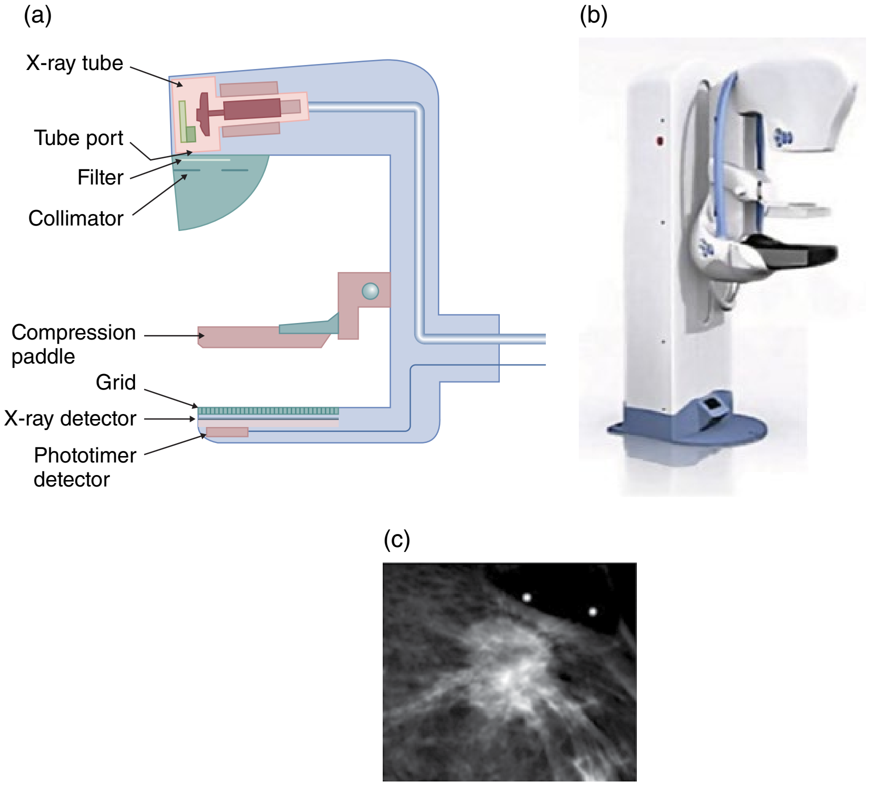

Figure 2.13 (a) Design of a mammography imaging system. *Source:* Bushberg et al. [8]. Reproduced with permission of Wolters Kluwer. (b) Clinical mammography system. (c) Mammogram demonstrating a small breast cancer lesion. *Source:* Chapter 9 (figure 9.13).

compression using a compression paddle is employed in mammography to decrease breast thickness to minimize degradation of the image by overlying tissues and scattered X-rays, to decrease motion artifacts, and to minimize the radiation dose to the breast [8]. An anti-scatter lead grid with holes analogous to a collimator on a gamma camera in nuclear medicine (see Chapter 3) rejects scattered X-rays that are not aligned with the X-ray tube source [8]. For many decades, screen-film image formation was used until the advent of digital mammography. Most mammography systems now use digital image formation using a thin film transistor (TFT) and flat panel display [8]. In one type of detector, the X-rays interact with a cesium iodide (CsI) phosphor that converts the X-rays into light photons that interact with a photodiode to convert the light into electrons, which ultimately form the image. Another type of detector directly converts X-rays into electrons using an amorphous selenium (a-Se) semiconductor.

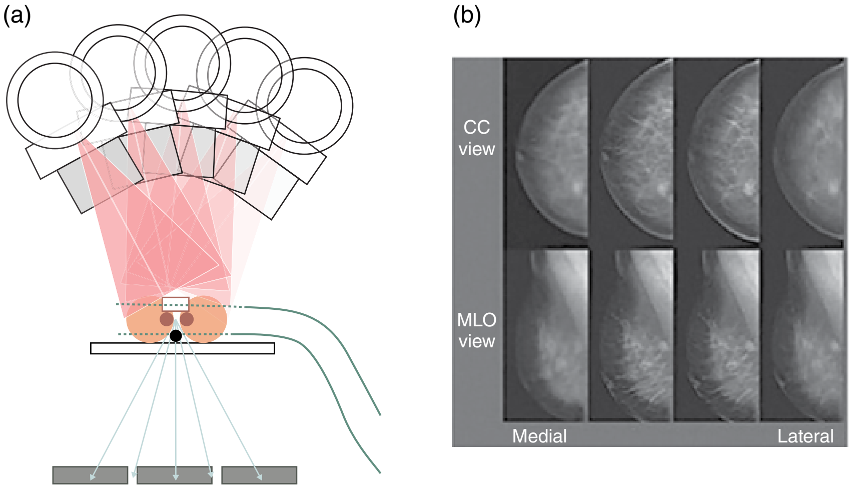

Figure 2.14 (a) Tomosynthesis mammography obtains images of the breast from different angles. (b) Tomosynthesis provides tomographic images of the breast, which may be helpful to visualize a lesion. *Source:* Bushberg et al. [8]. Reproduced with permission of Wolters Kluwer.

2.5.2 Tomosynthesis

A challenge in mammography is interference by overlying normal breast tissues, which may obscure a lesion. Tomosynthesis (Figure 2.14a) aims to overcome this limitation by acquiring a series of images (10–50) of the breast through an arc, which can be reconstructed to create a slice through the breast in a particular plane (Figure 2.14b) [8]. The radiologist may view sequential planes to more closely inspect a lesion. Tomosynthesis does not significantly increase the radiation dose compared to conventional mammography.

2.6 Summary

X-rays are a form of electromagnetic radiation produced by the interaction of a high-energy incident electron with orbital electrons in a target element, usually tungsten. X-rays are attenuated differentially by tissues when they pass through the body, which creates an X-ray image. CT is a three-dimensional image of the body obtained by taking attenuation measurements 360° around the patient. This three-dimensional image may be "sliced" to obtain tomographic images at different locations in the body and in different directions (axial, sagittal, and coronal). Mammography is a specialized X-ray of the breast used to screen for breast cancer in women at risk, and to detect breast cancer in women who are symptomatic. Tomosynthesis is a tomographic form of mammography that allows “slices” through the breast to be examined for lesions. X-ray, CT, and mammography are the most common forms of medical imaging.

References

1 Seibert, J.A. (2004). X-ray imaging physics for nuclear medicine technologists. Part 1: basic principles of X-ray production. *J. Nucl. Med. Technol.* 32: 139–147.

2 Bushberg, J.T., Seibert, J.A., Leidholdt, E.M. Jr., and Boone J.M. (2012). X-ray production, X-ray tubes, and X-ray generators. In: The Essential Physics of Medical Imaging, 3e, 171-206. Philadelphia, PA: Lippincott Williams & Wilkins.

3 Bushberg, J.T., Seibert, J.A., Leidholdt, E.M. Jr., and Boone, J.M. (2012). Radiography. In: The Essential Physics of Medical Imaging, 3e, 207-237. Philadelphia, PA: Lippincott Williams & Wilkins.

4 Seibert, J.A. and Boone, J.M. (2005). X-ray imaging physics for nuclear medicine technologists. Part 2: X-ray interactions and image formation. *J. Nucl. Med. Technol.* 33: 3–18.

5 Bushberg, J.T., Seibert, J.A., Leidholdt, E.M. Jr., and Boone, J.M. (2012). Computed tomography. In: *The Essential Physics of Medical Imaging*, 3e, 312–374. Philadelphia, PA: Lippincott Williams & Wilkins.

6 Goldman, L.W. (2007). Principles of CT and CT technology. *J. Nucl. Med. Technol.* 35: 115–128.

7 Loveless, V.S. (2012). Adjunct agents used in X-ray imaging. In: *Diagnostic Imaging for Pharmacists* (ed. B. Templar Smith and K.D. Weatherman), 43–64. Washington, DC: APhA.

8 Bushberg, J.T., Seibert, J.A., Leidholdt, E.M. Jr., and Boone, J.M. (2012). Mammography. In: *The Essential Physics of Medical Imaging*, 3e, 238–281. Philadelphia, PA: Lippincott Williams & Wilkins.

Additional Reading

Duncan, C. (2012). Review of imaging procedures using X-rays. In: *Diagnostic Imaging for Pharmacists* (ed. B. Templar Smith and K.D. Weatherman), 25–42. Washington, DC: APhA.

3

Nuclear Medicine Imaging Technology

Raymond M. Reilly

3.1 Introduction

Nuclear medicine imaging includes single photon emission computed tomography (SPECT) and positron emission tomography (PET). The principles of SPECT and PET are described in this chapter. Nuclear medicine imaging differs from other forms of radiological imaging such as X-ray, CT, MRI, and ultrasound through the use of radiopharmaceuticals (see Chapter 4), which are administered to patients, localize in certain organs or tissues in the body, and emit γ-photons or positrons that are imaged using a gamma camera or PET tomograph, respectively. The theoretical potential to design radiopharmaceuticals that could probe almost any physiological, biological, or molecular property of a tissue in the body makes nuclear medicine very powerful and the most functional of all imaging modalities. Moreover, the high sensitivity of the gamma camera or PET tomograph for the detection of γ-photons or positrons, respectively, requires that only "tracer" amounts (i.e. very small mass) of radiopharmaceuticals need to be administered to obtain images. This avoids adverse reactions that are more commonly associated with contrast agents for CT or MRI, which need to be administered at much higher amounts for imaging (see Chapters 2 and 5). Moreover, these small "tracer" amounts of radiopharmaceuticals permit imaging without perturbing the functional or molecular properties of tissues (i.e. there is no pharmacological effect of radiopharmaceuticals). The main limitation of SPECT and PET compared to other imaging modalities such as X-ray, CT, or MRI is its relatively poor spatial resolution. Spatial resolution refers to the ability of an imaging technology to differentiate between two anatomically close structures. X-ray, CT, and MRI have tens of micrometers spatial resolution whereas the spatial resolution of clinical SPECT and PET systems is 5–10 mm. To take advantage of the ability of nuclear medicine to image organs and tissues but retain the high spatial resolution of CT or MRI, hybrid imaging systems have been

Medical Imaging for Health Professionals: Technologies and Clinical Applications, First Edition.
Edited by Raymond M. Reilly.
© 2019 John Wiley & Sons, Inc. Published 2019 by John Wiley & Sons, Inc.

introduced (e.g. SPECT/CT, PET/CT, and PET/MRI). These hybrid systems obtain both a nuclear medicine image and a CT or MRI image and co-register these images to reveal the anatomy at tens of micrometers resolution as well as the functional properties of the tissues at lower spatial resolution.

3.2 Scintillation Detectors

To understand how nuclear medicine imaging technology works, it is important to appreciate the principles of solid scintillation detectors. These detectors are composed of inorganic crystalline materials that emit flashes of light (scintillations) when a γ-photon interacts with the material. The most common solid scintillator used for SPECT in nuclear medicine is sodium iodide containing a small amount of thallium impurity (NaI(Tl); Table 3.1) [1]. The thallium impurity traps the energy deposited by γ-photons in electron–hole pairs that is then emitted as light. For PET, commonly used scintillators are bismuth germinate (BGO), lutetium silicate (LSO), lutetium yttrium oxyorthosilicate (LYSO), or gadolinium orthosilicate (GSO) [2].

The density of NaI(Tl) scintillation crystals (3.7 $\mathrm{g\,cm^{-3}}$) is most effective for absorbing the relatively low energy (80–364 keV) γ-photons emitted by radionuclides commonly used for SPECT (^{99m}Tc, ^{123}I, ^{111}In, ^{67}Ga, ^{131}I; Table 3.2).

Absorption of the two high-energy 511 keV annihilation γ-photons created by positron decay employed in PET requires higher density scintillators such as BGO (7.1 $\mathrm{g\,cm^{-3}}$), LSO (7.4 $\mathrm{g\,cm^{-3}}$), LYSO (7.1 $\mathrm{g\,cm^{-3}}$), or GSO (6.7 $\mathrm{g\,cm^{-3}}$) [1]. Common radionuclides used for PET include ^{18}F, ^{11}C, ^{18}O, ^{13}N, ^{64}Cu, ^{68}Ga, ^{89}Zr, and ^{124}I (Table 3.3). More dense BGO, LSO, LYSO, and GSO crystals have higher attenuation coefficients than NaI(Tl) detectors, providing greater

Table 3.1 Properties of solid scintillators used in nuclear medicine imaging [1].

Property	NaI(Tl)	BGO	LSO	GSO
Density ($\mathrm{g\,cm^{-3}}$)	3.67	7.13	7.40	6.71
Attenuation coefficient ($\mathrm{cm^{-1}}$)	0.34	0.92	0.87	0.62
Light yield (relative to NaI(Tl))	1.0	0.15	0.75	0.41
Peak wavelength (nm)	410	480	420	430
Decay constant (ns)	230	300	40	56
Hygroscopic	Yes	No	No	No
Fragile	Yes	No	No	No

NaI(Tl), sodium iodide with thallium impurity; BGO, bismuth germinate; LSO, lutetium silicate; GSO, germanium silicate.

Table 3.2 Common radionuclides used for SPECT imaging.

Radionuclide	**$T_{1/2}$p**	**Eγ**	**β-Particle emission**	**Production**
^{99m}Tc	6 h	140 keV	—	Generator
^{111}In	2.8 d	171, 245 keV	—	Cyclotron
^{201}Tl	3.0 d	69–83, 167 keV	—	Cyclotron
^{123}I	13.2 h	159 keV	—	Cyclotron
^{131}I	8.0 d	364 keV	0.6 MeV	Reactor
^{67}Ga	3.2 d	93, 184, 300, 393 keV	—	Cyclotron

$T_{1/2}$p, physical half-life; Eγ, energy of gamma photon; β-particle emission, β-particle emissions in addition to γ-photon emissions.

Table 3.3 Common radionuclides used for PET imaging.

Radionuclide	**$T_{1/2}$p**	**$E\beta^+$**	**Spatial resolution**	**Production**
^{15}O	2.0 min	1.72 MeV	2.7 mm	Cyclotron
^{13}N	10.0 min	1.19 MeV	1.8 mm	Cyclotron
^{11}C	20.4 min	0.96 MeV	1.7 mm	Cyclotron
^{68}Ga	68.0 min	1.9 MeV	2.4 mm	Generator
^{18}F	1.8 h	0.64 MeV	0.8 mm	Cyclotron
^{64}Cu	12.7 h	0.70 MeV	0.7 mm	Cyclotron
^{89}Zr	78.4 h	0.36 MeV	0.5 mm	Cyclotron
^{124}I	4.2 d	0.8–2.1 MeV	2.3 mm	Cyclotron

$T_{1/2}$p, physical half-life; $E\beta^+$, energy of positron.

γ-photon absorption. However, the efficiency of conversion of γ-photon energy to light for BGO, LSO, or GSO detectors is 6.7-, 2.4-, and 1.3-fold lower than for NaI(Tl), which is about 13% [1]. Another important factor is the time for the light scintillations generated to decay away (decay time). This should be as short as possible, so that subsequent γ-photons interacting with the crystal will generate new discrete scintillation events. LSO and GSO provide the shortest decay times (40 and 56 nanoseconds [ns], respectively), while NaI(Tl) and BGO exhibit the longest decay times (230 and 300 ns, respectively) [1]. Another limitation of NaI(Tl) crystals is their hygroscopic nature, i.e. their tendency to absorb moisture from the air. Due to this property, NaI(Tl) detectors are hermetically sealed to prevent moisture from the ambient room air from degrading the crystal. NaI(Tl) crystals are also very fragile and can easily be cracked, destroying the crystal. BGO, LSO, and GSO crystals are not hygroscopic and are less fragile [1]. The spatial resolution of PET depends in part on the energy of the positron, with higher energies providing poorer spatial resolution than lower energy positrons (Table 3.3). This is because the distance that the positron travels before annihilation generating the two 511 keV γ-photons used for PET is greater for higher energy positrons.

3.2.1 Conversion of Light to an Electronic Signal

The photomultiplier tube (PMT; Figure 3.1a) converts the light scintillations resulting from interaction of γ-photons with the scintillation crystal into an electronic signal that can be measured and which is directly proportional to the number of γ-photons interacting with the crystal [1]. The PMT consists of a glass vacuum tube with a photocathode at one end nearest to the crystal that emits electrons when light interacts with the photocathode, in sequence with a series of diodes that greatly amplify the number of electrons produced and finally, an anode at the opposite end of the PMT. The anode is connected to a preamplifier and then to an amplifier. In a γ-camera (see Section 3.3), there is an array of PMTs that completely covers the imaging surface of the scintillation crystal [3]. These are in direct contact with a glass cover on the crystal by a layer of UV-transparent film that transmits the light photons produced into the PMTs. An alternative to PMTs are avalanche photodiodes, which directly convert light into an electronic signal. These have recently been introduced into some state-of-the-art γ-cameras.

3.2.2 Amplification and Analysis of the Electronic Signal

The electronic signal generated by the PMTs is further amplified by a preamplifier and amplifier, and then analyzed. The first analysis is performed by a multichannel analyzer (MCA), which determines the energy spectrum of the γ-photons. An example of the γ-spectrum of ^{99m}Tc is shown in Figure 3.1b. The spectrum includes the photopeak due to complete absorption of the 140 keV γ-photons by the scintillation crystal (photoelectric effect) as well as the Compton region due to absorption of scattered photons, which have lower energies [1]. There are also some smaller low-energy X-ray peaks caused by interaction of the 140 keV γ-photon of ^{99m}Tc with the crystal and the lead shield that surrounds the detector. The MCA is used to set energy windows to only register detection events for γ-photons with energies that fall within these ranges. Importantly, this allows elimination of scattered low-energy γ-photons outside the window of the photopeak, but it also permits the detection of two or more photopeaks for a single radionuclide that emits γ-photons of different energies, in order to maximize the count rate to increase the sensitivity of detection and improve image quality. Energy discrimination also permits

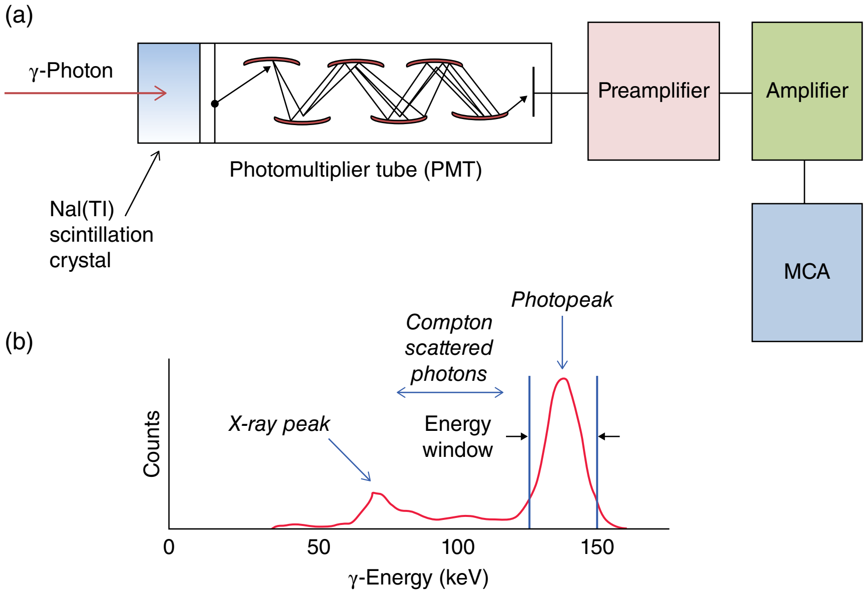
(a)
γ-Photon
NaI(Tl) scintillation crystal
Photomultiplier tube (PMT)
Preamplifier
Amplifier
MCA
(b)
Photopeak
Compton scattered photons
X-ray peak
Energy window
Counts
0
50
100
150
γ-Energy (keV)

Figure 3.1 (a) Detection of γ-photons. A γ-photon is absorbed by the NaI(Tl) scintillation crystal generating small flashes of light (scintillations). The light scintillations are converted to electrons by a photomultiplier tube (PMT), which also amplifies the number of electrons generated. The electronic signal is further amplified by a preamplifier and amplifier. The multichannel analyzer (MCA) selects the photopeak energy of the γ-photons to form the image and rejects scattered γ-photons that do not directly originate from the source of radioactivity in the patient since these have lower energy. (b) The gamma spectrum of ^{99m}Tc showing the photopeak at 140 keV, scattered γ-photon energies in the Compton region, and a lead X-ray peak at 80 keV. The MCA sets an energy window around the photopeak to eliminate scattered γ-photons and X-rays.

simultaneous detection of two or more radionuclides that have different γ-photon energies (dual-isotope detection) to visualize the uptake of two different radiopharmaceuticals labeled with two different radionuclides in an organ.

3.3 The Gamma Camera

The γ-camera used for planar and SPECT imaging of single γ-photon-emitting radionuclides (Table 3.2) was originally designed by Dr. Hal Anger at the University of California, Berkley, in 1958 and was originally called the "Anger camera" [4]. Many technological improvements have been made since then, such that the modern γ-camera (Figure 3.2a) barely resembles the original "Anger camera" (Figure 3.2b). Nonetheless, the basic principles for producing an

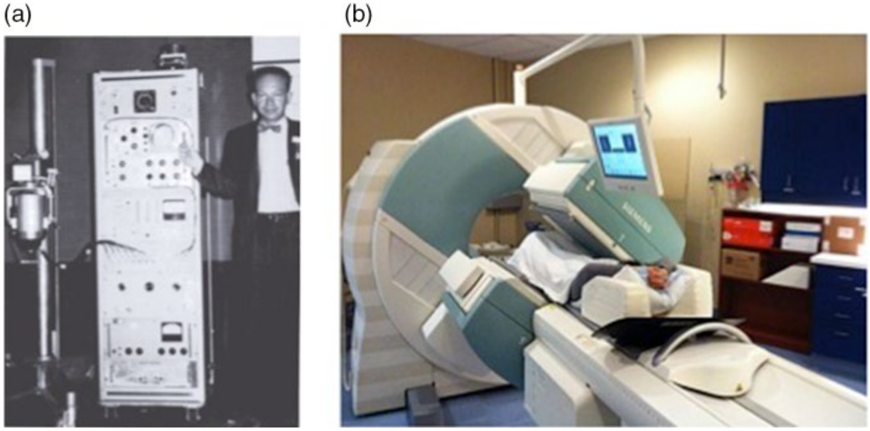

Figure 3.2 (a) Dr. Hal Anger showing the first gamma camera ("Anger camera") invented at the University of California, Berkley, in 1958. Source: From Myers [4]. Reproduced with permission from the Society of Nuclear Medicine and Molecular Imaging (SNMMI). (b) A modern SPECT/CT gamma camera . Source: https://en.wikipedia.org/wiki/Single-photon_emission_computed_tomography.

image remain the same. In order to create an image of the distribution of a radiopharmaceutical in a patient, it is necessary to identify the anatomical location of radioactive decay events, as well as the number of decays that are occurring at that location, in order to provide intensity information. This is achieved by positioning the γ-camera head over the patient. The head (Figure 3.3a) incorporates a large field-of-view scintillation crystal, most often composed of NaI(Tl), interfaced with an array of PMTs [3]. A lead collimator is affixed to the γ-camera head. The collimator consists of a sheet of lead (several centimeters thick) in which there are holes of precise diameter that only permit γ-photons perpendicular to the γ-camera head to interact with the scintillation crystal. Any γ-photons that are not perpendicular to the head impact on the lead septa between the holes and are absorbed and not detected. These stray γ-photons that may originate in nearby anatomical regions or may be scattered from other regions in the body, and detection of these photons would degrade the image, thus collimation is used to eliminate them. The major disadvantage of collimation is that only γ-photons that pass through the holes in the collimator are detected. The vast majority of γ-photons emitted from the radiopharmaceutical in the patient impact with the lead septa of the collimators and are not detected – in fact, <0.1% of the emitted γ-photons pass through the holes and are detected! The requirement for collimation with the γ-camera makes SPECT several orders of magnitude less sensitive than PET, which works on a different principle and does not require lead collimation.

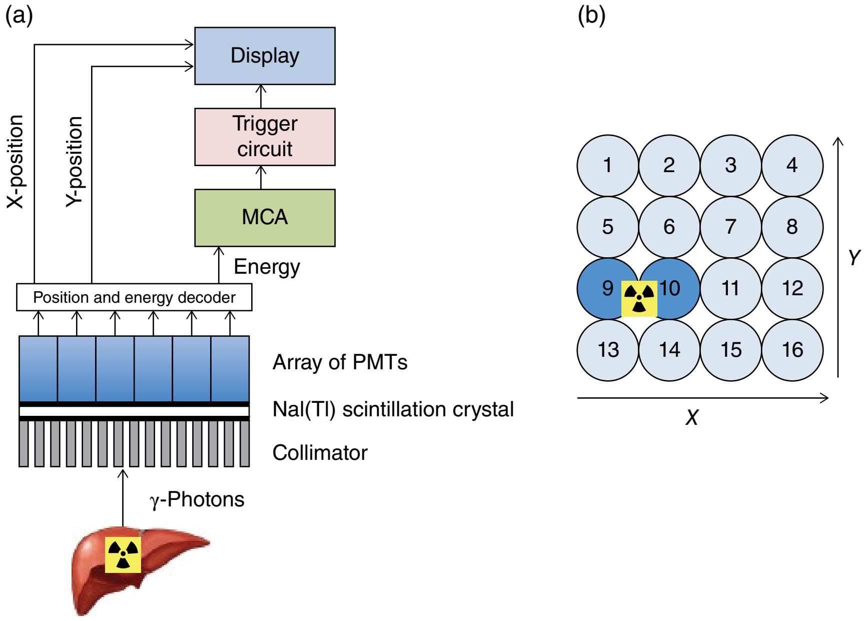

Figure 3.3 Principle of image formation using a gamma camera [3]. (a) γ-Photons emitted by a radiopharmaceutical pass through the collimator and are absorbed by the NaI(Tl) scintillation crystal. The collimator is composed of a sheet of lead with holes that permit only γ-photons directly originating from the radioactive source to interact with the scintillation crystal (i.e. stray γ-photons are eliminated). The scintillation crystal generates small light flashes that are converted to electrons by an array of photomultiplier tubes (PMTs) in direct contact with the crystal. The position and energy of the γ-photons interacting with the crystal and array of PMTs is decoded and the *X*- and *Y*-positions of the γ-photon interaction events are sent to the display. A multichannel analyzer (MCA) selects the energy of the γ-photons to be displayed on the image, further eliminating scattered γ-photons. (b) The position of the γ-photon interaction with the crystal is deduced by monitoring the intensity of electrons generated by an array of PMTs using an *X*, *Y*-circuit. Those PMTs closest to the position of the radioactive source (darker shading) generate the most intense electronic signal response.

A digital *X*, *Y* circuit deduces the anatomical position of the radioactive decay event (Figure 3.3b), and a *Z*-circuit provides information on the number and energy of events [3]. A computer monitors the *X*,*Y*-circuit and records the intensity of the electronic signal created at each PMT in the array – PMTs closest to the source of radioactive decay generate the most intense signal, while those farther away generate a weaker signal. By monitoring the PMT signals generated in both the *X*- and *Y*-direction, the location of the radioactive decay can be deduced in a two-dimensional plane. Tomographic SPECT imaging requires 180° or 360° rotation of the γ-camera head around the patient to acquire a series of two-dimensional images that are then reconstructed into a three-dimensional image (see Section 3.4) [2]. The Z-circuit signal is further analyzed by an MCA to determine the energy of the γ-photons being detected. The MCA eliminates any γ-photons outside of a preselected energy window centered around the photopeak of the radionuclide being imaged. For example, if ^{99m}Tc was being imaged (Table 3.2), then a 20% window is set around the 140 keV photopeak, i.e. 112–168 keV (Figure 3.1b). Any γ-photons with energy higher or lower than this range would be eliminated. Most scattered γ-photons have lower energy than the photopeak and are eliminated by energy discrimination, improving image quality. However, depending on the width and position of the energy window, some scattered γ-photons may still be detected. In addition, coincidence γ-photons may be detected. These are γ-photons that have an energy below the energy window (e.g. scattered γ-photons), but because two γ-photons by chance interacted simultaneously with the scintillation crystal, their energies are summed bringing the total energy into the range of the energy window [3]. Scattered and coincidence photons decrease image resolution and quality.

3.3.1 Collimator Designs

Most imaging with a γ-camera is performed using a parallel hole collimator (Figure 3.4a) in which a sheet of lead has thousands of small parallel holes [3]. This type of collimator provides a 1 : 1 image size relative to the area of the body being imaged. Sometimes, it is necessary to magnify the image size for an organ that is small (e.g. the thyroid). In these cases, a pinhole collimator may be used (Figure 3.4b) [3]. A pinhole collimator has one small hole through which the γ-photons pass. Similar to a pinhole aperture on a camera, it magnifies but reverses the image. The smaller the holes on a collimator, the greater the spatial resolution of the image. However, this comes at a great cost, as the sensitivity of detection is greatly decreased since there is less opportunity for a γ-photon to pass through a hole in the collimator. Thicker septa on the collimator are better at collimating and eliminating scattered γ-photons, especially those with high energy that may pass through a less thick collimator (septal penetration). Depending on the collimator thickness and size of the holes, collimators may be classified as low energy-high sensitivity, low energy all-purpose (LEAP), low energy-high resolution, medium energy, high energy, and ultra-high energy [3]. The LEAP collimator is most commonly used for nuclear medicine imaging.

3.3.2 Image Acquisition, Display, and Analysis

A computer interfaced with the γ-camera controls image acquisition and display. The field-of-view of the scintillation detector is only about 40 cm × 60 cm, and so the detector heads must be slowly moved from the head to the feet of the patient in order to obtain a whole-body image [3]. In addition, for tomographic

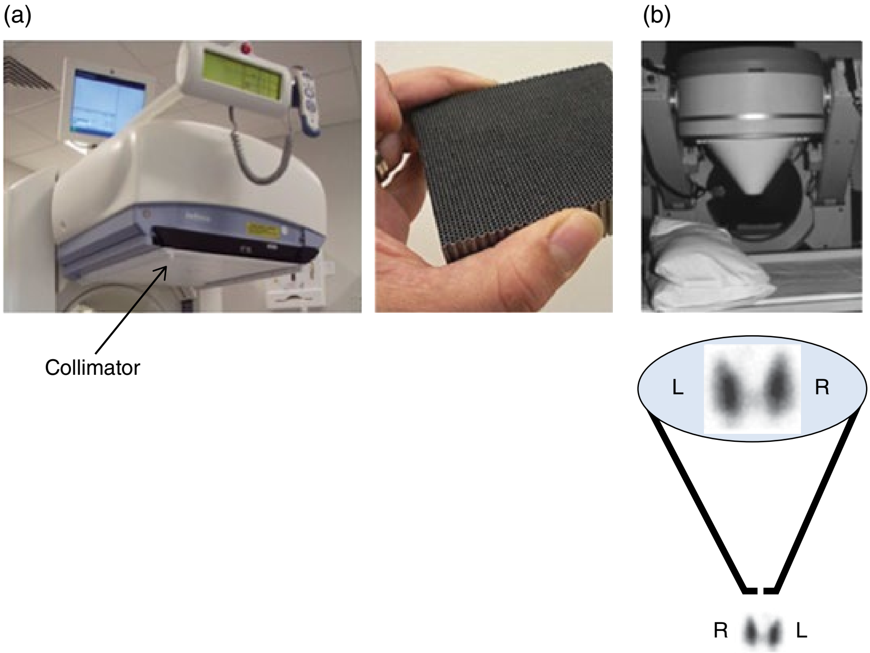

Figure 3.4 Collimators used for gamma camera imaging. (a) Most commonly used are parallel collimators (left image). Source: From http://www.nuclearmedicine.ie/Gamma_Camera.html. These are composed of a sheet of lead with holes precisely drilled to permit only γ-photons directly originating from the radioactive source in the patient from interacting with the scintillation crystal (right image). Source: Obtained from http://www.nuclearfields.com/collimators-nuclear-medicine.htm. (b) Pinhole collimators magnify the image of small organs and are commonly used to image the thyroid gland. Pinhole collimation also reverses the image (note "L [left]" and "R [right]").

SPECT imaging, the γ-camera heads need to be rotated around the patient 180° or 360° (see Section 3.4) [2]. Planar images are constructed of pixels in a 64 × 64 or 128 × 128 matrix or a 128 × 1024 pixel matrix for whole-body images [3]. An image may be acquired over a predetermined time period (static image), or a series of images may be obtained over time (dynamic), or multiple images may be obtained registered with a physiological event in the patient (gated). An example employing dynamic imaging is a hepatobiliary study in which images of the uptake of ^{99m}Tc-disofenin by the liver and gallbladder and its elimination into the small bowel are acquired over a period of 30–60 minutes (Figure 3.5a) [5]. An example in which gated imaging is performed is radionuclide ventriculography (MUGA scan) with ^{99m}Tc-labeled red blood cells, which aims to measure the percentage of blood ejected by the left ventricle of the heart at end systole (left ventricular ejection fraction [LVEF]) (Figure 3.5b) [6]. A region-of-interest

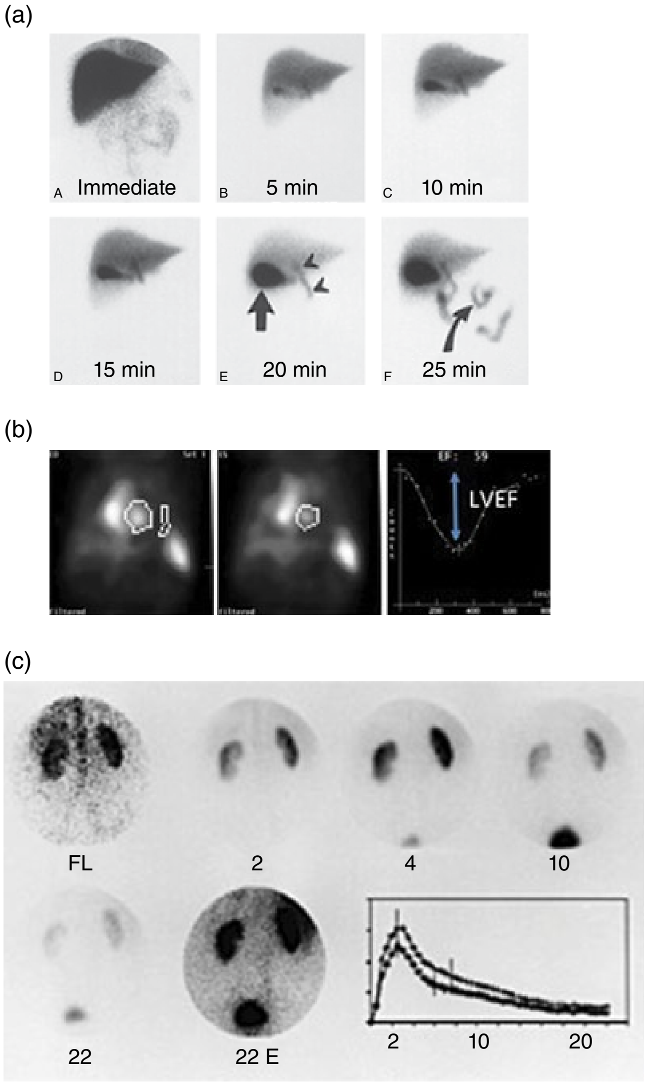

Figure 3.5 (a) Dynamic images acquired for a hepatobiliary imaging study using ^{99m}Tc-disofenin showing uptake of the radiopharmaceutical into the liver and gallbladder and elimination into the small intestine. Source: Brant and Helms [5]. Reproduced with permission of Wolters Kluwer. (b) Gated images acquired at end diastole and end systole in a MUGA scan of the heart used to measure the left ventricular ejection fraction (LVEF). The radioactivity in the left ventricle is quantified by a region-of-interest (ROI) and plotted for one cardiac cycle to estimate the LVEF. Source: Reprinted with permission from Szmit et al. [6]. (c) Dynamic images acquired for a renal imaging study using ^{99m}Tc-MAG3. The radioactivity in each kidney is quantified by ROI analysis and plotted versus time to evaluate the function of each kidney independently. Source: From Sfakianakis et al. [7]. Reproduced with permission from the Society of Nuclear Medicine and Molecular Imaging (SNMMI).

(ROI) may be set on an image and the counts obtained in that region. In a dynamic or gated study such as a MUGA scan, a ROI may be set for a series of images and the changes in counts in the ROI determined over time. This provides the opportunity to plot time–activity curves that provide information on the elimination of a radiopharmaceutical from an organ, e.g. elimination of ^{99m}Tc-MAG$_3$ in a renal imaging study (Figure 3.5c) [7].

3.4 Single Photon Emission Computed Tomography

Planar imaging generates two-dimensional images of the body, which means that it is not possible to visualize the distribution of radioactivity that lies in the plane of the image if there is interference by radioactivity above or below the plane. Thus, radiopharmaceutical uptake by other organs or tissues above or below the image plane interferes with image quality and resolution. SPECT (Figure 3.6a) is a technique which acquires multiple planar images around the patient in 180° or 360° that are then stored by a computer, and mathematically reconstructed into a three-dimensional tomographic image of the body or region of the body [2]. This tomographic image can then be "sliced" by the computer to eliminate interference with radioactivity that lies above or below the area of interest. SPECT was invented by Drs. David Kuhl and Roy Edwards at the University of

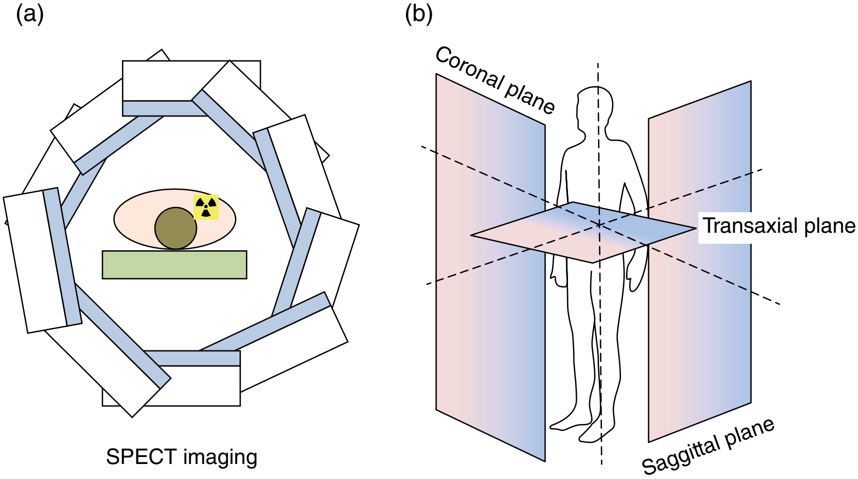

Figure 3.6 (a) Single photon emission computed tomography (SPECT) acquires images 360° around the patient, which are stored by a computer and reconstructed using mathematical algorithms to provide a three-dimensional image of the body. (b) The SPECT images can be "sliced" in the coronal, sagittal, or transaxial planes to provide a series of images at the selected level within a plane in the body.

Pennsylvania in 1963 [2]. Two γ-camera heads each rotate 180° around the body such that the entire series of images are obtained over 360°, in either a circular orbit, or in a noncircular orbit that adjusts for the patient's body contours (referred to as "body contouring"). Transverse images (slices) through the body are most often reconstructed using "filtered backprojection," a mathematical algorithm that removes statistical "noise" and backprojects the individual images to reconstruct the transverse section slice. Iterative backprojection is an improved mathematical algorithm that is used in some γ-cameras to reconstruct higher resolution transverse images. SPECT images must be corrected for tissue attenuation to avoid artifacts. Most SPECT systems now incorporate a CT module (i.e. SPECT/CT) to visualize the patient's anatomy for registration with the radionuclide distribution. The attenuation of the CT X-ray source can also be used to correct the SPECT images for tissue attenuation [2]. Three different transverse section planes through the body are shown in Figure 3.6b. The coronal plane slices the body from anterior to posterior (front to back); the sagittal plane slices the body from lateral to medial (left to right); and the transaxial plane sections the body from the head to feet. Other tomographic images obtained at angles to the body are used for myocardial imaging (e.g. oblique images).

3.5 Positron Emission Tomography

PET is a tomographic imaging technology that detects the two 511 keV γ-photons simultaneously created by the annihilation of a positron by interaction with an electron in tissues (Figure 3.7a) [2]. These γ-photons travel out at ~180° to each other and are detected by two opposing scintillation crystals. The positron travels a small distance in tissue before interacting with an electron, which depends on the energy of the positron. For example, the moderate-energy positron emitted by ^{18}F ($E\beta^+$ = 0.6 MeV) travels 0.7 mm before being annihilated, while the high-energy positron emitted by ^{124}I ($E\beta^+$ = 0.6 MeV) travels 2.3 mm. This finite distance traveled by the positron contributes to uncertainty in precisely locating the position of the decay event, and leads to decreased image resolution. Thus, images obtained with ^{124}I are poorer resolution than those obtained with ^{18}F (Table 3.3). In PET, a ring of scintillation crystals surrounds the patient (Figure 3.7b). If two opposing crystals detect interaction of a 511 keV γ-photon within a very short time period (5–10 ns), this is registered by an annihilation coincidence detection (ACD) circuit as a "true" coincidence (Figure 3.7b) and a line-of-response (LOR) is established between these two opposing crystals [2]. The LOR will pass through the location of the positron decay. Multiple LOR are established due to many positron decays that generate multiple γ-photon coincidences. These LOR will intersect precisely at the location of the positron decay in the patient and this information is used by the computer to form PET images. Unlike SPECT, no collimation is required in

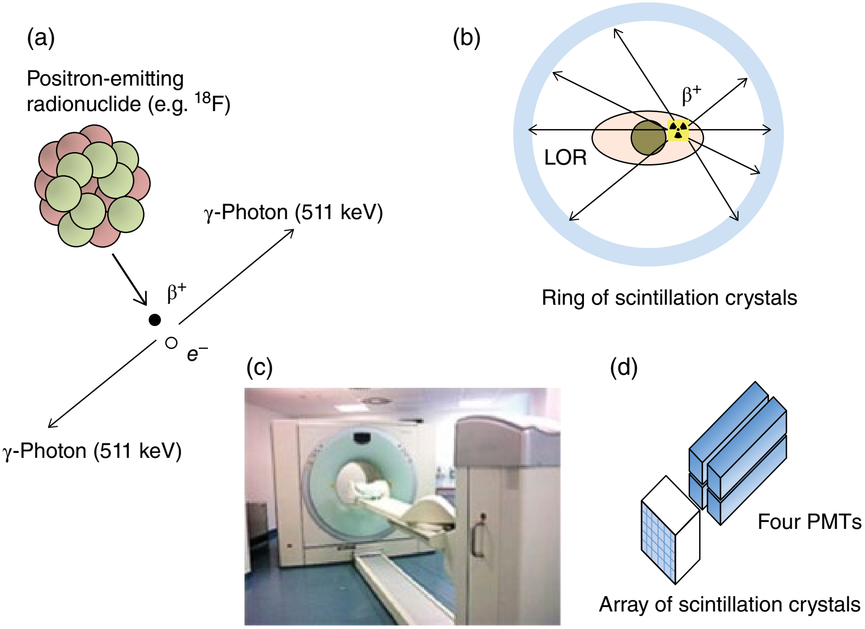
(a)
Positron-emitting
radionuclide (e.g. ^{18}F)
γ-Photon (511 keV)
β+
e−
γ-Photon (511 keV)
(b)
β+
LOR
Ring of scintillation crystals
(c)
(d)
Four PMTs
Array of scintillation crystals

Figure 3.7 (a) Decay of a positron-emitting radionuclide (e.g. ^{18}F) results in the emission of a positron (β^+), which quickly interacts with an electron (e^-) in tissues and is annihilated (destroyed). Annihilation of the positron creates two 511 keV γ-photons, which travel out at ~180° to one another. (b) In positron emission tomography (PET), coincidence detection of these two 511 keV γ-photons resulting from positron decay, by two opposing crystals in a ring of scintillation crystals surrounding the patient generates a line-of-response (LOR). Multiple LOR generated by different positron annihilation events intersect at the position of the radioactive decay and this information is used to produce the PET image. (c) A modern PET/CT tomograph. Source: https://en.wikipedia.org/wiki/PET-CT. (d) The ring of scintillation crystals in PET is composed of an array of small, divided scintillation crystals interfaced each with a series of four photomultiplier tubes (PMTs) that deduce the signal from each of the crystal elements. The array of scintillation crystals has been separated from the PMTs in the figure for clarity, but these are in fact in contact with each other.

PET although collimation is sometimes used in the detector design to eliminate scattered γ-photons from being detected (see Section 3.5.1). Since there is no collimator used in PET, this dramatically increases the sensitivity compared to SPECT. In addition to true coincidences, there may also be “random” coincidences as well as scattered coincidences detected by the scintillation crystals, which cause artifacts in the image and degrade image quality [2]. Random coincidences occur when by chance, two 511 keV γ-photons simultaneously interact with two opposing crystals, but each γ-photon actually originates from a different positron decay at different locations in the body. Thus, the LOR established by interaction of these random coincidences with the two opposing crystals will not pass through the location of the positron decay, but causes artifacts in the image. Scattered coincidences occur when γ-photons scattered by tissues in the patient interact with two opposing crystals generating a LOR, which again does not pass through the location of the positron decay. Scattered γ-photons have energies lower than 511 keV and can be eliminated by the computer using energy discrimination with a MCA as described earlier for the gamma camera (Section 3.3).

3.5.1 Design of the PET Tomograph

The PET tomograph detector incorporates a ring of scintillation crystals that surround the patient (Figure 3.7c) [2]. As mentioned earlier, the material used for scintillation crystals for PET is BGO, LYSO, LSO, or GSO (Table 3.1) due to their superior ability to absorb the high-energy 511 keV annihilation γ-photons [1]. GSO and BSO have shorter decay times than BGO, and are more commonly used as detectors (Table 3.1). Image resolution depends on the size of the scintillation crystals, with better resolution obtained as the crystal size is decreased. However, there is a limit to the size and number of crystals that can be feasibly incorporated into the detector. Thus, in modern PET tomograph designs, a larger crystal element is subdivided into an array of small segments and interfaced with four PMTs (Figure 3.7c) [2]. The use of this array of small segments in a single crystal element provides spatial resolution similar to very small crystals. The precise location of the γ-photon interaction in individual crystal segments is deduced by monitoring the signal intensity sensed by the PMTs across the array of segments, analogous to the *X*,*Y*-circuit used in the gamma camera (Section 3.3). In order to image a section of the body, PET tomographs incorporate multiple rings of detectors along the axial direction and the patient is advanced through these rings of detectors on a moving bed. To separate the individual slices acquired by each ring of detectors and avoid any scattered coincidences caused by positron decay in neighboring slices, PET tomographs may incorporate thin tungsten collimators between each ring of detectors [2]. The images created by each ring are ultimately assembled into a three-dimensional image of the body. Images are also corrected for tissue attenuation, which is achieved using the CT X-ray in PET/CT systems. Following acquisition of the images, tomographic sections are reconstructed by similar mathematical algorithms as in SPECT (Section 3.4).

3.5.2 Time-of-Flight PET

In theory, it is possible to determine the precise location of a positron decay by determining the time taken for each of the two 511 keV γ-photons to reach the two opposing detectors without relying on the intersection of multiple LOR [2].

Since the γ-photons travel at the speed of light ($3 \times 10^8\,\mathrm{m\,s^{-1}}$), extremely rapid decay times for the scintillation crystals are required to differentiate interactions of the two γ-photons with opposing crystal elements. LSO and LYSO crystals offer the possibility of time-of-flight (TOF) PET. Image reconstruction is not required with TOF-PET and image resolution is improved.

3.6 Multimodality Imaging – SPECT/CT, PET/CT, and PET/MR

Most nuclear medicine systems combine SPECT or PET imaging with anatomical imaging obtained by CT (Figure 3.8a) or magnetic resonance imaging (MR) (Figure 3.8b). These systems co-register the CT and MR images with the SPECT or PET image to provide anatomical reference for the distribution of the radiopharmaceutical in the patient. This aids the radiologist in determining the anatomical location of the radioactivity, which helps in diagnosing disease.

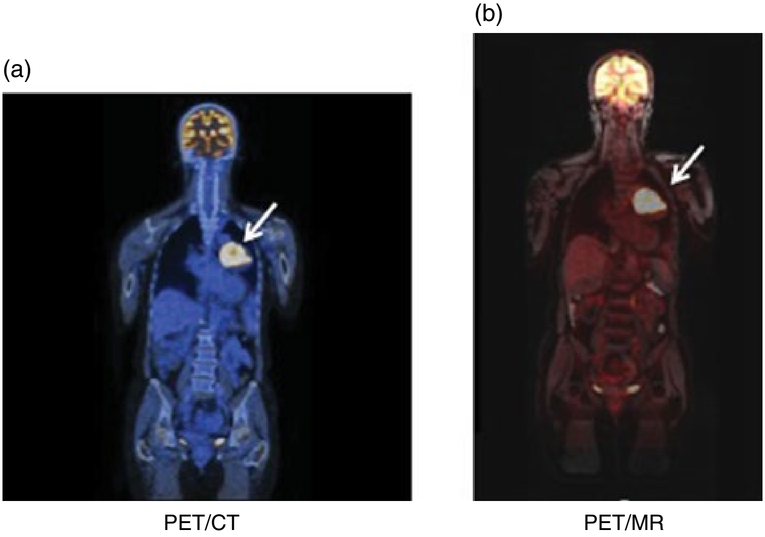

Figure 3.8 (a) PET/CT combines functional and molecular imaging obtained by PET with the high spatial resolution anatomical imaging provided by CT. A whole-body CT image was co-registered with the PET image obtained with ^{18}F-2-fluorodeoxyglucose (^{18}F-FDG) in a patient with lung cancer (arrow) to provide a multimodality PET/CT image. (b) PET/MR similarly combines PET with high spatial resolution MR images. A whole-body PET image obtained with ^{18}F-FDG was co-registered with the MR image of a patient with lung cancer (arrow) to provide a multimodality PET/MR image. Source: Images provided by Dr. Patrick Veit-Haibach, Joint Department of Medical Imaging, University Health Network, Toronto, Canada. (*See insert for color representation of the figure.*)

As mentioned earlier, the X-ray in the CT module in PET/CT is also used to correct the PET images for tissue attenuation. Spatial registration artifacts may occur in SPECT/CT and PET/CT imaging due to slight patient movement between the CT and radionuclide images. A technical problem with PET/MR systems is that the PMTs used in the PET detectors are adversely affected by the strong magnetic field used for MR (see Chapter 5). To avoid this problem, PET/MR systems may employ avalanche diode detectors which is a detector design not affected by the magnetic field instead of PMTs, or the PET and MR modalities may be physically separated by about 2 m to avoid the negative effects of the magnetic field on the PMTs [2].

3.7 Summary

Nuclear medicine imaging technology employs a gamma camera for SPECT imaging of single γ-photon-emitting radionuclides or a PET tomograph to image positron-emitting radionuclides. The gamma camera forms images by scintillation detection of γ-photons combined with an *X,Y*-circuit to deduce the position of the radioactive decay. Collimation and energy discrimination is used to avoid detection of scattered γ-photons. PET relies on coincidence detection of the two 511 keV γ-photons produced by the annihilation of a positron by interaction with an electron in tissues. Coincidence detection generates a LOR that passes through the point of positron annihilation. Intersection of multiple LOR from many positron annihilation events precisely localizes the position of the radioactive decay. PET does not require collimation and is much more sensitive than SPECT. Both SPECT and PET are now combined with CT or MR to co-register the functional and molecular imaging provided by these nuclear medicine technologies with the high spatial resolution anatomical imaging provided by CT and MR.

References

1 Saha, G.B. (2010). Instruments for radiation detection and measurement. In: *Fundamentals of Nuclear Pharmacy*, 6e. New York: Springer.

2 Bushberg, J.T., Seibert, J.A., Leidholdt, E.M. Jr., and Boone, J.M. (2012). Nuclear imaging – emission tomography. In: *The Essential Physics of Medical Imaging*, 3e, 705–748. Philadelphia, PA: Lippincott Williams & Wilkins.

3 Bushberg, J.T., Seibert, J.A., Leidholdt, E.M. Jr., and Boone, J.M. (2012). Nuclear imaging – the scintillation camera. In: *The Essential Physics of Medical Imaging*, 3e. Philadelphia, PA: Lippincott Williams & Wilkins.

4 Myers, W.G. (1979). The Anger scintillation camera becomes of age. *J. Nucl. Med.* 20: 565–567.

5 Brant, W.E. and Helms, C.A. (2012). Gastrointestinal, liver–spleen, and hepatobiliary scintigraphy. In: *Fundamentals of Diagnostic Radiology*, 4e, 1309. Philadelphia, PA: Wolters-Kluwer.
6 Szmit, S., Nurzyński, P., Szaluś, N. et al. (2009). Reversible myocardial dysfunction in a young woman with metastatic renal cell carcinoma treated with sunitinib. *Acta Oncol.* 48: 921–942.
7 Sfakianakis, G.N., Cohen, D.J., Braunstein, R.H. et al. (2000). MAG3-F0 scintigraphy in decision making for emergency intervention in renal colic after helical CT positive for a urolith. *J. Nucl. Med.* 41: 1813–1822.

Noor Al-saden

Noor Al-saden is a PhD student in the Graduate Department of Pharmaceutical Sciences at the Leslie Dan Faculty of Pharmacy, University of Toronto. She holds a Master of Science in Pharmaceutical Technology from King's College London, London, United Kingdom and a Bachelor of Science in Pharmacy from the University of Sharjah, Sharjah, United Arab Emirates. She joined the Laboratory of Molecular Imaging and Targeted Radiotherapeutics team under the supervision of Dr. Raymond Reilly to pursue her PhD studies. Her research focuses on developing PET molecular imaging probes for predicting response or resistance to antibody–drug conjugates in patients with HER2-positive metastatic breast cancer.

Medical Imaging for Health Professionals: Technologies and Clinical Applications, First Edition.
Edited by Raymond M. Reilly.
© 2019 John Wiley & Sons, Inc. Published 2019 by John Wiley & Sons, Inc.

4

Radionuclide Production and Radiopharmaceuticals

Noor Al-saden and Raymond M. Reilly

4.1 Introduction

Radiopharmaceuticals are agents used in nuclear medicine (see Chapter 3) composed of a radionuclide linked to a carrier molecule, which selectively delivers the radionuclide to an organ or disease site mainly for the purpose of diagnostic imaging (Figure 4.1) or in some cases for radiotherapeutic applications. The radionuclide most often has no organ or disease selectivity, but relies on the carrier molecule for this property. There are a few cases in which a radionuclide has organ selectivity, e.g. thyroid imaging with ^{99m}Tc pertechnetate or ^{123}I/^{131}I sodium iodide. However, the physical properties of the radionuclide, especially its radiation emissions (see Chapter 3), are important for the clinical application of the radiopharmaceutical – gamma (γ) or positron (β^+) emissions are needed for imaging, while beta (β-) emissions are used for treatment of disease (e.g. cancer). The physical half-life ($t_{1/2p}$) of the radionuclide is also an important consideration since it must be sufficiently long to permit imaging at the time postinjection when the radiopharmaceutical exhibits optimal localization in the organ or disease site of interest, but should not be too long, since this unnecessarily increases the radiation dose for a diagnostic imaging procedure. Generally, radionuclides used for imaging studies with radiopharmaceuticals have $t_{1/2p}$ of only a few hours to a few days. In this chapter, we will discuss the production of medically-useful radionuclides and the properties and clinical applications of commonly used radiopharmaceuticals in nuclear medicine.

Medical Imaging for Health Professionals: Technologies and Clinical Applications, First Edition.
Edited by Raymond M. Reilly.
© 2019 John Wiley & Sons, Inc. Published 2019 by John Wiley & Sons, Inc.

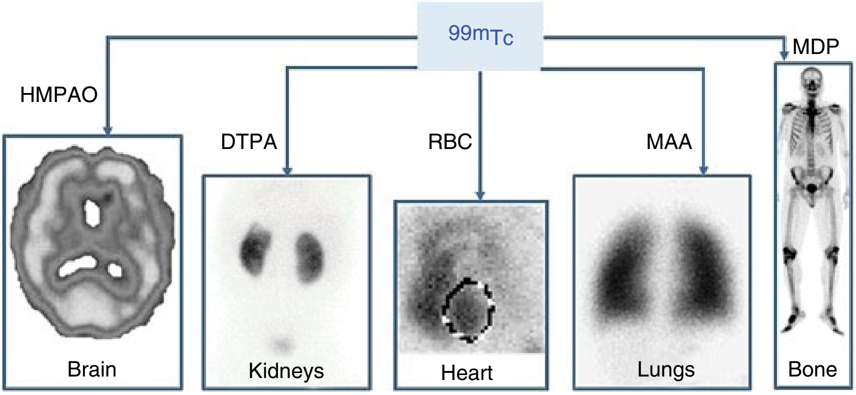

Figure 4.1 The concept of a radiopharmaceutical is illustrated by ^{99m}Tc that has restricted normal organ affinity (mainly thyroid) but may be complexed to HMPAO, a lipophilic chelate, which crosses the blood–brain-barrier, enabling imaging of the brain. ^{99m}Tc may be complexed to DTPA, a water-soluble chelator, which is eliminated renally in order to image the kidneys to evaluate renal function. ^{99m}Tc may be linked to a patient's red blood cells (RBCs) to provide a blood pool marker to assess the ejection fraction in the heart. ^{99m}Tc may be linked to a macroaggregated albumin particle that is trapped in the capillaries of the lungs in order to assess the lungs for pulmonary embolism. Finally, ^{99m}Tc may be complexed by a bisphosphonate and used to image the bones to identify fractures, osteomyelitis, or metastases of cancer to the bone.

4.2 Production of Radionuclides

Radionuclides for medical imaging may be produced in a reactor, cyclotron, or by using a radionuclide generator system. In a reactor, a stable target element is irradiated with neutrons to produce a radionuclide or alternatively uranium (e.g. ^{235}U) undergoes fission caused by neutrons to produce a series of daughter radionuclides, some of which are medically useful. Medical cyclotrons are becoming more commonplace and have the capability to produce radionuclides locally in a hospital, especially short-lived positron-emitting radionuclides (e.g. ^{18}F; half-life [$t_{1/2p}$] = 2 hours). Cyclotron production of radionuclides involves irradiation of a stable target element with high-energy protons or deuterons. Radionuclide generator systems rely on the production of a short-lived daughter radionuclide by the decay of a longer-lived parent radionuclide (e.g. ^{99m}Tc [$t_{1/2p}$ = 6 hours] is produced from ^{99}Mo [$t_{1/2p}$ = 66 hours]). These systems also permit local production of the radionuclide, since the generator incorporating the longer-lived parent radionuclide may be shipped to a hospital, where it then locally produces the short-lived daughter radionuclide. Longer-lived radionuclides are most commonly produced by a radiopharmaceutical company either using a cyclotron or reactor and then shipped to a hospital for radiopharmaceutical preparation. Alternatively, the final radiopharmaceutical preparation may be prepared by the company and shipped to the hospital.

4.2.1 Reactor Production

Radionuclides may be produced in a reactor (Figure 4.2a) through the fission of ^{235}U by neutrons (*n, f*) or by neutron irradiation of a stable target element (*n, γ*). ^{235}U undergoes spontaneous fission to produce two series of fission products (Figure 4.2b) with the release of two or three fission neutrons and high thermal energy (200 MeV). These neutrons then cause the fission of other ^{235}U atoms sustaining the nuclear chain reaction and resulting in repeated production of fission products. The chain reaction is moderated by insertion of control rods composed of cadmium or boron into the reactor, which absorb neutrons. The fission products decay to daughter radionuclides or stable elements in complex decay schemes. Iodine-131 (^{131}I), molybdenum-99 m (^{99}Mo, which decays to ^{99m}Tc), and strontium-90 (^{90}Sr, which decays to ^{90}Y) are examples of medically-useful fission-produced radionuclides. These radionuclides are chemically purified from other fission products but trace amounts of radionuclide impurities may still be found (e.g. ^{131}I

(a)

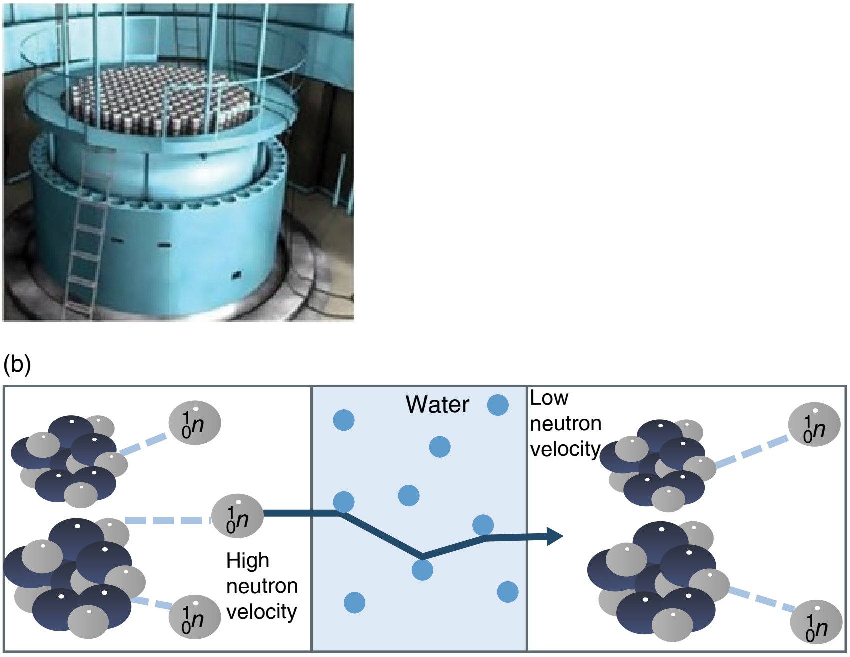

$$^{235}_{92}\mathrm{U} + {}^{1}n \rightarrow {}^{236}\mathrm{U} \rightarrow {}^{131}_{53}\mathrm{I} + {}^{102}\mathrm{Y} + 3\,{}^{1}_{0}n \rightarrow {}^{99}_{42}\mathrm{Mo} + {}^{135}\mathrm{Sn} + 2\,{}^{1}_{0}n$$

Figure 4.2 (a) Some radionuclides are produced in a nuclear reactor through neutron activation of a stable element or by fission of ^{235}U. (b) Fission of ^{235}U by neutrons results in the production of many different fission products, some of which are medically useful. These include ^{131}I and ^{99}Mo.

may be present in ^{99}Mo, and thus may be detected in trace amounts in ^{99m}Tc eluates obtained from a ^{99}Mo/^{99m}Tc generator). In neutron irradiation, the radionuclide is produced when a stable target element is irradiated with neutrons leading to the addition of one neutron to the nucleus of the atom (increase of one atomic mass unit [AMU]) and the emission of γ rays. Since the radionuclide produced is the same element as the target, but only having a different atomic mass, purification is normally not required. However, chemical and isotopic impurities in the stable target element may result in the production of radionuclide impurities through side-reactions, which may require removal or sometimes waiting for a sufficient time to allow for their complete decay (if the radionuclide impurities have a much shorter $t_{1/2}$ than the desired radionuclide). Another limitation of radionuclide production by neutron irradiation is that the specific activity (SA; the amount of radioactivity per unit mass) is low, since most atoms remain in a stable form with only a fraction being converted to the radionuclide. This low SA may cause challenges in achieving a high radiolabeling efficiency of the carrier molecule to prepare the radiopharmaceutical. This problem has been found for neutron-produced ^{99}Mo [^{98}Mo(n, γ)^{99}Mo] used to construct a ^{99}Mo/^{99m}Tc generator. Low SA neutron-produced ^{99}Mo is more likely to cause ^{99}Mo "breakthrough" in eluting ^{99m}Tc, resulting in contamination of the ^{99m}Tc eluate with ^{99}Mo, since the alumina column used may not be able to bind all molybdenum atoms loaded onto the column (both stable ^{98}Mo and radioactive ^{99}Mo). This problem is very rare with generators constructed using fission-produced ^{99}Mo, since this form is carrier-free (no stable ^{98}Mo) and has very high SA. Some common examples of neutron-produced radionuclides are ^{99}Mo, ^{186}Re, ^{188}Re, ^{177}Lu, ^{67}Cu, and ^{131}Te, which decay to produce ^{131}I (Table 4.1). Since radionuclides produced in a reactor by neutron irradiation have an excess of neutrons, they decay by β^- emission, which converts a neutron into a proton with the simultaneous emission of a neutrino ($\bar{\nu}$): $n \rightarrow p + \beta^- + \bar{\nu}$. The result of this decay is no change in the mass number but an increase in the atomic number by one unit, which produces a different daughter element (next element in the Periodic Table). For example, ^{177}Lu decays to hafnium-177 (^{177}Hf) by β^- emission:

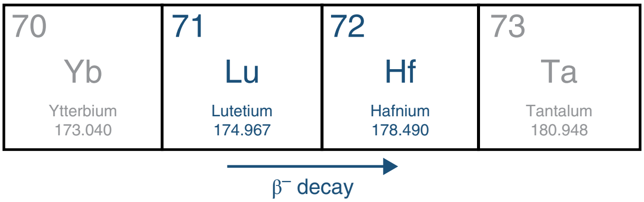

$$^{177}_{71}\text{Lu} \rightarrow \, ^{177}_{70}\text{Hf} + \beta^- + \bar{\nu}$$

Table 4.1 Production of radionuclides by neutron irradiation.

Radionuclide	Production	$t_{1/2p}$	Decay product	Radiation emissions (energy [abundance])
^{99}Mo	^{98}Mo(n, γ)^{99}Mo	66 h	^{99m}Tc	β^- (1.2 MeV [87.5%]), γ (740 keV [12.3%]), γ (778 keV [4.3%]), γ (181 keV [6.1%])
^{186}Re	^{185}Re(n, γ)^{186}Re	89 h	^{186}W	β^- (1.069 MeV [71%]), β^- (932 keV [21%]), γ (137 MeV [21%]), EC (582 MeV [5.8%])
^{188}Re	^{187}Re(n, γ)^{188}Re	17 h	^{188}Os	β^- (2.12 MeV [71.1%]), β^- (1.96 MeV [25.6%]), γ (155 keV [15%])
^{177}Lu	^{176}Lu(n, γ)^{177}Lu	6.6 d	^{177}Hf	β^- (498 keV [79%]), β^- (385 keV [9.1%]), β^- (177 keV [11.6%]), γ (113 keV [20%]), γ (208 keV [11%])
^{67}Cu	^{66}Zn(p, $2p$)^{67}Cu	2.6 d	^{67}Zn	β^- (477 keV [20%]), β^- (486 keV [35%]), β^- (395 keV [45%]), γ (91 keV [7%]), γ (93 keV [17%]), γ (184 keV [47%])
^{131}Te	^{130}Te(n, γ)^{131}Te	25 min	^{131}I	β^- (2.23 MeV [100%])

Since the decay product following β-emission remains unstable, there is often release of excess energy as γ radiation.

4.2.2 Cyclotron Production

A cyclotron (Figure 4.3) is an instrument used to produce radionuclides through the interaction of high-energy atomic particles (e.g. protons or deuterons) with the nucleus of a stable element. A medical cyclotron can be housed in a room about the size of a small bedroom, and these instruments are becoming more commonplace in major hospitals with active nuclear medicine departments, that routinely provide positron emission tomography (PET) imaging studies (see Chapter 3). In most cases, a proton source (H^+) is generated in the cyclotron by extraction of an electron from hydrogen gas, and the proton is then accelerated in an expanding circular path across a gap between two powerful D-shaped electromagnets that alternately change their polarity. The protons gain energy each time they pass across the gap between the electromagnets, reaching very high energies (e.g. 11 MeV). Ultimately, the protons are focused on a target element, which gains one proton, converting the target element to a radioactive element with an atomic number one unit higher than the target. Often, during the production of the radionuclide, neutrons are also released, so the cyclotron room is shielded with concrete to absorb these neutrons. An example of a cyclotron-produced radionuclide is fluorine-18 (^{18}F),

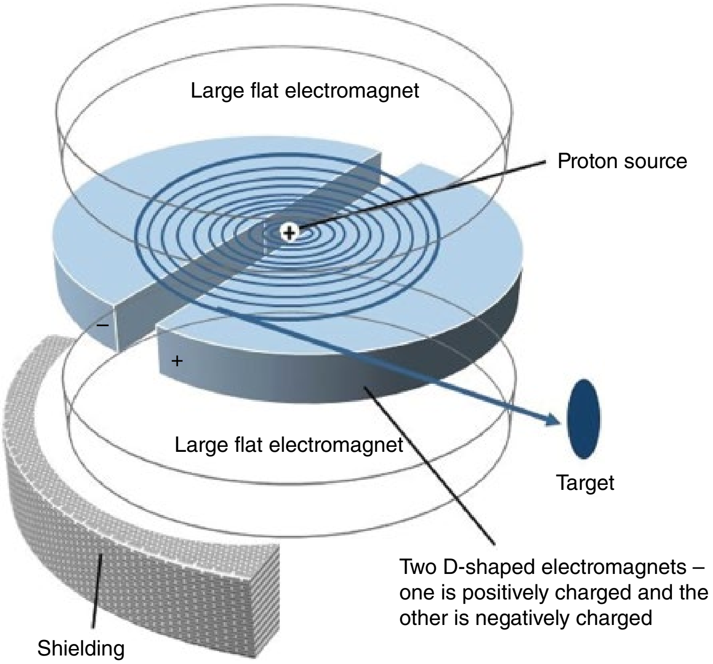
Large flat electromagnet
Proton source
−
+
Large flat electromagnet
Target
Two D-shaped electromagnets – one is positively charged and the other is negatively charged
Shielding

Figure 4.3 A cyclotron accelerates charged particles, usually protons, across a gap between two powerful electromagnets. Once the protons have acquired sufficient energy, they are used to bombard a stable target element, resulting in the addition of one proton to the nucleus of the element, thereby creating a new element, which is unstable and radioactive. Cyclotron-produced radionuclides decay by positron emission, which converts a proton to a neutron through the emission of a positively-charged electron (positron), or by electron capture, in which a proton captures an inner orbital electron converting the proton into a neutron.

which is produced by interaction of protons with oxygen-18 water: $^{18}O(p,n)^{18}F$. It is important that the target element be chemically and isotopically pure, since interaction of protons with impurities may generate radionuclide impurities through side-reactions. It is interesting to note that in the production of ^{18}F, isotopically pure ^{18}O water must be used, but ^{18}O represents only 0.2% of naturally occurring oxygen! Thus, pure ^{18}O water is very expensive, costing hundreds of dollars per milliliter. Target elements used to produce other radionuclides in a cyclotron are also very expensive due to the requirement for rare and isotopically pure elements. Cyclotron targets may be constructed in an aqueous, solid, or gas form. Solid targets may be designed as a foil, disk, or powder. Targets need to be cooled since excessive heat is generated by the high-beam current during the production of the radionuclide, and this can be challenging for gas targets, which do not dissipate heat as easily as solid or liquid targets. The radionuclide produced is extracted by ion exchange, solvent extraction, precipitation, or distillation and the target element is recovered and reused to generate radionuclides, due to its high cost.

Since radionuclides produced in a cyclotron have an excess of protons, they often decay by positron (β^+) emission, which converts a proton into a neutron with the simultaneous emission of an anti-neutrino (ν): $p \rightarrow n + \beta^+ + \nu$. The result of this decay is no change in the mass number but a decrease in the atomic number by one unit, which regenerates the same target element used to produce the radionuclide, i.e. the previous element in the Periodic Table. For example, ^{18}F decays to ^{18}O by β^+ emission:

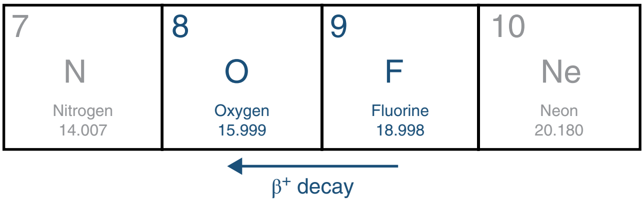

$$^{18}_{9}F \rightarrow {}^{18}_{8}O + \beta^+ + \nu$$

Alternatively, some radionuclides produced in a cyclotron decay by electron capture (EC). In EC, a proton in the nucleus captures an electron from an inner orbital shell, converting the proton into a neutron: $p + e^- \rightarrow n$. Again, this decreases the atomic number by one unit but with no change in the mass number and regenerates the target element used to produce the radionuclide (i.e. the previous element in the Periodic Table). For example, ^{111}In is produced in a cyclotron by the $^{111}Cd(p,n)^{111}In$ reaction and then decays back to ^{111}Cd by EC:

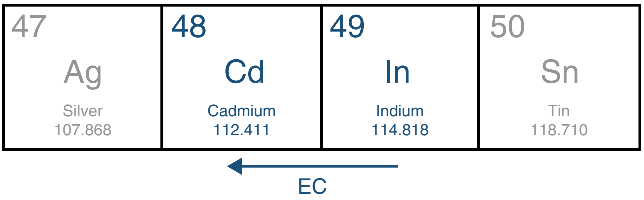

$$^{111}_{49}\mathrm{In} \xrightarrow{\mathrm{EC}} {}^{111}_{48}\mathrm{Cd}$$

Some common examples of cyclotron-produced radionuclides are ^{11}C, ^{13}N, ^{15}O, ^{18}F, ^{67}Ga, ^{201}Tl, ^{111}In, ^{64}Cu, and ^{123}I (Table 4.2).

4.2.3 Generator Production

The concept of producing radionuclides using a generator system is very attractive and is based on the long and successful experience in producing ^{99m}Tc using the $^{99}Mo/^{99m}Tc$ generator. ^{99m}Tc decays to ^{99}Tc with a $t_{1/2p}$ of 6 hours

Table 4.2 Production of radionuclides in a cyclotron.

Radionuclide	Production	$t_{1/2p}$	Decay product	Radiation emissions (energy [abundance])
^{11}C	$^{11}B(p, n)^{11}C$ $^{10}B(d, n)^{11}C$ $^{14}N(p, \alpha)^{11}C$	20.3 min	^{11}B	β^+ (960.5 keV [99.8%]), γ (511 keV [200%]), EC (1982.5 keV [0.25%])
^{13}N	$^{12}C(d, n)^{13}N$ $^{16}O(p, \alpha)^{13}N$	10 min	^{13}C	β^+ (1198.4 keV [99.8%]), γ (511 keV [200%]), EC (2220.4 keV [0.18%])
^{15}O	$^{14}N(d, n)^{15}O$	123 s	^{15}N	β^+ (1735 keV [99.8%]), γ (511 keV [200%]), EC (2757 keV [0.11%])
^{18}F	$^{16}O(p, n)^{18}F$ $^{16}O(^{3}He, 3n)^{18}F$	109.7 min	^{18}O	β^+ (633.5 keV [96.8%]), γ (511 keV [194%]), EC (1655.5 keV [3.1%])
^{67}Ga	$^{67}Zn(p, n)\ ^{67}Ga$ $^{65}Cu(\alpha, 2n)\ ^{67}Ga$	77.9 h	^{67}Zn	γ (184 keV [21%]), γ (93 keV [70%]), γ (300 keV [16.9%]), γ (393 keV [4.7%]), EC (907.6 keV [50%]), EC (607 keV [24%])
^{201}Tl	$^{203}Pb(p, 3n)\ ^{201}Tl$	74 h	^{201}Hg	γ (135.5 keV [11.6%]), γ (167 keV [28.9%]), EC (316 keV [41%]), EC (482 keV [25%])
^{111}In	$^{111}Cd(p, n)\ ^{111}In$ $^{109}Ag(\alpha, 2n)\ ^{111}In$	2.8 d	^{111}Cd	EC (445 keV [100%]), γ (171 keV [100%]), γ (245 keV [100%])
^{64}Cu	$^{64}Ni(p, n)^{64}Cu$	12 h	^{64}Ni, ^{64}Zn	β^- (579 keV [39%]), β^+ (653 keV [18%]), EC (1675 keV [43%]), γ (1346 keV [0.47%])
^{123}I	$^{122}Te(d, n)\ ^{123}I$	13.3 h	^{123}Te	EC (1075 keV [97%]), γ (159 keV [99%])

emitting highly abundant γ-rays (140 keV [99%]) that are ideal for single photon emission computed tomography (SPECT) imaging using a gamma camera (see Chapter 3). The ^{99}Tc decay product of ^{99m}Tc is almost a stable element, because its $t_{1/2p}$ is 200 000 years! Many carrier molecules can be easily labeled with ^{99m}Tc to produce radiopharmaceuticals (e.g. Figure 4.1) and the short $t_{1/2p}$ minimizes the radiation dose to a patient. However, this short $t_{1/2p}$ presents a major challenge for maintaining a continuous and readily available supply of ^{99m}Tc for radiopharmaceutical preparation. Fortunately, Powell Richards and Walter Tucker at Brookhaven National Laboratory in the United States invented the ^{99}Mo/^{99m}Tc generator in 1960, which enables daily production of ^{99m}Tc in high yield and purity in a nuclear pharmacy for more than a week before the generator must be replaced. The original ^{99}Mo/^{99m}Tc generator designed by Powell and Richards and a modern version of the generator are shown in Figure 4.4a and b, respectively. As mentioned earlier, the generator principle is based on the decay–growth relationship between a long-lived parent radionuclide and its daughter, in this case ^{99}Mo ($t_{1/2p} = 66$ hours) and ^{99m}Tc ($t_{1/2p} = 6$ hours), respectively. The useful lifetime of a generator system is approximately three to four half-lives of the parent radionuclide, i.e. about 7–10 days for the ^{99}Mo/^{99m}Tc generator. To obtain a pure daughter radionuclide, the chemistry of the parent and daughter should be different to allow chromatographic separation. The major advantage of a generator system is the ability to ship a source of a short-lived radionuclide to nuclear medicine facilities that do not have local access to a cyclotron or reactor-produced radionuclides. Modern ^{99}Mo/^{99m}Tc generators reliably produce ^{99m}Tc as a sterile, non-pyrogenic solution of ^{99m}Tc sodium pertechnetate (^{99m}TcO$_4^-$), which is used for the preparation of injectable ^{99m}Tc radiopharmaceuticals. The ^{68}Ge/^{68}Ga and ^{82}Sr/^{82}Rb generators (Figure 4.5) have been developed for the production of positron-emitting radionuclides to enable PET imaging without access to a cyclotron. The ^{99}Mo/^{99m}Tc generator and these other generator systems are described in more detail in the next sections.

4.2.3.1 ^{99}Mo/^{99m}Tc Generator

The ^{99}Mo/^{99m}Tc generator (Figure 4.4b) is the most commonly used generator system in nuclear medicine. The parent radionuclide, ^{99}Mo ($t_{1/2p} = 66$ hours), decays by a combination of β^- and γ-emission to the daughter, ^{99m}Tc ($t_{1/2p} = 6$ hours). The ^{99}Mo is strongly adsorbed as sodium molybdate onto an alumina chromatography column. ^{99m}Tc builds up on the column reaching a maximum after about four half-lives (~24 hours). After 24 hours, there is equilibrium between ^{99}Mo decay and ^{99m}Tc production, such that the yield of ^{99m}Tc obtainable from the generator decreases with the half-life of the parent radionuclide (Figure 4.4c), ^{99}Mo. As mentioned earlier, the useful lifetime of a ^{99}Mo/^{99m}Tc generator is three to four half-lives of ^{99}Mo (7–10 days), beyond which the yield of ^{99m}Tc is impractical for the production of radiopharmaceuticals. Since ^{99m}Tc has different chemistry than ^{99}Mo, it does not remain bound to the alumina column and is readily eluted by passing sterile normal saline through the column, leaving the ^{99}Mo bound to the column to produce more ^{99m}Tc. The eluate is passed through a 0.22 μm sterilizing filter and collected into an evacuated, lead-shielded glass multidose vial (Figure 4.4d). More than 100 GBq of ^{99m}Tc can be eluted from a ^{99}Mo/^{99m}Tc generator, but the yield decreases each day until the generator is no longer useful and must be replaced. Quality control testing of the ^{99m}Tc eluate includes an assay to determine ^{99}Mo "breakthrough," i.e. the proportion of ^{99}Mo present in the eluate, and alumina "breakthrough," which measures the concentration of alumina ions in the eluate. ^{99}Mo radionuclide impurities are required to be very low (<0.03 kBq ^{99}Mo/MBq ^{99m}Tc)

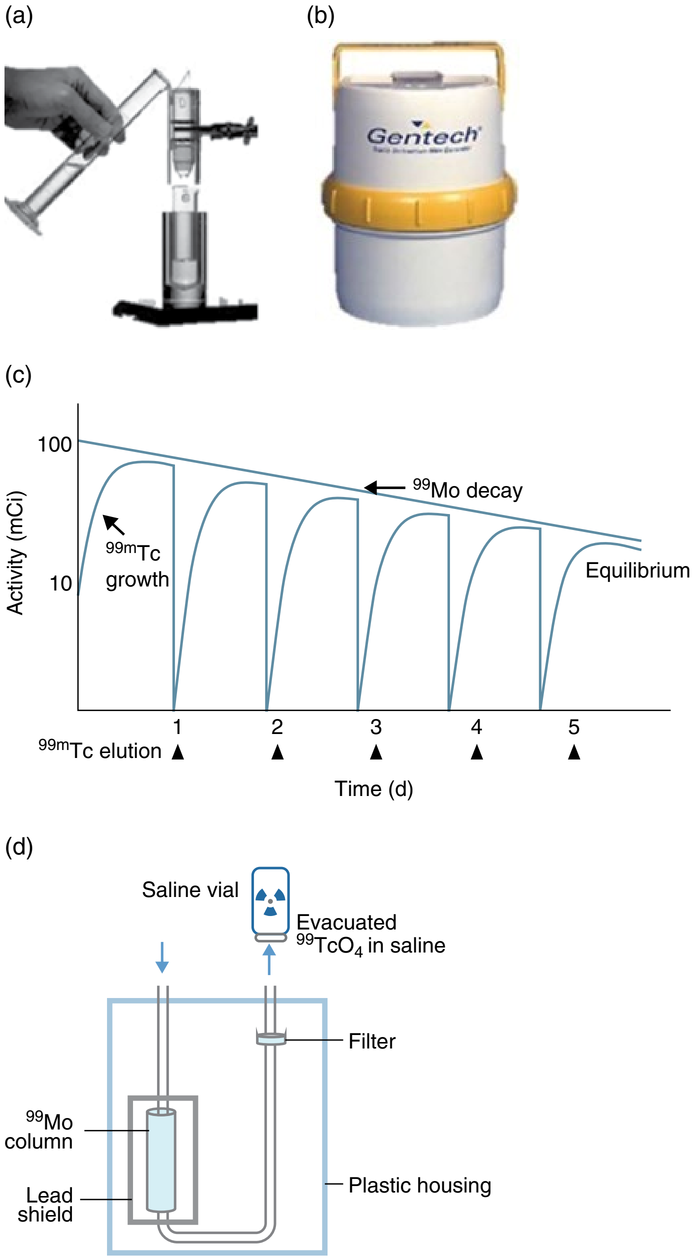
(a)
(b)
Gentech
(c)
100
10
Activity (mCi)
^{99m}Tc growth
^{99}Mo decay
Equilibrium
1
2
3
4
5
^{99m}Tc elution ▲ ▲ ▲ ▲ ▲
Time (d)
(d)
Saline vial
Evacuated $^{99}TcO_4$ in saline
Filter
^{99}Mo column
Lead shield
Plastic housing

Figure 4.4 (a) The original ^{99}Mo/^{99m}Tc generator invented by Powell Richards in 1957. The ^{99}Mo was adsorbed onto an alumina chromatography column and the pure ^{99m}Tc daughter product of ^{99}Mo was obtained by passing normal saline through the column and collecting the eluate in a lead-shielded container. (b) A modern ^{99}Mo/^{99m}Tc generator. (c) The kinetics of buildup of ^{99m}Tc due to decay of ^{99}Mo following each elution of the generator. The yield of ^{99m}Tc will decrease over time due to decay of the ^{99}Mo parent radionuclide and eventually the generator will need to be replaced. (d) The internal schematic for a ^{99}Mo/^{99m}Tc generator showing the alumina column, normal saline port, and collection port for the ^{99m}Tc eluate as well as the sterilizing filter for the eluate.

because they unnecessarily increase the radiation dose to a patient since ^{99}Mo is long-lived ($t_{1/2p}$ = 66 hours) and emits β-radiation and high-energy γ-rays. The limit for alumina ions is <10 µg ml^{-1}, since these interfere with the radiolabeling of some radiopharmaceuticals with ^{99m}Tc (e.g. ^{99m}Tc sulfur colloid). An interesting aspect of the ^{99}Mo/^{99m}Tc generator is that if the generator is not eluted for a few days, there is buildup of the ^{99}Tc decay product of ^{99m}Tc. This decay product adds to the total technetium atoms present in the ^{99m}Tc eluate and may cause low radiolabeling efficiency in the preparation of certain radiopharmaceuticals from kits, especially those kits containing low amounts of stannous chloride (Sn^{2+}), which is used to reduce ^{99m}Tc in order to bind to the carrier molecule. This problem does not occur if the generator is eluted at least every 24 hours, or for kits that contain high amounts of Sn^{2+}.

4.2.3.2 ^{68}Ge/^{68}Ga and ^{82}Sr/^{82}Rb Generators

The ^{68}Ge/^{68}Ga and ^{82}Sr/^{82}Rb generator systems enable local production of positron-emitting radionuclides in a nuclear medicine department without the need for a cyclotron. The ^{68}Ge/^{68}Ga generator (Figure 4.5a) relies on the decay of germanium-68 (^{68}Ge; $t_{1/2p}$ = 271 days) by EC to gallium-68 (^{68}Ga; $t_{1/2p}$ = 68 minutes). ^{68}Ga decays to zinc-68 (^{68}Zn) by positron emission (2.92 MeV [89%]). The parent radionuclide, ^{68}Ge, is adsorbed to stannic dioxide column and the

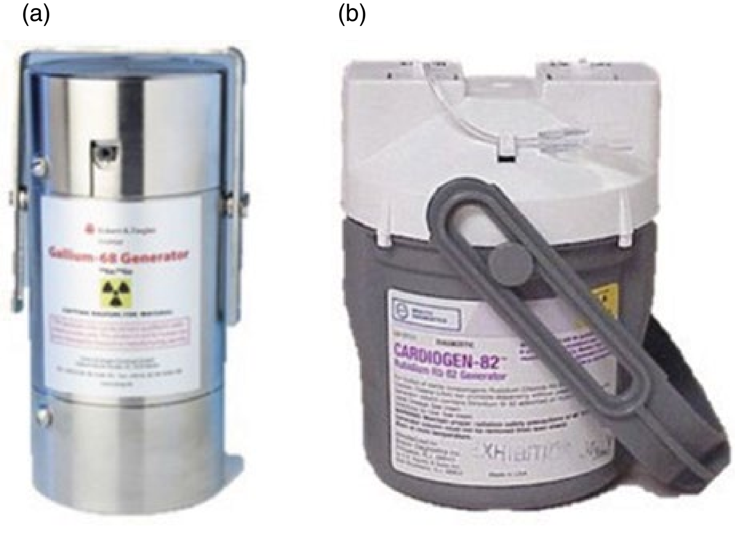

Figure 4.5 (a) A ^{68}Ge/^{68}Ga generator is used to produce the short-lived positron-emitter, ^{68}Ga ($t_{1/2p}$ = 68 minutes), for PET imaging of cancer using ^{68}Ga-labeled peptides. (b) A ^{82}Sr/^{82}Rb generator is used to produce the very short-lived positron-emitter, ^{82}Rb ($t_{1/2p}$ = 75 seconds), for myocardial perfusion imaging using PET.

daughter, ^{68}Ga, is eluted using sterile 1 M HCl. The eluate must be concentrated and neutralized to about pH 6 for labeling of radiopharmaceuticals. The generator may be eluted often, since ^{68}Ga quickly rebuilds to its maximum yield within six hours after a previous elution. The generator has a useful lifetime of more than a year due to the long $t_{1/2p}$ of ^{68}Ge. Although the $t_{1/2p}$ of ^{68}Ga is short (68 minutes), it has been found very useful for radiolabeling of peptides for PET imaging of certain cancers (e.g. ^{68}Ga-DOTATOC for imaging somatostatin receptor-positive tumors).

The ^{82}Sr/^{82}Rb generator (Figure 4.5b) relies on the decay of strontium-82 (^{82}Sr; $t_{1/2p} = 25$ days) by EC to rubidium-82 (^{82}Rb; $t_{1/2p} = 75$ seconds). ^{82}Rb decays to krypton-82 (^{82}Kr) by positron emission (3.15 MeV [95%]). The parent radionuclide, ^{82}Sr, is adsorbed to stannic oxide column and the daughter, ^{68}Ga, is eluted using sterile normal saline. The generator may be eluted frequently since only about 15 minutes are required for buildup of ^{82}Rb on the generator after a previous elution. The generator has a useful lifetime of one to two months. An interesting aspect of the ^{82}Sr/^{82}Rb generator is that since the ^{82}Rb has an extremely short $t_{1/2p}$ (75 seconds), a system has been developed that permits direct infusion of the eluate into the patient. ^{82}Rb is a potassium analog and is avidly accumulated into the myocardium via the Na^+/K^+ ATP-ase transporter in proportion to myocardial blood flow. Thus, ^{82}Rb is employed for myocardial perfusion imaging (MPI) studies using PET.

4.3 Radiopharmaceutical Preparation and Supply

Radiopharmaceuticals are prepared or supplied by two main routes: locally prepared radiopharmaceuticals using kits that can be labeled with a suitable radionuclide (e.g. ^{99m}Tc kits and ^{111}In kits) or commercially prepared finished radiopharmaceuticals (e.g. ^{201}Tl, ^{67}Ga, etc.). Most ^{99m}Tc-labeled radiopharmaceuticals are prepared locally from a kit. The kit consists of the ligand (for ^{99m}Tc complexation), reducing agent, buffer suitable for radiolabeling, stabilizing agent, and excipients. The kit is manufactured by a commercial supplier in a freeze-dried form to ensure long shelf-life at 2–8 °C storage conditions. When the radiopharmaceutical is required for patient administration, the kit will be reconstituted and labeled locally by a nuclear pharmacist or technologist with ^{99m}Tc. The labeling process has to be performed under aseptic conditions inside a laminar air flow hood. After labeling, the final radiopharmaceutical will undergo quality control testing to ensure a high radiochemical purity, sterility, and apyrogenicity. The main advantage of the kit is that radiopharmaceuticals can be prepared using short-lived generator-produced radionuclides quickly when needed at the hospital/imaging facility. Other radiopharmaceuticals, usually labeled with longer-lived radionuclides are supplied by commercial companies in their final form. Before administration to patient, all radiopharmaceuticals are assayed to assure the correct patient dose. Aseptic procedure and radiation shielding are required, while handling and preparing radiopharmaceuticals.

4.4 Radiopharmaceuticals for Cardiac Imaging

Radiopharmaceuticals for cardiac imaging are used to assess regional myocardial blood flow to diagnose ischemia or infarction, to assess left ventricular ejection fraction (LVEF), to detect metabolic abnormalities, such as changes in glucose or fatty acid utilization associated with myocardial ischemia, or to evaluate cardiac innervation implicated in some cardiomyopathies. MPI is used to assess regionally decreased coronary blood flow to differentiate between ischemia that may be treated by angioplasty and infarction, which is not reversible (see Chapter 7). Most MPI utilizes SPECT with ^{99m}Tc radiopharmaceuticals (^{99m}Tc-sestamibi or ^{99m}Tc-tetrofosmin; Figure 4.6) or thallium-201 (^{201}Tl) (Table 4.3). In some cases, PET may be performed using rubidium-82 (^{82}Rb). ^{201}Tl and ^{82}Rb are both K^+ analogs that are taken up by the myocardium via the Na^+/K^+ ATP-ase pump, while the ^{99m}Tc agents are organic cationic complexes of ^{99m}Tc that are passively taken up by the myocardium in proportion to blood flow but are not transported by the Na^+/K^+ ATP-ase pump. Another important difference between ^{201}Tl and the ^{99m}Tc agents is that the ^{99m}Tc agents do not redistribute to poorly perfused areas of the myocardium at rest, thus two separate injections are required to differentiate ischemia from infarction – one injection for the exercise stress or pharmacological stress study, and one for the rest study (see Chapter 7). In contrast, since ^{201}Tl redistributes to poorly perfused (but not infarcted) regions of the myocardium at rest, both the stress and rest studies may be acquired with a single injection of the radiopharmaceutical. Stressing of the myocardium may be achieved by exercise on a treadmill or by administering a pharmacological stress agent (e.g. dipyridamole or adenosine) that dilates non-stenosed blood vessels more than stenosed vessels, thereby revealing poorly perfused regions of the myocardium (see Chapter 7). Infarction may be recognized and differentiated from ischemia as a lesion that remains fixed in the stress and rest studies (i.e. a nonreversible defect; see Chapter 7).

^{99m}Tc-labeled red blood cells (^{99m}Tc-RBCs) may be used to image blood flowing through the ventricles of the heart, which is used to measure the fraction of blood ejected from the left ventricle at end systole (LVEF) (see Chapter 7). These imaging procedures are called MUGA (multigated acquisition) scans since a series of images are obtained coordinated with the ECG events (systole and asystole). The procedures are also known as radionuclide angiography. Decreased LVEF is a dose-limiting side effect of anthracycline chemotherapeutic agents and cancer patients may undergo MUGA scans to assess this toxicity.

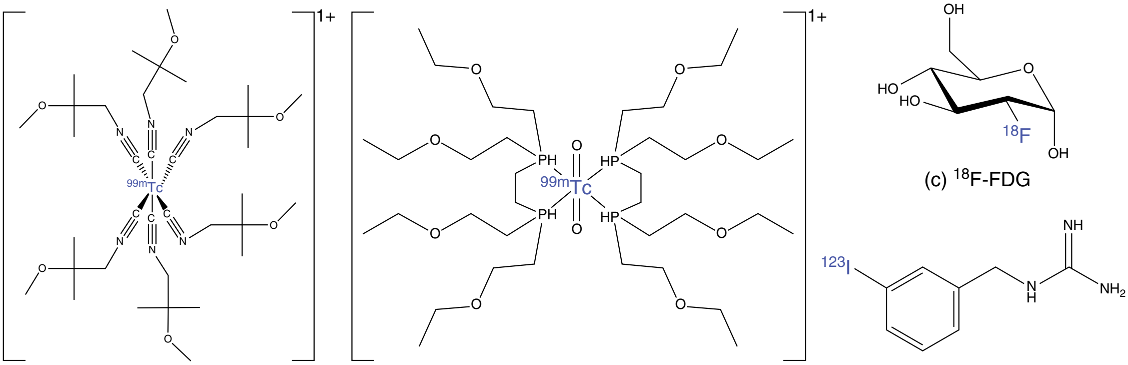
1+
^{99m}Tc
1+
^{99m}Tc
PH
HP
OH
HO
HO
O
^{18}F
OH
NH
^{123}I
N
H
NH$_2$

(a) ^{99m}Tc-sestamibi (b) ^{99m}Tc-tetrofosmin (c) ^{18}F-FDG (d) ^{123}I-MIBG

Figure 4.6 (a–d) Cardiac imaging radiopharmaceuticals.

The normal LVEF is 50–55% but may be decreased in patients who are receiving anthracyclines, who have had a myocardial infarct, or who have other cardiomyopathies. LVEF may also be determined as part of the MPI study by measuring the changes in left ventricular volume between asystole and systole (see Chapter 7). MUGA scans also allow assessment of myocardial wall motion, which can aid in detecting areas of infarcted myocardium.

Myocardial glucose utilization is associated with ischemia since under normal perfusion conditions, the myocardium metabolizes long-chain fatty acids for energy. This switch from fatty acid to glucose metabolism is imaged by PET using ^{18}F-2-fluorodeoxyglucose (^{18}F-FDG) (see Chapter 15). Oxygen utilization of the myocardium is sensitive for detecting ischemia and this may be imaged by PET using ^{15}O water ($H_2{}^{18}O$). Ammonia is involved in many metabolic activities in several organs among which is the myocardium, therefore it is used to assess regional blood perfusion for detection of ischemia by PET imaging using ^{13}N ammonia ($^{13}NH_3$). ^{123}I-Metaiodobenzylguanidine (^{123}I-MIBG) is another radiopharmaceutical that can detect the likelihood of cardiac ischemia. Since cardiac ischemia is associated with alterations in myocardial sympathetic nerve activity, ^{123}I-MIBG (an analog of guanethidine) is used to image cardiac innervation using SPECT. Radiolabeled fatty acids (e.g. ^{123}I-(*p*-iodophenyl)-pentadecanoic acid [^{123}I-IPPA] and ^{123}I-β-methyl-*p*-iodophenylpentadecanoic acid [^{123}I-BMIPP]) may also be used to image the myocardium to assess an increase in fatty acid utilization associated with ischemia, since fatty acids will be the main source of ATP production in ischemic myocardium. In the following sections, a brief description of the most common radiopharmaceuticals used for cardiac imaging is provided.

4.4.1 ^{99m}Tc-Sestamibi

^{99m}Tc-sestamibi (Figure 4.6a) is a lipophilic cationic complex of ^{99m}Tc that is passively taken up in myocardial cells in proportion to regional myocardial blood flow and is used for MPI by SPECT. ^{99m}Tc-sestamibi binds intracellularly to mitochondria and its washout from myocardial cells is very slow. Thus, ^{99m}Tc-sestamibi does not redistribute to poorly perfused myocardium at rest, requiring two separate injections for the stress and rest MPI studies. ^{99m}Tc-sestamibi has higher liver uptake than ^{99m}Tc-tetrofosmin (Table 4.3), which may result in lower sensitivity for detecting lesions in the inferior region of the heart. ^{99m}Tc-sestamibi has also been used for imaging parathyroid adenomas (see Chapter 10) as well as for imaging breast cancer (scintimammography; see Chapter 9), especially in women with dense breasts for whom mammography is less sensitive.

4.4.2 ^{99m}Tc-Tetrofosmin

^{99m}Tc-tetrofosmin (Figure 4.6b) is a lipophilic cationic complex of ^{99m}Tc that is taken up by myocardial cells localizing mainly in the cytosol with a small

Table 4.3 Radiopharmaceuticals for myocardial perfusion imaging.

Property	^{201}Tl	^{99m}Tc-sestamibi	^{99m}Tc-tetrofosmin	^{82}Rb
Physical half-life	3.0 d	6.0 h	6.0 h	75 s
γ-Energy (keV)	71	140	140	511 (β^+ annihilation)
Charge	+1	+1	+1	+1
Myocardial uptake (%)	4	1	1	70
Redistribution	Yes	No	No	Yes
Lung uptake (%)	0.9	2.6	1.7	31
Liver uptake (%)	4–7	20	7	5
Dose (MBq)	74–111	370–1110	185–925	1480–2200

fraction binding to mitochondria. ^{99m}Tc-tetrofosmin is used for MPI SPECT imaging. Similar to ^{99m}Tc-sestamibi, this agent also does not redistribute to poorly perfused myocardium at rest, and thus, two separate injections are required for the stress and rest studies. ^{99m}Tc-tetrofosmin exhibits much lower liver uptake than ^{99m}Tc-sestamibi, which improves its sensitivity for detection of lesions in the inferior region of the myocardium.

4.4.3 ^{201}Tl Thallous Chloride

^{201}Tl is a monovalent cationic radiometal (Tl^+), which has comparable biological behavior as potassium (K^+). ^{201}Tl is taken up by viable cardiac myocytes via the Na^+/K^+ ATP-ase pump in proportion to regional myocardial blood flow. SPECT images are obtained soon after administering the radiopharmaceutical at peak exercise or pharmacological stress (see Chapter 7). Imaging is repeated a few hours later with the patient at rest to determine if a perfusion defect in the myocardium is reversible. No second injection is required since ^{201}Tl redistributes from well-perfused to poorly perfused myocardium at rest. Disadvantages of ^{201}Tl include its suboptimal γ-energy for SPECT ($E\gamma = 71$ keV) that can cause tissue attenuation artifacts and its long $t_{1/2p}$ (3.0 days), which delivers a higher radiation dose than ^{99m}Tc agents. Consequently, for dosimetry reasons the administered radioactivity dose for ^{201}Tl is 5–10-fold lower than ^{99m}Tc agents (Table 4.3). Combined with higher attenuation of the low-energy γ-photons emitted by ^{201}Tl by overlying tissues results in lower quality images. An advantage of ^{201}Tl, however, is that the images directly reflect myocardial cell viability, since only viable cells have an active Na^+/K^+ ATP-ase transporter required to accumulate the radiopharmaceutical. ^{201}Tl is also used in combination with ^{99m}Tc sodium pertechnetate to image the parathyroid gland (see Chapter 10).

4.4.4 ^{82}Rb Rubidium Chloride

^{82}Rb is a monovalent cationic radiometal (Rb^+), which is accumulated by cardiac myocytes via the Na^+/K^+ ATP-ase pump in proportion to regional myocardial blood flow, similarly to ^{201}Tl. The advantage of ^{82}Rb compared to ^{201}Tl is that since it is a positron-emitter, PET can be performed for MPI. Moreover, ^{82}Rb is produced locally using a ^{82}Sr/^{82}Rb generator, making the radiopharmaceutical readily available without the need for a cyclotron. Since ^{82}Rb has a very short $t_{1/2p}$ (75 seconds), it delivers a lower radiation dose than ^{201}Tl or the ^{99m}Tc agents, and thus the administered dose of the radiopharmaceutical is up to 20-fold higher than ^{201}Tl and 2-fold higher than ^{99m}Tc agents (Table 4.3). However, due to the short $t_{1/2p}$, two separate infusions of the radiopharmaceutical are required for stress and rest MPI studies, but both studies may be completed in only an hour.

4.4.5 ^{15}O Water ($H_2{}^{15}O$)

$H_2{}^{15}O$ is water labeled with the very short-lived positron-emitter, ^{15}O ($t_{1/2p}$ = 2.4 minutes). This agent has been studied for evaluating regional blood flow in the myocardium (MPI) using PET, but has limitations because it is freely diffusible and circulates in the blood as well, requiring subtraction of the blood pool to estimate uptake in the heart muscle. The administered dose of $H_2{}^{15}O$ is 3.0–3.7 GBq.

4.4.6 ^{13}N Ammonia ($^{13}NH_3$)

$^{13}NH_3$ is ammonia labeled with the very short-lived positron-emitter, ^{13}N ($t_{1/2p}$ = 10 minutes). $^{13}NH_3$ is accumulated in cardiac myocytes in proportion to blood flow and is incorporated into glutamine by the enzyme glutamine synthase. The radiopharmaceutical has been used for MPI by PET, but has limitations due to variable uptake in different regions of the heart muscle, export of $^{13}NH_3$ from cardiac myocytes, and high liver uptake, which interferes with the detection of lesions in the inferior region of the heart. The administered dose of $^{13}NH_3$ is 370–555 MBq.

4.4.7 ^{99m}Tc Red Blood Cells

The patient's own RBCs may be radiolabeled *in vitro* by obtaining a small sample (about 8 ml) of blood and incubating the RBCs with stannous ion (Sn^{2+}), washing the RBCs to remove excess Sn^{2+}, and then incubating with ^{99m}Tc sodium pertechnetate. The Sn^{2+} ions act to reduce ^{99m}Tc to allow it to bind to the RBCs. Kits are available for facile *in vitro* radiolabeling of blood samples with ^{99m}Tc. Alternatively, the patient's RBCs may be radiolabeled *in vivo* by injecting stannous pyrophosphate (a source of Sn^{2+}) 30 minutes prior to injecting ^{99m}Tc sodium pertechnetate. Higher radiolabeling efficiencies are obtained for the *in vitro* method (>95%) than the *in vivo* method (>80%) providing higher quality images, but *in vivo* radiolabeling of RBCs with ^{99m}Tc is the most commonly used procedure due to its convenience. Imaging with ^{99m}Tc-RBCs can also be used to detect gastrointestinal bleeding or hemangiomas (see Chapter 11). The administered dose of ^{99m}Tc-RBCs is 555–925 MBq.

4.4.8 ^{18}F-2-Fluorodeoxyglucose (^{18}F-FDG)

^{18}F-FDG (Figure 4.6c) is an analog of glucose, which is transported into cells including cardiac myocytes via glucose transporters (GLUT) and metabolized intracellularly to ^{18}F-FDG-6-phosphate via hexokinase. ^{18}F-FDG-6-phosphate cannot be further metabolized in the glycolytic pathway since it is not recognized by phosphoglucose isomerase or exported and thus becomes trapped within cells. In ischemic myocardium, there is increased utilization of glucose compared to fatty acids, and thus PET with ^{18}F-FDG is sensitive for revealing regions of ischemia. However, ^{18}F-FDG uptake is decreased after myocardial infarction. The administered dose of ^{18}F-FDG is 74–370 MBq and imaging of the heart is performed 45 minutes after radiopharmaceutical injection.

4.4.9 ^{123}I-Metaiodobenzylguanidine (^{123}I-MIBG)

^{123}I-MIBG (Figure 4.6d) is an analog of norepinephrine that is accumulated in the myocardium and is used for SPECT imaging of cardiac innervation. Decreased uptake of ^{123}I-MIBG is associated with decreased function of the myocardium in heart transplant patients, as well as in other cardiomyopathies. The administered dose of ^{123}I-MIBG is 370 MBq and imaging is performed at four hours postinjection. ^{123}I-MIBG is also used to image certain types of tumors (e.g. pheochromocytoma, neuroblastoma, and neuroendocrine malignancies – see Chapter 10).

4.5 Radiopharmaceuticals for Tumor Imaging

Imaging of cancer with radiopharmaceuticals that probe the biology or physiology of tumors is known as “molecular imaging” (MI) and is a rapidly expanding area of medical imaging, which has an important role in diagnosing and staging cancer, characterizing the tumor phenotype to select targeted cancer therapies, as well as monitoring metabolic response to treatment (see Chapter 15). The advancement of hybrid modality imaging systems that combine PET or SPECT with computerized X-ray tomography (CT; see Chapter 2) or magnetic resonance imaging (MRI; see Chapter 5) takes advantage of the high sensitivity of PET and SPECT for probing cancer biology with the exquisite anatomical spatial resolution of CT and MRI to co-register these images to clearly identify and characterize cancerous lesions. MI offers the potential to personalize cancer treatment by probing the biological properties of tumors in an individual patient. MI may also accelerate the development of new cancer therapies and reduce costs to the health-care system by identifying subpopulations of patients who are most likely to respond to molecularly-targeted cancer treatment. A summary of the radiopharmaceuticals used for MI of cancer is shown in Table 4.4. These agents are described in the following sections.

4.5.1 ^{18}F-Fluoro-L-Thymidine (^{18}F-FLT)

^{18}F-FLT (Figure 4.7a) is a thymidine nucleoside analog labeled with ^{18}F that enables PET imaging of tumor proliferation. ^{18}F-FLT is taken up by tumor cells by nucleoside transporters, phosphorylated by thymidine kinase-1 to ^{18}F-FLT 3′-monophosphate, but is not incorporated into DNA. Nonetheless, since thymidine kinase-1 is elevated in proliferating tumor cells, ^{18}F-FLT is considered a tumor proliferation marker. ^{18}F-FLT is considered more specific in differentiating malignant tumors from normal tissues than ^{18}F-FDG, since there is enhanced uptake of ^{18}F-FDG by inflammatory cells, especially at sites of infection. The administered dose of ^{18}F-FLT is 185–370 MBq and tumor imaging is performed 1 h after radiopharmaceutical injection.

4.5.2 ^{18}F-Fluorodeoxyglucose (^{18}F-FDG)

As described earlier, ^{18}F-FDG (Figure 4.6c) is an analog of glucose that is transported into cells via GLUT and metabolized intracellularly by hexokinase to ^{18}F-FDG-6-phosphate, which is not metabolized further but becomes trapped within the cells. There are increased levels of GLUT and hexokinase in cancer cells compared to normal cells and this results in strong accumulation of ^{18}F-FDG in tumors. PET imaging with ^{18}F-FDG provides information on tumor glucose utilization, which reflects tumor viability (see Chapter 15). Cancer treatment, which reduces the viability of cancer cells, often results in decreased uptake of ^{18}F-FDG on PET scans. ^{18}F-FDG PET is useful for diagnosing a wide variety of malignancies, for tumor staging and for monitoring response to treatment. A limitation of ^{18}F-FDG PET is uptake of the radiopharmaceutical in inflammatory cells, but quantitative assessment of tumor uptake (standard uptake value [SUV]) is helpful to differentiate tumors from non-cancerous lesions. Tumors exhibit higher SUV values. Another limitation of ^{18}F-FDG is high uptake in the brain, which limits its ability to detect brain tumors. The administered dose of ^{18}F-FDG is 74–370 MBq and tumor imaging is performed 45 minutes after radiopharmaceutical injection.

Table 4.4 Radiopharmaceuticals used for cancer imaging.

Radiopharmaceutical	Tumor property	Types of cancer	Dose	Imaging modality
^{18}FLT	DNA synthesis	Many	185–370 MBq	PET
^{18}F-FDG	Glucose metabolism	Many	74–370 MBq	PET
^{18}F-choline	Cell membrane phospholipids	Many	4.07 MBq kg^{-1}	PET
^{18}F-FET	Cerebral proteins	Brain tumors	400 MBq	PET
^{18}F-FAZA	Hypoxia marker	Many	37–370 MBq	PET
^{111}In-pentetreotide	Somatostatin receptor binding	Neuroendocrine tumors	111–222 MBq	SPECT
^{68}Ga-DOTATOC/ DOTATATE	Somatostatin receptor binding	Neuroendocrine tumors	100–200 MBq	PET
^{123}I-MIBG	Norepinephrine analog	Neuroendocrine tumors	370 MBq	SPECT
^{123}I sodium iodide	Thyroid hormone analog	Thyroid and parathyroid tumors	3.7–14.8 MBq	SPECT
^{131}I sodium iodide	Thyroid hormone analog	Thyroid and parathyroid tumors	148–370 MBq	SPECT
^{67}Ga gallium citrate	Plasma transferrin and lactoferrin binding	Many	74–370 MBq	SPECT
^{111}In-ibritumomab tiuxetan	Cell membrane protein	Non-Hodgkin’s lymphoma	185 MBq	SPECT
^{111}In-capromab pendetide	Prostate-specific membrane antigen	Prostate tumors	185 MBq	SPECT

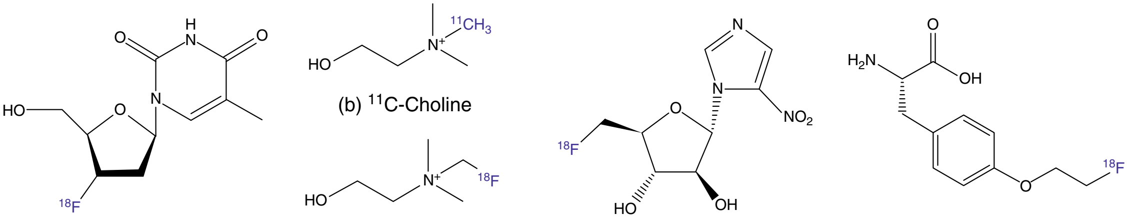
HO
^{18}F
O
N
H
^{11}CH$_3$
N$^+$
(b) ^{11}C-Choline
^{18}F
NO$_2$
OH
H$_2$N

(a) ^{18}F-FLT (b) ^{18}F-Choline (c) ^{18}F-FAZA (d) ^{18}F-FET

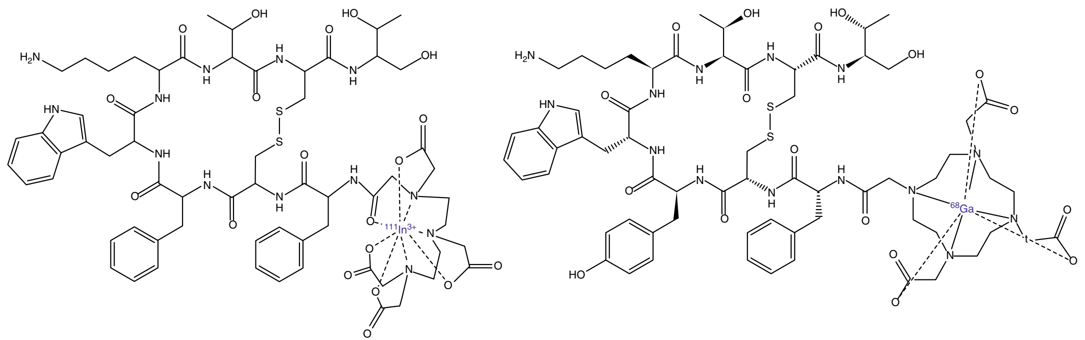
H$_2$N
HN
NH
OH
S
^{111}In^{3+}
^{68}Ga
HO

(e) ^{111}In-Pentetreotide (f) ^{68}Ga-DOTATOC

Figure 4.7 (a–f) Tumor imaging radiopharmaceuticals.

4.5.3 ^{18}F- and ^{11}C-Choline

Choline is an essential component of phospholipids that form cell membranes. Increased choline utilization to synthesize cell membranes is a property of some tumors. Choline taken up by cells is phosphorylated by choline kinases to produce phosphorylcholine, which then undergoes a series of biosynthesis processes resulting in integration into the cell membrane. PET imaging with ^{18}F- or ^{11}C-labeled choline (Figure 4.7b) is useful for detecting prostate cancer, lung cancer, or esophageal cancer. The administered dose of ^{18}F-choline and ^{11}C-choline are 4.07 MBq kg^{-1} and 370–740 MBq, respectively, and tumor imaging is performed 60–90 minutes or 2 minutes, respectively, after the radiopharmaceutical injection.

4.5.4 ^{18}F-FAZA

1-(5-^{18}F-Fluoro-5-deoxy-α-D-arabinofuranosyl)-2-nitroimidazole (^{18}F-FAZA; Figure 4.7c) is 2-nitroimidazole derivative, which undergoes reductive metabolism in regions of hypoxia in a tumor. Hypoxia is often observed in solid tumors due to their outgrowth of the blood supply and disorganized tumor vascularization. Hypoxic tumors are resistant to both radiation and chemotherapy treatment. Radiolabeled 2-nitroimidazole can noninvasively image a hypoxic tumor since the radiopharmaceuticals are trapped in hypoxic regions of the tumor upon reduction of the 2-nitroimidazole group. PET imaging using ^{18}F-FAZA allows assessment of hypoxia in various tumors including head and neck carcinoma, sarcomas, brain tumors, breast cancer, and lung cancer (see Chapter 15). The administered dose of ^{18}F-FAZA is 37–370 MBq, and tumor imaging is performed two to three hours after radiopharmaceutical injection.

4.5.5 ^{18}F-Fluoroethyltyrosine (^{18}F-FET)

^{18}F-FET (Figure 4.7d) is a synthetic amino acid that is transported into tumor cells via the L-amino acid transporter (LAT 1), which is increased in cancer. ^{18}F-FET can readily cross the blood brain barrier (BBB). Due to the high uptake of ^{18}F-FET in brain tumors in comparison to healthy brain tissue, PET imaging with ^{18}F-FET offers a high background contrast for tumor detection and to predict response to treatment. ^{18}F-FET is used for imaging brain tumors including glioma. The administered dose of ^{18}F-FET is 400 MBq and the patient is imaged one to three hours after radiopharmaceutical injection.

4.5.6 ^{111}In-Pentetreotide and ^{68}Ga-DOTATOC/DOTATATE

^{111}In-pentetreotide (Figure 4.7e) is a radiolabeled form of octreotide, an 8-amino acid synthetic cyclic peptide analog of somatostatin, which is a 14- or 28-amino acid neuropeptide ligand for somatostatin receptors (SMSR). There are seven subtypes of SMSR. Tumors that arise in both the endocrine and neural systems (neuroendocrine malignancies) frequently overexpress SMSR, especially subtypes 1 and 2, which bind ^{111}In-pentetreotide permitting SPECT imaging (see Chapter 10). Tumors that express SMSR include sympathoadrenal system tumors, gastroenteropancreatic tumors, medullary thyroid carcinoma, pituitary adenoma, and other neuroendocrine tumors. ^{68}Ga-DOTATOC (Figure 4.7f) and ^{68}Ga-DOTATATE are ^{68}Ga-labeled analogs of octreotide peptides with high affinity for the SMSR subtype 2, while ^{68}Ga-DOTATOC has affinity for SMSR subtype 5 as well. Despite imaging with ^{68}Ga-DOTATOC and ^{68}Ga-DOTATATE yielding the same diagnostic accuracy, the main difference is that ^{68}Ga-DOTATOC exhibits higher tumor uptake than ^{68}Ga-DOTATATE. These agents allow PET imaging of SMSR-positive tumors. The administered dose of ^{111}In-pentetreotide and ^{68}Ga-DOTATOC/DOTATATE are 111–222 MBq and 100–200 MBq, respectively, and tumor imaging is performed at 4–48 hours or 45–90 minutes, respectively, after injection of these radiopharmaceuticals. The shorter time after injection of the ^{68}Ga-labeled peptides is required due to the short $t_{1/2p}$ of ^{68}Ga (68 minutes). ^{90}Y-DOTATOC/DOTATATE and ^{177}Lu-DOTATOC/DOTATATE are radiotherapeutic analogs, which emit β-radiation and are administered at much higher doses (2.6 and 3.7 GBq, respectively) to treat SMSR-positive malignancies. ^{177}Lu-DOTATOC/DOTATATE also emits γ-radiation, which allows imaging of tumors by SPECT but ^{90}Y-DOTATOC/DOTATATE cannot be imaged since it is a pure β-emitter.

4.5.7 ^{123}I-Metaiodobenzylguanidine (^{123}I-MIBG)

As described earlier, ^{123}I-MIBG (Figure 4.6d) is a guanethidine analog. This agent is accumulated in tumor cells via norepinephrine transporters (NET) and is used to image pheochromocytoma (see Chapter 10), an adrenal medullary tumor, as well as neuroblastoma in children. The administered dose of ^{123}I-MIBG is 370 MBq and imaging is performed at 4–48 hours postinjection. ^{131}I-MIBG is a radiotherapeutic analog, which emits β- and γ-radiation and is used at much higher doses (3.7–11.2 GBq) to treat neuroblastoma. The uptake of ^{131}I-MIBG can also be imaged in tumors by SPECT due to the γ-emissions.

4.5.8 ^{123}I and ^{131}I Sodium Iodide

^{123}I and ^{131}I sodium iodide are avidly taken up into the thyroid gland via the sodium iodide symporter and incorporated into thyroid hormones. These radiopharmaceuticals are administered in an oral dosage form (capsule or liquid) and are used to image the thyroid gland to diagnose hypo- or hyperthyroidism and to identify any lesions present in the thyroid (see Chapter 10). They can also be used to sensitively detect primary and metastatic thyroid cancer by SPECT. ^{123}I sodium iodide is preferred for imaging due to its shorter $t_{1/2p}$ (13 hours) and absence of β-radiation, which reduces the radiation dose to patients compared to ^{131}I that has a longer $t_{1/2p}$ (8 days) and emits β-radiation. Also, the γ-energy of ^{123}I (159 keV) is more suited to imaging with the γ-camera than the higher γ-energy of ^{131}I (364 keV). ^{131}I sodium iodide is used to treat hyperthyroidism (see Chapter 10) as well as for treatment of thyroid cancer. The dose of ^{123}I and ^{131}I sodium iodide for imaging is 3.7–14.8 MBq and 148–370 MBq, respectively, and imaging is performed at 24 hours after radiopharmaceutical administration.

4.5.9 ^{67}Ga Gallium Citrate

^{67}Ga gallium citrate is bound by transferrin and lactoferrin in the plasma and taken up by tumor cells via transferrin receptors, which are overexpressed on certain malignancies. ^{67}Ga gallium citrate is used mainly for SPECT imaging of lymphomas, melanoma, hepatocellular carcinoma, and lung cancer. The administered dose of ^{67}Ga citrate is 185–370 MBq and imaging is performed at 48–72 hours postinjection. ^{67}Ga gallium citrate is accumulated at sites of infection and has also been used for this purpose. Similar to the mechanism of tumor cells uptake, ^{67}Ga gallium citrate binds to transferrin in the circulation, which then binds to circulating leukocytes. Also, ^{67}Ga has a high affinity for bacterial siderophores, which increases its uptake at sites of infection. The limitations of ^{67}Ga gallium citrate include its higher energy γ-photons (93, 184, and 300 keV) that are not optimal for imaging with the γ-camera and its high uptake by the liver as well as excretion into the bowel, which may interfere with tumor imaging.

4.5.10 ^{111}In-Ibritumomab Tiuxetan

^{111}In-ibritumomab tiuxetan is a murine IgG_1 monoclonal antibody directed against the CD20 antigen expressed on B-cell lymphomas and normal B-cells modified with a form of DTPA (tiuxetan) to complex ^{111}In. It is mainly used for SPECT imaging of non-Hodgkin's lymphoma to predict the radiation-absorbed dose to the whole body from ^{90}Y-ibritumomab tiuxetan (Zevalin), used to treat non-Hodgkin's B-cell lymphoma. The administered dose of ^{111}In-ibritumomab tiuxetan is 185 MBq and imaging is performed at 2–72 hours postinjection.

4.5.11 ^{111}In-Capromab Pendetide

^{111}In-capromab pendetide is a murine IgG_1 monoclonal antibody targeting intracellular prostate-specific membrane antigen (PSMA) linked to a form of DTPA (pendetide), which complexes ^{111}In. PSMA is overexpressed in prostate cancer. ^{111}In-capromab pendetide is used for SPECT imaging of prostate cancer, lymph node metastasis, and recurrence post prostatectomy. The administered dose of ^{111}In-capromab pendetide is 185 MBq and imaging is performed at 72–120 hours postinjection.

4.6 Radiopharmaceuticals for Brain/CNS Imaging

The main biological requirement for radiopharmaceuticals used for brain or CNS imaging is the ability to cross the BBB. The vasculature supplying the CNS is highly selective and semipermeable for many substances due to the tight junctions in the blood epithelial membrane. The vasculature allows the passage of water, lipid-soluble molecules, some gases, glucose, and amino acids. Radiopharmaceuticals for brain imaging are usually lipophilic complexes or molecules, which are able to penetrate the BBB. In some cases (e.g. ^{99m}Tc-bicisate) the radiopharmaceutical is metabolized in the brain to a less lipophilic agent, which is retained in the brain since it cannot cross the BBB to be exported. Radiopharmaceuticals used for brain imaging (Table 4.5) are categorized into three main classes: (i) cerebral metabolism agents, (ii) cerebral perfusion imaging agents, and (iii) receptor binding agents.

4.6.1 ^{18}F-Fluorodeoxyglucose (^{18}F-FDG)

^{18}F-FDG (Figure 4.6c) crosses the BBB readily via GLUT where it gets phosphorylated and trapped in brain cells as discussed earlier. Improved uptake in the brain is achieved if the patient fasts for six hours prior to injecting the radiopharmaceutical. ^{18}F-FDG is used to evaluate regional cerebral glucose consumption by PET (see Chapter 13), which allows assessment of Alzheimer's disease, frontotemporal dementia, epilepsy, and movement disorders (e.g. Parkinson's disease and atypical Parkinsonian syndromes). In case of epilepsy, the brain metabolism will increase, therefore an increase in ^{18}F-FDG uptake. The administered dose of ^{18}F-FDG is 370–555 MBq and imaging is performed at 45–60 minutes postinjection.

4.6.2 ^{99m}Tc-HMPAO (^{99m}Tc-Exametazime)

^{99m}Tc-Hexamethylpropylene Amine Oxime (^{99m}Tc-HMPAO; ^{99m}Tc-exametazime; Figure 4.8a) is a lipophilic complex of ^{99m}Tc that passively diffuses across the BBB into the brain and is reduced by glutathione in the brain to a more hydrophilic complex, which is not able to escape and remains trapped. ^{99m}Tc-HMPAO distributes in the brain according to regional blood flow, and the agent is used for cerebral perfusion imaging by SPECT to detect cerebrovascular events (i.e. stroke and cerebral infarction). The administered dose of ^{99m}Tc-HMPAO is 555–740 MBq and imaging is performed immediately postinjection.

Table 4.5 Radiopharmaceuticals used for brain imaging.

Radiopharmaceutical	Mechanism of localization	Type of study	Dose (MBq)	Imaging modality
^{18}FDG	Glucose metabolism	Many neurologic disorders	370–555	PET
^{99m}Tc-HMPAO	Intracellular passive diffusion	Perfusion	555–740	SPECT
^{99m}Tc-ECD	Intracellular passive diffusion	Perfusion	370–740	SPECT
$H_2{}^{15}O$	Oxygen metabolism	Perfusion	3000–3700	PET
$^{13}NH_3$	Ammonia transporter	Perfusion	370–555	PET
^{123}I-IBZM	Dopamine receptor agonist	Parkinson's disease	370	SPECT
^{11}C-raclopride	Dopamine receptor agonist	Addiction and many neurologic and psychiatric disorders	370–555	PET
^{11}C-methylspiperone	Dopamine and serotonin receptor antagonist	Many neurologic and psychiatric disorders	150–350	PET
^{18}F-FDOPA	Protein synthesis	Many neurologic disorders	220–440	PET
^{11}C-flumazenil	GABA receptor agonist	Epilepsy	220–440	PET
^{123}I-iomazenil	GABA receptor agonist	Epilepsy	220–440	SPECT
^{111}In-DTPA	Cisternography	CSF leakage	18.5	SPECT

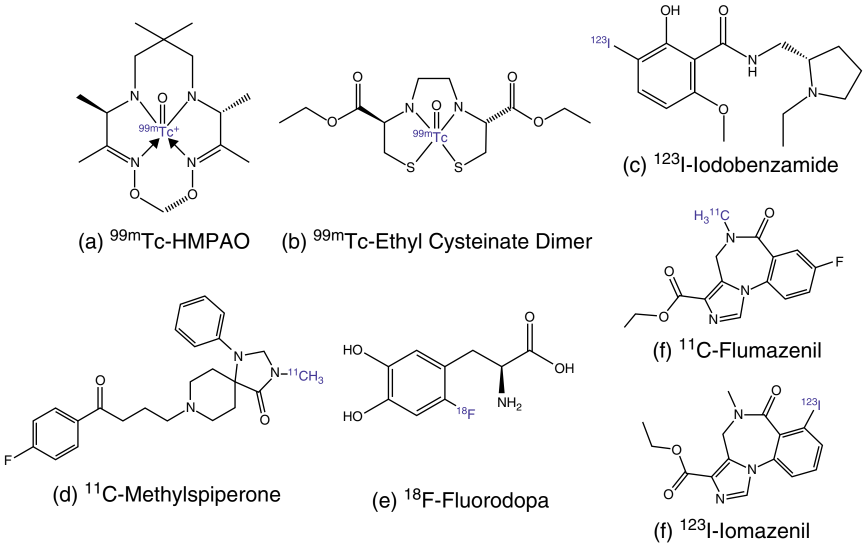

(a) ^{99m}Tc-HMPAO

(b) ^{99m}Tc-Ethyl Cysteinate Dimer

(c) ^{123}I-Iodobenzamide

(d) ^{11}C-Methylspiperone

(e) ^{18}F-Fluorodopa

(f) ^{11}C-Flumazenil

(f) ^{123}I-Iomazenil

Figure 4.8 (a–f) Brain/CNS imaging radiopharmaceuticals.

4.6.3 ^{99m}Tc-ECD (^{99m}Tc-Bicisate)

^{99m}Tc-Ethyl Cysteinate Dimer (^{99m}Tc-ECD; ^{99m}Tc-bicisate; Figure 4.8b) is a lipophilic complex of ^{99m}Tc that diffuses passively across the BBB and is metabolized intracellularly by esterases to a more hydrophilic compound, which is trapped in the brain. The agent is used to image cerebral perfusion by SPECT to detect stroke. The administered dose of ^{99m}Tc-ECD is 555–740 MBq and imaging is performed within 30 minutes postinjection.

4.6.4 ^{15}O Water ($H_2{}^{15}O$) and ^{13}N Ammonia ($^{13}NH_3$)

These radiopharmaceuticals discussed earlier are used to assess regional cerebral perfusion by PET in order to measure cerebral blood flow. The administered dose of $H_2{}^{15}O$ and $^{13}NH_3$ are 3000–3700 MBq and 370–555 MBq, respectively, and imaging is performed immediately postinjection. The high administered dose of $H_2{}^{15}O$ is permissible to the very short $t_{1/2p}$ of ^{15}O (2.4 minutes), which minimizes the radiation dose to the patient.

4.6.5 ^{123}I-Iodobenzamide (^{123}I-IBZM) and ^{11}C-Raclopride

^{123}I-IBZM (Figure 4.8c) is a dopamine receptor subtype 2 (D2R) agonist, while ^{11}C-raclopride is a D2R antagonist. These agents are used to image D2R in the brain by SPECT or PET, respectively. The main application of ^{123}I-IBZM is to predict the responsiveness of Parkinson's disease to treatment and to differentiate Parkinson's disease from basal ganglia disorders (e.g. multiple-system atrophy). ^{11}C-raclopride has been used to assess D2R occupancy in patients with addiction to cocaine or methylphenidate (see Chapter 13) and to detect neurological disorders (e.g. Parkinson's disease and schizophrenia). Patients with addiction have a lower dopamine receptor availability, which can be detected by PET using ^{11}C-raclopride. Similar to ^{123}I-IBZM, ^{11}C-raclopride is used to predict the response to treatment in patients with Parkinson's disease. An increase in synaptic dopamine level leading to a reduction in ^{11}C-raclopride binding has been shown in schizophrenic patients, especially after the administration of amphetamine (dopamine inducer). The administered dose of ^{123}I-IBZM and ^{11}C-raclopride are 185 MBq and 370–555 MBq, respectively, and imaging is performed at 2 hours postinjection for ^{123}I-IBZM and at 30 minutes postinjection for ^{11}C-raclopride.

4.6.6 ^{11}C-Methylspiperone

^{11}C-methylspiperone (Figure 4.8d) is a dopamine D2/3 and 5-HT2A (subtype of 5-hydroxytryptamine [5-HT2] serotonin receptors) receptor antagonist. Depletion of dopamine contributes to various psychiatric disorders, including Parkinson's disease, schizophrenia, autism, and attention-deficit hyperactivity disorder. Serotonin is a neurotransmitter implicated in depression, anxiety, obsessive–compulsive disorder, and schizophrenia. ^{11}C-methylspiperone has been used to image Parkinson's disease, Alzheimer's disease, and schizophrenia by PET. The administered dose of ^{11}C-methylspiperone is 150–350 MBq and imaging is performed at 20 minutes postinjection.

4.6.7 ^{18}F-Fluorodopa (^{18}F-FDOPA)

^{18}F-FDOPA (Figure 4.8e) is a precursor that is decarboxylated by aromatic amino acid decarboxylase (AAAD) and undergoes O-methylation by catechol O-methyl transferase (COMT) in the brain to ^{18}F-dopamine and 3-*O*-methyl-6-^{12}F-fluoro-L-DOPA. ^{18}F-fluorodopamine is further oxidized by monoamine oxidase (MAO) to l-3,4-dihydroxy-6-^{18}F-fluorophenylacetic acid, which then undergoes O-methylation by COMT to 6-^{18}F-fluoro-homovanillic acid. Decarboxylase inhibitors such as carbidopa have been used to minimize the metabolism of ^{18}F-FDOPA in the plasma in order to maximize brain uptake. ^{18}F-FDOPA is used to image dopamine receptors in the brain by PET. The agent is used for imaging neurodegenerative diseases (e.g. Parkinson's disease), but has also been used to image neuroendocrine tumors elsewhere in the body (e.g. pheochromocytoma). The administered dose of ^{18}F-FDOPA is 220–440 MBq and imaging is performed at 20–30 minutes postinjection.

4.6.8 ^{11}C-Flumazenil and ^{123}I-Iomazenil

^{11}C-flumazenil and ^{123}I-iomazenil (Figure 4.8f) are ligands for benzodiazepine-gamma aminobutyric acid (GABA) receptors in the brain. There are decreased levels of GABA receptors in regions of the brain where there are epileptogenic foci. ^{11}C-flumazenil and ^{123}I-iomazenil are used to localize seizure onset in epilepsy patients and to assess neuronal integrity (e.g. ischemic stroke) by PET and SPECT, respectively. The administered dose of ^{11}C-flumazenil and ^{123}I-iomazenil is 220–440 MBq and imaging is performed at 20 minutes or 1 hour postinjection, respectively.

4.6.9 ^{111}In-Diethylenetriaminepentaacetic Acid (^{111}In-DTPA)

^{111}In-DTPA is a water-soluble complex of the metal chelator, DTPA, labeled with ^{111}In. The agent is administered intrathecally to visualize CSF flow (cisternography) to detect leakage or blocks in patients with CSF shunts by SPECT imaging. It is approved for intrathecal administration since it has very low endotoxin levels and is a sterile injectable product. The administered dose of ^{111}In-DTPA is 18.5 MBq and imaging is performed at 4 hours and 24–48 hours postinjection.

4.7 Radiopharmaceuticals for Renal Imaging

Radiopharmaceuticals used for renal imaging (Table 4.6) are agents that are eliminated by the kidneys by glomerular filtration or a combination of filtration and tubular secretion. Imaging is able to independently evaluate the function of each kidney (renograms) and provide estimates of glomerular filtration rate (GFR) and effective renal plasma flow (ERPF) (see Chapter 12). ERPF is a measure of filtration and tubular function. GFR or ERPF may be measured indirectly by imaging or by collecting plasma samples from the patient at selected times postinjection and plotting the elimination of radioactivity from the plasma over time. The elimination curves can then be fitted to a pharmacokinetic model to estimate the clearance, which is an estimate of GFR in the case of ^{99m}DTPA or ERPF for ^{99m}Tc-MAG$_3$. Renal imaging can also identify renal masses, but CT and ultrasound are more commonly used for this purpose (see Chapter 12).

4.7.1 ^{99m}Tc-Diethylenetriaminepentaacetic Acid (^{99m}Tc-DTPA)

^{99m}Tc-DTPA (Figure 4.9a) is eliminated almost entirely by glomerular filtration but a small fraction (<10%) of the injected dose of the radiopharmaceutical is bound to plasma proteins, which results in an underestimation of GFR. The

Table 4.6 Properties of renal imaging agents.

Radiopharmaceutical	Glomerular filtration	Tubular secretion	Binding to renal cortex	Imaging application	Dose (MBq)
^{99m}Tc-DTPA	Yes	No	No	GFR	370–555
^{99m}Tc-MAG$_3$	Yes	Yes	No	ERPF	185–370
^{99m}Tc-glucoheptonate	Yes	No	Yes	Morphology	370–555
^{99m}Tc-DMSA	Yes	No	Yes	Morphology	74–185

GFR, glomerular filtration rate; ERPF, effective renal plasma flow.

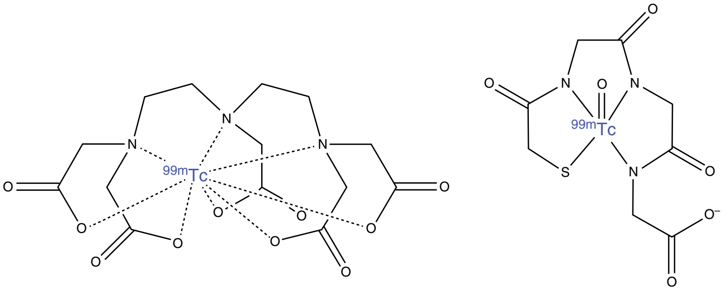

(a) ^{99m}Tc-DTPA (b) ^{99m}Tc-MAG$_3$

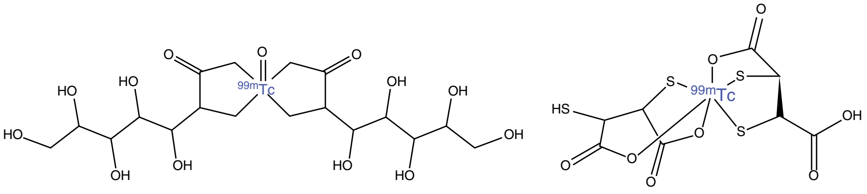

(c) ^{99m}Tc-Glucoheptonate (d) ^{99m}Tc-Succimer

Figure 4.9 (a–d) Renal imaging radiopharmaceuticals.

plasma protein binding fraction varies with the kit formulation used to prepare ^{99m}Tc-DTPA. If required, the free nonprotein-bound ^{99m}Tc-DTPA can be isolated from plasma samples by ultrafiltration to obtain a more accurate estimate of GFR, when the pharmacokinetic modeling approach is taken. A limitation of ^{99m}Tc-DTPA for renal imaging is its relatively low extraction fraction (20%), which makes it less sensitive for evaluation of patients with more severe renal impairment, and also, it only assesses glomerular filtration and does not provide an estimate of complete renal function (i.e. ERPF). The administered dose of ^{99m}Tc-DTPA is 370–555 MBq and images are obtained immediately after injection and then sequentially up to 30 minutes (see Chapter 12).

4.7.2 ^{99m}Tc-MAG$_3$ (^{99m}Tc-Mertiatide)

^{99m}Tc-Mercaptoacetylglycine (^{99m}Tc-MAG$_3$; ^{99m}Tc-mertiatide; Figure 4.9b) is eliminated by a combination of glomerular filtration and tubular secretion, which provides an estimate of ERPF. It has a renal extraction fraction of 40–50%, which is more than twofold higher than ^{99m}Tc-DTPA, thus it has become the preferred renal imaging agent, especially in patients with severe renal impairment. ^{99m}Tc-mertiatide is highly plasma protein-bound, so its clearance does not reflect glomerular filtration, but more than 90% is excreted by tubular secretion. The administered dose of ^{99m}Tc-DTPA is 37–370 MBq and images are obtained immediately after injection (see Chapter 12).

4.7.3 ^{99m}Tc-Glucoheptonate

^{99m}Tc-glucoheptonate (Figure 4.9c) is eliminated by glomerular filtration but about 15% binds to the renal cortex, which allows imaging of any masses present in the kidneys. There is some hepatobiliary excretion, which may interfere with visualization of the kidneys. The administered dose of ^{99m}Tc-glucoheptonate is 370–555 MBq and images are obtained immediately after injection.

4.7.4 ^{99m}Tc-DMSA (^{99m}Tc-Succimer)

^{99m}Tc-Dimercaptosuccinic Acid (^{99m}Tc-DMSA; ^{99m}Tc-succimer; Figure 4.9d) is eliminated by glomerular filtration with minor tubular secretion, but localizes in the renal cortex. The radiopharmaceutical is highly plasma protein-bound (>90%) and 5% is associated with red blood cells (RBCs). ^{99m}Tc-succimer is mainly used to image the morphology of the kidneys to visualize any lesions. The administered dose of ^{99m}Tc-succimer is 74–185 MBq and images are obtained at 30–120 minutes postinjection.

4.8 Radiopharmaceuticals for Hepatobiliary Imaging

Radiopharmaceuticals for hepatobiliary imaging exploit the Kupffer cells (^{99m}Tc sulfur colloid) to image the morphology and phagocytic function of the liver and the spleen or probe hepatobiliary clearance mediated by the hepatocytes (^{99m}Tc iminodiacetic acid derivatives). Changes in the phagocytic function of the liver are associated with cirrhosis as well as focal nodular hyperplasia (FNH), a benign liver tumor (see Chapter 11). Imaging of the hepatobiliary excretory pathway is used to assess the patency of the cystic bile duct in patients with suspected acute cholecystitis (see Chapter 11). These radiopharmaceuticals are discussed in more detail below.

4.8.1 ^{99m}Tc Sulfur Colloid

^{99m}Tc sulfur colloid is an inorganic colloidal form of ^{99m}Tc ($^{99m}Tc_2S_7$) with a particle size of about 300 nm. The radiopharmaceutical is one of the few ^{99m}Tc agents that is not a chelate complex of ^{99m}Tc. It is formed by heating ^{99m}Tc sodium pertechnetate in the presence of sodium perrhenate carrier (ReO_4^-) with sodium thiosulphate at 100 °C under acidic conditions (by addition of 1 N HCl) for a defined period of time (usually two to three minutes). The reaction is stopped by adding sodium phosphate buffer, pH 7.4. It is very important that the reaction be heated for the precise time period, since too short a time will result in very small particles that are taken up by the bone marrow, while too long a time will produce much larger particles that deposit in the lungs. About 85% of ^{99m}Tc sulfur colloid localizes in the liver and about 7% in the spleen with 5% in the bone marrow. In cirrhosis of the liver, there is higher uptake by the spleen and bone marrow and lower accumulation in the liver (see Chapter 11). FNH is associated with high focal uptake of ^{99m}Tc sulfur colloid in the liver. The administered dose of ^{99m}Tc sulfur colloid is 74–185 MBq and images are obtained immediately or up to 10 minutes postinjection. ^{99m}Tc sulfur colloid that has been filtered to obtain small particles is used for sentinel lymph node detection in breast cancer using an intraoperative probe (see Chapter 9).

4.8.2 ^{99m}Tc-Iminodiacetic Acid Derivatives

^{99m}Tc iminodiacetic acid (^{99m}Tc-IDA) derivatives, which include ^{99m}Tc-disofenin (Figure 4.10a) and ^{99m}Tc-mebrofenin (Figure 4.10b), are taken up by hepatocytes via organic anion pathways and excreted through the cystic and common bile ducts into the small intestine. ^{99m}Tc-mebrofenin exhibits the highest liver uptake and lowest renal elimination and is the most commonly used agent for imaging the hepatobiliary tract. Blockage of the cystic duct by gallstones (acute cholecystitis) causes poor and delayed elimination of ^{99m}Tc-IDA agents and non-visualization of the gallbladder. The administered dose of ^{99m}Tc-mebrofenin is 150–185 MBq and serial images are obtained immediately after injection up to one hour or more postinjection to visualize the elimination of the radiopharmaceutical through the hepatobiliary tract.

4.9 Radiopharmaceuticals for Bone Imaging

Bone scans are the most common diagnostic imaging procedure in nuclear medicine. In most cases, bone imaging is performed by SPECT with ^{99m}Tc-labeled bisphosphonates but more recently, PET with ^{18}F sodium fluoride has been used. Bone scans reveal fractures, osteomyelitis, arthritis, osteoporosis, and metastasis of cancer to the bone. Bone scans are often used to stage cancer by identifying metastatic spread to the bone. Bone scanning exploits remodeling

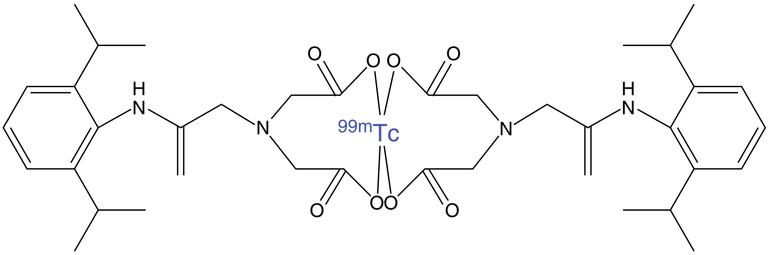

(a) ^{99m}Tc-Disofenin

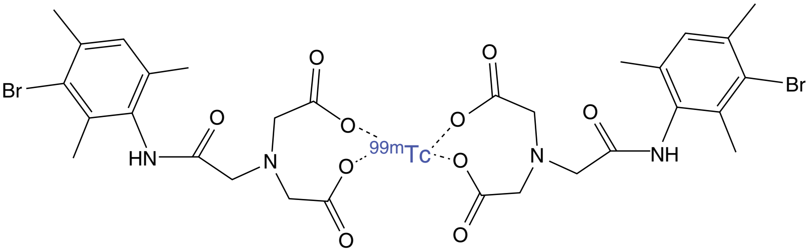

(b) ^{99m}Tc-Mebrofenin

Figure 4.10 (a, b) Hepatobiliary imaging radiopharmaceuticals.

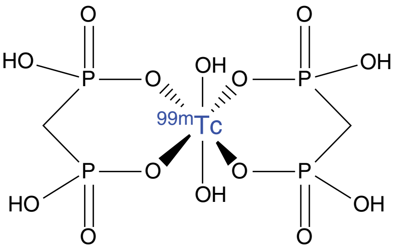

^{99m}Tc-Medronate

Figure 4.11 Bone imaging radiopharmaceutical, ^{99m}Tc-MDP.

of bone due to the activity of osteoblasts and osteoclasts and in some cases, can be more sensitive than X-rays for detecting fractures (see Chapter 14).

4.9.1 ^{99m}Tc-Bisphosphonates

The most common ^{99m}Tc-bisphosphonate used for bone scanning is ^{99m}Tc-methylene diphosphonate (^{99m}Tc-medronate; Figure 4.11). This agent, first introduced in 1975 by Gopal Subramanian [1] is structurally similar to bisphosphonates currently used to treat osteoporosis. ^{99m}Tc-medronate incorporates a methylene bridge between two phosphate groups (P–C–P), which provides stability to degradation by phosphodiesterases. An earlier agent used for bone scanning was ^{99m}Tc-pyrophosphate, which incorporated a phosphoester linkage (P–O–P), but this radiopharmaceutical was found to be unstable *in vivo*, resulting in poor-quality images. About 50% of the injected dose (370 MBq) of ^{99m}Tc-medronate binds to hydroxyapatite in the bone matrix with the remainder eliminated renally in the first 24 hours. Images are acquired at two to three hours postinjection when bone uptake is maximal and blood levels of radioactivity are low. The radiopharmaceutical is excreted into the urine, and patients are advised to void their bladder to minimize radiation dose to the pelvis.

4.9.2 ^{18}F-Sodium Fluoride (Na^{18}F)

Na^{18}F exchanges with hydroxyl anions in the hydroxyapatite matrix of the bone and is accumulated in the bone at sites undergoing remodeling. This agent was first studied for bone scanning by PET more than 40 years ago but was supplanted by SPECT imaging using ^{99m}Tc-bisphosphonates. With recent shortages of reactor-produced ^{99}Mo to produce ^{99m}Tc, there has been a resurgence in the use of cyclotron-produced Na^{18}F for bone scanning. The sensitivity of PET scans with Na^{18}F to detect bone lesions is greater than with ^{99m}Tc-bisphosphonates. The administered dose of Na^{18}F is 148 MBq and images are obtained at 15–30 minutes postinjection.

4.10 Radiopharmaceuticals for Lung Imaging

The aim of lung imaging in nuclear medicine is to identify pulmonary embolism (PE; see Chapter 8). This is achieved by comparing the results of a ventilation imaging study of the lungs with those of a perfusion study (i.e. V/Q scan). The ventilation study is performed by the patient breathing in an aerosol of ^{99m}Tc, while the perfusion study is acquired after intravenous injection of ^{99m}Tc-macroaggregated albumin (^{99m}Tc-MAA). PE is recognized on the V/Q scan as a defect in the distribution of ^{99m}Tc-MAA in the lungs, i.e. abnormal perfusion study, but normal ventilation of the lungs on images obtained with ^{99m}Tc-aerosols ("mismatch"). PE is differentiated from chronic obstructive pulmonary disease (COPD) on a V/Q scan, since in COPD, there is a matching defect on both the ventilation and perfusion studies.

4.10.1 ^{99m}Tc-Macroaggregated Albumin (^{99m}Tc-MAA)

^{99m}Tc-MAA is a suspension of denatured human serum albumin particles (10–90 μm) in sterile normal saline that is injected intravenously to perform perfusion imaging of the lungs. The particles are quickly trapped (>90%) by the lung capillaries, which have a diameter of 5–8 μm by a first-pass effect. Approximately 1.5–3 × 10^5 ^{99m}Tc-MAA particles are injected, which block <0.01% of the lung capillaries, so the risk to the patient is very low. Moreover, ^{99m}Tc-MAA particles are biodegradable, and are eventually eliminated from the lungs by disaggregation and dissolution following completion of the imaging procedure. The administered dose of ^{99m}Tc-MAA is 74–148 MBq and SPECT images are obtained immediately postinjection.

4.10.2 ^{99m}Tc-Aerosols

^{99m}Tc aerosols are employed for ventilation imaging of the lungs and are most commonly produced by aerosolizing ^{99m}Tc-DTPA or by creating an ultrafine dispersion of ^{99m}Tc-labeled carbon particles (Technegas). The aerosol particles are typically 0.5–3 μm in diameter and are breathed in by the patient for about three to five minutes before obtaining the ventilation images. The particles are eliminated by diffusion across the alveolar epithelium into the blood and excreted into the urine. ^{99m}Tc-Technegas has a particle size of 7–23 nm that agglomerate into bigger particles 60–160 nm in size. ^{99m}Tc-Technegas is generator-produced and commercially available aerosol paired with an efficient inhalation delivery system. It requires two to five inhaled breaths of ^{99m}Tc-Technegas before imaging. The administered dose of ^{99m}Tc-DTPA and ^{99m}Tc-Technegas aerosol is 1110 MBq and SPECT images are obtained immediately or up to five minutes.

4.11 Radiopharmaceuticals for Thyroid/Parathyroid Imaging

Radiopharmaceuticals used for thyroid imaging (Table 4.7) include radioiodine ($Na^{123}I$ and $Na^{131}I$) and ^{99m}Tc sodium pertechnetate ($^{99m}TcO_4^-$) as well as ^{18}F-FDG and ^{18}F-FDOPA. Radioiodine is actively taken up by the thyroid gland by anion transporters and incorporated into the thyroid hormones, tri-iodothyronine (T3) and thyroxine (T4). Thus, imaging with radioiodine or measurement of the uptake of radioiodine into the thyroid using a γ-probe provides information on thyroid function (see Chapter 10). This is used to diagnose hyperthyroidism or hypothyroidism. In contrast, since $^{99m}TcO_4^-$ is accumulated by the thyroid gland via anion transporters but is not incorporated into thyroid hormones, it is used mainly to image the thyroid to identify any anatomical lesions. Radioiodine is also used to diagnose thyroid cancer and to assess metastatic spread of this disease using whole-body SPECT imaging (see Chapter 10). There are four main forms of thyroid cancer. Papillary thyroid cancer accounts for 80–85% of cases, while follicular accounts for

Table 4.7 Properties of radiopharmaceuticals used for thyroid or parathyroid imaging.

Radiopharmaceutical	Uptake mechanism	Dose (MBq)	Clinical application
^{123}I-sodium iodide	Anion transporters and incorporation into thyroid hormones	0.37–3.7 p.o.	Thyroid uptake study and imaging of the thyroid
^{131}I-sodium iodide	Anion transporters and incorporation into thyroid hormones	3.7–11.1 p.o.	Thyroid uptake study and imaging of the thyroid and whole-body imaging of metastases from thyroid cancer
^{99m}Tc-sodium pertechnetate	Anion transporters	370 i.v.	Imaging of thyroid morphology. Parathyroid gland imaging in combination with ^{201}Tl
^{18}F-FDG	Glucose transporters	370–740 i.v.	Imaging of medullary or anaplastic thyroid cancer
^{18}F-FDOPA	Amino acid transporters	100–200 i.v.	Imaging of medullary or anaplastic thyroid cancer
^{201}Tl thallous chloride	Na^+-K^+-ATPase transporters	74 i.v.	Parathyroid gland imaging incombinationwith $^{99m}TcO_4^-$
^{99m}Tc-sestamibi	Passive diffusion	74 i.v.	Parathyroid gland imaging

anaplastic thyroid cancer (1–2%). Both papillary and follicular thyroid cancer take up radioiodine for imaging and are very effectively treated with high doses of Na^{131}I. In contrast, medullary and anaplastic thyroid cancer do not take up radioiodine and are imaged with other radiopharmaceuticals such as ^{18}F-FDG and ^{18}F-FDOPA. Parathyroid gland imaging involves a combination of radiopharmaceuticals (Table 4.7) including an agent to image the thyroid and an agent that has both thyroid and parathyroid uptake (see Chapter 10). Na^{123}I and $^{99m}TcO_4^-$ radiopharmaceuticals localize in the thyroid, while ^{99m}Tc-sestamibi and ^{201}Tl localize in both thyroid and parathyroid glands. After image subtraction and normalization the image of the parathyroid gland can be obtained. Imaging with these agents is used to diagnose parathyroid adenomas or parathyroid carcinomas, which are more rare.

4.11.1 ^{123}I- and ^{131}I Sodium Iodide (Na^{123}I and Na^{131}I)

Na^{123}I or Na^{131}I are administered orally as a capsule or solution. For diagnosing hyper- or hypo-thyroidism, the administered dose is 37–74 MBq for Na^{123}I and 37–185 MBq for Na^{131}I. Radioiodine uptake in the thyroid is measured using a γ-probe placed at a precise distance from the neck. The counts obtained with the γ-probe are converted to the percent uptake of the administered dose of radioiodine (see Chapter 10). Normal radioiodine uptake in the thyroid is 7–20% at 6 hours and 10–35% at 24 hours. Imaging of the thyroid is then performed at 24 hours to assess if there are any lesions present (e.g. thyroid nodules). The administered dose of $Na^{131}I$ to detect metastases from thyroid cancer is 296–370 MBq, and whole-body imaging is performed at 82 hours post-administration (see Chapter 10). Radioiodine is excreted into the urine with smaller amounts excreted in the feces and sweat. Higher doses of $Na^{131}I$ are used to treat hyperthyroidism (185–555 MBq) or thyroid cancer (1850–9250 MBq).

4.11.2 ^{99m}Tc Sodium Pertechnetate ($^{99m}TcO_4^-$)

^{99m}Tc sodium pertechnetate ($^{99m}TcO_4^-$) is used to image the morphology of the thyroid gland to identify lesions since it is taken up by anion transporters but not incorporated into thyroid hormones. The administered dose of $^{99m}TcO_4^-$ to image the thyroid is 74–185 MBq i.v., and imaging is performed at 15–20 minutes post-administration.

4.11.3 Other Thyroid Imaging Agents

Other radiopharmaceuticals used for thyroid imaging include ^{18}F-FDG and ^{18}F-DOPA. These agents are used to detect medullary or anaplastic thyroid carcinoma and have a high sensitivity to detect metastatic lesions. PET images of ^{18}F-FDG and ^{18}F-DOPA are obtained one hour after injection of 370–740 MBq and 100–200 MBq, respectively. Pentavalent ^{99m}Tc-dimercaptosuccinic acid ($^{99m}Tc^{5+}$-DMSA) and ^{111}In-pentetreotide are other radiopharmaceuticals used for the detection of primary medullary thyroid carcinoma and its metastatic lesions.

4.11.4 Parathyroid Gland Imaging Agents

As mentioned earlier, parathyroid gland imaging often involves dual-imaging with two different radiopharmaceuticals (see Chapter 10), one of which has preferential uptake into the thyroid, while the other has uptake into both thyroid and parathyroid glands. Combinations of $^{99m}TcO_4^-$/^{201}Tl thallous chloride, $Na^{123}I$/^{201}Tl thallous chloride, and $Na^{123}I$/^{99m}Tc-sestamibi are used for parathyroid imaging. $^{99m}TcO_4^-$ and $Na^{123}I$ are taken by thyroid gland, while ^{201}Tl thallous chloride and ^{99m}Tc-sestamibi are taken by thyroid and parathyroid glands. After the administration of either $Na^{123}I$ (11 MBq, oral) or $^{99m}TcO_4^-$ (74 MBq, i.v.), SPECT images are obtained four hours post-administration. Then the patient will receive the second dose of either ^{201}Tl thallous chloride (74 MBq, i.v.) or ^{99m}Tc-sestamibi (925–1110 MBq, i.v.). SPECT images are again obtained 15 minutes postinjection.

4.12 Radiopharmaceuticals for Imaging Infection/Inflammation

Imaging studies with radiopharmaceuticals such as ^{67}Ga gallium citrate, ^{111}In- or ^{99m}Tc-labeled leukocytes, or ^{99m}Tc-sulesomab Fab' fragments (Leukoscan) (Table 4.8) are performed to identify inflammatory bowel disease (IBD), soft-tissue sepsis, post-operative infection, abscess, osteomyelitis, and other infectious or inflammatory processes.

4.12.1 ^{67}Ga Gallium Citrate

The mechanism of uptake of ^{67}Ga in inflammatory or infectious processes is different than that responsible for tumor uptake of the radiopharmaceutical. ^{67}Ga behaves similarly to ferric iron (Fe^{3+}) and binds to lactoferrin secreted by leukocytes attracted to sites of infection as well as complexed by bacterial siderophores. ^{67}Ga is useful for imaging osteomyelitis as well as sites of infection including abscess and peritonitis as well as inflammatory processes such as sarcoidosis. ^{67}Ga has also been used to identify sites of opportunistic infections in patients with AIDS, sarcoidosis, and tuberculosis. The administered dose of ^{67}Ga to image infections or inflammation is 370 MBq, and imaging is performed at 24–72 hours postinjection.

4.12.2 ^{111}In- or ^{99m}Tc-Labeled Leukocytes (^{111}In- or ^{99m}Tc-WBC)

A patient's own leukocytes (WBC) can be isolated from a blood sample (~60 ml) and labeled *in vitro* with ^{111}In-oxine or ^{99m}Tc-HMPAO, then reinjected into the patient to image sites of infection or inflammation. ^{111}In-WBC allow imaging up to 24 hours postinjection due to the longer $t_{1/2p}$ (2.8 days) resulting

Table 4.8 Properties of radiopharmaceuticals used for imaging infection or inflammation.

Radiopharmaceutical	Uptake mechanism	Dose (MBq)	Clinical application
^{67}Ga-gallium citrate	Uptake by leukocytes due to binding lactoferrin	74–370	Detection of infectious foci
^{111}In-leukocytes	Immune response	18.5–37	Detection of inflammation, abscesses, and infections
^{99m}Tc-leukocytes	Immune response	296–370	Detection of inflammation, abscesses, and infections
^{99m}Tc-sulesomab Fab'	Affinity for granulocytes	370–555	Detection of infections and inflammation

in enhanced resolution images, while images with ^{99m}Tc-WBC are usually performed at 1–4 hours postinjection, due to the shorter $t_{1/2p}$ of ^{99m}Tc (6 hours). Both ^{111}In-oxine and ^{99m}Tc-HMPAO are lipophilic complexes that diffuse across the cell membrane and are trapped intracellularly in WBC, allowing radiolabeling. ^{111}In- or ^{99m}Tc-WBC are used to image sites of infection in patients with "fever-of-unknown-origin (FUO)", osteomyelitis, abscess, IBD, bacterial endocarditis, and other infections. The administered dose of ^{111}In-WBC or ^{99m}Tc-WBC to image infections or inflammation is 18.5 MBq and 296–370 MBq, respectively.

4.12.3 ^{99m}Tc-Sulesomab Fab'

^{99m}Tc-sulesomab Fab' are fragments of a murine anti-granulocyte reacting antigen (NCA90) monoclonal antibody labeled with ^{99m}Tc. The monoclonal Fab' fragments exhibit high sensitivity and specificity. The radiolabeling of leukocytes (^{99m}Tc-WBC) requires ex-vivo blood handling, special handling techniques, and risk of patient infection. Therefore, ^{99m}Tc-sulesomab Fab' overcomes all these issues associated with ^{99m}Tc-WBC. The administered dose of ^{99m}Tc-sulesomab Fab' is 1110 MBq, SPECT images are obtained 1, 4, and 24 hours postinjection of the radiopharmaceutical.

4.13 Therapeutic Radiopharmaceuticals

Radiopharmaceuticals are not only used for diagnostic imaging but also for therapeutic purposes, commonly referred to as radionuclide therapy (RNT). The most commonly used RNTs are ^{131}I sodium iodide, ^{177}Lu and ^{90}Y-DOTATOC/DOTATATE, ^{90}Y-ibritumomab (Zevalin), and ^{223}Ra dichloride. ^{131}I sodium iodide (HICON) is used for the treatment of hyperthyroidism and thyroid carcinoma. The administered therapeutic dose of ^{131}I sodium iodide is 1110–7400 MBq. ^{177}Lu/^{90}Y-DOTATOC/DOTATATE are radiolabeled peptides used to treat somatostatin receptor-positive malignancies. These are administered at high doses, i.e. 3.7 GBq for ^{177}Lu-DOTATOC/DOTATATE and 2.6 GBq for ^{90}Y-DOTATOC/DOTATATE. ^{90}Y-ibritumomab is a monoclonal antibody conjugated with DTPA for complexing the β-emitter, ^{90}Y. It is used to treat relapsed or refractory low-grade, follicular, or CD20-positive B-cell non-Hodgkin's lymphoma and rituximab-refractory follicular non-Hodgkin's lymphoma. ^{223}Ra dichloride (Xofigo) is an α-particle emitter used to treat castration-resistant prostate cancer in patients with symptomatic bone metastases but no known visceral metastatic disease. The administered dose of ^{223}Ra dichloride 50 kBq kg^{-1} is given at four-week intervals for six cycles.

4.14 Summary

Radiopharmaceuticals have been used for almost three-quarters of a century since the introduction of the first agent in 1946 (iodine-131). This field continues to evolve and grow since new radiopharmaceuticals and advanced imaging modalities are emerging. The introduction of medical cyclotrons has made locally available short-lived positron-emitting radionuclides for PET imaging, while radionuclide generators are the mainstay of SPECT imaging with ^{99m}Tc. Other longer-lived radionuclides may be produced commercially and shipped to nuclear medicine departments in hospitals. The application of radiopharmaceuticals to imaging diseases is highly diverse. They play a significant role in assessing myocardial function, imaging of neurological disorders, evaluation of renal function, imaging the morphology and function of the hepatobiliary system, imaging of bone diseases, imaging of PE, determination of thyroid and parathyroid function, and diagnosing and staging of cancer as well as monitoring response to treatment. In the future, imaging with radiopharmaceuticals will be used to characterize tumors (MI) and select the most appropriate treatment for patients. A major strength of radiopharmaceuticals is their ability to be used both for imaging disease as well as treating disease ("theranostic" concept). Several radiopharmaceuticals are already in use for treatment of cancer.

Reference

1 Subramanian, G., McAfee, J.G., Blair, R.J. et al. (1975). Technetium-99m-methylene diphosphonate – a superior agent for skeletal imaging: comparison with other technetium complexes. *J. Nucl. Med.* 16 (8): 744–755.

Additional Reading

Ackerhalt, R.E., Blau, M., Bakshi, S., and Sondel, J.A. (1974). A comparative study of three ^{99m}Tc-labeled phosphorus compounds and ^{18}F-fluoride for skeletal imaging. *J. Nucl. Med.* 15 (12): 1153–1157.

Delbeke, D. and Israel, O. (2010). *Hybrid PET/CT and SPECT/CT Imaging: A Teaching File*, 760. New York: Springer.

Dunet, V., Rossier, C., Buck, A. et al. (2012). Performance of ^{18}F-fluoro-ethyl-tyrosine (^{18}F-FET) PET for the differential diagnosis of primary brain tumor: a systematic review and metaanalysis. *J. Nucl. Med.* 53 (2): 207–214.

Ekhtiari, H. and Paulus, M. (2016). *Neuroscience for Addiction Medicine: From Prevention to Rehabilitation: Methods and Interventions*, 461. Amsterdam: Elsevier.

Emran, A.M. (1995). *American Chemical Society Symposium on Chemists' Views of Imaging Centers*, 537. New York: Springer.

Gratz, S., Schipper, M.L., Dorner, J. et al. (2003). LeukoScan for imaging infection in different clinical settings. *Clin. Nucl. Med.* 28 (4): 267–276.

Khalil, M.M. (2016). *Basic Science of PET Imaging*. Cham, Switzerland: Springer.

Mettler, F.A. and Guiberteau, M.J. (2012). *Essentials of Nuclear Medicine Imaging*, 607. Philadelphia, PA: Elsevier/Saunders.

Owunwanne, A., Patel, M., and Sadek, S. (1995). *The Handbook of Radiopharmaceuticals*, 236. London: Chapman & Hall Medical.

Pak, Y., Kim, E.E., and Isawa, T. (1998). *Nuclear Imaging of the Chest*, 336. New York: Springer.

Palestro, C.J., Brown, M.L., Forstrom, L.A. et al. (2004). Society of Nuclear Medicine Procedure Guideline for Gallium Scintigraphy in Inflammation. http://snmmi.files.cms-plus.com/docs/Gallium_Scintigraphy_in_Inflammation_v3.pdf (accessed 3 August 2018).

Patterson, C. and Willis, M.S. (2012). *Translational Cardiology: Molecular Basis of Cardiac Metabolism, Cardiac Remodeling, Translational Therapies and Imaging Techniques*. New York: Humana Press.

Saha, G.B. (2010). Production of radionuclide. In: *Fundamentals of Nuclear Pharmacy*. New York: Springer.

Scott, P.J. and Hockley, B.G. (2012). *Radiochemical Synthesis Volume I, Radiopharmaceuticals for Positron Emission Tomography*, 343. Hoboken, NJ: Wiley.

Tsopelas, C. (2015). Radiotracers used for the scintigraphic detection of infection and inflammation. *ScientificWorldJournal* 676719. doi: 10.1155/2015/676719.

Vallabhajosula, S. (2009). *Molecular Imaging: Radiopharmaceuticals for PET and SPECT*. Berlin: Springer-Verlag.

5

Magnetic Resonance Imaging (MRI) Technology

Raymond M. Reilly

5.1 Introduction

Magnetic resonance imaging (MRI) is a high spatial resolution imaging technology that does not employ ionizing radiation, but rather relies on the magnetic properties of protons in the body, mostly in the form of water molecules. MRI is a Nobel Prize-winning technology. Dr. Paul C. Lauterbur at the University of Illinois in the United States conceived the idea of using localized gradients in a strong magnetic field to determine the position of proton resonances in the body. Dr. Peter Mansfield at the University of Nottingham, in the United Kingdom further advanced this idea by using radiofrequency (RF) and phase-encoding to precisely identify the position of proton resonances and applied Fourier transform mathematical algorithms to reconstruct MRI images. They jointly shared the Nobel Prize for Physiology or Medicine in 2003 for their invention of MRI. MRI has since become a widely used medical imaging technology that is essential for patient care. In this chapter, only the fundamental principles of MRI technology are discussed. The reader is referred to the references and additional reading list for more detailed information on the physics of MRI. In particular, an excellent text from which much of the material for this chapter was taken is "MRI in Practice, 4th ed." edited by Westbrook, C., Roth, C.K. and Talbot J., Wiley-Blackwell, 2011.

5.2 Principles of MRI

MRI is a high spatial resolution imaging technology that does not employ ionizing radiation, but rather is based on absorption of RF energy by hydrogen nuclei (^1H) in the body placed into a strong magnetic field, and the subsequent release and detection of this energy. Atoms are composed of a nucleus surrounded by a

Medical Imaging for Health Professionals: Technologies and Clinical Applications, First Edition.
Edited by Raymond M. Reilly.
© 2019 John Wiley & Sons, Inc. Published 2019 by John Wiley & Sons, Inc.

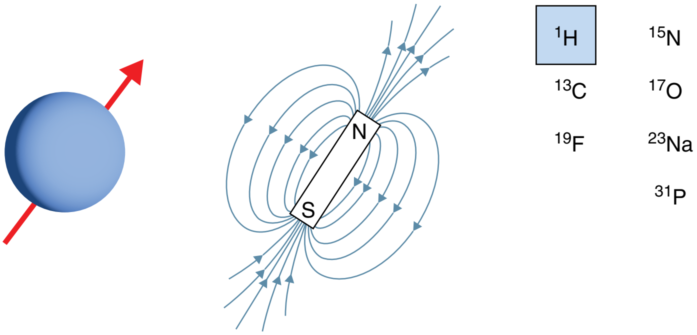

Figure 5.1 Magnetic moment (depicted by the arrow) is caused by an uneven number of protons and neutrons in nuclei. Thus, the "spin" of the protons is not completely counterbalanced by the opposite spin of the neutrons. The magnetic moment of nuclei is similar to a small magnet. Several nuclei have net magnetic moment but ^{1}H is the most abundant in tissues and is most commonly used for MRI.

cloud of electrons. The nucleus is composed of protons and neutrons, which spin in opposite directions. If the number of protons in the nucleus equals the number of neutrons, these opposing spins cancel each other and the nucleus has no overall net spin. If the number of protons does not equal the number of neutrons, then the nucleus has an overall net spin called *angular momentum* [1,2]. For example, the nucleus of ^{12}C has six protons and six neutrons, and has no net spin. In contrast, the nucleus of ^{13}C has six protons and seven neutrons and therefore has angular momentum. The nucleus of an atom can also be envisioned as a tiny magnet with a "north" and "south" pole [1]. The nucleus has a *magnetic moment* (vector) that describes the magnetic strength and orientation in space (Figure 5.1) [1,2]. Since the body is composed of 60–70% water (H_2O), the most important atomic nucleus is the hydrogen nucleus (^{1}H), which has one proton and no neutrons, and thus has a net magnetic moment. Other examples of atoms with a magnetic moment are ^{13}C, ^{15}N, ^{17}O, ^{19}F, ^{23}Na, and ^{31}P. In the absence of a strong external magnetic field denoted B_0, the magnetic moments of the hydrogen nuclei (protons) are not aligned with each other (Figure 5.2, left panel). However, once exposed to a strong magnetic field, almost all of the protons align their magnetic moments parallel to the direction of the field ("spin-up"; Figure 5.2, right panel). A small number of protons have their magnetic moment aligned in an unfavorable (higher energy) "spin-down" orientation opposite to the direction of the field [2]. The *net magnetization vector* (NMV) describes the net alignment of the magnetic moments of all the protons with the magnetic field [2].

5.2.1 Precession

In addition to alignment of their magnetic moments in the direction of the magnetic field, protons placed into a strong magnetic field spin around their axis, which is called *precession* (Figure 5.3) [1,2]. The speed of precession is termed

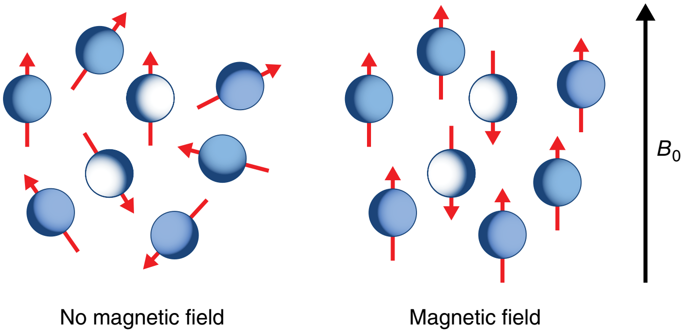
B_0
No magnetic field
Magnetic field

Figure 5.2 In the absence of a magnetic field (B_0) the magnetic moments of protons are randomly aligned. In the presence of a strong magnetic field, the magnetic moments of the protons align with the field. Most protons have their magnetic moment parallel to the field (spin-up direction) and a minority have their magnetic moment, anti-parallel (spin-down direction). *Source:* Figure adapted from Westbrook et al. [2]. Reproduced with permission of John Wiley & Sons.

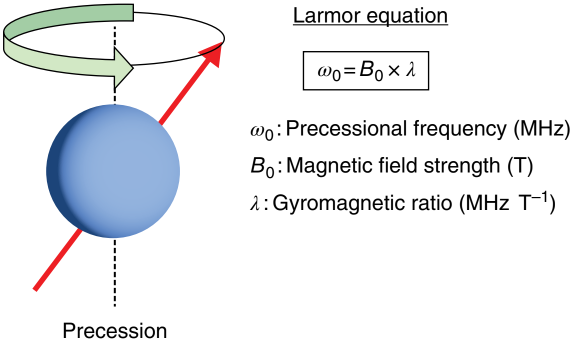
Larmor equation
$\omega_0 = B_0 \times \lambda$
ω_0: Precessional frequency (MHz)
B_0: Magnetic field strength (T)
λ: Gyromagnetic ratio (MHz T^{-1})
Precession

Figure 5.3 Protons placed into a strong magnetic field "spin" on their axis, which is called precession. The precessional frequency (ω; MHz) is dependent on the magnetic field strength (B_0; T) and the gyromagnetic ratio for protons (MHz T^{-1}). This relationship is described by the Larmor Equation. *Source:* Figure adapted from Westbrook et al. [2]. Reproduced with permission of John Wiley & Sons.

the precessional frequency and is measured in units of megahertz (1 MHz = 1 million cycles per second). The precessional frequency (ω) is dependent on the magnetic field strength (B_0) given in units of Tesla (T) and a constant (gyromagnetic ratio; λ), which relates precessional frequency to field strength (MHz T^{-1}):

$$\omega_0 = B_0 \times \lambda$$

This equation is called the Larmor equation, and provides the precession frequency (Larmor frequency) for nuclei at a particular magnetic field strength. For example, since $\lambda = 42.57\,\text{MHz}\,\text{T}^{-1}$ for ^{1}H nuclei, the Larmor frequency (ω) of protons is 42.57 MHz at a magnetic field strength of 1 T. At a field strength of 1.5 T, $\omega = 63.86$ MHz, and at 0.5 T, $\omega = 21.28$ MHz [2]. The Larmor frequency is critically important in MRI because it describes the precise energy that must be applied to cause protons to resonate (described in the next section).

5.2.2 Resonance and Phase

Application of energy at the precise Larmor frequency (RF energy) will cause protons placed in a magnetic field of a particular strength to resonate (Figure 5.4a) [1,2]. *Resonance* describes the absorption of RF energy by the protons causing more nuclei to flip to the higher energy, *spin-down* orientation,

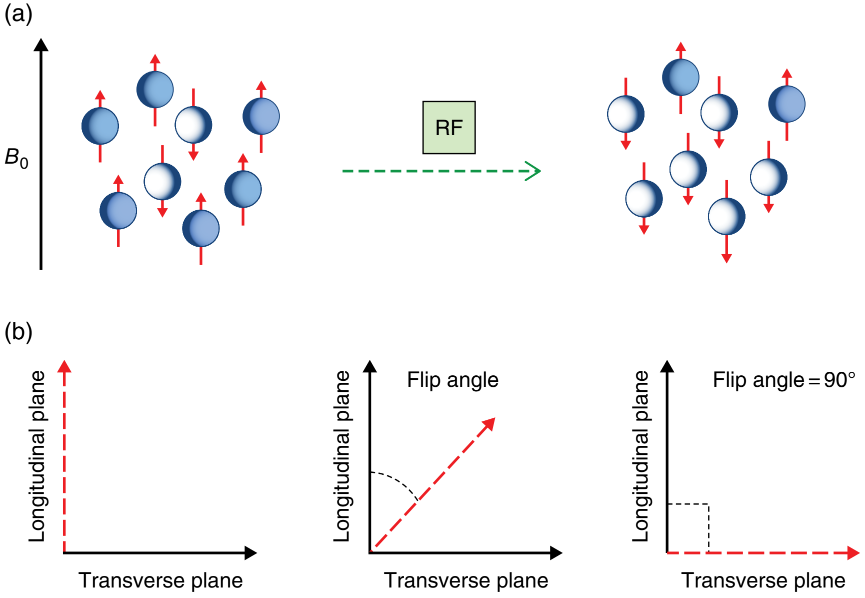

Figure 5.4 (a) Radiofrequency (RF) energy applied at the Larmor frequency will cause the magnetic moment of some protons to "flip" to the higher energy "spin-down" orientation with the magnetic field – this is called "excitation." (b) In the absence of RF energy, the net magnetization vector (NMV) shown with the broken line of all the protons is aligned with the magnetic field in the longitudinal plane. After application of RF energy, the NMV is displaced towards the transverse plane. The extent of displacement is described by the flip angle, which ranges up to 90°, depending on the proportion of the magnetic moments of the protons that are displaced. *Source:* Figure adapted from Westbrook et al. [2]. Reproduced with permission of John Wiley & Sons.

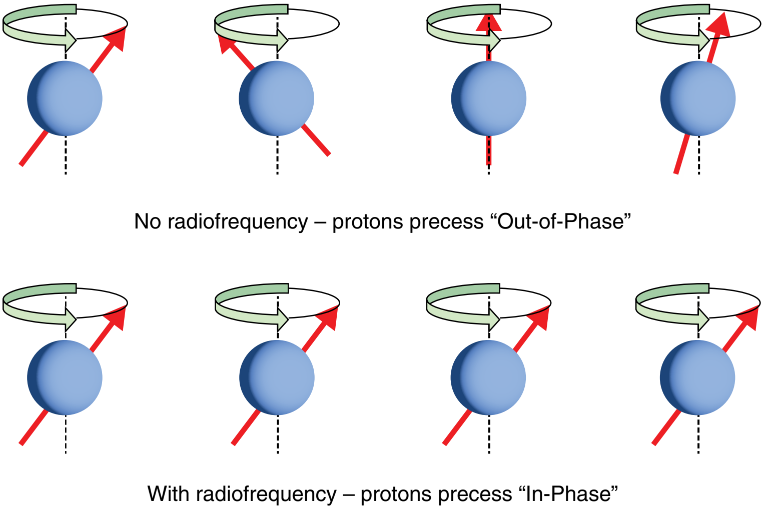
No radiofrequency – protons precess "Out-of-Phase"
With radiofrequency – protons precess "In-Phase"

Figure 5.5 In the absence of RF energy, the protons precess in an uncoordinated "out-of-phase" manner. Application of RF energy causes the protons to precess in a coordinated "in-phase" manner. *Source:* Westbrook et al. [1], chapter 1. Reproduced with permission of John Wiley & Sons.

opposite to the direction of the magnetic field. The result is that the NMV is no longer aligned with the magnetic field, but rather has an angle relative to the field direction, called the *flip angle* (Figure 5.4b) [2]. The flip angle depends on the amplitude and duration of the RF pulse applied, but is usually 90°. The orientation of the magnetic field is plotted as a vector in the longitudinal plane, while the displaced NMV is shown in the transverse plane (Figure 5.4b) [2]. Another effect of RF energy is to cause the protons to precess "in-phase" with each other (coordinated precession), whereas in the absence of such energy, they precess "out-of-phase" (uncoordinated precession) (Figure 5.5) [2].

5.2.3 The Magnetic Resonance Signal

MRI is based on placing protons in the body into a strong magnetic field, then applying RF energy at the precise Larmor frequency to cause the magnetic moment of some of the protons to flip to an orientation opposite to the field direction. A signal is then received once the RF pulse is turned off and the protons relax and give up the absorbed energy. During the relaxation process, the flip angle decreases and the NMV realigns with the magnetic field [2]. There is a decrease in the transverse vector and an increase in the longitudinal vector. The time taken for 63% of the protons to realign with the magnetic field (longitudinal vector) is known as the T1 recovery time and is due to the protons releasing their energy to the surrounding environment or lattice (Figure 5.6) [2].

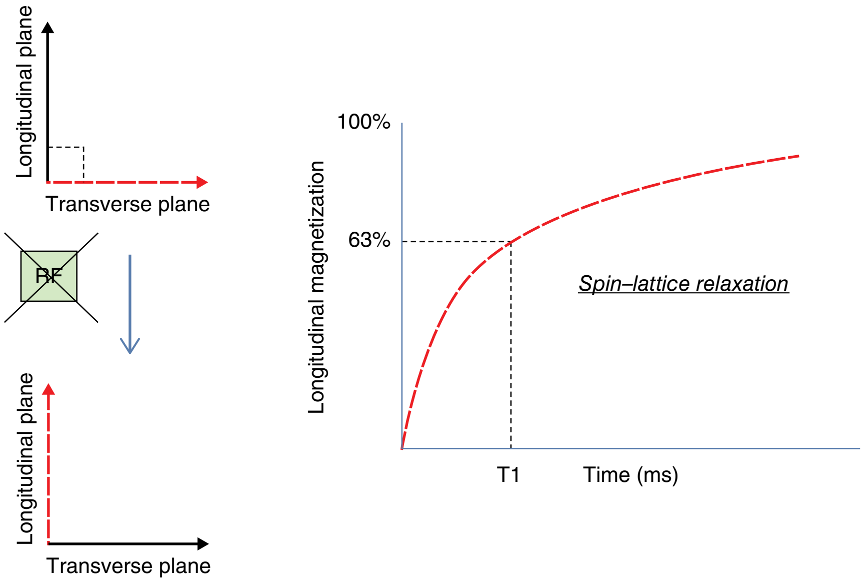

Figure 5.6 Removing the RF energy causes the magnetic moment of the protons with "spin-down" orientation to realign in a "spin-up" orientation in the direction of the magnetic field i.e. longitudinal plane (B_0). T1 is the time required for 63% of the protons to realign their magnetic moment with the direction of the magnetic field. In this process, which is termed "spin-lattice relaxation", the NMV shown by the broken line reorients from the transverse to the longitudinal plane. *Source:* Figure adapted from Westbrook et al. [2]. Reproduced with permission of John Wiley & Sons.

Thus, T1 is also known as *spin lattice relaxation*. The time taken for 63% of the protons to lose their transverse vector (i.e. 37% retaining this vector) is known as the T2 decay time (Figure 5.7) [2]. This is due to interactions between neighboring protons, and is known as *spin–spin relaxation*. It is associated with a loss of "in-phase" precession of the protons.

5.2.4 RF Pulse Sequences

In MRI, a single RF pulse is not used but rather multiple RF pulses are employed that are repeated in a particular time interval (Figure 5.8). Commonly, one RF pulse is applied at 90° to the direction of the magnetic field, then a second pulse at 180° to the field, and the signal is then acquired (*spin-echo* sequence) [3]. The repetition time (TR) in milliseconds is the time interval between the application of one pulse and the next pulse. TR determines the amount of *longitudinal relaxation* which occurs between one RF pulse and the next pulse. The echo time (TE) is the time in milliseconds between the application of the RF pulse and the acquisition of the relaxation signal (echo). TE determines the amount of *transverse decay* which occurs between pulses. There are many different RF

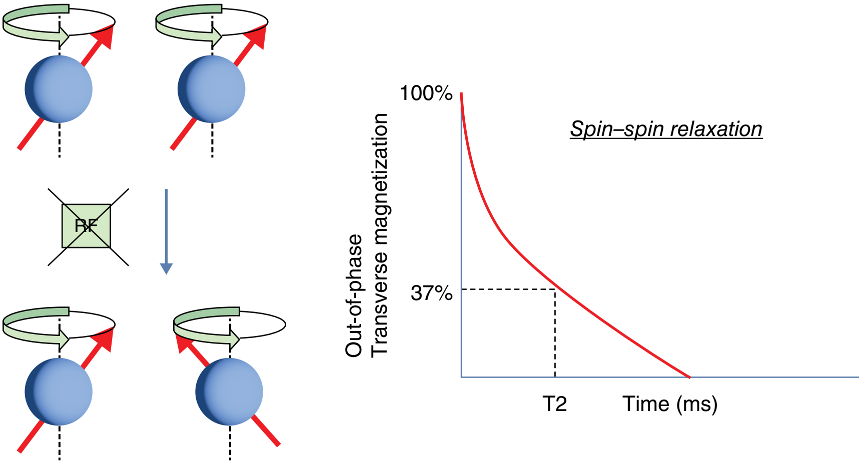
RF
100%
Spin–spin relaxation
Out-of-phase
Transverse magnetization
37%
T2
Time (ms)

Figure 5.7 Removing the RF energy causes the protons to become "out-of-phase." T2 is the time required to decrease the proportion of protons that are "in-phase" to 37%. This process is termed "spin-spin relaxation." *Source:* Figure adapted from Westbrook et al. [2]. Reproduced with permission of John Wiley & Sons.

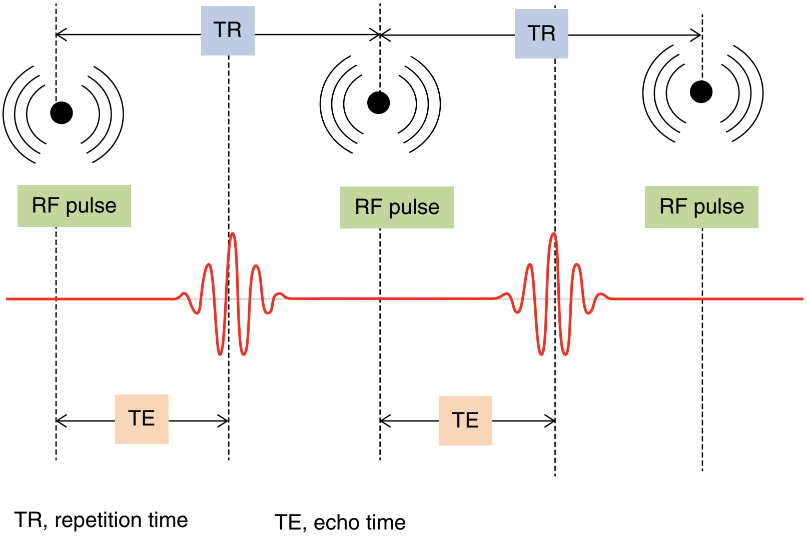
TR
TR
RF pulse
RF pulse
RF pulse
TE
TE
TR, repetition time
TE, echo time

Figure 5.8 Multiple RF pulses are used in MRI to emphasize the differences in T1 or T2 times of tissues to improve contrast. The time between one RF pulse and the next pulse is termed the repetition time (TR). The time between delivery of a RF pulse and acquisition of the relaxation signal is termed the echo time (TE). A short TR emphasizes differences in T1 times between tissues (T1-weighted MRI), while a long TE emphasizes differences in T2 times (T2-weighted MRI). Many different RF pulse sequences are available in MRI to improve image contrast. *Source:* Figure adapted from Westbrook et al. [2]. Reproduced with permission of John Wiley & Sons.

pulse sequences used in MRI to emphasize contrast between different types of tissues, which are beyond the scope of this chapter. The reader is referred to Ref. [3] for more detailed information.

5.2.5 T1- and T2-Times

MRI is excellent for visualizing soft tissues in the body. An MRI image is composed of areas of high signal intensity (bright), intermediate intensity (shades of gray), and low intensity (dark). A tissue exhibits a high signal if it has a large transverse component of the NMV at the time the signal is acquired (TE). If the transverse component of the NMV is small, then the tissue appears dark [4]. The two extremes of tissue signals in MRI are those for fat and water. *Spin–lattice* recovery occurs much slower in water than in fat and thus, T1 is much longer for water (2500 milliseconds) than for fat (200 milliseconds; Table 5.1) [1]. Since the *longitudinal vector* just prior to applying the next RF pulse is greater for fat than water, it creates a greater *transverse vector* when this second pulse is applied, resulting in a brighter (whiter) signal. In contrast, the *longitudinal vector* for water is small just before the next RF pulse is applied, creating a smaller *transverse vector* and a lower (darker) signal. These images are called T1-weighted MRI, and are favored by using a short TR [1,4]. If the TR is too long, both fat and water recover all of their longitudinal vector and there is no difference in the signals obtained. The *spin–spin* decay is faster for fat than water, and thus T2 times are much shorter for fat (100 milliseconds) than water (2500 milliseconds). In general, T2 times are always much shorter than T1 times (Table 5.1) and are emphasized by a long TE [1,4].

5.2.6 T1- and T2-Weighted MRI

By selecting the appropriate TR and TE times for the RF pulses, MRI images may be weighted for T1 (longitudinal or *spin–lattice relaxation*) or T2 (transverse or *spin–spin decay*) [1]. To weight the image for T1 (Figure 5.9), the TR must be short enough so that the magnetic moments for different tissues (e.g. fat or water) do not have sufficient time to completely realign with the magnetic

Table 5.1 T1 and T2 values for different tissues [1].

Tissue	T1 (milliseconds)	T2 (milliseconds)
Skeletal muscle	870	47
Myocardium	600	40
Liver	490	43
Fat	260	84
Blood	1210	35

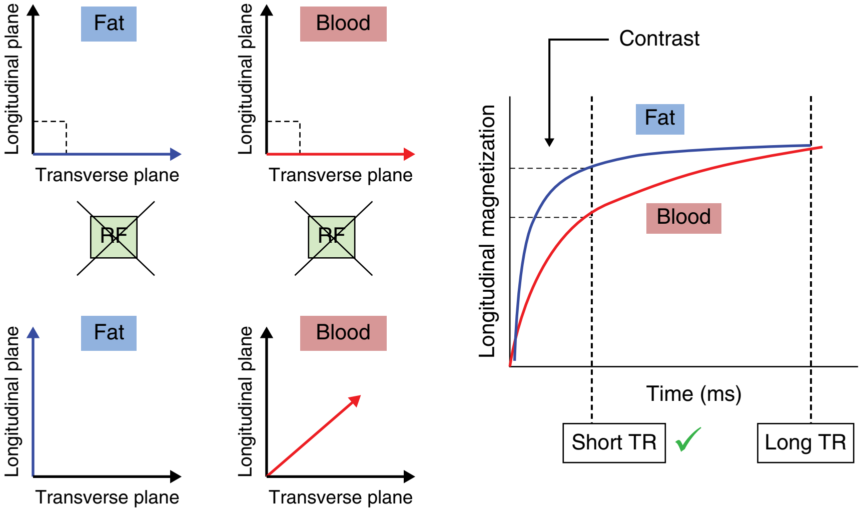
Fat
Longitudinal plane
Transverse plane
Blood
Longitudinal plane
Transverse plane
RF
RF
Fat
Longitudinal plane
Transverse plane
Blood
Longitudinal plane
Transverse plane
Contrast
Fat
Blood
Longitudinal magnetization
Time (ms)
Short TR ✓
Long TR

Figure 5.9 The shorter T1 time of fat (260 milliseconds) compared to water (blood; 1210 milliseconds) results in faster reorientation of protons in the longitudinal plane (aligned in the direction of the magnetic field) once the RF energy is removed (left panels). Thus, if the time between the first RF pulse and a second pulse (TR) is short, this will emphasize differences in T1 times between these two tissues (right panel) providing improved MRI contrast (T1-weighted MRI). *Source:* Figure adapted from Westbrook et al. [4]. Reproduced with permission of John Wiley & Sons.

field (B_0) [4]. This exploits differences in the T1 relaxation times between the different tissues to create image contrast. To weight the image for T2 (Figure 5.10), the TE must be long enough to exploit differences in the transverse relaxation times (*spin–spin* decay) between different tissues [4]. Generally, *TE must be long for T2-weighted MRI.* A long TR and a short TE weight the image for proton density rather than relaxation times. T2* decay is the T2 signal obtained when the RF pulse is removed. T2* is shorter than T2 due to inhomogeneities in the magnetic field strength of the MRI system, which accelerates *spin–spin* de-phasing [1,4]. A comparison of T1- and T2-weighted MRI is shown for a patient with a glioblastoma (a type of brain tumor) in Figure 5.11 [5]. Brain tissue, which has a high fat content, appears bright on the T1-weighted image (Figure 5.11 left panel), while the tumor, which is surrounded by edema (water), appears dark [1]. In the T2-weighted image (Figure 5.11 right panel), the brain tissue is dark, and the tumor appears bright [1].

5.2.7 Signal Encoding Using Magnetic Gradients

To form an image with MRI, it is necessary to spacially encode the location of the signal in three-dimensional space (*X, Y, Z*). This is achieved by magnetic field gradients. Using electromagnets (*gradient coils*), the field strength of the

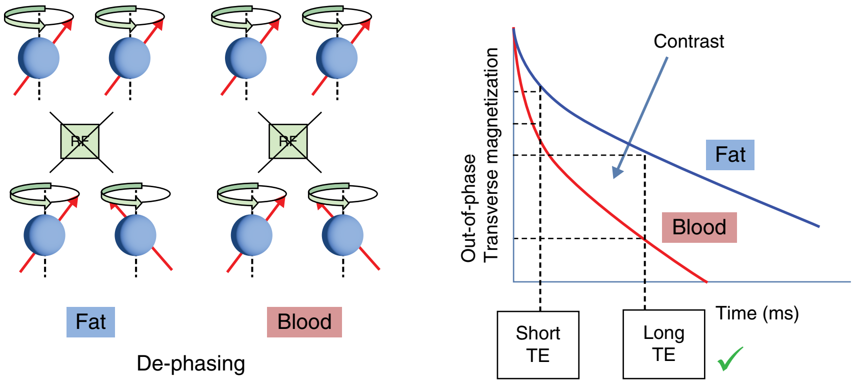

Figure 5.10 The shorter T2 time of water (blood; 35 milliseconds) compared to fat (84 milliseconds) results in faster *spin–spin* de-phasing once the RF energy is removed (left panels). Thus, if the time to acquisition of the relaxation signal is long (TE), this will emphasize differences in T2 times between these two tissues (right panel) providing improved MRI contrast (T2-weighted MRI). *Source:* Figure adapted from Westbrook et al. [4]. Reproduced with permission of John Wiley & Sons.

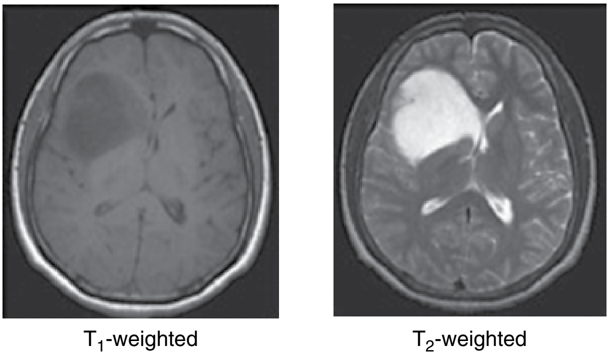
T_1-weighted

T_2-weighted

Figure 5.11 A 36-year-old female patient with large glioblastoma (GBM), a type of brain tumor. On a T1-weighted image obtained using a short TR (left panel), fat appears bright while water appears dark. In a T2-weighted image obtained using a long TE (right panel), fat appears dark but water (or blood) appears bright. *Source:* Pouratian et al. [5]. Reproduced with permission of Springer Nature.

permanent superconducting magnet in MRI is systematically and slightly altered along the X, Y, or Z-direction (Figure 5.12) [1,2]. For example, for a 1.0 T magnetic field, the field strength along the Z-axis (sagittal plane) may range from 1.005 T at the head of the patient to 0.9995 T at the patient's feet [6]. Since the magnetic field strength is slightly different along the Z-axis, this means that the precise Larmor frequency required to excite protons will also vary along the Z-axis, and conversely, the RF signal received when the protons relax along the

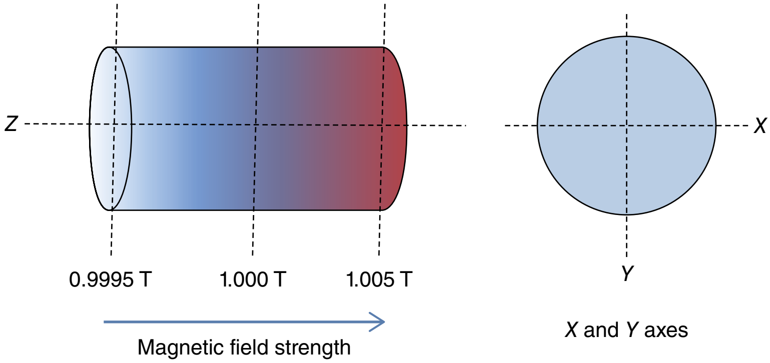

Figure 5.12 Electromagnets slightly alter the magnetic field experienced by protons along the *X*, *Y*, and *Z* directions, thereby changing the Larmor frequency required for excitation at different positions ("slices") through the body. The relaxation signal of protons within a particular slice in the *X*, *Y*, or *Z*-direction is emitted at a Larmor frequency that corresponds to the magnetic field strength at this slice in the body, providing spatial information to form the image. *Source:* Figure adapted from Westbrook et al. [6]. Reproduced with permission of John Wiley & Sons.

Z-axis will be slightly different. Gradient coils in the *X*-direction (axial plane) and in the *Y*-direction (coronal plane) similarly create small differences in the magnetic field strength, which generate different Larmor frequencies [6]. A particular slice through the body can easily be selected by applying a RF pulse that corresponds to the Larmor frequency at that position in the magnet (and patient's body). A slice in the *Z*-direction is selected using the *Z*-gradient coil, one in the *Y*-direction using the *Y*-gradient coil, and one in the *X*-direction using the *X*-gradient coil (Figure 5.13) [6]. *Frequency encoding* is used to select the slice, and a process called *phase encoding* is used to identify the position of the signal within a slice (Figure 5.14) [6]. This process also employs a magnetic gradient and takes advantage of different rates of precession for protons (phasing) depending on the field strength that they experience.

5.2.8 *K*-Space and Image Formation

Frequency-encoded data and phase-encoded data, which spatially define the position of the signal in MRI, are stored in *K-space*. *K*-space represents a mathematical matrix of all of the data acquired, which provides the information for constructing the image. For a more detailed description of *K*-space, the reader is referred to Ref. [6]. A Fast Fourier Transform (FFT) algorithm converts the *K*-space data into a gray scale MRI image. A detailed explanation of the FFT is beyond the scope of this chapter. The reader is referred to Ref. [6].

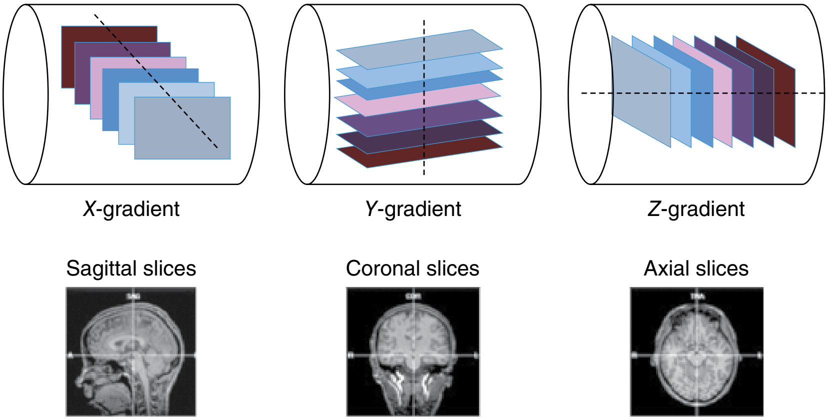
X-gradient
Y-gradient
Z-gradient
Sagittal slices
Coronal slices
Axial slices

Figure 5.13 Magnetic gradients in the *X*, *Y*, and *Z* directions allow slices along the sagittal, coronal, and axial planes as shown in the MRI images of the brain at the bottom. *Source:* Figure adapted from Westbrook et al. [6]. Reproduced with permission of John Wiley & Sons.

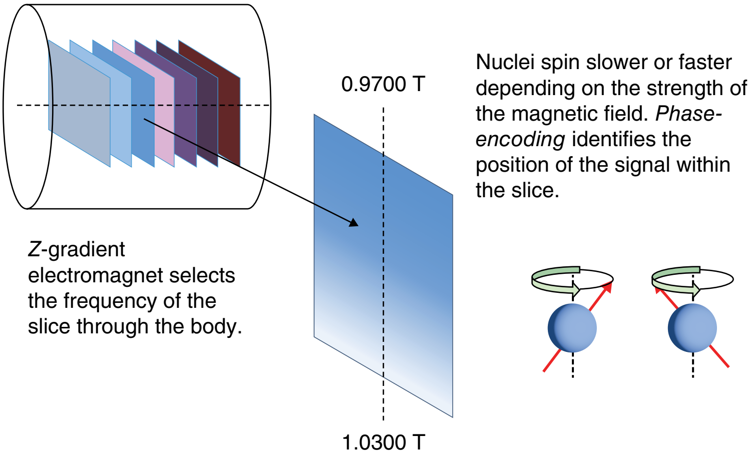
0.9700 T
1.0300 T
Nuclei spin slower or faster depending on the strength of the magnetic field. *Phase-encoding* identifies the position of the signal within the slice.
Z-gradient electromagnet selects the frequency of the slice through the body.

Figure 5.14 A particular slice through the body is selected by the gradient magnet (e.g. Z-magnet). The position of the relaxation signal within the slice is determined based on magnetic gradients, which cause protons within the slice to spin at different precession rates ("phase-encoding"). *Source:* Figure adapted from Westbrook et al. [6]. Reproduced with permission of John Wiley & Sons.

5.3 Components of the MRI System

The MRI system (Figure 5.15) consists of a powerful superconducting magnet to provide a strong magnetic field (B_0), a RF source for excitation of protons in the body and a receiver to receive the signals, magnetic field gradients to

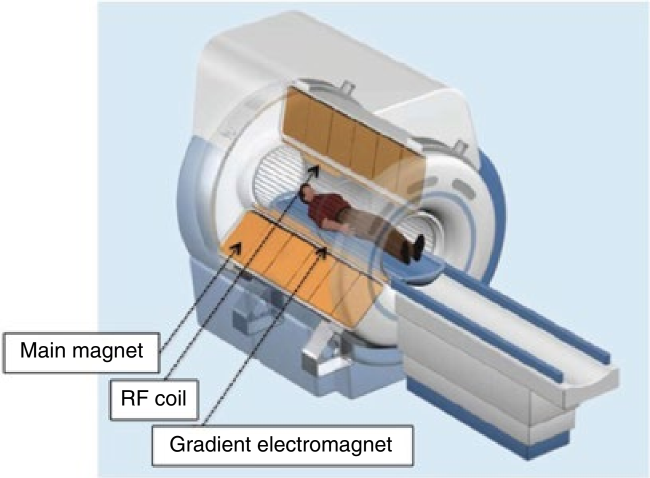

Figure 5.15 Components of an MRI system showing the main magnet, gradient electromagnets, and RF coil. *Source:* From https://www.symmetrymagazine.org/article/december-2008/deconstruction-mri.

spatially encode the signals, and a computer and image processing station to convert the signals into images and display these for the radiologist [7].

5.3.1 Superconducting Magnet

A *superconducting magnet* used for MRI employs wires made of niobium or titanium [7]. These materials exhibit the property of superconductivity such that when cooled below an extremely low temperature (4°K = −269 °C), they will conduct a current without resistance indefinitely, and will not heat up. Application of voltage is only required to ramp up the magnet and then is no longer needed, thus greatly reducing operating costs. A superconducting magnet produces field strengths of 0.5–3 T, or higher needed for MRI. The magnetic coil is supercooled by submerging in liquid nitrogen or liquid helium contained in a stainless-steel tank known as a cryostat. There are several safety considerations in MRI that pertain to the strong and continuous magnetic field risk associated with superconducting magnets for ferromagnetic objects (see section on *Safety Considerations*). The magnet cannot be turned off, and therefore, there is always a high magnetic field risk in the MRI suite.

5.3.2 Gradient Coils

Gradient coils (Figure 5.15) are less powerful electromagnets that surround the main superconducting magnet and create magnetic field gradients in the *X*, *Y*, and *Z*-directions to spatially encode the signals acquired from different positions in the body based on their Larmor frequency and phasing (Figures 5.12 and 5.13) [7]. These are not superconducting magnets but are instead electromagnets, and thus they generate heat as current is passed through the wire coils, requiring water cooling.

5.3.3 RF Coils

The RF coils include both transmitter coils and receiver coils [7]. An RF coil that both transmits and receives is known as a transceiver coil. The MRI system (Figure 5.15) has an integrated whole body transceiver coil which creates RF pulses at 90° to the direction of the main magnetic field (B_0). Other designs of RF coils (local coils) may be used to image the chest, head, abdomen or extremities (e.g. knee or wrist) [7]. Such local coils provide greater spatial resolution of small structures. In some cases, the body RF coil may be used to send the RF pulse and the local coil used to receive the signals. There are safety considerations in MRI that pertain to the use of RF coils (see Section 5.4). Patients may accidentally receive burns from the cables connecting the RF coil to the system if these are not properly insulated.

5.3.4 Computer and Image Storage System

The MRI system is interfaced with a computer work station that enables the technologist to set the parameters and acquire images [7]. Preassigned protocols may be used or the technologist may manually select a protocol for imaging. Each protocol includes settings for image contrast (e.g. TR and TE), resolution (field-of-view [FOV], slice thickness, matrix), and scan time [7]. Images are stored on the hard drive of the computer on a Picture Archiving and Communication System (PACS) or may be transferred to a CD or DVD.

5.4 MRI Safety Considerations

MRI employs a strong magnetic field (0.5–3.0 T) and the superconducting magnet is continuous, i.e. it cannot be turned off. Thus, any ferromagnetic materials brought into the MRI suite will be rapidly and strongly drawn into the MRI bore [8,9]. Serious accidents have occurred with oxygen cylinders acting as projectiles and being quickly drawn into the MRI bore, in one case fatally injuring a patient. Rules are strictly enforced in the MRI suite to prohibit any ferromagnetic materials from being brought into the room. Furthermore, ferromagnetic materials in the patient (e.g. shrapnel, bullets, ocular or cochlear implants, intraocular ferrous foreign bodies) may pose a risk for the patient to receive an MRI, due to the potential for movement caused by the strong magnetic field [8,9]. In addition, cardiac pacemakers may be affected by both the magnetic field and RF pulses used in MRI, preventing the patient from undergoing an MRI scan [8]. For a list of implants in patients that are safe or unsafe, see Table 5.2 and Ref. [8]. There is a risk of skin heating and burns from RF coils, especially if the cables from local RF coils are placed too close to the patient and if high RF frequencies are used. Noise is also an issue with MRI, since operation of the gradient magnets generates a loud sound. Patients should wear ear protection (e.g. earplugs or headphones). Rupture and a subsequent catastrophic loss of cryogens from the main magnet will cause a loud rapid release of a large volume of gases into the room displacing the room oxygen [8]. In these cases, which are very rare, patients need to be evacuated from the MRI suite and assessed for asphyxia, hypothermia, and eardrum damage [8,9].

Table 5.2 Safety of patient implants in MRI.[a]

Metallic implant	Complications in MRI	Safety recommendation
Ocular implants and intra-ocular ferrous bodies	May move	MRI not safe
Bullets, pellets, and shrapnel	May move	MRI may be unsafe
Orthopedic implants	Minor. RF heating of implants	MRI safe
Surgical clips and pins	Minor. RF heating of implants	MRI safe but should be delayed for four to six weeks after surgery
Cochlear implants	May move	MRI not safe
Cardiac pacemakers	Effected by RF pulse and magnetic field	MRI not safe
Intracranial vascular clips	May move	MRI not safe unless clip proven to be safe for MRI
Intravascular coils, filters, and stents	Unlikely to move	MRI safe but should be delayed for several weeks after implantation
Extracranial vascular clips (e.g. carotid artery)	May move slightly	MRI should be delayed for four to six weeks
Vascular access ports	None	MRI safe
Heart valves	May move slightly	MRI safe

[a] For a more detailed discussion, see Ref. [8].

5.5 MRI Contrast Agents

To improve the contrast between tissues in MRI, contrast agents are often administered. Most commonly, chelates of gadolinium (Gd^{3+}) are used (Figure 5.16) [10–12]. Gd exhibits paramagnetic properties, in that it mostly

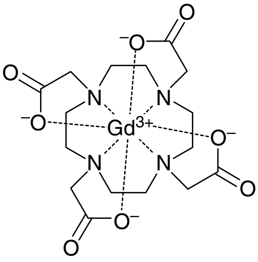

Gd-DOTA
Dotarem®
(Guerbet)

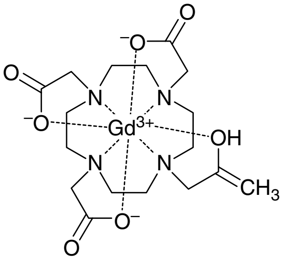

Gd-HP-DO3A
ProHance®
(Bracco)

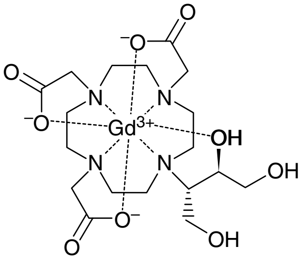

Gd-BT-DO3A
Gadovist®
(Schering)

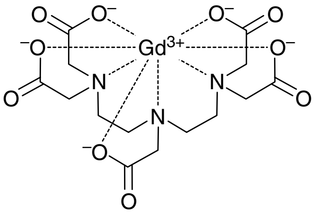

Gd-DTPA
Magnevist®
(Schering)

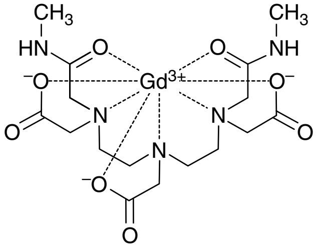

Gd-DTPA-BMA
Omniscan®
(Amersham)

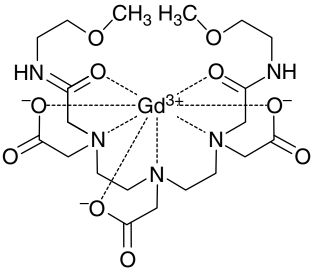

Gd-DTPA-BMA
OptiMARK®
(Malincksodt)

Figure 5.16 Gd chelates approved in the United States as MRI contrast agents.
Source: Xiao et al. [10]. Reproduced with permission of Royal Society of Chemistry.

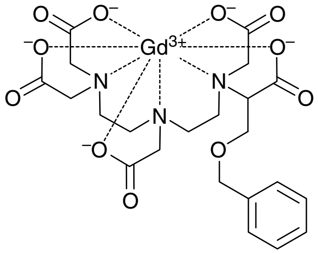

Gd-BOPTA
MultiHance®
(Bracco)

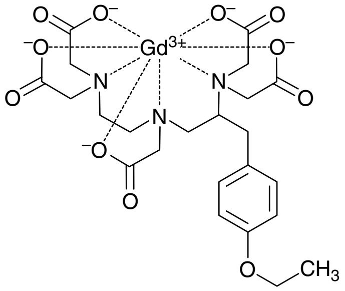

Gd-EOB-DTPA
Primovist® (Eovist®)
(Schering)

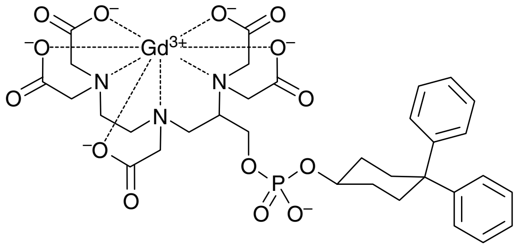

MS-325
Vasovist® (AngioMARK®)
(EPIX/Schering, Malincksodt)

Figure 5.16 (Cont'd)

shortens T1 times of the protons in water molecules, which enhances the relaxation signal. Thus, tissues that accumulate high concentrations of Gd chelates will appear brighter on T1-weighted MRI, and those that have low concentrations will appear darker, thereby improving contrast. Contrast agents are most commonly administered by i.v. injection, but in some cases may be administered orally for imaging of the GI tract. The effect of contrast agent on improving image quality is shown in Figure 5.17. An important issue in the use of Gd to improve image contrast in MRI is the toxicity of Gd. The LD_{50} for uncomplexed Gd in mice is 0.4–0.8 mmol kg^{-1}, but when chelated by diethylentriaminepentaacetic acid (DTPA) as in gadopentate dimeglumine (GD-DTPA; Magnevist) contrast used for MRI, the toxicity is reduced by 100-fold (LD_{50} = 40–80 mmol kg^{-1}). The dose of Gd-DTPA used for MRI in humans is 0.05–0.2 mmol kg^{-1}, providing a wide safety margin [11]. Nonetheless, Gd contrast agents are cleared by the kidneys and these agents have caused nephrogenic systemic fibrosis (NSF) in patients with poor renal function [11]. NSF is a fatal condition that can be treated but there is no cure. Gd-agents are thus contraindicated for patients with poor renal function.

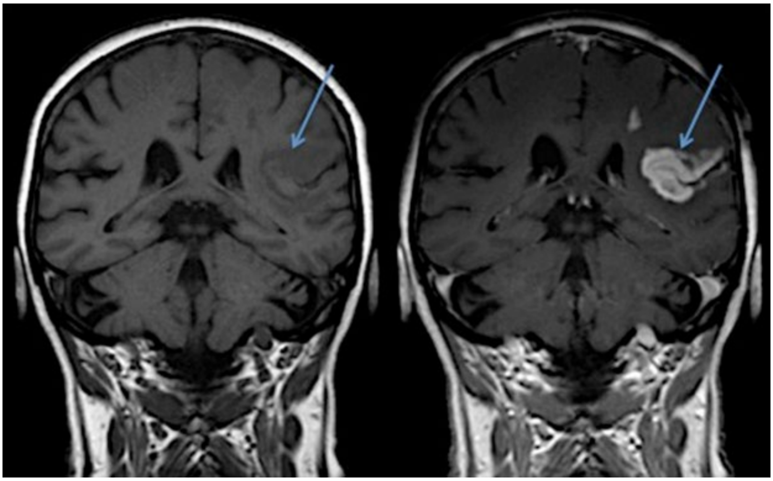

Figure 5.17 T1-weighted MRI image without contrast (left) or with contrast (right), demonstrating an abnormality (arrows) associated with a stroke that is more clearly visualized with contrast. *Source:* Image obtained from Wikipedia (https://en.wikipedia.org/wiki/MRI_contrast_agent).

5.6 Summary

MRI exploits the magnetic moment of protons (^{1}H), which are ubiquitous in the body. Placed into a strong magnetic field, the magnetic moments of protons align in the direction of the field and the protons precess (spin). Application of RF energy at the precise Larmor frequency (resonance) causes the magnetic moments of some protons to be displaced away from the direction of the magnetic field and the protons to precess in a coordinated manner (in-phase). Removal of the RF energy causes proton relaxation with release of RF energy associated with realignment of the magnetic moments of the protons in the direction of the magnetic field direction, and de-phasing of proton spins. The times taken for realignment with the magnetic field (T1) and de-phasing of proton spins (T2) are used to form MRI images. Spatial information is provided using small gradients in the magnetic field from the head to the feet of the patient, which cause protons at different positions in the body to resonate at different Larmor frequencies. Frequency encoding of different rates of proton precession in magnetic field gradients is also used to identify the position of proton resonance. Contrast agents are commonly used in MRI to improve the contrast between different tissues. These are composed of Gd complexed to chelators that reduce its toxicity. MRI is one of the most widely used medical imaging technologies, essential for patient care.

References

1 Bushberg, J.T., Seibert, J.A., Leidholdt, E.M. Jr., and Boone, J.M. (2012). Magnetic resonance basics: magnetic fields, nuclear magnetic characteristics, tissue contrast, image acquisition. In: *The Essential Physics of Medical Imaging*, 402–448. Philadelphia, PA: Wolters Kluwer.
2 Westbrook, C., Roth, C.K., and Talbot, J. (2011). Basic principles. In: *MRI in Practice*, 4e, 1–20. Chichester, UK: Wiley-Blackwell.
3 Westbrook, C., Roth, C.K., and Talbot, J. (2011). Pulse sequences. In: *MRI in Practice*, 4e, 140–197. Chichester, UK: Wiley-Blackwell.
4 Westbrook, C., Roth, C.K., and Talbot, J. (2011). Image weighting and contrast. In: *MRI in Practice*, 4e, 21–58. Chichester, UK: Wiley-Blackwell.
5 Pouratian, N., Asthagiri, A., Jagannathan, J. et al. (2007). Surgery insight: the role of surgery in the management of low-grade gliomas. *Nat. Clin. Pract. Neurol.* 3 (11): 628–639.
6 Westbrook, C., Roth, C.K., and Talbot, J. (2011). Encoding and image formation. In: *MRI in Practice*, 4e, 59–102. Chichester, UK: Wiley-Blackwell.
7 Westbrook, C., Roth, C.K., and Talbot, J. (2011). Instrumentation and equipment. In: *MRI in Practice*, 4e, 307–340. Chichester, UK: Wiley-Blackwell.
8 Westbrook, C., Roth, C.K., and Talbot, J. (2011). MRI safety. In: *MRI in Practice*, 4e, 341. Chichester, UK: Wiley-Blackwell.
9 Bushberg, J.T., Seibert, J.A., Leidholdt, E.M. Jr., and Boone, J.M. (2012). Magnetic resonance imaging: advanced image acquisition methods, artifacts, spectroscopy, quality control, siting, bioeffects, and safety. In: *The Essential Physics of Medical Imaging*, 449–499. Philadelphia, PA: Wolters Kluwer.
10 Xiao, Y.-D., Paudel, R., Liu, J. et al. (2016). MRI contrast agents: classification and application [review]. *Int. J. Mol. Med.* 38: 1319–1326.
11 Westbrook, C., Roth, C.K., and Talbot, J. (2011). Contrast agents in MRI. In: *MRI in Practice*, 4e, 372–395. Chichester, UK: Wiley-Blackwell.
12 Hermann, P., Kotek, J., Kubicek, V., and Lukes, I. (2008). Gadolinium(III) complexes as MRI contrast agents: ligand design and properties of the complexes. *Dalton Trans.* 23: 3027–3047.

Additional Reading

Westbrook, C., Roth, C.K., and Talbot, J. (2011). Functional imaging techniques. In: *MRI in Practice*, 4e, 396. Chichester, UK: Wiley-Blackwell.

6

Ultrasound Imaging Technology

Raymond M. Reilly

6.1 Principles of Ultrasound Imaging

Ultrasound (US) imaging employs high-frequency sound waves that penetrate the body and are reflected back (i.e. echo) at tissue interfaces to generate an image (Figure 6.1). The principles are summarized in this chapter, but the reader is referred to Ref. [1] for more detailed information. The sound waves are both produced and detected by an US transducer (Figure 6.2; for description see next section). Sound waves with very low frequencies <15 cycles per second (Hz) are in the *infrasound* range (Figure 6.3), while humans hear sounds with intermediate frequencies between 15 Hz and 20 kHz (*audible* range). Sound waves with very high frequencies of 2–10 MHz are in the *US* range and these are employed for US imaging. The speed at which US waves propagate through tissues varies greatly with tissue density, with higher speeds found for more dense tissues such as bone (4000 $\mathrm{m\,s^{-1}}$) compared to soft tissues such as kidneys or liver (1500 $\mathrm{m\,s^{-1}}$) or the lungs (600 $\mathrm{m\,s^{-1}}$), which are composed mostly of air (300 $\mathrm{m\,s^{-1}}$) [1]. The depth of penetration of US waves is inversely proportional to their frequency with higher frequencies penetrating less deeply into tissues and lower frequencies penetrating more deeply. Thus, lower frequencies (3–5 MHz) are used to image deep-seated structures (e.g. abdominal US), while higher frequencies (7–10 MHz) are used to image superficial structures (e.g. breast US) [1]. The intensity of the US wave ($\mathrm{mW\,cm^{-2}}$) is a measure of the power applied per unit area of tissue by the transducer. The relative intensity (RI) describes the intensity of the incident US wave (I_2) relative to the reflected wave at the tissue interface (echo; I_1) and is given in units of decibels (Db) [1]:

$$\text{Relative Intensity, RI}\left(\text{Db}\right) = 10 \times \text{Log}\left(\frac{I_2}{I_1}\right)$$

Medical Imaging for Health Professionals: Technologies and Clinical Applications, First Edition.
Edited by Raymond M. Reilly.
© 2019 John Wiley & Sons, Inc. Published 2019 by John Wiley & Sons, Inc.

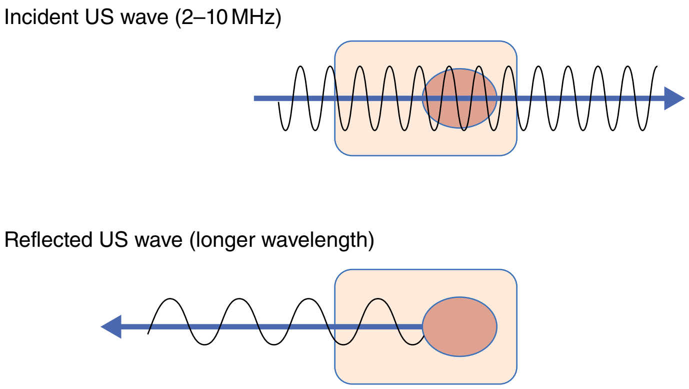
Incident US wave (2–10 MHz)
Reflected US wave (longer wavelength)

Figure 6.1 Ultrasound imaging is based on the reflection of a high-frequency sound wave at tissue interfaces. The reflected ultrasound wave has a longer wavelength (lower energy) than the incident sound wave (2–10 MHz).

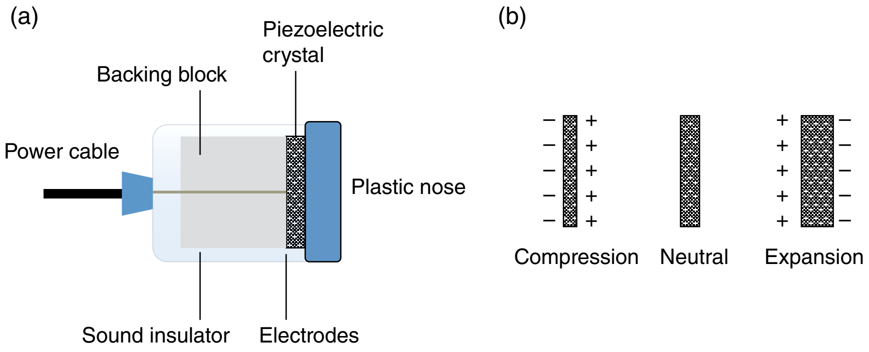
(a)
Piezoelectric crystal
Backing block
Power cable
Plastic nose
Sound insulator
Electrodes
(b)
Compression
Neutral
Expansion

Figure 6.2 (a) Ultrasound transducer. (b) Application of a charge (several hundred volts) to the transducer deforms the PZT (lead–zirconium–titanium) piezoelectric crystal from a compressed state through neutral to an expanded state. This results in a change in the arrangement of the dipoles of the crystal creating a surface charge, which creates a high-frequency (2–10 MHz) incident ultrasound (US) wave. The piezoelectric crystal similarly deforms when the reflected sound wave is returned from tissue interfaces, resulting in a change in the arrangement of the dipoles, a change in the surface charge of the crystal, and transmission of a small charge, which contributes to forming the US image. Figure adapted from Ref. [1].

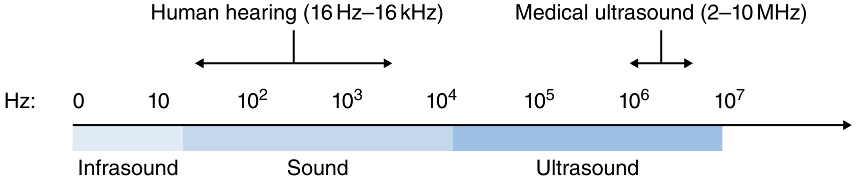
Human hearing (16 Hz–16 kHz)
Medical ultrasound (2–10 MHz)
Hz:
0
10
10²
10³
10⁴
10⁵
10⁶
10⁷
Infrasound
Sound
Ultrasound

Figure 6.3 Range of sound frequencies. The infrasound range is from 0 to 10 Hz. Humans can hear sounds with frequencies of 16 Hz–16 kHz. The ultrasound range is from 10^4 to 10^6 Hz. Medical ultrasound utilizes sound with frequency between 2 and 10 MHz to form images of the body.

Table 6.1 Fraction of reflected ultrasound energy at tissue interfaces.

Tissue interface	Fraction reflected
Liver–kidney	0.000 03
Liver–fat	0.011
Fat–muscle	0.015
Soft tissue–water	0.20
Muscle–bone	0.41
Muscle–lung	0.65
Soft tissue–air	0.99

An intensity ratio of 1 million (10^6) corresponds to 60 Db, while a ratio of 100 (10^2) corresponds to 20 Db. A twofold decrease in US intensity is equivalent to −3 Db, since RI = 10 × Log (1/2) = 10 × −0.3 = −3 Db. This is known as the half-value thickness (HVT) and corresponds to the thickness of medium that reduces the intensity of the US wave by half [1]. US waves interact with tissues by several processes: refraction, scattering, absorption, and reflection [1]. Refraction is a change in the direction of the incident US wave. Scattering occurs due to refraction or reflection and produces the "gray scale" of US images. Absorption is the loss of US energy to heat as the sound wave propagates through tissues, resulting in attenuation. Reflection is the most important process for generating the US image, and occurs when two adjacent tissues have different *acoustic impedance*. Acoustic impedance describes the compressibility of tissues to sound waves. Small differences in compressibility between two tissues permit transmission of the US wave and result in only a small amount of reflected energy, whereas large differences in tissue compressibility cause a high proportion of the US energy to be reflected back towards the transducer. An example of a major difference in acoustic impedance is between air and the surface of the body, which results in almost 100% of the US energy to be reflected (Table 6.1). This is the reason why a gel is applied to the skin for US imaging – the gel eliminates this interface, so that the US wave can penetrate the body and is not completely reflected back to the transducer (Table 6.1).

6.1.1 US Transducer

A transducer (Figure 6.2a) produces the US wave and also detects the reflected US wave. The transducer incorporates a piezoelectric ceramic crystal that in response to an electronic charge mechanically deforms to generate the incident

US wave (Figure 6.2b) [1]. A voltage of 150 V applied for a very short period of time (1 μs) causes the crystal to deform and generate the US wave. The frequency of the wave generated depends on the thickness of the piezoelectric crystal – higher frequencies are produced by thinner crystals, and lower frequencies by thicker crystals. The reflected sound wave interacts with the piezoelectric crystal similarly deforming the crystal, which generates an electronic charge resulting in a signal (Figure 6.2b). The piezoelectric crystal is composed of lead–zirconate–titanate (PZT), which forms an array of charged dipoles that when compressed or expanded results in different charges on the opposing surfaces (positive or negative) [1]. Electrodes attached to each surface measure changes in this potential difference over time to produce the image. In most clinical US transducers, there is an array of 128 to 512 PZT crystals arranged in a linear or curvilinear geometry [1]. A linear array produces a rectangular field-of-view. A curvilinear array produces a trapezoidal field-of-view. In a phased array, individual PZT crystals are sequentially activated with a time-delay (phase), which allows scanning of an area of the body without moving the transducer. Other components of the transducer include the damping block and matching layer. The damping block at the back of the PZT crystal array absorbs any US energy that passes through the PZT crystal and is not detected. The matching layer at the front of the PZT crystal provides an interface between the crystal and the body and has an acoustic impedance similar to that of soft tissue, to permit transmittance of the sound wave into the body [1].

6.1.2 Image Acquisition and Display Modes

US images are obtained by transmitting a pulse of US energy into the body and then recording the US wave reflected from tissue interfaces (i.e. echo). A typical US imaging system is shown in Figure 6.4a. The US system has a beam former, which shapes the US beam for the particular application [1]. A pulser or transmitter provides voltage to the PZT crystals in the transducer to create the US wave and adjust its intensity. A transmit/receive switch changes the transducer from pulse mode to receive mode. In *pulse-echo mode*, the US wave is only occasionally but repeatedly emitted, while most of the time the transducer is in receive mode [1]. The pulse repetition frequency (PRF) is the number of pulses per second, which is most often 2000–4000. The pulse repetition period (PRP) is the inverse of PRF, i.e. the number of seconds per pulse, usually 500 μs. The duty cycle is the fraction of time that the transducer is transmitting and not receiving. This is very low with only about 0.2–0.4% of the time spent producing pulses, while 99.6–99.8% of the time, the transducer is receiving echos [1]. The US signal received by the PZT crystals creates a small voltage, which is amplified and converted to a digital signal by an analog-to-digital converter (ADC). The echo data may be displayed as A-mode, B-mode, or M-mode. A-mode displays the signal as a

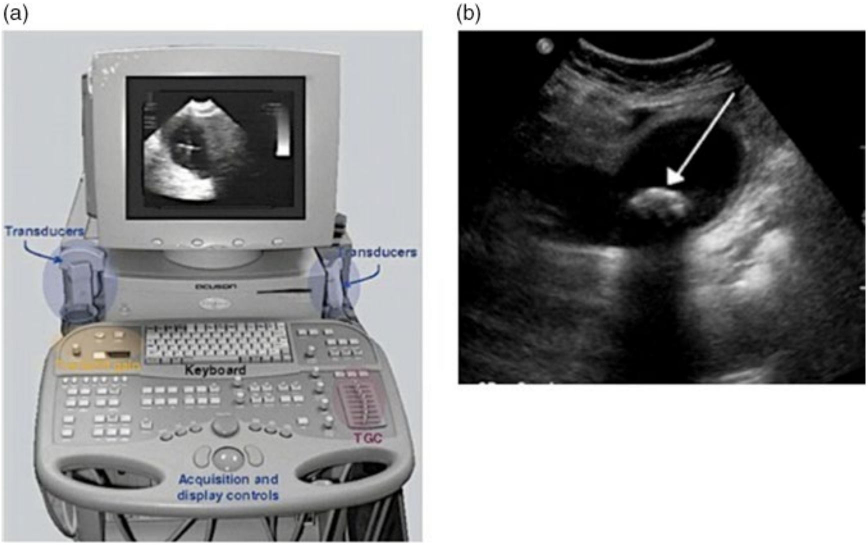

Figure 6.4 (a) Medical ultrasound imaging system. *Source:* Bushberg et al. [1]. Reproduced with permission of Wolters Kluwer. (b) Ultrasound image of the abdomen, revealing a gallstone in a bile duct. *Source:* Obtained from https://en.wikipedia.org/wiki/Biliary_colic.

function of time, and was originally used to determine the depth of a lesion in the body based on the speed of sound [1]. However, most US imaging employs B-mode ("brightness mode"), which is a display of the reflected US wave intensity (amplitude) versus distance in the body. M-mode ("motion mode") displays changes in the B-mode signal over time, and is sometimes used to image the heart valves. M-mode is different than Doppler US (described below), which is used to image blood flow [1]. The scan converter creates two-dimensional images from the data received from each of the transducer PZT elements, and displays these images on a screen (Figure 6.4b). A typical image is 512 × 512 pixels with each pixel consisting of 8 bits (1 byte) of data to provide the gray scale.

6.2 Doppler US

Doppler US is based on the principle that the frequency of sound changes as the sound wave approaches and then recedes from a detector. This is often said to be similar to the sound of an approaching train, which increases but then decreases as the train passes and recedes into the distance. Doppler US is used to image blood flow to an organ, since sound waves reflected off red blood cells create different frequencies if the blood is moving towards the detector than if

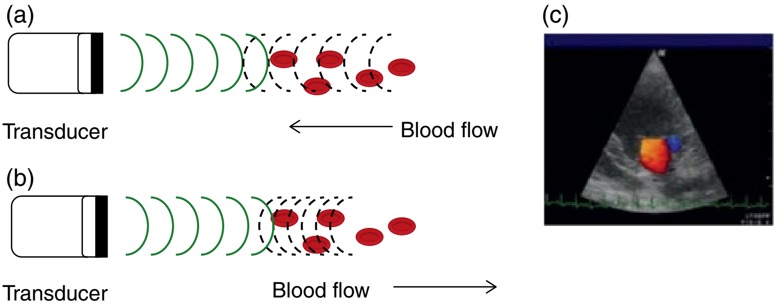

Figure 6.5 Doppler ultrasound is a technique to visualize blood flow. (a) The incident ultrasound wave created by the transducer (green solid lines) is reflected off the surface of red blood cells. If the blood is moving away from the transducer, the frequency of the reflected sound wave (black broken lines) decreases due to expansion of the wave. (b) If the blood is moving toward the transducer, the reflected sound wave is compressed, resulting in an increase in frequency. (c) Doppler ultrasound is often used to image blood flow in the heart (echocardiogram) to assess valve function. *Source:* Panel (c). Obtained from https://en.wikipedia.org/wiki/Doppler_echocardiography. (*See insert for color representation of the figure*.)

it is moving away (Figure 6.5a and b) [1]. The Doppler shift is a term that describes the differences in the incident US frequency and the reflected US frequency [1]. The Doppler shift frequency is in the audible range and this provides an audio sound that assists the radiographer in performing the imaging study. A continuous Doppler imaging system employs two transducers – one to transmit the sound, and one to receive the echos. Pulsed Doppler employs pulse-echo mode in acquiring the image. Color flow Doppler US superimposes Doppler shift data (blood flow) on the conventional B-mode (gray scale) US image of an organ (Figure 6.5c). Blood moving toward the transducer is shown in red, while blood moving away from the transducer is shown in blue.

6.3 US Contrast Agents

Most often, contrast agents are not used in US imaging, but some agents have been developed to enhance imaging. US contrast agents are “microbubbles” (<7 μm diameter) of perfluorocarbon encapsulated in phospholipids or albumin [2]. Two examples are Definity® (Lantheus) and Optison® (GE Healthcare). The microbubbles enhance the US signal up to 300-fold using specialized imaging techniques. Application of US energy causes the microbubbles to oscillate or burst, which greatly enhances the reflected sound signal. Definity® is prepared before use with a device (Vialmix®). The dose is $10\,\mu\text{l}\,\text{kg}^{-1}$ bolus followed by a 10 ml saline flush [2]. Adverse effects include injection site reactions, chest pain, dizziness, nausea, flushing, and hypersensitivity reactions.

Optison® is provided ready to use but must be gently resuspended. The dose is 0.5 ml administered by bolus injection over <1 minute followed by a 10 ml saline flush [2]. Adverse effects include headache, warm sensation, flushing, chills/fever, flu-like symptoms, malaise/weakness/fatigue, dizziness, chest pain, nausea, vomiting, dyspnea, injection site reactions, erythema, altered taste, and hypersensitivity including rare anaphylactic reactions.

6.4 Summary

US imaging relies on high-frequency (2–10 MHz) sound waves, which reflect off-tissue interfaces. The sound waves are generated by a transducer and the reflected waves are detected by a receiver. A piezoelectric crystal in an US imaging system acts as both a transducer and receiver. Doppler US detects the different frequencies of reflected sound waves when blood is moving toward or away from the transducer. Doppler US is able to evaluate blood flow in tissues and is often used to image the heart (echocardiogram). US contrast agents consist of microbubbles of perfluorocarbon gas encapsulated in lipoproteins or albumin. US contrast agents are associated with some adverse reactions.

References

1 Bushberg, J.T., Seibert, J.A., Leidholdt, E.M. Jr., and Boone, J.M. (2012). Ultrasound. In: *The Essential Physics of Medical Imaging*, 3e. Philadelphia, PA: Lippincott Williams & Wilkins.

2 Turner, J. (2012). Adjunct agents used in ultrasound imaging: contrast media. In: *Diagnostic Imaging for Pharmacists* (ed. B. Templar Smith and K.D. Weatherman), 219–230. Washington, DC: APhA.

Additional Reading

Minnigan, H.J. (2012). Review of imaging procedures using ultrasound. In: *Diagnostic Imaging for Pharmacists* (ed. B. Templar Smith and K.D. Weatherman), 197–218. Washington, DC: APhA.

Laura Jimenez-Juan

Dr. Laura Jimenez-Juan is a cardiothoracic radiologist at the Sunnybrook Health Sciences Centre (SHSC) in Toronto, an Assistant Professor in the Department of Medical Imaging of the University of Toronto, and an Affiliate Scientist at the Sunnybrook Research Institute. Dr. Jimenez-Juan completed her residency training in the Complutense University of Madrid (Spain). Before being appointed as a faculty member, she was a clinical and research cardiothoracic imaging fellow at the Department of Medical Imaging of the University of Toronto. Her main research interests include the application of advanced cardiovascular imaging techniques to improve the understanding, risk stratification and outcomes of cardiovascular diseases.

Shaheeda Ahmed

Dr. Shaheeda Ahmed is an Assistant Professor in the Department of Medicine at the University of Toronto. She is a Cardiologist in the Division of Cardiology at the Schulich Heart Centre at Sunnybrook Health Sciences Centre (SHSC) in Toronto. She completed her subspecialty fellowships in echocardiography at McGill University in Montreal, Canada and clinical trials in acute coronary syndromes at Harvard University in Boston, USA. She is certified in transthoracic, transesophageal, and stress echocardiography by the American Society of Echocardiography. Her clinical interests are in acute care, cardio-oncology, and echocardiography. Her academic focus is education. She is the site Director of the Cardiology training program at SHSC and a national Cardiology board examiner for the Royal College of Physicians and Surgeons of Canada.

Medical Imaging for Health Professionals: Technologies and Clinical Applications, First Edition.
Edited by Raymond M. Reilly.
© 2019 John Wiley & Sons, Inc. Published 2019 by John Wiley & Sons, Inc.

Katherine Zukotynski

Dr. Katherine Zukotynski is an Associate Professor in the Departments of Medicine and Radiology at McMaster University. After completing an undergraduate degree in Engineering Science at the University of Toronto, Dr. Zukotynski completed medical training followed by residency in radiology, also at the University of Toronto. She completed nuclear medicine training through the Joint Program in Nuclear Medicine at Harvard in 2009. She is board-certified in nuclear cardiology as well as in nuclear medicine and radiology in both the United States and Canada. Dr. Zukotynski is Secretary/Treasurer of the Society of Nuclear Medicine and Molecular Imaging (SNMMI) as well as President of the PET Center of Excellence and Eastern Great Lakes Chapter. She is also the Chair of the American Roentgen Ray Society (ARRS) Nuclear Medicine Section, and Vice-Chair of the Radiologic Society of North America (RSNA) Research and Education Public Relations Committee. Dr. Zukotynski's main areas of interest are in nuclear medicine and radiology as it relates to medical education, oncology, and neurodegenerative disease.

7

Cardiac Imaging

Laura Jimenez-Juan, Shaheeda Ahmed, and Katherine Zukotynski

7.1 Introduction

Cardiac imaging is an essential tool in assessing the function of the heart including the perfusion of the myocardium and dysfunctional wall motion, ventricular ejection fraction, and cardiac valve function. Assessment of the heart employs several different imaging modalities (MRI, ultrasound, and nuclear medicine), which are discussed in this chapter. Cardiovascular Magnetic Resonance imaging (CMR) has revolutionized the diagnosis and evaluation of the cardiovascular diseases. The accurate quantification of ventricular volumes and function along with the ability for myocardial tissue characterization makes CMR the most complete imaging modality to assess the cardiovascular system. However, ultrasound imaging of the heart (echocardiography) is essential to determine cardiac valve function and nuclear medicine imaging provides important information on myocardial perfusion and cardiac viability and function that affect patient management.

7.2 Cardiovascular Magnetic Resonance Imaging (CMR)

CMR has been increasingly used in the evaluation of cardiovascular diseases and for monitoring treatment. There is enough evidence that CMR is the most accurate imaging technique used for the functional evaluation of the ventricles [1, 2]. MRI allows scanning in different planes and allows three-dimensional coverage of the whole heart in contrast to other commonly used imaging modalities such as echocardiography and nuclear medicine. CMR provides high-resolution images that allow detailed evaluation of the cardiovascular

Medical Imaging for Health Professionals: Technologies and Clinical Applications, First Edition.
Edited by Raymond M. Reilly.
© 2019 John Wiley & Sons, Inc. Published 2019 by John Wiley & Sons, Inc.

Table 7.1 Most common clinical indications for cardiovascular magnetic resonance imaging (CMR).

Detection of myocardial infarction and assessment of viability
Ventricular function assessment
Nonischemic cardiomyopathies
Valve pathology
Aortic pathology
Congenital heart disease
Pericardial disease
Cardiac mass/tumor

structures, with no exposure to ionizing radiation. The most common clinical indications of CMR are summarized in Table 7.1. In this section, the basic techniques used in CMR as well as the main clinical indications of CMR will be reviewed, illustrated by case examples. Some recommendations for analysis and interpretation of clinical cases, with focus on ischemic heart disease will also be provided.

7.3 Cardiovascular MRI Techniques

7.3.1 Cardiac Anatomy

CMR allows detailed anatomical assessment of the heart. Two types of techniques are widely used to assess anatomy: *black/dark-blood* and *white/bright-blood sequences* (Figure 7.1). Black/dark-blood sequences utilize inversion recovery (IR) prepulses (see Chapter 5) to null the signal from blood alone (double IR), or from both blood and fat (triple IR). This sequence allows optimal visualization of the myocardium. Rapid signal generation is usually based upon variants of the Half-Fourier Acquisition Single-shot Turbo spin Echo (HASTE) technique (see Chapter 5). White/bright-blood sequences are typically based on the balanced Steady-State Free Precession (b-SSFP) technique (see Chapter 5), which reflects the relatively high T2/T1 ratio of blood. This is a relatively fast sequence to acquire and allows a rapid overview of the cardiovascular anatomy.

7.3.2 Cardiac Function

CMR is the gold standard imaging modality for the quantitative assessment of the right and left ventricular (LV) volume and ejection fraction using steady-state free precision (SSFP) cine (multiple images linked to provide a “movie”)

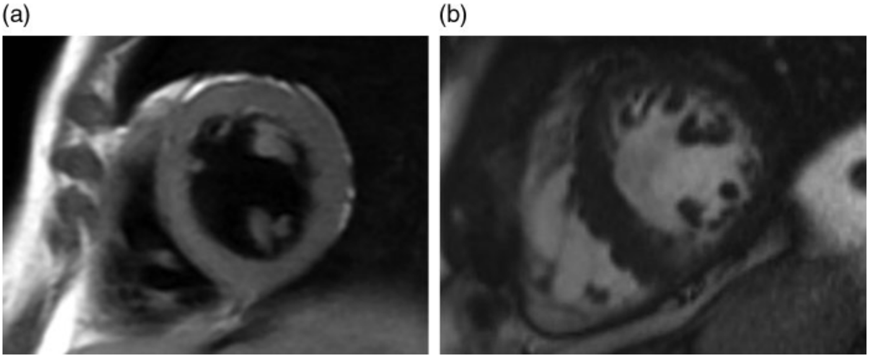

Figure 7.1 Examples of (a) T2-weighted MRI imaging ("Black-blood") and (b) Steady-state free precession MRI imaging ("White-blood") in short-axis orientation, typically used to evaluate cardiac anatomy.

imaging. It is obtained by imaging the heart at a single slice location throughout the cardiac cycle, covering the whole heart, from base to apex. Between 16 and 32 cardiac phases are usually sampled (typically 20–25) and displayed in a movie loop. SSFP cine imaging provides accurate measurements of the ventricular volumes, mass, and function. It also allows the qualitative evaluation of wall motion abnormalities and the valves. The short-axis view (see Figure 7.2 illustrating the different views of the heart) is the standard plane acquired to obtain quantitative measurements of the left ventricle (LV, Figure 7.3). It is included in almost every clinical CMR protocol. For the right ventricle (RV), both axial and short-axis views are used in for the volumetric and functional ventricular quantification. Additional SSFP cine imaging views in four-chamber, two-chamber, and three-chamber orientation are routinely acquired to provide a complete visualization of the heart (Figure 7.4). Once the images are acquired, they are transferred to a dedicated workstation for contour tracing. The quantitative analysis of the left and right ventricles starts by selecting the end-diastolic phase and the end-systolic phase. This is followed by tracing a line through the endocardium from basal to apical images in these two phases. The end-diastolic and end-systolic volumes, derived ejection fractions, stroke volumes, and cardiac outputs are obtained. For the measurement of the LV mass, the epicardial border in the end-diastolic phase is also contoured.

7.3.3 Myocardial Tissue Characterization

Late gadolinium enhancement (LGE) imaging is the standard MRI technique used to characterize myocardial tissue after the administration of gadolinium-based contrast agents (GBCA). It was first introduced to detect infarction in the context of ischemic heart disease but it is not specific of myocardial

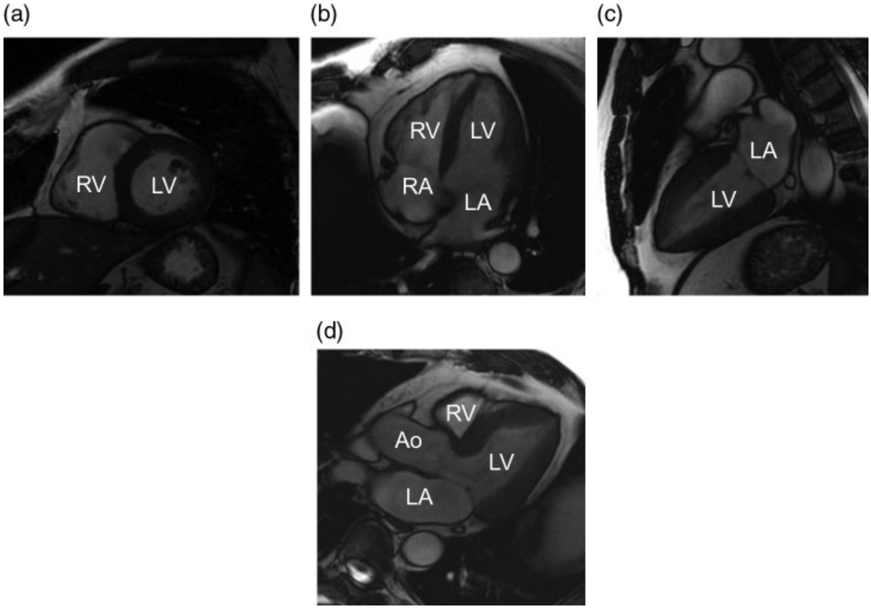

Figure 7.2 Standard cardiac views. (a) Short-axis view demonstrates the right and the left ventricle perpendicular to the long axis of the heart. (b) Four-chamber view shows the left atrium next to the left ventricle and the right atrium next to the right ventricle. (c) Two-chamber view gives an overview of the left atrium, the left ventricle, and the mitral valve. (d) Three-chamber view shows the left atrium, the left ventricle, the aortic root as well as mitral and aortic valves. Ao, aorta; LA, left atrium; LV, left ventricle; RA, right atrium; RV, right ventricle.

infarction. Therefore, LGE imaging is also used in a large number of other clinical scenarios [3] such as inflammatory and infectious diseases of the myocardium, cardiac tumors, and congenital heart diseases. LGE imaging uses segmented, T1-weighted, inversion-prepared fast gradient echo sequences (see Chapter 5). Precontrast images are first obtained followed by injection of half-dose gadolinium with first-pass perfusion imaging. An additional half-dose of gadolinium is then injected. A total of 0.1–0.2 mmol kg^{-1} of GBCA is injected at 1–2 ml s^{-1}. After one to three minutes of contrast administration, images can be acquired, and this is known as *early gadolinium enhancement* (EGE). After 8–10 minutes of contrast administration, an inversion time (TI) is chosen to null the signal from myocardium, typically in the range of 250–350 ms at 1.5 T magnetic field LGE imaging. LGE imaging is started ~10 minutes after injection with a stack of images in short-axis view followed by additional single two-, three-, and four-chamber views. The patterns of LGE imaging are typically divided into subendocardial, subepicardial, and mid myocardial (Figure 7.5). The distribution of LGE imaging in myocardial infarction

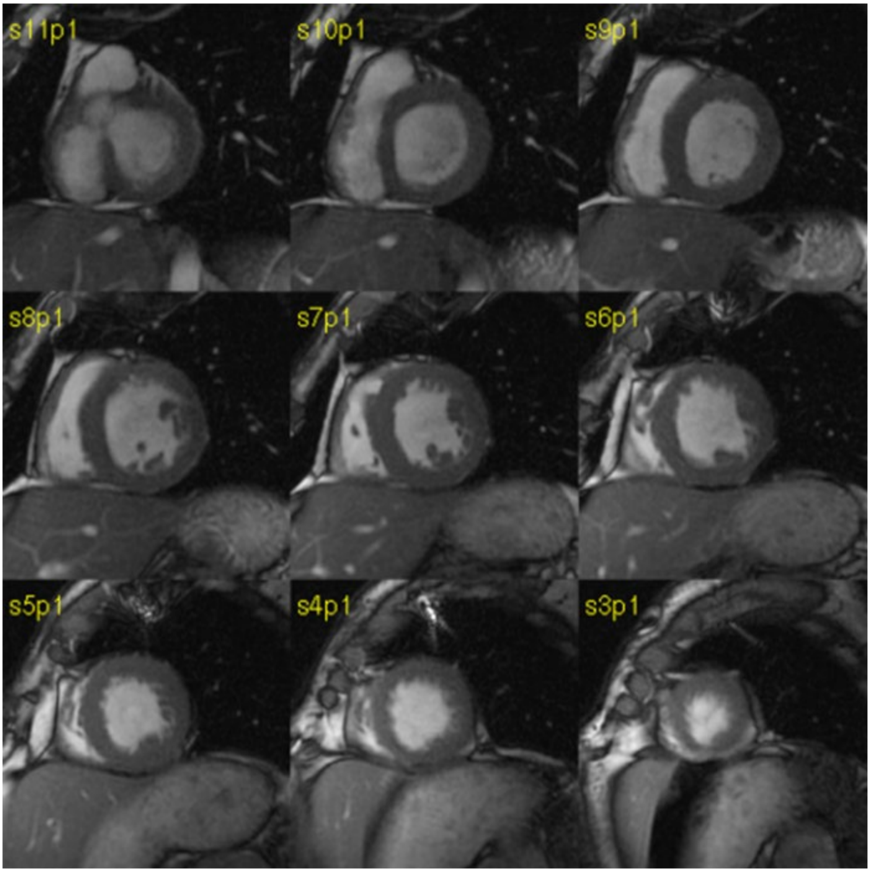
s11p1
s10p1
s9p1
s8p1
s7p1
s6p1
s5p1
s4p1
s3p1

Figure 7.3 Contiguous stack of steady-state free precession (SSFP) cine MRI images in short-axis view used for the qualitative and quantitative functional assessment of the heart.

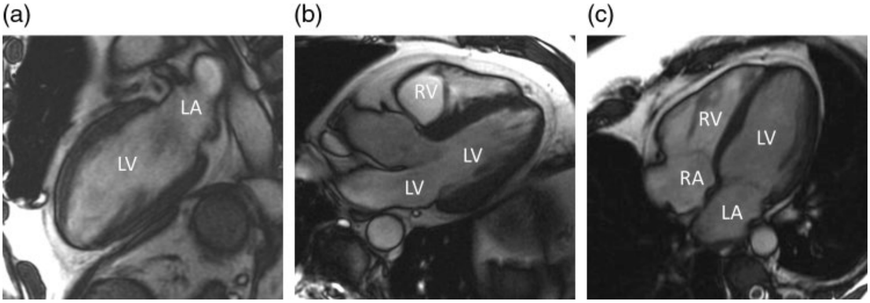
(a)
LA
LV
(b)
RV
LV
LV
(c)
RV
LV
RA
LA

Figure 7.4 Steady-state free precession (SSFP) MRI images in (a) two-chamber, (b) three-chamber, and (c) four-chamber views, which provide a complete visualization of the heart in different orientations. LA, left atrium; LV, left ventricle; RA, right atrium; RV, right ventricle.

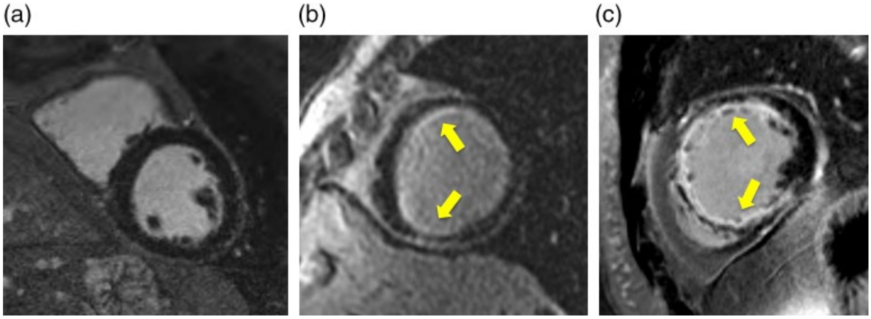

Figure 7.5 Patterns of late gadolinium enhancement (LGE) in short-axis images of the heart. (a) No LGE (no areas of intense brightness on the images). (b) Subendocardial LGE in the left anterior descending coronary artery territory (arrows). (c) Transmural (>50% myocardial thickness) LGE in the left anterior descending artery territory (arrows).

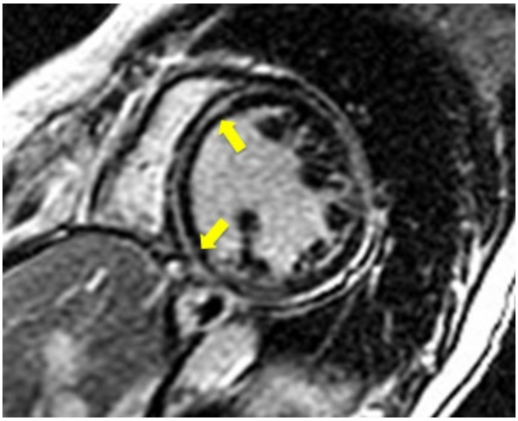

Figure 7.6 Nonischemic cardiomyopathy in a 76-year-old male with left ventricular dysfunction. Late gadolinium enhancement (LGE) imaging in short-axis view showing mid wall myocardial enhancement with subendocardial sparing (arrows) in keeping with dilated idiopathic cardiomyopathy. The coronary arteries demonstrated no significant coronary artery disease in angiocatheterization (not shown).

typically involves at least subendocardium, since it is the most sensitive myocardial layer to ischemia. In addition, abnormal enhancement follows a vascular territory. Patterns of LGE imaging in nonischemic cardiomyopathies tend to spare the subendocardium or, if this is affected, it does not follow a specific vascular territory (Figure 7.6). Therefore, LGE imaging is particularly useful in differentiating ischemic from nonischemic cardiomyopathies based on the location of the myocardial fibrosis/scar (Figures 7.7–7.9). Basic knowledge of the pharmacokinetics of extracellular GBCA is important to understand LGE

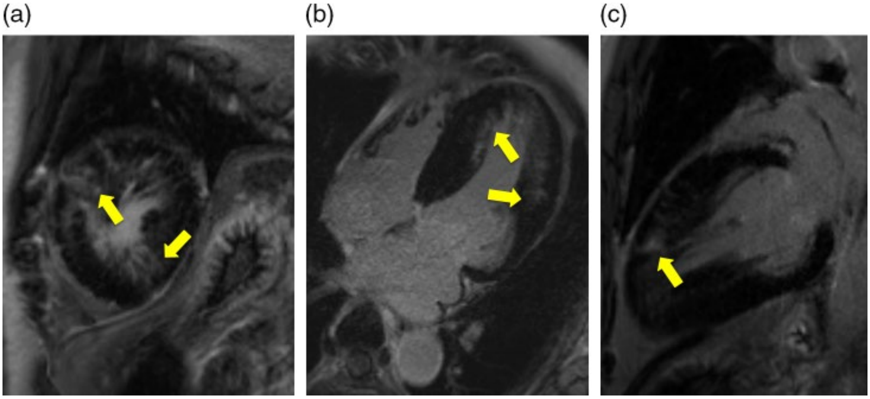

Figure 7.7 Hypertrophic cardiomyopathy (HCM). Late gadolinium enhancement (LGE) images in (a) short-axis, (b) four-chamber, and (c) two-chamber views, demonstrating areas of patchy LGE (arrows) nonischemic in distribution, in a patient with marked left ventricular wall thickening due to HCM.

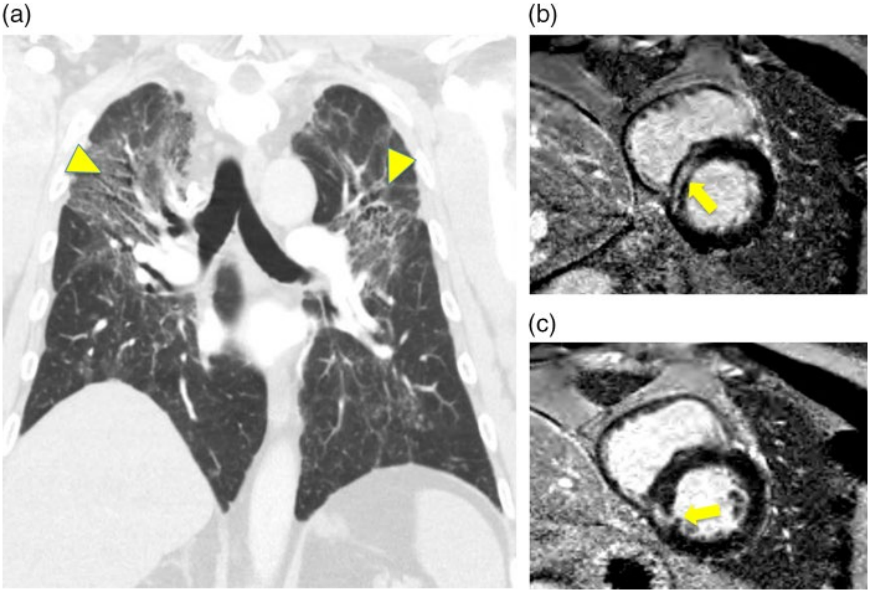

Figure 7.8 A 55-year-old female with known pulmonary sarcoidosis, presenting now with conduction abnormalities. (a) Coronal CT image of the chest demonstrating areas of fibrosis predominantly involving both upper lobes and peri-bronchovascular regions in both lower lobes (arrowheads). These findings are in keeping with stage 4 pulmonary sarcoidosis. (b) and (c) Short-axis late gadolinium enhancement (LGE) images of the heart demonstrating mid wall and patchy areas of fibrosis in the basal inferoseptum extending into the mid inferior wall (arrows) typical for cardiac sarcoidosis.

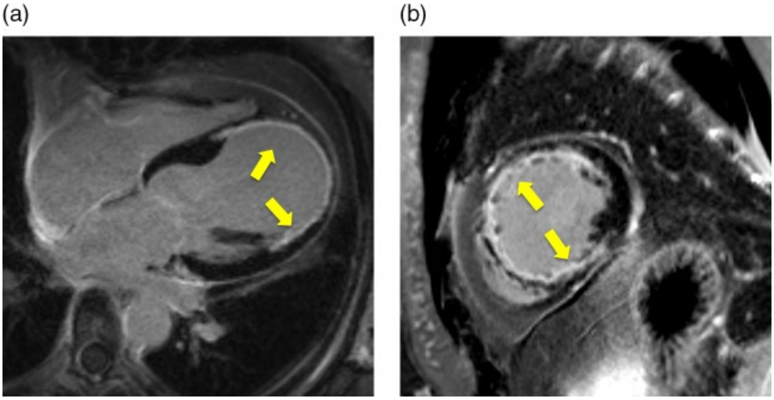

Figure 7.9 Late gadolinium enhancement (LGE) imaging in a 75-year-old patient who was a potential candidate for an implantable cardioverter defibrillator. (a) Four-chamber and (b) mid cavity short-axis views demonstrating left ventricular dilatation, marked left ventricular wall thinning of the mid cavity and apex (arrows) corresponding to a transmural infarction in the left anterior descending territory.

imaging techniques. After bolus injection of GBCA, the extravasation of contrast into the interstitial space (including myocardium) occurs along a gradient (wash-in) and only reverses (wash-out) over time with continuous renal excretion of GBCA. These processes are altered in the setting of myocardial infarction. In acute myocardial infarction, the distribution of GBCA in the interstitial space is markedly increased due to cell membrane ruptures. In chronic myocardial infarction there is increased extracellular space of collagen resulting in accumulation of GBCA in the area of infarction [4–6]. Myocardial perfusion imaging using GBCA allows for the characterization of blood flow in the myocardium by measuring the amount of contrast that traverses a unit of volume of tissue per unit of time. It reflects myocardial blood flow through the coronary microcirculation. Myocardial regions with poor perfusion show decreased contrast enhancement and are identified as perfusion defects. The sensitivity of gadolinium-enhanced CMR to evaluate myocardial ischemia can be improved by combining first-pass cine perfusion and delayed imaging in conjunction with pharmacological stress testing, most widely performed with adenosine or dipyridamole (Persantine) (Figure 7.10).

7.3.4 Clinical Importance of the Assessment of Myocardial Viability

Risk stratification of patients after myocardial infarction is crucial for effective treatment planning. The steady improvement of the outcome of patients with acute coronary syndrome (ACS) has resulted in a higher incidence of patients with chronic LV dysfunction. Therefore, there is increasing interest in

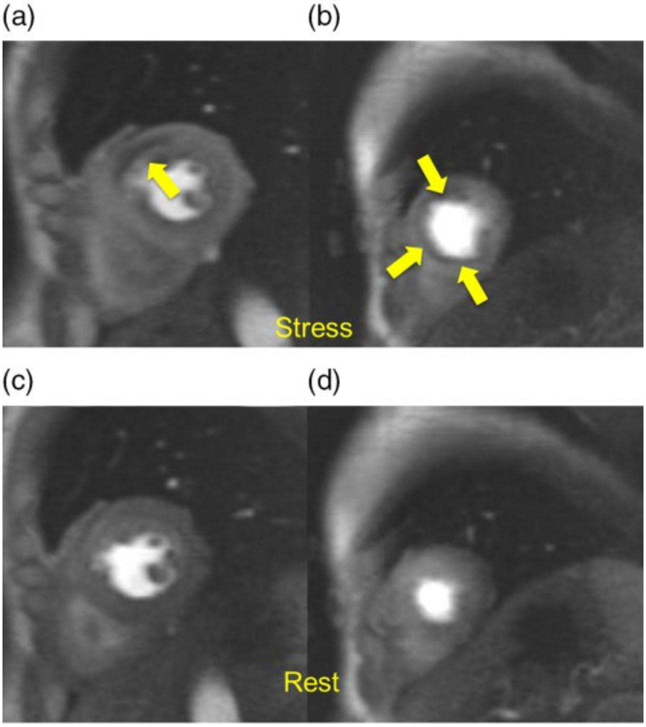

Figure 7.10 Vasodilator stress myocardial perfusion imaging in a 60-year-old male with a 90% lesion in the left anterior descending artery. (a) and (b) show a perfusion defect (darker area) in the anteroseptal wall of the mid cavity (a, arrow) and anterior, septal, and inferior walls of the apex (b, arrows), which disappears at rest imaging (c) and (d). No infarction was demonstrated in the late gadolinium enhancement (LGE) imaging (not shown). Findings are in keeping with stress-induced ischemia in the left anterior descending territory.

identifying accurate predictors of outcome that may improve risk stratification and guide patient management [7–9]. The differentiation of dysfunctional myocardium as viable or nonviable is an important predictor of outcome after myocardial infarction. A large number of studies have supported that ischemic cardiomyopathy in patients with dysfunctional but still viable myocardium benefit from revascularization and do poorly if treated medically [10]. In contrast, there is low likelihood that patients with nonviable myocardium will benefit from coronary revascularization [11, 12].

7.3.5 Prognostic Value of LGE Imaging After Myocardial Infarction

CMR is a valuable noninvasive tool for the assessment and risk stratification of patients after myocardial infarction. Particularly, the contribution of LGE imaging to viability imaging has supposed a paradigm shift in the assessment of myocardial viability [13]. Besides being an important diagnostic tool, LGE imaging is also able to provide prognostic information. There is substantial evidence that the infarct extent assessed by LGE imaging correlates with the likelihood of functional recovery of dysfunctional myocardium after coronary revascularization [14, 15]. Kim and coworkers validated the ability of LGE imaging to distinguish between ischemic but viable myocardium, which showed no hyperenhancement versus infarcted myocardium that showed hyperenhancement in acute and chronic myocardial infarction in animal experiments with histopathologic validation [16]. A pioneering human study demonstrated an inversely proportional relationship between the likelihood of improvement in regional contractility after revascularization and the transmural extent of hyperenhancement in LGE imaging prior to revascularization [14]. Since then, multiple CMR studies have been performed with the primary outcome of evaluating the recovery in contractility and LV systolic function after revascularization, based on the amount of viable myocardium [17, 18].

It has been shown that changes in LV ejection fraction after revascularization are linearly correlated with the number of viable segments and baseline amount of scar resulting in a general consensus about patient-based criteria for prediction of global LV improvement after revascularization [18–20]. While no LGE or <25% transmurality is the best predictor of recovery, generally segments with <50% of transmural LGE extent are considered viable [21]. The latter threshold has also been implemented in current guidelines as an established predictor of significant LV function improvement after coronary revascularization [20] (Figure 7.11). Although it is not routinely part of myocardial viability assessment in cardiac MR [20, 22], several studies have demonstrated the prognostic value of MR stress perfusion in the assessment of myocardial ischemia and an improved accuracy of LGE imaging in viability imaging (Figure 7.12) [15, 23–25].

7.3.6 Other Imaging Modalities for Assessment of Myocardial Viability

Other imaging modalities for assessment of myocardial viability usually rely on the injection of a radiotracer (see Section 7.5 on radionuclide imaging of the heart) or highlight the presence of viability based on functional recovery under pharmacologic challenges. As discussed later in this chapter, in single photon emission computed tomography (SPECT), cardiomyocytes accumulating the radiopharmaceutical are, by definition, viable. Thallium-201 (^{201}Tl) imaging is dependent upon the integrity of the cardiomyocyte cell membrane Na^+/K^+-ATPase pump while technetium-99m (^{99m}Tc) myocardial perfusion imaging agents are retained in cardiomyocytes by interacting with mitochondria, but are accumulated in proportion to myocardial blood flow. Maximal ^{201}Tl uptake may not occur within the first 3–4 hours and therefore may require delayed

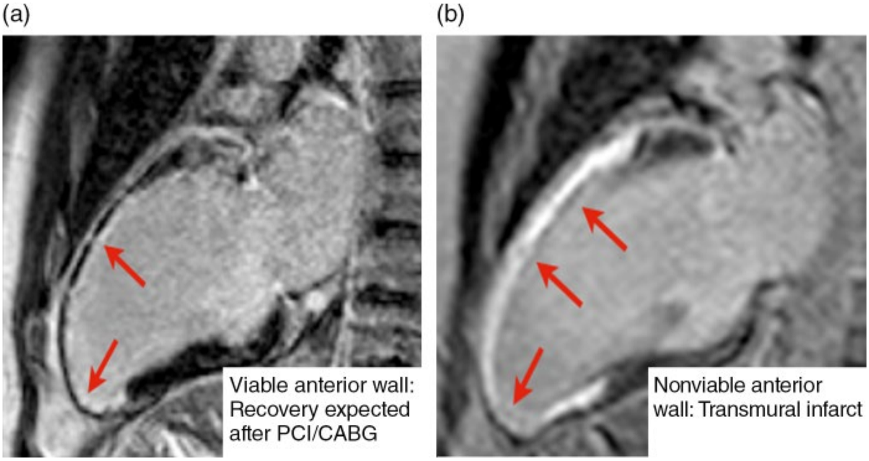
(a)
(b)
Viable anterior wall: Recovery expected after PCI/CABG
Nonviable anterior wall: Transmural infarct

Figure 7.11 Two-chamber late gadolinium enhancement (LGE) images demonstrating (a) subendocardial enhancement (brightness) in the anterior wall (arrows) in keeping with viable myocardium (<50% of myocardial involvement), which is associated with high likelihood of recovery after revascularization and (b) transmural enhancement (>50% of myocardial involvement; arrows), in keeping with nonviable myocardium.

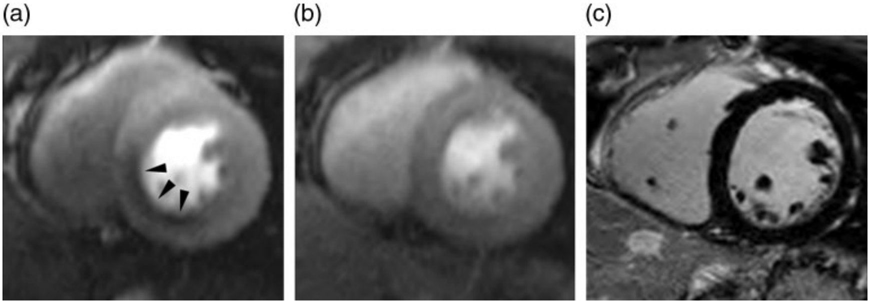

Figure 7.12 A 60-year-old male with a 90% lesion in the right coronary artery. (a) Vasodilator stress MRI myocardial perfusion imaging shows a perfusion defect in the mid cavity inferoseptal region (dark area, arrowheads), which disappears at (b) rest imaging. No infarction was demonstrated in (c) the late gadolinium enhancement (LGE) imaging. Findings are in keeping with stress-induced ischemia in the right coronary artery territory, with no established infarction.

imaging to assess uptake at 24 hours postinjection (rest-redistribution study). ^{99m}Tc agents (e.g. ^{99m}Tc-sestamibi or ^{99m}Tc-tetrofosmin – see Chapter 4) do not redistribute to any great extent but require tracer reinjection for rest redistribution imaging. As the gamma photon energy of both radiotracers is relatively low, especially for ^{201}Tl, attenuation artifacts caused by overlying tissues may reduce accuracy. In addition, spatial resolution is limited and thus thinned but

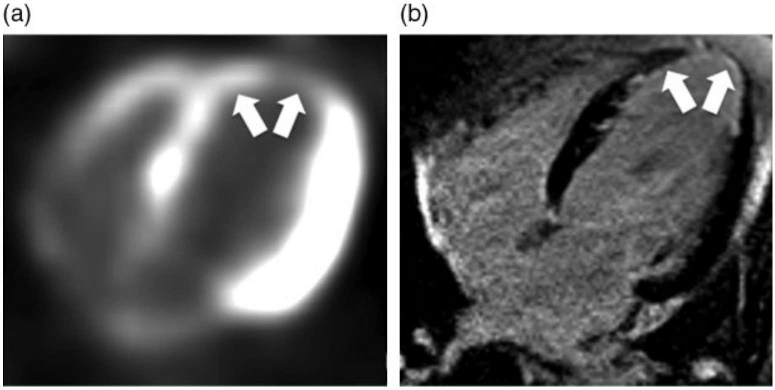

Figure 7.13 (a) A 75-year-old woman with abnormal ^{18}F-FDG myocardial PET scan. Note the decreased radiotracer uptake in the distal septum and left ventricular apex (arrows). (b) Late gadolinium enhancement (LGE) MRI imaging of the same patient demonstrates a transmural scar in the same region (bright areas; arrows). Note the relatively good agreement between the two modalities.

hibernating segments may appear as fixed defects. In addition, SPECT has been shown to miss up to ~45% of subendocardial infarctions [13].

The metabolic signature of viable but oxygen-depleted myocytes is a switch from fatty acid metabolism to dominance of glucose metabolism, which can be exploited by positron emission tomography (PET) imaging (see Chapter 15). Segments on PET imaging with little or no uptake of a blood flow radiotracer (e.g. ^{13}N ammonia or ^{82}Rb) at rest but extensive uptake of ^{18}F-2-fluorodeoxyglucose (^{18}F-FDG PET) demonstrate a perfusion/metabolism mismatch, which is characteristic of hibernating myocardium. Matched defects in blow flow imaging and ^{18}F-FDG PET are characteristic of transmural scar/infarct extent. While PET provides improved spatial resolution, identification of subendocardial infarcts is still limited and again sensitivity is higher than specificity [26] (Figure 7.13).

In echocardiography (see the next section), residual viability is demonstrated by the presence of a "biphasic response" to a dobutamine challenge in segments with resting dysfunction. While hibernating myocardium responds with an appearance of improved contractility reserve at low doses of dobutamine (max. $10\,\mu g\,kg^{-1}\,min^{-1}$), segmental function deteriorates once again with further dose increase ($-40\,\mu g\,kg^{-1}\,min^{-1}$). Such a response pattern predicts recovery after revascularization with pooled sensitivity and specificity of 79 and 87%, respectively [27]. General echocardiography limitations apply such as operator dependency and the subjective nature of wall motion interpretation. In addition, echocardiography does not directly visualize the extent of nonviable myocardium.

Similarly low-dose dobutamine cardiac MR was reported to predict functional recovery in much the same way as with echocardiography, albeit with improved diagnostic accuracy [28]. In addition, simple end-diastolic wall thickness assessment with a threshold of <5.5–6 mm was used to indicate non-viability in cardiac MR prior to the LGE era [29]. This, however, ignores the significant thinning that may occur *without scar* in hibernating segments. In recent years, cardiac CT has been explored with regard to viability assessment but for now remains the least-explored technique. Basic principles of iodinated contrast agent distribution patterns are quite similar to LGE MRI referring to the term *late iodine enhancement* to identify regions of infarcted myocardium [30]. Limitations to CT viability imaging include radiation dose, the poor contrast to noise ratio compared to LGE MR techniques, and the potentially high amount of iodinated contrast agent that may be required. Recently, the use of dual-energy CT has demonstrated promise in animal and patient studies of myocardial infarction [31, 32]. The development of hybrid MR-PET imaging also holds great promise in further improvement of viability assessment and even more precise prediction of functional recovery after revascularization [33]. Most importantly, the likely higher costs of such hybrid examinations would demand a clear benefit with respect to the predictive value and specificity of viability assessment.

7.4 Echocardiography

Echocardiography is a widely available inexpensive imaging test central to the diagnosis and treatment of cardiac pathology. Echocardiography uses ultrasound, high-frequency sound waves >2 MHz (see Chapter 6), to provide fundamental information on cardiac structure and function [34]. Images are acquired using a probe applied to the chest wall (transthoracic) and in select cases, via the esophagus (transesophageal) [34]. Transmitted ultrasound beams are reflected from cardiac structures and processed to create anatomic images [34]. This was initially displayed as a still view of the heart (m-mode) but has evolved into detailed 2D moving cardiac images (Figure 7.14) [34]. Blood flow within the heart (across valves or between chambers) and great vessels is measured from Doppler signals (see Chapter 6) [34]. These are changes in ultrasound frequency generated by moving red blood cells, color coded based on the direction of flow (red toward and blue away from the probe), and degree of turbulence (shades of green) (Figure 7.15) [34]. Doppler and 2D imaging are complementary, basic techniques [34]. M-mode is still used for measurements, detecting high-velocity structures not seen by 2D, and distinguishing ultrasound artifacts from pathology [34, 35]. Evolving techniques include the ability to create 3D images of the cardiac chambers and valves (Figure 7.16) and strain imaging, an analysis of tissue deformation [35].

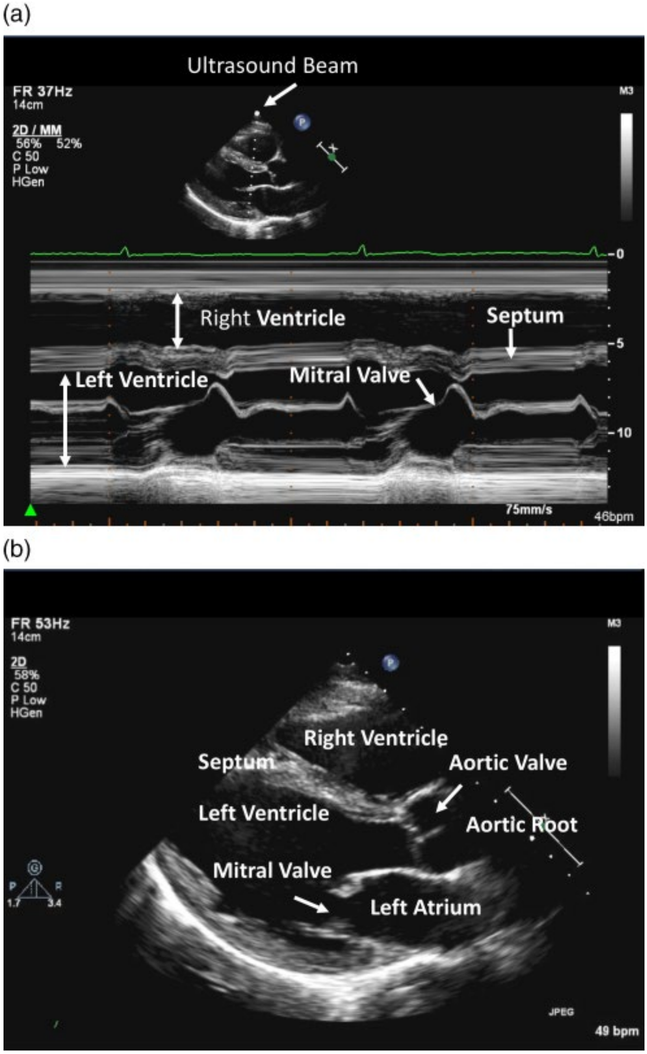
(a)
Ultrasound Beam
FR 37Hz
14cm
2D / MM
56% 52%
C 50
P Low
HGen
M3
0
Right Ventricle
Septum
5
Left Ventricle
Mitral Valve
10
75mm/s
46bpm
(b)
FR 53Hz
14cm
2D
58%
C 50
P Low
HGen
M3
Right Ventricle
Septum
Aortic Valve
Left Ventricle
Aortic Root
Mitral Valve
Left Atrium
P R
1.7 3.4
JPEG
49 bpm

Figure 7.14 M-Mode and two-dimensional cardiac imaging. (a) M-Mode (bottom) displaying ultrasound signals from cardiac structures (top) in a single vertical plane across time from the parasternal window. (b) Two-dimensional image of the heart from the parasternal window.

7.4.1 Clinical Applications of Echocardiography

7.4.1.1 The Cardiac Chambers

LV function assessment is a common test indication. Global and regional LV functional abnormalities are identified by 2D/3D imaging, complemented by strain [35]. The proportion of blood ejected by the LV or ejection fraction (LVEF)

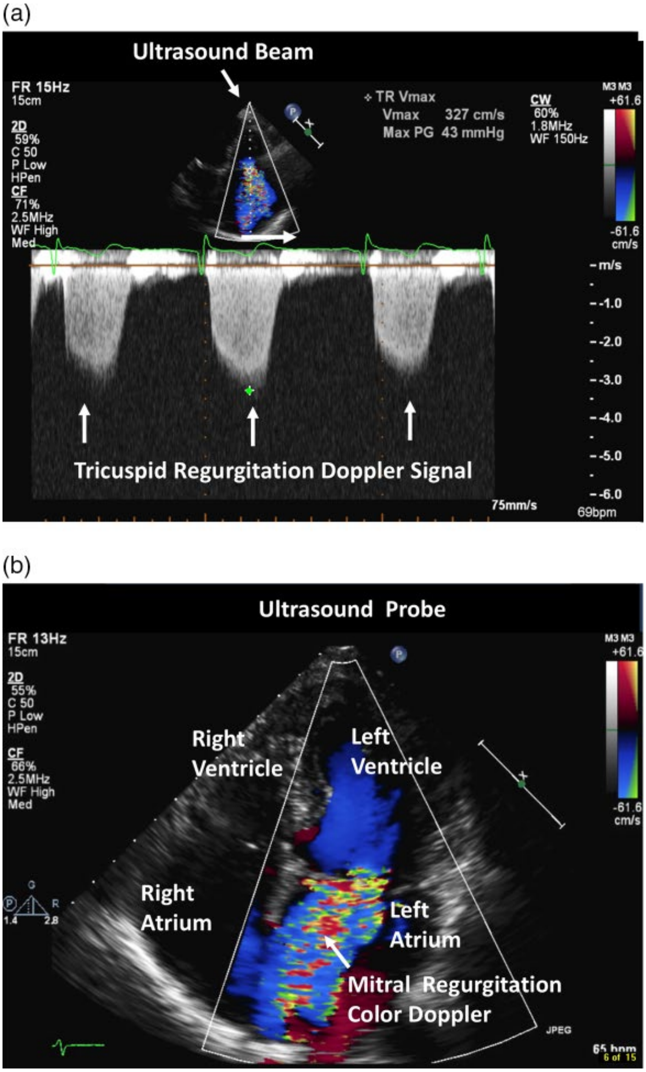
(a)
Ultrasound Beam
FR 15Hz
15cm
2D
59%
C 50
P Low
HPen
CF
71%
2.5MHz
WF High
Med
TR Vmax
Vmax 327 cm/s
Max PG 43 mmHg
CW
60%
1.8MHz
WF 150Hz
M3 M3
+61.6
-61.6
cm/s
m/s
-1.0
-2.0
-3.0
-4.0
-5.0
-6.0
Tricuspid Regurgitation Doppler Signal
75mm/s
69bpm
(b)
Ultrasound Probe
FR 13Hz
15cm
2D
55%
C 50
P Low
HPen
CF
66%
2.5MHz
WF High
Med
M3 M3
+61.6
-61.6
cm/s
Right Ventricle
Left Ventricle
Right Atrium
Left Atrium
Mitral Regurgitation Color Doppler
JPEG
65 bpm
6 of 15

Figure 7.15 Two-dimensional and color Doppler. (a) Doppler signal from the tricuspid valve across time; the velocity of the regurgitant jet is measured and used to estimate the right ventricular systolic pressure. (b) Color Doppler showing systolic blue flow with shades of green within the left atrium due to a turbulent jet of mitral regurgitation. (*See insert for color representation of the figure.*)

is a key clinical quantitative measure of LV systolic function (normal ≥54% in women, ≥52% in men) [35]. LVEF by 3D is preferred over 2D, as it more closely approximates LVEF by MRI and unlike 2D EF, is not derived by geometrical formulas that make assumptions on the shape of the LV [35]. In patients with

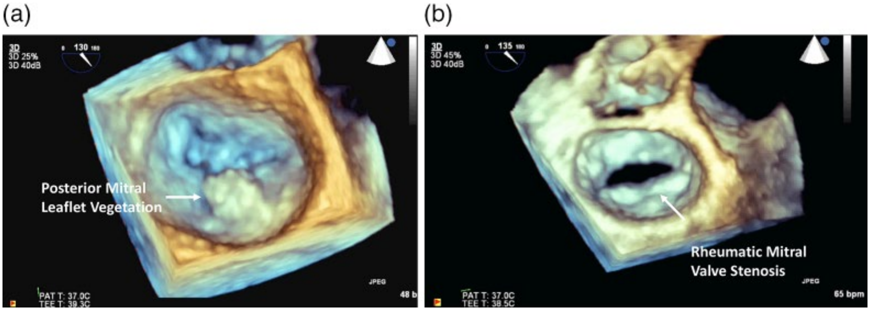

Figure 7.16 Three-dimensional images of the mitral valve. (a) 3D facilitates localization of a vegetation (bacterial infection) to a particular portion or scallop of the posterior mitral valve leaflet. (b) 3D can be used to determine mitral valve area by tracing the edges of its borders (planimetry) in mitral stenosis.

suboptimal images, echo contrast (microbubbles of perfluorocarbon gas; see Chapter 3) can be administered intravenously to enhance visualization of the LV [35]. In clinical practice, decisions to initiate medical or device therapy in systolic heart failure [36] or to withhold cardiotoxic chemotherapy hinge on LVEF [37]. Note that LVEF can also be assessed by nuclear medicine imaging techniques using ^{99m}Tc-labeled red blood cells (see Section 7.5). Echocardiography also assesses LV diastolic (or relaxing) function [38]. Diastolic abnormalities signal elevated left-sided pressures and may be the only clue that dyspnea is cardiac in origin [38]. Measurements of LV size and thickness are important [35]. For example, an enlarged LV suggests an ischemic or nonischemic cardiomyopathy; thickened walls may suggest hypertrophic cardiomyopathy or another process (e.g. hypertension, aortic stenosis, infiltration, or physiologic changes from exercise) [34]. Ancillary findings can support one diagnosis over another. However, unlike MRI, echocardiography does not characterize tissue and unlike angiography, does not visualize coronary stenosis.

The RV geometry is complex, wrapping around the LV like a croissant [35]. It is challenging to measure and simplified formulas for RVEF are lacking. Despite this, echocardiography identifies RV enlargement, based on size relative to the LV and normal population values [35]. RV function is described qualitatively based on visual appearance and quantitative parameters that measure the degree of movement of the basal part of the RV or the change in RV area during contraction (systole) compared with relaxation (diastole) [35]. Right ventricular systolic pressure can be estimated in conjunction with the inferior vena cava appearance and is a surrogate for pulmonary systolic pressure [34]. This is clinically informative in pulmonary conditions (e.g. pulmonary embolism, obstructive lung disease), systemic diseases (e.g. scleroderma, sarcoidosis), and cardiac abnormalities (e.g. myocardial infarction, cardiomyopathies, intracardiac shunts) that may affect the right side of the heart. Atrial abnormalities have prognostic significance in atrial arrhythmias [39]. Static blood within the atrium and the appendage, its embryological remnant, appears like smoke (spontaneous echo contrast), sludge, or thrombus and increases the risk of thromboembolism [39]. Enlarged left atrial volumes are associated with stroke risk, mortality, and recurrent atrial fibrillation post cardioversion [39].

7.4.1.2 Cardiac Valves

Echocardiography is the main diagnostic test for native and prosthetic valvular heart disease [34, 40–42]. Multiple valvular pathologies (e.g. infective endocarditis, degenerative changes, rheumatic disease) resulting in stenosis or incompetence are imaged in detail in 2D and 3D [34, 40–42]. The hemodynamic significance of a lesion, once obtained only from invasive cardiac catheterization, is now largely obtained by Doppler ultrasound (see Chapter 6) (e.g. valve area, pressure gradient, and regurgitant volume) [34, 40–42]. These data categorize a lesion's functional significance (mild, moderate, or severe) and are integrated in practice guidelines on valvular heart disease management [43]. Echocardiography is also used during valvular procedures and assesses technical success [43].

7.4.1.3 Pericardial Disease and the Great Vessels

Echocardiography diagnoses a pericardial effusion, like MRI and CT, but has the advantage of determining its hemodynamic significance based on signs of increased pericardial pressure and chamber compression (tamponade) [44]. Prompt treatment with percutaneous drainage (pericardiocentesis) can be performed at the bedside under ultrasound guidance [44]. Echocardiography screens for proximal ascending and descending thoracic aortic abnormalities (e.g. some aneurysms and aortic coarctation, a congenital discrete narrowing of the descending aorta associated with hypertension and structural anomalies) [45]. In cases of acute aortic syndromes (e.g. dissection or intramural hematomas), a transthoracic echocardiogram lacks diagnostic sensitivity; additional imaging with CT or transesophageal echocardiography is essential [45].

7.5 Nuclear Cardiology

Imaging the heart using radiopharmaceuticals, or in other words, radioactive diagnostic imaging agents approved for administration to patients (see Chapter 4), are among the most common tests done in nuclear medicine today (for additional reading on nuclear cardiology, see Refs. [46–49]). These imaging studies provide useful clinical information on blood flow to the heart (*myocardial perfusion*), function of the heart, and motion of the heart walls. Also, nuclear medicine studies help to assess if the heart muscle is *viable*. There are a few radiopharmaceuticals that can be used to image the heart. The most common are: (i) Thallium-201 (^{201}Tl); (ii) Technetium-99m (^{99m}Tc)-labeled compounds, ^{99m}Tc-Sestamibi (Cardiolite), and ^{99m}Tc-Tetrofosmin (Myoview); (iii) Rubidium-82 (^{82}Rb); and (iv) Fluorine-18-labeled fluorodeoxyglucose (^{18}F-FDG). ^{201}Tl, ^{99m}Tc-Sestamibi/Tetrofosmin, and ^{82}Rb are used to evaluate myocardial perfusion and function, while ^{201}Tl and ^{18}F-FDG may be used to determine if the heart muscle is viable. Although ^{201}Tl was the first clinically successful radiopharmaceutical used to image the heart, today the ^{99m}Tc-labeled agents are the most commonly used radiopharmaceuticals for myocardial perfusion imaging due to their easy availability, relatively low radiation dose, and good imaging characteristics. ^{18}F-FDG is the most commonly used radiopharmaceutical to evaluate myocardial viability. The probability of a reaction to any one of these radiopharmaceuticals is negligible and the radiation exposure risk associated with these studies is low.

There are a few different imaging systems that can be used to obtain images of the heart in a patient following administration of a radiopharmaceutical. The most common imaging system used in nuclear medicine today is the gamma camera (see Chapter 3). Typically, myocardial perfusion images of the heart are acquired using electrocardiogram (ECG) gating and a gamma camera with SPECT capabilities, where the detectors of the camera rotate 360° around the patient during imaging and tomographic slices of the distribution of the radiopharmaceutical in the heart may be obtained. Recent technological advances have led to the development of cadmium zinc telluride (CZT) detectors for gamma cameras and positron emission tomography computed tomography (PET/CT) scanners. When available, the use of CZT gamma camera detectors or PET/CT scanners may help decrease imaging time, radiation dose, and improve image quality. Multi-gated cardiac acquisitions (MUGA scans) also called radionuclide ventriculography studies (RVG scans) are typically acquired using ^{99m}Tc-labeled red blood cells (see Chapter 4) and a gamma camera (with or without SPECT) with ECG gating. Myocardial viability scans may be acquired using ^{201}Tl and a gamma camera but are more commonly acquired with ^{18}F-FDG PET/CT.

7.5.1 Myocardial Perfusion Imaging

Blood is supplied to the heart by the coronary arteries. In most patients, the left coronary artery divides into the *left anterior descending* (LAD) and *circumflex* coronary arteries, where the LAD supplies the interventricular septum anteriorly and the anterolateral wall of the LV. The circumflex artery supplies the left atrium and the posterolateral wall of the LV. The right coronary artery supplies the right atrium, RV, inferior wall of the LV, and a variable portion of the interventricular septum. Normal coronary blood flow is ~0.6–0.8 $\mathrm{ml\,min^{-1}\,g^{-1}}$ of myocardium; however, with exercise or stress, this can increase four to six times as a result of coronary artery dilation. The ability of a coronary artery to increase blood flow to the heart with exercise and/or stress is called *coronary reserve.*

The evaluation of coronary artery disease and/or myocardial ischemia is made by detecting relatively decreased blood flow to the heart distal to a site of coronary artery narrowing. With <50% narrowing (also called *stenosis*) of the diameter of a coronary artery, the effect on the blood flow to the heart is typically clinically insignificant. However, a stenosis of 50% or more can be detected with myocardial perfusion imaging at times of maximal exercise or stress. When the coronary artery stenosis approaches 90%, the effect on myocardial perfusion can also be seen at rest.

There are a few ways in which myocardial perfusion imaging can be done but most commonly it is done using ^{99m}Tc-Sestamibi and a gamma camera with SPECT and ECG gating first with the patient at rest and then with imaging repeated after the patient is stressed with exercise or by using pharmacological agents that dilate non-stenosed coronary arteries (e.g. persantine). When possible, both rest and stress images are done on the same day and the patient is asked to fast for four to six hours prior to the study. Patients may also be asked to discontinue certain medications prior to the study such as β-blockers, which blunt the ability of exercise or pharmacological stress agents to reveal perfusion abnormalities. With this technique, 296–370 MBq of ^{99m}Tc-sestamibi or ^{99m}Tc-tetrofosmin is given intravenously at rest and imaging is done ~30–60 minutes later. About 1–4 hours after these images are acquired, the patient is stressed either by exercising on a treadmill or by using a pharmacological stress agent and, at peak stress, the patient is then administered 925–1110 MBq of ^{99m}Tc-sestamibi or ^{99m}Tc-tetrofosmin intravenously with imaging ~15–45 minutes later. The two sets of images, one set acquired with the patient at rest and the other shortly following stress, are then compared to look for differences in regional myocardial blood flow and function. This protocol is known as the "same-day" protocol in which both the rest and stress images are obtained on the same day using a low dose for the rest study and a higher dose for the stress study. The higher dose for the stress study overcomes interference in the images caused by any residual radioactivity in the heart present from the rest study. There is also a two-day protocol in which the rest and stress studies are obtained on two separate days using equal doses of ^{99m}Tc-Sestamibi or ^{99m}Tc-Tetrofosmin.

The results of a myocardial perfusion imaging test allows assessment of the LV cavity size and the presence of transient LV cavity dilation with exercise, which may suggest stenosis of more than one coronary artery. The motion of the LV walls is evaluated and described using terms such as: (i) *Hypokinetic* (diminished wall motion), (ii) *Akinetic* (absent wall motion), and (iii) *Diskinetic* (the motion is not expected, i.e. the wall moves outward when it should move inward). Diskinetic wall motion may suggest past injury leading to formation of an aneurysm. The fraction of blood ejected from the LV during a contraction, or the LVEF, is calculated from analysis of the images pre- and post-systole at rest and stress. Furthermore, the size, severity, and location of abnormal myocardial perfusion can be determined and each perfusion abnormality is classified as an area of ischemia or suspected scar (infarct). Typically, when there is a perfusion defect on images after stress that is not seen on images at rest, we say this is an area of ischemia (Figure 7.17). When the perfusion defect is the same on both images at stress and at rest, we say this is an area of scar or possibly hibernating myocardium. Hibernating heart muscle (i.e. does not function well but is still viable) usually occurs when there is chronically decreased blood flow to an area of the heart. To be able to tell the difference between an area of scar (often from a myocardial infarction) and an area of hibernating heart muscle, an ^{18}F-FDG PET/CT scan can be very helpful since this assesses glucose utilization by the myocardium, a measure of viability (Figure 7.18). Ultimately, a myocardial perfusion imaging study correlates wall motion, perfusion, and ECG abnormalities to help determine the extent of myocardial disease as well as the risk of a future cardiac event such as myocardial infarction.

7.5.2 PET Myocardial Viability Imaging

Under normal conditions, heart muscle cells primarily use long-chain fatty acids to meet energy demands; however, in cases of ischemia, the myocardium may convert to using glucose. Since ^{18}F-FDG is a radioactive glucose analog, it is taken up by heart muscle cells that are viable but ischemic. Often, a myocardial viability assessment includes perfusion imaging at rest with ^{82}Rb PET/CT (see Chapter 4) and subsequent glucose metabolic imaging with ^{18}F-FDG PET/CT. To perform the ^{18}F-FDG PET/CT component of the study, patients are asked to fast for six to eight hours to maximize the uptake of ^{18}F-FDG by the heart in the imaging study. Subsequently, a mix of glucose and insulin is given to force viable heart muscle cells to convert from using primarily long-chain fatty acids to meet their energy demands to using primarily glucose. At this point 370–555 MBq of ^{18}F-FDG is given intravenously and imaging is performed using a PET/CT scanner. Hibernating myocardium classically presents as a perfusion–metabolism mismatch, meaning an area of myocardium with decreased perfusion at rest and stress but normal or even increased glucose metabolism (Figure 7.18). Patients with hibernating myocardium may benefit from revascularization, which improves the blood flow to the area of hibernating heart muscle. Nonviable or scarred myocardium classically shows little or no perfusion and little or no glucose metabolism. In these patients, treatment that improves the blood flow to the area of nonviable heart muscle would be unlikely to benefit the patient.

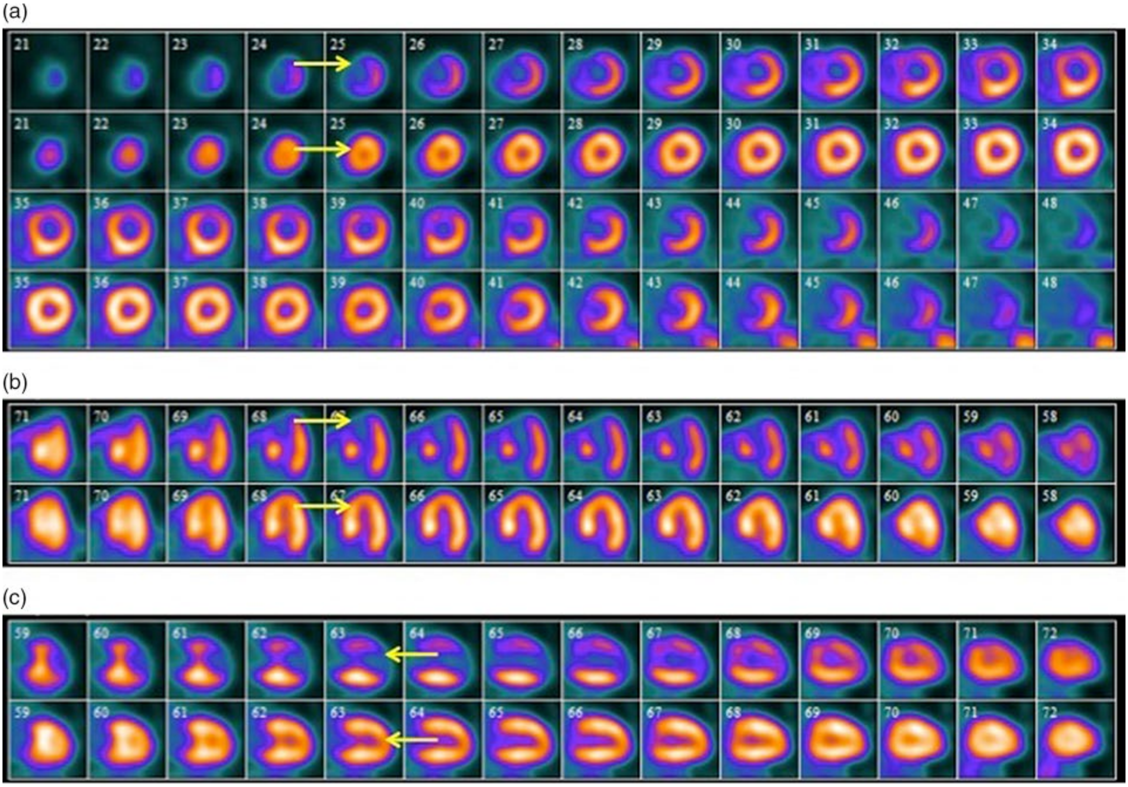
(a)
21 22 23 24 25 26 27 28 29 30 31 32 33 34
21 22 23 24 25 26 27 28 29 30 31 32 33 34
35 36 37 38 39 40 41 42 43 44 45 46 47 48
35 36 37 38 39 40 41 42 43 44 45 46 47 48
(b)
71 70 69 68 66 65 64 63 62 61 60 59 58
71 70 69 68 67 66 65 64 63 62 61 60 59 58
(c)
59 60 61 62 63 64 65 66 67 68 69 70 71 72
59 60 61 62 63 64 65 66 67 68 69 70 71 72

Figure 7.17 Perfusion images of the heart showing ischemia. (a) Short-axis projection images of the heart after stress (top and third row) compared with rest (second and bottom row) show reduced perfusion following stress that is not seen at rest suggesting ischemia (arrows). (b) Horizontal long-axis images of the heart after stress (top row) compared with rest (bottom row) also show ischemia (arrows). (c) Vertical long-axis images of the heart after stress (top row) compared with rest (bottom row) also show ischemia (arrows). (*See insert for color representation of the figure*.)

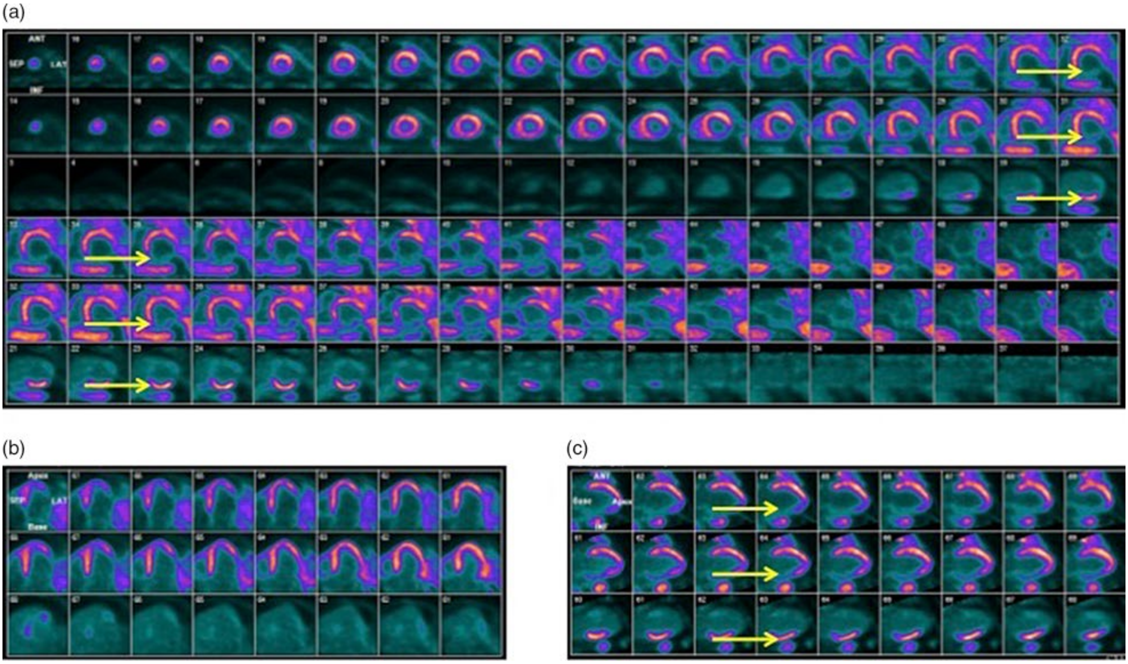

Figure 7.18 Perfusion and viability images of the heart showing hibernating myocardium. (a) Short-axis perfusion images of the heart after stress (top and fourth row) and after rest (second and fifth row) as well as viability images (third and bottom row) are shown. (b) Horizontal long-axis images of the heart after stress (top row) and after rest (middle row) as well as viability images (bottom row) are shown. (c) Vertical long-axis images of the heart after stress (top row) and after rest (middle row) and viability images (bottom row) are shown. The area of reduced perfusion in the inferior wall seen on stress/rest images (arrows) has mismatched increased glucose metabolism (arrows) and is alive, i.e. hibernating. The segments other than the inferior wall on ^{18}F-FDG images that do not show ^{18}F-FDG uptake can sometimes be due to intense glucose avidity of the hibernating segment resulting in apparent lack of uptake in the normal segments. Radiotracer uptake is seen in the lungs as well as below the diaphragm in this patient with heart failure. *With acknowledgement to Dr. Sharmila Dorbala at Brigham and Women's Hospital*. (*See insert for color representation of the figure*.)

7.5.3 MUGA Scans

There are several tests that can be used to qualitatively evaluate cardiac wall motion and quantitatively estimate the LVEF. Perhaps, the most common test done for this is echocardiography (see the earlier section on Echocardiography). A MUGA scan done using ^{99m}Tc-labeled red blood cells and a gamma camera with ECG gating is another way to determine the LVEF. Based on clinical experience, today, MUGA scans are most commonly done in patients where echocardiography is challenging, in patients on chemotherapy that has the potential to damage heart muscle cells or in patients prior to a stem cell transplant. To

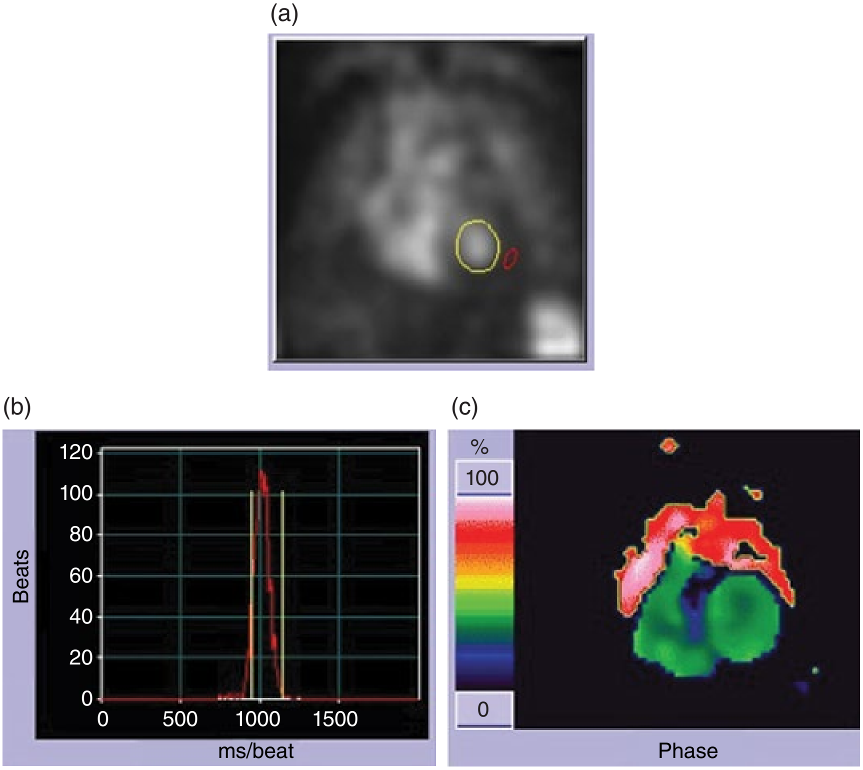

Figure 7.19 Images from a MUGA scan in a patient with LVEF of 65%. (a) An image of the heart with a region of interest drawn over the left ventricle (yellow circle) and background (red circle) so that the amount of radioactivity within the left ventricular cavity may be estimated during the cardiac cycle. (b) Graph showing all of the cardiac beats were at the same rate, indicating that the cardiac rhythm was regular during the study. (c) A "phase" image of the heart, showing that the atria (red) and ventricles (green) had uniform contraction (were uniform in color throughout) and that the atrial contraction was at a different time from the ventricular contraction, as would be expected in a normal heart. (*See insert for color representation of the figure*.)

perform a MUGA scan, red blood cells are labeled with ^{99m}Tc (see Chapter 4) and a region of interest is drawn over the LV so that the amount of radioactivity within the LV cavity may be estimated during the cardiac cycle and the LVEF can be calculated (Figure 7.19). In a patient being treated with a medication that has the potential to damage the ability of the heart to contract (such as trastuzumab [Herceptin] combined with anthracyclines therapy in patients with breast cancer) serial MUGA scans are often done to estimate changes in LVEF with time. If a significant decrease in LVEF is found, the medication may be discontinued with the hope that the LVEF will return to normal.

7.6 Summary

Cardiac MR (CMR) is an established advanced imaging modality, which provides the most accurate information of cardiac anatomy and function. It plays an important clinical role in the assessment of myocardial viability for decision making of myocardial revascularization. Echocardiography is a sophisticated yet simple diagnostic tool that provides a window into cardiac structure and function. Real-time imaging provides invaluable clinical information on cardiac physiology in health and disease. Nuclear medicine imaging studies have long been used to evaluate cardiac structure and function. These tests are very important and, in general, are complementary to echocardiography, CT, MRI, and angiography for assessing the heart and determining the most effective patient care.

References

1 Hendel, R.C., Kramer, C.M., Poon, M. et al. (2006). ACCF/ACR/SCCT/SCMR/ASNC/NASCI/SCAI/SIR 2006 appropriateness criteria for cardiac computed tomography and cardiac magnetic resonance imaging: a report of the American College of Cardiology Foundation Quality Strategic Directions Committee Appropriateness Criteria Working Group, American College of Radiology, Society of Cardiovascular Computed Tomography, Society for Cardiovascular Magnetic Resonance, American Society of Nuclear Cardiology, North American Society for Cardiac Imaging, Society for Cardiovascular Angiography and Interventions, and Society of Interventional Radiology. *J. Am. Coll. Cardiol.* 48: 1475–1497.

2 Schulz-Menger, J., Bluemke, D.A., Bremerich, J. et al. (2013). Standardized image interpretation and post processing in cardiovascular magnetic resonance: Society for Cardiovascular Magnetic Resonance (SCMR) Board of Trustees Task Force on Standardized Post Processing. *J. Cardiovasc. Magn. Reson.* 15: 35.

3 Vogel-Claussen, J., Rochitte, C.E., Wu, K.C. et al. (2006). Delayed enhancement MR imaging: utility in myocardial assessment. *Radiographics* 26: 795–810.

4 Flacke, S.J., Fischer, S.E., and Lorenz, C.H. (2001). Measurement of the gadopentetate dimeglumine partition coefficient in human myocardium in vivo: normal distribution and elevation in acute and chronic infarction. *Radiology* 218: 703–710.

5 Wendland, M.F., Saeed, M., Arheden, H. et al. (1998). Toward necrotic cell fraction measurement by contrast-enhanced MRI of reperfused ischemically injured myocardium. *Acad. Radiol.* 5 (Suppl 1): S42–S44. discussion: S45–S46.

6 Mewton, N., Liu, C.Y., Croisille, P. et al. (2011). Assessment of myocardial fibrosis with cardiovascular magnetic resonance. *J. Am. Coll. Cardiol.* 57: 891–903.

7 Gheorghiade, M. and Bonow, R.O. (1998). Chronic heart failure in the United States: a manifestation of coronary artery disease. *Circulation* 97: 282–289.

8 Jessup, M. and Brozena, S. (2003). Heart failure. *N. Engl. J. Med.* 348: 2007–2018.

9 Hung, J., Teng, T.-H.K., Finn, J. et al. (2013). Trends from 1996 to 2007 in incidence and mortality outcomes of heart failure after acute myocardial infarction: a population-based study of 20,812 patients with first acute myocardial infarction in Western Australia. *J. Am. Heart Assoc.* 2: e000172.

10 Camici, P.G., Prasad, S.K., and Rimoldi, O.E. (2008). Stunning, hibernation, and assessment of myocardial viability. *Circulation* 117: 103–114.

11 Beller, G.A. (1997). Assessment of myocardial viability. *Curr. Opin. Cardiol.* 12: 459–467.

12 Wijns, W., Vatner, S.F., and Camici, P.G. (1998). Hibernating myocardium. *N. Engl. J. Med.* 339: 173–181.

13 Wagner, A., Mahrholdt, H., Holly, T.A. et al. (2003). Contrast-enhanced MRI and routine single photon emission computed tomography (SPECT) perfusion imaging for detection of subendocardial myocardial infarcts: an imaging study. *Lancet* 361: 374–379.

14 Kim, R.J., Wu, E., Rafael, A. et al. (2000). The use of contrast-enhanced magnetic resonance imaging to identify reversible myocardial dysfunction. *N. Engl. J. Med.* 343: 1445–1453.

15 Kelle, S., Roes, S.D., Klein, C. et al. (2009). Prognostic value of myocardial infarct size and contractile reserve using magnetic resonance imaging. *J. Am. Coll. Cardiol.* 54: 1770–1777.

16 Kim, R.J., Fieno, D.S., Parrish, T.B. et al. (1999). Relationship of MRI delayed contrast enhancement to irreversible injury, infarct age, and contractile function. *Circulation* 100: 1992–2002.

17 Selvanayagam, J.B., Kardos, A., Francis, J.M. et al. (2004). Value of delayed-enhancement cardiovascular magnetic resonance imaging in predicting myocardial viability after surgical revascularization. *Circulation* 110: 1535–1541.

18 Pegg, T.J., Selvanayagam, J.B., Jennifer, J. et al. (2010). Prediction of global left ventricular functional recovery in patients with heart failure undergoing surgical revascularisation, based on late gadolinium enhancement cardiovascular magnetic resonance. *J. Cardiovasc. Magn. Reson.* 12: 56.

19 Bondarenko, O., Beek, A.M., McCann, G.P., and van Rossum, A.C. (2012). Revascularization in patients with chronic ischaemic myocardial dysfunction: insights from cardiovascular magnetic resonance imaging. *Eur. Heart J. Cardiovasc. Imaging* 13: 985–990.

20 Mancini, G.B.J., Gosselin, G., Chow, B. et al. (2014). Canadian Cardiovascular Society guidelines for the diagnosis and management of stable ischemic heart disease. *Can. J. Cardiol.* 30 (8): 837–849.

21 Choi, K.M., Kim, R.J., Gubernikoff, G. et al. (2001). Transmural extent of acute myocardial infarction predicts long-term improvement in contractile function. *Circulation* 104: 1101–1107.

22 Selvanayagam, J.B., Jerosch-Herold, M., Porto, I. et al. (2005). Resting myocardial blood flow is impaired in hibernating myocardium: a magnetic resonance study of quantitative perfusion assessment. *Circulation* 112: 3289–3296.

23 Jahnke, C., Nagel, E., Gebker, R. et al. (2007). Prognostic value of cardiac magnetic resonance stress tests: adenosine stress perfusion and dobutamine stress wall motion imaging. *Circulation* 115: 1769–1776.

24. Ingkanisorn, W.P., Kwong, R.Y., Bohme, N.S. et al. (2006). Prognosis of negative adenosine stress magnetic resonance in patients presenting to an emergency department with chest pain. *J. Am. Coll. Cardiol.* 47: 1427–1432.

25 Klem, I., Heitner, J.F., Shah, D.J. et al. (2006). Improved detection of coronary artery disease by stress perfusion cardiovascular magnetic resonance with the use of delayed enhancement infarction imaging. *J. Am. Coll. Cardiol.* 47: 1630–1638.

26 Bax, J.J., Valkema, R., Visser, F.C. et al. (1997). Detection of myocardial viability with F-18-fluorodeoxyglucose and single photon emission computed tomography. *G. Ital. Cardiol.* 27: 1181–1186.

27 Heijenbrok-Kal, M.H., Fleischmann, K.E., and Hunink, M.G.M. (2007). Stress echocardiography, stress single-photon-emission computed tomography and electron beam computed tomography for the assessment of coronary artery disease: a meta-analysis of diagnostic performance. *Am. Heart J.* 154: 415–423.

28 Sandstede, J.J., Bertsch, G., Beer, M. et al. (1999). Detection of myocardial viability by low-dose dobutamine cine MR imaging. *Magn. Reson. Imaging* 17: 1437–1443.

29 Cwajg, J.M., Cwajg, E., Nagueh, S.F., and He, Z.X. (2000). End-diastolic wall thickness as a predictor of recovery of function in myocardial hibernation: relation to rest-redistribution Tl-201 tomography and dobutamine stress echocardiography. *J. Am. Coll. Cardiol.* 35: 1152–1161.

30 Gerber, B.L., Belge, B., Legros, G.J. et al. (2006). Characterization of acute and chronic myocardial infarcts by multidetector computed tomography: comparison with contrast-enhanced magnetic resonance. *Circulation* 113: 823–833.

31 Deseive, S., Bauer, R.W., Lehmann, R. et al. (2011). Dual-energy computed tomography for the detection of late enhancement in reperfused chronic infarction: a comparison to magnetic resonance imaging and histopathology in a porcine model. *Investig. Radiol.* 46: 450–456.

32 Kartje, J.K., Schmidt, B., Bruners, P., and Mahnken, A.H. (2013). Dual energy CT with nonlinear image blending improves visualization of delayed myocardial contrast enhancement in acute myocardial infarction. *Investig. Radiol.* 48: 41–45.

33 Nensa, F., Poeppel, T.D., Beiderwellen, K. et al. (2013). Hybrid PET/MR imaging of the heart: feasibility and initial results. *Radiology* 268: 366–373.

34 Oh, J.K., Seward, J.B., and Tajik, A.J. (2006). *The Echo Manual*, 3e. Philadelphia, PA: Lippincott Williams & Wilkins.

35 Lang, R.M., Badano, L.P., Mor-Avi, V. et al. (2015). Recommendations for cardiac chamber quantification by echocardiography in adults: an update from the American Society of Echocardiography and the European Association of Cardiovascular Imaging. *J. Am. Soc. Echocardiogr.* 28: 1–39.

36 Yancy, C.W., Jessup, M., Bozkurt, B. et al. (2013). 2017 ACC/AHA/HFSA focused update of the 2013 ACCF/AHA guideline for the management of heart failure: a report of the American College of Cardiology/American Heart Association Task Force on Clinical Practice Guidelines and the Heart Failure Society of America. *J. Am. Coll. Cardiol.* 62: 495–439.

37 Plana, J.C., Galderisi, M., Barac, A. et al. (2014). Expert consensus for multimodality imaging evaluation of adult patients during and after cancer therapy: a report from the American Society of Echocardiography and the European Association of Cardiovascular Imaging. *J. Am. Soc. Echocardiogr.* 27: 911–939.

38 Nagueh, S.F., Smiseth, O.A., Appleton, C.P. et al. (2016). Recommendations for the evaluation of LV diastolic function by echocardiography: an update from the American Society of Echocardiography and the European Association of Cardiovascular Imaging. *J. Am. Soc. Echocardiogr.* 29: 277–314.

39 Saric, M., Armour, A.C., Arnaout, M.S. et al. (2016). Guidelines for the use of echocardiography in the evaluation of a cardiac source of embolism. *J. Am. Soc. Echocardiogr.* 29: 1–42.

40 Zoghbi, W.A., Adams, D., Bonow, R.O. et al. (2017). Recommendations for noninvasive evaluation of native valvular regurgitation. A report from the American Society of Echocardiography developed in collaboration with the Society of Cardiovascular Magnetic Resonance. *J. Am. Soc. Echocardiogr.* 30: 303–371.

41 Baumgartner, H., Hung, J., Barmejo, J. et al. (2017). Recommendations on the echocardiographic assessment of aortic valve stenosis: a focused update from the European Association of Cardiovascular Imaging and the American Society of Echocardiography. *J. Am. Soc. Echocardiogr.* 30: 372–392.

42 Zoghbi, W.A., Dumesnil, J.G., Foster, E. et al. (2009). Recommendations for evaluation of prosthetic valves with echocardiography and Doppler ultrasound. *J. Am. Soc. Echocardiogr.* 9: 975–1014.

43 Nishimura, R.A., Otto, C.M., Bonow, R.O. et al. (2014). 2014 AHA/ACC guideline for the management of patients with valvular heart disease. *J. Am. Coll. Cardiol.* 63: e57–e185.

44 Klein, A.L., Abarra, S., Agler, D.A. et al. (2013). American Society of Echocardiography clinical recommendations for multimodal cardiovascular imaging of patients with pericardial disease. *J. Am. Soc. Echocardiogr.* 26: 965–1012.

45 Goldstein, S.A., Evangelista, A., Abarra, S. et al. (2015). Multimodality imaging of diseases of the thoracic aorta in adults: from the American Society of Echocardiography and the European Association of Cardiovascular Imaging. *J. Am. Soc. Echocardiogr.* 28: 119–182.

46 Mettler, F.A. Jr. and Guiberteau, M.J. (2012). Cardiovascular system. In: *Essentials of Nuclear Medicine Imaging*, 6e, 131–194. Philadelphia, PA: Elsevier Saunders.

47 Ziessman, H.A., O'Malley, J.P., Thrall, J.H., and Fahey, F.H. (2014). Cardiac system. In: *Nuclear Medicine: The Requisites*, 4e, 378–423. Philadelphia, PA: Elsevier Saunders.

48 Heller, G.V. and Hendel, R.C. (2011). *Nuclear Cardiology: Practical Applications*, 2e. New York: McGraw-Hill.

49 Walker, J., Bhullar, N., Fallah-Rad, N. et al. (2010). Role of three-dimensional echocardiography in breast cancer: comparison with two-dimensional echocardiography, multi-gated acquisition scans, and cardiac magnetic resonance imaging. *J. Clin. Oncol.* 28: 3429–3436.

Anastasia Oikonomou

Dr. Anastasia Oikonomou is an Assistant Professor in the Medical Imaging Department of University of Toronto. She is a Cardiothoracic Radiologist and Head of the Cardiothoracic Imaging division in the Medical Imaging Department of Sunnybrook Health Sciences Centre in Toronto. Her fellowship training included clinical and research fellowships in thoracic and cardiac imaging in London – UK and Ottawa, Vancouver – Canada. Her main field of expertise is thoracic imaging and evaluation of interstitial lung diseases and lung malignancies. Her research interests are focused on primary and metastatic lung cancer imaging with survival and clinical outcome analysis based on radiomics, postradiation lung imaging, and metastatic workup algorithms.

Medical Imaging for Health Professionals: Technologies and Clinical Applications, First Edition.
Edited by Raymond M. Reilly.
© 2019 John Wiley & Sons, Inc. Published 2019 by John Wiley & Sons, Inc.

8

Lung Imaging

Anastasia Oikonomou

8.1 Introduction

The role of imaging in the diagnosis of chest diseases is crucial and is the mainstay for accurate treatment. The rapid and technological advancement of imaging modalities has created a major breakthrough in the past decades. The journey from the exclusive use of chest radiograph to the implementation of multidetector thin-slice chest CT and integrated PET/CT in clinical practice is a never-ending story giving new insights into the pathophysiology of the various diseases and redefining guidelines for monitoring and treatment leading to constant improvement of patient care.

8.2 Chest Radiograph – Projections

The standard views of a chest radiograph (chest X-ray) are the posteroanterior (PA) and lateral projections with the patient in standing position. These projections provide adequate three-dimensional evaluation of the chest. The *PA view* is the most common of all the chest radiographic projections. It is taken with the patient facing the image-forming screen (see Chapter 2), the chin slightly raised upward, and the backs of the hands on the hips with the elbows flexed (Figure 8.1a). The tube–image screen distance is at least 1.8 m according to the American College of Radiology standards to minimize the beam divergence effect and magnification of chest structures [1]. The *lateral view* is obtained with the patient in erect position, left or right side of the chest wall placed against the image screen (usually the left side if no special request stated), chin up, arms raised above head, and looking straight forward (Figure 8.1b). By placing the left side of the chest against the image screen, the

Medical Imaging for Health Professionals: Technologies and Clinical Applications, First Edition.
Edited by Raymond M. Reilly.
© 2019 John Wiley & Sons, Inc. Published 2019 by John Wiley & Sons, Inc.

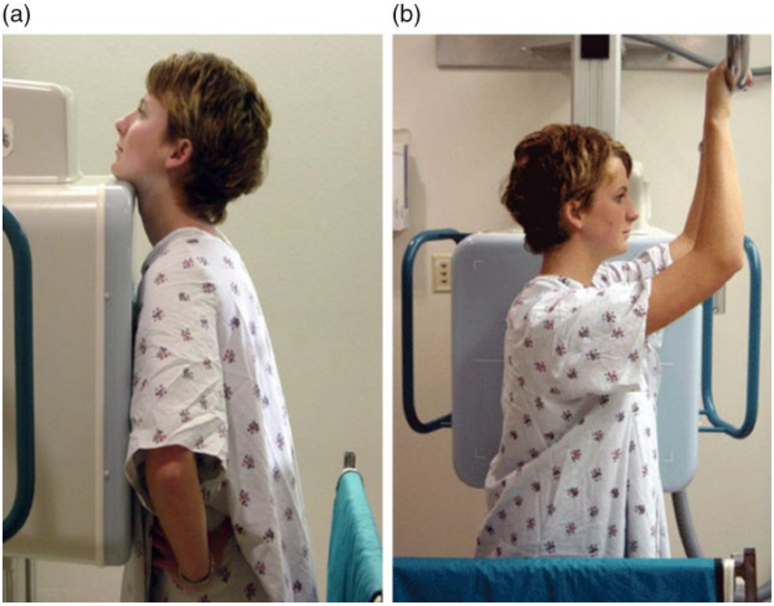

Figure 8.1 Positioning of a simulated patient for the posteroanterior (a) and lateral (b) view of the chest radiograph. *Source:* From https://www.med-ed.virginia.edu/courses/rad/cxr/technique1chest.html. Reproduced with permission of Rector and Visitors of the University of Virginia.

effect of magnification of the heart is diminished. Both views are obtained with the patient taking a deep breath (inspiration view), so that the lungs are captured at maximum volume and "false enlargement of the mediastinum and cardiovascular" structures is minimized. An *expiratory view* is obtained at deep expiration in cases where a small pneumothorax (abnormal collection of air within the pleura) is suspected and cannot be detected on an inspiration view alone or in the case of inhaled foreign body or air-trapping due to COPD [2]. If the patient is unable to stand facing the screen, then an *anteroposterior* (*AP*) *projection* (preferably) upright or even supine is obtained with a tube–screen distance of 1.2 m. In the latter cases, there is some magnification of the cardiomediastinal silhouette and equalization of the upper and lower vascular structures. Finally, a less commonly used view is the *decubitus* one obtained as a frontal projection with a horizontal X-ray beam and the patient lying in the right or left side down (according to the side of interest) (Figure 8.2). This view is used to detect a small effusion (abnormal collection of fluid within the pleura) not seen in an upright chest radiograph or to identify if the effusion is free-flowing (will change position in the decubitus view) or loculated (will not change morphology in the decubitus view) [3].

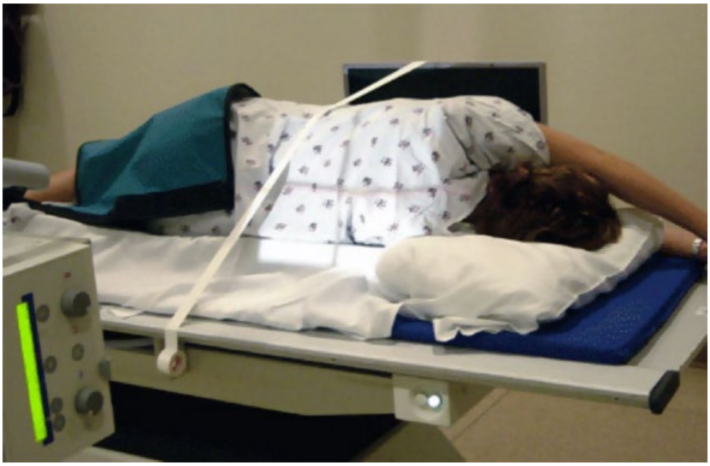

Figure 8.2 Positioning of a simulated patient for the decubitus view of the chest radiograph. *Source:* From https://www.med-ed.virginia.edu/courses/rad/cxr/web%20 images/RLD-technique.jpg. Reproduced with permission of Rector and Visitors of the University of Virginia.

8.3 Normal Findings in a Chest X-Ray

A normal chest radiograph demonstrates the right and left lung, which are normally radiolucent (dark since they do not absorb the X-ray) as they are inflated with air, the trachea and the central airways and the mediastinum in the midline, which contains the heart and the large vessels, and is radiopaque (white since they absorb the X-ray). The thoracic skeleton is composed by the 12 ribs bilaterally and the thoracic spine in the midline. The inferior margin of the thorax is the right and left hemidiaphragm, which is the border between the thorax and the abdomen (Figure 8.3).

8.3.1 Airways – Pulmonary Lobes and Segments

The trachea is a tubular radiolucent (black) structure in the midline that is usually 6–9 cm long (Figure 8.4). The trachea bifurcates into the right and left main stem bronchi at the carina. The angle of the carina is usually 60°, but this can be variable. The right main stem bronchus has a more vertical course and is shorter compared to the left. The right lateral and posterior walls of the trachea are bordered by aerated lung parenchyma and therefore are visible as “straight lines” called the right paratracheal and posterior tracheal stripes [4]. The right main stem bronchus gives rise to the right upper lobe bronchus and continues as the intermediate bronchus, which then continues distally to

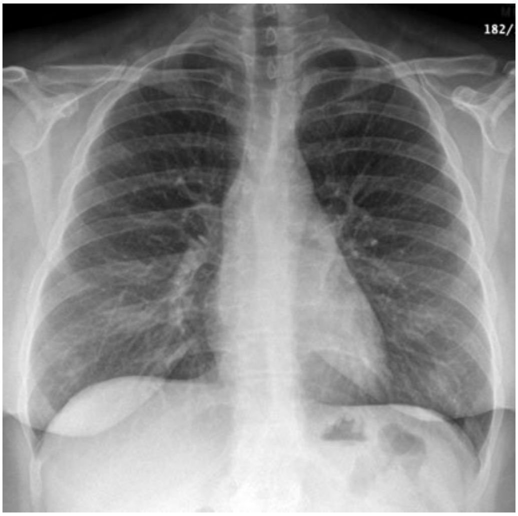

Figure 8.3 Posteroanterior view of a normal chest radiograph of a 29-year-old male.

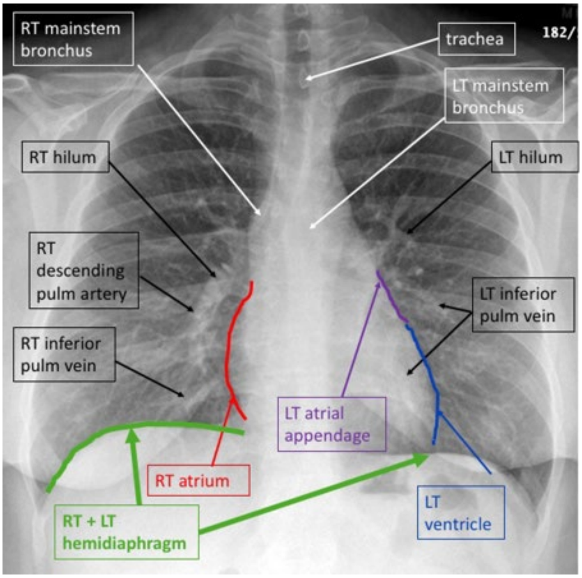
RT mainstem bronchus
trachea
182/
LT mainstem bronchus
RT hilum
LT hilum
RT descending pulm artery
LT inferior pulm vein
RT inferior pulm vein
LT atrial appendage
RT atrium
LT ventricle
RT + LT hemidiaphragm

Figure 8.4 Posteroanterior view of a normal chest radiograph of a 29-year-old male. Arrows added pointing out the anatomical features.

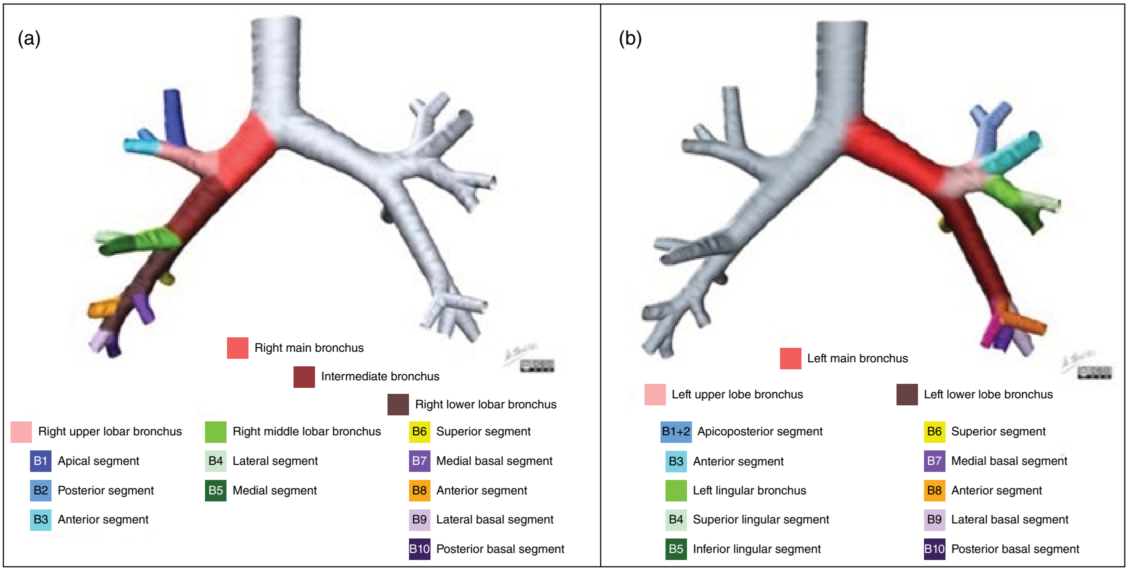
(a)
Right main bronchus
Intermediate bronchus
Right lower lobar bronchus
Right upper lobar bronchus
B1 Apical segment
B2 Posterior segment
B3 Anterior segment
Right middle lobar bronchus
B4 Lateral segment
B5 Medial segment
B6 Superior segment
B7 Medial basal segment
B8 Anterior segment
B9 Lateral basal segment
B10 Posterior basal segment
(b)
Left main bronchus
Left upper lobe bronchus
B1+2 Apicoposterior segment
B3 Anterior segment
Left lingular bronchus
B4 Superior lingular segment
B5 Inferior lingular segment
Left lower lobe bronchus
B6 Superior segment
B7 Medial basal segment
B8 Anterior segment
B9 Lateral basal segment
B10 Posterior basal segment

Figure 8.5 Lobar and segmental bronchial anatomy.

bifurcate to the middle lobe and right lower lobe bronchus (Figure 8.5). The right upper lobe bronchus divides into the apical (B1), anterior (B3), and posterior (B2) segmental bronchi. The middle lobe bronchus divides into the lateral (B4) and medial (B5) segmental bronchi and the right lower lobe bronchus divides into the superior (B6), medial basal (B7), anterior basal (B8), lateral basal (B9), and posterior basal (B10) segmental bronchi. The left main stem bronchus bifurcates into left upper lobe and left lower lobe bronchi. The left upper lobe bronchus gives off the upper division, which bifurcates to apicoposterior (B1 and B2) and anterior (B3) segmental bronchi and the lower division, which is the lingular bronchus that divides into superior (B4) and inferior (B5) segmental bronchi. The left lower lobe bronchus divides into superior (B6), anteromedial basal (B7 and B8), lateral basal (B9), and posterior basal (B10) segmental bronchi. The segmental bronchi supply bilaterally the equivalent segments in each lung (Figure 8.5) [1].

8.3.2 Pulmonary Arteries and Veins

8.3.2.1 Pulmonary Hila

The pulmonary hila are the regions at the right and left off the midline of the thorax that connect the mediastinum to the lungs (Figure 8.4). The density of the hila is largely formed by the pulmonary and bronchial arteries and veins, and to a lesser extent by the bronchi, nerves, lymphatic vessels, and lymph nodes. The main pulmonary artery bifurcates into right and left pulmonary artery. The right pulmonary artery courses to the right behind the ascending thoracic aorta before dividing behind the superior vena caca and anterior to the right main bronchus into a right upper branch and the descending or interlobar branch (Figure 8.6). The left pulmonary artery is at a higher position than the right as it passes over the left main bronchus. It usually continues as a left vertical interlobar artery that lies posterior to the left lower lobe bronchus and then divides into segmental branches for the left upper and lower lobes (Figure 8.6). The pulmonary veins are four, including right and left superior and inferior pulmonary veins. They all drain in the left atrium and have a more horizontal course compared to the pulmonary arteries, which are more vertically oriented (Figure 8.6). On a PA radiograph the right hilum is formed mainly by the interlobar artery and the right superior and inferior pulmonary vein. On the left, the hilum is mainly formed by the distal left pulmonary artery, the left interlobar artery, and the left superior and inferior pulmonary vein (Figure 8.4). On a lateral radiograph the anterior portion of the hilar structures is made up mainly by the right pulmonary artery. The left hilum, mostly composed by the left pulmonary artery, is seen as a longitudinal structure arching over and passing posterior to the left main stem or left upper lobe bronchus (Figure 8.7) [2].

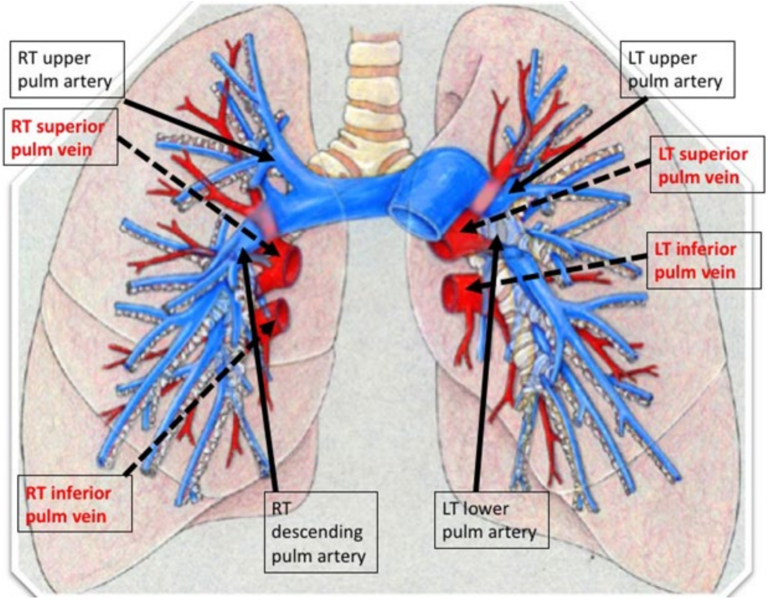
RT upper pulm artery
RT superior pulm vein
LT upper pulm artery
LT superior pulm vein
LT inferior pulm vein
RT inferior pulm vein
RT descending pulm artery
LT lower pulm artery

Figure 8.6 Diagrammatic presentation of the anatomy of the pulmonary arteries and veins. (*See insert for color representation of the figure*.)

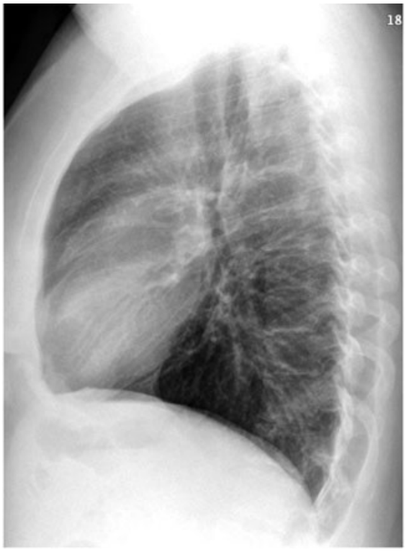

Figure 8.7 Lateral view of a normal chest radiograph of a 29-year-old male.

8.3.2.2 Radiographic Density and Pulmonary Markings

The density of the lungs depends on the X-ray absorptive power of each one of its three components: air, blood, and tissue. On a properly positioned radiograph there should be symmetry of the density of the two lungs. Any asymmetry in the radiodensity of the two lungs should be interpreted as abnormal. In a normal radiograph there are bilateral linear markings that are formed by the pulmonary arteries, veins, and bronchi. The vessels are normally seen up to 1–2 cm from the pleura and on an upright radiograph they are smaller in caliber in the upper lung zones compared to the lower lung zones (Figures 8.3 and 8.7).

8.3.3 Pleura – Fissures

The pleural space is made of the visceral pleura, which covers the lungs and the parietal pleura that lines the chest wall, mediastinum, and diaphragm. There is ~8–10 ml of physiologic fluid in the pleural space bilaterally. The fissures are invaginations of the pleura that extend from the outer surface of the lung into its substance. There are two fissures in the right lung – the minor and the major – and one major fissure in the left lung (Figure 8.8). The minor fissure may be seen on a frontal radiograph, while the two major fissures are rarely seen on a frontal radiograph. All three fissures are commonly seen on a lateral radiograph but usually incomplete (Figure 8.7).

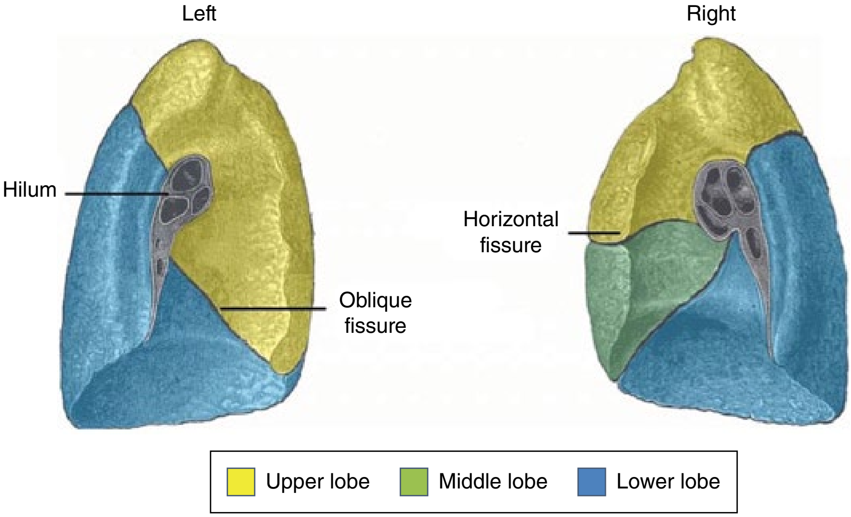

Figure 8.8 Diagrammatic presentation of the horizontal fissure (right lung) and bilateral oblique fissures separating the different lobes in the right and left lungs. *Source:* From http://teachmeanatomy.info/thorax/organs/lungs. (*See insert for color representation of the figure.*)

8.3.4 Mediastinum

The mediastinum separates the thoracic cavity into two compartments and is divided itself into three compartments: (i) the anterior mediastinum extends from the sternum up to a line drawn along the anterior border of the trachea and the posterior surface of the heart, (ii) the middle – posterior mediastinum that extends between the previous line and a line drawn 1 cm behind the anterior margin of the vertebral bodies, and (iii) the paravertebral region that extends between the previous line and the posterior surface of the vertebral bodies (Figure 8.9) [5].

8.3.5 Heart

On a frontal radiograph the right heart border is formed by the right atrium (Figure 8.4). The upper part of the left heart border is formed by the left atrial appendage and the lower heart border is formed by the left ventricle (Figure 8.4). The right ventricle is not visible on a frontal radiograph. The heart size on a PA

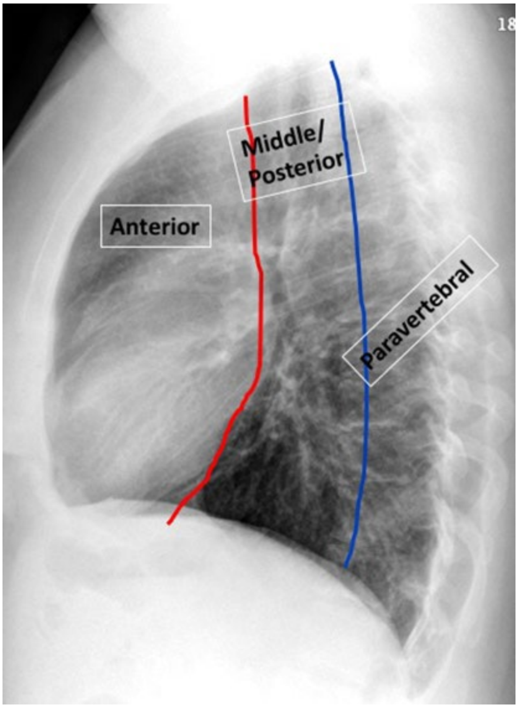

Figure 8.9 The compartments of the mediastinum as seen on a lateral view of a chest radiograph.

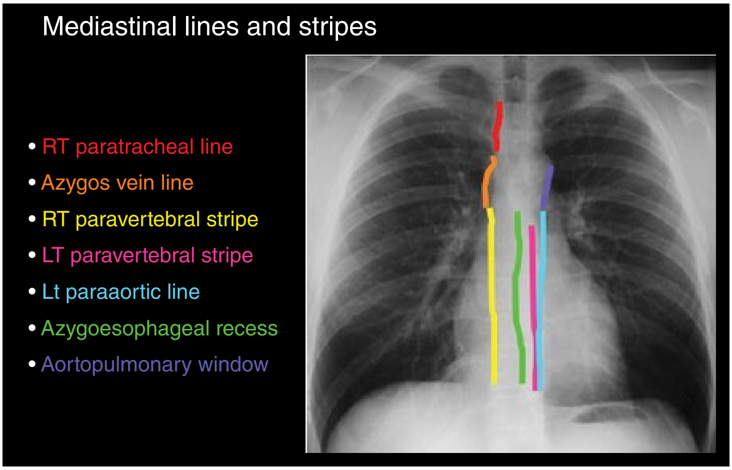
Mediastinal lines and stripes
• RT paratracheal line
• Azygos vein line
• RT paravertebral stripe
• LT paravertebral stripe
• Lt paraaortic line
• Azygoesophageal recess
• Aortopulmonary window

Figure 8.10 Mediastinal lines and stripes. (*See insert for color representation of the figure.*)

radiograph is measured by the cardiothoracic ratio, which is the ratio of the widest cardiac diameter to the widest inside thoracic diameter. A cardiothoracic ratio >50% on a PA radiograph is a reliable index of cardiomegaly (enlarged heart) [5].

8.3.6 Diaphragm

The diaphragm is a dome-shaped central tendon surrounded by muscle, which is attached to ribs 7–12 and to the xiphisternum (most inferior part of the sternum). Usually the right hemidiaphragm is higher than the left by 1.5–2.5 cm (Figures 8.4 and 8.7).

8.3.7 Chest Wall

On a well-exposed radiograph, the thoracic spine and intervertebral discs should be barely visible (Figures 8.3 and 8.7). The thoracic spine should be straight on the frontal view and slightly concave anteriorly on the lateral view. The paravertebral stripes (Figure 8.10) are formed by the contact between the lower lobes and the paravertebral soft tissues. Displacement of the right or left paravertebral stripe may be an indirect sign of a mass, adenopathy, or infection/inflammation of the thoracic spine [5].

8.4 Normal Findings in a Chest CT

The CT image is a two-dimensional representation of a three-dimensional cross-sectional slice (see Chapter 2), with the third dimension being the slice thickness. The CT image is composed of multiple picture elements called pixels. Each pixel on a CT image reflects the average attenuation of tissues – structures within this region expressed as Hounsfield Units (HU). The newer CT scanners are multidetector systems, which have the ability to obtain images in a volumetric fashion and can be reconstructed in multiple different planes [1]. The standard planes are three: axial, coronal, and sagittal (see Chapter 2) and the standard window settings are the *mediastinal window*, which allows the radiologist to see the mediastinal and cardiovascular structures and the soft tissues of the chest wall and the *lung window*, which allows visualization of the lung parenchyma, airways, and the interstitium. The anatomy and the relationship with adjacent structures on each slice of every plane are depicted with high spatial resolution and accuracy. Different anatomic landmarks are seen on different levels of each plane. On the mediastinal window at the *level of the great vessels* anterior to the central rounded structure that represents the trachea, starting from left to right we see the superior vena cava, the brachiocephalic artery, the left common carotid artery, and the left subclavian artery (Figure 8.11a). The vessel overlying anterior to the previously mentioned four branches is the left innominate vein.

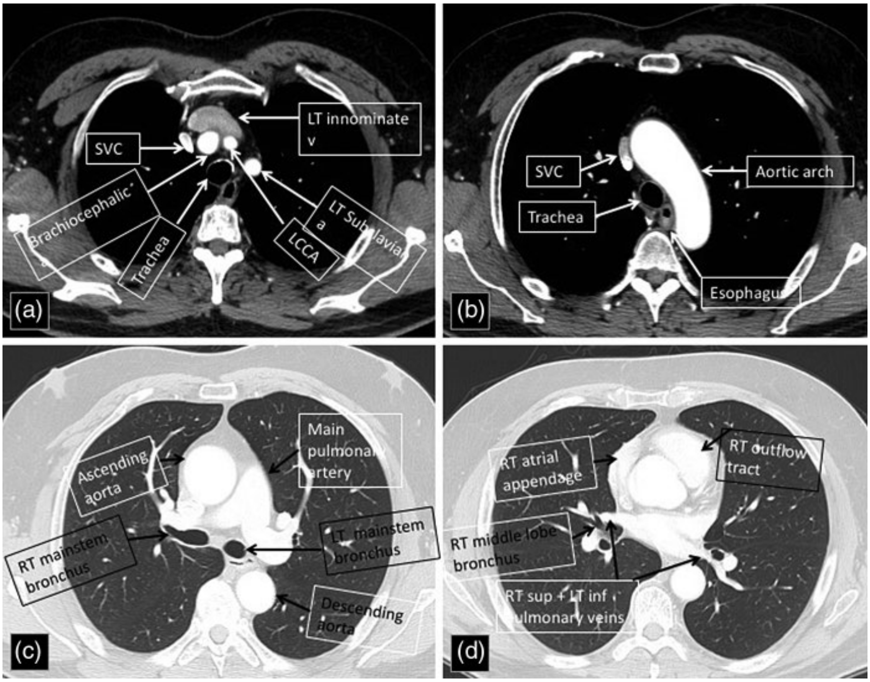
LT innominate v
SVC
Brachiocephalic
Trachea
LCCA
LT Subclavian a
(a)
SVC
Aortic arch
Trachea
Esophagus
(b)
Main pulmonary artery
Ascending aorta
RT mainstem bronchus
LT mainstem bronchus
Descending aorta
(c)
RT atrial appendage
RT outflow tract
RT middle lobe bronchus
RT sup + LT inf pulmonary veins
(d)

Figure 8.11 Normal anatomy at different levels of a chest CT: (a) level of the great vessels (mediastinal window – darker), (b) level of the aortic arch (mediastinal window), (c) level just below the carina (lung window intensity – brighter), and (d) level of the left atrium (lung window).

The two symmetric bilateral "black" regions represent the lung parenchyma, which on mediastinal window are completely black when normal. Anteriorly in the chest wall we see the major and minor pectoralis muscles. Bilateral ribs, scapulae, and the sternum are seen in the thoracic wall. At the level of the *aortic arch* (Figure 8.11b) we see the trachea in the middle mediastinum, with the arch located left to the trachea, the superior vena cava anteriorly, and the esophagus located posteriorly and to the left. Anteriorly to the aortic arch we may see some soft tissue, which represents normal thymus in the young patients. At the level just below the *bifurcation of the trachea* we see the right and left main stem bronchus, the ascending thoracic aorta anterior to the bifurcation, the descending thoracic aorta posterior to the bifurcation, and anterior and left of the spine, the left pulmonary artery left to the left main stem bronchus (Figure 8.11c). The esophagus is easily seen as it contains air in the middle/posterior mediastinum posterior and left to the trachea (Figure 8.11b). Bilaterally in the anterior chest wall the symmetric heterogeneous soft tissue represents normal fibroglandular breast tissue [6]. *At a level a few centimeter below* we see the main and right pulmonary artery, the right and left superior pulmonary vein, the right lower and left lower bronchus, the right middle lobe bronchus, and the left interlobar artery. *At the level of the left atrium*, which is located anterior to the descending thoracic aorta, we see the right atrial appendage on the right, the right outflow tract (where the main pulmonary trunk comes out of the right ventricle) on the left, the right superior and left inferior pulmonary veins, the right middle lobe bronchi, and the right and left lower lobe bronchi (Figure 8.11d). *At the level of the left ventricle* we see the left ventricle anteriorly and to the left of the midline, the right ventricle in an anterior retrosternal location right to the left ventricle, posterior to the right ventricle is the right atrium, and posterior to the left ventricle is the left atrium. Note that the myocardium of the left ventricle is thicker than the wall of the right ventricle. The normal pericardium is seen as a thin line in the epicardial fat surrounding the heart. The normal pleura are not appreciated on the chest CT. *At the level of the right dome of the diaphragm* we see the dome of the liver on the right side, the intrahepatic part of the inferior vena cava, the descending thoracic aorta anterior to the spine, and the distal esophagus anterior to thoracic aorta [7, 8].

On lung window settings we see the trachea and the bronchial tree bilaterally with the lobar, segmental and subsegmental bronchi, the lobes, the fissures, the interstitium, and the size and morphology of the pulmonary arteries and veins without being able to assess for possible intraluminal defects (pulmonary arterial emboli or venous thrombi). The smallest anatomic unit in the lung that is surrounded by interlobular septa is called the secondary pulmonary lobule, which contains a central bronchiole and pulmonary artery and is surrounded by septa, which contain lymphatics and veins. Normally, they are not visible in the normal lung apart from the lung base or in various diseases, for example, in interstitial pulmonary edema [1].

8.5 Pneumonia

Pneumonia is an infection of the pulmonary parenchyma. Pneumonia causes significant morbidity and mortality in the United States, resulting in 5.6 million cases per year and 1.7 million hospitalizations. In the United States, it is the eighth leading cause of death and the most common cause of death from infection [9]. It is associated with clinical symptoms of infection, such as cough, productive sputum, dyspnea, fever, and is accompanied by new air-space or interstitial opacities on the chest radiograph. The causative organisms can be classified as gram-positive bacteria (*Streptococcus pneumoniae, Staphylococcus aureus*), gram-negative bacteria (*Haemophilus influenzae, Escherichia coli, Klebsiella pneumoniae*), atypical bacteria (*Mycoplasma pneumoniae, Chlamydia pneumoniae, Legionella pneumophila*), anaerobes, and viruses. When pneumonia is suspected in a patient, then the role of chest radiograph is crucial as it is the first-line examination to confirm the diagnosis. Pulmonary opacities are usually visible on a chest radiograph within 12 hours from the onset of symptoms. Usually findings will improve following appropriate treatment within three weeks. The role of the chest radiograph in identifying the causative organism is limited; however, it provides useful information regarding the extent of the disease and possible complications, for example, cavitation (an intrapulmonary lesion with a thick wall and presence of air centrally), abscess formation, necrotizing pneumonia, pneumatocele formation (lesion filled in with air within the lung parenchyma surrounded by a very thin wall), pneumothorax (abnormal air within the pleural space), pleural effusion (fluid collection within the pleura), and empyema (infected loculated fluid collection within the pleura) [10]. The most common radiographic patterns are (i) focal nonsegmental (occupies an area smaller than a segment) or lobar pneumonia, (ii) multifocal bronchopneumonia or lobular pneumonia, and (iii) focal or diffuse interstitial pneumonia.

Lobar pneumonia usually appears in the periphery of the lung abutting the pleura and spreads toward the center of the lung. On the chest radiograph, there is a nonsegmental (occupies an area smaller than a segment), homogeneous air-space opacity with air bronchograms (bronchi filled with air "black" and surrounded by lung parenchyma that is "white" because of an infectious/inflammatory or hemorrhagic process) involving one lobe (Figure 8.12). The most characteristic causative organism is *Streptococcus pneumoniae.* Occasionally some pneumonias, predominantly in children, may present as round areas of consolidation (area in the lung parenchyma, which is "white" because there is abnormal filling of the alveoli with infectious/inflammatory or hemorrhagic process) usually caused by *Staphylococcus pneumoniae* and accompanied by thin-walled pneumatoceles.

Bronchopneumonia is most commonly caused by *Staphylococcus aureus, Haemophilus influenzae,* and fungi when the causative organisms produce inflammation of the bronchial wall that extends through the airway walls and into the adjacent pulmonary lobules. On a chest radiograph this is manifested

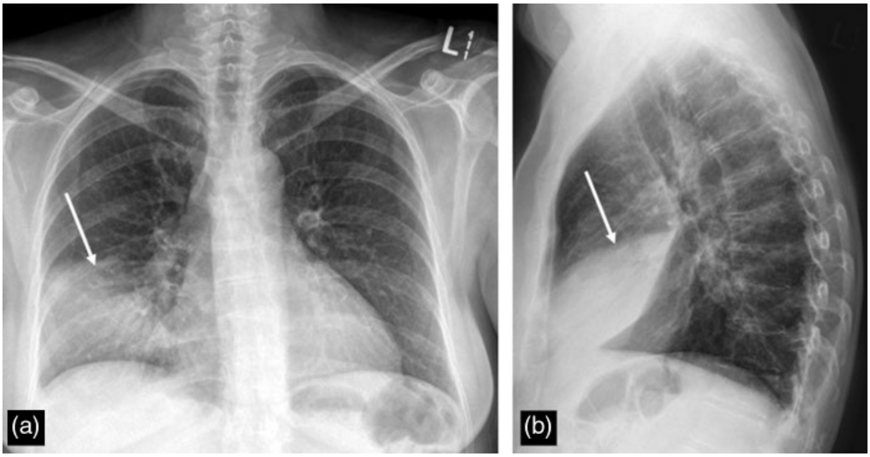

Figure 8.12 Middle lobe lobar pneumonia (white arrow) on the frontal (a) and lateral (b) view.

by patchy areas of consolidation, which may be lobular, segmental, or subsegmental (Figure 8.13). When they coalesce they may involve an entire lobe and mimic lobar pneumonia or they may cavitate [11, 12].

In interstitial pneumonia the damage and inflammation is centered in the wall of the bronchioles extending to the peribronchial tissue and interlobular septa. Radiographically, there is extensive peribronchial thickening and ill-defined reticulonodular (made up of combination of “linear” and “nodular”) opacities (Figure 8.14a). On CT there may be thickening of the interstitium associated with ground glass opacities (opacities that are not very densely white so that you can still “see through” them to the vessels and bronchi) (Figure 8.14b and c) or centrilobular nodules with a tree-in-bud pattern (pattern that resembles a tree that has small buds at the edge of its branches) representing bronchiolitis (Figure 8.15). CT has higher sensitivity in depicting small abnormalities compared to a chest radiograph [13].

8.6 Tuberculosis

Pulmonary tuberculosis (TB) is a chronic recurrent contagious infection caused by *Mycobacterium tuberculosis* that is transmitted by person to person mainly by coughing. Risk factors for TB include HIV infection (which is the greatest risk factor), immunosuppression, extremes of age, renal disease, diabetes, chemotherapy and biological agents, intravenous drug use, and cancer. More than 10 million new TB cases with more than 2 million deaths are reported worldwide every year. The majority of cases occur in Southeast Asia

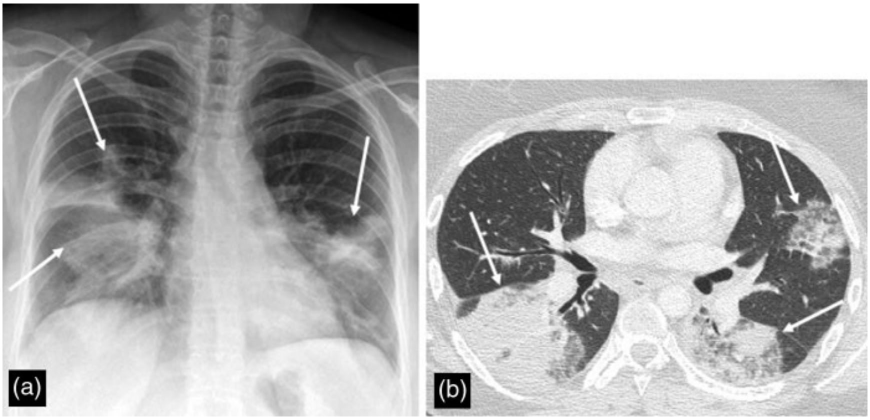

Figure 8.13 Bilateral multifocal post-viral *Streptococcus* pneumonia (arrows) on frontal chest radiograph (a) and chest CT on lung windowing intensity (b).

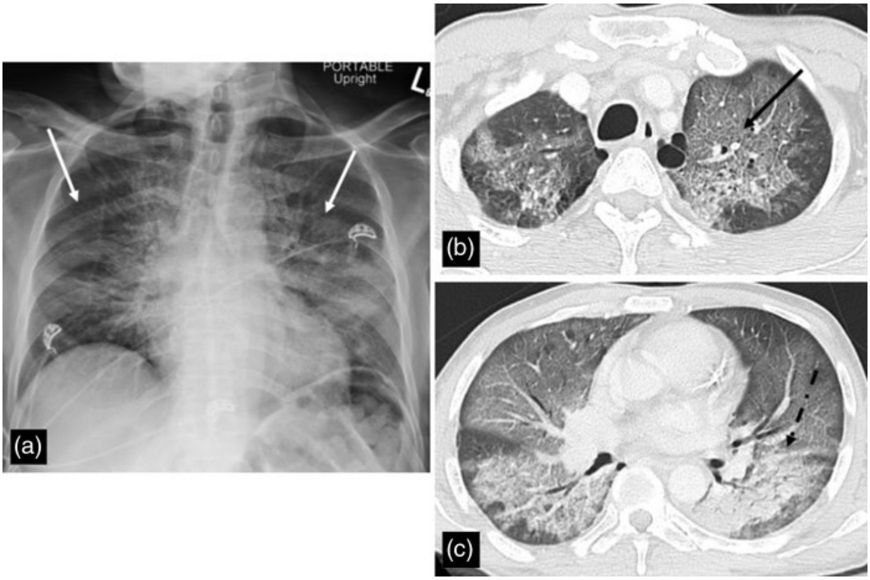

Figure 8.14 *Pneumocystis jirovecii* pneumonia in a 64-year-old female with lymphoma. (a) Frontal portable chest radiograph shows bilateral perihilar reticular and ground glass opacities (white arrows) suggestive of interstitial pneumonia. Chest CT at the level of the upper lobes (b) and lower lobes (c) shows geographic areas of ground glass opacity (black arrow) associated with thickened interlobular septa in keeping with "crazy paving pattern" (areas of ground glass opacity surrounded by thickened interlobular septa). More confluent consolidation is noted in the left lower lobe (dotted dashed arrow) (c). The findings are characteristic of *Pneumocystis jirovecii* pneumonia in the appropriate clinical context.

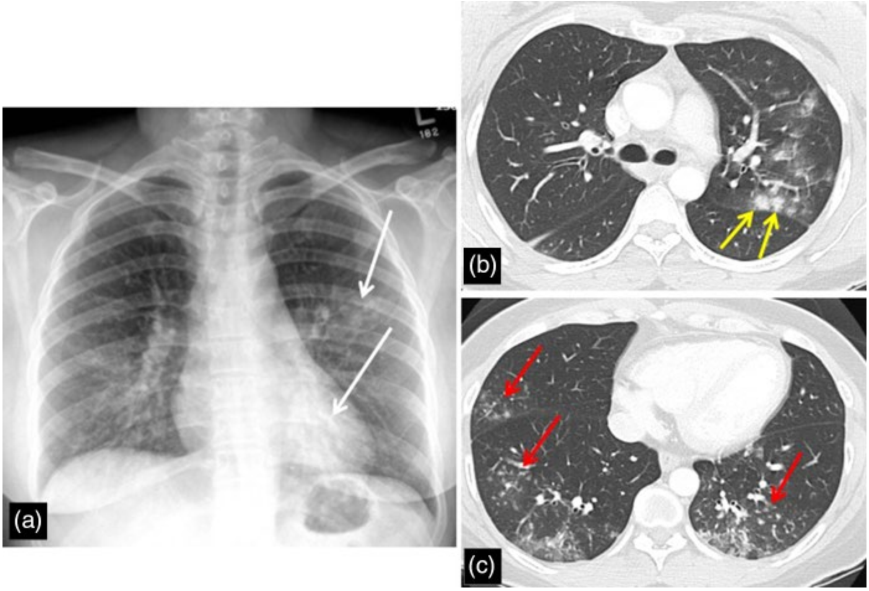

Figure 8.15 Influenza viral pneumonia in a 32-year-old female, with no previous medical history. (a) Posteroanterior chest radiograph shows bilateral perihilar and lower lobe small nodular and ground glass opacities (white arrows). Chest CT at the level of carina (b) and lower lobes (c) shows patchy areas of "tree-in-bud" nodularity (arrows in panel c) and larger ill-defined nodules (arrows in panel b) in bilateral lower lobes and in the left upper lobe suggestive of acute infectious bronchiolitis.

and Africa. Patients may be asymptomatic or present with mild or progressive dry or productive cough, fever, fatigue, weight loss, hemoptysis, and night sweats. The initial parenchymal focus of injury is called the "Ghon focus," which may be completely healed or calcify. The Ranke complex is the combination of the parenchymal focus and of the involved (usually unilateral) hilar lymph nodes [1]. TB can manifest in active and latent forms. Active disease can be seen both in primary and post-primary TB. Patients who develop the disease for the first time after initial exposure are considered to have primary TB, while patients who develop the disease as a result of reactivation of a previous focus of TB or reinfection are considered to have post-primary TB. Traditionally it is believed that these two phases of disease manifest with different radiographic findings [14].

The chest radiograph is the main imaging modality for the initial evaluation and follow-up of patients. Patients may have active TB and a normal chest radiograph and this may occur more commonly in miliary disease (hematogenous dissemination of the disease) or severely immunocompromised patients. However, CT is more sensitive than a chest X-ray in depicting subtle abnormalities especially in diffuse abnormalities such as miliary disease or endobronchial spread in patients with normal or equivocal radiographic findings. Primary TB is seen more often in children and immunocompromised patients. The most common imaging findings include necrotic lymphadenopathy (lymph nodes that have “fluid-like” density centrally secondary to necrosis), parenchymal consolidation in the lower lung zones, and pleural effusion. In post-primary TB the most common imaging manifestations are cavitary lesions, parenchymal consolidations, and tree-in-bud centrilobular branching micronodules, which are predominant in the upper lung zones (Figure 8.16). Miliary TB occurs when there is hematogenous dissemination of the disease and it occurs most commonly in the immunocompromised patients. Radiographically it presents with randomly distributed small nodules that have the same size and are symmetrically distributed bilaterally with no zonal predominance. Latent TB describes the asymptomatic phase of infection that can lead to post-primary TB after many years if the disease is reactivated [15].

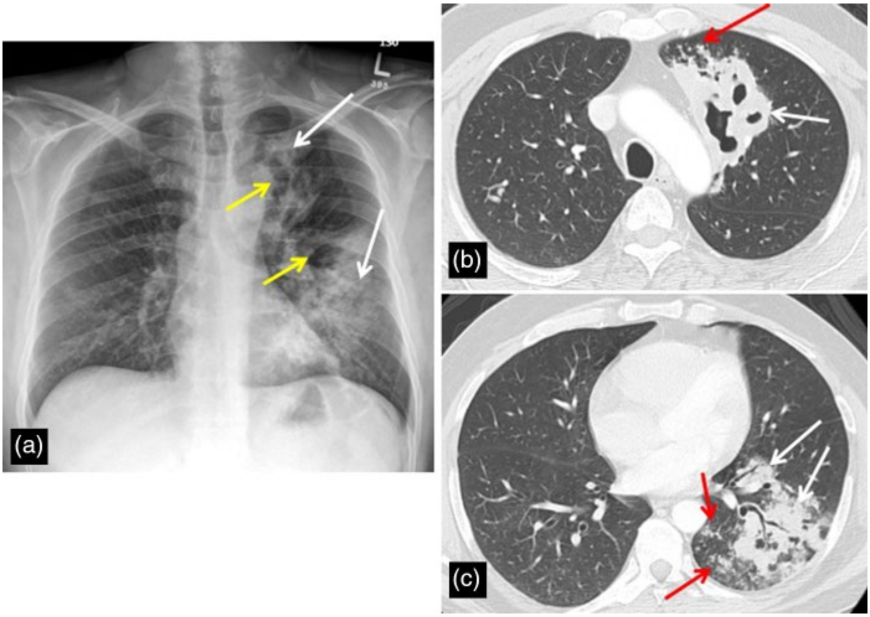

Figure 8.16 Postprimary reactivation tuberculosis in a 53-year-old male with prior history of tuberculosis. (a) Posteroanterior chest radiograph shows left upper and lower lobe confluent opacities (white arrows) with central areas of cavitation (broken black arrows). Chest CT at the level of the upper lobes shows a left upper lobe cavitary consolidation (white arrow) surrounded by tree-in-bud nodularity (broken black arrow) (b) and in the left lower lobe peribronchial areas of consolidation (white arrow) and tree-in-bud nodularity (broken black arrows) (c).

8.7 Chronic Obstructive Pulmonary Disease

According to the World Health Organization by the year 2030, COPD will be the third leading cause of death worldwide. COPD is a heterogeneous disease with different contributions from the airways (airways phenotypes) and parenchymal abnormalities (emphysema phenotypes) leading to pulmonary functional deficiencies characterized by airflow limitation [16].

8.7.1 Emphysema

Emphysema is the abnormal irreversible enlargement of airspaces distal to the terminal bronchiole, accompanied by destruction of bronchiolar walls. In the early stage, patients may be asymptomatic; however, in advanced stages, dyspnea may occur even at rest. Up to 30% of lung parenchyma may be destroyed without pulmonary function tests being abnormal. It is strongly associated with smoking history; however, only 40% of smokers will develop significant emphysema [17]. Chest X-ray has low specificity and sensitivity in detecting mild disease and cannot quantify severity. The radiographic findings include areas of increased lucency, paucity of lung vessels with tapering of the vessel caliber at the lung periphery, and flattening of the diaphragm with increased retrosternal space (Figure 8.17) [18]. Thin-section CT is the imaging modality of choice to detect the presence, extent, and quantify the severity of emphysema.

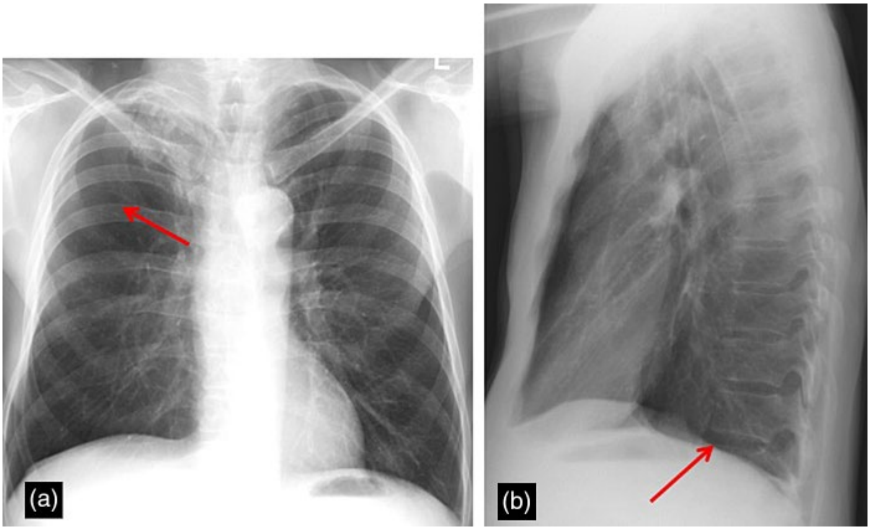

Figure 8.17 Emphysema on the frontal (a) and lateral (b) view of a chest X-ray in a 63-year-old male. The lungs appear hyperinflated with a paucity of lung vessels predominantly in the upper lung zones (arrow), and mild flattening of the hemidiaphragms (arrow).

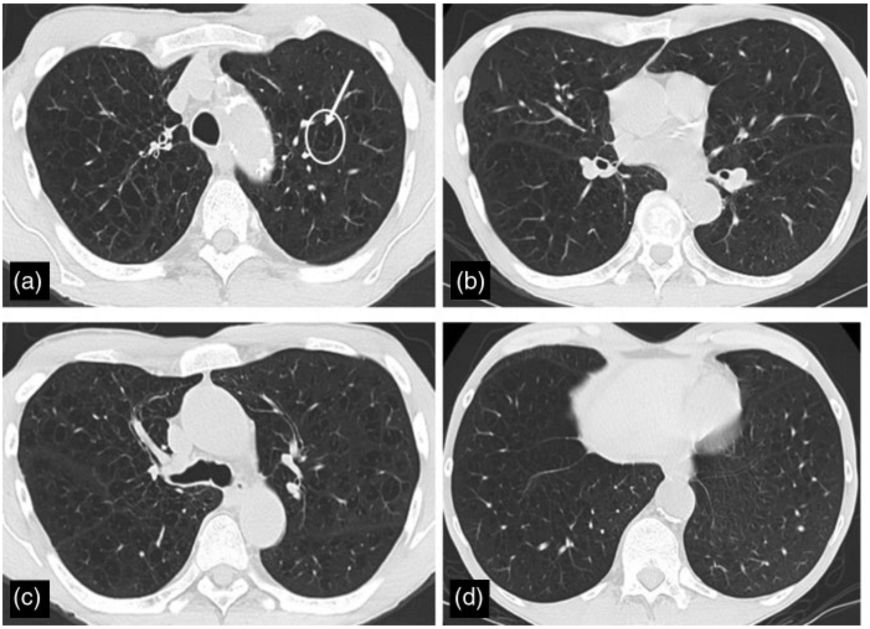

Figure 8.18 (a–d) Centrilobular emphysema predominantly in the upper lobes as shown on chest CT images and mediastinal windowing at four different anatomical cross-sectional levels. There are multiple centrilobular or panlobular areas of hyperlucency throughout the lung parenchyma including a central white dot, which represents the bronchial artery (circle and arrow in a).

The classification of emphysema into centrilobular, panlobular, and paraseptal type can be easily appreciated on CT. In centrilobular emphysema there are multiple centrilobular areas of decreased attenuation with no delineated surrounding walls (as opposed to "true pulmonary cysts," which are surrounded by a very thin wall), that spare the periphery of the secondary pulmonary lobule (Figure 8.18). In paraseptal emphysema there are multiple subpleural bullae (well defined air-filled cysts) adjacent to the pleura or fissures. Both centrilobular and paraseptal emphysema are upper lobe predominant. Panlobular emphysema is lower lobe predominant and associated with alpha-1 antitrypsin deficiency. It is characterized by diffuse homogeneous areas of low attenuation (involving the entire secondary pulmonary lobule) [18].

8.7.2 Chronic Bronchitis

Chronic bronchitis is mostly a clinical diagnosis based on a history of chronic sputum expectoration for three months of the year for two consecutive years. Imaging has a limited role in diagnosing chronic bronchitis. Usually the chest radiograph is normal or demonstrates increased lung markings (linear opacities that are similar to vessels and bronchi) reflecting bronchial wall thickening. The utility of a chest X-ray lies in excluding complications such as pneumonia or other pathology. The role of CT is also limited and the findings are nonspecific including bronchial wall thickening and air-trapping [19].

8.7.3 Bronchiectasis

Bronchiectasis is characterized by abnormal, irreversible dilatation of the airways with or without associated thickening of the bronchial walls. Chest radiography has limited sensitivity in detecting mild bronchiectasis, but is the first imaging modality requested. In advanced stage, the chest X-ray will demonstrate ring shadows (dilated bronchus seen "end-on") and tubular shadows ("tram lines") (Figure 8.19). CT is the imaging modality of choice and depicts to a great detail the "signet ring" sign when the dilated bronchus is seen end-on and the "tram-lines" representing thick-walled non-tapered bronchi when cut longitudinally in one slice (Figure 8.20). Tree-in-bud nodularity may also be seen reflecting mucus plugging in small peripheral airways as well as areas of air-trapping and decreased attenuation [19].

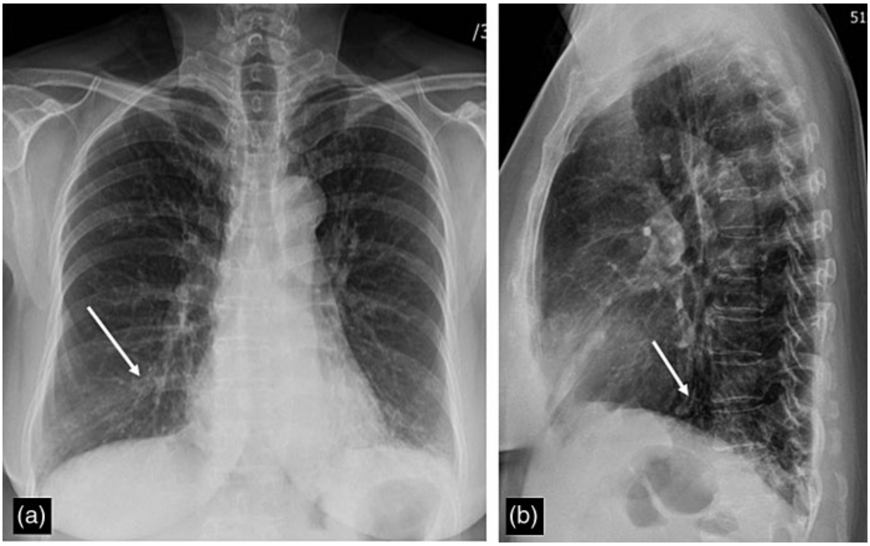

Figure 8.19 Bronchiectasis on the frontal (a) and lateral (b) view of a chest X-ray in a 53-year-old female. There are parallel linear opacities mimicking "tram lines" (white arrow), which are suggestive of bronchial wall thickening and dilated bronchi. The lungs are hyperinflated with "barrel" deformity of the thorax and mild flattening of the hemidiaphragms seen on the lateral view (white arrow).

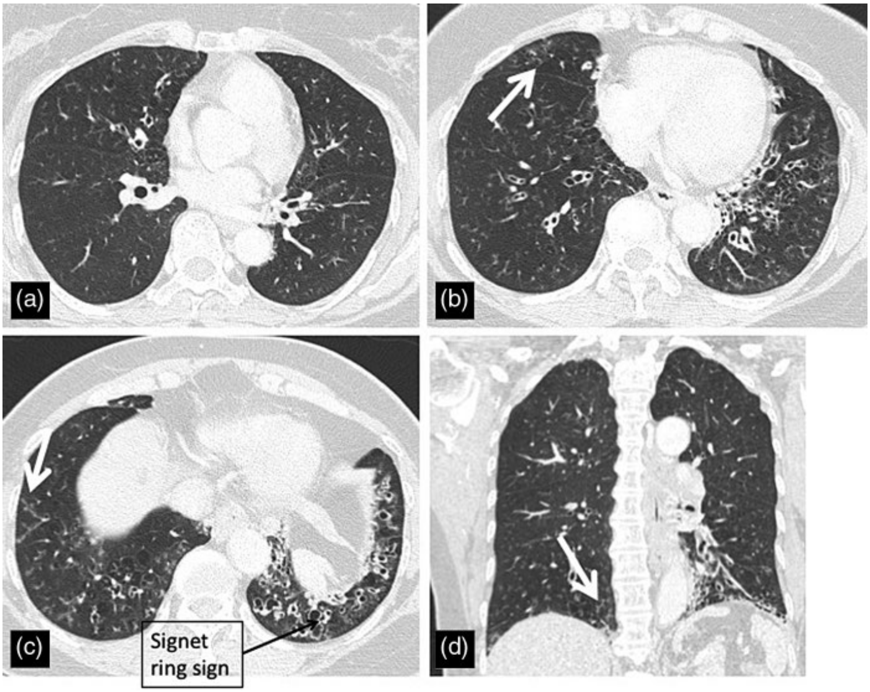

Figure 8.20 Bronchiectasis is noted in all lung lobes on CT scan at different cross-sectional levels (a–d) characterized by non-tapered thick-walled bronchi, and "signet-ring sign" representing dilated bronchi seen "end-on" with the adjacent pulmonary arterial branch represents the "signet" of the ring (circle enhancement and arrow in c). Scattered areas of tree-in-bud nodularity are also seen representing acute bronchiolitis (arrows in b–d).

8.7.4 Asthma

Asthma is a chronic inflammatory disease of the airways characterized by increased airway reactivity and air flow limitation that is at least partially reversible and results in recurrent episodes of wheezing, chest tightness, shortness of breath, and cough. The role of imaging in asthma is limited and the chest X-ray or chest CT may be normal during an attack. The chest radiograph may show hyperinflation and bronchial wall thickening and the CT may demonstrate luminal narrowing and paucity of lung vessels or few areas of bronchiectasis and air-trapping accentuated on expiratory CT. The utility of chest imaging is primarily in detecting complications of asthma such as pneumonia atelectasis (collapsed lung), pneumomediastinum (abnormal collection of air within the mediastinum), and pneumothorax (abnormal collection of air within the pleura) [20].

8.8 Pleural Effusion

Pleural effusion is the accumulation of pleural fluid within the pleural space due to imbalance of the homeostatic forces that are responsible for the movement of pleural fluid through the visceral and parietal pleura. The effusions are mainly classified as transudates (protein level $<30\,\mathrm{mg\,dl^{-1}}$ or pleural fluid protein/serum protein ≤ 0.5) and exudates (protein level $>30\,\mathrm{mg\,dl^{-1}}$ or pleural fluid protein/serum protein ≥ 0.5). The differentiation of transudate from exudate is also based on the measurement of pleural fluid and serum lactic dehydrogenase (LDH). The most common causes of pleural transudates are left-sided heart failure, liver failure, hypoproteinemia, renal failure, and constrictive pericarditis. Pleural exudates are most commonly caused by pneumonia, lung and pleural malignancy, pulmonary embolism (PE), drug toxicity, and connective tissue diseases [21].

Chest radiography is insensitive in detecting small pleural effusions. The classic sign of pleural effusion is the meniscus sign characterized by peripheral homogeneous opacity in the lateral costophrenic angle (where the lateral/inferior part of the diaphragm meets the lateral ribs on the frontal view) (frontal view) or posterior costophrenic angle (where the posterior/inferior part of the diaphragm meets the ribs on the lateral view) (lateral view) with concave upper border, which is higher laterally than medially (Figure 8.21). It requires ~200 ml of fluid to cause blunting of the costophrenic angle on a frontal view (Figure 8.21a), while even 50 ml of fluid is enough to be visible on a lateral view (Figure 8.21b). Supine view on the other hand has low sensitivity in depicting small pleural effusions or underestimates the fluid volume and it may show "apical pleural cap" (focal thickening of the pleura at the lung apex) in 50% of cases and a hazy opacification of the involved hemithorax (right or left chest) with preservation of the underlying bronchovascular markings (the linear opacities/markings that represent the pulmonary vessels and bronchi). The most sensitive view to depict a small pleural effusion is the lateral decubitus view where free fluid gravitates to the most-dependent part of the hemithorax (Figure 8.21c). Accumulation of fluid in the subpulmonic (at a location that is below the most inferior part of the lung) region on the frontal view causes flattening of the hemidiaphragm and "more lateral placement of the apex" of the "pseudodiaphragmatic contour" (the contour of the lowest part of the lung, which is mistakenly perceived as "diaphragmatic contour" as the "true" diaphragm is effaced by the presence of the subpulmonic pleural effusion) [22]. CT is more sensitive in depicting small pleural effusions and associated parenchymal abnormalities, differentiating pleural from ascitic fluid and free-flowing from loculated (trapped, not able to move freely) effusion. Contrast-enhanced CT helps in depicting pleural thickening, internal septations (thick, organized bands of fibrous tissue within the pleural fluid), and pleural-based masses

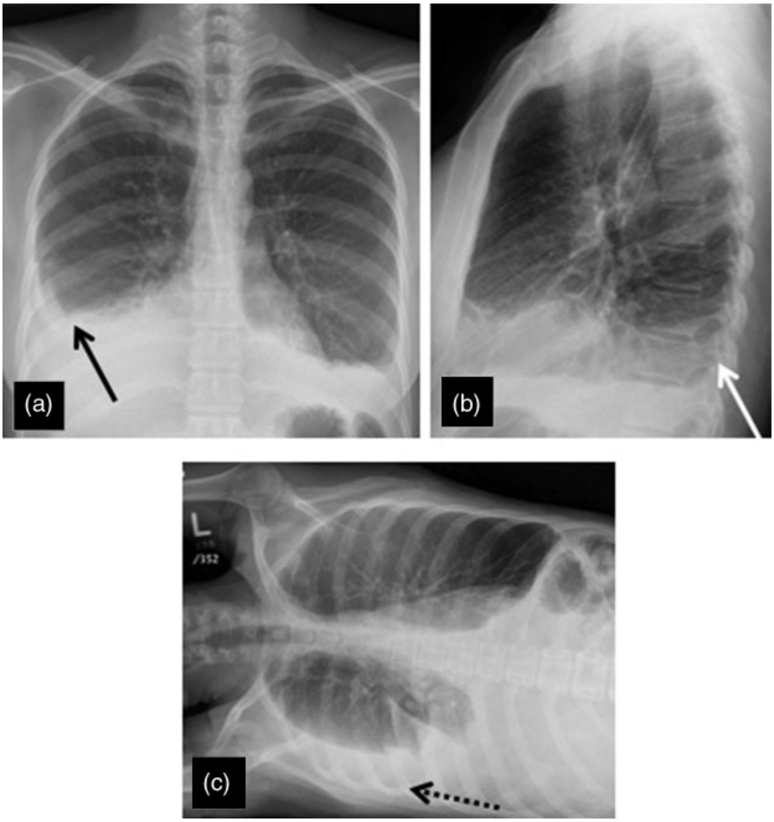

Figure 8.21 Bilateral pleural effusion on the frontal (a) and lateral view (b) of a chest radiograph. The classic sign of pleural effusion is the meniscus sign characterized by peripheral homogeneous opacity in the lateral costophrenic angle (frontal view; black arrow) or posterior costophrenic angle (lateral view; white arrow) with concave upper border, which is higher laterally than medially. The decubitus view (c) is the most sensitive one in depicting even a small amount of fluid as the free pleural fluid gravitates to the most-dependent part of the hemithorax (broken black arrow).

suggestive of malignant etiology. Free-flowing effusion on CT manifests as a "sickle-shaped" opacity in the most-dependent part of the pleura, while loculated effusion has a biconvex morphology with or without homogeneous thickening of the parietal and visceral pleura (split pleura sign). The usual range of HU (see Chapter 2) for a transudate is between 0 and 20 HU and it may be up to 100 HU for an exudate; however, the CT density alone is not reliable in differentiating a transudate from an exudative effusion [22].

8.9 Pneumothorax

Pneumothorax is the abnormal collection of air within the pleural space. Pneumothorax may be spontaneous – in a previously healthy person without preceding trauma or interventional procedure – or secondary to trauma, pre-existing medical conditions, or iatrogenic causes [1]. The chest radiograph is the first and usually the only imaging modality used to diagnose pneumothorax. It manifests on the frontal view as a homogeneously thin white line (<1 mm) that is parallel to the lateral chest wall or apex and when it is large enough it may also parallel the mediastinal or diaphragmatic pleura (Figure 8.22). The space between the white line and the lateral chest wall (which delineates the dilated pleural space) should be homogeneously hyperlucent (dark) containing no vessels or lung markings, just air. Occasionally an expiratory view may be necessary to accentuate a small pneumothorax that is not visible on the inspiratory view, by causing decrease in lung volume and enlargement of the pleural space. On supine view (lying on back) small-to-moderate pneumothoraces may not be visible [23]. A sign that raises suspicion for pneumothorax on the supine view is the "deep sulcus" (a diaphragmatic contour that is "deeper" than usually expected) sign. This is caused by the accumulation of air in the most-dependent part of the hemithorax in the supine view, which

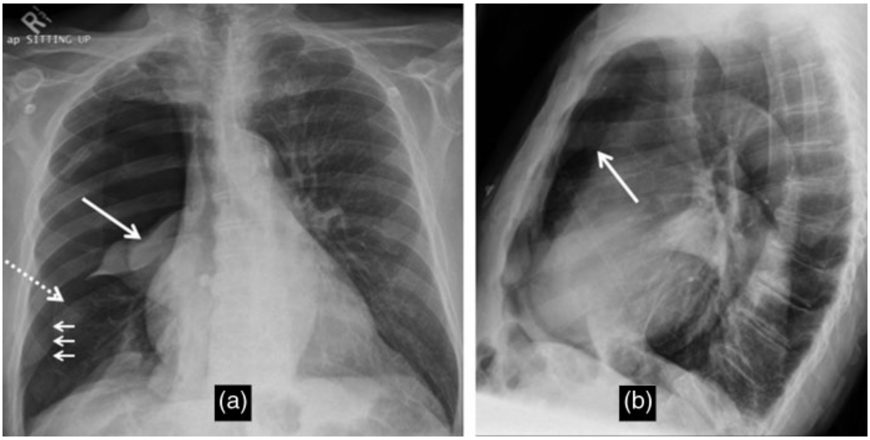

Figure 8.22 Right-sided pneumothorax on the frontal (a) and lateral view (b) of a chest radiograph. On the frontal view, there is almost complete collapse of the right lung toward the right hilum (white triangular area, white arrow in a) with only part of the right lower lobe remaining aerated. There is a thin line parallel to the right lower chest wall representing the visceral pleura (broken arrow in a). There is complete absence of vessels within the distended pleural space, which is filled with air. On the lateral view (b) there is barrel-like deformity of the thorax, flattening of the diaphragm, and retrosternal hyperlucency (dark area) (white arrow in b).

is the inferior lateral hemithorax that displaced inferiorly the hemidiaphragm and causes a very deep radiolucent sulcus [24]. CT of the chest may rarely be performed to investigate for the cause of spontaneous pneumothorax and it has been found that in 80% of patients with primary spontaneous pneumothorax there are apical bullae or blebs (small subpleural cysts).

8.10 Pulmonary Embolism

Acute PE is defined as the complete or partial obstruction of one or more branches of the pulmonary artery by thrombi that usually develop initially in the deep veins of the lower extremities and migrate centrally. PE is a frequent and potentially fatal condition with a highly effective treatment; however, if left untreated, the mortality rate is high, reaching up to 30%. It is the third most common cause of death after myocardial ischemia and stroke. The most common clinical presentation usually includes sudden onset of dyspnea, tachypnea, and pleuritic chest pain. PE remains a diagnostic challenge as its clinical presentation is usually nonspecific and mimics other clinical conditions [25]. Recent advances in imaging with fast imaging acquisition techniques and use of lower doses of radiation and contrast medium have led to the recognition of pulmonary CT angiography as the imaging modality of choice for the diagnosis of PE [26].

The role of the chest radiograph in PE is primarily to exclude other diagnoses that mimic PE such as pneumothorax, acute pneumonia, pulmonary abscess, pleural or pericardial effusion, pneumomediastinum, and dissection of aortic aneurysm. However, a chest X-ray has low sensitivity and specificity, especially in patients with preexisting cardiorespiratory disease. In the absence of preexisting radiographic abnormalities, pulmonary hemorrhage or lung infarction caused by PE is manifested as areas of consolidation accompanied by volume loss and elevation of the affected hemidiaphragm [27]. A more specific sign of infarction is the "Hampton's hump," which is characterized by a homogeneous wedge-shaped consolidation in the periphery of the lung with a rounded, convex apex toward the hilum. The "Westermark sign" indicates peripheral oligemia (fewer vessels seen and the lung is darker as the perfusion [blood going into the lung parenchyma] is reduced)), which is usually caused by occlusion of a large pulmonary arterial branch. The "Fleischner sign" describes the dilatation of a major pulmonary artery branch, usually in the hilum, accompanied by direct cutoff at the periphery of the vessel indicating abrupt occlusion. Pleural effusion is seen as an isolated finding or accompanies pulmonary hemorrhage or infarction. The imaging findings on CT pulmonary angiography (CTPA) include a complete or partial filling defect within an opacified arterial lumen characterized by either low attenuation that occupies the entire luminal area or a central area of low attenuation surrounded by a circumferential

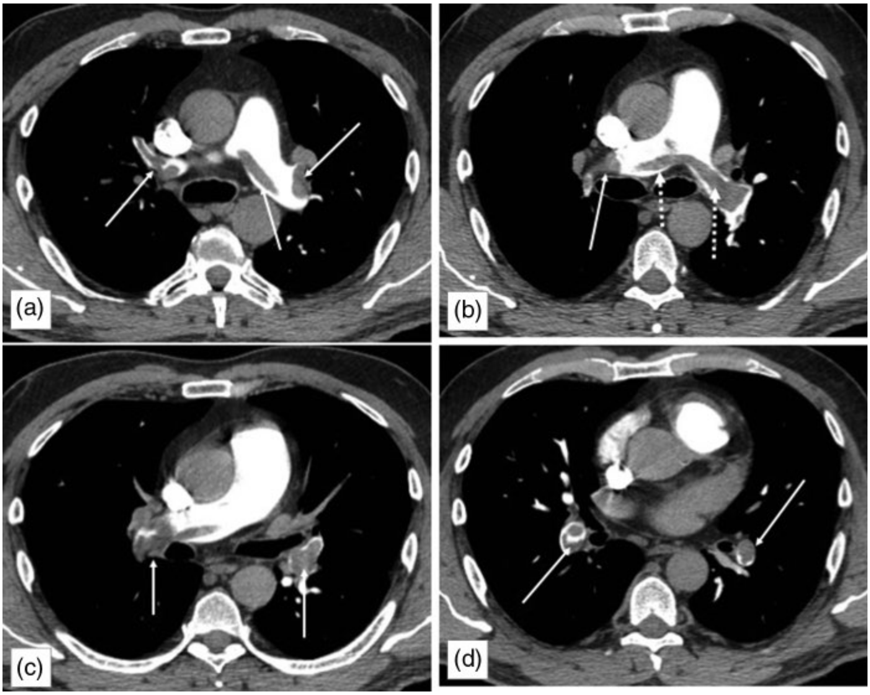

Figure 8.23 CT pulmonary angiography at multiple levels (different image panels) shows central "gray density" filling defects within the opacified "white" lumen of the central, lobar, and segmental pulmonary artery branches, which represent pulmonary emboli (white arrows in a–d). Note the "saddle embolus" (an embolus that is seen at the bifurcation of the main pulmonary artery and extends uninterrupted within the right and left pulmonary artery) at the bifurcation of the main pulmonary artery (solid arrow in b) extending within the right and left central branches (broken arrows in b).

peripheral area of contrast opacification (Figure 8.23). Ancillary nonvascular features of PE on CTPA include subpleural airspace or groundglass opacities, pleural effusions, and areas of decreased attenuation with paucity of vessels within them. Alternative diagnoses that mimic PE are easily diagnosed on CTPA including pneumonia, pneumothorax, pneumomediastinum, lung abscess, pleural or pericardial effusion as well as coronary artery disease if the study is performed with ECG gating. Incidental findings such as lung cancer may also be seen at the same time [28, 29].

Ventilation-perfusion (*V*/*Q*) lung scintigraphy is a nuclear medicine procedure to diagnose PE that is performed with the use of an inhaled ^{99m}Tc-labeled aerosol (see Chapter 4) or less commonly, ^{133}Xe gas (ventilation [*V*] scan) and intravenously-injected ^{99m}Tc-labeled macroaggregated albumin particles (perfusion [*Q*] scan). Mismatch of ventilation- perfusion areas in a patient with a normal chest radiograph is suggestive of PE, while if there is match of *V*/*Q* areas, this is likely to represent chronic obstructive pulmonary disease (Figure 8.24).

According to the recommendations based on the results of the prospective investigation of pulmonary embolism diagnosis (PIOPED) II trial [30] and the American College of Physicians [31], stratification of patients suspected for PE in the following three categories should be based on clinical assessment prior to imaging: low, intermediate, and high probability. In patients with low and intermediate probability, D-dimer test should be used and in case this is negative, then no further imaging is required. In case D-dimer is positive, then further imaging with CTPA combined with CT venography (CTV) should be used. If the latter imaging test is positive then the patient should be treated. In patients with high probability for PE, D-dimer test should not be used as it will not exclude the presence of PE if it is negative and further investigation with CTPA with CTV is recommended. If the latter is positive, treatment should be initiated, while if the latter is negative, then further investigation with venous ultrasound or ventilation/perfusion scan should be performed. *V*/*Q* scintigraphy is a good alternative for patients with allergy to iodinated contrast medium or impaired renal function. In case of pregnancy and suspected PE, then the clinical practice guidelines of the American Thoracic Society/Society of Thoracic Radiology recommend that D-dimer test not be used to exclude PE as it may falsely be positive in pregnancy. In case there are signs and symptoms of deep venous thrombosis (DVT), they recommend bilateral venous compression ultrasound (CUS) of lower extremities followed by anticoagulation treatment, if positive and further testing, if negative. If there are no signs of DVT they recommend a CXR for further assessment. If the CXR is normal, then lung *V*/*Q* scintigraphy is recommended as the next step. If the latter is nondiagnostic, then further investigation with CTPA is recommended. In case the CXR is abnormal, then further investigation with CTPA rather than lung scintigraphy is recommended [32].

8.11 Solitary Pulmonary Nodule

A solitary pulmonary nodule (SPN) is a round opacity that is at least moderately well-defined and measures 3 cm or less in diameter. A SPN can be solid or subsolid in density. The subsolid nodules include those that exhibit pure ground glass opacity or have mixed ground glass and solid components. Small SPNs are considered those that are smaller than 1 cm. The advent of multidetector CT has significantly improved the detection and characterization of small solid and subsolid pulmonary nodules [33]. Although a chest X-ray has limited sensitivity in depicting small pulmonary nodules, larger nodules are visible radiographically. Smooth margins, central or homogeneous calcification, and stability over

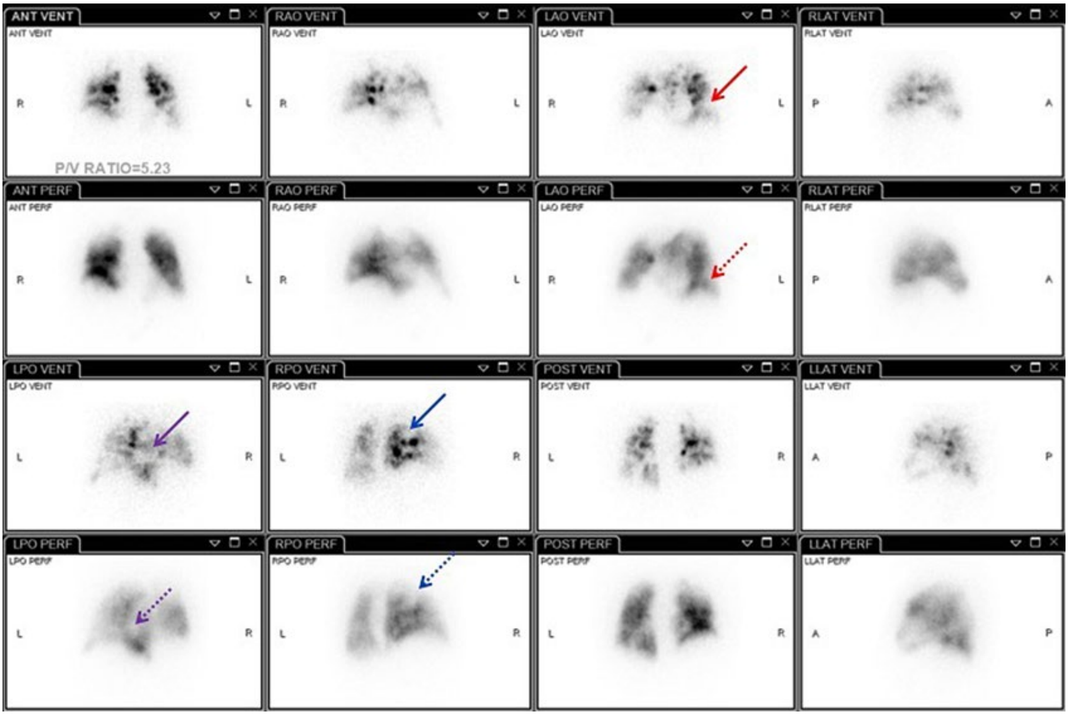
ANT VENT
RAO VENT
LAO VENT
RLAT VENT
P/V RATIO=5.23
ANT PERF
RAO PERF
LAO PERF
RLAT PERF
LPO VENT
RPO VENT
POST VENT
LLAT VENT
LPO PERF
RPO PERF
POST PERF
LLAT PERF
R
L
P
A

Figure 8.24 Ventilation/perfusion (*V*/*Q*) nuclear medicine scan in a 68-year-old male following oral inhalation of aerosolized ^{99m}Tc-medronate as well as following intravenous injection of ^{99m}Tc-macroaggregated albumin particles (^{99m}Tc-MAA). Single photon emission computed tomography (SPECT) and reconstructed planar images in different views demonstrate numerous matched ventilation/perfusion defects (solid and broken arrows in each pair of PERF and VENT images demonstrate matched defects in ventilation and perfusion images of the same plane accordingly), in keeping with advanced emphysema. The study is negative for pulmonary embolism (PE), which would require a mismatch between the ventilation (normal) and perfusion (abnormal) images. The views shown are anterior (ANT), right anterior oblique (RAO), left anterior oblique (LAO), right lateral (RLAT), posterior (POST), left lateral (LLAT). Perfusion is indicated as "PERF" and ventilation as "VENT." *P*/*V* is the ratio of blood perfusion to ventilation on the lung scan.

two years follow-up favor a benign nodule (Figure 8.25). On the contrary, spiculated or lobulated contour and interval increase in size are more commonly seen in malignant nodules. The role of a chest radiograph is crucial to determine stability or interval increase over time. Most of the time, nodules that are detected on a chest radiograph require further characterization with CT [34].

On CT, specific morphologic features are useful in determining benign or malignant potential of a nodule such as size, contour, density, the presence of air-bronchograms, the thickness of the wall of the cavitary nodules, and the growth rate. Solid nodules smaller than 4 mm have <1% likelihood of being primary lung cancer even in smokers, whereas nodules bigger than 8 mm have 10–20% risk for malignancy. Regarding the contour and margins of the nodule, typically a smooth contour favors a benign nodule whereas spiculated and lobulated contour favors malignancy (Figure 8.26). However, less commonly, benign conditions such as lipoid pneumonia, atelectasis, tuberculoma, and progressive massive fibrosis may have spiculated margins while on the other hand, most pulmonary metastases and 20% of primary lung cancers have

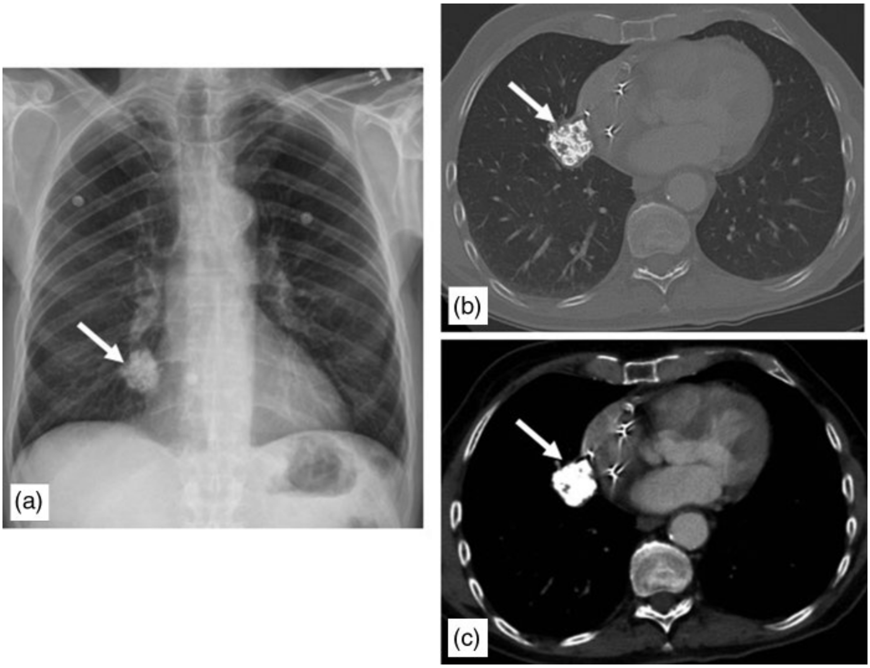

Figure 8.25 Posteroanterior chest radiograph (a) and chest CT images at the same level in lung (b) and mediastinal (c) windowing intensities show a coarsely calcified nodule (arrow) in the right paramediastinal area abutting the minor lung fissure and extending between the middle and right lower lobe. The findings are in keeping with a calcified granuloma or hamartoma, which are benign lesions.

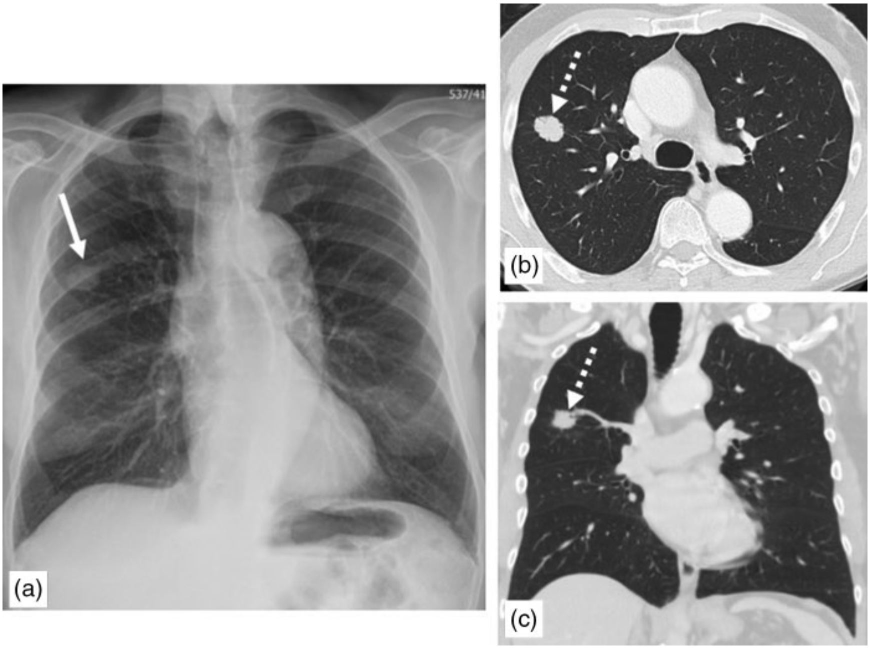

Figure 8.26 Posteroanterior chest radiograph shows a rather ill-defined solitary pulmonary nodule in the right upper lobe (solid white arrow in a). Chest CT axial (b) and coronal (c) images reveal a spiculated nodule (broken white arrow) in the right upper lobe highly suspicious for primary malignancy. CT-guided biopsy revealed histology consistent with adenocarcinoma of the lung.

smooth margins. The presence of fat attenuation (−40 to −120 HU) is characteristic of hamartoma (a benign tumor). Most of the calcification patterns (diffuse, central, laminated, and popcorn patterns) are seen in benign nodules as opposed to suspicious patterns of calcifications (punctuate, eccentric, and amorphous) that are seen in malignant nodules. In benign cavitary nodules usually the wall is thin, whereas in malignant cavitary nodules the wall is thick and irregular. About 95% of malignant cavitary nodules have a wall thickness >15 mm and 92% of benign cavitary nodules have a wall thickness <5 mm.

In terms of growth rate, volumetric assessment is a more accurate and reproducible way compared to measurement of diameter for determining the growth of a SPN. Malignant solid nodules have a volume doubling time of <100 days (20–400 days). This is in contrast to the volume doubling time of infectious/inflammatory nodules, which is <20 days, and of benign nodules, which is >400 days. Therefore, for solid nodules, stability over a 2-year period (doubling time >730 days) is a reliable factor a benign lesion [34]. The criteria are different in subsolid nodules. Size has been found to have limited value in determining malignancy. In terms of shape, it has been reported that a round shape is more

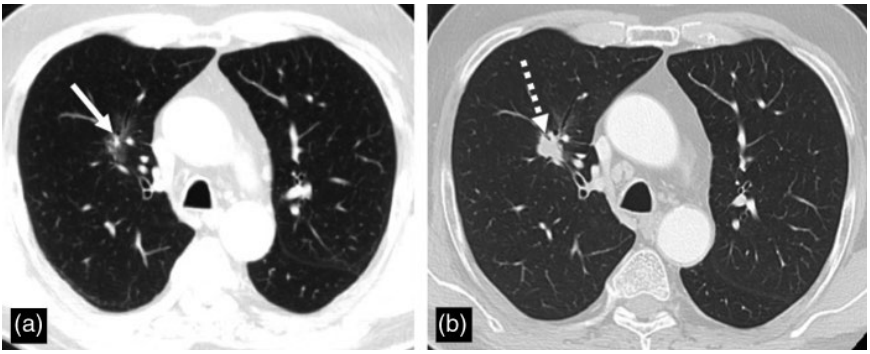

Figure 8.27 Pure ground glass opacity nodule in the right upper lobe on a chest CT (a) in 2012 (solid white arrow) performed for irrelevant clinical indication. Follow-up chest CT in 2015 (b) showed development of significant solid component and mild increase in size (broken white arrow). Histologic study revealed invasive adenocarcinoma of the lung.

common in malignant subsolid nodules. In addition to that, lobulation, spiculation, and a well-defined but course interface (the border with the surrounding tissues) are more common in malignant rather than in benign nodules. Regarding the growth rate, in subsolid nodules this may manifest in three different ways: increase in size, development of new solid component, and interval increase of solid component (Figure 8.27). All these three features favor malignancy [34, 35]. Once a subsolid nodule is detected, a follow-up CT in three months should be performed in order to confirm if it is persistent or has resolved since many of those are infectious or inflammatory in etiology. According to the most recent Fleischner guidelines for the management of pulmonary nodules, persistent subsolid pulmonary nodules must be reassessed for at least five years since the volume doubling time of slowly growing subsolid adenocarcinomas may be around 1346 days [36].

Nodule metabolism is assessed with the use of ^{18}F-FDG PET/CT (see Chapter 15), which is based on the semi-quantification of glucose uptake by the lesion. The metabolism of glucose is increased in malignancies with a commonly used threshold of standardized uptake value (SUV) >2.5 for ^{18}F-FDG. The sensitivity and specificity of PET/CT in detecting malignant nodules is increased for solid pulmonary nodules with a diameter >8 mm (~97 and 78%, respectively). However, the sensitivity and specificity of PET/CT for differentiating malignant-form benign subsolid nodules is very limited and is not recommended [37, 38].

8.12 Lung Cancer

Lung cancer remains the most common cancer worldwide and the leading cause of cancer death with an estimated 224 390 cases and 158 080 deaths in the United States in 2016. The primary risk factor for the development of lung cancer is smoking, which accounts for 85–90% of all lung cancers. However, ~15% of lung cancers occur in never smokers with a predilection in Asian women [39]. According to the 2015 World Health Organization classification, lung cancer histologic types are adenocarcinoma, adenosquamous carcinoma, squamous cell carcinoma, large cell carcinoma, sarcomatoid carcinoma, neuroendocrine tumors including small cell and carcinoid tumors, and DIPNECH (diffuse idiopathic pulmonary neuroendocrine cell hyperplasia). Approximately 95% of all lung cancers are classified as either small cell (SCLC) or non-small cell lung cancers (NSCLC) including adenocarcinoma, squamous cell carcinoma, and large cell carcinoma. The most common histologic type is the lung adenocarcinoma, which accounts for ~30% of lung cancers. The remaining 5% are other histologic types that arise in the lung [40]. The tumor node metastasis (TNM) staging system of lung cancer is based on the assessment of tumor size (T), extent of regional lymph node involvement (N), and status of distant metastasis (M). The combination of T, N, and M components determines the overall stage of the disease (stage I–IV). The different stage groups correlate with survival and prognosis and are linked to specific recommendations for treatment. The most recent TNM staging system is the eighth, which is in effect worldwide since 1 January 2017, except in the United States and will be in effect in the United States on 1 January 2018 [41].

The role of imaging in patients with suspected lung cancer is to detect the tumor characteristics, to determine the radiologic stage of the disease, identify the target lesion for tissue sampling, and assist in planning for surgery or radiation oncology and to monitor response to therapy. Chest radiography has low accuracy in diagnosing and staging lung cancer. The advantage of chest radiography is the immediate availability, low cost, and minimal radiation dose. Classic features that favor primary lung malignancy in a lesion are spiculated margins, large size, upper lobe location, mass-like opacity, and central mass with peripheral atelectasis (collapsed lung) (Figure 8.28). CT of the chest and upper abdomen (including adrenals) should be performed in all patients with suspected NSCLC to characterize the primary tumor and assess for involved lymph nodes and distant metastases. The tumor may present as nodule (<3 cm) or as a mass (>3 cm). It may rarely present as air-space consolidation with air-bronchograms mimicking pneumonia. When it presents as a nodule or a mass, it usually has spiculated margins (corona radiata) and may be solid, or have both solid and ground glass opacity components. Linear tags extending from the tumor to the pleura (pleural tags) are associated with increased likelihood of pleural invasion. In case of adenocarcinoma there may be central "bubble" lucencies or air-bronchogram, and in case of squamous there may be central cavitation with thick wall of the surrounding cavity. Occasionally the tumor may present as a central perihilar mass causing peripheral post-obstructive pneumonitis or atelectasis. Mediastinal and hilar adenopathy can be accurately evaluated on CT. The evaluation of malignant pleural effusion and possible

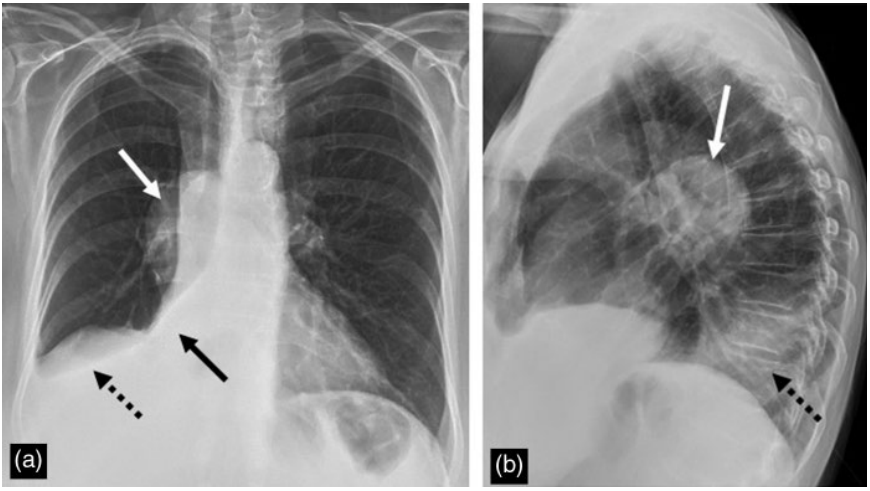

Figure 8.28 Posteroanterior (a) and lateral (b) views of a chest radiograph in a 70-year-old female show a large right hilar/mediastinal mass (white solid arrow in a and b) causing atelectasis (collapse) of the right middle (solid black arrow in a) and right lower lobes (broken black arrow in a). A small right small pleural effusion is also noted (broken black arrow in b).

pleural metastatic masses is significantly enhanced by the use of contrast medium administration (Figure 8.29). CT is also useful in assessing the extent of disease within the neighboring structures and for assessment of metastatic disease [42]. Although chest CT is the standard imaging modality of choice for assessing the primary tumor size, and margins, it has been reported that the role of ^{18}F-FDG PET/CT in staging lung cancer is crucial (see Chapter 15) as it reduces the number of unnecessary thoracotomies by usually upgrading the stage of the patient. However, ^{18}F-FDG PET/CT is indicated only if the tumor is localized on CT. PET detects ^{18}F-FDG-avid metastatic regional lymph nodes and distant metastases (Figure 8.30). It can also differentiate tumor from surrounding atelectasis. It has high sensitivity in detecting bone metastases obviating the need for a bone scan in many cases. ^{18}F-FDG PET/CT is reliable for nodules >8 mm and may show low or no ^{18}F-FDG avidity in carcinoid tumors and subsolid tumors (minimally invasive forms of adenocarcinoma) [38].

8.13 Summary

The chest radiograph is the most common imaging modality used in chest imaging. The accurate interpretation of high-quality chest radiographs and a good clinical history allows radiologists and physicians managing respiratory

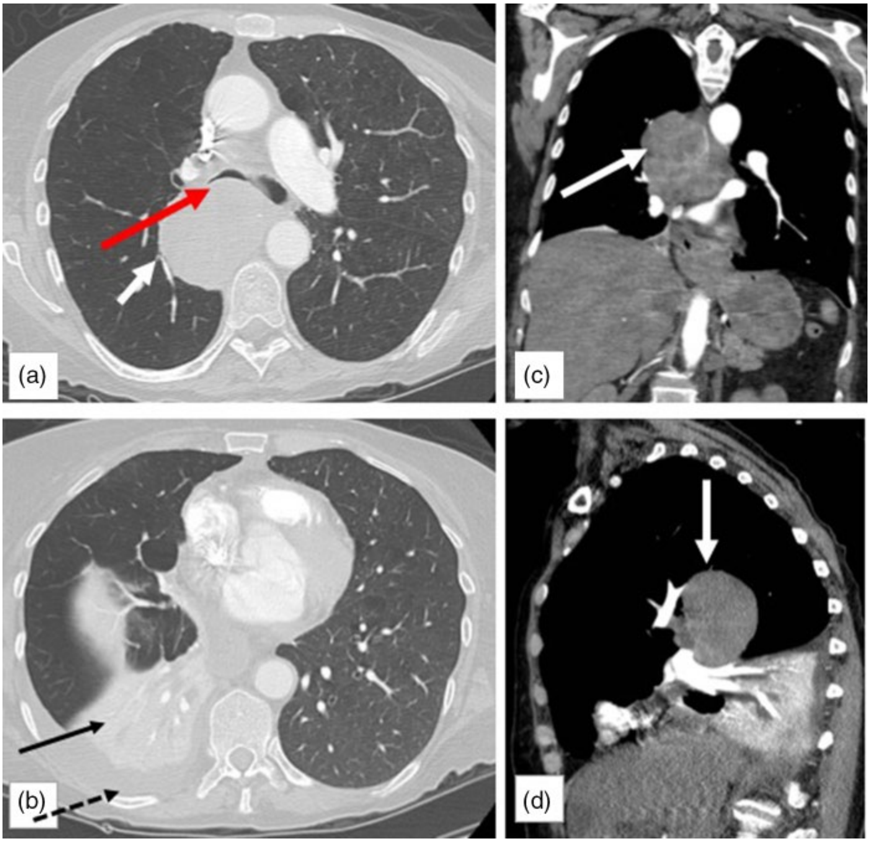

Figure 8.29 Chest CT of the same patient as in Figure 8.26 in axial plane with lung windowing intensity (a, b) and in coronal (c) and sagittal plane (d) in mediastinal windowing. There is a large heterogeneous soft tissue mass in the middle/posterior mediastinum extending into the right lower lobe (white arrow in a, c, d) and causing severe narrowing of the right main stem bronchus (broken black arrow in a). Complete atelectasis (collapse) of the right lower lobe (solid black arrow in b) and a small right pleural effusion (dotted black arrow in b) are also seen. The mass was biopsied and was consistent with small cell lung cancer.

diseases to accurately diagnose or to significantly narrow the differential diagnosis of many chest diseases. However, the chest radiograph has low sensitivity compared to the newer imaging modalities such as multidetector thin-slice chest CT and CTPA that can be used for further investigation and diagnosis of pulmonary infections, interstitial lung disease, airway disease, pleural and cardiovascular abnormalities, PE, and primary or metastatic malignancies. Imaging guidance is also used for interventional procedures, such as lung or mediastinal biopsy or pleural drainage. The role of ventilation perfusion

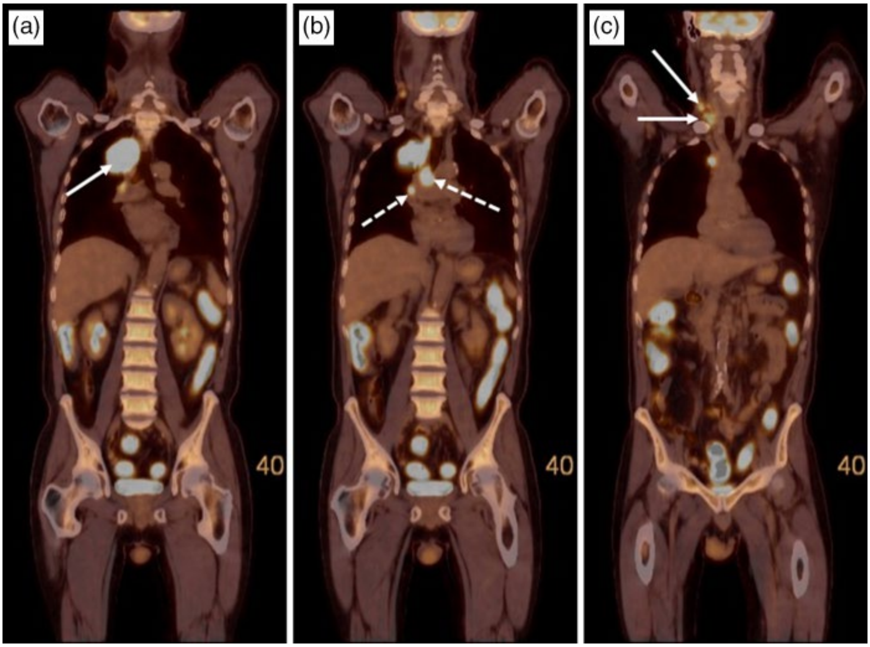

Figure 8.30 ^{18}F-2-fluorodeoxyglucose (^{18}F-FDG) PET/CT in a 72-year-old male for staging of lung cancer. FDG-avid right upper lobe mass (solid white arrow) is consistent with the known diagnosis of lung cancer (a). FDG-avid right hilar and right mediastinal (white dotted arrows in panel b) and right lower cervical and supraclavicular (white arrows in panel c) lymph nodes are consistent with metastatic nodal disease. No other distant metastatic disease is noted. The stage according to the PET/CT findings is IIIB (any T [size of tumor or invasion of chest wall or mediastinal structures], N3 [infiltration of supraclavicular nodes], and M0 [no distant metastases found]). (*See insert for color representation of the figure.*)

scintigraphy in PE is invaluable in patients with allergy to iodinated contrast medium, impaired renal function, or pregnant women. Finally, the use of integrated PET-CT has revolutionized the staging of lung cancer and other primary lung malignancy.

References

1 Muller, N.L. and Silva, C.I.S. (2008). Normal chest radiograph. In: *Imaging of the Chest*, 1e (ed. N.L. Muller and C.I.S. Silva), 3–33. Philadelphia: Saunders Elsevier.

2 Adam, A., Dixon, A.K., Gillard, J.H. et al. (2015). *Grainger & Allison's Diagnostic Radiology. A Textbook of Medical Imaging*, 6e. Edinburgh: Churchill Livingstone Elsevier.

3 Metersky, M.L. (2003). Is the lateral decubitus radiograph necessary for the management of a parapneumonic pleural effusion? *Chest* 124: 1129–1132.

4 Raoof, S., Feigin, D., Sung, A. et al. (2012). Interpretation of plain chest roentgenogram. *Chest* 14: 545–558.

5 Marano, R., Liguori, C., Savino, G. et al. (2011). Cardiac silhouette findings and mediastinal lines and stripes: radiograph and CT scan correlation. *Chest* 139: 1186–1196.

6 Sussmann, A.R. and Ko, J.P. (2010). Understanding chest radiographic anatomy with MDCT reformations. *Clin. Radiol.* 65: 155–166.

7 Gibbs, J.M., Chandrasekhar, C.A., Ferguson, E.C., and Oldham, S.A. (2007). Lines and stripes: where did they go? From conventional radiography to CT [Review]. *Radiographics* 27: 33–48.

8 Whitten, C.R., Khan, S., Munneke, G.J., and Grubnic, S. (2007). A diagnostic approach to mediastinal abnormalities [Review]. *Radiographics* 27: 657–671.

9 Sharma, S., Maycher, B., and Eschun, G. (2007). Radiological imaging in pneumonia: recent innovations. *Curr. Opin. Pulm. Med.* 13: 159–169.

10 Washington, L. and Palacio, D. (2007). Imaging of bacterial pulmonary infection in the immunocompetent patient. *Semin. Roentgenol.* 42: 122–145.

11 Vilar, J., Domingo, M.L., Soto, C., and Cogollos, J. (2004). Radiology of bacterial pneumonia. *Eur. J. Radiol.* 51: 102–113.

12 Herold, C.J. and Sailer, J.G. (2004). Community-acquired and nosocomial pneumonia. *Eur. Radiol.* 14 (Suppl 3): E2–E20.

13 Kim, E.A., Lee, K.S., Primack, S.L. et al. (2002). Viral pneumonias in adults: radiologic and pathologic findings. *Radiographics* 22: S137–S149.

14 Kim, H.Y., Song, K.S., Goo, J.M. et al. (2001). Thoracic sequelae and complications of tuberculosis. *Radiographics* 21: 839–858.

15 Nachiappan, A.C., Rahbar, K., Shi, X. et al. (2017). Pulmonary tuberculosis: role of radiology in diagnosis and management. *Radiographics* 37: 52–72.

16 Labaki, W.W., Martinez, C.H., Martinez, F.J. et al. (2017). The role of chest computed tomography in the evaluation and management of the patient with chronic obstructive pulmonary disease. *Am. J. Respir. Crit. Care Med.* 196 (11): 1372–1379.

17 Kirby, M., van Beek, E.J., Seo, J.B. et al. (2017). Management of COPD: is there a role for quantitative imaging? *Eur. J. Radiol.* 86: 335–342.

18 Litmanovich, D., Boiselle, P.M., and Bankier, A.A. (2009). CT of pulmonary emphysema-current status, challenges, and future directions. *Eur. Radiol.* 19: 537–551.

19 Little, B.P. and Duong, P.T. (2016). Imaging of diseases of the large airways. *Radiol. Clin. N. Am.* 54: 1183–1203.

20 Silva, C.I., Colby, T.V., and Müller, N.L. (2004). Asthma and associated conditions: high resolution CT and pathologic findings. *AJR Am. J. Roentgenol.* 183: 817–824.

21 Light, R.W. (2006). The undiagnosed pleural effusion. *Clin. Chest Med.* 27: 309–319.

22 Qureshi, N.R. and Gleeson, F.V. (2006). Imaging of pleural disease [Review]. *Clin. Chest Med.* 27: 193–213.

23 Hallifax, R.J., Talwar, A., Wrightson, J.M. et al. (2017). State-of-the-art: radiological investigation of pleural disease. *Respir. Med.* 124: 88–99.

24 Kong, A. (2003). The deep sulcus sign. *Radiology* 228: 415–416.

25 Muller, N.L. and Silva, C.I.S. (2010). Acute pulmonary embolism. In: *High Yield Imaging Chest*, 1e (ed. N.L. Muller and C.I.S. Silva), 390–392. Philadelphia: Saunders Elsevier.

26 Albrecht, M.H., Bickford, M.W., Nance, J.W. Jr. et al. (2017). State-of-the-art pulmonary CT angiography for acute pulmonary embolism. *AJR Am. J. Roentgenol.* 208: 495–504.

27 Wittram, C., Maher, M.M., Yoo, A.J. et al. (2004). CT angiography of pulmonary embolism: diagnostic criteria and causes of misdiagnosis. *Radiographics* 24: 1219–1238.

28 Ruggiero, A. and Screaton, N.J. (2017). Imaging of acute and chronic thromboembolic disease: state of the art. *Clin. Radiol.* 72: 375–388.

29 Yazdani, M., Lau, C.T., Lempel, J.K. et al. (2015). Historical evolution of imaging techniques for the evaluation of pulmonary embolism. *Radiographics* 35: 1245–1262.

30 Stein, P.D., Woodard, P.K., Weg, J.G. et al. (2007). Diagnostic pathways in acute pulmonary embolism: recommendations of the PIOPED II investigators. *Radiology* 242: 15–21.

31 Raja, A.S., Greenberg, J.O., Qaseem, A. et al. (2015). Evaluation of patients with suspected acute pulmonary embolism: best practice advice from the clinical guidelines committee of the American College of Physicians. *Ann. Intern. Med.* 163: 701–711.

32 Leung, A.N., Bull, T.M., Jaeschke, R. et al. (2012). ATS/STR Committee on Pulmonary Embolism in Pregnancy. American Thoracic Society documents: an official American Thoracic Society/Society of Thoracic Radiology clinical practice guideline – evaluation of suspected pulmonary embolism in pregnancy. *Radiology* 262: 635–646.

33 Raad, R.A., Suh, J., Harari, S. et al. (2014). Nodule characterization: subsolid nodules. *Radiol. Clin. N. Am.* 52: 47–67.

34 Truong, M.T., Ko, J.P., Rossi, S.E. et al. (2014). Update in the evaluation of the solitary pulmonary nodule. *Radiographics* 34: 1658–1679.

35 Cohen, J.G., Reymond, E., Lederlin, M. et al. (2015). Differentiating pre- and minimally invasive from invasive adenocarcinoma using CT-features in persistent pulmonary part-solid nodules in Caucasian patients. *Eur. J. Radiol.* 84: 738–744.

36 MacMahon, H., Naidich, D.P., Goo, J.M. et al. (2017). Guidelines for management of incidental pulmonary nodules detected on CT images: from the Fleischner society 2017. *Radiology* 284: 228–243.

37 Groheux, D., Quere, G., Blanc, E. et al. (2016). FDG PET-CT for solitary pulmonary nodule and lung cancer: literature review. *Diagn. Interv. Imaging* 97: 1003–1017.

38 Usmanij, E.A., de Geus-Oei, L.F., Bussink, J., and Oyen, W.J. (2015). Update on F-18-fluoro-deoxy-glucose-PET/computed tomography in nonsmall cell lung cancer. *Curr. Opin. Pulm. Med.* 21: 314–321.

39 Spira, A., Halmos, B., and Powell, C.A. (2016). Update in lung cancer 2015. *Am. J. Respir. Crit. Care Med.* 194: 661–671.

40 Travis, W.D., Brambilla, E., Nicholson, A.G. et al. (2015). The 2015 World Health Organization classification of lung tumors: impact of genetic, clinical and radiologic advances since the 2004 classification. *J. Thorac. Oncol.* 10: 1243–1260.

41 Detterbeck, F.C., Boffa, D.J., Kim, A.W., and Tanoue, L.T. (2017). The eighth edition lung cancer stage classification. *Chest* 151: 193–203.

42 Patil, S.S., Godoy, M.C., Sorensen, J.I., and Marom, E.M. (2014). Lung cancer imaging. *Semin. Diagn. Pathol.* 31: 293–305.

Hemi Dua

Dr. Hemi Dua is a fellowship-trained staff radiologist at the Toronto Joint Department of Medical Imaging, which services the University Health Network, Mount Sinai Hospital and Women"s College Hospital in Toronto. She is an Assistant Professor in the Department of Medical Imaging at the University of Toronto. She has special interest is all aspects of breast imaging including image-guided breast intervention, and has an emphasis on teaching and education.

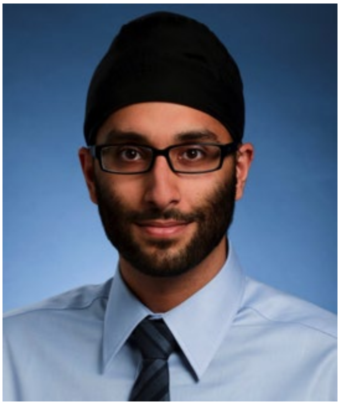

Jagbir Khinda

Dr. Jagbir Khinda is a final year resident in the Department of Medical Imaging at the University of Toronto. He will be completing a Women's Imaging fellowship at the University of Toronto following the residency. His research interests are focused on breast and abdominal imaging.

Medical Imaging for Health Professionals: Technologies and Clinical Applications, First Edition.
Edited by Raymond M. Reilly.
© 2019 John Wiley & Sons, Inc. Published 2019 by John Wiley & Sons, Inc.

9

Breast Imaging

Hemi Dua and Jagbir Khinda

9.1 Introduction

Breast cancer is the most common female malignancy globally, and a leading cause of cancer-related death in women. In the United States, ~1 in 8 women will develop breast cancer in their lifetime, while Canadian statistics predict 1 in 9, with 1/30 not surviving from the disease. Breast cancer incidence is far lower in males (1 in 1000), with only 1% of all breast cancers occurring in men. Breast cancer-related deaths have significantly declined since the implementation of widespread screening programs, in which breast imaging plays a central role.

9.2 Risk Factors for Breast Cancer

A variety of factors predispose individuals to an increased risk of developing breast cancer (Table 9.1). Female gender and advancing age represent the most significant of those. Breast cancer risk steadily increases to the age of 80, with decreasing incidence beyond this age. A family history of breast or ovarian cancer in a first-degree relative (e.g. mother, daughter, or sister) confers a substantial 50% added risk of developing breast cancer. In contrast, there is no associated increased risk by having a non-first-degree relative diagnosed with breast cancer. Inherited genetic mutations may also result in predisposition to breast cancer. Women with a BRCA1 or BRCA2 gene mutation have a nearly doubled risk of developing breast cancer in their lifetime (45–55% and 45% lifetime risk, respectively). Furthermore, BRCA1/2 gene mutation carriers often develop breast cancer at a much younger age, of a more aggressive type, and more commonly involving multiple sites within the breast(s). Prolonged

Medical Imaging for Health Professionals: Technologies and Clinical Applications, First Edition.
Edited by Raymond M. Reilly.
© 2019 John Wiley & Sons, Inc. Published 2019 by John Wiley & Sons, Inc.

Table 9.1 Breast cancer risk factors.

Female gender
Advancing age
Personal history of breast cancer
High-risk lesion diagnosed on image-guided or surgical biopsy (e.g. ADH, LCIS)
Early menarche
Late menopause
Nulliparity
First childbirth/breastfeeding beyond age 30
Radiation exposure (particularly thoracic radiation)
First-degree relative with premenopausal breast cancer
Known predisposing genetic mutations (e.g. BRCA1, BRCA2, PTEN [Cowden syndrome], ATM, TP53, and numerous other genes)
Personal history of breast cancer

ADH, atypical ductal hyperplasia; LCIS, lobular neoplasia in situ.

lifetime exposure to estrogen by means of early menarche (i.e. before age 12), late menopause (i.e. after age 55), late first pregnancy (i.e. beyond age 30), nulliparity, or in the setting of obesity (due to increased estrogen production by adipocytes) have all also been shown to increase the risk of breast cancer. Additional risk factors for breast cancer include prior chest radiation exposure (e.g. mantle radiation for Hodgkin's lymphoma treatment), previous breast biopsy yielding a high-risk lesion (e.g. atypical proliferative changes, lobular neoplasia), and a prior personal history of breast cancer. Several models have been developed for calculation of lifetime risk of developing breast cancer (e.g. IBIS, BOADICEA, Gail, and Claus). These models take a variety of risk factors into account to provide an overall estimate: hereditary gene mutations, biologic hormonal events, personal life choices (i.e. parenthood), age, family history, and now more recently mammographic breast density. Individuals calculated at a 20–25% or greater lifetime risk of developing breast cancer with these models are considered "high risk." Despite the many identified risk factors, 70% of women newly diagnosed with breast cancer have NO identifiable risk factors, aside from female gender and advancing age.

9.3 Guidelines for Breast Cancer Screening

Screening mammography is aimed at detecting malignancy in asymptomatic patients. Reports have found that screening mammography detects 2–8 cancers per 1000 women screened with an overall ~20% reduction in breast cancer mortality in screened patients [1].

9.3.1 Screening in Average Risk Women

There is a lack of global consensus with regard to the age of screening initiation and frequency of examinations. Current American College of Radiology (ACR) guidelines for women of average risk recommend suggest yearly mammographic screening from the age of 40 onward. Screening should continue as long as the patient is healthy and desires ongoing mammograms [2]. Canadian guidelines, by contrast, vary by province. Current Ontario Breast Screening Program (OBSP)/Cancer Care Ontario (CCO) [3] guidelines are identical to those outlined by the US Preventative Services Task Force [4], which recommend mammograms every other year between the ages of 50 and 74. Women may choose to begin biennial screening at the age of 40 if desired. Please refer to Table 9.2 for current American and Canadian screening guidelines in asymptomatic women.

9.3.2 High-risk Screening

Screening guidelines for high-risk women take into account the increased predisposition for developing cancer at a younger age and of a higher grade. Inclusion criteria and screening regimens for high-risk patients are generally region specific (Table 9.3). Some institutions also adapt further syndromic associations, which pose increased breast cancer risk into their high-risk screening criterion (e.g. personal history of or a first-degree relative with Li-Fraumeni syndrome, Cowden syndrome, or Bannayan–Riley–Ruvalcaba syndrome). The potential adverse effects of breast cancer screening include the minimal radiation exposure and false-positive diagnoses resulting in additional workup. Radiation doses from mammographic screening (see Chapter 1) are outlined in Table 9.4. These doses are considered acceptable given the high risk of breast cancer in the female population and the benefits of early detection.

Table 9.2 Breast cancer screening recommendations in average risk women.

Organization	Screening recommendations
American College of Radiology [2]	• Mammograms annually • Age 40 onward • Continue as long as the patient is healthy and desires ongoing screening
US Preventative Services Task Force [4] Current Ontario Breast Screening Program Cancer Care Ontario [3]	• Mammograms every other year • Ages 50–74

Table 9.3 Breast cancer screening recommendations in high-risk women.

Organization	High risk criteria	Screening recommendations
American College of Radiology [2]	• BRCA gene mutation and their untested first-degree relatives • Chest irradiation between the ages of 10–30 • ≥20% lifetime risk of breast cancer	• Annual mammogram and MRI beginning at age 25–30 or 10 yr before age of first-degree relative with breast cancer or 8 yr after radiation therapy
Ontario Breast Screening Program/ Cancer Care Ontario [3]	• Carriers of a deleterious gene mutation (e.g. BRCA1, BRCA2) • First-degree relative of a mutation carrier (e.g. BRCA1, BRCA2) and have declined genetic testing • ≥25% lifetime risk of breast cancer • Chest irradiation treatment before age 30 and at least 8 yr previously	• Annual mammogram and MRI from age of 30 to 69 (may occur together or at staggered intervals)

Table 9.4 Radiation doses for mammographic screening.

Procedure	Adult approximate radiation dose	Comparable to natural background radiation exposure for
Annual background	2.7 mSv	–
X-Ray extremity	0.001 mSv	3 h
Transatlantic flight	0.08 mSv	8 d
Chest X-ray	0.1 mSv	10 d
Mammogram (two views each breast)	0.4 mSv	7 wk
CT head	2 mSv	8 mo
CT chest	7 mSv	2 yr
CT abdomen and pelvis	10 mSv	3 yr

Source: Data from American College of Radiology [5].

9.4 Breast Anatomy

The normal breast is composed of central glandular elements with surrounding supportive stromal/connective tissue (Figure 9.1). The ductal and glandular breast tissue form a conical distribution converging to the lactiferous ducts in the retroareolar region. The breast glandular elements are composed of

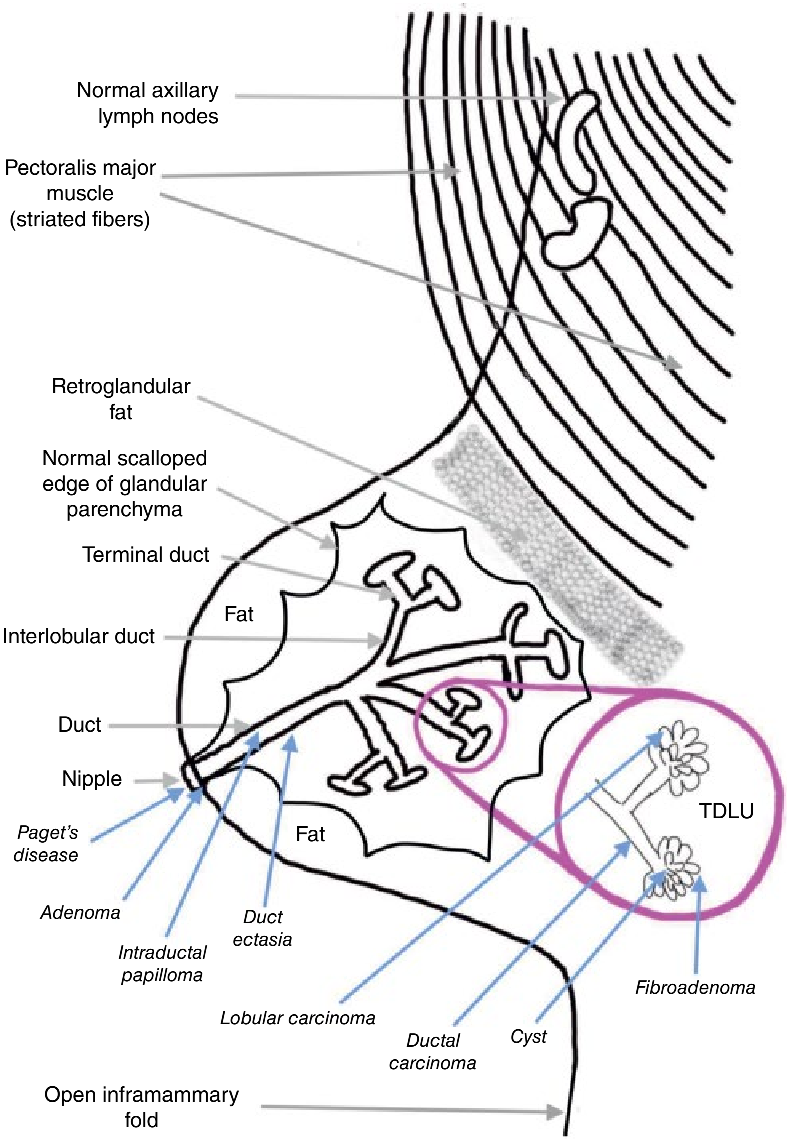
Normal axillary lymph nodes
Pectoralis major muscle (striated fibers)
Retroglandular fat
Normal scalloped edge of glandular parenchyma
Terminal duct
Fat
Interlobular duct
Duct
Nipple
Paget's disease
Adenoma
Intraductal papilloma
Duct ectasia
Fat
TDLU
Lobular carcinoma
Ductal carcinoma
Cyst
Fibroadenoma
Open inframammary fold

Figure 9.1 Schematic of normal breast anatomy.

milk-producing acini, which drain to the terminal ducts (a *lobule*), interlobular ducts, excretory ducts, and ultimately to the lactiferous ducts that lead to the nipple. A *lobe* (segment) is a drainage territory corresponding to one lactiferous duct. Each breast contains a total of 15–20 lobes (segments). The ducts are lined along their length by an inner secretory cell layer and outer myoepithelial layer. The majority of breast cancers arise from the cells of the lobules and terminal ducts. The stromal and connective tissues circumferentially encompass the glandular tissue, and include fat, suspensory (Cooper's) ligaments, lymphatics, vasculature, and nerves. Fat posterior to the gland is termed retroglandular fat, deep to which lies the pectoralis muscle.

9.5 Imaging Techniques

A variety of imaging techniques are available for the evaluation of the breast, primarily a mammogram and ultrasound. Magnetic resonance imaging (MRI) is discussed later in this chapter.

9.6 Mammography

Mammography serves as the mainstay of breast imaging with respect to screening, initial diagnostic workup, and disease monitoring.

9.6.1 Mammography System

A mammogram is a radiograph of the breast, acquired on specially designed X-ray machines. Each mammography unit (see Chapter 2) consists of an anode X-ray tube, breast compression plate, and image detector/cassette. Images are captured with either digital detectors or X-ray film. Various compression paddles are available and may be exchanged depending on the size of the breast and type of examination. The unit is mounted on a rotating C-arm to allow for the acquisitions of various projections. A trained technologist aids the patient in placing the breast between the compression plate and image detector. The breast is compressed to spread the fibroglandular tissue, thereby decreasing the amount of overlapping parenchyma. The mammogram is acquired and the patient is repositioned for additional views, as necessary. Current mammography units deliver a relatively low radiation dose to the breast with the average glandular radiation dose of 2 mSv per acquisition (4 mSv per breast for routine two-view examination; see Chapter 1). Examinations of denser breasts require a higher radiation dose compared to thin breasts as denser breasts attenuate a larger number of X-rays. Thus, in order to preserve image quality, a larger number of X-rays must be employed.

9.6.2 Image Review and Mammography Views

All mammograms are reviewed at a specialized workstation by a radiologist. Given the often subtle mammographic signs of malignancy, workstations must meet standardized criteria (e.g. high monitor resolution) to allow for accurate interpretation. Radiologists may request additional views of the breast as necessary. The craniocaudal (CC) and mediolateral oblique (MLO) views serve as the standard mammographic views (Figure 9.2). Additional views are acquired as indicated for better visualization of the breast or further characterization of abnormalities detected on these initial views.

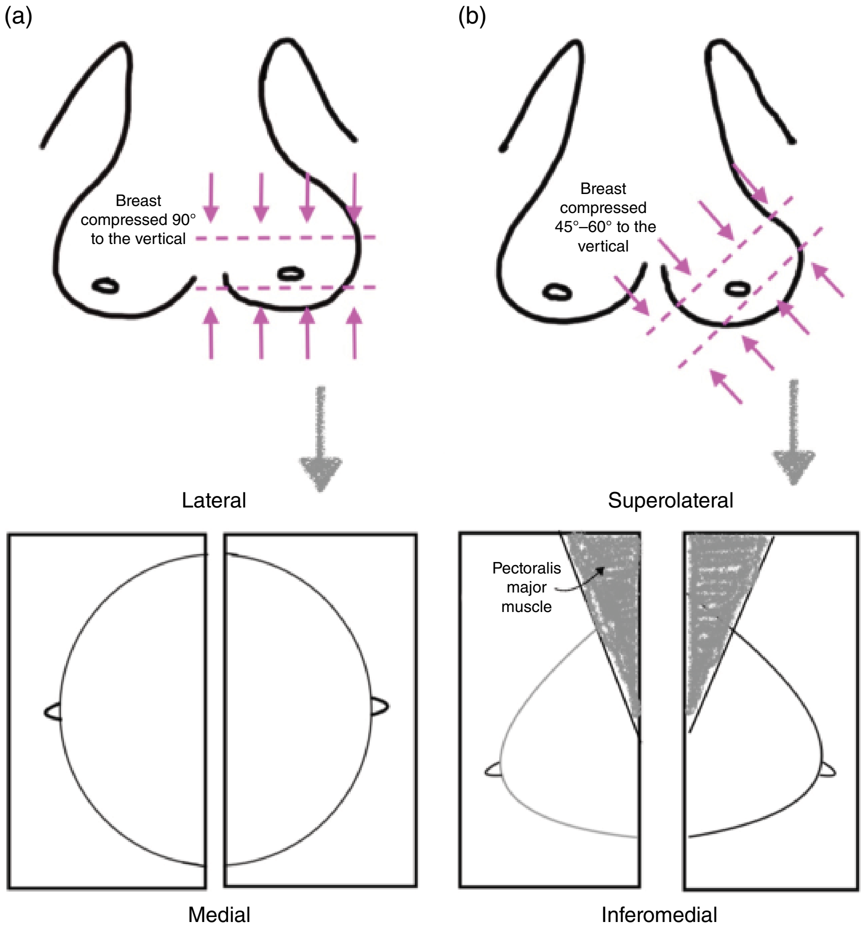
(a)
(b)
Breast compressed 90° to the vertical
Breast compressed 45°–60° to the vertical
Lateral
Superolateral
Pectoralis major muscle
Medial
Inferomedial

Figure 9.2 Standard craniocaudal (CC) (a) and mediolateral oblique (MLO) (b) mammographic views.

9.6.2.1 Craniocaudal (CC) View

CC views (Figure 9.2a) are acquired in a plane perpendicular to the floor with horizontal compression of the breast. CC views allow for greater compression of the breast and improved visualization of posteromedial breast tissue.

9.6.2.2 Mediolateral Oblique (MLO) View

MLO views (Figure 9.2b) are acquired parallel to the axis of the pectoralis major muscle (beam trajectory 45–60° to the horizontal plane) with accompanying breast compression in the same plane. The MLO view accordingly allows for superior visualization of the upper outer breast tissue bordering the axilla (i.e. axillary tail), which is not as well included on true lateral views. Additional specialized views may be acquired for assessment of breast tissue not well visualized on the MLO and CC views or further characterization of abnormalities detected on the initial views (Table 9.5).

9.6.3 Normal Mammogram

Mammographic assessment relies on the variation in X-ray absorption of the different tissue elements of the breast – namely fat, fibroglandular tissue, the pectoral muscle, and calcification. Fat is black on a mammogram while glandular tissue and muscle are gray/white. Thus, a "dense" breast will appear mostly white on mammography while a "less dense" or "fatty" breast will be predominantly black. Calcifications are also white but typically denser than glandular tissue and muscle. There is diverse variation in the amount (density) of fibroglandular tissue between patients. As per the BI-RADS lexicon (discussed below), breasts may be assigned one of four composition categories based on the relative volume of fibroglandular tissue in a breast (Figure 9.3):

1) The breasts are almost entirely fatty.
2) There are scattered areas of fibroglandular density.
3) The breasts are heterogeneously dense, which may obscure small masses.
4) The breasts are extremely dense, which lowers the sensitivity of mammography.

Table 9.5 Additional mammographic views.

Lateral (mediolateral [ML] and lateral-medial [LM]) views
Cleavage (CV) view
Laterally/medially exaggerated craniocaudal (XCCL/XCCM) view
Spot compression view
Magnification view
Tangential view
Tomosynthesis
Lateral (mediolateral [ML] and lateral-medial [LM]) views

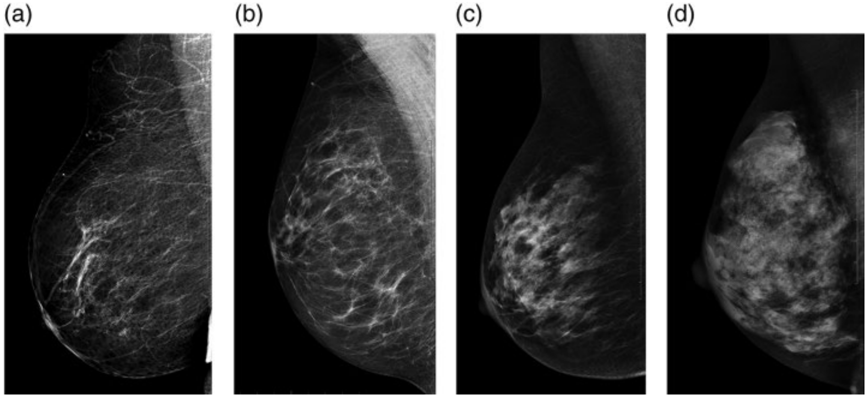

Figure 9.3 BIRADS breast fibroglandular composition categories. Categories are assigned on the basis of fibroglandular tissue density. (a) The breasts are almost entirely fatty. (b) There are scattered areas of fibroglandular density. (c) The breasts are heterogeneously dense, which may obscure small masses. (d) The breasts are extremely dense, which lowers the sensitivity of mammography.

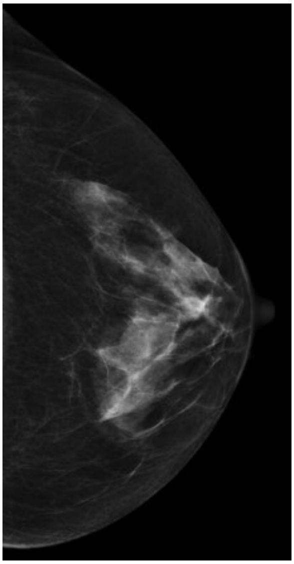

Figure 9.4 Craniocaudal (CC) mammogram anatomy.

Breast tissue is generally symmetric between the left and right breast. Occasionally, the medial and left breast may demonstrate greater density relative to the lateral and right breast, respectively. Typically, the amount of glandular tissue within the breast decreases with age as a result of fatty involution. Rapid change in breast density should prompt thorough investigation to exclude underlying malignancy. Exceptions to this pattern are pregnant/lactating women, those starting exogenous hormone replacement therapy, and patients with weight fluctuation.

On the normal CC projection, fibroglandular breast tissue extends from the retroglandular fat to the nipple (Figure 9.4). The pectoralis muscle generates a convex margin along the posterior breast. Fat immediately anterior to the pectoralis muscle is referred to as retroglandular fat and typically devoid

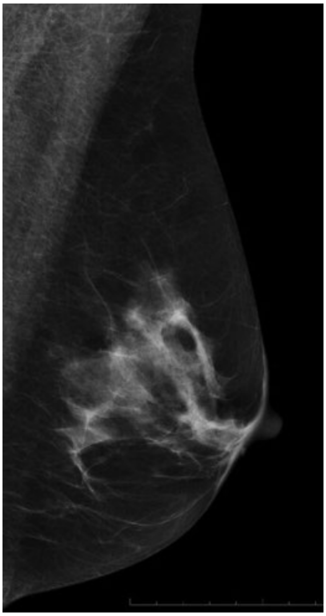

Figure 9.5 Mediolateral oblique (MLO) mammogram anatomy.

of fibroglandular tissue ("no man's land"). Any nonfat density in this region should be closely scrutinized with low threshold for further workup. Similar to the retroglandular fat, the medial breast on the CC view should typically contain only fatty tissue. On the normal MLO projection, the pectoralis muscle assumes an oblique orientation, again located in posteriorly (Figure 9.5). Retroglandular fat and fibroglandular tissue are located anterior to the muscle, respectively. The axilla is also captured in the MLO projection, often containing lymph nodes. The retroglandular fat spans ~3–4 cm anterior to the pectoralis muscle, any abnormal density in this region should be closely scrutinized (often referred to as to searching for stars in the Milky Way). A key component of the mammographic assessment is comparison to prior examinations. Apart for fatty involution, a normal mammographic examination should not change significantly in appearance between routine examinations. Careful comparison to not only the most recent examination but also to multiple prior examinations allows for the identification of gradual changes, which may represent a slow-growing malignancy.

9.6.4 Screening vs. Diagnostic Mammogram

Mammography may be performed as a screening (discussed above) or diagnostic examination. Diagnostic mammography is performed to address an abnormality detected on screening mammography, a specific clinical concern (e.g. palpable lump, nipple discharge, or skin thickening), in follow-up of patients with a prior history of breast cancer, and for the follow-up of BI-RADS 3 lesions (see the next section). An on-site radiologist guides imaging workup in the diagnostic mammography setting. If not previously obtained, routine mammographic views (CC and MLO) are acquired with additional views and/or ultrasound assessment for further characterization of an abnormality. In addition to mammogram, palpable lumps should always be assessed by ultrasound, regardless of whether a mammographic correlate is demonstrated. Once workup is completed, a BI-RADS assessment category is assigned.

9.6.5 Mammographic BI-RADS Lexicon

The breast imaging and reporting data system (BI-RADS) is a standardized reporting system, which provides strict criteria for the terminology, structure, and follow-up/further assessment of breast abnormalities. Specific BI-RADS criteria are set out by the ACR for mammography, ultrasound, and MRI. All mammographically significant findings are reported as per the BI-RADS lexicon, which highlights several categories (Figure 9.6). The calcification type/pattern (discussed below) and distribution should be closely assessed and reported. Architectural distortion results from tethering of the fibroglandular tissue, presenting as thin straight lines or spiculations radiating from a central point with no definite mass. An area of abnormal density is demonstrated only on a single mammographic projection. This is in contrast to a mass, which is seen in two projections. Asymmetries often result from summation of normal breast tissue; however, they should be scrutinized closely and worked up as necessary. Skin lesions on a breast may be superimposed on the underlying breast parenchyma on a standard two-view mammogram, and resultantly mistaken for intraparenchymal abnormalities. If skin lesions (e.g. nevi) are overtly clinically visible, a small, round metallic radiopaque marker (typically called a “BB”) may be placed on the skin by the technologist performing the mammogram. This is done to avoid unnecessary workup of these benign skin lesions, which can falsely project within the breast due to the 2D nature of the mammographic image.

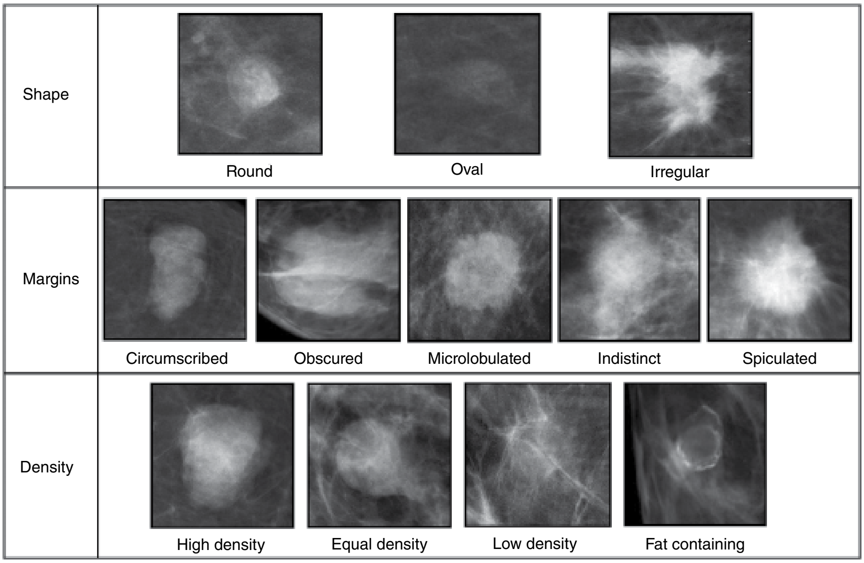

Figure 9.6 BIRADS mammography lexicon descriptors for a mass.

9.6.6 Breast Tomosynthesis

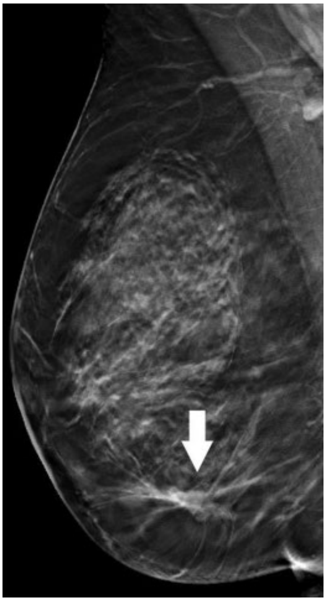

Figure 9.7 A digital breast tomosynthesis synthesized 2D view (C-view) demonstrating a suspicious mass in the inferior breast with accompanying architectural distortion (arrow).

Digital breast tomosynthesis (DBT) employs a modified digital mammography unit (see Chapter 2) to acquire a series of mammographic images from varying angles in order to establish a three-dimensional dataset. Reconstruction algorithms are then applied in order to view the breast in the standard mammography views (MLO and CC) as well as a series of sequential thin slices, much like a CT scan of the breast. The ability to analyze the breast tissue in slices in breast tomosynthesis rather than a single projection of overlapping tissues provides a number of added benefits over conventional mammography, including improved lesion identification and delineation of lesion margins. These benefits particularly hold true in dense breasts where the overlapping fibroglandular tissue often poses an increased risk potential for erroneous reporting (Figure 9.7). A growing body of literature highlights the many benefits of breast tomosynthesis in screening and diagnostic assessment, suggesting this technique will likely play a larger role in future breast imaging. Of note, total radiation dose in breast tomosynthesis ranges from lower to slightly higher than the dose in conventional mammography. Studies have shown stand-alone DBT to conventional mammography dose ratios of 0.34–1.0 for one-view DBT and 0.68–1.17 for two-view DBT [6]. If DBT is combined with conventional mammography, the overall dose is additive, yet still remains within recommended allowable dose exposure limits.

9.7 Ultrasound Imaging

Ultrasound primarily serves as a complementary imaging modality to mammography in the workup of breast disease. Indications for breast ultrasound include:

- Characterization of abnormalities demonstrated on mammogram.
- Evaluation of a palpable abnormality (regardless of whether there is a correlate on initial mammographic assessment).
- Imaging of lactating, and/or pregnant patients.

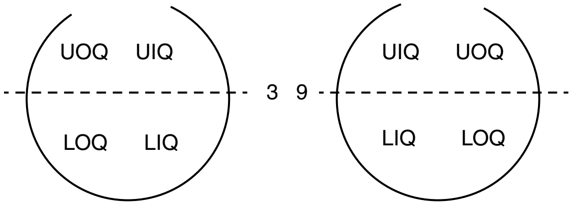

Figure 9.8 Conventional breast clockface and quadrant annotation. UOQ, upper outer quadrant; UIQ, upper inner quadrant; LOQ, lower outer quadrant; LIQ, lower inner quadrant.

- Guidance of interventional procedures.
- Second look ultrasound post MRI.

9.7.1 Ultrasound Technique

Breast ultrasound is typically performed by a trained sonographer with guidance from the interpreting radiologist. Generally, high-frequency linear transducers (7.5–13.5 MHz) are utilized in assessment of the breast and axilla (see Chapter 6). When assessing the entire breast, either a transverse/longitudinal or a radial/antiradial orientation is employed to ensure thorough, systematic assessment. Images are acquired of pertinent findings and annotated with the side (left or right) of the finding, clockface position of the lesion (Figure 9.8), distance from the nipple, and plane of imaging (transverse or longitudinal). Depending on the indication, the entire breast and/or axilla (e.g. for multifocal disease) or a targeted area of concern (e.g. for the assessment of a focal mammographic abnormality) may be assessed. An ultrasound examination of a complex breast may take up to 30 minutes.

9.7.2 Ultrasound BI-RADS Lexicon

As with mammography, a strict BI-RADS lexicon is in place for the reporting of findings on breast ultrasound examination (Figure 9.9). While calcifications may be visualized, often appearing as hyperechoic (increased intensity) foci with posterior acoustic shadowing, ultrasound is not a reliable imaging modality for the assessment of calcifications. The workup of calcifications is best performed under mammography with additional views. Axillary ultrasound is often performed in combination with breast ultrasound, primarily as a means of assessing for metastatic nodal involvement.

9.8 Breast MRI

Dynamic contrast-enhanced breast MRI is a growing tool in breast imaging. Gadolinium-based contrast agents are utilized in breast MRI (see Chapter 5). Breast MRI demonstrates over 90% sensitivity for invasive breast cancer.

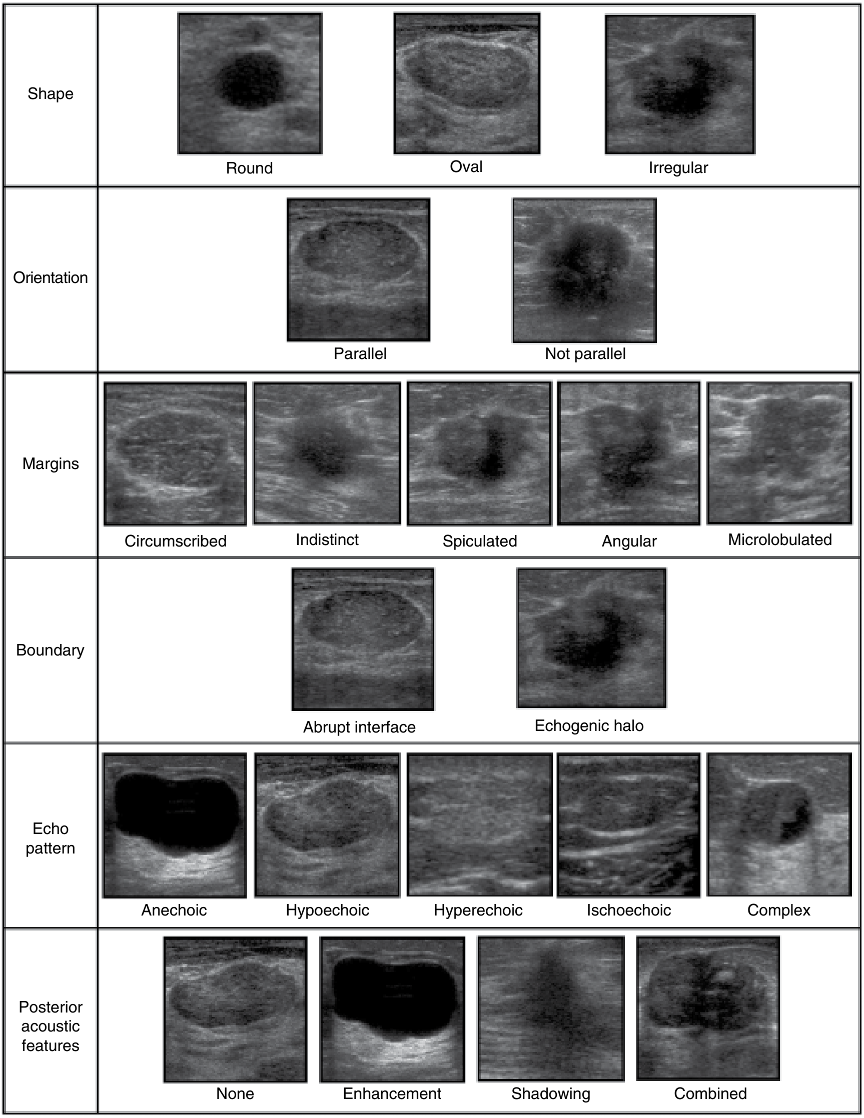
Shape
Round
Oval
Irregular
Orientation
Parallel
Not parallel
Margins
Circumscribed
Indistinct
Spiculated
Angular
Microlobulated
Boundary
Abrupt interface
Echogenic halo
Echo pattern
Anechoic
Hypoechoic
Hyperechoic
Ischoechoic
Complex
Posterior acoustic features
None
Enhancement
Shadowing
Combined

Figure 9.9 BIRADS ultrasound lexicon descriptors for a mass.

A fundamental principle of MRI breast imaging relies on the tumor angiogenesis of invasive breast cancers. Breast tumors characteristically demonstrate abundant neovascularity with resultant increased perfusion and leaky endothelium. Consequently, there is both an exaggerated rate of enhancement and washout (spread to the surrounding extracellular tissue) of contrast material in a tumor when compared to background breast parenchyma. In premenopausal patients, breast MRI should be performed on days 7–14 following the onset of menses in order to minimize false-positive background enhancement.

9.8.1 Indications

Breast MRI often plays a complementary role to mammography and ultrasound in detection, assessment, and management of lesions (Figure 9.10; Table 9.6). In patients with an established diagnosis of breast cancer, breast MRI plays an important role in the evaluation of disease extent and staging. Pectoralis muscle invasion and the extent of nodal involvement is best evaluated on MRI. A thorough understanding of disease extent is particularly useful in surgical planning (e.g. breast conservation therapy versus mastectomy).

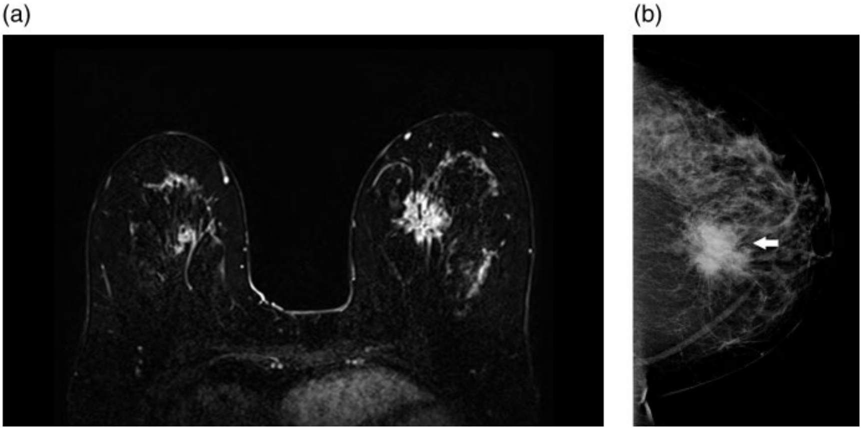

Figure 9.10 (a) Delayed T1-weighted fat saturation post-contrast image demonstrating an irregular mass in the left breast with spiculated margins and avid enhancement (arrow). (b) Note the similarities on the corresponding mammogram (arrow).

Table 9.6 Breast MRI indications.

Screening in high-risk patients (discussed above)
Evaluation of disease extent and staging in patients with established diagnosis of breast cancer
Positive surgical margins
Screening for recurrent malignancy
Differentiating postoperative scar from recurrence
Assessing response to neoadjuvant chemotherapy
Evaluation of breast implants
Diagnostic problem solving

9.8.2 Enhancement Kinetics

The acquisition of a temporal series of sequential post-contrast sequences in breast MRI allows for assessment of enhancement of a lesion over time. This data can be used to generate lesion enhancement kinetic curves. Lesion enhancement is divided into the initial (within two minutes of contrast administration or when the curve starts to change) and delayed (beyond two minutes) phases and defined by a strict BI-RADS lexicon. Stratification of the enhancement pattern is crucial as each pattern of delayed enhancement carries a different positive predictive value for malignancy (Figure 9.11). While delayed enhancement kinetics play an important role in characterization of a lesion, it should be noted that morphology is a stronger predictor for malignancy.

9.8.3 Breast MRI BI-RADS

In addition to enhancement characteristics, breast mass shape, margin, and internal enhancement pattern are all assessed with MRI. As with mammography and ultrasound, a BI-RADS lexicon provides a standardized lexicon for breast MRI findings. A small (<5 mm) dot of enhancement demonstrated on the post-contrast images is referred to as a *focus*. Given their small size, these lesions cannot be further assessed with regard to other characteristics. Three to 15% of foci represent malignancy. *Non-mass enhancement* (NME)

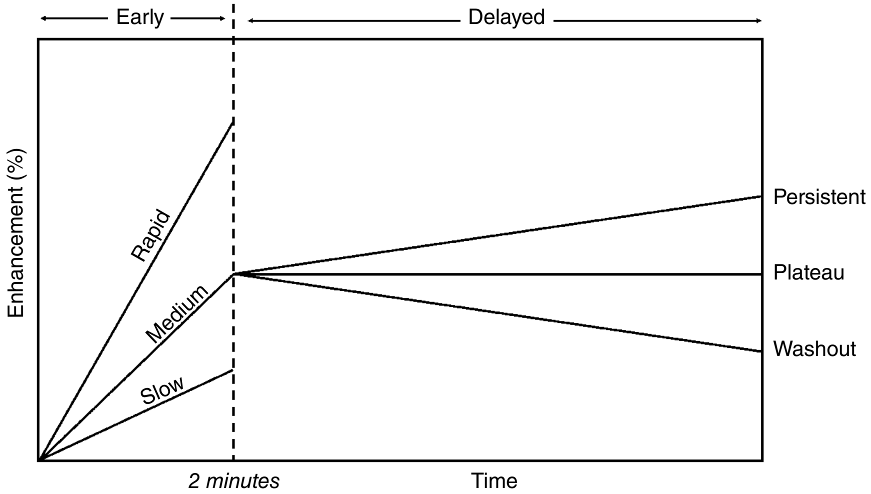

Figure 9.11 Breast MRI enhancement kinetic curves. Lesion enhancement is divided into the initial (within two minutes of contrast administration) and delayed (beyond two minutes) phases. Initial enhancement may be rapid, medium, or slow. Delayed enhancement is categorized as persistent, plateau, or washout. A washout type of delayed enhancement carries the highest positive predictive value for malignancy.

refers to a region of enhancement that is not a mass (convex borders) or a focus. NME may be benign or malignant, depending on the distribution and pattern of internal enhancement.

9.9 PEM and Breast-Specific Gamma Camera Imaging

Positron emission mammography (PEM) and breast-specific gamma imaging/molecular breast imaging (BSGI/MBI) are emerging imaging modalities providing potential for local staging of breast cancer, and monitoring of neoadjuvant chemotherapeutic response. PEM utilizes a technique similar to whole-body PET-CT, but is instead specifically targeted to the breast tissue, providing for a breast-centered field of view. A pair of gamma detectors is positioned above and below the breast and ^{18}F-FDG (^{18}F-2-fluorodeoxyglucose; see Chapters 3 and 4) is administered. This technique provides improved spatial resolution over whole-body PET-CT, allowing for detection of lesions as small as 1–2 mm (vs. 5–10 mm for whole-body PET). Although a promising alternative for those patients unable to undergo/tolerate MRI, it shares with MRI a high sensitivity yet low specificity for cancer detection – i.e. many benign lesions (e.g. fibroadeoma) show increased uptake similar to cancerous lesions. BSGI is a similar technique to PEM, but is based on single photon emission computed tomography (SPECT) imaging using ^{99m}Tc-sestamibi (see Chapters 3 and 4). A very significant disadvantage of both PEM and BSGI is the radiation exposure, which is not only limited to the breast, but can expose all body organs. This can result in radiation doses totaling up to 20–30 times that of standard digital mammography, which employs X-rays. As a result, the technique discussed in the next section may often be a preferred alternative, especially in younger women.

9.10 Contrast-Enhanced Spectral Mammography

Contrast-enhanced spectral mammography (CESM) is an emerging technique that acquires dual low- and high-energy X-ray images of the breast almost simultaneously following the administration of intravenous iodinated contrast (see Chapter 2). This allows for tumor detection by highlighting areas of angiogenesis/increased blood flow (Figure 9.12). Early studies suggest that CESM may provide higher sensitivity and greater diagnostic accuracy for breast cancer detection than conventional mammography, particularly in dense breasts. It may also provide a much lower cost and more readily available alternative for breast cancer staging and in those patients with contraindications to, or who cannot tolerate MRI.

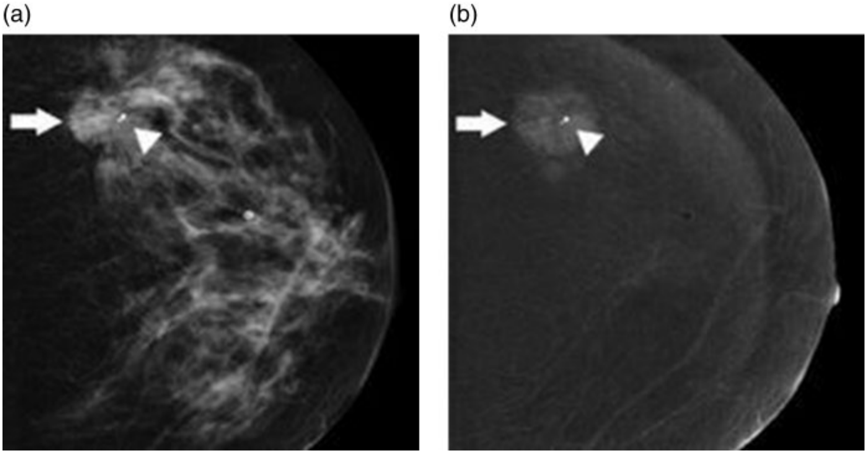

Figure 9.12 Standard (a) and subtracted (b) contrast-enhanced spectral mammography (CESM) images demonstrating avid enhancement corresponding to the biopsy-proven malignancy in the outer breast (arrow). A small metallic marker is demonstrated within the breast from prior biopsy (arrowhead).

9.11 The ABCs of Breast Imaging – Image Interpretation

9.11.1 Benign vs. Malignant Imaging Features

A variety of lesion characteristics on mammogram and ultrasound may aid in differentiating between malignant and benign disease. While there is considerable overlap in the imaging findings between different lesions, being able to identify these features allows for additional workup when necessary and avoids unneeded additional assessments (see Figures 9.13–9.16 and corresponding tables).

9.11.2 Breast Masses

9.11.2.1 Fat-containing Breast Masses

Fat-containing breast masses can be identified by their low density fat content. In general, these masses are benign. Examples of fat-containing breast masses include lipomas, oil cysts, hamartomas, galactoceles, and intramammary lymph nodes (Figure 9.17).

9.11.2.2 Circumscribed Solid Masses

Circumscribed masses demonstrate a clear, discernable border on both the mammogram and ultrasound images. The solid nature may be reliably confirmed by the presence of internal vascularity and the absence of cystic features

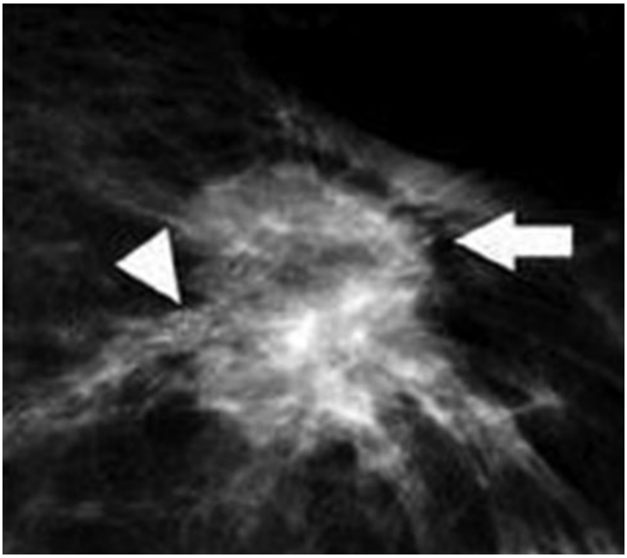

Figure 9.13 A mass demonstrating typical mammographic signs of malignancy, including spiculated margins (arrow), pleomorphic calcifications (arrowhead), and architectural distortion. Characteristic mammographic signs of malignancy may include: (i) mass with spiculated or indistinct margins, (ii) architectural distortion, (iii) asymmetry of breast parenchyma (focal or global), (iv) developing density, (v) skin thickening, (vi) nipple retraction, (vii) abnormal ductal patterns, and (viii) unilateral axillary lymphadenopathy.

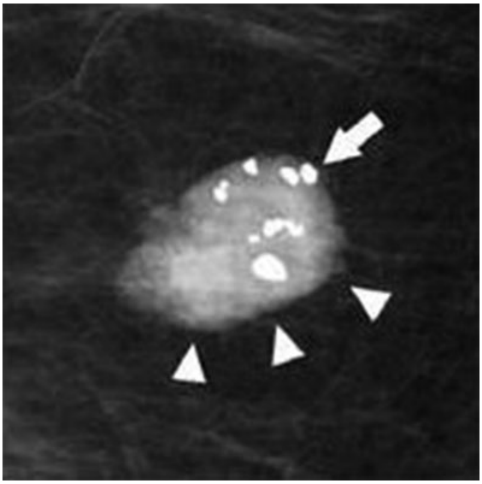

Figure 9.14 A mass demonstrating typical mammographic signs of benign disease, including circumscribed margins (arrowheads), benign calcifications (arrow), and absence of architectural distortion. Mammographic signs of benign disease may include: (i) a circumscribed lesion, (ii) benign calcifications, (iii) a fat-containing lesion, (iv) long-term stability, and (v) absence of suspicious findings.

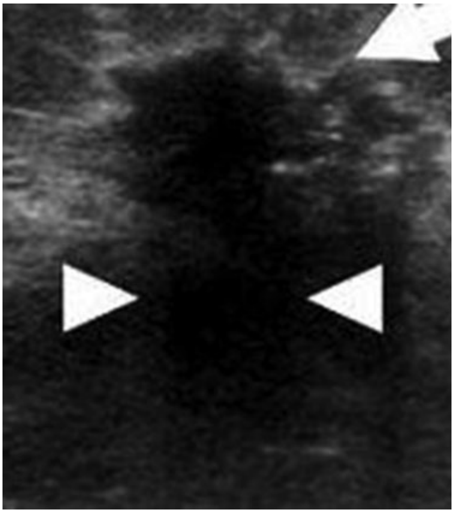

Figure 9.15 A mass demonstrating typical sonographic signs of malignancy, including spiculated margins (arrow), not parallel orientation, markedly hypoechoic echotexture, and posterior acoustic shadowing (arrowheads). Ultrasound features of a malignant lesion may include: (i) spiculated margins, (ii) nonparallel orientation (relative to the skin surface), (iii) angular or microlobulated margins, (iv) markedly hypoechoic (low signal intensity) echotexture, (v) posterior shadowing, (vi) suspicious calcifications, and (vii) lesion boundary with a wide zone of transition (a gradual, ill-defined border with the surrounding breast parenchyma).

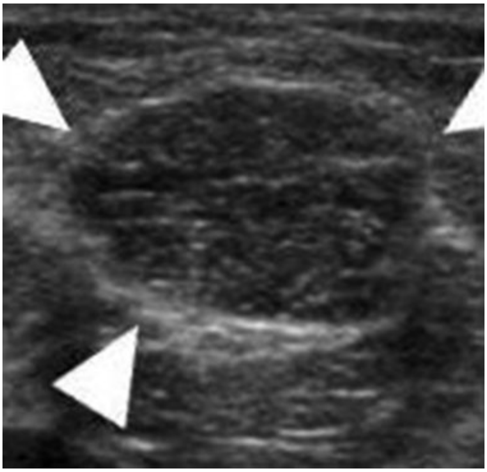

Figure 9.16 A mass demonstrating typical sonographic signs of benign disease (in this case a fibroadenoma), including circumscribed margins (arrowheads), an ellipsoid shape, and parallel orientation. Ultrasound features of a benign lesion may include: (i) circumscribed margins, (ii) parallel orientation, (iii) marked hyperechogenicity, (iv) round or ellipsoid shape, (v) a few gentle macrolobulations, and (vi) absence of suspicious features.

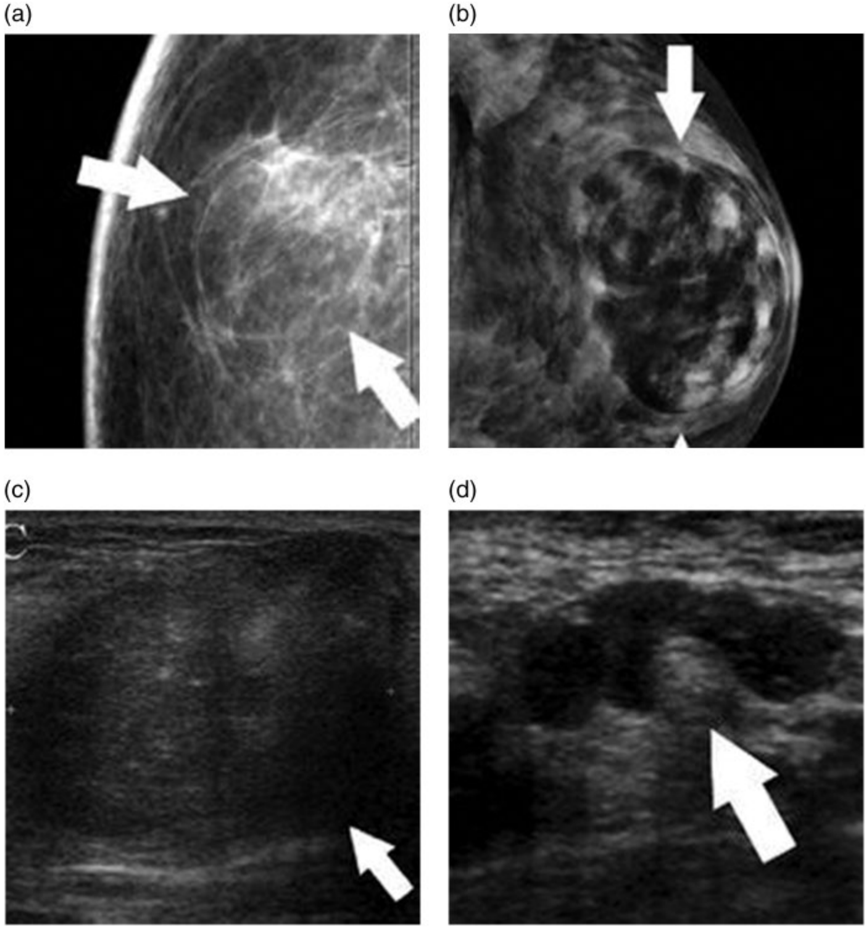

Figure 9.17 Fat-containing breast masses. (a) Lipomas are entirely fat-containing masses (arrows). Oil cysts (a sequelae of fat necrosis) vary from lipomas in that they demonstrate peripheral rim calcification. (b) A hamartoma (fibroadenolipoma; arrows) is a benign mass containing both fat and fibroglandular tissue. As these lesions have contents similar to the background breast parenchyma, they produce a characteristic "breast within a breast" appearance. (c) Galactoceles (arrow) occur in lactating women, appearing as a circumscribed, macrolobulated, mixed high density/fatty mass. On ultrasound (not demonstrated here), these masses are cystic (fluid-filled). (d) An intramammary lymph node (arrowhead) is a circumscribed mass easily identified by its hallmark kidney (reniform) shape and central echogenic fat (hilum, arrow). While lymph nodes may occur anywhere in the breast, they are most frequently seen in the superolateral quadrant, in close proximity to the axilla. Hilar vascularity is commonly seen on Doppler ultrasound assessment.

on ultrasound. A mammogram cannot reliably differentiate between a solid and cystic lesion (Figure 9.18).

9.11.2.3 Cystic Breast Masses

Ultrasound is the main imaging modality for characterizing cystic lesions. Cystic lesions may change shape/size on compression mammography views; however, this is not a reliable tool in differentiating cystic from solid lesions (Figure 9.19).

9.11.2.4 Malignant Masses

Masses with suspicious features on mammography or ultrasound are highly concerning for malignancy, requiring complete workup (Figure 9.20). Radial scar, post-procedural changes, and abscess are benign masses that may also demonstrate suspicious mammographic and/or ultrasound appearances, commonly seen as spiculated lesions on mammography. Clinical history is often useful in discerning these lesions from malignant processes; however, if uncertainty exists, these lesions should undergo full diagnostic workup to exclude malignancy.

9.11.2.5 Axillary Masses

Axillary masses in the breast typically correspond to lymph nodes. Features of malignant axillary nodes include a thickened peripheral/outer cortical layer (>3 mm), rounded overall lymph node shape (as opposed to a more normal ovoid reniform shape), focal bulge of the lymph node capsule, and flattening or loss of the normal central (hilar) lymph node fat (Figure 9.21). Unilateral lymphadenopathy is typically concerning for breast cancer metastases while bilateral adenopathy is more commonly seen in the setting of systemic processes (e.g. lymphoma, leukemia, vasculitis, etc.).

9.11.2.6 Breast Calcifications

Calcifications are a common mammographic finding. While the majority of breast calcifications are benign, abnormal calcifications may be the earliest or only mammographic signs for malignancy. Suspicious breast calcifications demonstrated on routine views should always be further characterized with spot magnification views. Both distribution and morphology of calcifications are important in determining the likelihood of malignancy. Calcification distribution refers to the arrangement of multiple calcifications within the breast (Figure 9.22). The BI-RADS lexicon has established mammographic calcification terminology (Figure 9.23).

9.11.2.7 Breast Asymmetries

Breast asymmetries may be further classified as an asymmetry, global asymmetry, or focal asymmetry. An asymmetry is an area of abnormal density demonstrated only on a single mammographic projection (Figure 9.24). A focal

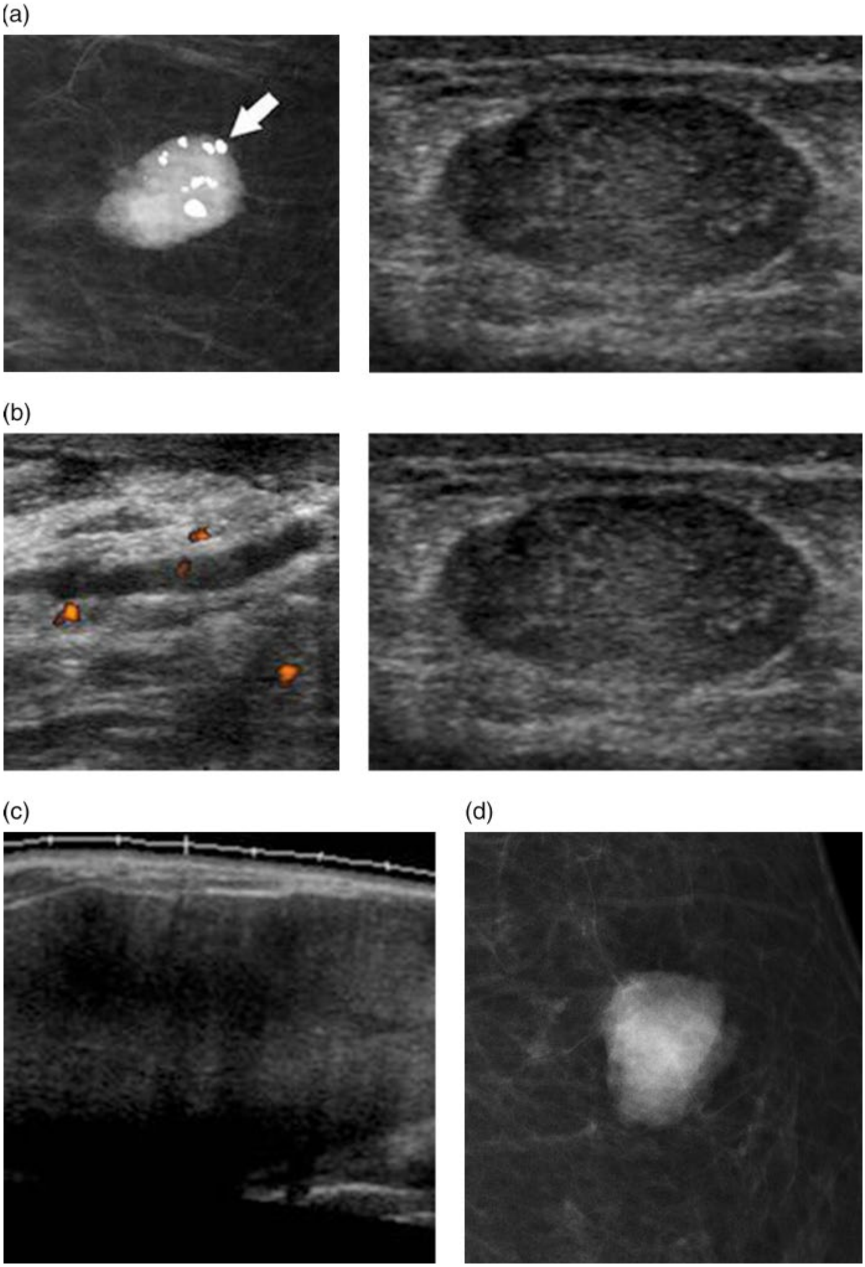

Figure 9.18 Circumscribed solid masses. (a) Fibroadenomas are benign neoplasms commonly presenting as palpable lesions in young women. These lesions are typically oval, circumscribed, equal density masses on mammography (left panel). On ultrasound, fibroadenomas commonly demonstrate an oval, circumscribed, homogeneously hypoechoic appearance (right panel). With advancing age, fibroadenomas may calcify,

asymmetry is seen on two projections but in contrast to a mass, does not demonstrate convex margins. Asymmetries often result from summation of normal breast tissue; however, they should be scrutinized closely and worked up as necessary.

9.12 BI-RADS Assessment Categories

All mammographic, tomosynthesis, ultrasound, and MRI reports conclude with a BI-RADS assessment category designation (Table 9.7). Seven BI-RADS assessment categories exist (BI-RADS 0–6), which provide a succinct means of communicating examination findings and suggestions for further workup or future follow-up. The approach to workingup screen-detected breast lesions is shown in Figure 9.25.

9.13 Image-Guided Breast Intervention

A variety of image-guided biopsy techniques may be utilized in acquiring specimens for tissue diagnosis. Selection of a technique is dependent on the modality by which the lesion is best visualized (ultrasound, mammogram, or MRI), radiologist preference, and patient-specific factors. In general, if a lesion is discernable under ultrasound, ultrasound-guided biopsy is the preferred means of sampling given the ability for real-time imaging, improved accuracy, relatively low cost, and most importantly patient comfort (i.e. lying supine without the breast in any kind of compression). Regardless of the method of tissue sampling, radiology–pathology correlation must be performed to ensure concordance between imaging and pathologic findings. This process involves the radiologist who performed the biopsy reviewing the pathology results and determining whether they are acceptable (i.e. within the differential diagnostic

◄

producing a "popcorn calcification" appearance (arrow in left panel). (b) Intraductal papillomas are benign tumors arising from the lactiferous ducts. These lesions commonly present with bloody, serosanguinous (blood – tinged serous fluid), or serous nipple discharge in women aged 30–50 years. Intraductal papillomas are often subareolar round/oval, circumscribed/irregular masses. Ultrasound appearances are that of an isoechoic (similar intensity as surrounding tissue) solid mass with internal vascularity on color Doppler imaging (bright orange areas), often with an accompanying duct dilated with fluid. On galactography (duct imaging performed by introducing contrast dye into the duct prior to mammography), intraductal papillomas often produce intraductal filling defects. (*See insert for color representation of the figure*.) (c) Phyllodes tumors are uncommon, rapidly growing lesions occurring most commonly in women 40–50 years of age. On mammography, these correspond to large, oval, circumscribed masses and are heterogeneous in echotexture on ultrasound as demonstrated above. The majority of these lesions are benign; however, there is a risk of malignancy in a quarter of cases. (d) Often, breast cancer may present as a circumscribed mass, particularly in cases of new lesions in postmenopausal females.

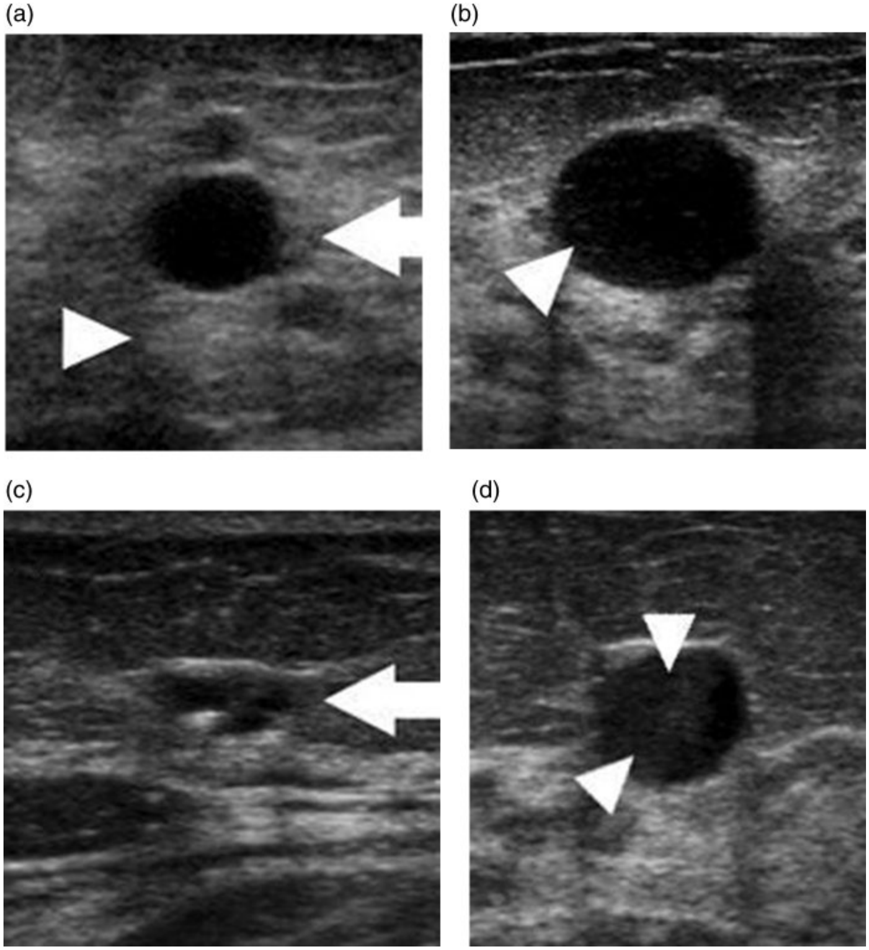

Figure 9.19 Cystic breast masses. (a) A simple cyst (arrow) is a benign fluid-filled lesion. On ultrasound, these lesions are typically round or oval in shape with an anechoic internal echo pattern and accompanying posterior acoustic enhancement (arrowhead). Simple cysts demonstrate thin, imperceptible walls and are avascular. (b) A cyst containing internal debris (appearing as low-level echos; arrowhead) is referred to as a complicated cyst. These cysts are typically benign; however, often warrant follow-up to ensure stability (BI-RADS category 3). (c) Clustered microcysts (arrow) are a benign group of multiple small cystic spaces. (d) A complex mass is a cystic lesion containing solid components (arrowheads) and/or thick walls or septations. The presence of complex features raises suspicion for malignancy and should be worked up.

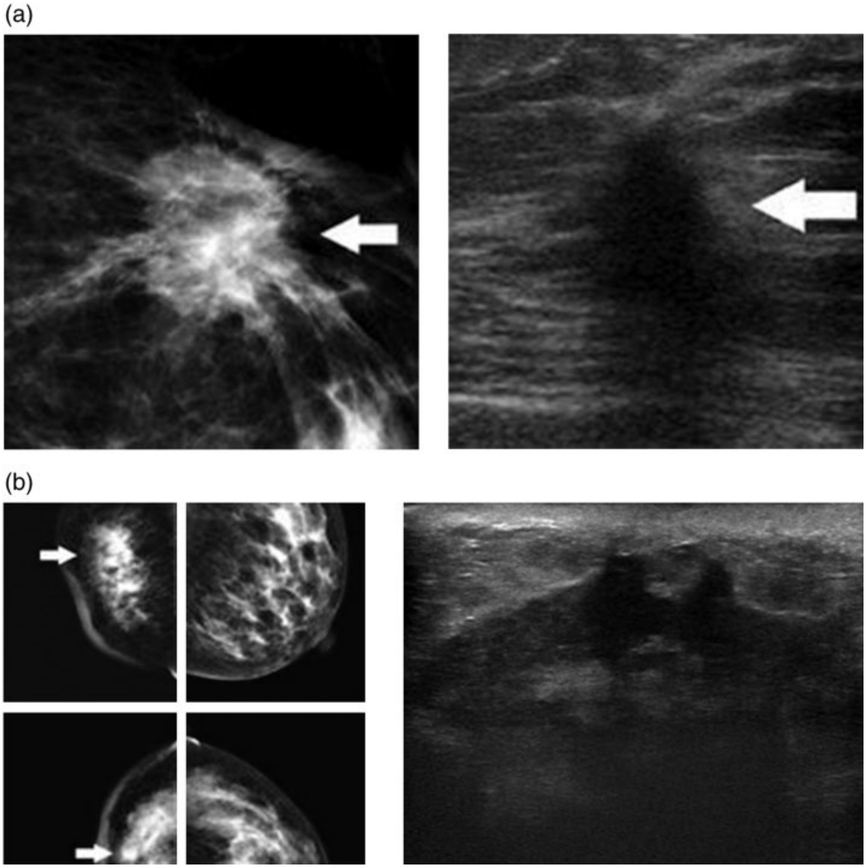

Figure 9.20 Malignant masses. (a) Invasive ductal carcinoma (arrow) on a mammogram (left panel) or ultrasound (right panel) is the most common type of breast cancer and often demonstrates a spiculated or ill-defined solid mass appearance. Concerning calcifications and architectural distortion further raise concern for malignancy in these lesions. The presence of axillary lymphadenopathy further raises concern for malignancy. This constellation of findings would be highly suggestive of malignancy (BI-RADS category 5). (b) Invasive lobular cancer (ILC, arrows) accounts for <10% of all breast cancer subtypes. This cancer is variable in its mammographic (left panels) and ultrasound appearance (right panels), including spiculated/ill-defined masses or architectural distortion without accompanying calcifications. Notice the decreased size of the right breast (left image panel) relative to the left – the "shrinking breast" appearance is considered a classic mammographic appearance for ILC. Given its variable and often subtle appearance, invasive lobular cancer often presents a diagnostic challenge, missed in up to 21% of mammographic examinations.

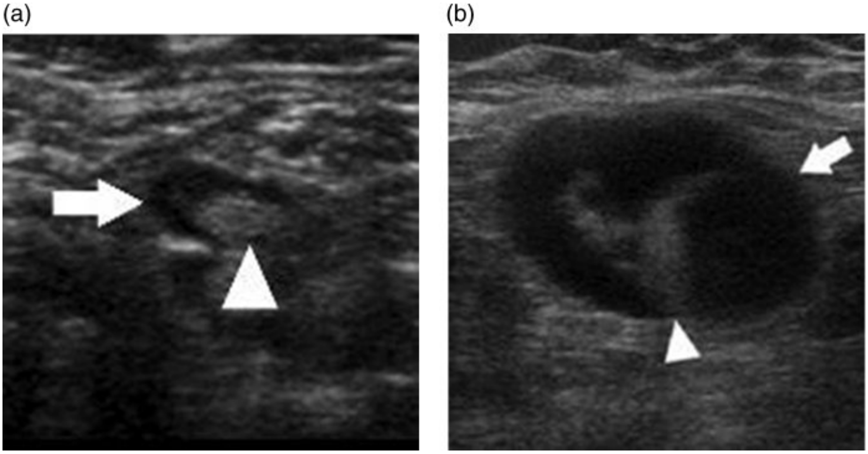

Figure 9.21 (a) A normal lymph node demonstrating a thin, hypoechoic peripheral cortex (arrow) and central fatty (echogenic) hilum (arrowhead). (b) Features of suspicious lymph node morphology, including a thickened cortex (arrow) and decrease in size of central fatty hilum (arrowhead).

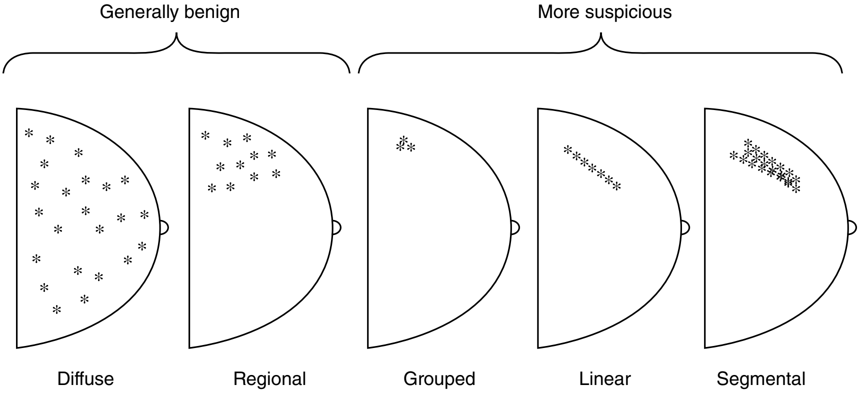

Figure 9.22 Schematic of breast calcification distribution. Diffuse and regional calcification distributions are generally considered benign. Grouped, linear, and segmental calcifications are more suspicious for malignancy and require additional workup (e.g. magnification views) and biopsy for further characterization.

possibilities for the imaging findings). For example, if a lesion with nonaggressive imaging features yielded a benign pathology result, this would be considered "concordant." By contrast, if a lesion with worrisome or aggressive imaging features returned a benign pathology result or vice versa, these results would be considered "discordant." In the setting of discordant findings, the radiologist

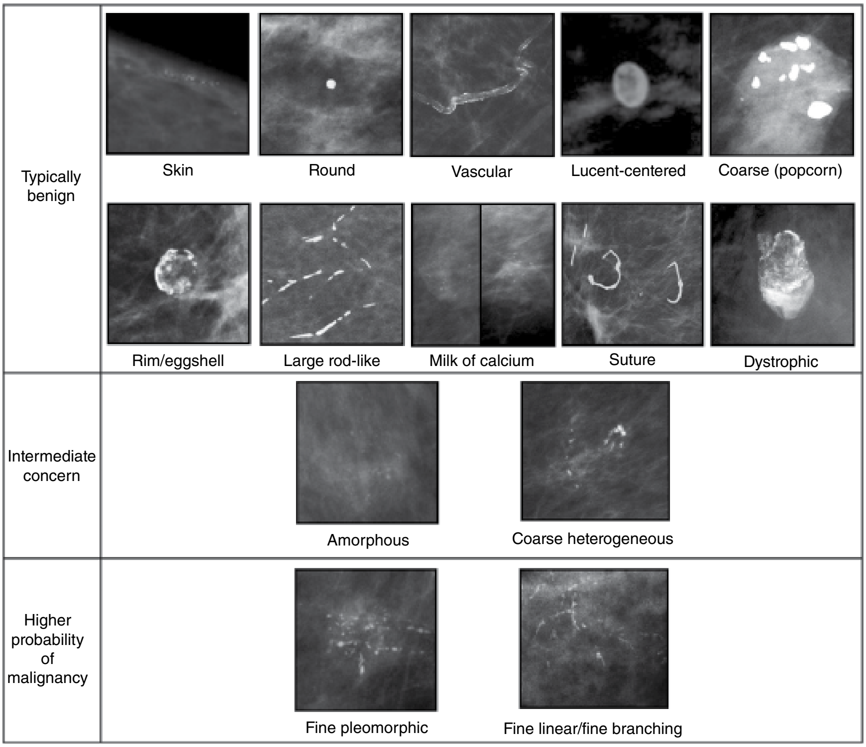
Typically benign
Skin
Round
Vascular
Lucent-centered
Coarse (popcorn)
Rim/eggshell
Large rod-like
Milk of calcium
Suture
Dystrophic
Intermediate concern
Amorphous
Coarse heterogeneous
Higher probability of malignancy
Fine pleomorphic
Fine linear/fine branching

Figure 9.23 BIRADS mammographic lexicon descriptors for breast calcifications.

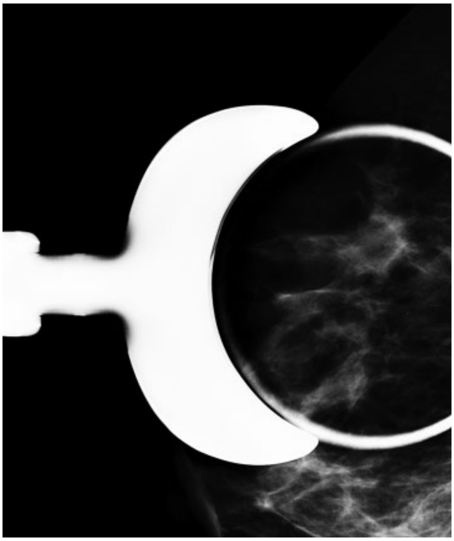

Figure 9.24 A asymmetry is demonstrated only on a single mammographic projection. Asymmetries can be further assessed with spot compression views, which employ the use of a compression paddle (shown as bright area). Asymmetries that result from overlapping breast tissue should resolve or spread out on compression views. Asymmetries that persist may relate to an underlying pathology and should be further worked up.

Table 9.7 BIRADS assessment categories.

BIRADS assessment category	Definition	Recommendations
0	**Incomplete examination** A BIRADS 0 designation is only appropriate for screening mammograms. All diagnostic mammograms require a BIRADS 1–6 assessment	Additional imaging evaluation with additional views (spot compression, magnification, etc.), ultrasound, and/or prior mammograms for comparison is necessary prior to a final BIRADS category [1–6] can be made
1	**Negative** The breasts are normal	Routine screening mammography
2	**Benign** A finding that is almost certainly benign. A BIRADS 2 classification infers a likelihood of cancer of essentially 0%	Routine screening mammography
3	**Probably benign** A finding that is most likely benign (>0% to ≤2% likelihood of malignancy) A full diagnostic workup (with additional views and/or ultrasound) is necessary prior to designating a BIRADS 3	Short interval (6 mo) follow-up is suggested. If a BIRADS 3 lesion demonstrates stability over 2 yr, it can be considered benign and redesignated as BIRADS 2. Interval change is suspicious and may require biopsy for further characterization
4	**4A**: Low suspicion for malignancy (>2% to ≤10% likelihood of malignancy) **4B**: Moderate suspicion for malignancy (>10% to ≤50% likelihood of malignancy) **4C**: High suspicion for malignancy (>50% to <95% likelihood of malignancy)	Proceed to biopsy/aspiration for tissue diagnosis
5	**Highly suggestive of malignancy** Assigned to findings with features highly concerning for malignancy. A BIRADS 5 classification suggests a ≥95% likelihood of malignancy	Proceed to biopsy for tissue diagnosis and/or surgical management
6	Known biopsy-proven malignancy Findings corresponding to prior pathology-proven malignancy (e.g. prior biopsy)	Dependent on biopsy results

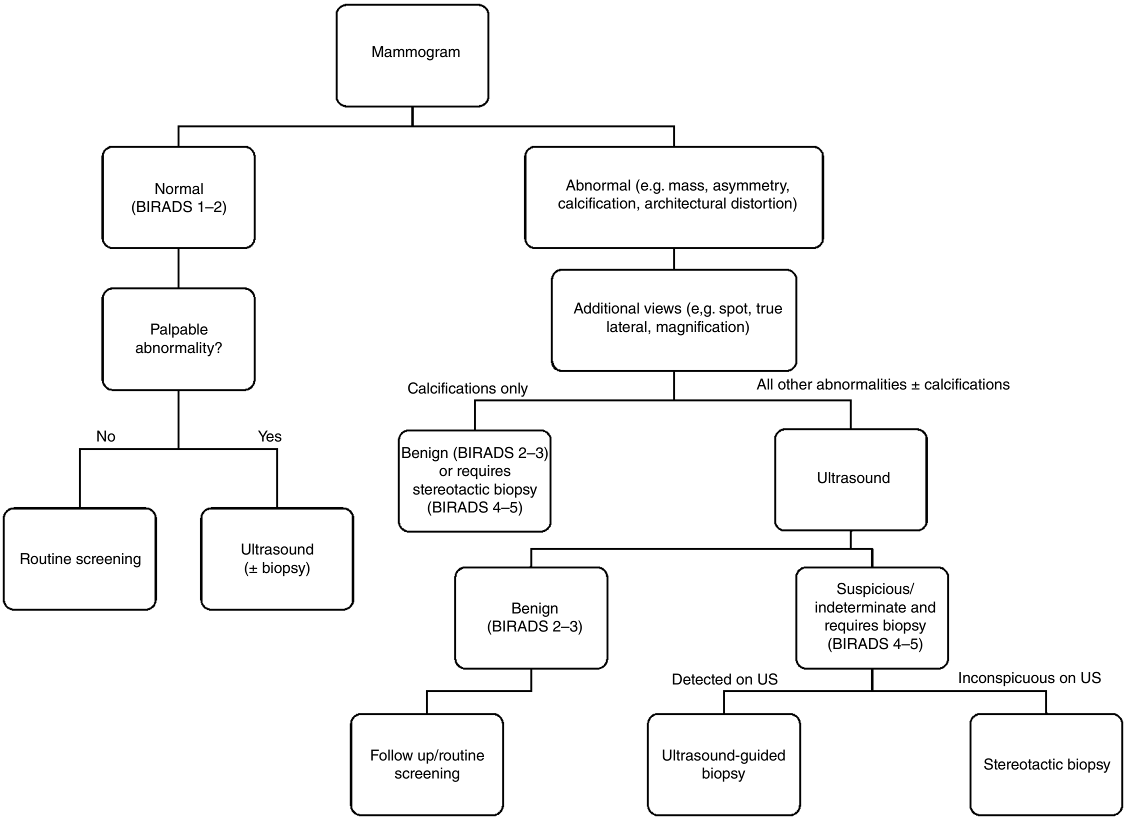
Mammogram
Normal (BIRADS 1–2)
Abnormal (e.g. mass, asymmetry, calcification, architectural distortion)
Palpable abnormality?
Additional views (e,g. spot, true lateral, magnification)
No
Yes
Calcifications only
All other abnormalities ± calcifications
Routine screening
Ultrasound (± biopsy)
Benign (BIRADS 2–3) or requires stereotactic biopsy (BIRADS 4–5)
Ultrasound
Benign (BIRADS 2–3)
Suspicious/ indeterminate and requires biopsy (BIRADS 4–5)
Detected on US
Inconspicuous on US
Follow up/routine screening
Ultrasound-guided biopsy
Stereotactic biopsy

Figure 9.25 An approach to workup of screen-detected breast lesions.

must then make a recommendation for the next appropriate action required (e.g. repeat biopsy possibly under another modality or with a larger bore needle, or surgical excision).

9.13.1 Ultrasound-Guided Core Needle Biopsy

Ultrasound-guided core needle biopsy involves the use of real-time ultrasound assessment to identify a lesion and guide biopsy. Once the lesion of interest is identified, the breast is cleaned and draped in a sterile fashion and local anesthetic is administered. A small incision is made in the skin and large bore (typically 14-guage) needle used to acquire core samples (Figure 9.26). Depending on radiologist and/or surgeon preference, a titanium tissue marker clip may be placed at the biopsy site with post-procedure mammography to confirm marker position and aid in future lesion follow-up/management.

9.13.2 Ultrasound-Guided Needle Aspiration

Ultrasound-guided needle aspiration can be performed for both diagnostic (e.g. deciphering if a mass is cystic or solid) as well as therapeutic purposes (e.g. abscess or hematoma drainage, and occasionally symptomatic benign cyst decompression). The technique and approach are very similar to that of the aforementioned core needle biopsy; however, a much smaller or finer (usually

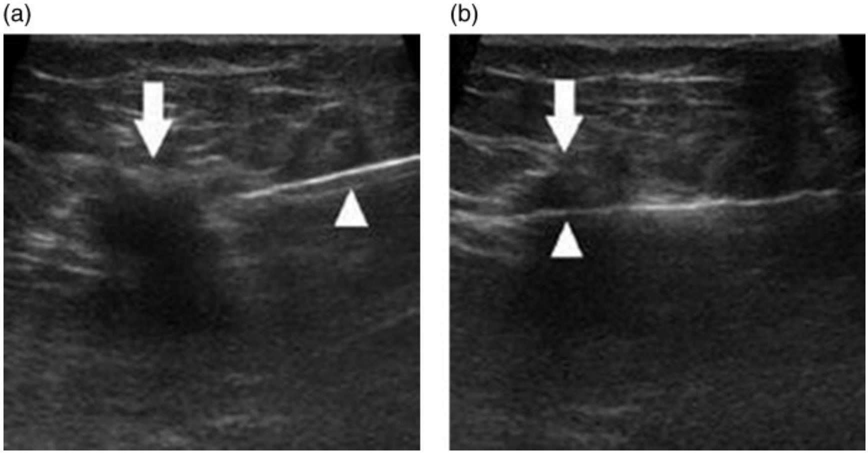

Figure 9.26 (a) A breast mass on ultrasound demonstrating suspicious morphology (arrow). The echogenic linear structure (arrowhead) corresponds to the biopsy needle advanced to its pre-fire position prior to biopsy. (b) Corresponding post-fire images confirming successful biopsy with biopsy needle (arrowhead) through the suspicious lesion (arrow).

22–25-gauge) needle is advanced into the target lesion for aspiration with larger gauge sizes (i.e. 18–20) required for drainage of a suspected purulent abscess or clotted hematoma. Accordingly, a cellular aspirate versus a tiny core block of intact tissue is obtained and sent for cellular analysis by a cytopathologist. Bloody or clear cyst aspirate may be a sign of malignancy and is sent to the pathology lab to be analyzed, while white creamy, green, yellow, or cloudy aspirate is considered benign and physiologic and may be discarded.

9.13.3 Stereotactic-Vacuum-Assisted Core Needle Biopsy

Stereotactic guidance is generally reserved for biopsy of suspicious calcifications. This technique utilizes a stereo pair of images, oriented 15° to the left and right of the area of concern. Once a user-selected target is determined, ample local anesthetic is administered, skin incision is made, and large bore biopsy needle advanced to the appropriate depth to obtain multiple samples of the area of concern. Specimen radiographs are then performed to ensure that the appropriate targeted calcifications are present and a titanium tissue marker clip is placed at the site of biopsy (Figure 9.27).

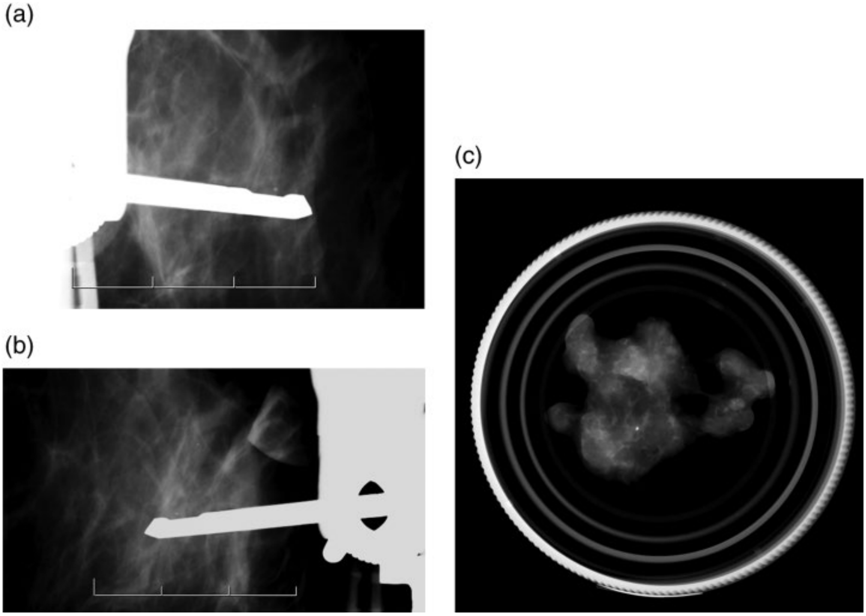

Figure 9.27 (a, b) Paired stereotactic biopsy images acquired demonstrating the biopsy needle (arrow) with the needle notch adjacent to the site of desired biopsy (arrowhead). (c) Specimen radiograph is acquired following stereotactic biopsy to confirm the presence of target calcification in the specimen (arrow).

9.13.4 MR-Guided Vacuum-Assisted Core Biopsy

In situations where a suspicious lesion is only evident on MRI, MRI-guided biopsy may be considered. The patient is placed in a prone position on the MRI scanner and a coordinate grid is applied to the breast to aid localization. Biopsies are then obtained in a fashion similar to stereotactic biopsy. A tissue marker clip is subsequently placed at the biopsy site to aid in future follow-up/management.

9.13.5 Radiopaque Markers

Metallic (radiopaque) marker insertion at the site of biopsy/region of concern is often indicated for small or subtle lesions, complex cysts/cysts, which collapse post sampling, or in the setting of diffuse disease (Figure 9.28). The placement of a marker allows for target correlation on additional imaging modalities and/or most importantly, reidentification of the sampled target if surgical resection is required, or at the time of follow-up imaging. Repeat sampling of the same lesion if a patient migrates geographically can also be avoided. Radiopaque marker placement in the tumor bed and/or axilla in the setting of advanced disease before starting neoadjuvant chemotherapy can also assist in delayed preoperative image-guided localization, especially if there is a good response (i.e. minimal residual detectable disease). Many of the radiopaque markers available today are also conspicuous on sonographic assessment, though may be very subtle and especially challenging in dense breast tissue containing many echogenic interfaces. More recently, markers specifically designed for detection under ultrasound or magnetic/electromagnetic systems have been developed. A primary advantage of these markers over wire localization techniques is the ability to temporally separate lesion localization and operative management, supplanting the need for same-day localization.

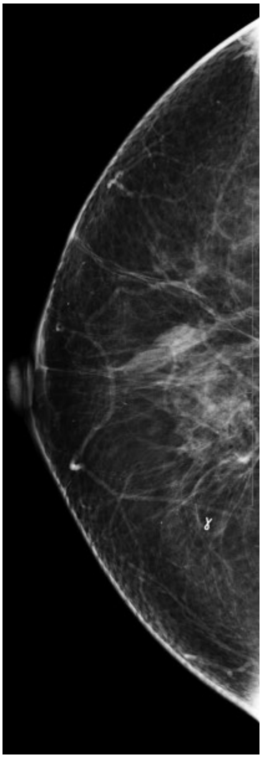

Figure 9.28 Radiopaque clip marker in situ post breast biopsy. The lesion biopsied was not conspicuous on mammogram in this case.

9.13.6 Pre-Operative Image-Guided Wire Localization and Specimen Imaging

Mammographic-guided wire localization is performed preoperatively as a means of lesion localization and to provide intraoperative tactile feedback to the

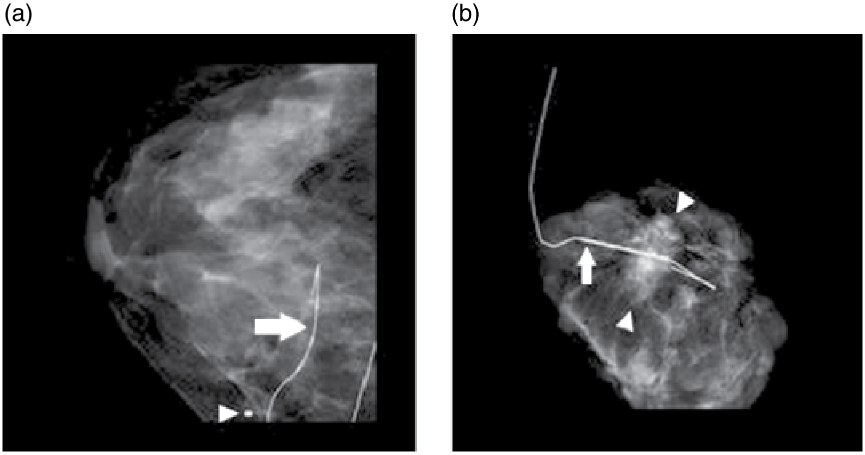

Figure 9.29 (a) Presurgical wire (arrow) localization of a lesion in the inner breast. The lesion was not conspicuous on this mammogram; however, palpable and thus marked with a round metallic marker ("BB", arrowhead). (b) Specimen radiograph of the surgical specimen post excision confirms the presence of the wire (arrow) within the lesion (arrowheads). Note that the lesion does not extend to the peripheral margins of the specimen, suggesting clear mammographic surgical margins.

surgeon. The procedure is often performed on the day of scheduled lumpectomy/excisional biopsy. Under orthogonal mammographic views or ultrasound guidance, a needle sheath containing a localization wire hook is advanced through and slightly beyond the lesion. Once in satisfactory position, the wire hook is unsheathed, deploying the wire in place (Figure 9.29). Post-lumpectomy/excision radiographs are acquired of the specimen to ensure the lesion has been removed in its entirety. Some institutions implement localization by radioactive (iodine-125) or magnetic seeds. In a fashion similar to wire localization, the localizer seeds are deployed in the region of planned excision, allowing for intraoperative detection by gamma or magnetic detection probe.

9.14 Extramammary Staging

Distant breast cancer metastases are typically spread hematogenously, most commonly to the bones, lung, liver, and brain. Cancer staging plays a pivotal role in guiding management decisions in the setting of malignancy and in prognostication of disease. The primary imaging modalities in evaluating for the extent of metastatic disease are computed tomography (CT), bone scan, and MRI. CT is the primary imaging modality for whole-body staging, including treatment response. A bone scan provides a higher sensitivity for skeletal metastatic involvement over CT. Positron emission tomography/computed tomography (PET/CT) may play a role as an adjunct to standard imaging modalities for staging of distant metastatic disease or in assessment of treatment response (see Chapter 15). Although useful in assessing for distant metastases, this modality is not a reliable tool for assessment of local (breast and axillary disease) due to its low spatial resolution, which is better visualized by PEM (see Section 9.9). Aside for assessment of local extent of ipsilateral or contralateral breast parenchyma and disease, MRI may be utilized in characterization of intracranial lesions, as well as spinal lesions suspicious for metastases.

9.15 Breast Lymphoscintigraphy

Breast lymphoscintigraphy, or sentinel lymph node mapping, allows for identification of the first-order (i.e. sentinel) lymph node along the lymphatic drainage pathway from a breast cancer. The procedure involves injection of radiocolloid around the region of the index breast lesion, followed by imaging with a gamma camera. The skin over the sentinel node is marked for intraoperative guidance.

9.16 Summary

As outlined in the chapter, breast imaging plays an important role in both the screening of healthy, asymptomatic patients (of average and high risk), as well as in the diagnostic workup of patients with concerning symptoms or abnormal screening findings. Medical imaging of the breast relies on several imaging modalities with mammography and ultrasound serving as the mainstay of breast assessment. More advanced imaging techniques, such as breast MRI, DBT, PEM, BSGI, and CESM, play a pivotal role in workup and problem solving, and can also be utilized to improve the sensitivity of mammographic screening in high-risk populations, or those with dense breasts. An understanding of the appearances of both suspicious and benign breast pathologies, on each of the aforementioned imaging modalities, is paramount in the accurate and timely detection of breast cancer at an early stage with a strong potential for cure.

References

1 Myers, E.R., Moorman, P., Gierisch, J.M. et al. (2015). Benefits and harms of breast cancer screening. *JAMA* 314 (15): 1615–1634.

2 Mainiero, M.B., Lourenco, A., Mahoney, M.C. et al. (2016). ACR appropriateness criteria breast cancer screening. *J. Am. Coll. Radiol.* 13 (11): R45–R49.

3 Cancer Care Ontario (2015). *Breast Cancer Screening Program Guidelines.* Toronto, ON: Cancer Care Ontario.

4 Siu, A.L. (2016). Screening for breast cancer: U.S. Preventive Services Task Force recommendation statement. *Ann. Intern. Med.* 164 (4): 279–296.

5 American College of Radiology (2017). *Radiation Dose to Adults from Common Imaging Examinations*. Reston, VA: ACR.

6 Svahn, T., Houssami, N., Sechopoulos, I., and Mattsson, S. (2015). Review of radiation dose estimates in digital breast tomosynthesis relative to those in two-view full-field digital mammography. *Breast* 24 (2): 93–99.

Katerina Mastrocostas

Dr. Katerina Mastrocostas, MBBS, is a Staff Specialist Radiologist at Concord Repatriation General Hospital, a teaching hospital of the University of Sydney, Australia. She completed Cross-Sectional Imaging and Abdominal Imaging Fellowships at the University of Toronto, Canada after completing Radiology training in Sydney, Australia. Her main clinical areas of interest are the gastrointestinal tract and other abdominal organs, and neuroradiology. Her research focus is in health-care efficacy and clinical governance.

Kim May Lam

Dr. Kim May Lam (MBBS) is currently undertaking fellowship training in Abdominal Imaging at the University of Toronto, Canada. She completed her radiology training in Sydney, Australia at Royal Prince Alfred Hospital and has also specialized in Breast Imaging with BreastScreen NSW, Australia. Her main clinical area of interest is the abdomen, and in particular, imaging of the GI tract and pelvic organs.

Shereen Ezzat

Dr. Shereen Ezzat is a Professor of Medicine and Oncology in the Endocrine Oncology Site Group at the Princess Margaret Cancer Centre, University Health Network, Toronto. He obtained his medical degree from the University of Manitoba, completed his residency training at the University of British Columbia, and his postdoctoral research training in molecular oncology at Cedars-Sinai-UCLA School of Medicine in Los Angeles. Dr. Ezzat has authored

Medical Imaging for Health Professionals: Technologies and Clinical Applications, First Edition.
Edited by Raymond M. Reilly.
© 2019 John Wiley & Sons, Inc. Published 2019 by John Wiley & Sons, Inc.

or coauthored more than 250 original research articles and 40 invited review articles, and he has delivered more than 150 invited lectures. He supervises undergraduate and graduate students, as well as postdoctoral fellows. He teaches a number of courses, including physiology, biochemistry, and developmental biology. Dr. Ezzat served as an Editorial Board member for a number of journals including *Endocrinology, Journal of Clinical Endocrinology & Metabolism, American Journal of Physiology, Journal of Endocrinology, Endocrine Practice,* and *BMJ-Endocrine*. He is a regular reviewer for the *New England Journal of Medicine* and the *Annals of Internal Medicine*. Dr. Ezzat belongs to a number of professional societies, including the Endocrine Society, Federation of American Societies for Experimental Biology (FASEB), the Pituitary Society, the American College of Physicians, and the Royal College of Physicians and Surgeons of Canada. He is equally committed to patient advocacy and serves as an advisor to a number of organizations including the Canadian Neuroendocrine Tumor Society (CNETS), Thyroid Cancer Canada, and the Pituitary Network Association.

Sangeet Ghai

Dr. Sangeet Ghai is an Associate Professor in the Joint Department of Medical Imaging (JDMI) at University Health Network (Toronto General Hospital – Princess Margaret Hospital) – Mount Sinai Hospital – Women's College Hospital, University of Toronto, Canada. He is also the Director of the Biopsy Center at JDMI and the Education Coordinator for the Abdominal Division. Prior to his present position, he worked as a Consultant Radiologist and was the College Tutor at University Hospital of North Staffordshire NHS Trust, UK. His main areas of interest and research include prostate and thyroid imaging and intervention. He is actively involved in prostate MRI techniques, high-resolution ultrasound imaging of prostate, and in-bore focal treatment for intermediate risk prostate cancer. Dr. Ghai is also a core member of an ongoing Active Surveillance Study for small (<2 cm) Papillary Thyroid Cancers.

10

Endocrine Gland Imaging

*Katerina Mastrocostas, Kim May Lam, Shereen Ezzat,
and Sangeet Ghai*

10.1 Introduction

The endocrine system is comprised of a group of hormone-secreting organs distributed throughout the body. These hormones are carried by the blood stream to distant targets, where they act to produce their effects. Diseases of endocrine organs can be classified into those that result in altered production of hormone by the gland or those resulting in a mass lesion in the gland. Endocrine organs include the pituitary and pineal glands in the brain, the thyroid and parathyroid glands (PTGs) in the neck, and the adrenal glands and endocrine pancreas in the abdomen. In this chapter, we will review common disorders involving some of these endocrine organs, and the most appropriate medical imaging technologies to investigate and monitor these diseases. The patient's clinical presentation and measurement of serum hormone assays related to the involved organ are critical to the correct diagnosis and disease surveillance. Apart from molecular imaging (i.e. PET and SPECT – see Chapters 3 and 15), other imaging modalities alone cannot differentiate between "functioning" and "nonfunctioning" diseases of the endocrine system, including cancer.

10.2 The Thyroid Gland

The thyroid gland (Figure 10.1) is located in the low anterior neck, wrapped around the anterior and lateral margins of the trachea in the visceral space (Figure 10.2a and b). The gland is comprised of two lateral lobes, joined across the midline by the isthmus. Its rich blood supply through the superior thyroidal and inferior thyroidal arteries derive from the external carotid artery and

Medical Imaging for Health Professionals: Technologies and Clinical Applications, First Edition.
Edited by Raymond M. Reilly.
© 2019 John Wiley & Sons, Inc. Published 2019 by John Wiley & Sons, Inc.

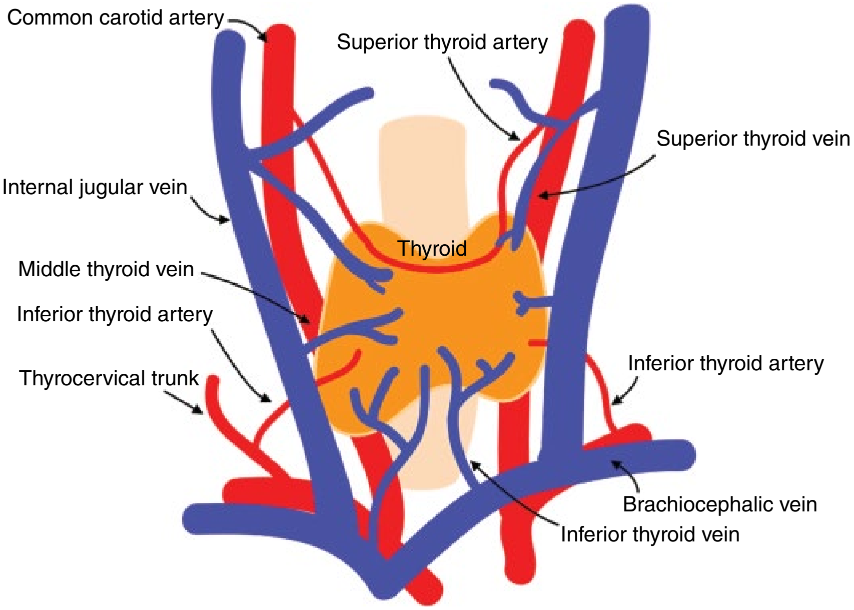
Common carotid artery
Superior thyroid artery
Superior thyroid vein
Internal jugular vein
Thyroid
Middle thyroid vein
Inferior thyroid artery
Thyrocervical trunk
Inferior thyroid artery
Brachiocephalic vein
Inferior thyroid vein

Figure 10.1 Arterial and venous supply of the thyroid gland. (*See insert for color representation of the figure.*)

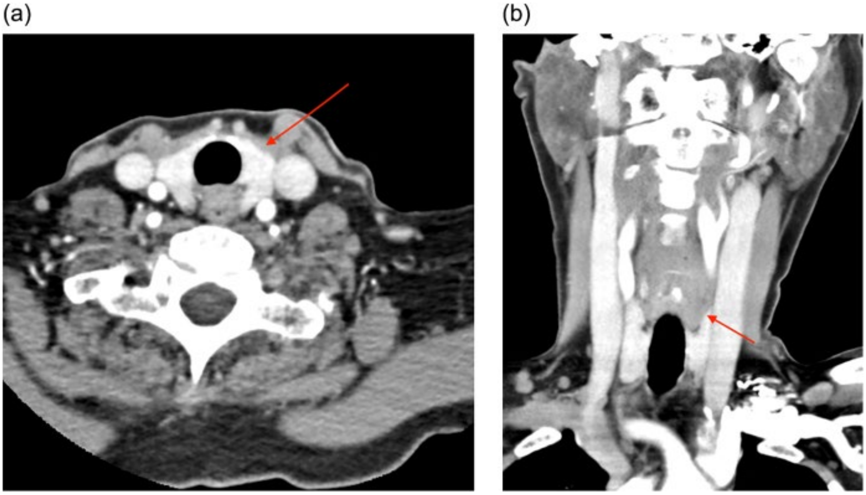

Figure 10.2 Axial (a) and coronal (b) MRI images of the thyroid (arrow), within the visceral space, wrapping around the trachea.

Figure 10.3 Feedback loop for thyroid hormones and TSH. Low serum thyroid hormones (T3 and T4) stimulate production of TSH by the pituitary gland in response to thyroid releasing hormone (TRH) secreted by the hypothalamus, which increases synthesis and release of T3 and T4 by the thyroid gland. Elevated serum T3 and T4 causes decreased TSH release by the pituitary gland.

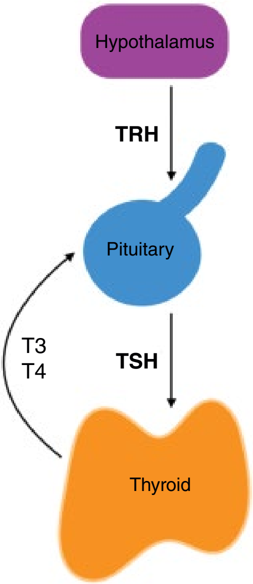

subclavian artery thyrocervical trunk, respectively (Figure 10.1). There is a venous plexus over the surface of the gland. This drains to the internal jugular veins, via the superior and middle thyroidal veins, and to the left brachiocephalic vein, via the inferior thyroidal veins. The lymphatic drainage is complex, draining to lymph nodes is the prelaryngeal, pretracheal, paratracheal, internal jugular chain, and spinal accessory chain (cervical lymph node levels II–VI). Thyroid stimulating hormone (TSH) that is secreted by the pituitary gland and thyroid releasing hormone (TRH) that is secreted by the hypothalamus in the brain work together to regulate the secretion of the thyroid hormones triiodothyronine (T3) and thyroxine (T4) from the thyroid gland. In turn, T3 and T4 levels work as a feedback mechanism to control the release of TSH and TRH (Figure 10.3). This feedback cycle regulates the normal levels of thyroid hormones in the circulation. Thyroid hormones have wide ranging effects on target cells in the body. The overall effect, however, is to increase the basal metabolic rate by regulating carbohydrate and fat catabolism, and protein synthesis. In the fetus and neonate, thyroid hormones also have an important role in brain development.

10.3 Thyroid Hormone Diseases

10.3.1 Increased Production of Thyroid Hormones

Clinically, increased thyroid hormone production is called thyrotoxicosis. Primary causes are those arising from an intrinsic thyroid disease that result in increased hormone release referred to as hyperthyroidism. Examples include

Graves disease, hyperfunctional multinodular goiter, or hyperfunctional thyroid adenoma. Thyroid inflammation or thyroiditis can also result in the release of stored thyroid hormone, and resulting thyrotoxicosis. Secondary causes of thyrotoxicosis are those arising from outside the thyroid. Once primary hyperthyroidism is suspected clinically and confirmed as evidenced by suppressed TSH and increased levels of circulating T3 and/or free T4 in the blood, the most appropriate medical imaging test is a nuclear medicine radioactive iodine uptake (RAIU) and thyroid scintigraphy study. While helping to confirm the diagnosis and etiology, this also serves as a baseline study prior to any treatment.

Thyroid scintigraphy is usually performed following the intravenous (i.v.) injection of technetium-99m sodium pertechnetate ($^{99m}TcO_4^-$), with imaging beginning 15 minutes after radiopharmaceutical administration (Figure 10.4).

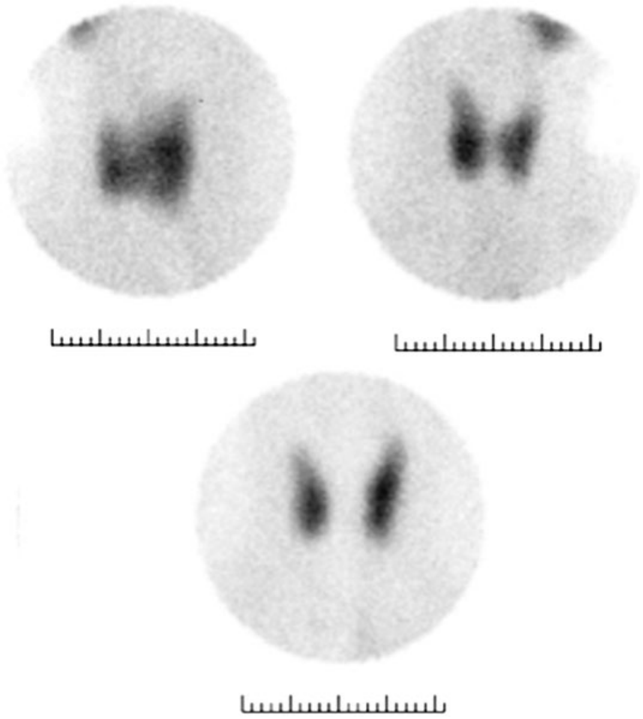

Figure 10.4 Preliminary flow and pool study (final phase demonstrating total tracer accumulation, usually in the diseased area) and delayed planar views of the thyroid using ^{99m}Tc pertechnetate thyroid scintigraphy demonstrate homogeneous uptake of the radiotracer with no focal hot or cold nodules, in keeping with a normal examination. Images are usually obtained from anterior, left anterior oblique, and right anterior oblique projections.

It should be appreciated that $^{99m}TcO_4^-$ is trapped in the thyroid by anion transporters that also trap radioactive iodine (RAI), but is not incorporated into thyroid hormones, thus it is not able to assess the hormone synthesis function of the thyroid gland (see Chapter 4). However, it is able to image the thyroid and detect any space-occupying lesions such as thyroid nodules. Imaging is completed on the same day. To assess the function of the thyroid gland, RAIU measurements are taken 24 hours after the oral ingestion of radioiodine (e.g. Iodine-131 [^{131}I] or iodine-123 [^{123}I]) in a capsule form, with the normal range at 24 hours between 5 and 35%. An alternative method of obtaining both a thyroid uptake measurement and scintigraphy image is with the administration of ^{123}I sodium iodide. This is taken orally in a capsule form, and both RAIU and scintigraphy scanning is performed 24 hours later. There are advantages in using ^{123}I, particularly in the detection of some types of malignant thyroid nodules. Disadvantages relate to the availability of the radioisotope, since ^{99m}Tc is readily available at any time by elution of a $^{99}Mo/^{99m}Tc$ generator (see Chapter 4) while ^{123}I must be ordered from a supplier and takes about one to two days to obtain. Ultimately, local practice will vary based on department preference.

The use of other imaging modalities for primary hyperthyroidism is determined by the RAIU and scintigraphy findings and the suspected etiology after these initial investigations, with some examples given below. In serum hormone assays, thyroid scintigraphy or RAIU do not support primary thyroid disease resulting in thyrotoxicosis, then a search for secondary causes is warranted. This may include pelvic ultrasound in women to assess for an ovarian teratoma subtype called struma ovarii that contains ectopic thyroid tissue. If TSH is increased as well as thyroid hormone levels, then imaging of the brain is the best first imaging investigation. An example is MRI imaging of the pituitary gland to assess for a rare TSH-secreting pituitary adenoma.

10.3.2 Graves Disease

The most common cause of primary hyperthyroidism is Graves disease, which is an autoimmune disease that results in diffuse hyperplasia of the gland and elevated levels of thyroid hormones. Autoimmune antibodies against TSH receptors on thyroid cells result in stimulation of the cells and release of thyroid hormone. Biochemically, serum thyroid hormone levels are elevated and TSH is low, due to feedback suppression (Figure 10.2). The most common subtype of auto-antibody is thyroid-stimulating immunoglobulin (TSI), elevated in 90% of cases. The imaging modality of choice varies by institution, and nuclear medicine or ultrasound assessment can be performed if required at diagnosis. RAIU demonstrates elevation of iodine uptake in the thyroid gland at 24 hours. Uptake values can be low (<5–10%), within normal limits (between 10 and 35%) or high (>35%). Patients with rapid turnover of iodine actually show normal RAIU at 24 hours, and the RAIU is actually elevated earlier (at 4–6 hours), termed "rapid iodine turnover." Thyroid scintigraphy (Figure 10.5) demonstrates that the thyroid gland is both enlarged and has diffusely increased radiotracer uptake throughout, with relative decreased activity within the rest of the body. The normal variant pyramidal lobe, which is a small remnant of normal thyroid tissue along the thyroglossal duct and that is not normally seen on scintigraphy, can be seen as it is also stimulated. Graves disease can coexist with multiple nodules, and is called "nodular Graves disease," "Graves disease coexistent with multinodular goiter," or Marine–Lenhart Syndrome. The nodule function is dependent on TSH, and because the TSH is suppressed in Graves disease, the nodules do not take up the radiotracer and appear as "cold nodules" on scintigraphy (Figure 10.6). There can be one or more of these "cold nodules" on a background of a diffusely enlarged gland with increased activity and relative decreased background activity.

Ultrasound in the acute phase of Graves disease demonstrates moderate diffuse enlargement of the thyroid gland, which appears diffusely hypoechoic with heterogeneous fine parenchymal hyperechoic foci. Doppler ultrasound (see Chapter 6) assessment demonstrates marked increased vascularity. There may be arterio-venous shunting and turbulent flow, giving a characteristic appearance on color Doppler termed "thyroid inferno." Ultrasound findings are compared with scintigraphy (Figure 10.7). Thyroid volume is useful in monitoring response to treatment in these patients. Ultrasound can also be used to localize and characterize coexistent nodules. Patients that develop thyroid-associated ophthalmopathy in Graves disease may require imaging of the orbits with CT or MRI to determine the extent of involvement and degree of extraocular muscle enlargement. This type of imaging is usually required to assist in decompressive surgical planning.

10.3.3 Hyperfunctional "Toxic" Thyroid Adenoma

Also called toxic autonomous nodule or Plummer disease, hyperthyroidism in this disease is caused by one or two nodules in the thyroid gland that are hyperfunctioning independent of the normal pituitary–thyroid feedback mechanism. This is due to gain-of-function mutations in the gene encoding the TSH receptor signaling pathway in follicular cells, leading the cells to continuously secrete thyroid hormone. RAIU demonstrates mild or moderate elevation, but can also be at the upper limit of normal. At thyroid scintigraphy, the nodule is hyperfunctioning, termed a "hot nodule" and the remaining thyroid tissue demonstrates decreased or absent uptake due to suppression of TSH by the thyroid–pituitary feedback mechanism. Ultrasound is performed to characterize the morphology and location of the "hot nodule" detected at thyroid scintigraphy, and to guide ultrasound-guided biopsy.

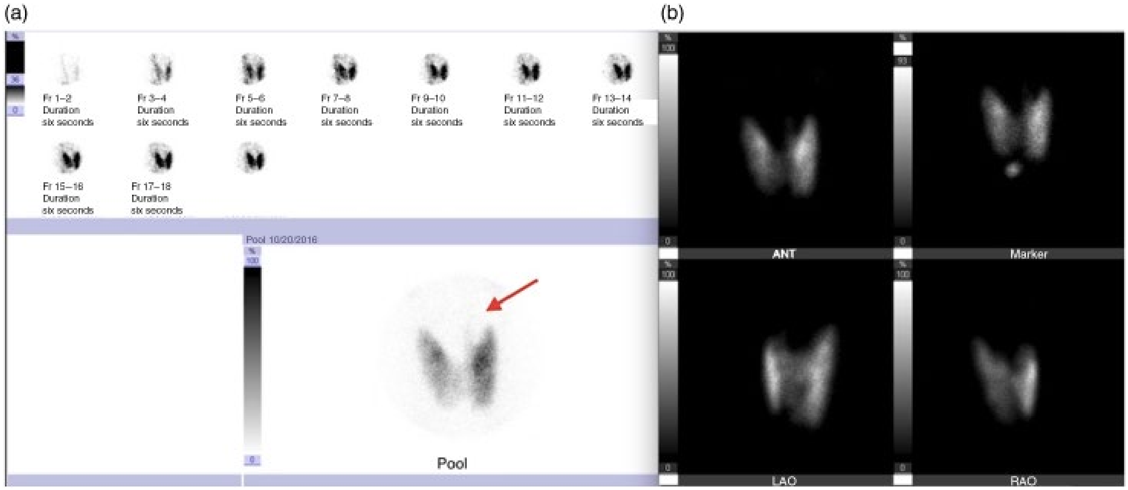
(a)
(b)
Fr 1–2 Duration six seconds
Fr 3–4 Duration six seconds
Fr 5–6 Duration six seconds
Fr 7–8 Duration six seconds
Fr 9–10 Duration six seconds
Fr 11–12 Duration six seconds
Fr 13–14 Duration six seconds
Fr 15–16 Duration six seconds
Fr 17–18 Duration six seconds
Pool 10/20/2016
Pool
ANT
Marker
LAO
RAO

Figure 10.5 Combined ^{99m}Tc pertechnetate (a) and ^{131}I scintigraphy (b) to obtain blood flow and pool images, and thyroid uptake, respectively. These demonstrate marked hyperemia on blood flow images, as demonstrated by increased uptake concentration. There is uniform increased uptake of radiotracer in the thyroid, including faint uptake within the pyramidal lobe (arrow), without a discrete nodule. Quantitative RAIU at 2 hours was 18.3% and at 24 hours was 53.8%, which are increased. The findings of both the scan and uptake images are in keeping with Graves disease. (Views in panel b: ANT, anterior; LAO, left anterior oblique; RAO, right anterior oblique.)

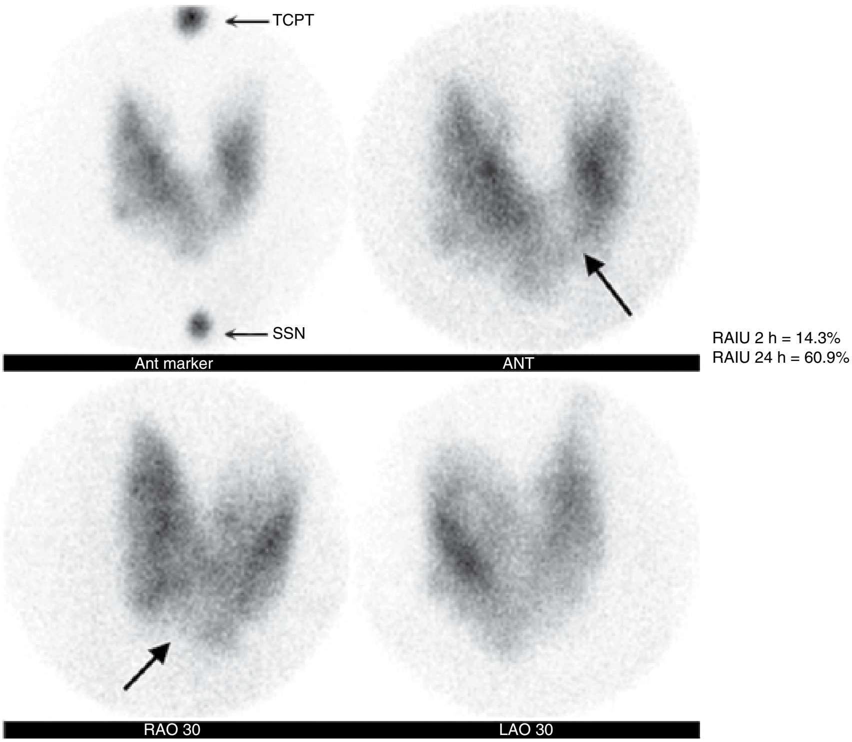

Figure 10.6 Thyroid scintigraphy demonstrating increased RAIU (60.9%) and diffuse increased radiotracer uptake through the gland with multiple "cold" nodules (arrows), in keeping with Graves disease superimposed on a background of multinodular goiter. "Hot spots" above and below the thyroid image in upper left panel are radioactive markers.

10.3.4 Hyperfunctional "Toxic" Multinodular Goiter

Multinodular goiter is asymmetrical enlargement of the thyroid gland containing two or more nodules. Multinodular goiter imaging will be discussed further below, but some of the nodules within the goiter can develop genetic abnormalities as seen in hyperfunctioning thyroid adenomas and result in "toxic" autonomously functioning nodules within the multinodular goiter. RAIU is normal or only slightly elevated. Thyroid scintigraphy demonstrates "hot nodules" that are hyperfunctioning scattered in the thyroid due to TSH suppression. There can also be "cold nodules" within the areas of suppressed background parenchyma due to the presence of nodules that are not hyperfunctioning, resulting in a heterogeneous appearance of the thyroid on RAIU. As in the case of a solitary toxic autonomous nodule, ultrasound is used to determine the location and morphology of these "hot" and "cold" nodules, and to enable image-guided biopsy.

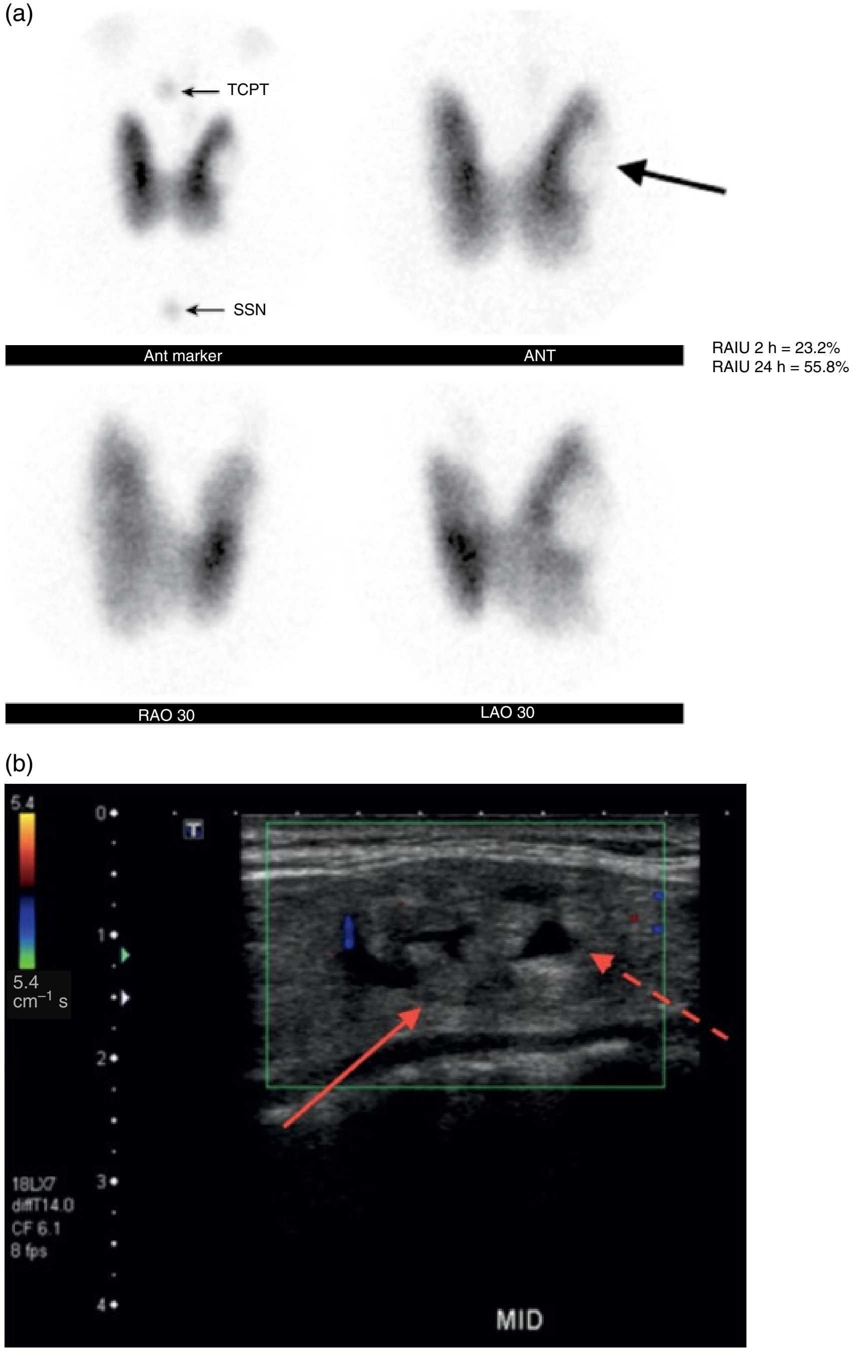
(a)
TCPT
SSN
Ant marker
ANT
RAIU 2 h = 23.2%
RAIU 24 h = 55.8%
RAO 30
LAO 30
(b)
5.4
5.4 cm⁻¹ s
0
1
2
3
4
T
18LX7
diffT14.0
CF 6.1
8 fps
MID

Figure 10.7 (a) Scintigraphic RAIU study in keeping with Graves disease with a "cold" nodule in the left upper to mid lobe (arrow). (b) Ultrasound of the same patient demonstrates a well-defined nodule with solid (solid arrow) and cystic components (broken arrow) at the site of "cold" nodule on scintigraphy, with no worrisome ultrasound features concerning for malignancy.

10.3.5 Granulomatous (de Quervain) Thyroiditis

Granulomatous thyroiditis is inflammation of the thyroid gland believed to be triggered by a viral infection, which results in an antigen that stimulates cytotoxic T lymphocytes that in turn damage thyroid follicular cells. The immune response is related to the viral infection and so the inflammation is limited. Initial inflammation of the thyroid gland results in thyroid pain, characteristic of this type of thyroiditis. Blood tests show increased thyroid hormone released from stores within the damaged gland and suppressed TSH. This acute phase lasts for two to six weeks. Recovery occurs in six to eight weeks and thyroid function gradually returns to normal. RAIU is very low during the initial inflammatory phase of the thyroiditis as the thyroid is unable to transport iodine. Likewise, scintigraphy with ^{99m}Tc pertechnetate shows very little or no radioactivity in the gland. This is due to damage of the follicular cell membrane and resulting inability to transport ^{99m}Tc pertechnetate. During the acute phase of granulomatous thyroiditis, there can be focal, ill-defined, subcapsular areas of reduced echogenicity of the thyroid parenchyma on ultrasound imaging. These regions demonstrate decreased or absent internal vascularity on color Doppler assessment, and there can be associated tenderness to ultrasound probe pressure. The intervening thyroid parenchyma can appear normal or mildly heterogeneous. Ultrasound during the subacute phase demonstrates progression with confluence of the patchy areas of involvement and enlargement of the thyroid gland. Regional lymph nodes may be enlarged or hypervascular, in keeping with reactive lymphadenopathy.

10.3.6 Subacute Lymphocytic Thyroiditis

Also called painless thyroiditis, subacute lymphocytic thyroiditis presents with mild thyrotoxicosis and/or mild enlargement of the thyroid gland. As a type of autoimmune thyroiditis, most patients have circulating auto-antibodies (such as antithyroid peroxidase antibodies) that result in lymphocyte infiltration of the thyroid follicular cells and disruption that leads to release of thyroid hormones into the circulation. In this thyrotoxic phase, which lasts from weeks to months, there is usually suppressed TSH and increased T3 and T4 levels. RAIU is very low during this phase as is uptake at thyroid scintigraphy with ^{99m}Tc pertechnetate, due to cell membrane damage and inability to take up iodine or ^{99m}Tc (Figure 10.8). This is followed by a period of hypothyroidism before the recovery phase. During this recovery phase, the patient can demonstrate thyrotoxicosis again. This is referred to as "rebound phenomenon." The RAIU increases and so does diffuse uptake on thyroid scintigraphy. These findings overlap with those seen in Graves disease, with the patient's clinical course helping to distinguish between the two. Patients with subacute lymphocytic thyroiditis usually have less marked symptoms of thyrotoxicosis and

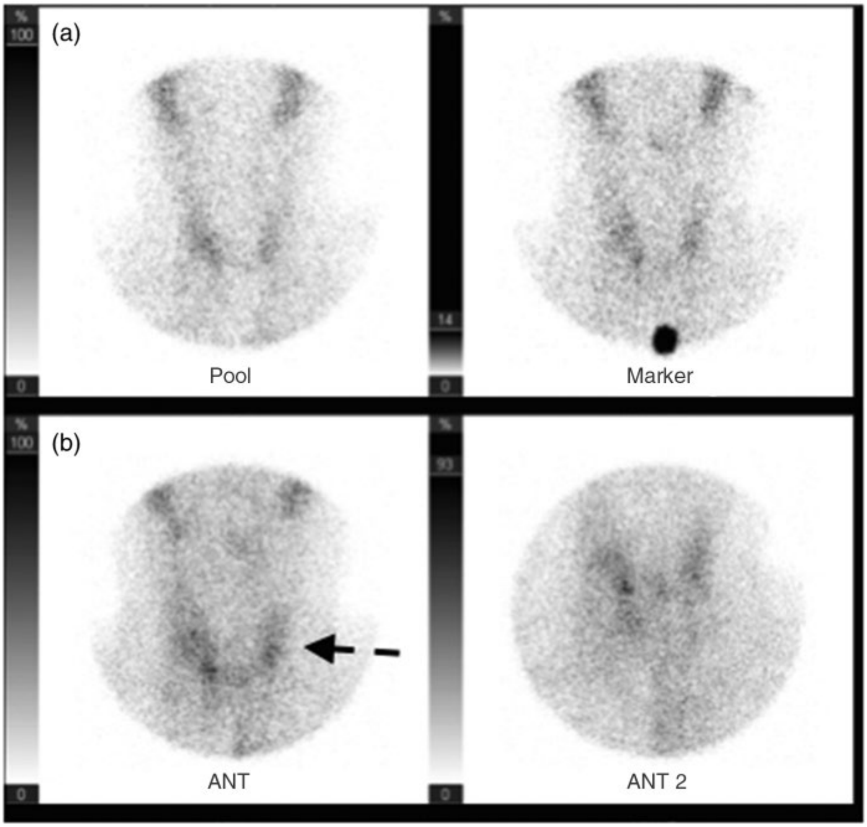

Figure 10.8 A 51-year-old female with subclinical hyperthyroidism was investigated with a combined ^{99m}Tc blood flow and pool study (a) that demonstrated decreased uptake in the thyroid gland. A ^{131}I RAIU study performed at the same time (b) demonstrated greatly reduced uptake in the thyroid gland (1.7% at 2 hours and 1.3% at 24 hours; broken arrow). These findings were most consistent with subacute thyroiditis.

demonstrate improvement over time with return to an euthyroid state. Up to one-third of patients progress to hypothyroidism over a 10-year period following the initial episode of thyroiditis.

10.3.7 Struma Ovarii

Rarely, thyrotoxicosis can be due to ectopic autonomously functioning thyroid tissue within an ovarian teratoma. This leads to increased T3 and T4, suppressed TSH, and suppression of the normal thyroid tissue function. RAIU is decreased, as is thyroid uptake at radioiodine scintigraphy. The ovarian tumor uptake can be seen on imaging the pelvis at scintigraphy (Figure 10.9a). In

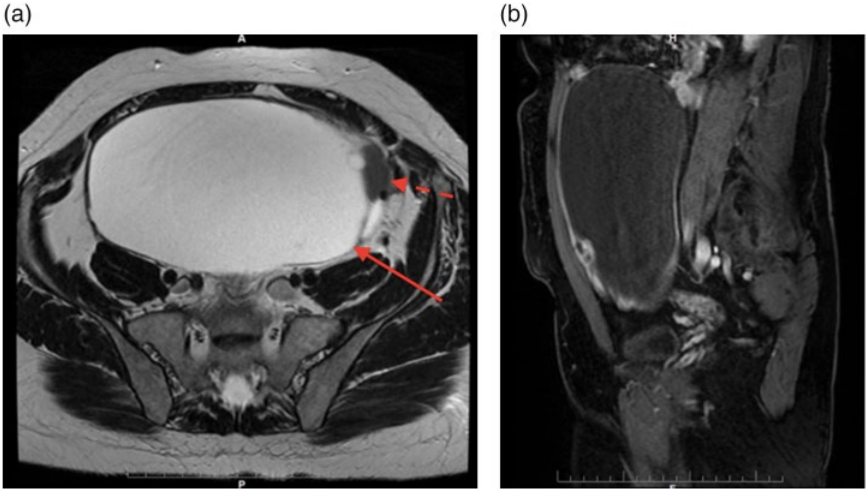

Figure 10.9 Axial (a) and sagittal (b) post-gadolinium contrast fat-saturated T2-weighted sequences. MRI images of the pelvis demonstrate a large cystic mass (solid arrow) with eccentric soft tissue at the left anterolateral margin of the mass (broken arrow). Thyroid scintigraphy in this patient demonstrated tracer uptake in the solid component of the mass. The surgical resection specimen was confirmed as the *struma ovarii* subtype of ovarian teratoma.

these cases, imaging of the pelvis with pelvic ultrasound and/or MRI is required to assess the pelvic mass prior to surgical resection (Figure 10.9b). The patient's thyroid function returns to normal following removal of the ovarian tumor.

10.3.8 Radioactive Iodine Treatment of Hyperthyroidism

RAI treatment of hyperthyroidism is the use of ^{131}I sodium iodide (see Chapter 4) to ablate the thyroid tissue and, therefore, stop the mechanism of increased circulating thyroid hormone. ^{131}I is one option for the treatment of Graves disease, except for patients that are pregnant, are lactating (due to excretion of ^{131}I in breast milk), or that have severe Graves ophthalmopathy, as symptoms may be potentially worsened. It is the preferred option for Marine–Lenhart Syndrome (a rare syndrome where the patient has both Graves disease and multinodular goiter), toxic autonomous nodules, and toxic multinodular goiter. Surgery is indicated when the thyroid is large and causing a mass effect on adjacent structures or the patient is refractory to medical treatment. A nuclear medicine physician performs RAI treatment. The dose of ^{131}I is based on the thyroid uptake of radioiodine and disease process affecting the thyroid gland, as well as the aim of the treatment, i.e. to render the patient hypothyroid or euthyroid. The patient must discontinue thyroid or any other interfering medications, and have not had i.v. iodinated CT contrast for four to six weeks prior to the procedure. The ^{131}I dose is administered orally as a capsule or liquid. Post-procedural complications most often manifest as radiation thyroiditis, which presents with pain and swelling of the thyroid gland and often requires corticosteroid treatment for symptom control. Appropriate radiation safety precautions to limit exposure of family members to radioiodine excreted in the saliva, sweat, and urine must be explained to the patient prior to treatment, and maintained for between 3 and 14 days following treatment depending on the dose administered.

10.3.9 Decreased Production of Thyroid Hormones

Hypothyroidism is a result of interference with the production of thyroid hormones that can be primary, due to diseases of the thyroid gland, or rarely secondary, due to pituitary or hypothalamic causes. The diagnosis is usually made from a combination of clinical findings and measurement of serum TSH and T4. All cases of hypothyroidism demonstrate reduced serum T4. Imaging plays a limited role in the investigation of hypothyroidism, as the clinical history and presentation are usually adequate for the determination of the etiology.

10.3.10 Primary Hypothyroidism

Primary hypothyroidism is characterized by low T4 and increased TSH on serum biochemistry. Congenital and genetic defects are rare causes for primary hypothyroidism. Postsurgical or post-ablative therapies (such as radioiodine therapy and external irradiation) are readily elicited from the clinical history. The most common remaining causes are autoimmune hypothyroidism, iodine deficiency, and medications (such as lithium, certain drugs used to treat hyperthyroidism, and interferon). These common causes also lead to enlargement of the thyroid gland. If required for confirmation, the medical imaging modality of choice is thyroid ultrasound. Autoimmune hypothyroidism, most commonly due to Hashimoto's thyroiditis, is associated with antimicrosomal, antithyroid peroxidase, and antithyroglobulin autoantibodies. Ultrasound demonstrates evolution of parenchymal changes based on the clinical stage and degree of involvement (Figure 10.10). In the acute stage, involvement can be focal (forming discrete nodules) or diffuse (resulting in diffuse enlargement of the gland and a micronodular heterogeneous pattern to the parenchyma). Acutely, the gland can be hypervascular, but not to the extent as seen with Graves disease. In the chronic stage, the thyroid is enlarged with a lobulated capsule. The parenchyma is hypoechoic and demonstrates a micronodular appearance. Echogenic septa can be seen running through the gland in some patients. In the end stage, there is atrophy of the gland, which is small and heterogeneous is echotexture.

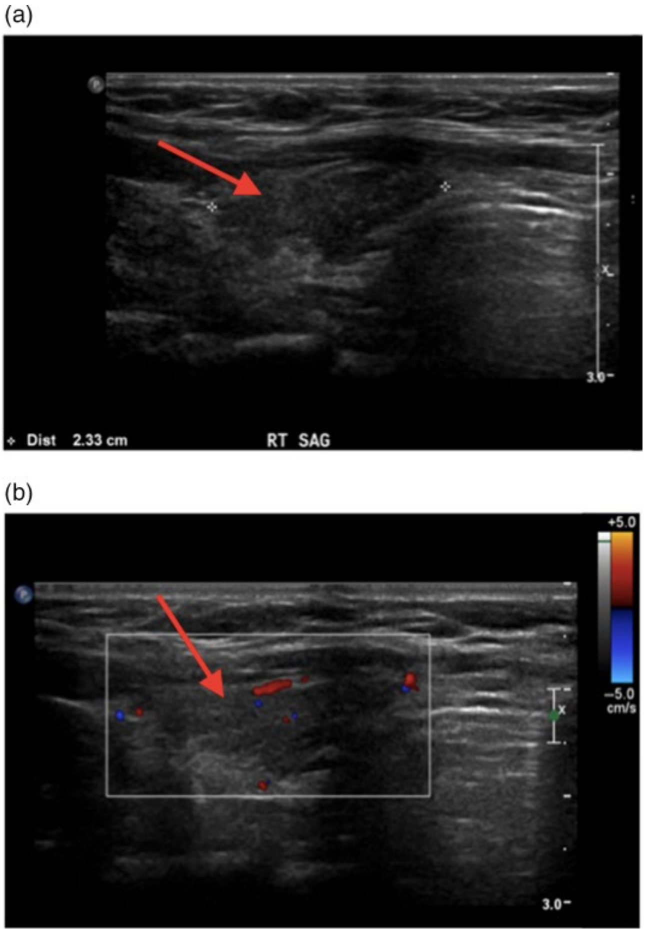

Figure 10.10 Sagittal ultrasound images through the right thyroid lobe (arrows) demonstrate atrophy of the lobe and diffuse hypoechoic parenchyma (a) with reduced internal vascularity on color Doppler assessment (b), in keeping with end-stage atrophy seen with chronic Hashimoto's thyroiditis. (*See insert for color representation of the figure*.)

10.3.11 Secondary Hypothyroidism

A rare cause for hypothyroidism, serum biochemistry in secondary hypothyroidism demonstrates reduced T4 and lack of elevation of TSH. In this situation, imaging should be directed to the brain to assess for rare central causes of hypothyroidism in the pituitary gland or hypothalamus. This is best assessed with MRI of the brain and pituitary fossa.

10.3.12 Use of Iodinated Contrast in Thyroid Disease

It is important to be cautious with the use of i.v. iodinated contrast, commonly used for CT and angiography, in patients with thyroid disease. Patients with multinodular goiter, especially those living in areas with endemic iodine deficiency, are at risk of developing an autonomous functioning nodule within the thyroid gland caused by delivery of excess iodine. The usual protective mechanism that results in inhibition of thyroidal iodine organification is termed the Wolff–Chaikoff effect. When a large dose of iodine is given, such as with the use of iodinated contrast, a previously low-functioning autonomous nodule within the gland can synthesize and release large amounts of thyroid hormone. This is called the Jod–Basedow phenomenon, and can lead to iodinated contrast-induced thyrotoxicosis. RAIU will be decreased and scintigraphy will demonstrate reduced radiotracer uptake, due to excess iodine within the gland. The use of i.v. iodinated contrast can also result in abnormal low RAIU and diminished radiotracer uptake at thyroid scintigraphy due to saturation of the thyroid gland with iodine. Therefore, examinations requiring i.v. contrast in those being investigated with thyroid disease should be used with caution or after consultation with the treating endocrinologist and/or nuclear medicine physician to avoid affecting the results of potential RAIU or scintigraphy studies. I.v. contrast should be used with caution in those with a history of thyroid disease, particularly in Graves disease or multinodular goiter, and in those living in areas of endemic iodine deficiency. If i.v. contrast cannot be avoided in patients at risk of developing thyroid-induced hyperthyroidism, they should be monitored closely for 2–12 weeks following the examination or procedure for the development of hyperthyroidism.

10.3.13 Mass Lesions in the Thyroid Gland

Thyroid nodules are reported in up to 68% of the adult population at ultrasound imaging, with the vast majority being benign. Whether suspected due to the presence of symptoms such as an enlarged palpable gland or nodule in the neck, or whether found incidentally at imaging for other indications, the appearance of the thyroid nodule on ultrasound can be used to determine whether the nodules are benign or suspicious for malignancy. Goiter is diffuse enlargement of the gland and occurs in endemic regions of iodine deficiency or sporadically. It has two phases: the initial diffuse hyperplastic phase, without producing nodularity, and the later phase of colloid involution, where follicles become filled with colloid, and subsequent rupture of these follicles causing inflammation. Patients are usually euthyroid. With time, repeated episodes of hyperplasia and involution result in nodularity of the enlarged thyroid gland, which is called a multinodule goiter.

The location of the thyroid anteriorly in the neck allows the gland to be readily imaged by ultrasound, which is the medical imaging modality of choice for characterization of nodules within it. The vast majority of thyroid nodules are nonneoplastic (such as simple cysts or a dominant nodule in a multinodular goiter) or benign neoplasms. Less than 1% of solitary thyroid nodules are malignant, and most are indolent with 90% of these patients alive 20 years after diagnosis. On ultrasound, nodules that are hypoechoic relative to the thyroid parenchyma and solid, taller than wide in dimensions, have irregular margins, contain microcalcifications or disrupted rim calcifications, and/or that demonstrate extrathyroidal extension are suspicious for thyroid cancer. Of note, microcalcifications have a reported sensitivity of 89%, a specificity of 95%, and an accuracy of 94% for the detection of malignant thyroid nodules. Each individual nodule >1 cm within the thyroid gland must be assessed for suspicious features, and every nodule with suspicious features should be considered for fine needle aspiration (FNA) biopsy. Extrathyroidal extension and extension of the thyroid into the superior mediastinum are also important factors to be assessed at the time of ultrasound. When the thyroid is markedly enlarged, it can develop retrosternal extension that is termed intrathoracic or "plunging" goiter. Mass effect on the aerodigestive tract or on the head and neck vessels, leading to dyspnea or dysphagia or to superior vena cava syndrome, respectively, may be indications for surgery. If goiter resection is considered, CT of the neck is usually performed for surgical planning.

10.4 Thyroid Cancer

While there are ultrasound features that are suspicious for thyroid cancer as outlined above, the definitive diagnosis is made by sampling the nodule either by FNA biopsy or at surgical resection. There are multiple guidelines, such as those published by the American Thyroid Association in 2015, which direct biopsy based on the morphology and size of the thyroid nodule in question. Most medical imaging departments have their own internal guidelines based on current evidence. The rate of thyroid cancer in the nodules that undergo FNA biopsy is reported to be around 10%. The addition of FNA biopsy to clinical practice has led to an increase in the likelihood of malignancy at thyroid resection from 14 to 50%, with a reduction in unnecessarily thyroidectomy for benign or nonneoplastic disease. Benign follicular adenomas contribute the majority of benign neoplasms of the thyroid gland. An intact capsule distinguishes follicular adenomas from follicular carcinomas, therefore, the diagnosis can only be definitively made after surgical resection at hemithyroidectomy. Carcinomas of the thyroid are differentiated in over 95% of cases, and the subtypes include: papillary (>85%), follicular (5–15%), or medullary (5%). Less than 5% of thyroid carcinomas are due to anaplastic (undifferentiated)

Table 10.1 Categories of the Bethesda System for Reporting Thyroid Cytopathology, risk of malignancy and the usual management.

Bethesda category	Category description	% Risk of malignancy	Usual management
I	Nondiagnostic or unsatisfactory cytopathology	1–4	Repeat FNA biopsy
II	Benign	0–3	Follow-up with clinical assessment
III	Atypia or follicular lesion of undetermined significance	5–15	Repeat FNA biopsy
IV	Follicular neoplasm or suspicious for follicular neoplasm	15–30	Hemithyroidectomy
V	Suspicious for malignancy	60–75	Hemithyroidectomy or (near) total thyroidectomy
VI	Malignant	97–99	(Near) total thyroidectomy

carcinoma. FNA biopsy performed under ultrasound guidance has been shown to have a 20% greater accuracy than palpation-guided FNA biopsy. Cytology reporting has been standardized and referred to as “The Bethesda System for Reporting Thyroid Cytopathology” (Table 10.1). This system stratifies results into diagnostic categories, each category implying a risk of malignancy and triggering different management strategies.

10.4.1 Thyroid Cancer Metastasis

At the time of ultrasound for suspected thyroid cancer, a thorough assessment of the cervical lymph nodes should also be performed. As discussed above, the thyroid lymphatics drain bilaterally to cervical levels II–VI (the cervical lymph nodes involving the internal jugular, spinal accessory, and pretracheal regions). If suspicious lymph nodes are seen, these should also be sampled with FNA biopsy. If involved, the surgical management is altered to include cervical lymph node dissection at the time of thyroidectomy. Cross-sectional imaging with contrast-enhanced CT or MRI of the neck is recommended as an adjunct to ultrasound in patients that have findings suspicious for advanced disease (Figures 10.11 and 10.12). Suspicious findings include a locally invasive primary thyroid tumor (with extrathyroidal extension on ultrasound), clinically palpable or ultrasound detected bulky lymph node involvement. Preoperative ^{18}F-FDG-PET scanning is not recommended as a routine preoperative investigation.

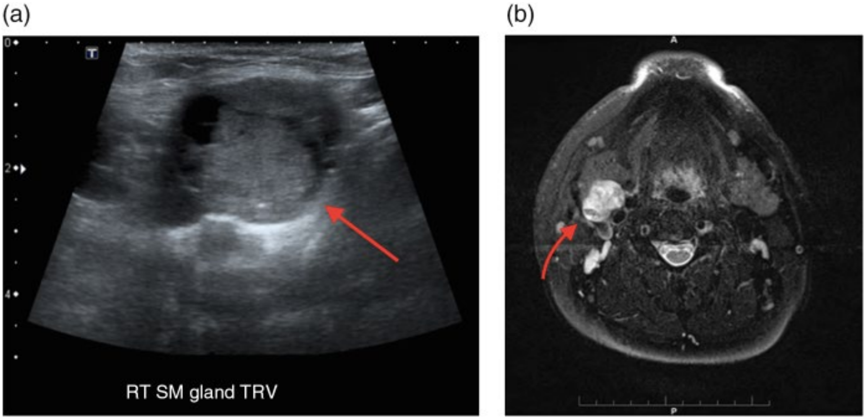

Figure 10.11 (a) Ultrasound of the neck in a patient with a suspicious thyroid nodule demonstrates a heterogeneous predominantly hyperechoic mass deep to and elevating the posterior margin of the right submandibular gland that was concerning for metastatic lymph node involvement from a suspected thyroid carcinoma. (b) Axial fat suppressed T2-weighted image of the upper neck of the same patient demonstrates an enlarged right level II cervical lymph node abutting the carotid space and deep to the submandibular gland that is hyperintense internally on T2-weighted MRI image. T1-weighted MRI (not shown) demonstrates internal areas of high T1 signal. This could represent either hemorrhage or colloid contents within the enlarged lymph node.

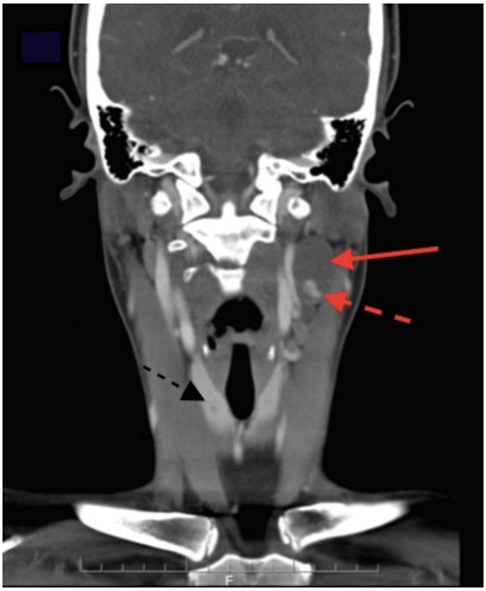

Figure 10.12 Coronal contrast-enhanced CT of the neck in a patient with a palpable left neck lump. This image demonstrated left level II–IV cystic lymphadenopathy (solid white arrow) with enhancing solid, nodular components (broken white arrow). Note the tiny 0.6 cm hypoattenuating nodule in the right thyroid gland (broken black arrow).
At thyroidectomy, this was shown to be the primary papillary carcinoma resulting in metastatic lymphadenopathy.

10.4.2 Imaging Thyroid Cancer Metastases

Whole-body radioiodine scans are performed to evaluate thyroid cancer metastases. As with RAI treatment (see below), only papillary and follicular thyroid cancer are RAI avid and, therefore, the pathological subtype of cancer plays a role in the use of this imaging approach. With increasing availability, this is now commonly performed with ^{123}I sodium iodide, but ^{131}I can also be used (see Chapter 4). Local practice varies on the availability of the radioisotopes. ^{123}I has been found to have improved imaging characteristics, a lower radiation dose, and a lower risk of thyroid "stunning" if used prior to RAI ablation treatment. A low dose of RAI is administered orally, and images are obtained within 6–48 hours. As with RAI treatment, the patient must have TSH stimulation (by withdrawal of thyroid hormone replacement therapy) and a low iodine diet prior to the study. Female patients must have negative pregnancy testing due to the risk of radioiodine to the fetus. If imaging cannot be avoided while lactating, women undergoing ^{123}I imaging are instructed to discard breast milk for two to three days post oral administration of the radioisotope, since it may contain radioiodine. Women imaged with ^{131}I must cease lactation for up to two months prior, as lactating breasts actively take up iodine resulting in inappropriate radiation to the breasts. Thyroid cancer metastases from medullary and anaplastic thyroid cancer types are best evaluated with CT imaging, and PET/CT can be useful in the setting of dedifferentiated thyroid cancer.

10.4.3 Radioactive Iodine Treatment of Thyroid Cancer

Further treatment with RAI is determined by a combination of postoperative disease status and clinical factors, including postoperative serum thyroglobulin. Stratification is also based on whether the differentiated thyroid cancer was found to be of low, intermediate, or high risk at histopathology. Only the papillary and follicular types of thyroid carcinoma take up RAI. Therefore, RAI is not used for treatment of medullary and anaplastic thyroid cancer. RAI treatment has a role in ablation of any thyroid remnant, as adjuvant therapy or for treatment of persistent disease. The current American Thyroid Association Guidelines give recommendations for the use of RAI based on the combined risk. In patients without metastatic disease, RAI ablation is not generally recommended for low-risk patients post thyroidectomy or in those with isolated subcentimeter unifocal papillary microcarcinoma. RAI should be considered for intermediate risk-level patients and is routinely recommended after total thyroidectomy for high-risk patients. Various features are taken into consideration for each individual patient, including recurrence risk, pathological features of the resected tumor, follow-up implications, and patient preferences. Patient age (>45 years), primary tumor size (>4 cm), and extrathyroidal extension or lymph node metastases are strong factors in recommending RAI treatment. Postsurgical RAI treatment is indicated for patients with gross extrathyroidal extension or distant metastases.

Patient preparation prior to RAI treatment includes excluding exogenous iodine, such as waiting four to six weeks after i.v. contrast-enhanced CT, cessation of amiodarone, and following a low-iodine diet for one to two weeks prior to treatment. Also, TSH must be elevated at the time of treatment. Thyroid hormone replacement withdrawal is recommended for three to four weeks prior to treatment, with the aim of producing elevated TSH (target TSH of $>30\,\mathrm{mIU\,l^{-1}}$). Female patients must have a negative urine or serum pregnancy test prior to treatment. Prior to oral therapy with ^{131}I at the therapeutic dose, a whole-body RAI scan is performed to assess for distant metastases. RAIU is also measured, and usually low at between 1 and 5%. Findings at these investigations as well as the risk profile of the patient contribute to determining the dose administered for therapy. A repeat RAI whole-body scan is performed 4–10 days following treatment, and has been found to detect additional sites of disease in up to a quarter of patients. Post-procedure instructions regarding recommencing thyroid replacement therapy, low-iodine diet, and radiation safety precautions are discussed with the patient prior to treatment.

10.5 The Parathyroid Glands

There are four PTGs, two on each side of the neck, immediately adjacent to the thyroid. Most commonly, the superior PTGs are located posterior to the mid-thyroid gland and the inferior PTGs are located lateral to the lower pole of the thyroid. The number of glands and their location, however, are variable. There can be up to a total of 12 PTGs, located anywhere from the angle of the mandible to the superior mediastinum, in the visceral space posterior to the thyroid, or even posterior to the pharynx or esophagus. Rarely, PTG can be intrathyroidal. Blood supply to the PTGs is from the superior and inferior thyroidal arteries. The role of the PTGs is in calcium homeostasis. Parathyroid hormone (PTH) is secreted by the glands in direct response to the free calcium level in the blood. When free calcium is low, the glands secrete PTH. In turn, PTH acts on the kidneys to reabsorb calcium and excrete urinary phosphate, to convert vitamin D to the active dihydroxy form in the kidneys, and to assist in calcium absorption in the gastrointestinal tract.

10.5.1 Altered Production of PTH

Hypoparathyroidism is a clinical diagnosis, and medical imaging plays a limited role. Hyperparathyroidism is a diagnosis that is determined clinically through a combination of clinical history and elevated serum PTH. It can be asymptomatic. It is classified into primary, secondary, and the rare tertiary forms. Scintigraphy (nuclear medicine imaging) and ultrasound are the two imaging modalities that are more often used in the detection and localization of diseases of the PTGs. Three main techniques are commonly used for parathyroid scintigraphy. Single-phase dual-isotope subtraction imaging uses ^{99m}Tc-sestamibi to visualize the hyperfunctioning PTG and the thyroid, while ^{123}I sodium iodide or ^{99m}Tc sodium pertechnetate is used for imaging of the thyroid gland only (see Chapter 4). The second set of images is digitally subtracted from the first to reveal the hyperfunctioning PTG. The second technique is single-isotope dual-phase imaging study that is based on the difference in washout rates of ^{99m}Tc-sestamibi from the thyroid and hyperfunctioning PTG. A single radiopharmaceutical injection is required, with patients imaged at 10–15 minutes and again at 90–180 minutes. The PTGs exhibit slower washout than the thyroid gland. The third technique is a combination of both of the above. More often, conventional two-dimensional planar imaging is being replaced by SPECT or SPECT/CT to improve contrast and/or spatial resolution.

10.5.2 Primary Hyperparathyroidism

Primary hyperparathyroidism due to autonomous overproduction of PTH from the PTG is usually a result of an adenoma in 85–95% of cases. Primary hyperplasia, which can be diffuse or nodular, accounts for a further 5–10% of cases. Parathyroid carcinoma is rare, and accounts for about 1% of cases. More common in women by 4 : 1, primary hyperparathyroidism is a disease of adults. It is often detected in an asymptomatic population with incidental hypercalcemia on serum electrolyte assessment. Serum PTH levels are raised. Only 20–25% of cases present with symptomatic disease due to hypercalcemia. Clinical manifestations are broad but include nausea or vomiting, bone pain, biliary or renal colic, and psychiatric symptoms. A sporadic solitary parathyroid adenoma is the most common cause, and is usually a monoclonal benign neoplasm pathologically. Familial syndromes such as Multiple Endocrine Neoplasia (MEN, types 1 and 2) and familial hypocalciuric hypercalcemia are far less common causes. Medical imaging plays a role in differentiating a solitary adenoma, nodular hyperplasia, and diffuse hyperplasia in patients deemed suitable for surgical exploration and excision as treatment. Scintigraphy and ultrasound are the two modalities used most frequently. The aim is preoperative localization to facilitate minimally invasive surgery. Dual-phase ^{99m}Tc-sestamibi scintigraphy as discussed earlier has been reported as superior to ultrasound in sensitivity for the detection of single adenomas (88 vs. 78%), double adenomas (44 vs. 35%), and multiple gland hyperplasia. Ultrasound is used in correlating or confirming findings at scintigraphy, or in those with negative initial imaging.

10.5.3 Parathyroid Adenoma

On early dual-phase scintigraphy imaging, parathyroid adenomas are detected only if they have accumulation greater to that of thyroid tissue, resulting in a contour bulge if adjacent to the thyroid or are not abutting/within the thyroid gland. Late dual-phase scintigraphy imaging relies on the difference in retention of radiotracer in the thyroid and PTGs. The PTGs rarely demonstrate early washout, with delayed washout more common. Delayed washout, or retention of radiotracer on a delayed phase study, is commonly seen in hyperfunctioning PTGs (Figure 10.13). Multiple adenomas can also be detected this way. SPECT/CT, which is tomographic imaging (see Chapter 3), has improved the localization of the parathyroid adenoma above conventional planar scintigraphy alone. Ultrasound is used in conjunction with parathyroid scans to localize enlarged PTGs in the neck (Figure 10.14).

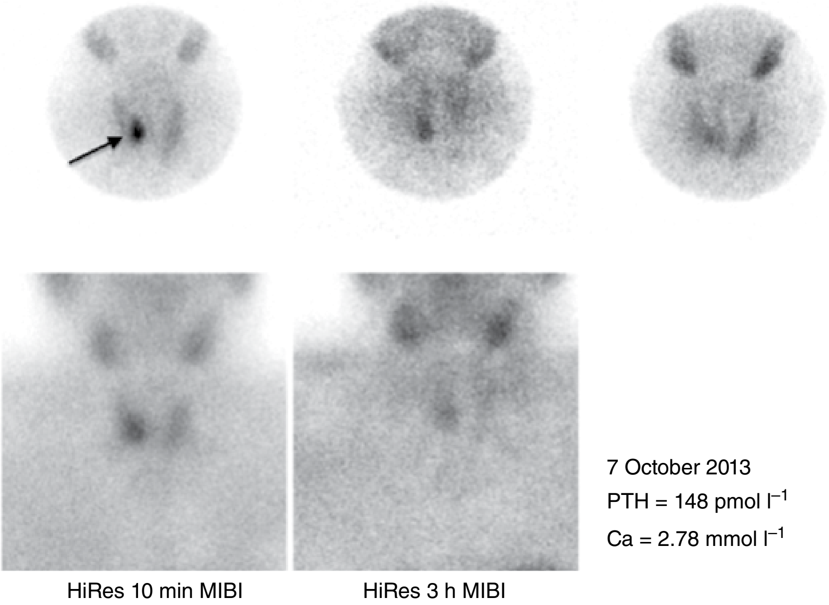

Figure 10.13 ^{99m}Tc-sestamibi parathyroid scan demonstrating a focus of persistent abnormal radioactivity posterior to the inferior pole of the right lobe of the thyroid on the delayed phase (arrow), likely a parathyroid adenoma. Top right image shows an image with ^{99m}Tc-sodium pertechnetate to reveal the thyroid gland. All other panels are images with ^{99m}Tc-sestamibi.

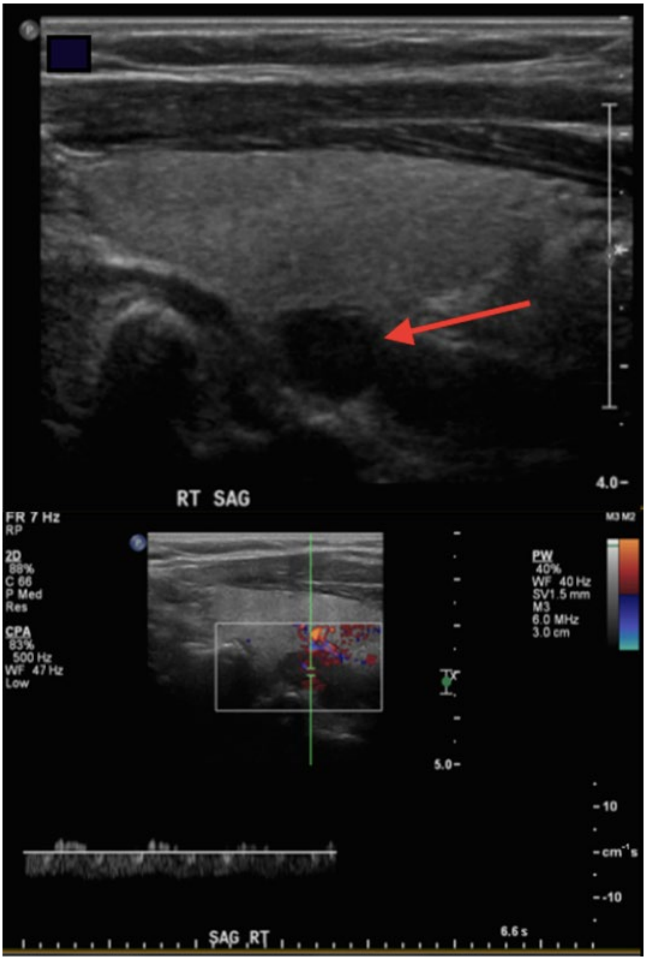
4.0
RT SAG
FR 7 Hz
RP
2D
88%
C 66
P Med
Res
CPA
83%
500 Hz
WF 47 Hz
Low
PW
40%
WF 40 Hz
SV1.5 mm
M3
6.0 MHz
3.0 cm
M3 M2
5.0
10
cm⁻¹s
-10
SAG RT
6.6 s

Figure 10.14 Selected ultrasound images from right neck of the same patient as in Figure 10.13 above demonstrates a hypoechoic vascular mass deep to the mid to lower pole of the right thyroid lobe (arrow). This is the typical ultrasound appearance of a parathyroid adenoma. (*See insert for color representation of the figure.*)

10.5.4 Parathyroid Hyperplasia

The same imaging characteristics seen on parathyroid scintigraphy for parathyroid adenoma also apply in parathyroid hyperplasia. Scintigraphy is less sensitive, however, for its detection. When primary hyperparathyroidism is suspected clinically and parathyroid scintigraphy is negative, the possibility of parathyroid hyperplasia or even multiple parathyroid adenomas should be considered.

10.5.5 Parathyroid Carcinoma

A rare diagnosis, the imaging findings on scintigraphy and ultrasound are the same as parathyroid adenoma and is often only diagnosed on pathological evaluation. Parathyroid carcinoma tend to behave as a low-grade malignancy and are suspected in a large nodule (>3 cm) or if there is invasion into adjacent structures such as the thyroid gland on imaging. The presence of a thick capsule around a hypoechoic mass on ultrasound can be suggestive, but diagnosis cannot be made on imaging findings alone.

10.5.6 Parathyroid 4D CT Imaging

CT imaging of the neck has been shown to have high accuracy in localizing parathyroid adenomas to a quadrant by up to 87%. A “4D CT” of the neck is performed from the carina of the trachea to the skull base prior to administering contrast, and in the arterial and delayed venous phases following i.v. contrast administration. The fourth dimension of the CT refers to the perfusion information in the multiple contrast phases, which allows for a more confident diagnosis of adenoma. A parathyroid lesion is typically hypoattenuating relative to the thyroid prior to contrast, but demonstrates avid arterial enhancement and “washout” of contrast on the delayed venous phase. These changes over time assist in the detection of parathyroid lesions on CT. Another benefit of CT imaging is the localization of PTGs away from the thyroid in the neck. With embryological origin from the third and fourth branchial pouches, from which many other structures from the ear and neck arise and then migrate to their final position, PTGs can, therefore, be located as high as the carotid bifurcation, significantly higher than their expected location adjacent to the thyroid. As the inferior PTGs descend during embryogenesis with the thymus, they can be detected as low as the anterior mediastinum.

10.5.7 Secondary and Tertiary Hyperparathyroidism

Most commonly seen in patients with chronic renal failure, secondary hyperparathyroidism is due to compensatory hypersecretion of PTH due to chronic hypocalcemia. Osteomalacia, rickets, and malabsorption can also cause secondary hyperparathyroidism. The rare tertiary hyperparathyroidism is due to persistently elevated PTH after correction of the cause for prolonged hypocalcemia, such as following renal transplant. Clinical findings and laboratory studies will make the diagnosis in these cases. Both secondary and tertiary hyperparathyroidism usually result in diffuse parathyroid changes, and, therefore, imaging of the neck is not usually necessary as in the case of primary hyperparathyroidism where the goal is to localize a parathyroid adenoma responsible for the patient’s symptoms. Parathyroid scintigraphy has a low sensitivity for the detection of all the PTGs in this setting, reported as low as 9% in tertiary hyperparathyroidism. Also, of patients found to have an ectopic mediastinal PTG intraoperatively, only 38% were detected at parathyroid scintigraphy prior to surgery. Finally, as standard of care is bilateral neck exploration, imaging findings will not alter surgical approach. The greatest utility of neck imaging in the setting of secondary and tertiary hyperparathyroidism is in the setting of recurrent or persistent hyperparathyroidism postoperatively, and in planning prior to reexploration. The reported rates of successful identification of parathyroid remnants at ^{99m}Tc-sestamibi scintigraphy are up to 85% in cases with underlying secondary hyperparathyroidism and up to 100% of cases with tertiary hyperparathyroidism.

10.6 The Adrenal Glands

The adrenal glands are located superior to the upper pole of the kidneys. They have two components: the adrenal cortex, which synthesizes glucocorticoids, mineralocorticoids, and sex steroids, and the adrenal medulla, which synthesizes catecholamines. As with most endocrine disorders, disorders of adrenal function can be primary, due to primary adrenal disease, or secondary, such as due to pituitary disease. Primary diseases of the adrenal cortex can lead to hyperfunction, termed hyperadrenalism, or hypofunction, called adrenocortical insufficiency. The various syndromes resulting from increased or decreased production of the adrenal cortical hormones are beyond the scope of this chapter. Generally, functional adenomas most often result in hyperaldosteronism and Cushing syndrome. Adrenal cortical carcinoma usually results in adrenocortical insufficiency. Furthermore, imaging cannot distinguish whether an adrenal neoplasm is “functional” or “nonfunctional.” Correlation with the clinical presentation and with measurement of the adrenal cortical hormones and their metabolites is required to determine this. The adrenal medulla is part of the paraganglion system, and is made of specialized neuroendocrine cells, called chromaffin cells, that are a major source of catecholamines (epinephrine and norepinephrine). Other extra-adrenal sites of paraganglia are branchiometric (related to the great vessels), intravagal (related to the vagus nerve), and aortico sympathetic (related to the sympathetic ganglia along the abdominal aorta, including the organs of Zuckerkandl near the aortic bifurcation). Mass lesions of the adrenal medulla and paraganglia can result in abnormal release of catecholamines.

The most common primary adrenal lesions and their imaging characteristics are discussed below. Other less common benign adrenal lesions include cysts, hemorrhage, ganglioneuromas, hemangiomas, neuroblastoma, and granulomatous disease. Combined, these benign lesions account for up to 2% of incidental adrenal lesions. Adrenal metastasis is important to consider in patients with a diagnosis of malignancy, especially pulmonary malignancy, with one study showing that 27% of patients with malignancy have microscopic adrenal metastases. PET and PET/CT have been shown to have a sensitivity and specificity between 80 and 100% for detecting malignant lesions. False positives include mild radiotracer uptake in some adrenal adenomas, adrenal endothelial cysts, and inflammatory or infectious lesions. False negatives include necrotic or hemorrhagic malignant adrenal lesions.

10.7 Mass Lesions of the Adrenal Cortex

10.7.1 Adrenocortical Adenoma

Most adrenocortical adenomas, commonly referred to as adrenal adenomas, are typically clinically silent and nonfunctional. They are benign neoplasms of the adrenal cortex that are usually small (up to 2.5 cm in size) and are commonly found incidentally at imaging or at autopsy. It has been reported that the incidence is up to 9% of the population, increasing with age. The finding of an incidental adrenal lesion at imaging for other indications, excluding in the setting of cancer staging, is commonly termed an "incidentaloma." Of these 94% of incidentalomas will be nonfunctioning adenomas, and 6% functioning. Whether an adenoma is functioning is determined by the clinical presentation and hormone/biochemical assays. As 70% of adrenal adenomas contain intracellular fat and are termed "lipid rich," CT and MRI imaging are used in characterization of adrenal lesions as both are highly sensitive for the detection of lipid. Generally, due to ease of availability and cost, CT is the best first test for the assessment of these adrenal lesions. Non-enhanced CT of the adrenal glands has a sensitivity of 71% and a specificity of 98% for the detection of lipid-rich adrenal adenomas when the attenuation of the adrenal lesion is ≤10 Hounsfield Units (HU; see Chapter 2). This is a quick method for characterizing the majority of adrenal adenomas with confidence. If the density of the adrenal nodule is >10 HU on a non-enhanced CT study, then further assessment with an adrenal washout CT study is required to assess the perfusion of the nodule. Most medical imaging departments have an "adrenal CT" protocol where the non-enhanced images are reviewed at the time of image acquisition, and the adrenal washout protocol is activated if the attenuation of the nodule is >10 HU. Images of the adrenal glands are obtained following the administration of i.v. contrast in the portal venous phase and following a 15-minute delayed phase (Figure 10.15). The other 30% of adrenal adenomas that are lipid-poor tend to washout i.v. contrast faster than malignant lesions, and so can be confirmed with this CT technique. This is done by determining the absolute percentage of washout (APW) and relative percentage of washout (RPW) of i.v. contrast in the nodule (Table 10.2). Nodules with an APW of >60% and a RPW of >40% can be confirmed as

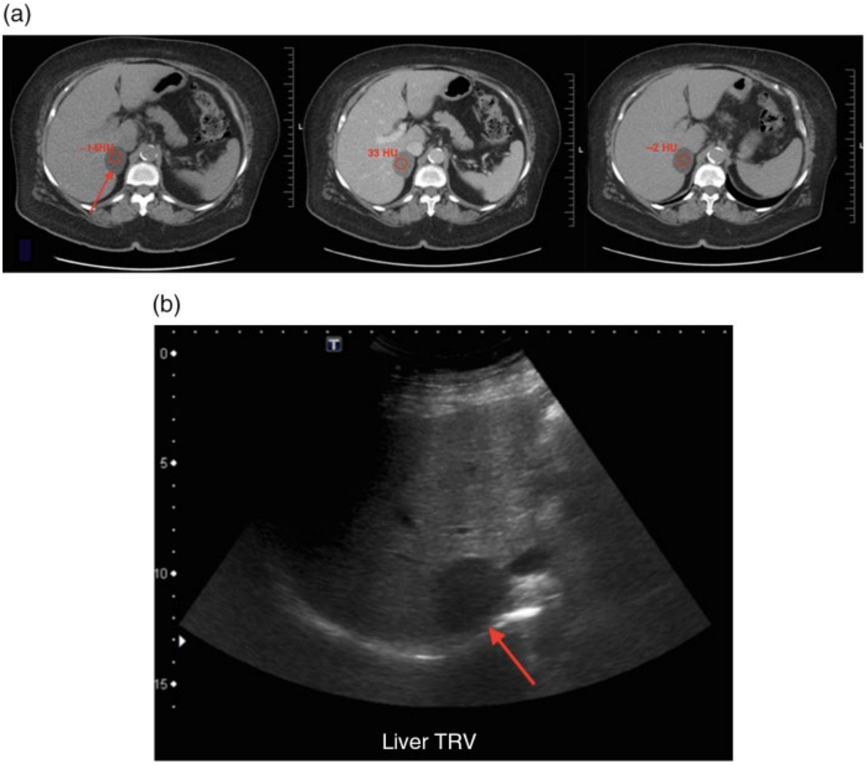

Figure 10.15 (a) Non-enhanced, portal venous, and 15-minute delayed phase transaxial CT images at the level of the right adrenal gland demonstrates a well-circumscribed mass in the right suprarenal lesion (arrow) that is continuous with the adrenal gland (not shown). Prior to contrast, the lesion has an attenuation of −14 HU. This is diagnostic of adrenal adenoma. Further phases were performed in this patient (for other indications). In the portal venous phase, the lesion has an attenuation of 33 HU. At 15 minutes delay, the lesion has an attenuation of −2 HU. The washout characteristics of the lesion are also in keeping with adrenal adenoma. (b) Ultrasound of the right upper abdomen in the same patient demonstrates a hypoechoic mass in the liver (arrow), corresponding to the adrenal adenoma as characterized on CT. Adrenal adenomas can vary in their ultrasound appearance, and can be either hyperechoic or hypoechoic relative to the liver. This is dependent on the macroscopic fat content of the adenoma.

Table 10.2 Calculation of APW and RPW for adrenal lesions.

Parameter	Calculation
Absolute percentage of washout (APW)	100 · [(Post HU – Delayed HU)/(Post HU – Pre HU)]
Relative percentage of washout (RPW)	100 · [(Post HU – Delayed HU)/Post HU]

HU, Houndsfield Units.

lipid-poor adrenal adenomas. Alternatively, if these criteria are not fulfilled, malignancy is the likely diagnosis.

MRI imaging can also be performed to characterize adrenal adenomas by utilizing the chemical shift artifact for the detection of intracellular lipid. This technique uses the phenomenon of loss of signal between the in-phase and opposed-phase on T1 weighted gradient echo sequences, which is due to canceling of signal from voxels containing both water and lipid. This phenomenon is observed in lipid-rich adrenal adenomas, but due to the lower lipid-to-water ratios in lipid-poor adrenal lesions, has limited utility in this setting. Therefore, CT remains the preferred imaging modality for the characterization of adrenal adenomas. Special care should be taken in the rare case of a concurrent adrenal adenoma and other adrenal lesion within the same location, termed a "collision tumor." Any heterogeneity or change in attenuation of an adrenal adenoma should be assessed with caution.

10.7.2 Adrenocortical Carcinoma

Adrenocortical carcinoma (ACC) is a rare neoplasm that occurs at any age, with a bimodal distribution peaking in young children <5 years and in adults aged between 30 and 40 years. Females are more commonly affected than males, and also more commonly have functional tumors. Males more commonly have nonfunctional tumors. Most patients present with Cushing syndrome, due to cortisol hypersecretion from the adrenal gland. Conn syndrome and adrenogenital syndrome are less-common clinical presentations. While large adrenal masses can be detected on ultrasound, details regarding the tumor characteristics, the presence of vascular extension, and invasion of adjacent organs is best delineated with CT or MRI. The tumor is bilateral in around 10% of cases. ACC are usually large at detection, measuring 5–10 cm at presentation. Functioning tumors tend to present at a smaller size than non-functioning tumors. On both CT and MRI, the tumor is typically heterogeneous with irregular margins. Up to 30% of cases have calcification within the mass. There may be areas of hemorrhage or cystic components. Venous invasion, such as into the inferior vena cava if right-sided, and direct extension into adjacent organs, such as the kidneys, liver, spleen, or diaphragm, can be best assessed on multiplanar imaging. On CT, the lesions enhance heterogeneously following i.v. contrast. Washout characteristics of the mass are similar to other malignant lesions, such as metastases. An assessment of metastatic disease via lymphatics to regional and periaortic lymph nodes, or hematogenous metastases to liver and lungs can be performed at the same time. Therefore, CT is the most appropriate initial modality for the assessment of ACC. ACC are characteristically hypointense on T1-weighted MRI and hyperintense on T2-weighted MRI relative to the liver. As on CT, there may be internal heterogeneity due to hemorrhage or cystic necrosis. The lesions enhance heterogeneously, and local invasion can be assessed. On ^{18}F-FDG PET imaging, the mass lesions demonstrate marked ^{18}F-FDG uptake.

10.7.3 Adrenal Myelolipoma

These are benign but uncommon tumors of the adrenal gland that are composed of mature fat and hematopoietic cells of all three lineages. They are most commonly unilateral and the incidence increases with age. Usually asymptomatic and an incidental finding, the larger tumors can be complicated by hemorrhage. CT and MRI are the imaging modalities that are best in characterizing these lesions. On CT imaging, the presence of macroscopic fat (of attenuation between −30 and – 90 HU) is diagnostic of adrenal myelolipoma. Rarely, myelolipomatous change can be seen in other cortical tumors or in cortical hyperplasia, so it is important to ensure the lesion is solitary. The lesions have a varying amount of macroscopic fat, with fat not seen in only a small proportion of these lesions. The hematopoietic component is seen as varying soft tissue attenuation within the lesion. Small areas of calcification can be seen in up to 20% of cases. Due to the high specificity of CT in determining the presence of macroscopic fat in the lesion, as well as the relative ease of availability and lower cost, it is preferred over MRI for the assessment of adrenal myelolipoma. If MRI is performed, the high fat component of the mass results in hyperintensity on T1-weighted and T2-weighted images relative to the liver, with suppression of this component on fat-suppressed images. In-phase and opposed-phase T1-weighted gradient echo sequences (see Chapter 5) have limited utility in characterization of macroscopic fat, as there tend to be less voxels that contain both water and fat to result in significant chemical shift artifact (see Chapter 5) and, therefore, signal drop on the opposed-phase T1 gradient echo sequence.

10.8 Mass Lesions of the Adrenal Medulla

10.8.1 Pheochromocytoma and Extra-adrenal Paraganglioma

Neoplasms containing chromaffin cells, called pheochromocytomas, often present due to symptoms related to the abnormal release of catecholamines and in some cases peptide hormones. The diagnosis is made through a combination of the clinical presentation, evaluation of serum and urinary catecholamine levels, and the appearance on imaging. There are classic features of pheochromocytomas that are referred to as the “rule of 10s,” as follows:

- 10% of cases are asymptomatic as the tumors are nonfunctioning.
- 10% of these tumors are extra-adrenal (found in the paraganglia, such as the carotid body or organ of Zuckerkandl, which is located along the abdominal aorta, most concentrated at the origin of the inferior mesenteric artery).

- 10% of cases are bilateral if sporadic (and this can rise to 50% if associated with a familial tumor syndrome).
- 10% are malignant, and can have metastatic disease.
- 10% are not associated with hypertension.

A previous further “rule of 10” regarding the percentage of patients that harbor a germline mutation has been revised up to 25%, as there are now six recognized genes that can result in pheochromocytomas. These tend to present in younger patients. If a familial case is suspected, this warrants a search for concurrent lesions in other organs at the time of imaging. For example, this would include a search for renal cysts, renal cell carcinoma, and pancreatic cystic neoplasms in patients suspected to have von Hippel Lindau syndrome.

Imaging for the presence of pheochromocytoma should cover the location of the paraganglia in the abdomen and pelvis to increase the detection of the 10% of extra-adrenal lesions. Paraganglia are located in the aortico sympathetic chain (including the organ of Zuckerkandl at the aortic bifurcation), the spleen, the bladder, and in the ovaries or testes. Therefore, extra-adrenal paragangliomas can occasionally be found in these sites. While large adrenal masses can be detected on ultrasound as a suprarenal mass, CT and MRI are the imaging modalities of choice if the diagnosis of pheochromocytoma is suspected. On CT, pheochromocytomas typically appear as a well-defined rounded and smoothly marginated mass. Prior to i.v. contrast, they are isoattenuating to soft tissue. Some may demonstrate areas of mural (i.e. involving the wall of the lesion) or curvilinear calcification. Macroscopic fat is rare within these tumors. Following contrast, they demonstrate avid enhancement (brighter on CT) (Figure 10.16a). If an adrenal washout study has been performed, they most commonly demonstrate washout characteristics of other malignant lesions. Some may have washout characteristics like adrenal adenomas. The larger

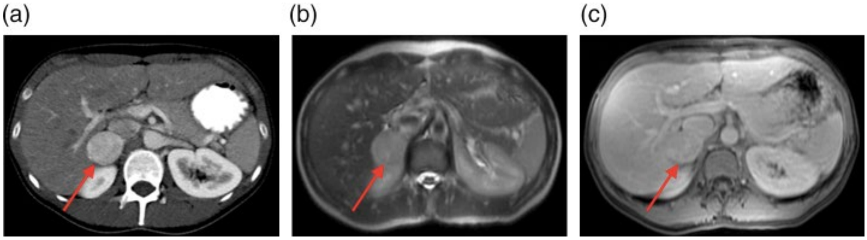

Figure 10.16 (a) Axial post-contrast CT of the abdomen demonstrates an avidly enhancing mass in the right suprarenal region (arrow). On MRI, T2-weighted image (b) demonstrates the lesion is hyperintense (arrow) and post-contrast T1-weighted image (c) demonstrates avid enhancement of the mass (arrow). At surgical resection, this was confirmed as a pheochromocytoma. The patient has a positive family history of and subsequent genetic testing for Von Hippel Lindau disease.

lesions can be heterogeneous in attenuation and enhancement, due to internal areas of necrosis and hemorrhage. On MRI, up to 70% of these lesions demonstrate hyperintensity on T2-weighted images (Figure 10.16b). This finding is sometimes referred to as “light bulb” appearance, and when present is characteristic. Lesions can, however, demonstrate heterogeneity on T2-weighted MRI due to internal hemorrhage and necrosis, with 30% having low signal intensity. On T1-weighted MRI, pheochromocytomas generally appear isointense relative to muscle and hypointense relative to liver (Figure 10.16c). Areas of hemorrhage can result in hyperintensity within the lesion on T1-weighted images. As with CT, they demonstrate avid enhancement with contrast. Some cases may demonstrate a “salt and pepper” appearance, with areas of enhancement (the “salt”) and flow-related signal voids (the “pepper”).

Paragangliomas have similar CT and MRI appearances to pheochromocytomas, occurring in characteristic locations as outlined above. Iodine-123 metaiodobenzylguanidine (^{123}I-MIBG; see Chapter 4) scintigraphy (Figure 10.17a and b) and ^{18}F-FDG PET have similar sensitivities for the detection of occult, recurrent, or metastatic disease. In the past, patients with known or suspected pheochromocytoma and/or paraganglioma were premedicated with α-adrenergic blockers prior to administration of i.v. contrast material for CT. This was to reduce the theoretical risk of elevated norepinephrine levels and precipitation of a hypertensive crisis. There have been a few recent studies, however, that failed to detect any symptoms of an adrenergic crisis in patients with pheochromocytoma or paraganglioma after contrast-enhanced CT. Premedication, therefore, is no longer routinely advocated in this group of patients.

10.9 Other Neuroendocrine Diseases

10.9.1 Pancreatic Neuroendocrine Tumors (PanNET)

Pancreatic neuroendocrine tumors (PanNET) account for 2% of all pancreatic primary malignancies and arise from the endocrine pancreas. They can arise from within or adjacent to the pancreas. While they can be benign or malignant, they also can be “functional” and produce hormones and resulting clinical syndromes. Insulinomas, the most common type of PanNET can secrete insulin leading to hypoglycemia. Gastrinomas, found in the pancreas, peripancreatic tissues, or the duodenum, produce gastrin that results in gastric acid secretion and severe peptic ulceration known as Zollinger–Ellison syndrome. Some cases are associated with MEN, and in these cases, a search for other associated neoplasms is warranted.

Cross-sectional imaging with CT or MRI is recommended when the diagnosis of PanNET is suspected (Figure 10.18a). Multiphase imaging is

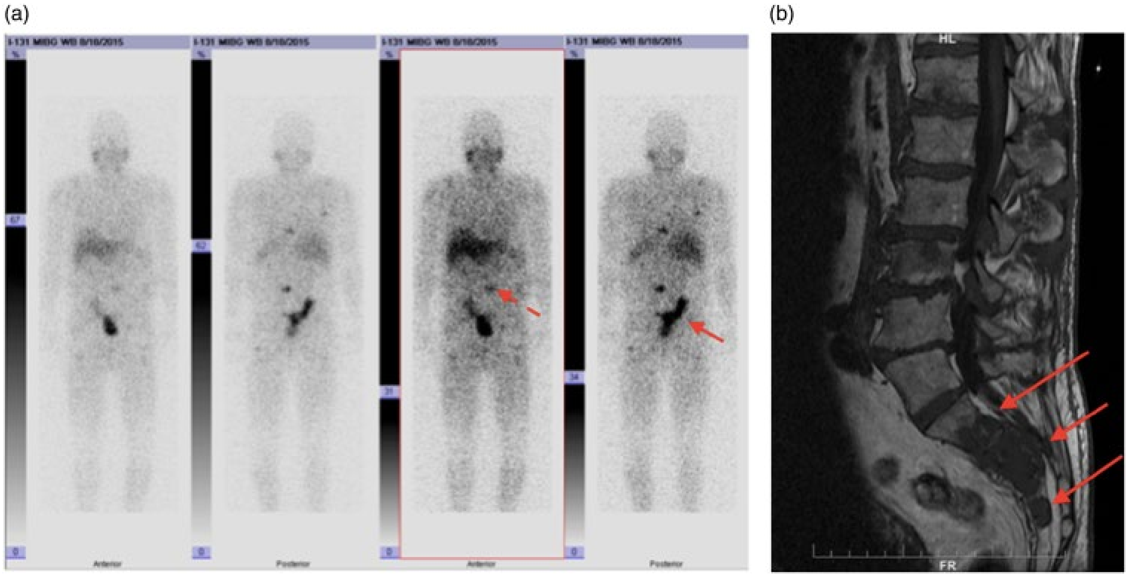
(a)
I-131 MIBG WB 8/10/2015
I-131 MIBG WB 8/10/2015
I-131 MIBG WB 8/10/2015
I-131 MIBG WB 8/10/2015
%
67
62
31
34
0
Anterior
Posterior
Anterior
Posterior
(b)
HL
FR

Figure 10.17 (a) ^{131}I-MIBG scintigraphy. The two sets of anterior and posterior views with varying signal intensity demonstrates multiple MIBG avid osseous masses within the spine and pelvis (solid arrow), with index lesions in the left of the L3 vertebral body (broken arrow), right upper sacrum, and right posterior ileum, in keeping with metastases from malignant pheochromocytoma. (b) T1-weighted image from MRI of the spine in the same patient confirms multiple masses in the sacrum from S1 to S3 (arrows) corresponding to the MIBG avid sites of metastatic disease. There is involvement of the right S1 to S3 nerve roots and epidural extension of the tumor into the sacral spinal canal.

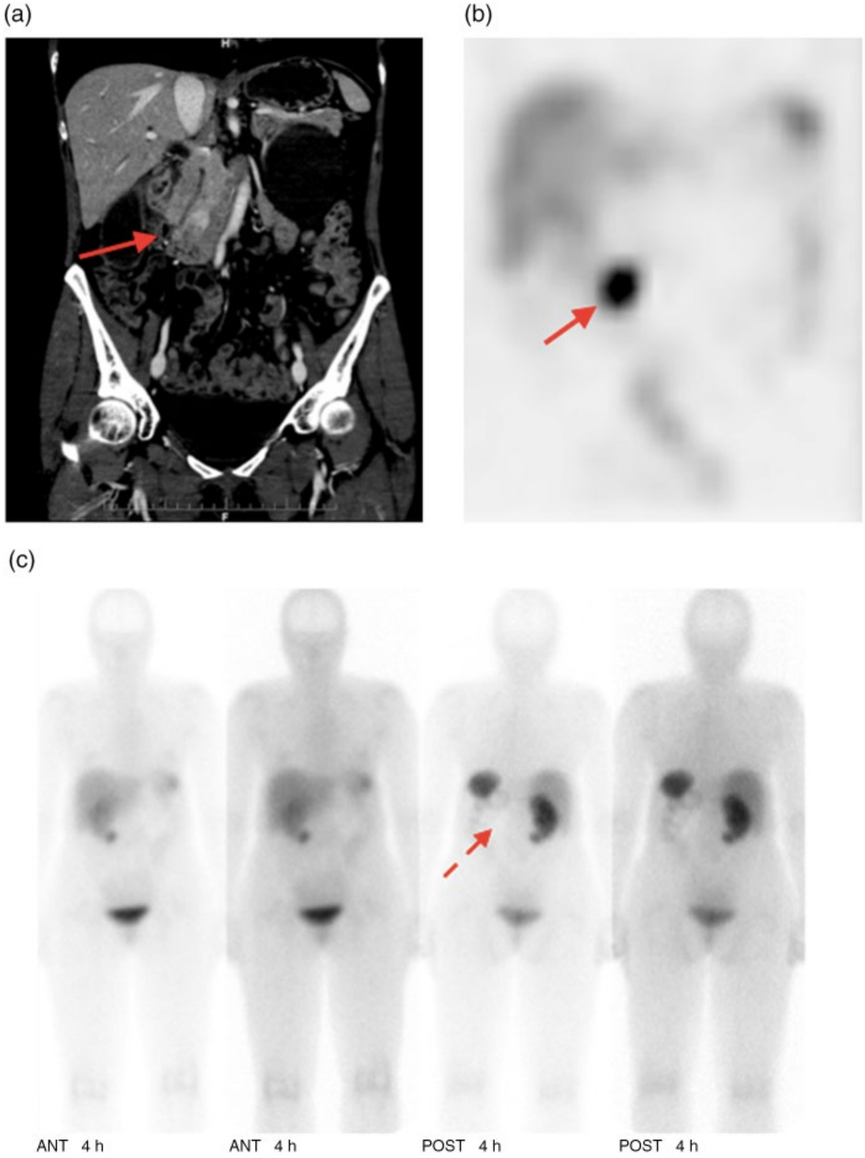

Figure 10.18 (a) Contrast-enhanced coronal CT demonstrates an enhancing mass (arrow) in the pancreatic uncinate process, which extends inferiorly from the pancreatic head. ^{111}In-pentetreotide scan (b) in the same patient demonstrates abnormal uptake in the region of the pancreatic head (arrow), corresponding to the mass detected on CT. (c) Incidental note is made of absent function in the left kidney (broken arrow) that is seen to be markedly hydronephrotic on CT due to incidental chronic ureteropelvic junction obstruction.

recommended on both CT and MRI assessment, with at least arterial and venous phases required for characterization. On CT, the lesions are usually well-circumscribed and do not result in pancreatic duct obstruction or dilation. The lesions are hypervascular and their enhancement is usually most avid in the arterial phase of enhancement. Nonfunctional tumors are usually large at presentation, and in this case may have areas of central necrosis, cystic change, or calcification. Metastases to local lymph nodes and the liver are also hypervascular, with avid enhancement in the arterial phase. MRI imaging demonstrates a lesion that is hypointense on T1-weighted images and hyperintense on T2-weighted images relative to the pancreas. The enhancement characteristics follow those as seen on CT. *trans*-Abdominal ultrasound assessment is of limited utility for PanNET, but endoscopic ultrasound has the ability to detect small lesions not seen on CT or MRI. Endoscopic ultrasound or intraoperative ultrasound can be used to localize small masses for preoperative marking to guide resection. Indium-111 pentetreotide scintigraphy (Octreotide scan), which detects expression of somatostatin receptors (see Chapter 4), has a high sensitivity of between 75 and 100% for PanNET (Figure 10.18b). This is lower in the setting of insulinoma. The utility of ^{111}In-pentetreotide scintigraphy is in confirming the diagnosis of neuroendocrine tumor. Both the primary mass and any metastases take up the radiopharmaceutical for detection using this modality.

10.9.2 Carcinoid Tumor

Carcinoid tumors are well-differentiated gastrointestinal tract neuroendocrine tumors (GI-NET). Less commonly, they arise from the lung or genitourinary tract. The primary locations of gastrointestinal carcinoids are distributed as follows:

- midgut (jejuno-ileal) – 45%
- colorectal – 31% (with 20% in the rectum)
- appendiceal – 16%
- gastric – 7%

Patients often present with carcinoid syndrome, which includes flushing, sweating, and diarrhea, and can progress to right heart failure. Carcinoid syndrome is a sign of metastatic involvement of the liver, as this allows the circulation of the hormonal factors produced by the tumors to reach the systemic circulation. When there is isolated gastrointestinal tract involvement, the hormonal factors produced drain via the portal venous system to the liver, where they are cleared by hepatic metabolism.

Cross-sectional imaging, with CT or MRI, is again the imaging modality of choice (Figure 10.19). Carcinoid tumors and their metastases are typically hypervascular, and, therefore, a biphasic study with an arterial and venous

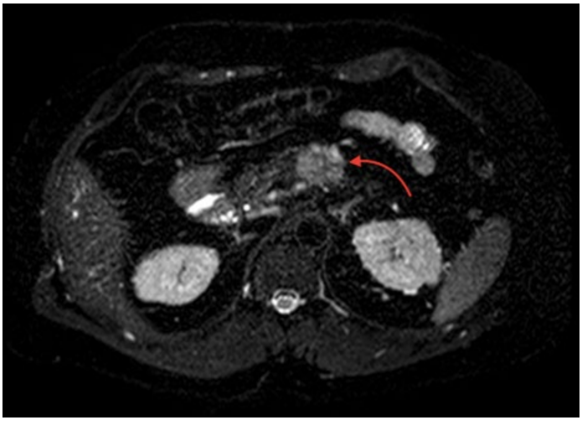

Figure 10.19 T2-weighted MRI image demonstrates a hyperintense mass (arrow) in the pancreatic body, confirmed to be a pancreatic neuroendocrine tumor.

phase is often employed. For primary lesion detection in the gastrointestinal tract, CT imaging with negative oral and, if appropriate, rectal contrast is utilized. This increases the conspicuity of the often small submucosal mass. Biphasic CT and MRI enterography protocols can also be used, with the addition of small bowel distension to maximize detection of the primary lesion. At CT, the primary carcinoid is usually a small hypervascular submucosal bowel wall mass. On MRI, the mass is usually isointense to muscle on T1-weighted images and isointense/hyperintense to muscle on T2-weighted images with enhancement following contrast. Metastatic disease is more readily detected than the primary lesion when present. There can be either direct extension through the bowel wall or metastasis to mesenteric lymph nodes. These lymph node masses can appear spiculated and result in tethering of the adjacent structures and desmoplastic reaction. Calcification is seen within these metastatic lymph node masses on CT. They demonstrate avid enhancement. Liver metastases are hypervascular, with avid enhancement on the arterial phase. Scintigraphy utilizing ^{111}In-pentetreotide (Figure 10.20) has a reported sensitivity and specificity of between 75 and 100% for carcinoid tumors, with the benefit of whole-body scanning for the detection remote metastases. The addition of SPECT/CT improves localization of involved sites.

10.10 Summary

Given the unique nature of the endocrine system in hormone production, many diseases present with unique syndromes and derangement of hormone assays that often lead to a clinical diagnosis. Clinical factors,

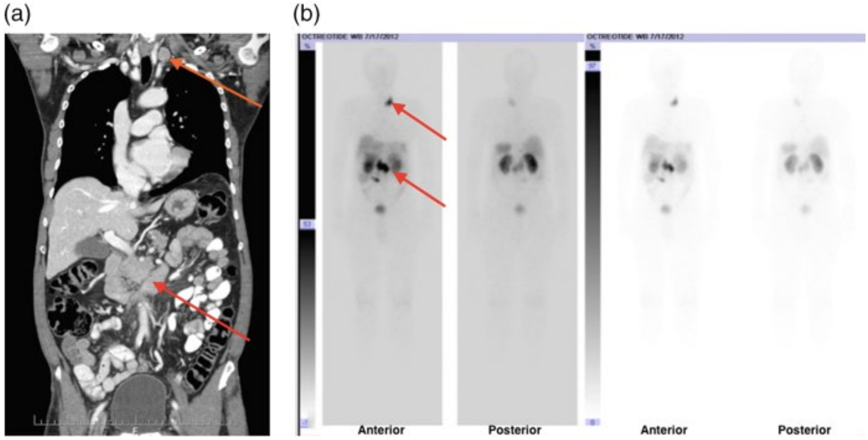

Figure 10.20 (a) Coronal contrast-enhanced CT of the chest, abdomen, and pelvis in a patient with a history of carcinoid tumor demonstrates lymphadenopathy in the left neck (top arrow) and proximal small bowel mesentery (bottom arrow). (b) These lymph node metastases are ^{111}In-pentetreotide avid at scintigraphy (arrows), in keeping with metastatic carcinoid (two sets of images are acquired at different intensities).

laboratory, and medical imaging findings all play an important role in the diagnosis and surveillance of diseases of the endocrine system as outlined in this chapter.

Additional Reading

Adami, S.Z., Nikolaidis, P., Horowitz, J.M. et al. (2016). Chemical shift MR imaging of the adrenal glands: principles pitfalls, and applications. *Radiographics* 36: 414–432.

Al-Sharif, A.A., Abujbara, M.A., Chiacchio, S. et al. (2010). Contribution of radioiodine uptake measurement and thyroid scintigraphy to the differential diagnosis of thyrotoxicosis. *Hell. J. Nucl. Med.* 13 (2): 132–137.

Boland, G.W., Blake, M.A., Hahn, P.F., and Mayo-Smith, W.W. (2008). Incidental adrenal lesions: principles, techniques, and algorithms for imaging characterization. *Radiology* 249: 756–775.

De Feo, M.L., Colagrande, S., Biagini, C. et al. (2000). Parathyroid glands: combination of ^{99m}Tc MIBI scintigraphy and US for demonstration of parathyroid glands and nodules. *Radiology* 214: 393–402.

Donahue, K.P., Shah, N.P., Lee, S.L., and Oates, M.E. (2008). Initial staging of differentiated thyroid carcinoma: continued utility of posttherapy 131-I whole body scintigraphy. *Radiology* 246: 887–894.

Dunne, P., Kaimal, N., MacDonald, J., and Syeed, A.A. (2013). Iodinated contrast-induced thyrotoxicosis. *Can. Med. Assoc. J.* 185 (2): 144–147.

Eslany, H.K. and Ziessman, H.A. (2008). Parathyroid scintigraphy in patients with primary hyperparathyroidism: ^{99m}Tc sestamibi SPECT and SPECT/CT. *Radiographics* 28: 1461–1476.

Haugen, B.R. (2009). Drugs that suppress TSH or cause central hypothyroidism. *Best Pract. Res. Clin. Endocrinol. Metab.* 23 (6): 793–800.

Haugen, B.R., Alexander, E.K., Bible, K.C. et al. (2016). 2015 American Thyroid Association Management guidelines for adult patients with thyroid nodules and differentiated thyroid cancer. *Thyroid* 26 (1): 1–133.

Heller, M.T., Gilbert, C., Ohori, N.P., and Tublin, M.E. (2013). Correlation of ultrasound findings with the Bethesda cytopathology classification for thyroid nodule fine-needle aspiration: a primer for radiologists. *AJR Am. J. Roentgenol.* 201: 487–494.

Hoang, J.K., Lee, W.K., Lee, M. et al. (2007). US features of thyroid malignancy: pearls and pitfalls. *Radiographics* 27: 847–860.

Hoang, J.K., Sung, W., Bahl, M., and Douglas Phillips, C. (2014). How to perform parathyroid 4D CT: tips and traps for technique and interpretation. *Radiology* 270: 15–24.

Hoang, J.K., Sung, W.K., Bahl, M., and Phillips, C.D. (2014). How to perform parathyroid 4D CT: tips and traps for technique and interpretation. *Radiology* 270 (1): 15–24.

Hudzik, B. and Zubelewicz-Szkodzinska, B. (2014). Radiocontrast-induced thyroid dysfunction: is it common and what should we do about it? *Clin. Endocrinol.* 80 (3): 322–327.

Intenzo, C.M., dePapp, A.E., Jabbour, S. et al. (2003). Scintigraphic manifestations of thyrotoxicosis. *Radiographics* 23: 857–869.

Johnson, P.T., Horton, K.M., and Fishman, E.K. (2009). Adrenal imaging with multidetector CT: evidence-based protocol optimization and interpretative practice. *Radiographics* 29: 1319–1331.

Kumbhar, S.S., O’Malley, R.B., Robinson, T.J. et al. (2016). Why thyroid surgeons are frustrated with radiologists: lessons learned from pre- and postoperative US. *Radiographics* 36: 2141–2153.

Maruko, Y., Abe, K., Baba, S. et al. (2012). Incremental diagnostic value of SPECT/CT with 131-I scintigraphy after radioiodine therapy in patients with well-differentiated thyroid carcinoma. *Radiology* 265: 902–909.

Mayo-Smith, W.W., Boland, G.W., Noto, R.B., and Lee, M.J. (2001). From the RSNA refresher courses: state-of-the-art adrenal imaging. *Radiographics* 21: 995–1012.

Nachiappan, A.C., Metwalli, Z.A., Hailet, B.S. et al. (2014). The thyroid: review of imaging features and biopsy techniques with radiologic-pathologic correlation. *Radiographics* 34: 276–293.

Nakajo, M., Nakajo, M., Jinguji, M. et al. (2013). Diagnosis of metastases from postoperative differentiated thyroid cancer: comparison between FDG and FLT PET/CT studies. *Radiology* 267: 891–901.

Nguyen, B.D. (1999). Parathyroid imaging with Tc-99m sestamibi planar and SPECT scintigraphy. *Radiographics* 19: 601–616.

Pitt, S.C., Sippel, R.S., and Chen, H. (2009). Secondary and tertiary hyperparathyroidism, state of the art surgical management. *Surg. Clin. North Am.* 89 (5): 1227–1239.

Ross, D.S., Burch, H.B., Cooper, D.S. et al. (2016). 2016 American Thyroid Association guidelines for diagnosis and management of hyperthyroidism and other causes of thyrotoxicosis. *Thyroid* 26 (10): 1343–1421.

Sachs, C.H. (2013). The transfer of drugs and therapeutics into human breast milk: an update on selected topics. *Pediatrics* 132 (3): e796–e809.

Smith, J.R. and Oates, E. (2004). Radionuclide imaging of the parathyroid glands: patterns, pearls and pitfalls. *Radiographics* 24: 1101–1115.

van Dalen, A., Smit, C.P., van Vroonhoven, T.J.M.V. et al. (2001). Minimally invasive surgery for parathyroid adenomas in patients with primary hyperparathyroidism: role of US with supplemental CT. *Radiology* 220: 631–639.

Vivek Singh

Dr. Vivek Singh completed his medical school training at Queen's University in Kingston, Ontario after which he completed a Diagnostic Radiology residency program at the University of Ottawa and an Abdominal Imaging Fellowship at Sunnybrook Health Sciences Centre, University of Toronto. He is currently a staff radiologist at Quinte Health Care in Belleville, Ontario.

Chirag Patel

Dr. Chirag Patel is an Assistant Professor in the Department of Medical Imaging at the University of Toronto. He is an Abdominal Radiologist and Head of Abdominal Imaging Division in the Department of Medical Imaging, Sunnybrook Health Sciences Centre and Site Lead for the Abdominal Imaging Fellowship program, at the University of Toronto. Dr. Patel has subspecialist training in Abdominal Imaging (University of Toronto) and Interventional Radiology (London, UK), having obtained his undergraduate and postgraduate qualifications in London, UK. His expertise is in hepato-pancreatic biliary and genitourinary imaging, and is involved in research and education in these areas.

Medical Imaging for Health Professionals: Technologies and Clinical Applications, First Edition.
Edited by Raymond M. Reilly.
© 2019 John Wiley & Sons, Inc. Published 2019 by John Wiley & Sons, Inc.

11

Abdominal Imaging

Vivek Singh and Chirag Patel

11.1 Introduction

Gastrointestinal imaging covers a vast array of organ systems and pathology, anatomically extending superiorly from the esophagus and inferiorly to the anal canal. Multiple interconnected organ systems located within the complex compartmental anatomy of the abdomen and pelvis can make for challenging imaging interpretation. This chapter features representative imaging examples of commonly encountered pathological processes involving the digestive, hepatobiliary, pancreatic, and lymphatic systems, together with those that affect the peritoneal compartment. The full armament of imaging modalities are used to characterize gastrointestinal pathology, which often have complementary roles. Plain film X-ray, ultrasound (US), fluoroscopy, CT, MRI, and nuclear medicine imaging all have a role in imaging, with a combination of imaging techniques often required to reach a conclusive diagnosis. Patient factors remain an important consideration when selecting an imaging method for a given clinical situation, including clinical stability of the patient, body habitus, pregnancy, age of the patient, allergy to contrast agents, impaired renal function, and cognitive status, to name of few. In addition to the diagnostic ability of medical imaging, there is (and will continue to be) progressive utilization of imaging for the purposes of guided intervention to achieve histological diagnosis (i.e. biopsy), assess functional parameters, and offer minimal access therapies in a wide range of clinical scenarios. This chapter provides an insight into abdominal imaging, highlighting commonly seen and major pathological processes through the lens of radiology, covering a broad array of organ systems.

Medical Imaging for Health Professionals: Technologies and Clinical Applications, First Edition.
Edited by Raymond M. Reilly.
© 2019 John Wiley & Sons, Inc. Published 2019 by John Wiley & Sons, Inc.

11.2 Surgical Sieve

The "surgical" sieve represents an approach to forming a cohesive list of diagnoses and differential diagnoses when presented with a clinical or imaging scenario. This works particularly well with respect to imaging findings, given that a certain imaging appearance could be attributed to several different causes/etiologies. Therefore, the surgical sieve allows one to approach an imaging finding or constellation of findings, to form a structured and reasoned response when asked about a particular condition, sign, or finding. Table 11.1 shows a commonly used mnemonic to serve this purpose and may be applied to any section of this chapter (and likely book) to expand upon the pathologies seen involving the various organs/organ systems.

11.3 Peritoneum/Mesentery

The peritoneum is a specialized membrane that lines the peritoneal cavity and covers the majority of the intra-abdominal and pelvic organs/structures and abdominal wall, although typically not seen on imaging unless affected by pathology. Importantly, the peritoneum not only provides a support structure for the abdominal organs (solid and hollow viscera), but also as a pathway for the vascular, lymphatic, and nervous system. By virtue of its elaborate configuration, it also provides a continual flow of fluid (typically trace amounts) through the peritoneal cavity, essential for normal physiological function. So why does a structure, by all accounts, "invisible" on almost all imaging modalities feature prominently in a chapter about abdominal imaging? Understanding this complex structure is essential in

Table 11.1 Surgical sieve – common root etiological processes, which may be used to form structured differential diagnoses for a given sign, symptom, or finding.

Mnemonic: VITAMIN	Etiologic process
V	Vascular
I	Infective/inflammatory
T	Traumatic
A	Autoimmune
M	Metabolic
I	Iatrogenic/idiopathic
N	Neoplastic

allowing one to grasp the complex anatomy of the abdomino-pelvic structures, their relationship with one another, understand localization and spread of disease processes, and formulate diagnoses and differential diagnoses by imaging. Ligaments and mesenteries represent specialized peritoneal folds that act as support structures, but also important pathways and barriers to the spread of disease.

Pathology involving the mesentery and peritoneum can be broadly divided into acute and non-acute etiologies for the purpose of this discussion. Acute pathology includes the presence of gas or blood within the peritoneal cavity, referred to as pneumoperitoneum and hemoperitoneum, respectively. Fluid within the peritoneal cavity may be seen with both acute and chronic pathologies. Commonly seen non-acute pathology includes malignant deposits and fluid involving the peritoneum and peritoneal cavity, referred to as peritoneal carcinomatosis and ascites, respectively.

11.4 Acute Peritoneal Pathologies

11.4.1 Pneumoperitoneum

Pneumoperitoneum refers to the presence of gas within the peritoneal cavity, which may be free or localized. The most concerning source of pneumoperitoneum is from bowel (including gastric) perforation, either related to traumatic injury or secondary to a disease process involving the gastrointestinal (GI) tract. Pneumoperitoneum from this source is generally treated as a surgical emergency, often requiring emergent surgery. While there are benign causes of pneumoperitoneum (e.g. postoperative state), the majority of patients with acute pneumoperitoneum have clinical features consistent with an emergent disease process.

Plain film X-ray assessment is usually the first imaging examination performed in patients with an acute abdomen, primarily to assess for the presence of free peritoneal gas. This study is best performed with patient sitting upright, where the air rises to the least-dependent portion of the abdomen (underneath the hemidiaphragms), resulting in a gas lucency seen between the hemidiaphragm and adjacent solid viscera, best seen on the right due to the presence of the liver (Figure 11.1). Gas under the left hemidiaphragm can be seen normally, due to the presence of normal gas within the stomach. CT is the imaging modality of choice in a patient with an acute abdomen. In the presence of pneumoperitoneum on plain film X-ray, patients may be taken straight to surgery without any further imaging investigations, in the correct clinical setting. However, more commonly, patients will undergo unenhanced or contrast-enhanced CT prior to surgery (given the rapidity of imaging acquisition) to identify the site of perforation and help plan the surgical approach. CT is highly

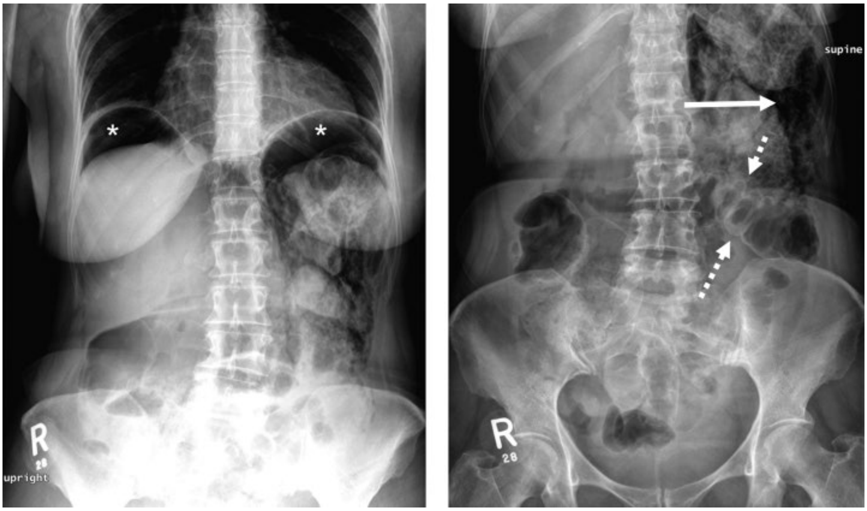

Figure 11.1 Pneumoperitoneum. Upright (left) and supine (right) abdominal plain films. Erect film (left) demonstrates free peritoneal gas below the diaphragm (*), located within the nondependent space. Supine film (right) demonstrates extra-luminal gas within the left abdomen (solid arrow), outlining the left kidney, consistent with retroperitoneal gas. Gas outlines the wall of the large bowel (both inner and outer margin – dashed arrow) signifying pneumoperitoneum (Rigler's sign).

sensitive in detecting localized and free peritoneal gas, together with identifying the source of the pneumoperitoneum and other complicating features elsewhere within the abdomen or pelvis.

11.4.2 Hemoperitoneum

Hemoperitoneum is most commonly seen in the setting of acute traumatic injury to the intraperitoneal organs where vascular injury to a specific organ causes blood loss into the peritoneal cavity. The most commonly injured intraperitoneal organs are the spleen and liver. In these cases, hematoma is generally seen surrounding the organ in question and tracking into the pelvis, often layering within the most-dependent portion of the peritoneal cavity (Figure 11.2). Mesenteric blood (hematoma) may be seen secondary to direct injury to the mesentery, usually related to trauma. Mesenteric hematoma is important to recognize due to the fact that the rich network of blood supply to the bowel runs through the mesentery and thus, injury to the mesentery may result indirectly in bowel ischemia and infarction.

Hemoperitoneum may be seen on US, typically as free fluid (often slightly complex in nature), commonly noted with a Focussed Assessment with Sonography in Trauma (FAST) scan performed following acute trauma.

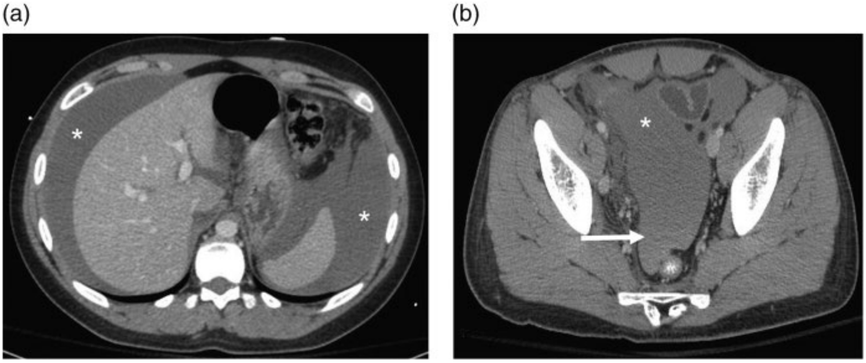

Figure 11.2 Hemoperitoneum. (a) Axial CT through the upper abdomen in a patient with abdominal trauma. Large volume fluid/blood is accumulated around the liver and spleen (*). (b) Axial CT image through the pelvis, demonstrating large volume fluid/blood (*) from abdominal trauma. Note, subtle change in shade of the pelvic fluid (darker to brighter from top to bottom), with brightest components within the most dependent part of the pelvis (arrow) signifying denser blood products, typical for hemoperitoneum.

However, unenhanced and contrast-enhanced CT remains the imaging modality of choice in assessing the distribution, volume, and site of origin of peritoneal blood in acute and non-acute settings. Blood may have a variable appearance on imaging, depending on its acuity/chronicity. Clotted blood is denser than unclotted blood and will therefore appear brighter on CT. This sign can be helpful to identify the site of bleeding as coagulated blood will often develop right at the site of bleeding, termed the *sentinel clot sign*. In the setting of active bleeding, contrast blush or extravasation (i.e. focal areas of contrast leak from blood vessel(s)) can often be seen at the site of bleeding, aiding in the treatment planning of patients acutely (i.e. image-guided embolization vs. surgery). Mesenteric hematoma is best detected by CT, seen as a focal/localized area of blood products accumulating within the mesentery, and often associated with free blood products elsewhere within the peritoneal cavity. Careful search must be performed of the bowel to look for injury, though bowel injury may be occult on CT.

11.4.3 Ascites

Ascites refers to excessive free fluid within the peritoneal cavity and can be subdivided based on the amount of protein present in the ascitic fluid; low protein content fluid called *transudative* and high protein fluid called *exudative*. Common causes of transudative ascites include liver cirrhosis, heart failure, renal failure, and fluid overload. Exudative ascites can be due to malignancy (associated with *peritoneal carcinomatosis,* discussed in the next section), infectious processes (e.g. tuberculosis), or inflammatory processes, among other causes. When large in volume, ascites may be detected on plain film X-ray imaging, seen by enlargement of the abdominal cavity with the obscuration of the normal solid visceral silhouettes, psoas muscles (hip flexor muscles, running adjacent to the lumbar spine), and loss or displacement of the lateral abdominal fat structures. Furthermore, bowel gas may be more centrally located.

US is highly sensitive in the detection of ascites and often the imaging modality of choice. When ascites is simple in nature, the presence of black-appearing fluid on the US image surrounding the intraperitoneal organs is seen; however, complexity may be seen depending upon the underlying cause. When large enough in volume, bowel loops will be seen floating within the fluid. US is particularly helpful to guide drainage of ascites. CT and MRI remain the mainstay of imaging techniques in the workup of patients with ascites, primarily to identify the cause of ascites (not diagnosed from history or physical examination), but also to assess for complex ascites (compartmentalized, hemorrhagic, or infected ascites), which can aid in patient management. Typically, intravenous contrast enhancement is required in this setting.

11.4.4 Peritoneal Carcinomatosis

Peritoneal carcinomatosis represents metastatic deposits within the peritoneal cavity, which is commonly accompanied by ascites (Figure 11.3). Numerous primary malignancies can cause peritoneal carcinomatosis, including tumors of ovarian, gastric, pancreatic, and colorectal origin, among others. While imaging is valuable in assessment of peritoneal carcinomatosis, subtle carcinomatosis is often not visible on imaging and surgical exploration may be required for complete staging.

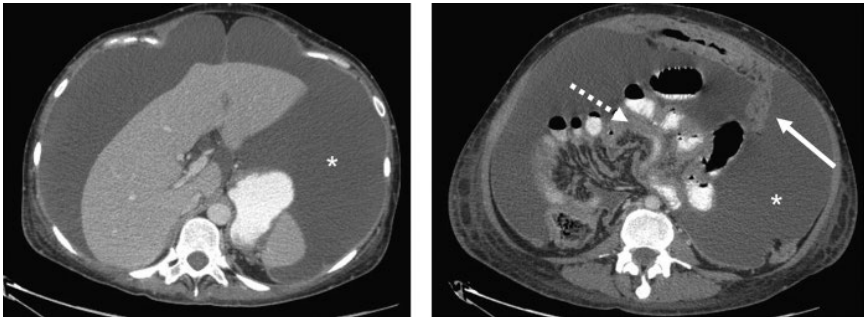

Figure 11.3 Peritoneal carcinomatosis. Axial contrast enhanced CT imaging demonstrating significant ascites in a patient with peritoneal carcinomatosis (*). Thickening of the omentum and mesenteric folds (both arrows – light gray areas) secondary to metastatic deposits to the peritoneum. Note that serosal thickening of the small bowel (dashed arrow) and transverse colon is present, predisposing this patient to bowel obstruction.

MRI is the most sensitive imaging modality in detecting peritoneal carcinomatosis, but it is seldom used as a primary method in its diagnosis, given it remains suboptimal compared to direct visualization. Contrast-enhanced CT remains the workhorse for imaging and staging of malignant disease within the abdomen and pelvis due to its availability, lower cost, higher spacial resolution, and better patient tolerance than MRI. Peritoneal carcinomatosis appears as nodularity or stranding within the peritoneal fat, with more advanced cases demonstrating measurable disease, sometime tending to form large confluent masses typically involving the greater omentum (a specialized peritoneal ligament), termed an "omental cake." ^{18}F-FDG PET-CT (see Chapters 3 and 4) is a useful staging tool for malignant disease, particularly in detecting occult peritoneal malignant disease, often changing patient management in these settings. However, peritoneal disease of <1 cm or smaller may sometimes be below the threshold of detection by PET. In addition, other causes of peritoneal disease (infection vs. inflammation) may lead to a false diagnosis of peritoneal carcinomatosis in certain clinical situations. Early, small volume, or diffuse tiny peritoneal malignant spread can be inconspicuous on any imaging and therefore, in those undergoing surgical intervention (particularly in those requiring potentially morbid surgery), patients may undergo initial minimally invasive laparoscopic assessment of the peritoneum to exclude such disease.

11.5 Gastrointestinal Tract

The GI or digestive tract extends from the mouth, all the way through to the anus. As such, its imaging can be complex, encompassing various body parts, including the head and neck, thorax, abdomen, and pelvis. Imaging of the mouth and throat (oropharynx and larynx) is typically incorporated by subspecialists in head and neck imaging and therefore beyond the scope of this section. This section aims to highlight imaging of some of the common presenting GI tract pathologies encountered in both the acute and non-acute setting.

Plain film radiography of the GI tract has seen a steady decline in its utility, but still serves as a valuable screening study, particularly in the acute setting. As mentioned, in a small proportion of cases, a grossly abnormal plain film X-ray examination (in the correct clinical context) may be enough to base further management, treatment, and/or surgery without the need for further complex imaging or work-up, although this is increasingly uncommon. CT, US, fluoroscopy, and MR imaging are the mainstay for more comprehensive imaging of the GI tract, with CT by far the most utilized in practice. CT allows rapid image acquisition with relatively high spatial and contrast resolution, but also allows for assessment of the peritoneal, retroperitoneal compartments, solid organs, together with their respective vascular and lymphatic structures, all at the same time. US and MRI are less commonly used in bowel imaging, but certainly have a specific role as detailed below. In a patient with an acute abdomen, an abdominal plain film X-ray series is typically the first-line imaging study, consisting of a supine film of the abdomen and pelvis, together with an erect/upright or decubitus film of the abdomen. Erect and decubitus films allow for the detection of free peritoneal gas (pneumoperitoneum) as previously discussed (Figure 11.1), air-fluid levels within the bowel (or other fluid collections) and the supine film allow assessment of the hollow and solid viscera to a limited extent. If this imaging series/screen is negative, the decision to move on to more comprehensive imaging (typically CT) becomes a clinical one, based on the patient's history, examination, and lab findings.

11.5.1 Bowel Obstruction

Bowel obstruction is a common cause of an "acute surgical abdomen", with radiology not only playing a key part in diagnosing the presence of an obstruction, but also identifying the site and cause of obstruction, together with any potential complicating features (such as bowel ischemia and/or perforation). The site of obstruction (gastric, small bowel vs. large bowel) is important to identify, as the cause of obstruction and subsequent management may differ between them. The common causes of small and large bowel obstruction are listed in Table 11.2.

Table 11.2 Common causes of bowel obstruction.

Small bowel obstruction (SBO)	Large bowel obstruction (LBO)
Adhesions	Primary colon cancer
Hernia	Malignant metastatic disease
Volvulus[a]	Diverticulitis
Extrinsic tumor	Volvulus[a]
Intraluminal lesions • Intussusception[b] • Tumor • Foreign body • Gallstones • Bezoar[c]	Ischemia

[a] When a bowel loop twists on the mesentery resulting in an obstruction.

[b] When a loop of bowel telescopes into adjacent bowel potentially causing obstruction.

[c] Ingested intraluminal foreign body, often composed of hair, causing obstruction.

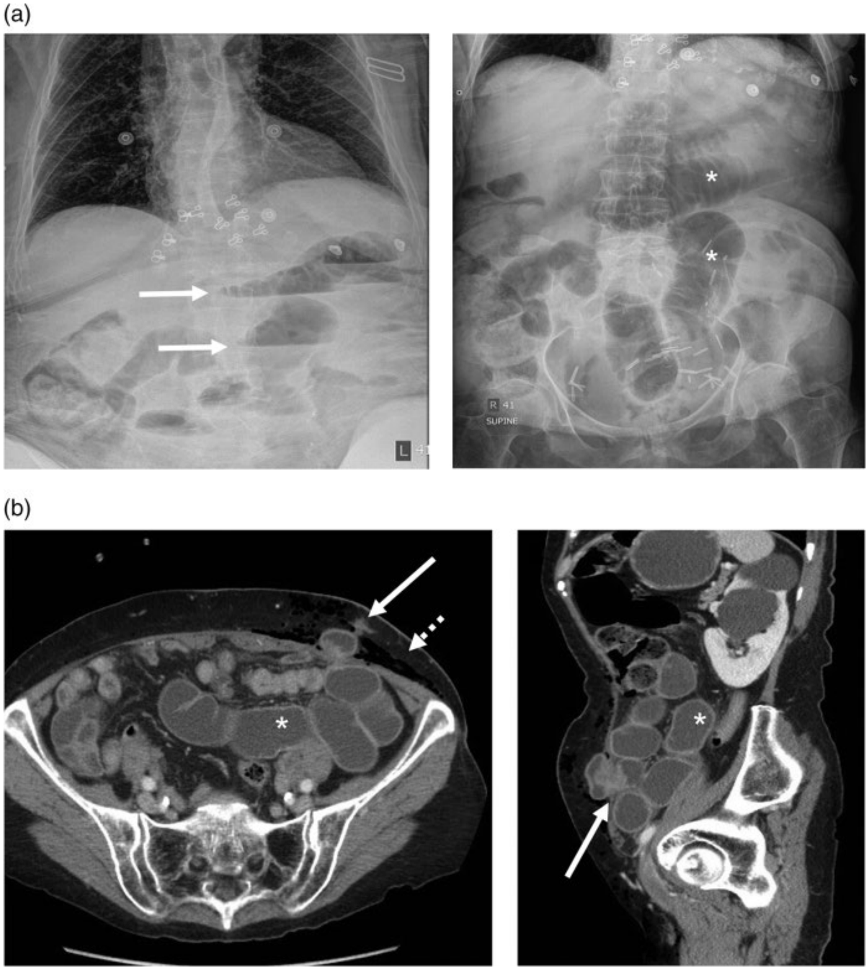

Figure 11.4 (a) Small bowel obstruction (SBO) – abdominal radiographs (top row). The upright view (left image) of the abdomen demonstrates multiple air-fluid levels (arrows) in dilated loops of small bowel. On the supine view (right image), multiple dilated loops of bowel (*) are present throughout the central abdomen. (b) SBO on CT (bottom row) in a different patient. Axial and sagittal images from a contrast-enhanced CT study, demonstrating dilated loops of small bowel within the abdomen (*) with focal herniation of a small bowel loop through the anterior abdominal wall (solid arrow), corresponding to port site from recent laparoscopic abdominal surgery. Note, associated gas within soft tissues of the anterior abdominal wall (dashed arrow), consistent with recent surgery.

Small bowel obstruction (SBO) on plain X-ray film imaging includes: dilation of the small bowel (measuring >3.0 cm in diameter), the presence of air-fluid levels (typically at different levels/heights) (Figure 11.4a), and the presence of gas trapped between folds in a dilated fluid-filled segment giving rise to the "string of pearls" sign. CT imaging is the modality of choice in imaging SBO. In addition to the above, CT allows demonstration of the degree and extent of dilated small bowel, identification of the location and cause of the obstruction, and allows assessment for complicating features (Figure 11.4b). Bowel ischemia may be seen as a complicating feature of high-grade bowel obstruction due to impairment of the blood supply to the dilated gut. On CT, features include thickening and edema of the bowel wall, decreased or lack of bowel mucosal (wall) enhancement, congestion and haziness of the surrounding bowel mesentery (including mesenteric hemorrhagic changes), culminating in bowel infarction and formation of gas within the bowel wall (pneumatosis) (Figure 11.5), which may ultimately extend into the mesenteric and portal venous circulation. Although the presence of pneumatosis (bowel wall gas), mesenteric, and portal venous gas may be seen in other states (some benign), in this clinical context/scenario these findings are associated with a high mortality rate. Bowel perforation may be identified on plain film X-ray with free peritoneal gas (as described above). Detection of bowel perforation is more sensitive with CT, particularly in cases with only a small amount of gas present, localized gas, or perforation involving a bowel loop that is retroperitoneal.

Large bowel obstruction (LBO) is a less commonly seen, although more prevalent in the older adult population. On imaging, the large bowel is dilated to measure >5.0 cm, although the cecum is required to be dilated >8.0 cm. Large bowel dilation >10 cm is associated with a high risk of perforation. On plain film X-ray, the dilated large bowel is typically seen at the periphery of the film and may be associated with bowel wall thickening, gas

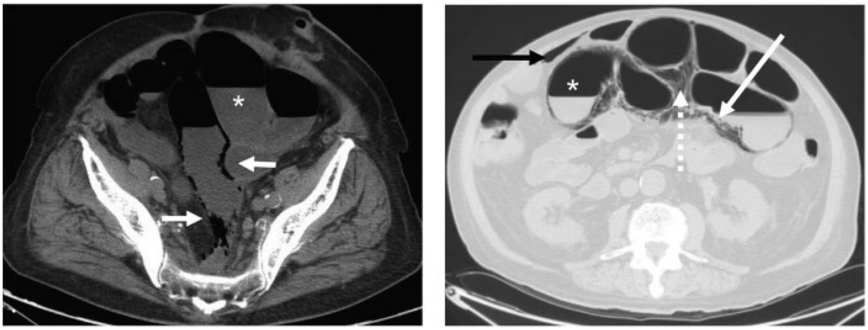

Figure 11.5 Small bowel obstruction (SBO) with ischemia and perforation. Unenhanced CT. In top image, dilated loops of small bowel with distinct air-fluid level (*) are consistent with SBO. Central small bowel loops demonstrate gas within the walls (solid white arrow) in keeping with pneumatosis, a finding that can be seen with established bowel ischemia. In bottom image, adjusting the intensity window levels when viewing the images allows greater differentiation, appreciation, and visualization of the distribution of gas within the abdomen. Gas seen tracking outside the bowel into its surrounding mesentery (dashed arrow) together with free peritoneal gas (black arrow) are consistent with perforation.

(pneumatosis), and/or the presence of free peritoneal gas, depending on the severity of obstruction. In cases of LBO, the small bowel may or may not be dilated, depending on the competency of the ileo-cecal valve. CT is the imaging modality of choice in further evaluating the extent and location of obstruction, but also in identifying the cause, which can significantly impact the patient's management. Given that colorectal carcinoma accounts for a significant proportion of LBO causes, identifying and planning in this group of patients is key to successful management. A typical plain film X-ray and CT of a colorectal cancer in a patient causing an acute LBO is shown in Figure 11.6. Ischemic change and perforation findings on CT are similar to those observed for SBO.

11.5.2 Diverticulitis

Characterized by the inflammation or perforation of small colonic outpouchings of the mucosa and submucosa, this most commonly involves the sigmoid colon. Diverticulosis simply refers to the presence of these outpouchings from the bowel (large bowel most common), but without inflammation, and these are often associated with bowel wall thickening of the involved segment and may be a cause of GI tract blood loss. Acute inflammation of a diverticulum (or several diverticula), results in abdominal pain that is often nonspecific and may mimic other pathological processes. CT is the imaging modality of choice in the detection of acute diverticulitis, demonstrating thickening of the involved segment of bowel wall and "culprit" diverticulum with surrounding inflammation, typified by stranding of the fat surrounding the bowel (Figure 11.7). Furthermore, CT allows assessment of any complicating features, primarily related to perforation and presence of an associated abscess, involvement of surrounding structures (bowel, abdominal wall, gynecological, or genito-urinary organs), or free peritoneal perforation and fecal contamination. In a small proportion of cases, diverticulitis (acute or chronic) may result in bowel stricturing, resulting in acute LBO.

In acute cases of diverticulitis, gas or thrombus may be seen in the associated bowel mesentery or portal venous system and these patients are at risk of developing hepatic abscesses (due to the GI tract venous circulation passing through the liver) (Figure 11.7). Ultrasonography is not typically used in patients with suspected diverticulitis (due to the high diagnostic accuracy of CT vs. US, and limitation of US to detect complicating features); however, US can be highly specific for acute diverticulitis, demonstrating bowel wall and culprit diverticulum thickening and increased echogenicity of the surrounding fat (signifying acute inflammation) with or without associated fluid/collection (Figure 11.8). CT and US are modalities typically used in managing abscesses (mesenteric and hepatic) by way of

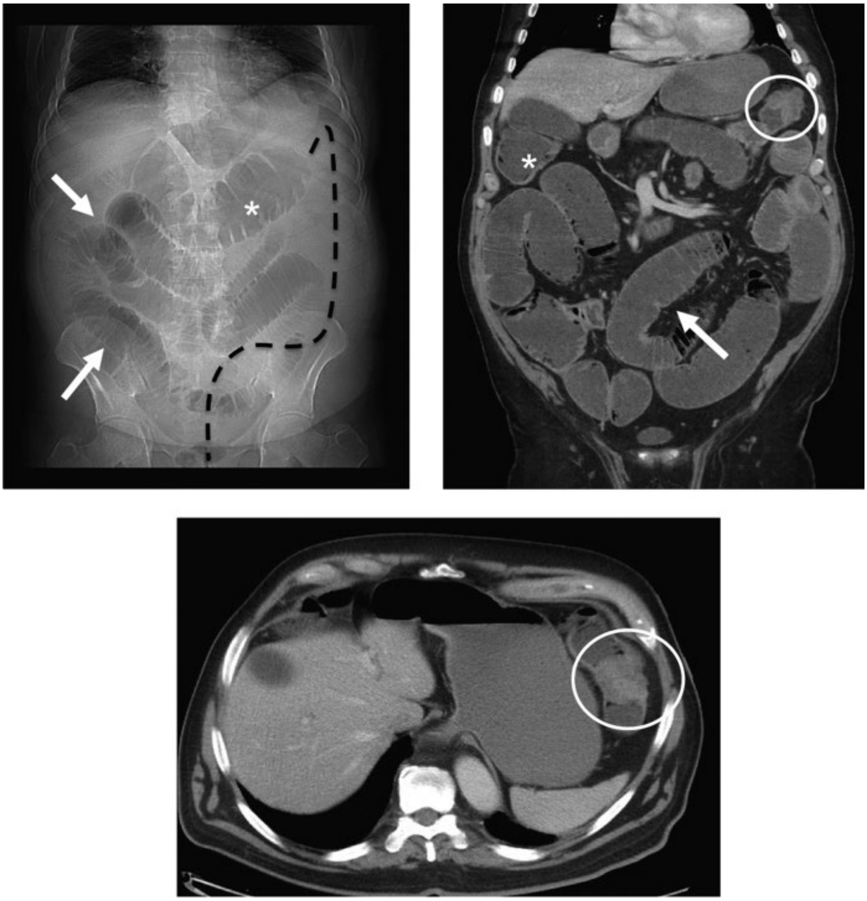

Figure 11.6 Acute large bowel obstruction (LBO) – plain X-ray film and contrast-enhanced CT. Plain film (top left image) shows dilated transverse colon (*) together with dilated small bowel loops (arrows) consistent with LBO. Note the paucity of gas within the expected location of the downstream large bowel (descending, sigmoid colon, and rectum) on plain film (dashed black line), due to a splenic flexure obstructing lesion. Coronal CT (top right image) and axial CT (bottom image) show dilated fluid-filled large (*) and small bowel loops (arrow) secondary to an "apple-core like" colonic tumor (circled) involving the splenic flexure, consistent with a colon cancer.

placement of drainage catheters. Fluoroscopic contrast enema imaging plays a limited role in the imaging of chronic complicated diverticulitis, primarily in confirming persisting bowel perforation or identifying and mapping of sinus/fistulous tracts for the purposes of surgical planning,

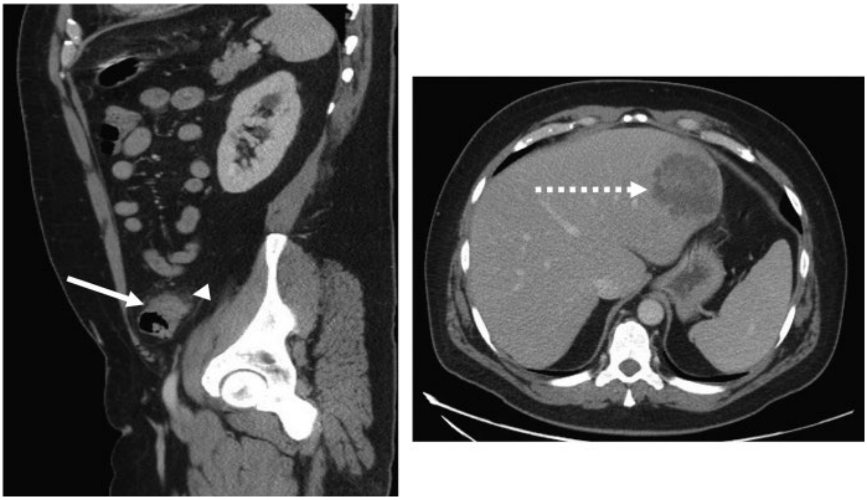

Figure 11.7 Complicated acute diverticulitis – contrast-enhanced CT. Left image shows a focal acute diverticulitis involving a segment of the proximal sigmoid colon demonstrating focal wall thickening (asymmetric) (solid arrow) due to an inflamed diverticulum. Haziness of the surrounding fat (fat stranding) adjacent to the inflamed diverticulum and bowel wall thickening (arrow head) is seen with inflammation. Right image shows a lobulated hypoattenuating (darker) lesion within the left lobe of the liver with peripheral/rim enhancement (brighter line outlining its contour), consistent with a hepatic abscess secondary to seeding of infective material from the infected/inflamed diverticulum, via the portal venous circulation.

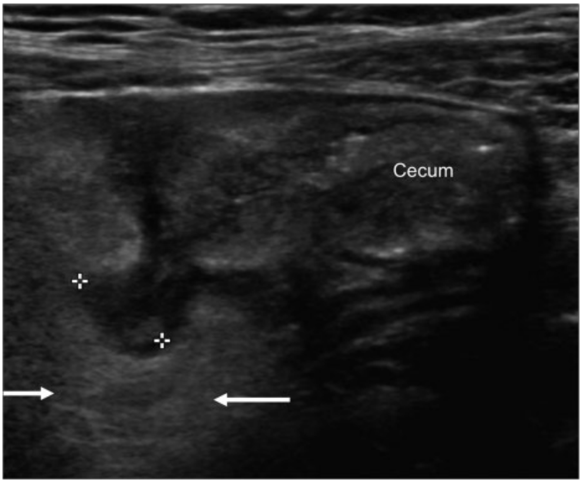

Figure 11.8 Acute cecal diverticulitis – ultrasound. Focal outpouching from the cecal wall (+ calipers) consistent with a diverticulum with associated diverticular wall thickening and inflammation of the surrounding fat, which becomes more echogenic (returns ultrasound signal) in this state (arrows). No focal collection/abscess or extra-luminal gas is seen in this case to suggest complicating features.

although by in large, this is now performed with CT with rectally instilled water-soluble contrast.

11.5.3 Appendicitis

Acute inflammation of the appendix is one of the most common causes of an acute abdomen. The clinical diagnosis is usually straightforward when a classic history and examination findings are present; however, a cohort of patients present with atypical features that pose a diagnostic challenge. Plain film X-ray has little utility in the diagnosis of acute appendicitis, although typically performed as a first-line "acute abdomen" screen, mainly to exclude major complications (pneumoperitoneum). In pediatric, thin young adult, and pregnant patients, US is used as the first-line imaging modality in the majority of centres. US allows for real-time imaging of the right lower quadrant, without exposing the patient to ionizing radiation and in experienced hands, has high diagnostic accuracy.

US signs of an acute appendix include: a noncompressible appendix measuring ≥7 mm, focal pain overlying the appendix (a sonographic McBurney's sign), the presence of an appendicolith (i.e. an obstructing body, often a stone, obstructing the lumen of the appendix), Doppler US vascular flow within the wall of the appendix, and surrounding echogenic fat indicating inflammation (Figure 11.9). In complicated cases, a focal defect in the wall of the appendix, surrounding fluid collection, and/or gas outside the appendix may be seen, suggesting perforation. There may be reactive changes to the adjacent small bowel and cecum and associated dilation of the bowel, related to reactive paralysis (i.e. ileus). CT remains the most used examination in those suspected of having an acute appendicitis, either as the initial imaging modality or when US findings are nondiagnostic or equivocal. Similar to US, the appendix appears dilated (≥7 mm) with abnormal enhancement, fat stranding around the appendix, surrounding small volume fluid, and the presence of an appendicolith (Figure 11.10). Other causes of appendiceal obstruction (as a cause of acute appendicitis) should be considered in the imaging workup, including an underlying cecal or appendiceal malignancy, although this is less common. Complicating features such as abscess formation and perforation are better assessed with CT compared to US and may also allow planning for percutaneous drainage catheter insertion or surgery. Furthermore, CT is the imaging modality of choice in assessing postsurgical complications following appendectomy, particularly related to abscess formation at the site of surgery or elsewhere within the peritoneal cavity. MR imaging of the appendix is typically reserved for cases of suspected appendicitis that are nondiagnostic or equivocal on US in pregnant or pediatric patients.

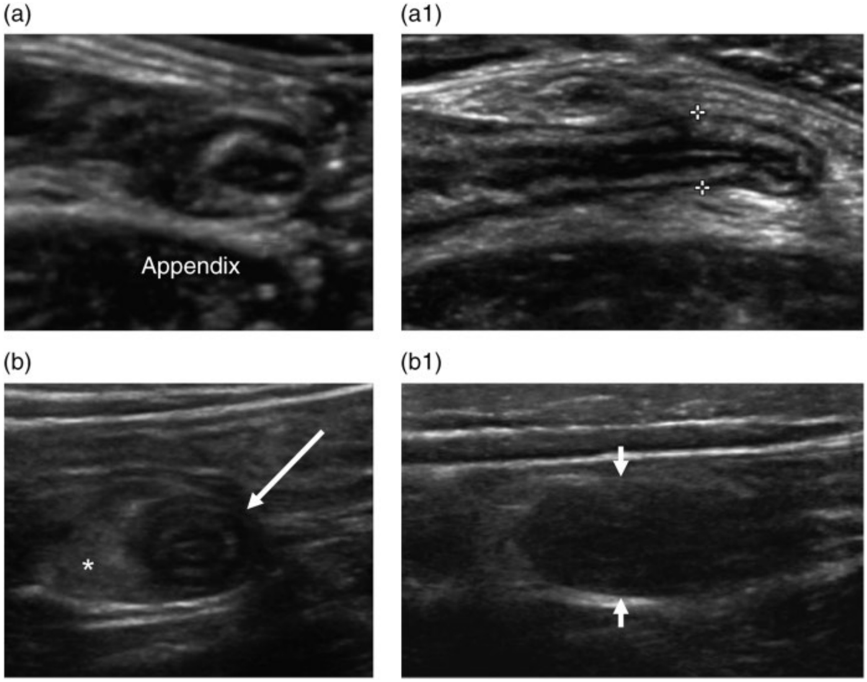

Figure 11.9 Acute appendicitis – ultrasound. Imaging of a normal appendix in cross-section (a) and long-axis (along its length) (a1). Note, nearly all of the bowel wall layers are visible in the normal appendix. A thickened and mildly dilated appendix (arrows) in cross-section (b) and long-axis (b1) with loss of the normal wall layer differentiation, together with surrounding echogenic fat (*) consistent with inflammation. No focal collection/abscess or extra-luminal gas is seen, which if present would suggest complicating features.

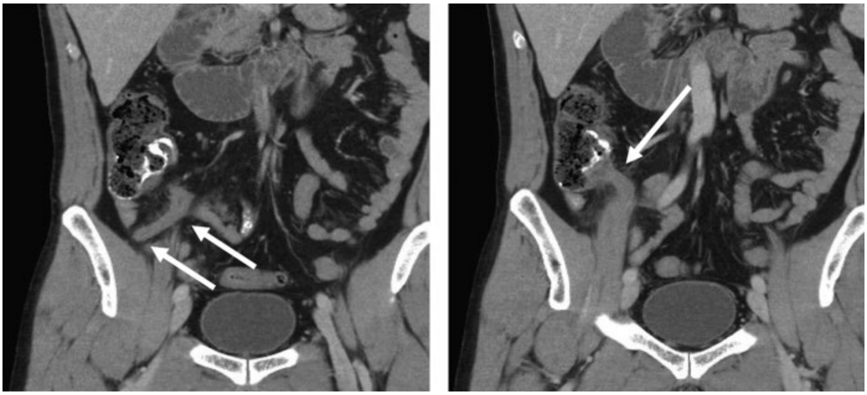

Figure 11.10 Acute appendicitis on coronal CT. Left image: A thickened appendix is seen in the right lower quadrant (arrows) with mild surrounding inflammatory stranding of the fat. The tip of the appendix is seen without evidence of perforation (no extra-luminal gas or focal wall defect). Right image: The inflamed appendix can be seen arising from the cecal pole (arrow).

11.6 Inflammatory Bowel Disease

While there are numerous underlying pathological processes responsible for this spectrum of disease, Crohn's Disease (CD) and ulcerative colitis (UC) are best known in this category, both with characteristic imaging features.

11.6.1 Crohn's Disease

CD may affect the GI tract anywhere from mouth to anus, but most commonly involves the terminal ileum and proximal colon. Terminal ileal involvement is by far the most common, followed by colonic and rectal involvement. Proximal small bowel involvement (without terminal ileal involvement) may be seen, although much less frequently.

Plain film X-ray, US, fluoroscopy, CT, MRI, and nuclear medicine imaging are used in the imaging of this complex disease. Endoscopic evaluation is almost always routinely performed on the upper and lower GI tract, not only allowing for visual assessment of active mucosal disease, but also having the advantage of obtaining tissue samples for histopathological analysis required for definitive diagnosis. However, limitations of conventional endoscopy include the inability to image the jejunum and ileum or assess for any extramural (i.e. outside of bowel) complicating features. In this group, some form of small bowel imaging is commonly performed. Barium small bowel follow-through (SBFT) (Figure 11.11) is a fluoroscopic imaging technique to assess the small bowel from the duodenum to terminal ileum, as a single contrast method, allowing one to determine the location, extent, and severity of mural (i.e. bowel wall) changes. Fluoroscopy essentially refers to the real-time acquisition of X-ray images in order to dynamically assess changes in structures such as bowel. Mucosal and deep ulcerations, fissures, fold thickening and distortion, mural fibrosis, stricturing, and fistula formation are some of the commonly seen bowel changes on fluoroscopy. Fluoroscopic real-time imaging of the bowel allows for assessment of bowel peristalsis and contrast propagation. Barium enteroclysis (i.e. barium instillation via a nasojejunal tube) is an invasive method of examining the small bowel, providing superior detail compared to SBFT; however, this study now is seldom performed. Together with conventional SBFT, most institutions have moved away from barium fluroscopic techniques to image the small bowel, instead using either CT (more commonly) or MR enterography.

CT and MR enterography are noninvasive techniques for imaging the small bowel, allowing high-resolution imaging of the bowel wall and extra-luminal structures together. Typically, the bowel is distended with ingestion of either a neutral (e.g. water, polyethylene glycol [PEG], electrolyte solution, or methyl cellulose) or positive (dilute barium) contrast agent, prior to scanning. Imaging with CT is performed with intravenous iodinated contrast injection, therefore

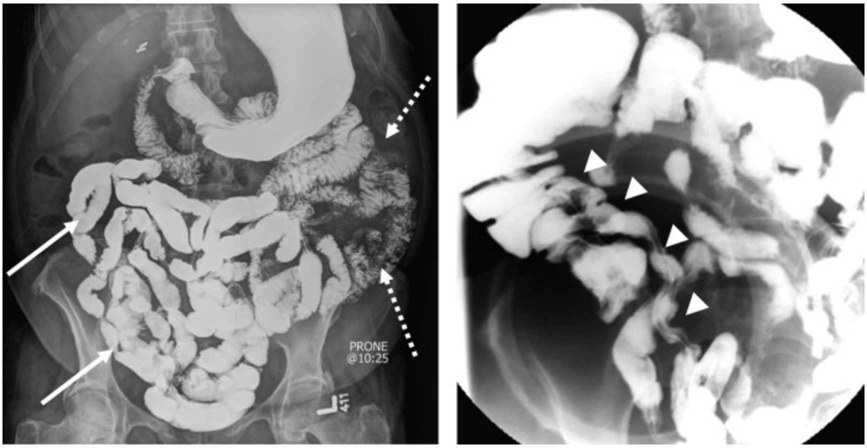

Figure 11.11 Normal small bowel follow-through (SBFT) study. Left image: Note the normal "feathered" appearance of the proximal small bowel (duodenum and jejunum [dashed arrows] typically located within the left upper abdomen vs. the "smoother" appearances of ileal loops [solid arrows], typically located within the mid and right lower abdomen). Right Image: Spot-magnified image of the distal ileum with interrogation of the terminal ileum (arrow heads), a segment of the small bowel associated with multiple different pathologies.

allowing assessment of bowel, mesenteric, and solid visceral enhancement. Figure 11.12 shows the typical example of ileal CD on a CT enterogram. MR enterography has the ability to assess mural and extramural manifestations of disease, without the use of ionizing radiation. This property makes MRI in Crohn's patients attractive, given the relatively young demographic commonly affected by this disease and the need for repeat/recurrent imaging leading to cumulative radiation doses with CT. MRI may also allow some functional imaging (cine [a type of "movie"] sequences) with visualization of bowel motion/peristalsis, similar to SBFT. Motion artifact is an issue with small bowel imaging, and routinely, these patients receive a short-acting antiperistaltic drug for imaging (e.g. *Hyoscine Butylbromide or Glucagon*). The key application of MRI in CD, however, is in the imaging of anal and peri-anal fistulous disease. The high contrast and soft-tissue resolution makes this imaging modality superior to all others for this indication.

11.6.2 Ulcerative Colitis

UC represents a chronic idiopathic inflammatory disease of the colon, involving the colorectal mucosa and submucosa, characterized by superficial ulcerations, increased vascularity, and edema. The imaging hallmark of this disease is its contiguous involvement of the bowel without skip areas

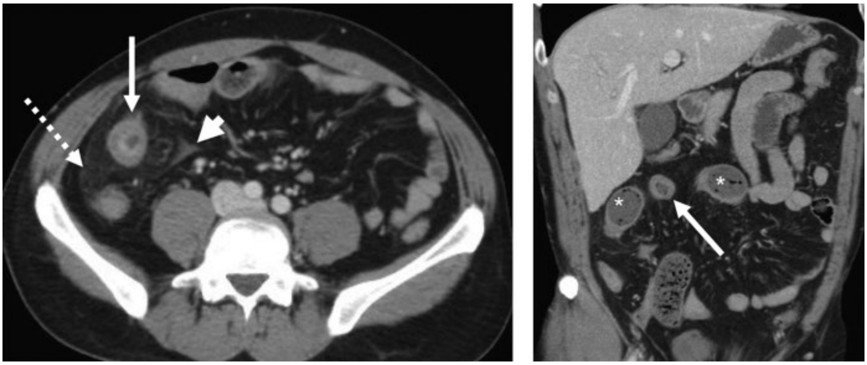

Figure 11.12 Small bowel Crohn's disease – contrast-enhanced CT. Left image: A loop of inflamed and thick-walled small bowel loop (ileum) is seen in the right lower quadrant on an axial CT image (solid arrow). Mild surrounding inflammatory stranding (dashed arrow) and trace-free fluid (short arrow) is also present. Right image: On a coronal image from the same study, focal loops of dilated small bowel with fluid within (*), immediately upstream from collapsed segments, representing pre-stenotic dilation secondary to inflamed ileal loops.

(i.e. the inflamed bowel is continuous without interspersed non-inflamed segments). The rectum is invariably always involved (unless treated with local rectal therapies) and typically shows contiguous involvement extending proximally along the sigmoid, descending colon, etc. Plain film X-ray imaging may be normal; however, it may show a spectrum of changes ranging from loss of normal haustral pattern (featureless bowel), mural thickening (thumbprinting) (Figure 11.13), and dilation (acutely related to toxic megacolon). Barium fluoroscopic enema is indicated in the imaging of UC; however, it is seldom performed in current clinical practice, but may show a fine mucosal granular pattern (related to edema and hyperemia), "collar-button" ulcers, eventually leading to pseudopolyp formation due to undermining of ulcers. More chronic changes related to bowel fibrosis, blunting or loss of the haustra, and strictures may be seen, usually post-inflammatory in nature; however, these patients remain at high risk of developing colorectal carcinoma (see below). Contrast-enhanced CT demonstrates concentric bowel mural thickening and edema, luminal narrowing, increased enhancement of the mucosa, submucosa, and muscularis propria (i.e. the muscular layer within the bowel wall), together with proliferation of the fat surrounding the colon and rectum. Toxic megacolon (dilated colon with loss of haustra, air-fluid levels, and mucosal islands) may be seen as an acute, severe life-threatening complication, requiring surgical intervention (colectomy). Nuclear medicine imaging, namely radiolabeled white blood cell scintigraphy (see Chapter 4), may be used in the imaging of acute inflammatory bowel disease. For this type of imaging, a patients' own

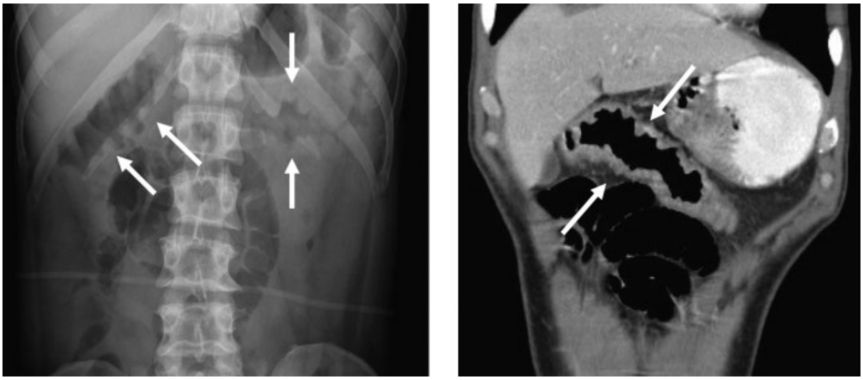

Figure 11.13 Thumbprinting in ulcerative colitis. Left image: Loops of transverse colon within the upper abdomen on X-ray demonstrate thickening of haustral folds due to edema, consistent with colitis (arrows). These thickened folds mimic thumbprints on imaging, hence the term "thumbprinting." Right image: On CT, the X-ray finding of transverse colon wall thickening (arrows) is seen in greater detail.

white blood cells separated from a blood sample are tagged with a radioisotope (e.g. ^{99m}Tc or ^{111}In) and injected back into the bloodstream, in turn migrating to areas of inflammation, useful in determining the presence of active inflammation and the site of inflammation (Figure 11.14).

11.7 Colorectal Adenocarcinoma

Numerous malignancies may arise from the GI tract; however, colorectal adenocarcinoma is by far the most commonly encountered, and therefore warrants specific discussion. The following sections provide an overview of imaging used in the diagnosis and treatment of colorectal cancer, together with surveillance strategies in place to detect premalignant and early malignant colorectal tumors.

11.7.1 Screening

This is the process of identifying people from a select population who appear healthy, but may be at increased risk of a particular disease or condition. In the case of the colorectal cancer-screening program, this may be a national, regional, or provincial-based organized system to detect malignant or premalignant colorectal tumors with the overall aim to reduce deaths from colorectal cancer. There may be variation in the presence, scale, and inclusion criteria of

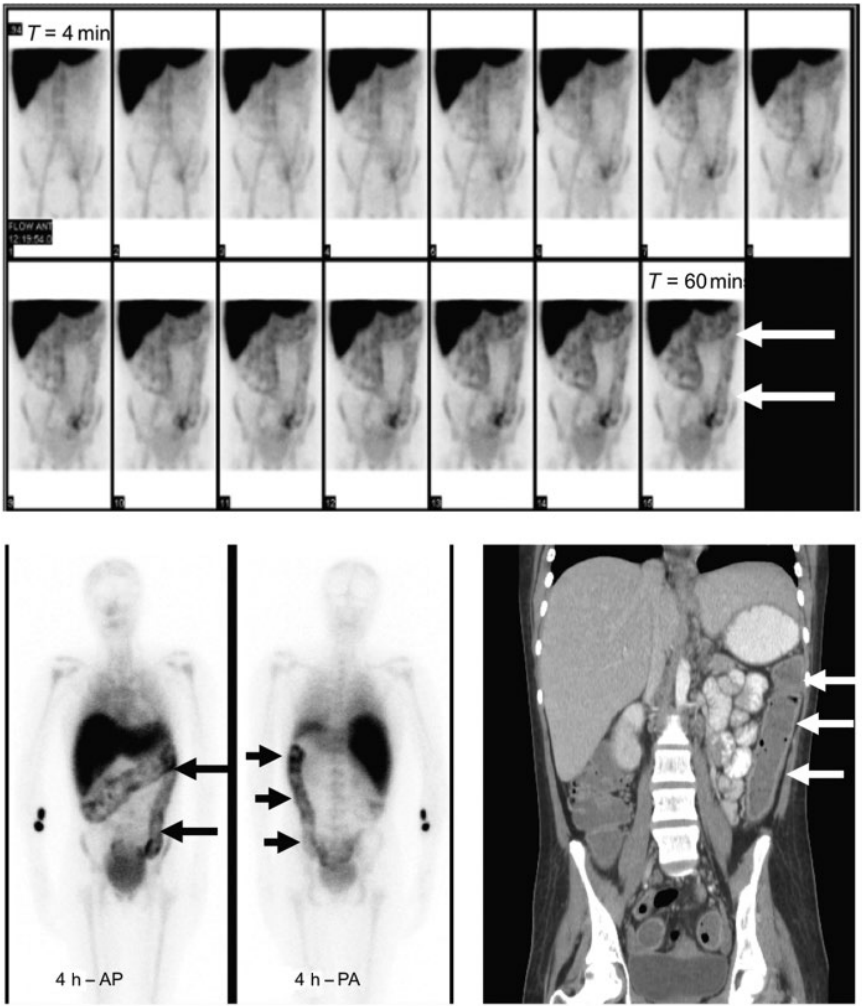

Figure 11.14 Ulcerative colitis on a radiolabeled white blood cell scan and CT. Top image: Serial image acquisition at four-minute intervals after injecting ^{99m}Tc-labeled white cells, up to one hour. There is abnormal diffuse radiotracer uptake from the hepatic flexure to the rectum (arrows). Bottom left image: At four hours after the injection, imaging acquired in the anterior–posterior (AP) and posterior–anterior (PA) planes. Colonic findings are more conspicuous, consistent with active inflammatory change from the hepatic flexure to the rectum (arrows). Bottom right image: On coronal CT, the involved descending colon has a featureless appearance with loss of normal haustral folds (arrows).

a colorectal screening program depending on the country, territory, region, or province – largely based on population needs and resources. The following colorectal screening program (Table 11.3) provides an overview of the screening program related to that in effect within the authors' province (Ontario, Canada).

The fecal occult blood test (FOBT) is a screening test that is relatively inexpensive and can be performed with a home test kit. The test involves collecting a small sample of stool (from three consecutive bowel movements) that is sent to a laboratory to detect the presence of blood within the fecal matter. The premise of the test is based on the fact that colonic tumors are associated with increased blood supply and these fragile tumors often release a small amount of blood (usually not visible to the naked eye) that may be detected by this test. Of note, this test cannot determine if the blood is from the colon or other parts of the GI tract, and therefore further testing (endoscopy) is required if occult blood is detected. If the test is positive (i.e. detected the presence of blood products within the stool) a colonoscopy is required. Colonoscopy is the gold standard in those with screen-positive FOBT or clinically suspected of having an underlying colorectal cancer. Direct visualization allows assessment of the location, size, and degree of bowel involvement, assess the potential for impending obstruction, and allow samples to be taken for histological confirmation.

CT colonography (CTC) (virtual colonoscopy) is a powerful and minimally invasive technique for imaging the large bowel, which may be used as a technique for the detection of colorectal carcinoma (or premalignant polyps), to

Table 11.3 Cancer care Ontario colorectal cancer (CRC) screening recommendations.

Screening average risk population
• Screening with fecal occult blood test (FOBT) every two years for asymptomatic people aged 50–74 without family history of CRC • Abnormal FOBT result should be followed up with colonoscopy within eight weeks • Those aged 50–74 without a family history of CRC who chose to be screened with endoscopy should be screened every 10 years • Recommendation against screening using metabolic (blood or urine), DNA, CT colonography, capsule colonoscopy, and double contrast barium enema due to insufficient evidence
Screening high-risk population
• Asymptomatic person screened with colonoscopy if they have a family history of CRC that includes one or more first-degree relatives with the disease • Screening should begin at age of 50, or 10 years earlier than the age their relative was diagnosed, whichever occurs first

Source: Adapted from www.cancercare.on.ca.

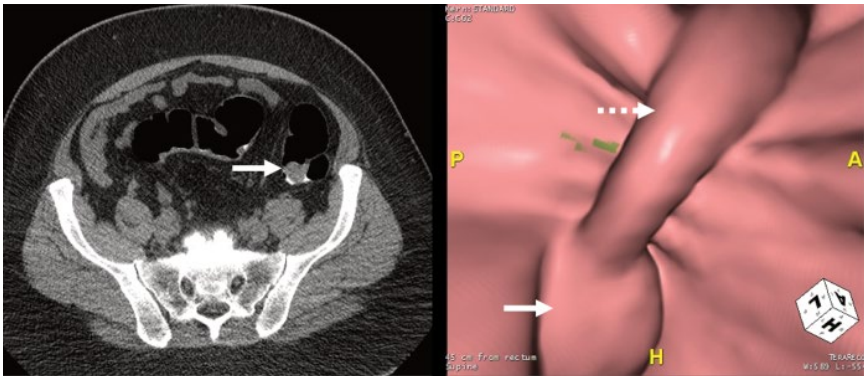

Figure 11.15 CT colonography. Axial CT colonography image (2D; left panel) demonstrates a focal polyp (arrow) with associated long stalk (not shown on 2D), best demonstrated on 3D reconstructed images (dashed arrow; right panel). This lesion was located ~45 cm from the ano-rectal junction, aiding localization for subsequent endoscopic assessment and treatment (polypectomy).

evaluate the large bowel in cases where optical colonoscopy was incomplete, unsuccessful or in those patients with a contraindication to, or declined optical colonoscopy. Of note, this technique/modality is not currently routinely indicated for use in the screening (asymptomatic) population in the author's province at time of writing. This technique essentially uses CT imaging of the abdomen and pelvis, following monitored insufflation of the large bowel with carbon dioxide via a rectal tube. Image processing allows 2D images together with 3D virtual modeling of the large bowel to detect polyps (benign, premalignant, or malignant) or frank cancer. In addition, this technique also allows for the structures beyond the GI tract to be imaged (e.g. lymph nodes and liver). Figure 11.15 demonstrates a typical CTC study with 2D and 3D reconstructions. Lesions detected on CTC require formal colonoscopy (unless otherwise contraindicated) for tissue (histological) confirmation.

11.7.2 Imaging

Plain film X-ray imaging may be useful in acute presentations of colorectal cancer. Mechanical bowel obstruction due to colorectal cancer is frequently seen in the acute setting, with dilated large bowel (with or without perforation) seen on plain films. However, CT (unenhanced vs. contrast enhanced) remains the imaging modality of choice in the assessment of acute abdomen suspected secondary to a colorectal cancer or in the routine staging of colorectal cancer, primarily to identify/confirm the location of the primary tumor (although some colorectal tumors may be inconspicuous on CT), to assess for extramural tumor extension, and identify the presence of local or distant spread of disease. CT chest,

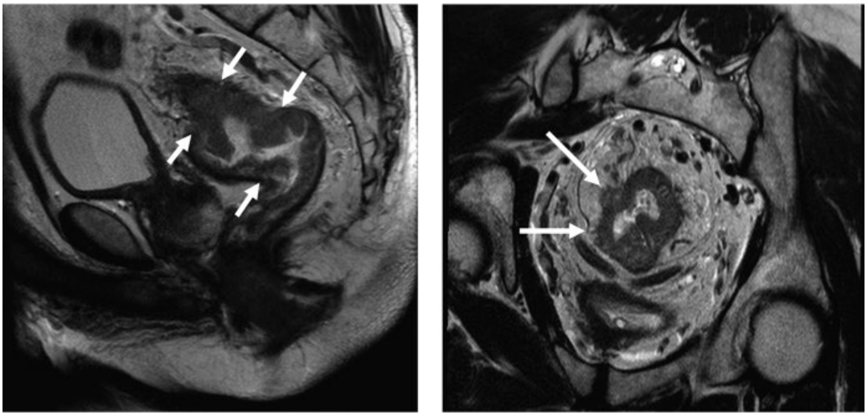

Figure 11.16 Rectal cancer on MRI. Left image: A sagittal T2-weighted image of the pelvis shows a high rectal cancer that involves the rectal wall, depicted by "light gray" signal soft tissue (arrows). Right image: An axial T2-weighted image through the rectum at the site of the tumor, showing the lesion in cross-section, depicted by "light gray" signal soft tissue and spiculated soft-tissue projections extending in a radial fashion outside of the bowel wall (arrows) into the surrounding fat (bright tissue surrounding the bowel), allowing accurate staging of the cancer and optimal treatment planning.

abdomen, and pelvis imaging remains the standard in staging colorectal cancer. Chest X-rays have essentially no role in the staging of colorectal cancer, due to their low sensitivity for small nodules. MRI plays a vital role in the imaging and local staging of primary rectal cancers, primarily due to the surgical technique of total mesorectal excision (TME). This technique (resection of the rectum, surrounding mesorectal fat, and perirectal nodes all together with its circumferential envelope) has revolutionized the surgical management of rectal cancers and now considered the gold standard technique. MRI is the modality of choice due to its high soft-tissue contrast, allowing assessment for the presence of tumor spread beyond the bowel wall (extramural) and its relationship with or distance from the planned TME excision plane. This preoperative MRI staging (together with CT staging described above), allows decision making between patients that may proceed directly to surgery, versus those that may need some adjunct therapy (chemotherapy and radiation) prior to surgery (to shrink the tumor and thus improving surgical outcome) versus those who have disease so advanced, that surgery may no longer be an appropriate option (palliative). Furthermore, it allows assessment of the relationship of the tumor with the ano-rectal sphincter complex and therefore allowing informed decisions to be made between surgical resection of tumors that may result in permanent bowel diversion (stoma formation) and those that may have their bowel reconstituted upfront. Figure 11.16 demonstrates MRI features of a typical rectal cancer (identified as requiring upfront chemoradiotherapy prior to definitive curative intent surgery).

In those who cannot undergo pelvic MRI or have equivocal findings on MRI, certain lower rectal cancers may be staged locally with trans-rectal ultrasound (TRUS). This technique is highly sensitive in assessing the presence of any extramural tumor extension (like MRI), thus allowing presurgical planning, as discussed above. Mesorectal lymph node assessment (and biopsy if needed) can also be performed with TRUS. ^{18}F-FDG PET/CT plays a role in colorectal cancer imaging (see Chapter 15), though its use is dependent upon availability, funding, and regional guidelines. More generally, PET/CT may be used in staging patients with synchronous metastatic disease at presentation and thus allowing assessment of resectability, particularly when findings are equivocal on conventional staging CT. Moreover, PET/CT is used in restaging of patients with prior treated colorectal cancer who have either a proven recurrence with plans to have radical treatment (to exclude other sites of disease) or in those suspected of having recurrent disease (rising tumor markers) with normal or equivocal CT/MRI findings. Figure 11.17 demonstrates typical PET/CT imaging in colorectal cancer.

11.8 Hepatic System

Imaging of the hepatic system encompasses assessment of the liver parenchyma, hepatic vascular structures, and biliary system, all of which are intimately related with one another. Imaging of the biliary tree has been separated from this section and is discussed later. US, CT, and MRI form the mainstay of hepatic imaging, both in emergent and non-acute clinical settings. US is often used as first-line imaging assessment, primarily related to its availability/access, cost, and nonionizing advantages, but US is also used as a problem-solving tool (related to incidental findings on clinical examination, CT, MRI, or PET) to characterize lesions/pathology, confirm, or refute findings from other tests. Furthermore, in sub-specialist expert centers, the use of intravenous contrast agent (microbubble) may be used to examine the vascular/enhancement properties of specific lesions (see Chapter 6), similar to that used to characterize lesions on CT and MRI.

CT (unenhanced, single, or multiphasic) imaging forms the "workhorse" of hepatic imaging, primarily for lesion/disease detection, but also for lesion characterization; the latter typically requiring multiphasic contrast imaging. MRI allows for comprehensive morphological and functional assessment of the liver with superior soft-tissue characterization related to liver parenchyma and lesion analysis, primarily related to greater contrast resolution. Liver MRI is generally used for lesion characterization that may remain indeterminate on other imaging modalities, but also plays a significant role in staging of malignant disease, particularly those with hepatic involvement. Furthermore, MRI

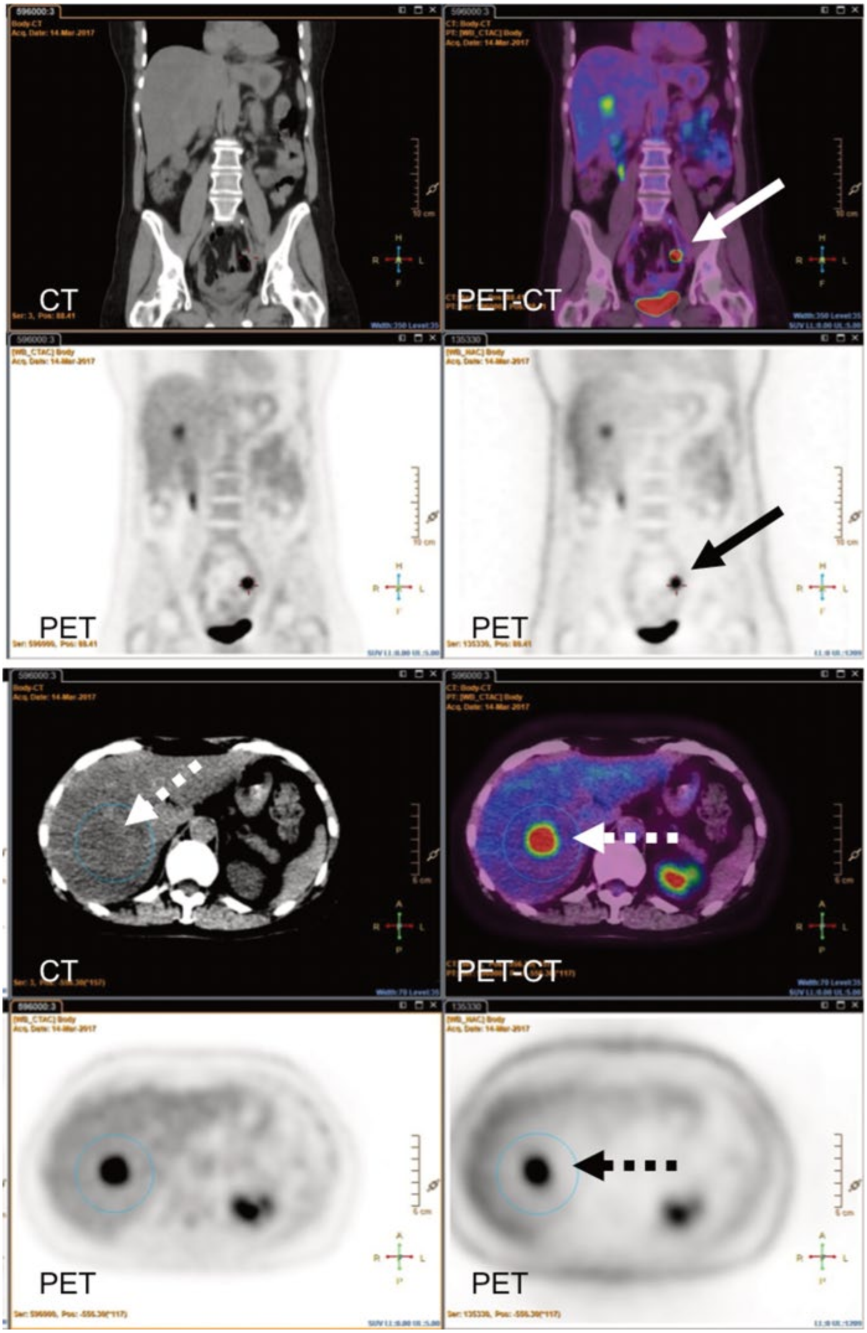

Figure 11.17 Colorectal cancer with synchronous liver metastasis on ^{18}F-FDG PET/CT. Top two image rows (Coronal CT only, PET-CT [fused], and PET only imaging): A hypermetabolic mass is seen in the left pelvis (solid arrow) corresponding to a primary sigmoid cancer. Bottom two image rows (Axial CT only, PET-CT [fused], and PET only imaging): A hypermetabolic lesion is seen in the right lobe of the liver (dashed arrow), consistent with synchronous metastasis. Of note, the liver metastasis is partially imaged on the coronal set of imaging on the PET-CT (fused) and PET only images. (*See insert for color representation of the figure*.)

allows assessment of the liver in those patients unable to receive iodinated intravenous CT contrast agents (i.e. severe contrast allergies) or ionizing radiation (i.e. in pregnancy) for hepatic lesion detection and characterization.

Radionuclide imaging (except for ^{18}F-FDG-PET) has a limited role in imaging of the liver, and is mainly used in very specific problem-solving roles (i.e. hepatic perfusion assessment or hemangioma confirmation). PET/CT has a wide spectrum of applications, although its application in cancer imaging is most notable, particularly for staging and monitoring of cancer disease activity. However, there remains significant constraints in PET access and infrastructure in Canada (compared to United States and Europe), which limits its utilization.

11.9 Diffuse Hepatic Disease

Diffuse hepatic disease is an important finding to recognize on imaging, as patients are often asymptomatic and may not have clinical or laboratory evidence of liver disease. Recognition may allow appropriate workup and mitigation of irreversible liver damage or complicating features. In addition, those with known underlying diffuse liver disease may require monitoring for complications. Some commonly encountered liver disease imaging is highlighted.

11.9.1 Fatty Infiltration

Fatty infiltration of the liver is a common response to hepatic cellular injury and toxins, manifesting as either focal or diffuse deposition of fat within the liver. Fatty (steatotic) infiltration may be seen throughout the liver (diffuse) or involve select geographic areas (focal). While the cause may be unknown in some cases, it is frequently associated with excess alcohol consumption, diabetes (including other metabolic conditions), obesity, drug therapies, and chronic hepatitis, to name a few. Typically, the degree of hepatic steatosis is graded (mild, moderate, or severe) by subjective measures, depending on the imaging used. On US, the liver parenchyma appears bright (compared to surrounding solid organs) and may limit sound waves penetration and thus assessment of the posterior part of the liver (Figure 11.18). However, increased echogenicity of the liver may be seen with other disorders (iron, copper deposition, etc.). On CT, fatty infiltration lowers the attenuation/density of the liver (Figure 11.18), best assessed on unenhanced CT imaging, demonstrating the difference between the liver and spleen attenuation ratio. MRI is most sensitive in assessing for the presence of fatty infiltration, but also has the ability to be able to quantify the degree of fatty deposition, using various techniques. The presence and extent (subjective) of fatty involvement is generally best demonstrated with MRI (Figure 11.18). It is important to identify patients with hepatic steatosis as a majority may be asymptomatic and have reversible/modifiable disease (e.g. excess alcohol intake). In a proportion of nonalcoholic patients, fatty

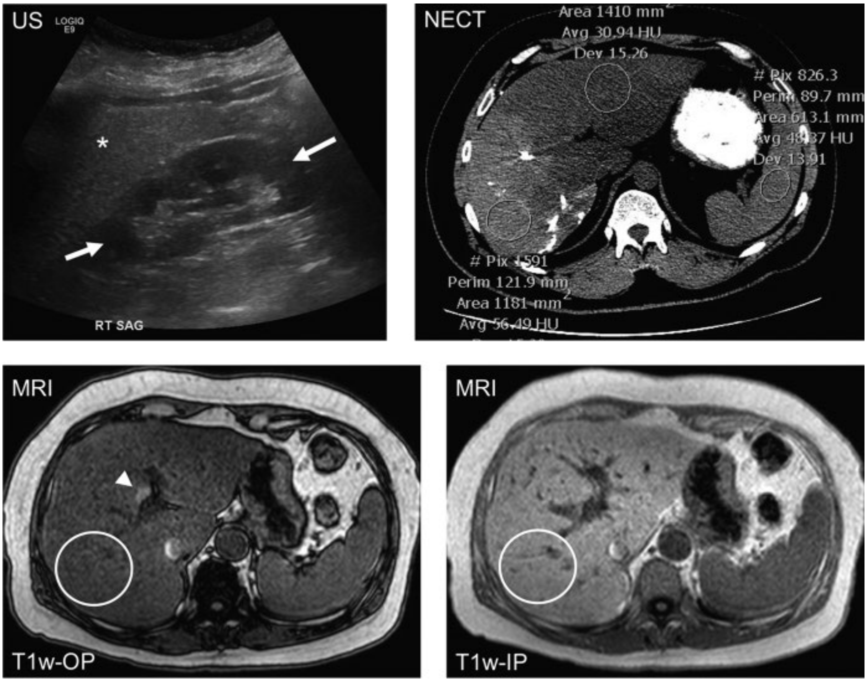
US
LOGIQ E9
*
RT SAG
NECT
Area 1410 mm²
Avg 30.94 HU
Dev 15.26
# Pix 826.3
Perim 89.7 mm
Area 613.1 mm
Avg 48.37 HU
Dev 13.91
# Pix 1591
Perim 121.9 mm
Area 1181 mm²
Avg 56.49 HU
MRI
T1w-OP
MRI
T1w-IP

Figure 11.18 Diffuse hepatic fat/steatosis – US, CT, and MRI. Top left image: Ultrasound demonstrates bright/echogenic liver (*) compared to the adjacent right kidney (arrows). Top right image: Unenhanced CT in a patient treated with chemotherapy demonstrates diffuse decreased attenuation/density (darker) of the left lobe of liver (upper middle circle) compared to the right lobe and spleen (circle at lower left and right respectively). Bottom images: MRI T1-weighted, in- and out-of-phase imaging (IP and OP) shows diffuse signal drop throughout the liver parenchyma (circled) on out-phase imaging, consistent with diffuse hepatic steatosis. Note, a focal area of liver showing lack of signal drop (arrow head) in OP imaging, in keeping with focal fatty sparing.

liver leads to hepatic inflammation (NASH – Non-Alcoholic Steato-Hepatitis), which may ultimately lead to fibrosis (cirrhosis) and liver dysfunction.

11.9.2 Hepatic Cirrhosis

Hepatic cirrhosis represents an endpoint to hepatic parenchymal insult resulting in tissue damage, fibrosis, and architectural distortion that ultimately may lead to hepatic dysfunction and failure. Causes include alcohol excess, viral hepatitis, drugs, autoimmune, and hereditary pathologies. Imaging in this group of patients serves two main goals. The first goal is to identify morphological features of cirrhosis in those are at risk, while the second is to screen for complicating features of hepatic cirrhosis, namely primary liver cancer (hepatocellular carcinoma [HCC]). It is important to note that imaging of the liver may be normal in the presence of pathological hepatic cirrhosis and therefore imaging cannot exclude this diagnosis (which remains strictly a histological diagnosis). However, the liver may show enlargement (hepatomegaly) during the early phase with the typical shrunken (i.e. atrophic) appearance seen during the later stages. Furthermore, the liver may show contour irregularity, lobar redistribution (enlargement of the caudate lobe and lateral segment of the left lobe with shrinkage of the right lobe and medial segment of the left lobe), widening of the fissures, and parenchymal nodularity (Figure 11.19). On imaging, nodules may be seen scattered

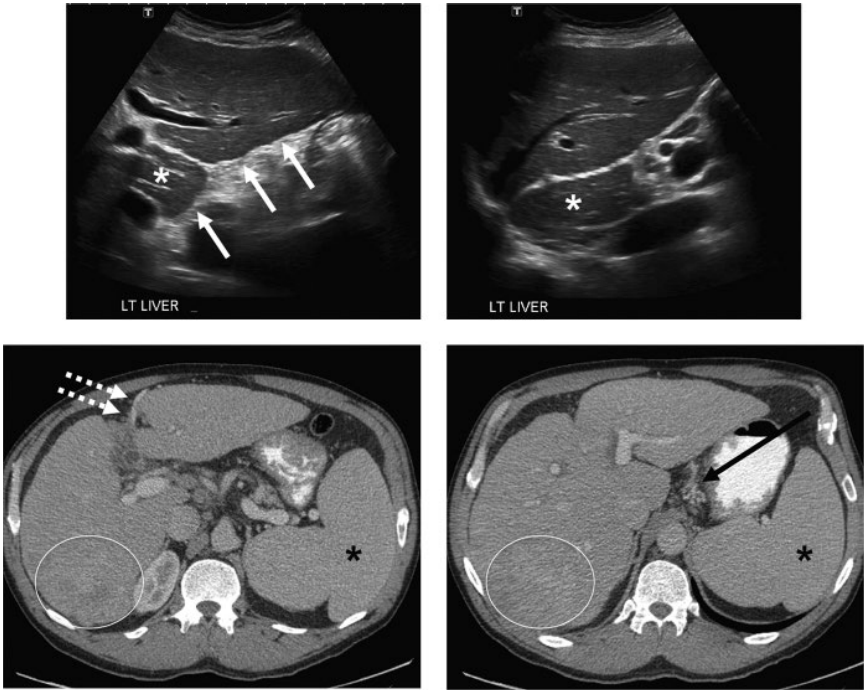

Figure 11.19 Hepatic cirrhosis. Top images: Ultrasound images of the left lobe of the liver demonstrating the nodular contour of the liver (arrows), best appreciated along the surface of the liver. Note, enlargement of the caudate lobe (white *) secondary to chronic liver disease. Bottom images: Axial contrast-enhanced CT images of the upper abdomen at two different levels. Both show the nodular contour of the liver and enlargement of the caudate and right lobe of liver, relative to the left lobe. Left image demonstrates contrast opacification (bright) of the paraumbilical vein (dashed arrows) seen in patients with liver cirrhosis, secondary to portal hypertension. Right image shows a leash of vessels adjacent to the stomach, consistent with varices (black arrow). Note, both images show enlargement of the spleen (*) secondary to portal hypertension. Subtle heterogeneity is noted within the right lobe of the liver (circled), which represents an underlying hepatocellular carcinoma.

throughout the liver, typically caused by reactive/regenerative nodules; however, these groups of patients are at risk of developing dysplastic and malignant nodules (i.e. HCC). Increased parenchymal fibrosis leads to decreased hepatic function and increased vascular resistance, leading to portal vein hypertension (extrahepatic portal vein dilation, opening up of portal-systemic venous collaterals, and formation of varices). Enlargement of the spleen (splenomegaly) together with varices and free fluid (ascites) may be seen in patients with established cirrhosis and secondary decompensation.

11.10 Focal Hepatic Disease

Discrete hepatic lesions are a common occurrence on imaging, and the majority are incidental in nature. However, the key is being able to differentiate common benign entities, from aggressive malignant pathology. The most commonly encountered focal hepatic lesions are highlighted below.

11.10.1 Hepatic Abscess

Localized collection of infected fluid within the liver, causing parenchymal damage, is the hallmark of a hepatic abscess. Pyogenic (bacterial) type is by far the commonest cause (typically from *E. coli* in adults) and may develop via infection of the biliary tract (usually secondary to obstruction), the portal venous system (i.e. phlebitis typically related to diverticulitis, colitis, or appendicitis), hepatic arterial system (i.e. infective endocarditis), or via direct extension from penetrating injury or adjacent infected collection. Amebic and fungal abscesses are much less common. US and CT are typically used in the diagnosis of these collections, with CT having the advantage of assessing for multifocality, hepatic and extrahepatic complications, and identification of potential sites of origin elsewhere within the abdomen or pelvis. Figure 11.20 demonstrates hepatic abscesses on CT, typically seen as a well-defined, round low-density lesions with rim/capsule. Occasionally, several small, low-density collections may be seen, coalescing to form a larger complex collection. US is particularly useful in demonstrating the fluid component of these collections, typically seen as a hypoechoic lesion/mass with through transmission (posterior acoustic enhancement), confirming its fluid component. In addition, US allows real-time imaging for therapeutic percutaneous aspiration and drainage of these collections. MRI may be occasionally used in the assessment of a hepatic abscess, particularly if there are equivalent features on CT or US, or in assessing a biliary cause for the collection (i.e. biliary obstruction).

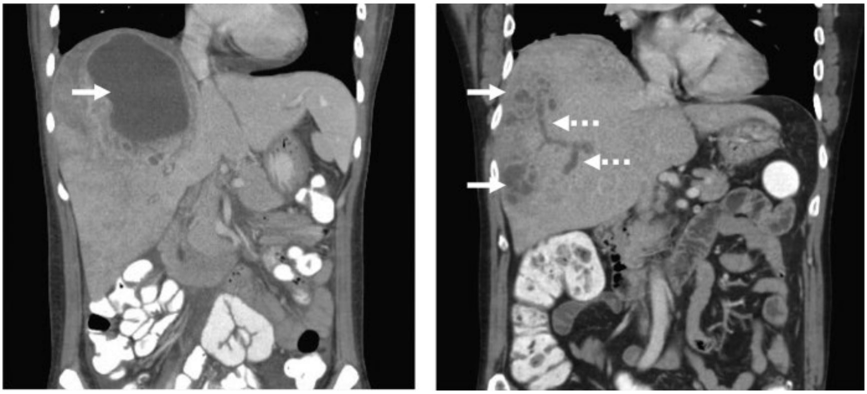

Figure 11.20 Hepatic abscesses – contrast-enhanced CT (CECT). Low-density hepatic abscesses may be either uni- or multi-loculated (multiple fluid compartments within an abscess; solid arrows) and typically show rim enhancement (bright line around the centrally low-density material). Satellite abscesses can be seen (often smaller) and may be associated with thrombophlebitis (venous blood clot) of adjacent portal vein branches (dashed arrows).

11.10.2 Cavernous Hemangioma

Hemangioma is the commonest tumor within the liver. These lesions are characterized by multiple endothelial-lined vascular channels forming focal masses that are typically asymptomatic and found incidentally. Typical hemangiomas are bright on US and depicted as well-defined lesions on US, likely due to the presence of innumerable tiny vascular spaces causing reflection of the US beam. While the vast majority of lesions require no further imaging, in some cases (particularly in patient with an underlying malignancy) these may require formal characterization. To definitively characterize these lesions, contrast enhanced imaging (US, CT, or MRI) is generally indicated. Typically, hemangiomas exhibit a classic enhancement pattern demonstrating contrast filling in the periphery of the lesion as tiny discontinuous bright nodules, which eventually progress to contrast filling the entire lesion resulting in a diffusely bright appearance (Figure 11.21). A nuclear medicine red blood cell scan uses the patients' own red blood cells (RBCs) labeled with ^{99m}Tc that are injected back into the patients' circulation. These radiolabeled RBCs accumulate within these vascular lesions, confirming the diagnosis of hemangiomas, although this study is not as commonly used more recently, given the high sensitivity and specificity of other imaging modalities as well as the ability to make alternate diagnoses with other modalities.

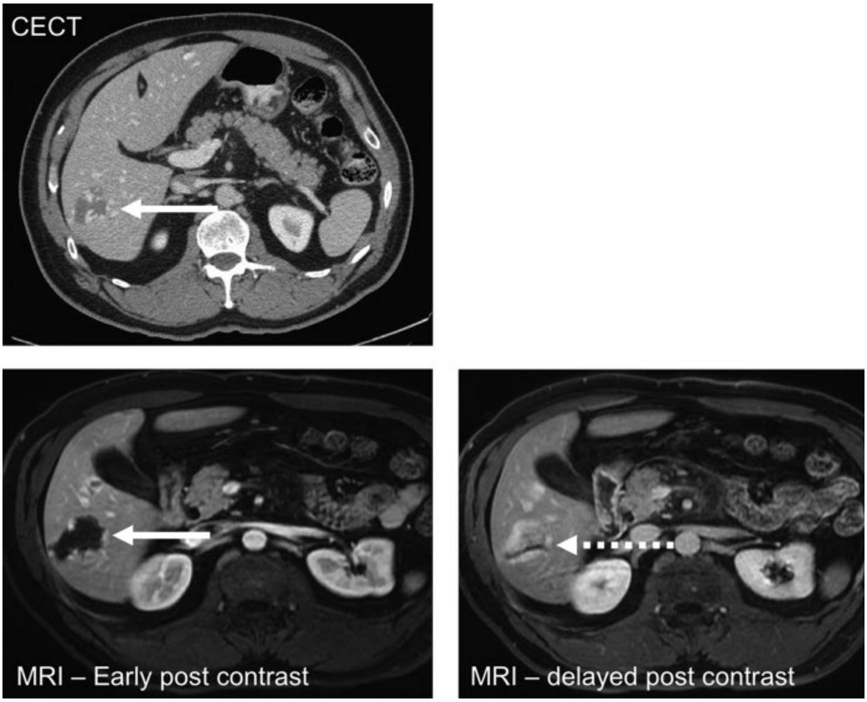

Figure 11.21 Hemangioma on CT and MRI. Top image: A right lobe liver lesion demonstrating peripheral discontinuous nodular enhancement (arrow) on a contrast-enhanced CT (CECT). Lower images: On dynamic contrast-enhanced MRI, hemangioma demonstrates peripheral nodular discontinuous enhancement (identical to CT) on early post-contrast imaging (solid arrow), with progressive central filling on delayed post-contrast imaging (dashed arrow), typical for a hemangioma.

11.10.3 Cysts

Cysts are benign congenital developmental lesions of the biliary duct and range in size from a few millimeters to over 10 cm and are common findings on hepatic imaging. The vast majority are asymptomatic and detected incidentally. On US, hepatic cysts are well-demarcated, hypoechoic lesions with imperceptible walls, showing acoustic through transmission (Figure 11.22). On CT, hepatic cysts are well demarcated and of water density (hypodense −10 to +10 HU) without internal nodules and an almost imperceptible wall. Cysts show no enhancement post-contrast administration either on CT or MRI, unless complicated. Occasionally, cysts may show complexity by way of wall thickening or internal smooth septations (i.e. thin soft-tissue divisions within the cyst). Furthermore, secondary cyst infection, trauma, and hemorrhage may

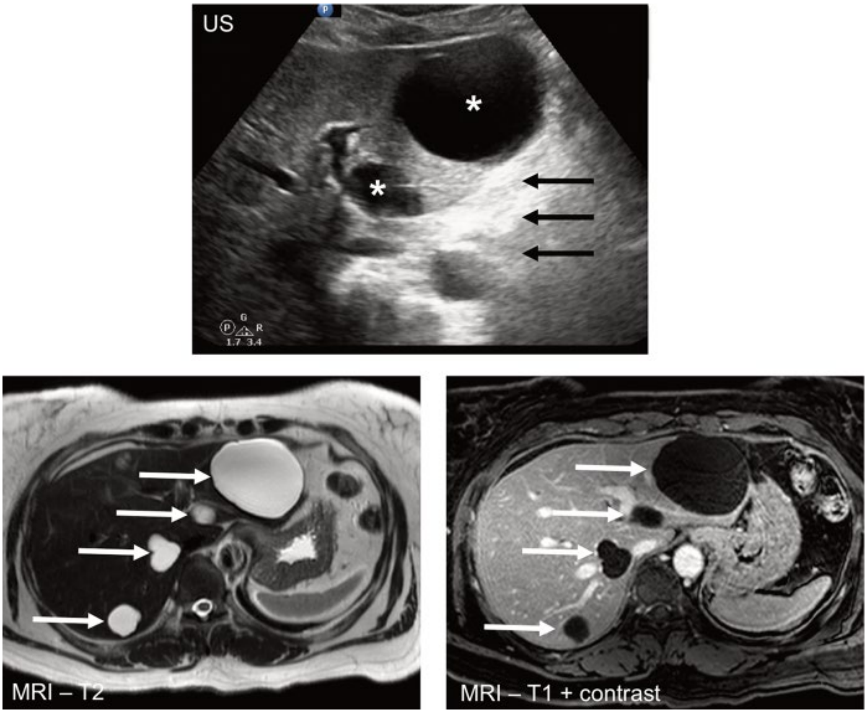

Figure 11.22 Hepatic cysts. Top image: Ultrasound image through the left lobe of the liver demonstrates a large homogenous hypoechoic lesion with thin, almost imperceptible walls, consistent with a hepatic cyst (*). There is typical increased through transmission (sound waves travel unimpeded through the fluid within the cyst, compared to surrounding tissues), resulting in increased echogenicity (brightness) behind the cyst (black arrows). Bottom images: Axial T2-weighted image (left) through the liver in the same patient shows the typical bright fluid signal of simple cysts (white arrows). Axial T1-weighted images following injection of IV gadolinium contrast, shows no enhancement within these cysts (hence the term simple). Both images again show the thin, almost imperceptible wall, of simple hepatic cysts.

be seen, making assessment by US and CT more challenging. Simple hepatic cysts, in general, require no follow-up or specific treatment.

11.10.4 Focal Nodular Hyperplasia

Focal nodular hyperplasia (FNH) is the second-most common benign hepatic tumor (after hemangiomas) and represents hyperplastic growth of normal hepatocytes with malformed biliary drainage, thought to be in response to an underlying congenital arterio-venous malformation. These hypervascular tumors are almost always asymptomatic and detected incidentally on imaging, but rarely may present with signs and symptoms of mass effect (i.e. compression of adjacent liver parenchyma or other structures), depending on its size and location. It is important to recognize and characterize these lesions accurately, as primary hepatic and metastatic hypervascular tumor may have some similar features, potentially leading to inappropriate management. FNH may show variable echogenicity on US, and often are difficult to detect with respect to the background liver parenchyma. Microbubble contrast-enhanced US has shown great utility in characterizing focal hepatic lesions such as FNH. A typical FNH will show hyperenhancement on early contrast imaging when arterial blood supply is more prominent, relative to the background liver with a prominent central vessel feeding the lesion. On portal venous phase imaging (i.e. when the circulation in the portal venous system is most prominent), the lesion will show central contrast filling (opposite of a hemangioma), which persists on delayed imaging (i.e. once contrast has had a chance to circulate through the body multiple times). CT and MRI will show a similar enhancement pattern, although MR is the imaging modality of choice (particularly in centers where contrast US is not readily available or the remainder of the liver needs to be assessed) in the imaging of FNH. More specifically, the use of a hepatocyte-specific contrast agent demonstrates uptake of contrast (since it is hepatocyte containing) and retains contrast (compared to the background liver) on delayed phase imaging, confirming the diagnosis. Figure 11.23 shows the typical MRI features of FNH, with Primovist™ (a hepatocyte-specific contrast agent). ^{99m}Tc-Sulfur Colloid can also be used for confirming the diagnosis of FNH, though is dependent on the concentration of cells taking off the sulfur colloid (i.e. Kupffer cells) within the FNH, which can limit the sensitivity of this technique.

11.10.5 Hepatic Metastases

Hepatic metastases represent the spread of malignant disease to the liver parenchyma and are the most common malignant tumor to involve the liver. The majority of hepatic metastases are hypovascular (e.g. those from GI tract, pancreas, breast, lymphoma, bladder, and uterine primary cancers), with a smaller proportion being hypervascular, arising from hypervascular primaries (e.g. renal, endocrine, melanoma, thyroid, and some breast cancers). Contrast-enhanced CT is the imaging modality of choice to detect hepatic metastases. Hypovascular metastases are characteristically of low attenuation with peripheral rim enhancement. Hypervascular tumors show increased enhancement (hyperdense) on arterial phase imaging (Figure 11.24) and are iso- or hypodense on portal venous phase imaging. Lesions may vary in size and number, ranging from a few millimeters, to over 10 cm. Cystic metastases may be seen from

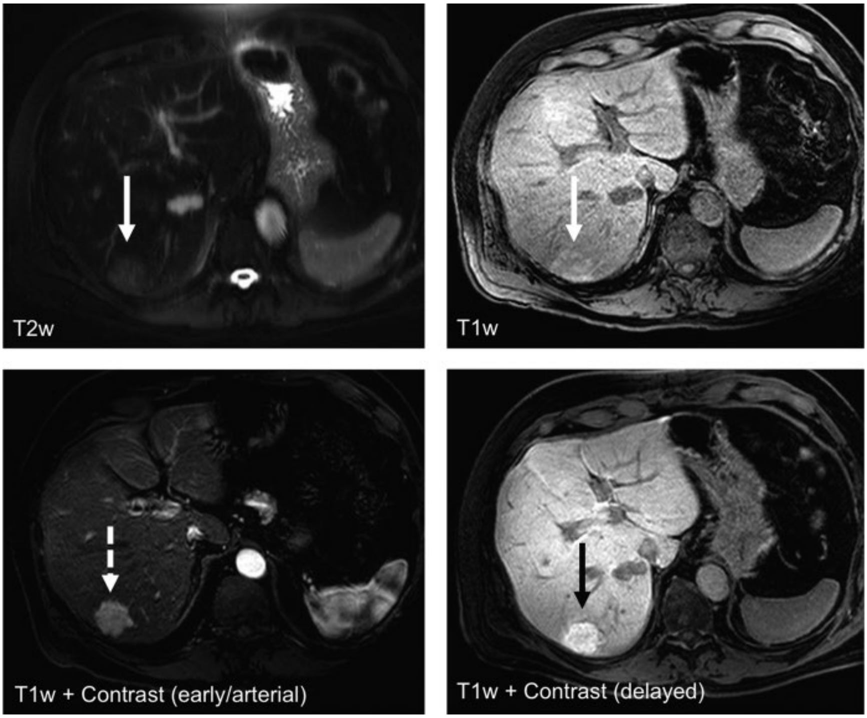

Figure 11.23 Focal nodular hyperplasia (FNH) on MRI + Gadoxetate (Primovist) hepatocyte-specific contrast agent. On MRI, typically FNH is subtle on T2 (top left) and T1-weighted (top right) imaging, barely visible on these sequences (white arrows). However, these lesions are typically hypervascular and markedly enhance on arterial phase imaging (bottom left image; dashed arrow) and retain hepatocyte-specific contrast agent on delayed phase post-contrast imaging (bottom right image; black arrow).

pancreatic cancer (neuroendocrine), cancers of the GI tract (mucinous adenocarcinomas), or ovarian primary malignancies, and care must be taken to differentiate them from benign complex cysts. MRI has two specific roles in imaging metastases. Firstly, indeterminate lesions may be further characterized (particularly cystic neoplasms) in the detection of malignant metastatic disease, particularly important in allowing decisions between curative versus palliative management of disease. The greater soft-tissue contrast resolution of MRI (compared to CT and US), together with some functional assessment, allows for this. Secondly, in patients who are deemed to have resectable liver metastases (primarily in the management of metastatic colorectal cancer), MRI, together with Primovist (hepatocyte-specific contrast agent) and diffusion-weighted imaging, allows for accurate tumor detection and mapping ideal for planning curative intent therapies (Figure 11.25). PET imaging

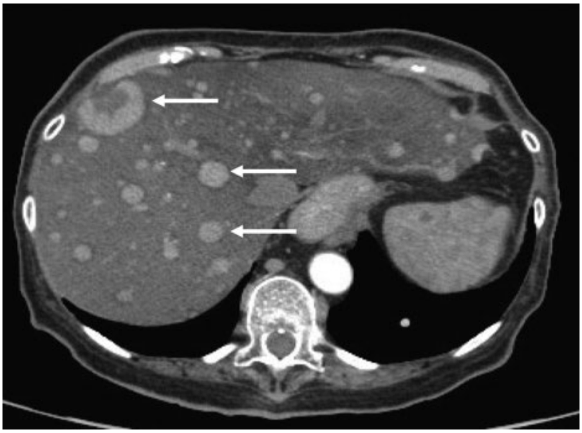

Figure 11.24 Hypervascular liver metastases – contrast-enhanced CT (CECT). Multiple hyper-enhancing lesions throughout the liver (arrows) ranging in size, consistent with liver metastases, confirmed secondary to a small bowel carcinoid primary tumor.

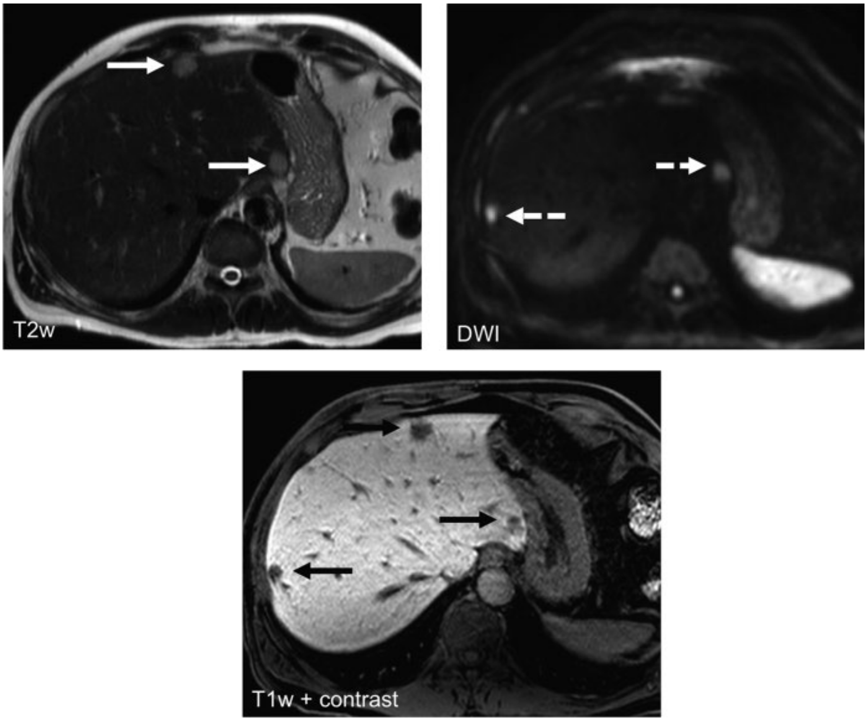

Figure 11.25 Colorectal liver metastases – MRI + Gadoxetate (Primovist) hepatocyte-specific contrast agent. Liver metastases are typically bright on T2-weighted imaging (top left image; solid arrows) and show diffusion restriction on diffusion-weighted (DWI) imaging (top right image; dashed arrows). Given that metastases do not contain any hepatocytes, they fail to retain a hepatocyte-specific contrast agent (Primovist) and appear as focal low signal areas (bottom image; black arrows), aiding their detection.

(more specifically ^{18}F-FDG PET/CT) has a specific role in staging of malignancies, depending on the primary site of disease, planned management, local, regional, and national guidelines/availability. Typically, PET/CT is most frequently used to detect sites of disease spread for a particular malignancy. Lung, colorectal, and pancreatic cancers and lymphoma are common malignancies for which PET/CT may be indicated (see Chapter 15). Furthermore, PET/CT is also indicated in the detection of recurrent disease for those already treated or in remission.

11.10.6 Hepatocellular Carcinoma

HCC represents the most common primary liver malignancy, although is ~18 times less common than metastatic liver disease. While HCC may occur de-novo, the vast majority are seen in those with chronic liver disease. Chronic viral hepatitis (Hepatitis B and C) and alcoholic liver disease are the most common risk factors for HCC. Recognition and management of patients with chronic liver disease are important in establishing a screening regime for the detection of HCC. Routine US monitoring (every six months) is the current standard for screening this group of patients. On US, the key element of screening is for the detection of a focal hepatic nodule or mass that thereafter requires further workup. An overview of the screening and assessment algorithm is given in Ref. [1]. On US, HCC have a variable appearance, typically of mixed echogenicity due to tumor necrosis and hemorrhage, although may be fully hypoechoic or hyperechoic (due to the presence of fat). Given the overlap with benign and other malignant lesions, further assessment with CT and/or MRI is usually required. Lesions typically show heterogeneity on CT and MRI with blood products (generally clotted blood from internal hemorrhage in the lesion) and internal fat components. The hallmark features of an HCC include hypervascularity on late arterial phase imaging with subsequent washout (tumor of lower attenuation/signal than the surrounding parenchyma) on portal venous or delayed post-contrast imaging. Lesions that have the classic appearance of HCC by imaging require no tissue sampling and this classic imaging appearance is deemed diagnostic. Figure 11.26 demonstrates a typical HCC on a background of chronic liver disease. Associated portal venous involvement and thrombosis is a common finding with HCC. In cases where the imaging features are atypical or equivocal for HCC, tissue sampling may be indicated and usually obtained using either US- or CT-guided percutaneous biopsy. Imaging plays a role in some treatments of HCC, usually as a temporizing measure for palliative indications (i.e. to minimize symptoms and/or prolong need for systemic treatment(s)) or as a “holding” measure for those awaiting liver transplantation (should the patient meet rigorous transplant criteria).

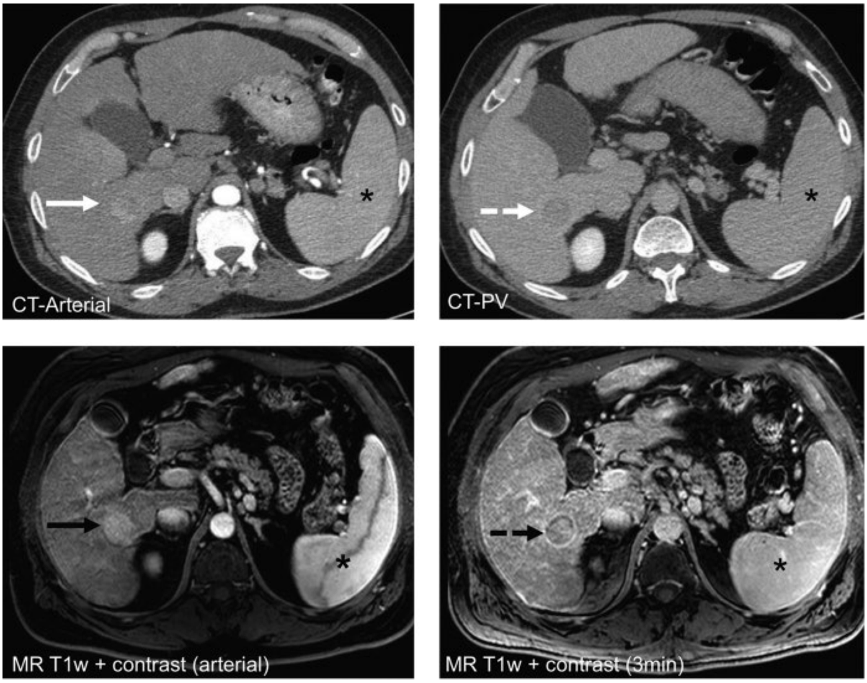

Figure 11.26 Hepatocellular carcinoma (HCC) in a patient with hepatic cirrhosis. CT demonstrates a focal hypervascular lesion seen on arterial phase imaging (top left image; white solid arrow) with subsequent contrast "washout" on portal venous phase imaging (top right image; white dashed arrow). Subsequent T1-weighted arterial phase MRI confirms the hypervascular nature of this lesion (bottom left image; solid black arrow), which again shows contrast "washout" on delayed imaging, together with apparent delayed rim enhancement, consistent with a pseudocapsule, typically seen with HCC (bottom right image; black dashed arrow). Background liver demonstrates a nodular contour (i.e. the edge of the liver is lobulated) and enlargement of the left and caudate lobes, consistent with cirrhosis. Note, splenic enlargement (*) secondary to portal hypertension.

11.11 Biliary Tract

Various methods may be used to image the biliary tract, but by far the most commonly used are US and CT. US is highly sensitive in the detection of biliary tract dilation and gallbladder pathology, and is commonly used in combination with other modalities (CT/MRI) either as part of the initial workup or for specific problem solving. CT (unenhanced and/or IV contrast-enhanced multiphase) imaging has high utility in both the workup of acute and chronic biliary tract pathologies, the most common of which are detailed below. MR cholangiopancreatography (MRCP), a special MRI sequence, which accentuates the pancreatic and biliary ducts, offers high-contrast resolution imaging of the biliary tract in both acute and chronic conditions that not only allows anatomic and pathological detail, but when combined with other specific MRI sequences and contrast agents, may allow functional assessment of the liver and biliary tree. Similar to CT, MRI also allows assessment of the extra-biliary structures, particularly when assessing for complicating features, such as concurrent pancreatitis/pancreatic duct obstruction. Finally, nuclear medicine imaging is less commonly used for biliary imaging, but remains valuable in specific cases. The commonest indication for hepatobiliary scintigraphy (^{99m}Tc-disofenin study – see Chapter 4) includes acute inflammation of the gallbladder (acute cholecystitis), chronic cholecystitis, identifying bile leaks and less commonly for bile duct sphincter (Odi) dysfunction.

11.12 Gallbladder

11.12.1 Cholelithiasis

Gallstones are a common finding in the general population; however, in the majority, these will be asymptomatic and only found incidentally. Most of these stones are located within the gallbladder (cholelithiasis) and may be made up of cholesterol, bile pigments, or a combination of materials. Their composition affects their visibility on various imaging modalities. In a proportion of cases, stones may be present within the biliary ducts (choledocholithiasis), either forming within the bile ducts (particularly in patients with prior gallbladder removal) or may enter the biliary system from the gallbladder. Although gall stones are usually asymptomatic, they can frequently lead to symptomatic presentation with acute biliary colic, ascending cholangitis (infection), obstructive jaundice (obstruction of the bile ducts), or acute pancreatitis (inflammation of the pancreas). US remains the imaging modality of choice in the detection and assessment of biliary tract calculi/stones and some of the complications related to them. On US, gallstones are echogenic structures, located within the dependent portion of the gallbladder, causing shadowing behind them (posterior acoustic shadowing) and may exhibit a “twinkle” artifact on color Doppler imaging (i.e. the stones demonstrate rapid changes in color when viewed on real-time Doppler US due to their dense nature). On CT, gallstones have a variable appearance/density based on their predominant composition, ranging from focal low-density stones (cholesterol containing) to densely calcified calculi, which may have a laminated appearance. Gallstones may be isodense to surrounding bile on CT and therefore, in patients with a high clinical suspicion of symptomatic gallstone disease, assessment with biliary tract US is warranted. MRI may be indicated in cases where the biliary system is suboptimally assessed by US and delineation of the biliary tract, presence and location of any stones (together with potential complications) may be required. On MRI, stones are typically dark on T2-weighted sequences (see Chapter 6) and either dark or bright on T1-weighted imaging (based on their content). Symptomatic gallstone disease may be treated surgically or with endoscopic retrograde cholangiopancreatography (ERCP) assisted stone extraction, where an endoscope is inserted through via the mouth to the level of the duodenum to allow stone extraction from the common bile duct.

11.12.2 Acute Cholecystitis

Acute cholecystitis is an acute inflammation of the gallbladder, typically caused by an obstructing lesion at the gallbladder neck or within the cystic duct, most commonly due to gallstones. This condition commonly presents with right upper quadrant (RUQ) pain and may be associated with fevers and elevated white blood cell count (leukocytosis). Untreated, complications include gallbladder infarction, perforation, abscess formation, bile peritonitis, and sepsis. In a very small proportion of patients (5–10%), acute gallbladder inflammation is unrelated to gallstones, but rather related to ischemia/reperfusion injury, seen in a specific group of patients (i.e. immunocompromised patients, following burns, trauma, on parenteral nutrition or following major surgery). US is the first-line imaging modality of choice for the gallbladder in acute cases rather than CT and MRI. US signs of acute cholecystitis include gallbladder luminal distension (>40 mm), wall thickening (>3 mm), sonographic Murphy sign (maximal tenderness over the gallbladder from imaging with an US probe), and fluid surrounding the gallbladder and/or liver (Figure 11.27). CT (contrast enhanced) imaging is particularly useful in demonstrating (or excluding) complicated gallbladder inflammation, but may be obtained as a first-line imaging study in patients where the clinical diagnosis is uncertain or differential diagnosis remains wide. On CT, the gallbladder is typically distended (unless decompressed due to perforation), showing stranding of the surrounding fat (due to immune reaction and fluid) and mild hyperperfusion in the surrounding liver parenchyma. Focal gallbladder perforation, gas, abscess formation, ischemia, or infarction (lack of mucosal enhancement) is preferentially assessed by CT. Hepatobiliary iminodiacetic acid (^{99m}Tc-disofenin) imaging (nuclear medicine) is a sensitive test in the diagnosis of acute cholecystitis, but is rarely used in clinical practice, due to the prolonged imaging time required and inability to assess for alternative diagnoses, except in cases of diagnostic uncertainty (Figure 11.28).

11.12.3 Neoplasms

Gallbladder polyps are small mucosal lesions that are commonly found in the general population. The vast majority (about 95%) are benign and found incidentally. Polyps may be imaged on US, CT, and MRI; however, US remains the preferred imaging modality due to its superior spatial resolution. Typically

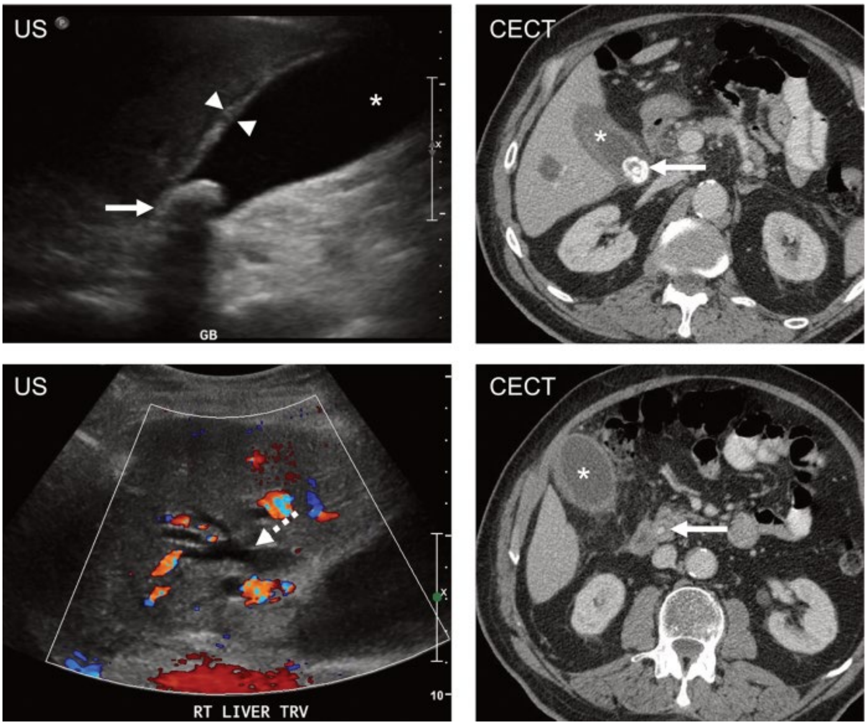

Figure 11.27 Acute cholecystitis and choledocholithiasis (i.e. stones in the common bile duct) – US and contrast-enhanced CT (CECT). US imaging (top left) shows a dilated gallbladder (*) with a dominant calculus (gallstone) at the gallbladder neck (solid arrow) showing classic shadowing below the stone. Note gallbladder wall thickening with surrounding trace fluid (arrow heads). Hepatic US imaging (bottom left) shows dilated intrahepatic bile ducts (dashed arrow). CECT (top right) shows same laminated stone in the gallbladder (solid arrow) within a thick-walled, inflamed gallbladder (*), consistent with acute cholecystitis. A small obstructing stone is noted at the distal common bile duct (bottom right image; solid white arrow), likely the cause of bile duct dilation and gallbladder inflammation. (*See insert for color representation of the figure.*)

small polyps are echogenic, protruding into the gallbladder lumen, and are non-shadowing (unlike gallstones). Larger polyps tend to be hypoechoic and may show internal vascularity. On CT and MRI, polyps demonstrate enhancement similar to the rest of the gallbladder, where hyper-enhancing polyps should be investigated further. There remains controversy with respect to polyps progressing to gallbladder cancers. Nonetheless, for polyps >10 mm, surgical consultation is advised. Those measuring ≤6 mm require no follow-up and 6–9 mm polyps require interval follow-up, typically with US. Gallbladder cancer (typically adenocarcinoma) remains asymptomatic until disease progresses to advanced stages, presenting with signs and symptoms of

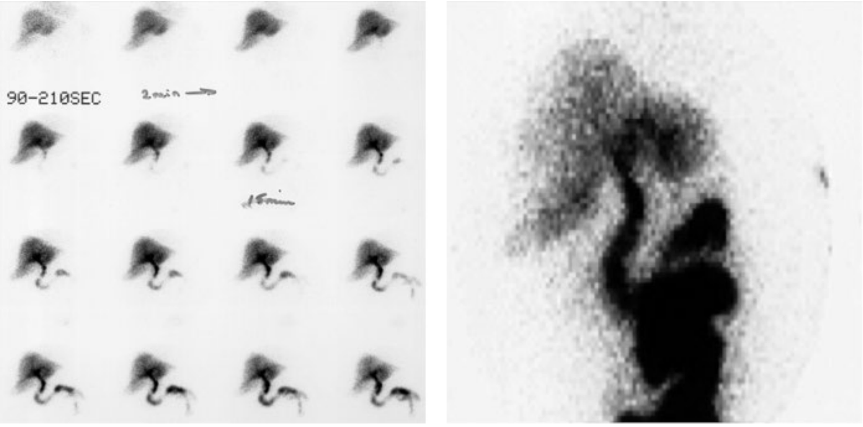

Figure 11.28 Acute cholecystitis on ^{99m}Tc-disofenin nuclear medicine scan. Left image: Early serial dynamic imaging after injection of the radiopharmaceutical (starting at 90–210 seconds post-injection acquisition [top left image] with serial imaging at 2-minute intervals, up to 35 minutes [bottom right image]). Serial imaging shows liver uptake followed by eventual excretion into the duodenum (at 15 minutes). No radiotracer uptake is seen in the gallbladder, indicating blockage of the cystic duct. Right image: An image taken four hours after injection shows significant excretion into the bowel with no gallbladder uptake, which is diagnostic of acute cholecystitis on a ^{99m}Tc-disofenin scan.

locally advanced or metastatic disease. US may identify early asymptomatic disease incidentally or potentially secondary to cholecystitis related to outflow obstruction. US allows identification of the primary tumor, usually as a soft-tissue mass with internal vascularity on color Doppler imaging (Figure 11.29). US may also allow assessment of extension of tumor beyond the gallbladder wall into adjacent structures, typically liver parenchyma. However, CT remains the imaging modality of choice in assessing the primary tumor, local-regional spread, and presence of metastatic disease.

11.13 Bile Ducts

11.13.1 Biliary Dilation

Bile duct dilation (intra and/or extrahepatic) has various causes; however, most typically it is seen due to a focal obstructing lesion. US, CT, and MRI are effective methods of imaging, although US is often used as first-line imaging. Dilated ducts appear as linear and branching hypoechoic (fluid-filled) structures extending through the liver, typically with abrupt transition/cutoff at the level of the obstruction. Similarly, CT and MRI allow further assessment of the

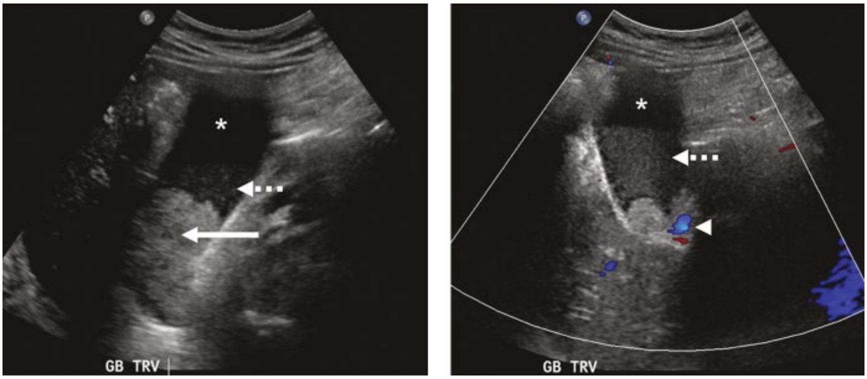

Figure 11.29 Gallbladder cancer – US. Left image: Focal soft-tissue mass located at the gallbladder neck (solid white arrow) causing mild distension of the gallbladder (*) and layering sludge above the tumor (white dashed arrow). Right image: Color Doppler US imaging shows focal vascularity within the soft-tissue component, allowing differentiation from dense sludge. (*See insert for color representation of the figure*.)

bile duct dilation, together with the site of obstruction. Furthermore, CT and MRI permit further characterization of an obstructing lesion.

11.13.2 Neoplasms

Benign and malignant bile duct tumors (either primary or secondary metastatic) account for a portion of cases of duct obstruction. Cholangiocarcinoma accounts for the second-most common primary hepatic malignancy, arising from the bile duct mucosa. Bile duct obstruction is an almost universal feature of this tumor by imaging, sometimes representing the only imaging finding and therefore warrants careful assessment with a low threshold for continued investigation. While US may be used first line in assessing bile duct dilation, multiphasic CT and/or MRI is required to characterize and stage these often complex tumors. Accurate staging by CT (and/or MRI) is crucial in determining the future management of these patients, particularly in determining curative intent of surgical resectability. On cross-sectional imaging, tumors may be intrahepatic, hilar, or extrahepatic in location, causing bile duct obstruction at any of these levels, depending on the location of the primary tumor. MRI and MRCP allow exquisite detail in imaging of the bile ducts and in soft-tissue characterization of the primary tumor. In addition, both CT and MRI allow assessment for local regional vascular involvement and the presence of nodal or visceral metastases. Other tumors of the bile ducts are pancreatic and ampullary carcinomas, which account for ~25% of obstructing biliary tumors; the former are discussed further in the pancreas imaging section below. Metastatic disease to the liver (from any extrahepatic primary tumor) causing biliary tree obstruction is uncommon; however, it is more commonly seen with advanced hepatic metastatic disease.

11.14 Pancreas

The pancreas is an endocrine and exocrine organ, secreting hormones into the bloodstream (such as insulin) as well as digestive enzymes into the GI tract. It is a retroperitoneal structure, which crosses midline with its head fitting within the groove of the C-shaped duodenum and its tail extending toward the splenic hilum (located within the left upper quadrant). An array of pathologies can involve the pancreas (either ad hoc or part of a multisystem process); however, these may be broadly divided into those that are acute, chronic, or neoplastic. The neuroendocrine pathologies involving the pancreas are described further in the endocrine imaging chapter (see Chapter 10).

11.14.1 Acute Pancreatitis

Inflammation of the pancreas (pancreatitis) is primarily a clinical diagnosis and relies heavily on biochemical markers of pancreatic inflammation such as elevated serum lipase and/or amylase. Imaging, however, plays an important role in determining the management of acute pancreatitis where it serves two major purposes. The first of these is to distinguish *gallstone pancreatitis* from *non-gallstone pancreatitis*. The second role for imaging is to assess for complications of acute pancreatitis. Imaging of the pancreas may be normal in cases of early or mild acute pancreatitis (hence the diagnosis cannot be excluded by imaging), although typically demonstrating pancreatic swelling, edema, and inflammatory changes within the surrounding (peri)-pancreatic fat. The distinguishing feature between acute *gallstone* and *non-gallstone* pancreatitis is the presence of biliary or pancreatic ductal stones, or signs of a recently passed stone. In addition, dilation of the biliary and/or pancreatic duct by an obstructing stone is an important diagnosis and it is important to identify these findings by imaging as this often leads to change in management in these patients. Obstructing stones usually originate from the gallbladder (or less commonly from the intrahepatic ducts), which may also contain numerous other stones at the time of imaging and may be an indication for a patient to undergo removal of the gallbladder, particularly if they present with recurrent episodes of gallstone pancreatitis. US is the first-line/imaging modality of choice in these cases, primarily to image the biliary tract and allows rapid and real-time assessment of the biliary tract, specifically in assessing for duct dilation and the presence of stones within the bile ducts. The gallbladder including its contents (e.g. gallstones) are generally well assessed with US. Visualization of the pancreas is often variable due to overlying gas and the deep location of the pancreatic tail on US, nonetheless pancreatic ductal dilation, stones, or focal lesions (which may occasionally be the cause of acute pancreatitis) are often seen.

The complications of acute pancreatitis are numerous and often correlate with the severity of clinical symptoms. Suspected complications are best imaged with a combination of unenhanced and contrast-enhanced CT, allowing full assessment of the pancreas, its surrounding spaces, and peritoneal/retroperitoneal compartments (Figure 11.30). Acute peri-pancreatic fluid collections are a common complication and may have some degree of organization (i.e. describing how well formed a collection is, typically depicted as a rim enhancing encapsulated pocket of fluid). Changes in the pancreatic parenchyma can also occur, including necrosis and hemorrhage from vascular disruption within the pancreatic bed. Leaking pancreatic enzymes may have significant local toxic soft-tissue effects, which may lead to injury of adjacent vascular structures, most notably arteries, leading to pseudoaneurysm formation and potentially life-threatening hemorrhage. Complications with necrosis and hemorrhage often require very aggressive clinical support, monitoring, and management given the high mortality associated with these findings. Unenhanced CT imaging is typically obtained to assess for calcifications related to biliary or pancreatic duct stones, pancreatic parenchymal calcification (a sign of chronic pancreatitis), and to assess for acute blood products. When uncomplicated, inflammatory changes may manifest as swelling of the

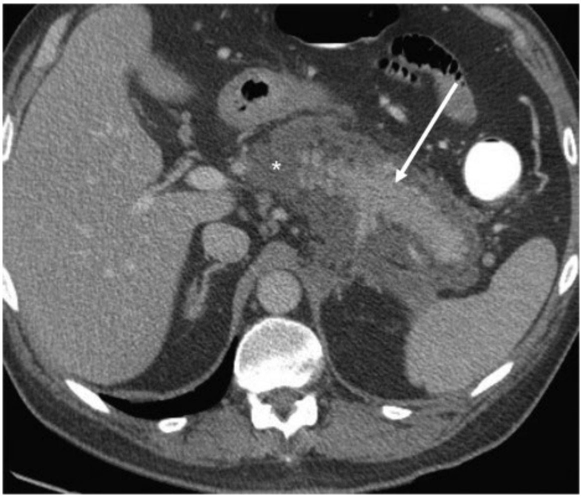

Figure 11.30 Severe acute pancreatitis – contrast-enhanced CT (CECT). Axial image shows findings of severe acute pancreatitis with significant edema/inflammatory changes (darker areas) surrounding the pancreas (*). However, the pancreatic parenchyma (arrow) enhances normally without evidence of necrosis or hemorrhage.

pancreas together with decreased attenuation related to edema. Stranding around the pancreatic tissue is usually the best imaging diagnostic clue for underlying pancreatic inflammation. A surrounding small volume of low-density fluid may also be seen. In gallstone pancreatitis, biliary stones may be seen (although a proportion is invisible on CT) and best assessed with US. Typically stones causing acute pancreatitis are seen within the mid and distal portion of the common bile duct, as it passes through the head of the pancreatic parenchyma. Upstream dilation of the intrahepatic ducts may be seen and the patient may be clinically jaundiced. Dilation of the pancreatic duct is also best demonstrated on CT (although can be seen with US) as its whole length is usually visualized by CT (uncommon on US).

Pancreatic necrosis is seen in acute severe cases, and if suspected, should be imaged with CT, which depicts areas of pancreatic parenchyma that fails to enhance following administration of IV contrast. On rare occasions of severe pancreatitis, the whole pancreas may be necrotic and non-enhancing. Pancreatic hemorrhage is typically related to pancreatic ischemia and necrosis. On unenhanced CT, areas of intermediate or increased attenuation are noted replacing the normal pancreatic parenchyma. However, in the case of a bleeding arterial pseudoaneurysm, blood products are typically seen around the pancreas, within the retroperitoneum and/or peritoneal cavity, depending on the anatomic location of the vessel involved. Moreover, following administration of IV contrast, arterial pseudoaneurysms appear as a very bright focal dilation of a peripancreatic artery (e.g. splenic, left gastric, pancreaticoduodenal artery, etc.) with possible active contrast leakage, in the case of a ruptured pseudoaneurysm, representing active extravasation of blood.

MRI has very specific utility in the workup of acute pancreatitis, primarily to establish the presence and extent of choledocholithiasis (stones in the biliary tract) when gallstone pancreatitis is suspected and CT and US are nondiagnostic. This is typically seen in cases where there is a stone suspected at the distal common bile duct, close to the ampulla, where US assessment is generally limited due to bowel gas. ERCP is an invasive technique of directly imaging the biliary and pancreatic ductal system via upper GI endoscopy and direct catheterization of the ductal system, which allows contrast injection of the biliary tree facilitating real-time X-ray assessment. In cases of acute pancreatitis (and other causes of ductal obstruction), this technique remains the treatment of choice in relieving ductal obstruction. In the case of gallstone pancreatitis causing ductal dilation (typically together with features of infection – cholangitis), the biliary stones may be removed (via sphincterotomy ± stone retrieval) or bypassed by placing a stent in cases where stones cannot be retrieved or other causes of obstruction are present (e.g. neoplasm). Of note, however, ERCP in itself is a cause of acute pancreatitis.

11.14.2 Pancreatic Trauma

Acute pancreatic trauma can be of varying degrees of severity from small contusions to complete disruption of the pancreatic head, seen with both blunt and penetrating traumatic mechanisms. CT remains the imaging modality of choice in the assessment of the pancreas in the setting of trauma. An important factor in assessing acute pancreatic trauma is the determination of the integrity of the pancreatic duct given that disruption of the duct will result in spillage of pancreatic fluid into the retroperitoneal space, which can be toxic to the surrounding tissues and therefore is an indication for surgery. Pancreatic contusions are more commonly seen that pancreatic disruption (Figure 11.31) or fracture (rare) and are depicted as areas of decreased attenuation on contrast-enhanced CT. Areas may be rounded, segmental, or linear. Pancreatic duct disruption results in discontinuity of the main pancreatic duct generally through the center of the pancreas, although this may be difficult to ascertain particularly when assessing patients with multi-visceral injuries. More severe disruption will result in the absence of the normal appearing lobulated pancreas, which will be replaced by devascularized non-enhancing necrotic areas and areas of acute hemorrhage.

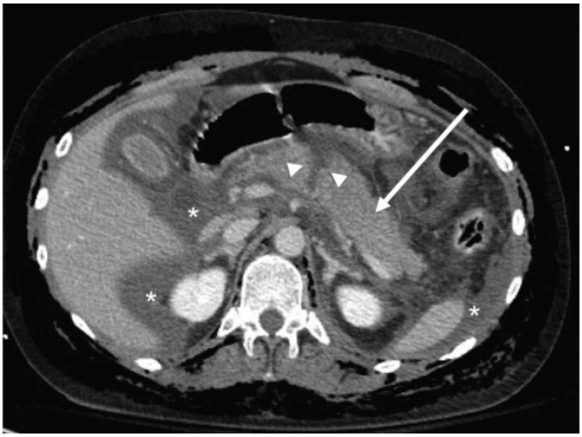

Figure 11.31 Pancreatic trauma – contrast-enhanced CT (CECT). Axial image through the pancreas with a linear area of non-enhancement within the pancreatic parenchyma (arrow heads), consistent with partial pancreatic transection. Note the pancreatic parenchyma remains enhancing elsewhere (arrow); however, the traumatic injury almost certainly transects the main pancreatic duct (not seen on CT). Moderate peripancreatic/retroperitoneal and peritoneal fluid/hemorrhage is noted (*).

11.14.3 Chronic Pancreatitis

Chronic pancreatitis is generally the result of repeated episodes of acute pancreatitis. Imaging features often include diffuse pancreatic atrophy, pancreatic calcifications, and peri-pancreatic collections (pseudocysts). Pseudocysts are collections of often-complex pancreatic fluid, which are generally, but not always, located in a peri-pancreatic distribution. They are referred to as pseudocysts due to their lack of a true epithelial lining and instead have a wall that is composed of fibrous tissue. Pseudocysts are "benign" entities, but may cause problems related to mass effect on adjacent structures or superinfection. They may also mimic cystic neoplasms of the pancreas, potentially posing a diagnostic dilemma for the clinical team.

Imaging is usually not indicated specifically to make a diagnosis of chronic pancreatitis, though is useful in cases where there are overlapping clinical and/or imaging features of chronic pancreatitis and other pathological processes. Coarse calcifications related to chronic pancreatitis may be seen on plain film X-ray radiography, but is of little clinical value. Equally, US assessment is limited primarily due to dense calcification typically seen in chronic pancreatitis interfering with US beam penetration. Unenhanced and multiphase contrast-enhanced CT imaging are most commonly used given their ability to comprehensively assess the pancreas and peri-pancreatic tissues (Figure 11.32). Thinning and heterogeneity of the pancreatic parenchyma are particularly well seen after the administration of IV contrast given that the normal uniform bright appearance of the parenchyma becomes more heterogeneous with loss of parenchymal bulk. Duct changes are readily apparent, typically with dilatation of the main duct and numerous side branches usually due to downstream post-inflammatory strictures. Note that early intraductal pancreatic cancers may give a similar imaging appearance, hence why these cases often pose a diagnostic dilemma. Pseudocysts on CT may contain blood, debris, and calcification and typically get smaller on subsequent imaging. Occasionally, these complex lesions may mimic a cystic primary pancreatic neoplasm (either that is typically malignant or has malignant potential). MRI is reserved in these patients in whom imaging features on CT have overlapping features of a malignant process (i.e. main duct dilation or complex pseudocysts mimicking malignancy). The superior soft-tissue and contrast resolution are the primary factors allowing for better characterization.

11.14.4 Pancreatic Neoplasms

Pancreatic neoplasms can be grouped into two main categories, namely solid and cystic lesions. The major solid malignant neoplasms of the pancreas include pancreatic ductal adenocarcinoma (most common), neuroendocrine tumors, metastases, and lymphoma (rare). Cystic tumors of the pancreas are

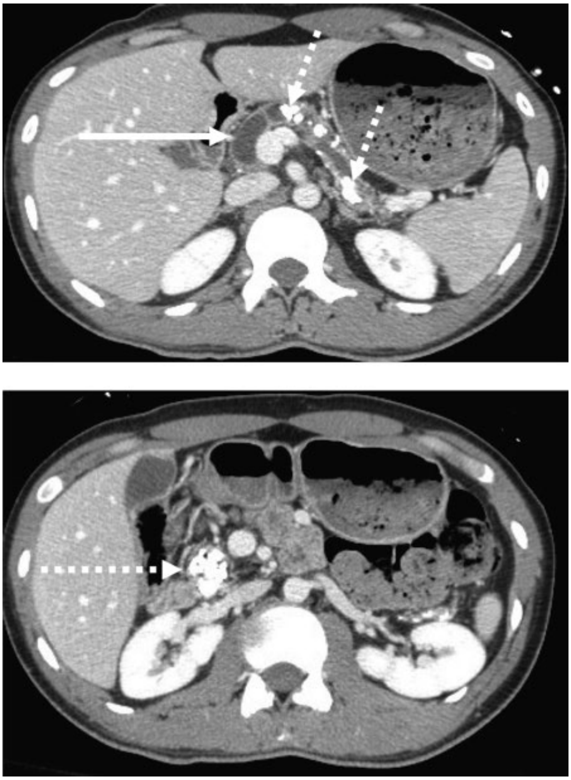

Figure 11.32 Chronic pancreatitis – axial CECT – Images taken at two different levels through the pancreas. Top image: The pancreatic head, neck, body, and tail, which shows significant parenchymal atrophy (thin rim of tissue surrounding the main pancreatic duct) with marked dilation of the main pancreatic duct (low-density tubular structure – solid arrow). Calcifications are also present throughout the pancreatic parenchyma and duct (dashed arrow). Bottom: Large confluent calcification within the region of the pancreatic head/uncinate process.

common and are often identified incidentally. Cystic tumors may be either benign, malignant, or have malignant potential and imaging is most commonly used to differentiate between lesions in this spectrum. Discussions of pancreatic cystic lesions are beyond the scope of this chapter, but further reading/information may be found in the suggested resource listing at the end of this chapter.

11.14.5 Pancreatic Ductal Adenocarcinoma

Pancreatic ductal adenocarcinoma manifests as a solid infiltrating tumor arising from the duct epithelium. These tumors often present with pancreatic duct obstruction and may have simultaneous obstruction of the common bile duct when in the head of the pancreas, causing a classic *double duct sign.* Pancreatic neoplasms causing bile duct obstruction tend to present earlier due to patients becoming jaundiced and seeking medical attention earlier. Conversely, tumors in the tail typically have a delayed presentation due to a lack of overt symptoms and frequently demonstrate metastases upon presentation. The major role for imaging, apart from diagnosis, is staging of these tumors for local extension and metastasis to determine whether they are surgically resectable. Unlike other lesions within the pancreas (such as pancreatic cystic and neuroendocrine tumors), adenocarcinomas tend to have a more infiltrative appearance with ill-defined borders, making them difficult to identify, especially when small. Importantly, signs such as main pancreatic duct obstruction (dilation) and associated parenchymal atrophy are imperative to recognize in identifying subtle malignant tumors that may be otherwise inconspicuous on conventional imaging.

In those identified with a pancreatic cancer, assessment of the mass in relation to the adjacent vascular structures involve determination of the presence/absence of arterial and portal venous involvement. Most importantly in terms of resectability (and therefore potential surgical cure) is encasement, narrowing, or obstruction of the major regional arteries (celiac axis, superior mesenteric, hepatic arteries, and aorta), as involvement of these vessels will generally preclude surgical management. Portal venous assessment, particularly of the portal confluence and superior mesenteric vein, is also important for assessing resectability and planning for potential vascular reconstruction at the time of surgery.

Finally, spread of disease to non-regional lymph nodes, liver, peritoneum, lung, or bone is vital to recognize, preventing patients from undergoing a highly morbid operation for no reasonable benefit and allowing the patient to explore a host of other palliative treatment options. Multiphasic CT (unenhanced, arterial, and portal venous phase) CT is the mainstay of imaging in the diagnosis and staging of pancreatic cancers. Typical appearances of adenocarcinoma often preclude the need for biopsy confirmation in those patients who may be surgically resectable. High contrast and spatial resolution of CT is particularly suited for assessment of vascular involvement, which as outlined above, is important for determining the feasibility of surgical resection. (Figure 11.33 demonstrates the typical appearance of a pancreatic adenocarcinoma.)

MRI is generally used as a problem-solving tool (particularly when a tumor is suspected though not definitively seen on another imaging modality) to characterize a focal pancreatic lesion (benign vs. malignant) or to identify the presence of metastatic disease (typically to exclude liver metastases) in a patient with a resectable tumor. ^{18}F-FDG PET/CT is of great utility in selecting patients with pancreatic cancer in whom the primary pancreatic tumor is

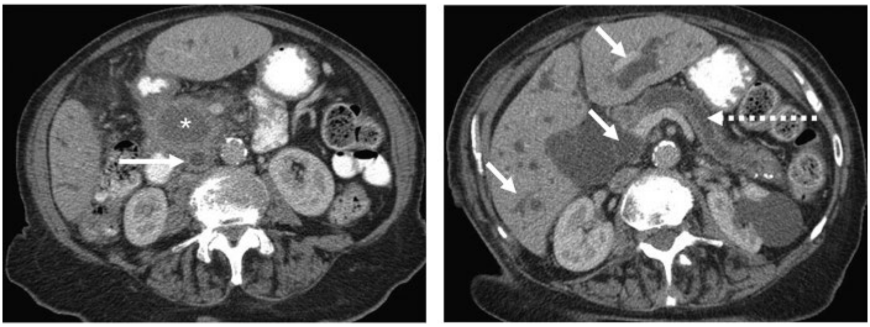

Figure 11.33 Pancreatic adenocarcinoma – axial contrast-enhanced CT (CECT). Images taken at two different levels through the pancreas. Top image: A large mass is present within the head of the pancreas (*) that has hypodense appearance after IV contrast administration relative to the remaining pancreatic tissue. Bottom image: The mass is causing upstream dilation of the biliary tree (solid arrows) and main pancreatic duct (dashed arrow), leading to the so-called double duct sign.

deemed resectable; however, staging imaging (CT) has identified findings that are indeterminate for metastatic disease, which PET/CT may help to further characterize, given that the presence of metastases would preclude curative surgery. Typically, these tumors are ^{18}F-FDG-avid and therefore PET/CT will identify the increased metabolic activity in the metastases as well. Figure 11.34 demonstrates a ^{18}F-FDG PET/CT study utilized in the staging of an otherwise resectable pancreatic tumor. Endoscopic Ultrasound (EUS) is a minimally invasive imaging tool that allows high resolution of imaging of the pancreas (among other abdominal structures). This technique combines fiber-optic endoscopy with high-frequency US (mounted at the tip of the endoscope) and therefore allows the US transducer to image the pancreas through the back wall of the stomach. This high-frequency imaging of the pancreas (by virtue of the close proximity to the stomach) allows greater lesion detection and characterization than conventional transabdominal US. Furthermore, a dedicated channel on the scope allows a biopsy needle to be guided into target organs/lesions through the scope and thus allowing pathological confirmation of lesions prior to definitive major surgery.

11.15 Spleen/Lymph Nodes

The spleen is a lymphoid organ whose major functions are sequestration of elements of blood as well as supporting the immune system. It is an intraperitoneal structure located within the left upper quadrant, under the left hemidiaphragm. Given its function, the spleen is a highly vascularized, supplied by a dominant splenic artery and splenic vein. Lymph nodes are also part of the

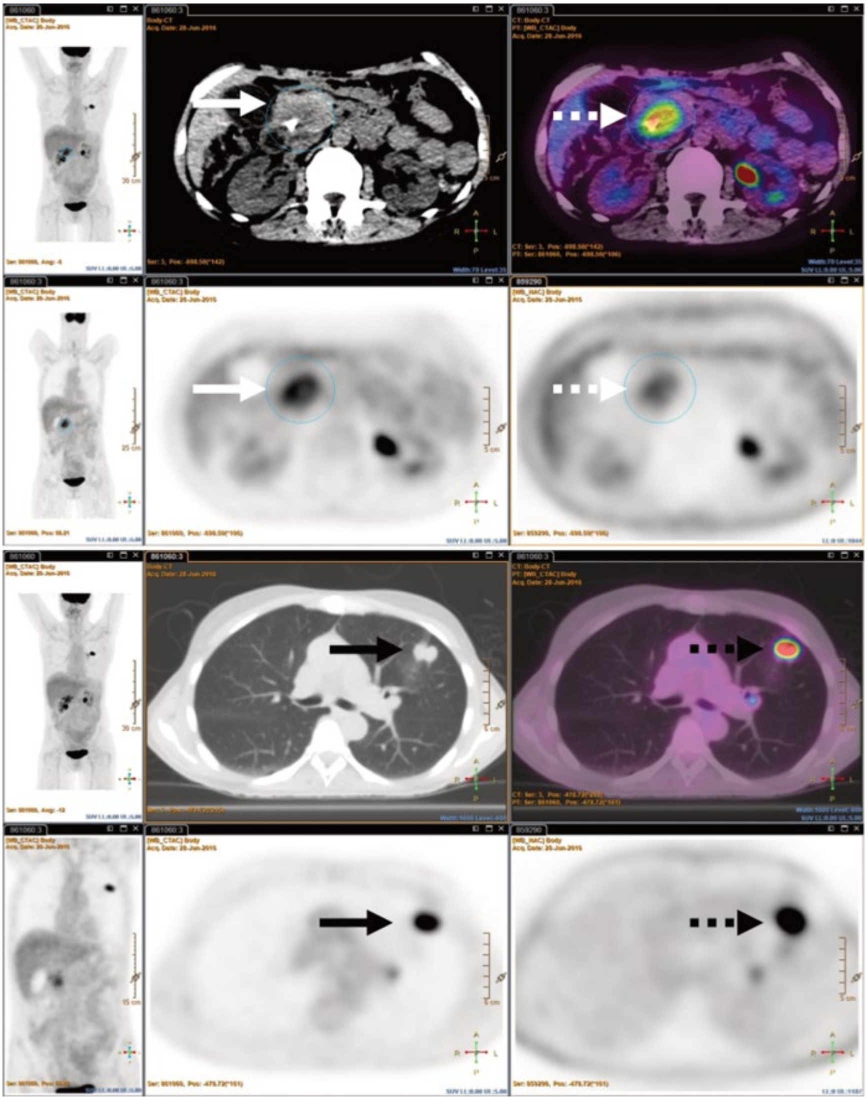

Figure 11.34 Pancreatic cancer on PET-CT. Top two rows of images represent the PET/CT and PET only images of the abdomen: A mass is seen within the pancreatic head (white solid arrow) on CT that demonstrates hypermetabolic activity (white dashed arrow), which was proven to be a pancreatic neuroendocrine tumor. Bottom two rows of images represent the PET/CT and PET only images of the chest: A hypermetabolic pulmonary metastasis is also seen in the left lung, both on CT (solid black arrow) and PET (black dashed arrow). (*See insert for color representation of the figure*.)

lymphatic/immune system and are found throughout the body, typically following the vascular pathways. A variety of pathological processes are known to involve these organ systems, a few common ones are detailed below with respect to their usual imaging features.

11.15.1 Splenic Trauma

The major cause of acute pathology to the spleen is trauma and, indeed, the spleen is the most commonly injured abdominal organ in the setting of trauma. Typical imaging findings in the setting of blunt trauma include splenic lacerations and hematoma. Hemorrhage from the spleen, as with other intraperitoneal organs, often settles within the pelvis due to gravity, making careful assessment of the spleen important in the setting of trauma, even in the absence of adjacent splenic hemorrhage. Contrast-enhanced CT is the imaging modality of choice in the assessment of abdomino-pelvic trauma. Splenic contusions and/or lacerations are depicted as hypodense areas within the splenic parenchyma and may be classified according to the American Association for the Surgery of Trauma (AAST) classification system, based on the degree, size, and involvement of splenic laceration and hematoma. Splenic injury may result in significant volume of blood loss. CT allows the detection of active bleeding by virtue of identifying contrast extravasating from the spleen or associated splenic vessel. Figure 11.35 demonstrates traumatic splenic injury and associated hematoma/hemorrhage.

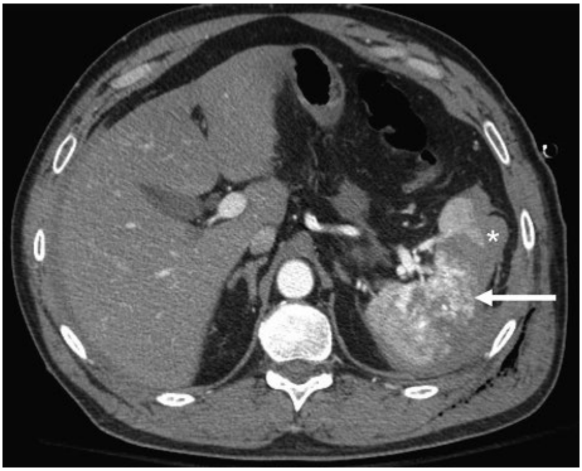

Figure 11.35 Splenic trauma on contrast-enhanced CT (CECT). Multiple lacerations are noted involving the splenic parenchyma (arrow), depicted as multiple areas of absent parenchymal enhancement. Surrounding blood products are seen (*) consistent with hemorrhage.

11.15.2 Splenomegaly/Splenic Masses

Splenomegaly (enlargement of the spleen) is often an indicator of more chronic pathology. This may be systemic (such as benign and malignant hematological disorders, infections, or inflammatory processes), chronic liver disease (i.e. cirrhosis with portal hypertension), or more rarely, due to a primary splenic pathology (such as primary splenic lymphoma). Focal splenic masses can be benign (such as hemangiomas) or malignant, most commonly secondary to lymphomatous/leukemic involvement. Other malignant lesions, such as splenic metastases are much less common. The size of the spleen can be reliably measured with US, conventionally measuring the cranio-caudal dimension (upper to lower-most part). US also allows interrogation of the splenic parenchyma for the detection of a focal splenic lesion. CT and MRI allow similar detection of focal splenic lesions, but with the advantage of allowing assessment of other abdomino-pelvic structures that may be involved by the same process or cause splenic enlargement/mass. Occasionally, US and CT are required to guide biopsy of focal lesions in the spleen to allow for definitive diagnosis.

11.15.3 Lymphadenopathy

Lymph node pathology is most commonly indicated on imaging by lymph node enlargement, though other features such as change in morphology or enhancement can also be helpful. Lymphadenopathy can be seen with a wide variety of benign and malignant conditions, including transient reactive enlargement, and therefore cannot be interpreted without appropriate clinical history. In the setting of oncologic imaging, lymph node enlargement and/or morphological abnormality (lymphadenopathy) signify the involvement of nodes by malignant disease. Generally, lymph nodes in the region of known primary malignancy are first to be involved (indicating regional spread of disease); however, the pattern of nodal involvement is very much dependent on the organ involved, its lymphatic drainage, and the histopathology of the malignancy. US, CT, MRI, and ^{18}F-FDG PET/CT are all highly useful imaging techniques in the detection/characterization of abnormal lymph nodes, with CT, MRI, and PET/CT reserved for staging of malignant disease. Imaging plays a vital role in image-guided sampling of pathological nodes to determine/confirm diagnosis and staging of the disease process.

11.16 Summary

Imaging of the abdomen requires the entire breadth of imaging techniques, with complementary information often provided by each in order to arrive at a final diagnosis. US and CT are the mainstay of imaging, with other techniques such as MRI or PET generally used for troubleshooting or for specialized purposes. It is important to remember that the abdominal organs are all interconnected and pathology affecting a single organ can often involve adjacent organs either by direct involvement (i.e. a tumor arising from the gallbladder and invading the liver) or spread to multiple organs (i.e. metastases to the liver and peritoneum from a pancreatic primary). Thus, despite the grouping of pathology by organ that has been outlined above, a comprehensive assessment of the abdominal structures is a necessity for full assessment of nearly all pathology.

Reference

1 Bruix, J., Sherman, M., and American Association for the Study of Liver Disease (2011). Management of hepatocellular carcinoma: an update. *Hepatology* 53 (3): 1020–1022. (Evidence-based guidelines in the diagnostic, therapeutic, and preventative aspects of care in liver disease.).

Additional Reading

Bran, W.E. and Helms, C.A. (2012). *Fundamentals of Diagnostic Radiology*. Philadelphia: Wolters Kluwer.

Cancer Care Ontario. Colorectal Screening Guidelines. https://www.cancercare.on.ca/colorectalscreening (accessed 30 April 2018).

Radiographics. www.pubs.rsna.org/journal/radiographics (accessed 30 April 2018). (Premier education journal in diagnostic radiology published by the Radiological Society of North America.)

Radiology Assistant (2017). www.radiologyassistant.nl (accessed 30 April 2018). (An online educational resource for the Radiology Society of the Netherlands, providing easily digestible topics on medical imaging.)

Radiopedia.org (2017). www.radiopedia.org (accessed 30 April 2018). (A free education radiological encyclopedia with access to cases and reference material.)

The American Association for the Surgery of Trauma (2017). www.aast.org (accessed 30 April 2018). (Provides grading scales for traumatic injury, including the abdominal organs.)

Dr. Sarah Johnson

Dr. Sarah Johnson graduated with Bachelor of Medical Science and Medical Doctor degrees from the University of Alberta and successfully completed the Diagnostic Radiology Residency Programme at the University of Toronto. She then commenced an Oncology Imaging fellowship at Memorial Sloan Kettering Cancer Centre and subsequently accepted a position as a staff radiologist in the Medical Imaging Consultants group at the University of Alberta, before joining the Joint Department of Medical Imaging/University Health Network at the University of Toronto. Dr. Johnson is also a Diplomate of the American Board of Radiology and an Associate of the Royal Conservatory of Music in Toronto in both Voice and Piano. Dr. Johnson is actively involved in teaching and research, serving as a member of several scientific associations including Radiological Society of North America (RSNA), Canadian Medical Associate (CMA), American Roentgen Ray Society (ARRS), and Society of Radiologists in Ultrasound (SRU), and as a reviewer for multiple Radiology journals. She has also published in peer reviewed journals, including *Radiology*. Dr. Johnson's current research interests include Gynecologic and Oncologic Imaging.

Medical Imaging for Health Professionals: Technologies and Clinical Applications, First Edition.
Edited by Raymond M. Reilly.
© 2019 John Wiley & Sons, Inc. Published 2019 by John Wiley & Sons, Inc.

12

Genitourinary Tract Imaging

Sarah Johnson

12.1 Introduction

The genitourinary (GU) system comprises a complex of organs, which are required for multiple vital physiologic functions. The kidneys have a major role in maintaining homeostasis. The collecting systems, involving the kidneys, ureters, and bladder, are responsible for transporting physiologic waste products for excretion. Male reproductive organs, namely the prostate gland, seminal vesicles, and testicles, are required for maintenance of sexual health and reproductive capability. The female reproductive organs, including the uterus and ovaries, are homologous for the female population with the added responsibility of sustaining and delivering pregnancy. The functions of the GU system are multiple and complex, and a disruption of any component of the system may have major adverse consequences.

Diseases and dysfunction of the GU system have a wide range of clinical presentations. Some of these are easy to identify and diagnose, for example, testicular trauma. Others are more subtle and frequently cause a diagnostic dilemma, including the many and variable diseases, which have a final common pathway of renal dysfunction. A comprehensive approach may be required for the diagnosis, treatment, and monitoring of GU system abnormalities, involving multiple medical specialties and various clinical tools. Medical imaging is widely applied as one of these tools in the investigation and characterization of suspected GU system abnormalities.

This chapter will outline the major applications of medical imaging for clinically-directed evaluation of the GU system. The discussion is organized by the organ of primary interest, namely the kidneys and collecting systems, and male and female reproductive organs. A section is separately devoted to GU system imaging in the pediatric population, given the multiple specialized

Medical Imaging for Health Professionals: Technologies and Clinical Applications, First Edition.
Edited by Raymond M. Reilly.
© 2019 John Wiley & Sons, Inc. Published 2019 by John Wiley & Sons, Inc.

clinical situations and imaging techniques among these patients. A clinically-oriented approach is chosen in order to facilitate an informed choice of medical imaging modality when faced with a patient in whom a GU system abnormality is suspected. Special attention is dedicated to appropriateness criteria, as the appropriate use of medical imaging is an important target in the current health-care environment. The material discussed in this chapter will hopefully inform the application of relevant medical imaging services to achieve optimal patient care.

12.2 GU System Imaging Modalities

As will be further discussed throughout this chapter, multiple medical imaging modalities may be applied to the evaluation of the GU tract (Table 12.1). Different modalities may be selected based on the clinical question and individual patient factors. Several common medical imaging modalities used for GU tract assessment are:

12.2.1 Ultrasound

This technique (see Chapter 6) does not use ionizing radiation and is very easily tolerated. Patients generally require no special preparation. This modality is especially useful in pregnant women and children, when limited radiation exposure is desirable. US is limited by its reliance on the skill of the operator and the inability to clearly visualize very deep structures (Figure 12.1).

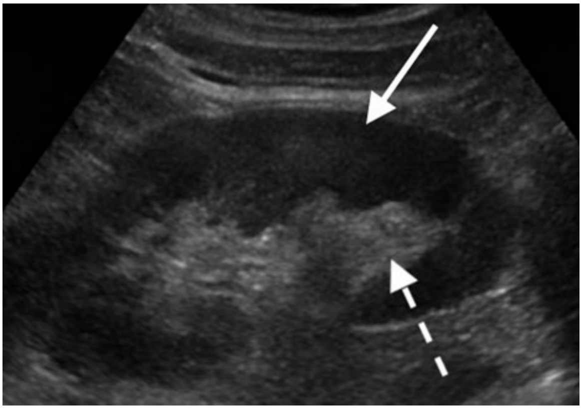

Figure 12.1 A normal kidney on ultrasound (US). The cortex is hypoechoic (solid arrow) while the central renal hilum is hyperechoic (dashed arrow) due to the normal renal sinus fat in this region. The collecting system is not dilated and no focal lesions are present.

Table 12.1 Quick guide to selection of medical imaging investigations of the genitourinary system.

Clinical history or suspected diagnosis	Recommended modality	Special considerations
Renal or ureteric calculi	CT is the most sensitive test. Ultrasound may be selected depending on local practice patterns	Ultrasound should always be the first-line test in pregnant or pediatric patients
Uncomplicated lower urinary tract infection	No imaging usually required	CT urogram or MR urogram if the patient has risk factors for complicated infection
Uncomplicated suspected pyelonephritis	No imaging usually required	Contrast-enhanced CT if the diagnosis is unclear or if the patient has risk factors for complicated infection
Renovascular hypertension	CT angiogram or MR angiogram	Ultrasound with Doppler assessment or nuclear scintigraphy with ACE-inhibitor administration are acceptable but require dedicated expertise
Renal mass	Contrast-enhanced CT or MRI	Contrast-enhanced ultrasound is an option if local expertise permits
Renal transplant	Ultrasound with Doppler assessment	
Renal function assessment	Radionuclide scintigraphy	For "dynamic" assessment (i.e. renal perfusion or collecting system clearance), ^{99m}Tc-DTPA or ^{99m}Tc-MAG3 is most common. For "static" assessment, ^{99m}Tc-DMSA is generally chosen
Bladder cancer	MRI for local bladder staging. CTU for staging upper urinary tract. Distant staging with CT	Distant abdominopelvic staging can be completed with CTU; chest CT can be performed simultaneously
Bladder trauma	CT cystogram	Only perform CT cystogram after urethral integrity has been confirmed on a retrograde urethrogram (see below)
Urethral trauma	Retrograde urethrogram	Suspected when blood is present at the urethral meatus and with straddle or trans-urethral penetrating mechanism of injury

Testicular cancer	Scrotal ultrasound	CT chest/abdomen/pelvis after diagnosis for completion of staging
Testicular pain	Scrotal ultrasound	
Suspected prostate cancer	Prostate MRI	Transrectal US (TRUS) may be appropriate as a screening evaluation or to guide biopsy
Known prostate cancer	Prostate MRI for local staging Contrast-enhanced CT abdomen/pelvis for distant staging Total body bone scan for distant staging	New techniques, for example, Na^{18}F-PET/CT, have been developed and may be available in some centers
Abnormal vaginal bleeding	First investigation: Pelvic and transvaginal ultrasound	Sonohysterogram and/or pelvic MRI may be recommended for further evaluation in some patients
Known endometrial carcinoma	Usually diagnosed based on biopsy after abnormal ultrasound. MRI for local staging. CT chest/abdomen/pelvis for distant staging	
Known cervical carcinoma	MRI for local staging. Distant staging with CT chest/abdomen/pelvis or 18-FDG-PET/CT	
Suspected adnexal mass	First investigation: Pelvic and transvaginal ultrasound MRI may be required for further evaluation	Staging CT chest/abdomen/pelvis if findings are diagnostic of ovarian carcinoma

(*Continued*)

Table 12.1 (Continued)

Clinical history or suspected diagnosis	Recommended modality	Special considerations
Acute pelvic pain, female	First investigation: Pelvic and transvaginal ultrasound	Pregnancy status should be determined in all patients of reproductive age by evaluation of serum β-hCG level prior to imaging evaluation
	CT abdomen/pelvis may be appropriate when non-gynecologic etiology of pain is suspected in a nonpregnant patient	MRI may be required for further characterization of any identified suspicious lesions among these patients
		MRI is also a follow-up modality among pregnant patients with noncontributory ultrasound as CT is relatively contraindicated in pregnant females
		MRI performed in pregnancy are performed WITHOUT gadolinium contrast administration
Pregnancy – first trimester	First investigation: Pelvic ultrasound	Transvaginal US may be required in some patients
Obstetrical evaluation	First trimester nuchal translucency assessment with ultrasound	Follow-up ultrasound may be required after the routine anatomic survey for optimal fetal visualization
	Routine second-trimester anatomic assessment with ultrasound	
Pregnancy – second/third trimester	First investigation: Pelvic ultrasound	
	Suspected placental abnormal invasion: Consider follow-up MRI	
Congenital renal or genital anomaly	First investigation: Abdominal and pelvic ultrasound	
Pediatric renal cystic disease	May be identified on prenatal ultrasound. Repeat ultrasound often recommended after birth	

Pediatric renal mass	First investigation: Abdominal ultrasound	CT or MR may be required for further characterization, staging, or surgical planning
Pediatric urinary tract infection (UTI), uncomplicated	Ultrasound on first UTI to assess for any relevant anomalies	Follow-up with voiding cystourethrography (VCUG) or radionuclide cystography (RNC) if vesicoureteral reflux (VUR) is suspected
Pediatric urinary tract infection (UTI), febrile with atypical features or recurrent febrile UTI	First investigation: Abdominal ultrasound. VCUG also often recommended	May consider renal DMSA scintigraphy in follow-up to assess for renal scarring
Acquired pediatric genital abnormality, i.e. trauma, mass	First investigation: Pelvic ultrasound	

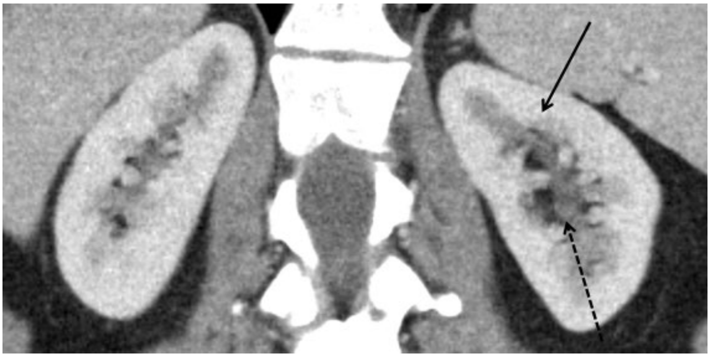

Figure 12.2 Normal bilateral kidneys on contrast-enhanced CT. The renal parenchyma enhances normally and symmetrically bilaterally (solid arrow). The more hypodense (darker) fluid-filled collecting system (dashed arrow) is not dilated. This patient has no renal lesions.

12.2.2 Computed Tomography

This technique (see Chapter 2) offers excellent spatial resolution and the ability to clearly visualize deep abdominal and pelvic structures. The patient is however exposed to a small amount of ionizing radiation (see Chapter 1) and some computed tomography (CT) protocols may require administration of intravenous or oral iodinated contrast ("CT dye"), which carry a small risk of allergic reaction. Despite these drawbacks, CT is very effective for a wide variety of clinical indications and is used extensively (Figure 12.2).

12.2.3 Magnetic Resonance Imaging

This modality (see Chapter 5) provides unparalleled imaging evaluation of soft tissues and does not use ionizing radiation. Spatial resolution is slightly less than on CT but often almost comparable. Magnetic resonance imaging (MRI) is especially valuable in clarifying soft-tissue characteristics but requires a high degree of patient cooperation and tolerance of often very long imaging examinations. MRI also often requires the administration of contrast (for MRI, gadolinium-based), which carries a small risk of inducing the severe condition of Nephrogenic Systemic Fibrosis (NSF) in patients with severe renal dysfunction and very rarely causes a severe allergy among the general population (Figure 12.3).

12.2.4 Nuclear Scintigraphy

This modality, which mainly employs SPECT (see Chapter 3) for GU imaging, involves the administration of radiopharmaceuticals to patients (see Chapter 4). Subsequent distribution in the patient often reflects radiotracer movement

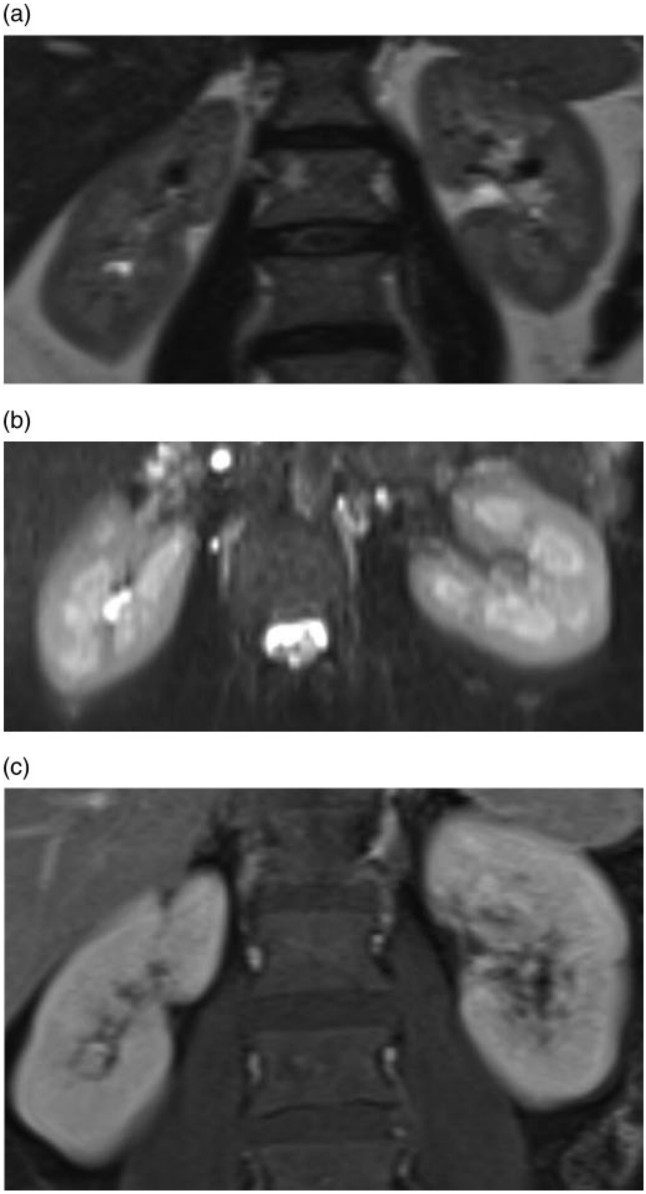

Figure 12.3 (a) Normal bilateral kidneys on T2-weighted MRI, coronal plane. (b) Normal bilateral kidneys on T2-weighted fat-saturated MRI. This is the same patient; the fat around the relatively bright renal kidneys is now dark (contrast to panel a where the fat surrounding the kidneys is bright). The change in fat signal intensity is achieved by applying a technique known as fat saturation. In this case, it makes the kidneys more visible against the background. (c) Normal bilateral kidneys on T1-weighted fat-saturated contrast-enhanced MRI. This is the same patient after gadolinium contrast has been injected. The appearance of the kidneys on contrast-enhanced MRI is similar to contrast-enhanced CT. This selected sequence of MR images demonstrates the reduced spatial resolution of MRI compared to CT (MR images are more blurry), but the improved soft-tissue contrast compared to CT (observe the difference between the renal peripheral cortex and central medullae in panel a).

and excretion through a physiologic pathway and therefore serves as a marker of function for that pathway. Scintigraphy thus provides a means of evaluating organ function while other imaging modalities such as CT and US mainly assess anatomical abnormalities. These techniques also involve a small amount of radiation exposure and are most appropriate when applied to a selected well-defined clinical indication.

12.3 Evaluation of the Kidneys and Collecting Systems

The bilateral kidneys are subject to a wide range of pathologic processes, including both reversible and irreversible, and benign and malignant, diseases. The bilateral ureters are affected by many similar processes, and may also be involved by other local ureteric diseases. The following discussion will address some of the most common collecting system abnormalities using clinical presentation or diagnosis as a starting point.

12.3.1 Urinary Tract Calculi (Nephroureterolithiasis)

Renal and ureteric calculi (kidney stones; nephroureterolithiasis) are extremely common and the prevalence is increasing, and has been related to increasing rates of diabetes and obesity [1]. In the United States, nephroureterolithiasis has been identified as the most expensive urologic disease, with an annual medical cost of ~$10 billion. Most cases are idiopathic, although a small minority occur secondary to metabolic disorders or genetic syndromes. Patients classically present with flank pain ipsilateral to the site of a calculus impacted within the collecting system and the pain can be excruciating. Recurrence is frequent (in approximately one-third of patients). An imaging study is often requested in patients when nephroureterolithiasis is suspected.

CT abdomen/pelvis without intravenous contrast has the highest sensitivity for diagnosis of urinary tract calculi [2] among the commonly utilized imaging modalities and is the modality recommended by the American College of Radiology (ACR) when this diagnosis is suspected [3]. Calculi may also be detected on renal/bladder ultrasound (US) but this modality is less sensitive. However, a large randomized controlled trial demonstrated that clinical outcomes were similar among patients with suspected nephroureterolithiasis in the Emergency setting when either US or CT was used as the initial imaging study [2]. Consequently, either modality may be acceptable as a first-line imaging evaluation and local practice habits may be considered when making the choice (Figure 12.4). US is the preferred modality in pregnant and pediatric patients when renal calculi are suspected in order to avoid the radiation

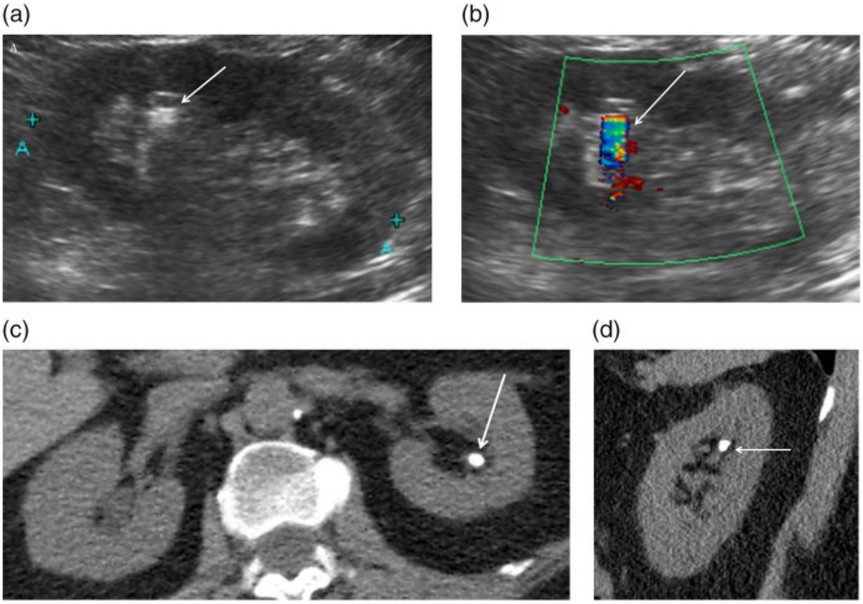

Figure 12.4 (a) An echogenic focus in the left renal upper pole (arrow) is suspicious for a small renal calculus without obstruction. (b) The echogenic focus shows "twinkle" artifact when color Doppler ultrasound (US) is applied (arrow), which suggests that the structure is mineralized, like most renal calculi. (*See insert for color representation of the figure*.) (c) CT was performed in the same patient. A calcified renal calculus in the left kidney is similar to the recent US (arrow). No calculi are found in the right kidney. (d) Sagittal reformat CT in the same patient again shows the left renal calculus in the upper pole (arrow), now in the same orientation as on the earlier US.

exposure associated with CT. Abdominal radiographs (X-rays often referred to as "KUB Radiographs," where KUB is an acronym for **K**idneys, **U**reters, and **B**ladder) are currently of limited use for the diagnosis of nephroureterolithiasis due to low sensitivity. However, these may be used as a screening test in centers where access to CT is delayed (Figure 12.5). KUB radiographs may also be ordered by urologists or other clinicians as follow-up examinations or for treatment (lithotripsy) planning [4].

12.3.2 Renal Infection and Inflammation

Infection may develop in any region of the GU tract. "Urinary tract infections," "UTI," or "bladder infections" are terms colloquially applied to infections of the lower tract, in particular the bladder and urethra, and are very common, especially among women. Among medical practitioners, these lower UTI may be more formally described as cystitis (bladder infection) or urethritis (infection

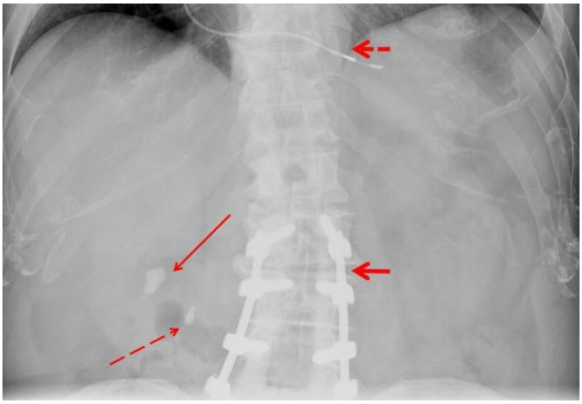

Figure 12.5 KUB radiograph in a patient with right flank pain demonstrating a large right renal pelvis calculus (long arrow) and a smaller calculus in the right proximal ureter (long dashed arrow). Incidental note of prior spinal surgery (thick solid arrow) and pacemaker lead incompletely imaged in the inferior heart (thick dashed arrow).

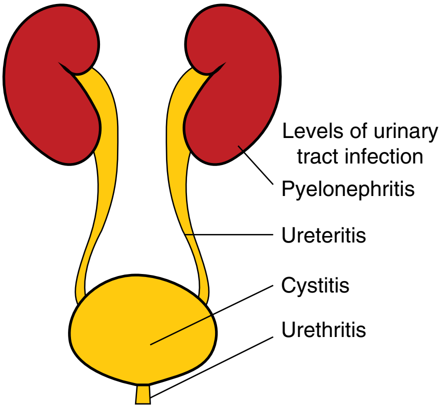

Figure 12.6 Schematic illustrating the anatomic levels corresponding to genitourinary (GU) tract infections. Infection of the kidneys is known as pyelonephritis; ureter infection as ureteritis, bladder infection as cystitis, and urethral infection as urethritis.

isolated to the urethra) (see Figure 12.6). These are generally diagnosed clinically [5] and a medical imaging investigation is not generally required. All imaging modalities have received a rating of “Usually not appropriate” from the ACR [6] when the infection is uncomplicated and the patient has no underlying risk factors for complicated infection. Risk factors include a known anatomic abnormality of the GU tract, immunosuppression or diabetes, and prior trauma. If these are present, or if the patient has symptoms of urinary obstruction, fever lasting over 72 hours after starting antibiotics, or rapidly recurrent infections, further assessment with medical imaging may be indicated. In these cases, CT urography (CTU) or MR urography

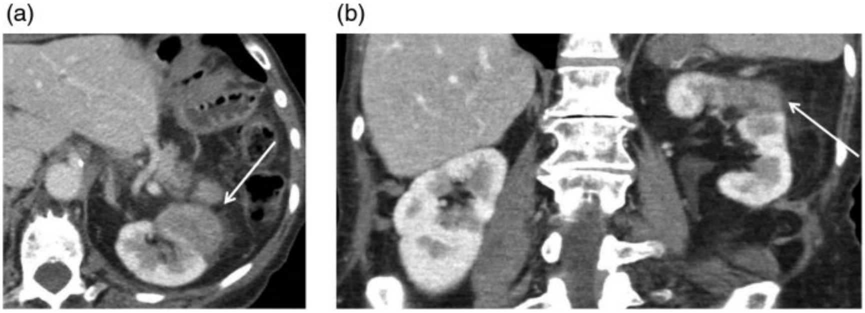

Figure 12.7 (a) Hypoenhancing left renal upper pole cortex with small-volume perinephric (around the kidney) free fluid and surrounding fat stranding (arrow). (b) Coronal projection more clearly outlines the zone of abnormal cortex, which enhances less than the background normal noninvolved renal cortex due to edema from infection, with associated left inflammatory change around the kidney (arrow). Compare this to the normal right kidney. In this patient with fever and flank pain, this likely represents acute left focal pyelonephritis.

(MRU) are considered most appropriate [6]. These are similar examinations involving both non-enhanced and contrast-enhanced imaging of the abdomen and pelvis, with a delayed phase acquired after contrast injection when contrast has accumulated in the urinary collecting system (see Section 12.3.7). These examinations offer an excellent anatomic assessment of the urinary tract.

Infections of the upper tract are often less straightforward to diagnose and have a more severe clinical course. Renal infection, or pyelonephritis, is associated with a classic diagnostic triad of fever, nausea/vomiting, and costovertebral angle (flank) tenderness. When the diagnosis is straightforward and the clinical course is uncomplicated, a medical imaging evaluation is usually unnecessary [7]. If the patient has risk factors for complicated infection (similar to those for lower UTI), or if the diagnosis is uncertain but pyelonephritis is suspected, contrast-enhanced CT is the most appropriate test. US has limited sensitivity for diagnosis of acute pyelonephritis [8], and unenhanced CT does not provide optimal evaluation of the kidneys and collecting systems. These modalities may be applied if iodinated contrast is contraindicated (see Chapter 2), or as follow-up examinations when obstruction is suspected, as both techniques are satisfactory to demonstrate a dilated obstructed collecting system. Contrast-enhanced CT, however, provides more detailed assessment, demonstrating hypoenhancing edematous parenchyma (Figure 12.7) and, when present, other signs of UTI such as enhancing collecting system urothelium. Unenhanced and contrast-enhanced CT may also be performed simultaneously, with the unenhanced phase used to assess for nephroureterolithiasis and the post-contrast phase for further details.

12.3.3 Renal Vascular Anomalies

Hypertension (known colloquially as high blood pressure) is an extremely common medical condition and may be idiopathic ("essential hypertension") or secondary to a wide range of underlying causes. Approximately 5% of cases in the United States are estimated to relate to "renovascular hypertension," which reflects underlying atherosclerosis of the renal blood vessels [9]. Atherosclerosis results in functional narrowing of blood vessels and when this occurs in the renal artery, the end effect in some patients will be the development of hypertension. This etiology of hypertension may be treatable by stenting (dilating the artery in an Interventional Radiology procedure then placing a narrow tube, or stent, in the involved renal artery to keep the vessel open). This treatment is still under some debate but remains an option in some centers. When hypertension cannot be controlled with noninvasive medical means, the diagnostic workup includes assessment for other etiologies of hypertension including renal artery stenosis (RAS).

Medical imaging tests are only recommended in selected patients who have clinical features leading to a high index of suspicion for renovascular hypertension. An imaging evaluation is not needed for every patient with essential hypertension [10]. In the appropriate clinical setting, the ACR appropriateness criteria indicate that an MR angiogram (MRA) or CT angiogram (CTA) of the renal arteries is the most appropriate first investigation if the patient's renal function is sufficient to allow safe administration of the intravenous contrast agents used during these examinations (Figure 12.8). Current criteria also recognize that an US with Doppler evaluation of the renal arteries or nuclear medicine scintigraphy using an angiotensin converting enzyme (ACE)-inhibitor (e.g. captopril) may also be reasonable evaluations in centers with sufficient experience in these specialized techniques or if MRA/CTA are contraindicated.

ACE-inhibitor scintigraphy is a functional assessment for RAS. Among patients with RAS, the administration of an ACE-inhibitor will lead to reduced renal function in the affected kidney compared with the baseline renal function, demonstrated by a change in the time–activity curves, which are calculated for each kidney before and after ACE-inhibitor administration (Figure 12.9). The time–activity curve becomes abnormal after ACE-inhibitor administration for kidneys with RAS [11]. Nuclear medicine scintigraphy with ACE-inhibitor is less reliable when renal function is poor, as the lack of response to the ACE-inhibitor may reflect RAS or renal dysfunction [10]. For patients with very poor renal function, non-gadolinium enhanced MRA may be performed although sensitivity is reduced; Doppler US is another option.

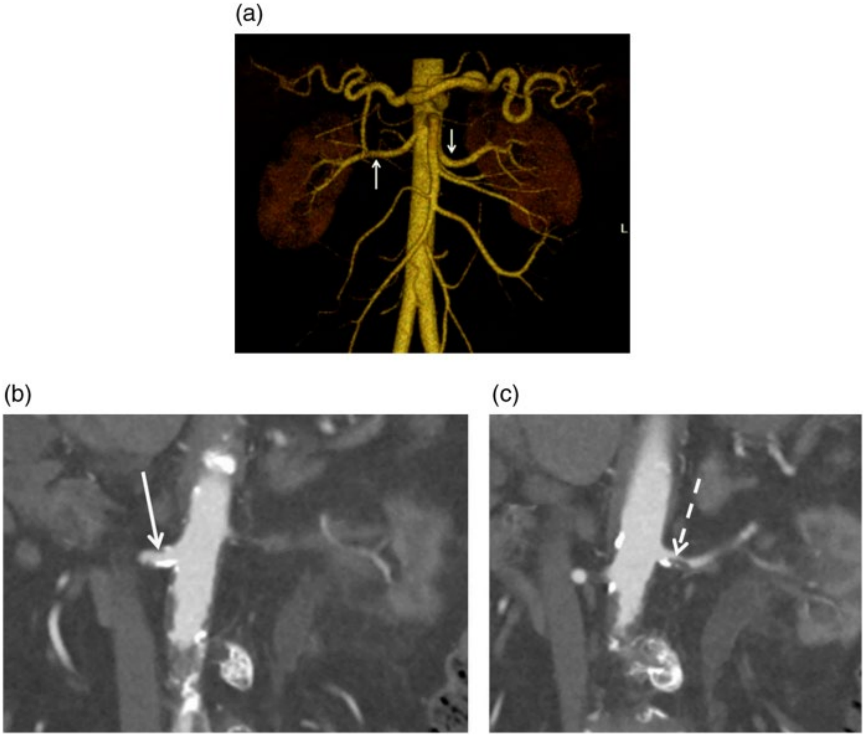

Figure 12.8 (a) Volumetric reconstruction of a renal CT angiogram demonstrating normal non-stenotic renal arteries bilaterally (arrows). (b) and (c) CT angiogram in this 90-year-old patient with hypertension and severe atherosclerotic vascular disease demonstrates mild narrowing of the patent lumen of the proximal right renal artery by a calcified atherosclerotic plaque (b; solid arrow) and moderate narrowing of the proximal left renal artery lumen by a noncalcified plaque (c; dashed arrow).

12.3.4 Renal Lesions

Several benign lesions are often found in healthy kidneys. Simple renal cysts are the most common and approximately half of adults over 50 years of age have at least one cyst [12]. Simple cysts are filled with simple fluid and have no malignant potential (Figure 12.10). Angiomyolipomas are more complex-appearing lesions and contain fat and smooth muscle tissue [13]. These may be complicated by hemorrhage but are also benign.

Renal cell carcinoma (RCC) is the most common renal neoplasm. Transitional cell carcinoma (TCC) is also quite common. More rare renal tumors are generally identified on histology. RCC may have a variety of clinical presentations but these lesions are increasingly found incidentally during medical imaging

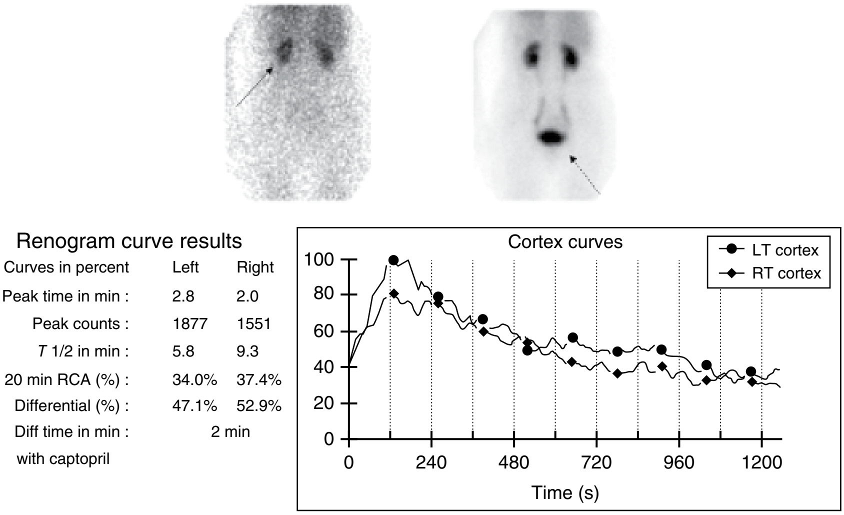

Renogram curve results

Curves in percent	Left	Right
Peak time in min :	2.8	2.0
Peak counts :	1877	1551
T 1/2 in min :	5.8	9.3
20 min RCA (%) :	34.0%	37.4%
Differential (%) :	47.1%	52.9%
Diff time in min : with captopril	2 min	

Figure 12.9 Normal captopril renogram. Low-resolution planar images demonstrate normal flow to both kidneys as radiolabeled tracer accumulates symmetrically in the kidneys (solid arrow), and the tracer is excreted normally into the bladder (dashed arrow). The Renogram Curve demonstrates appropriate renal function, as the tracer counts from both left and right renal cortex are similar, and the tracer counts decrease appropriately as the tracer is excreted from the kidneys into the bladder.

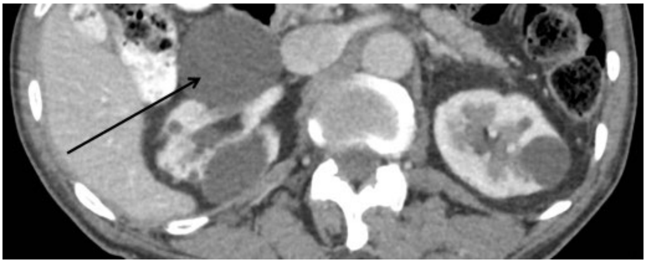

Figure 12.10 Abdominal CT demonstrating multiple bilateral renal lesions with attenuation similar to fluid consistent with simple renal cysts (arrow).

tests performed for other indications. When a solid or complicated/complex cystic renal mass is identified, further characterization with contrast-enhanced CT or MRI is acceptable; CT is, however, usually selected due to ease of access (Figure 12.11). If poor renal function prohibits contrast administration, US with Doppler interrogation and unenhanced MRI are options [14]. Contrast-enhanced (microbubble) US may also be used to characterize renal lesions in centers with expertise in this area. While key for initial diagnosis, medical imaging may have a role in management also; among certain patients with

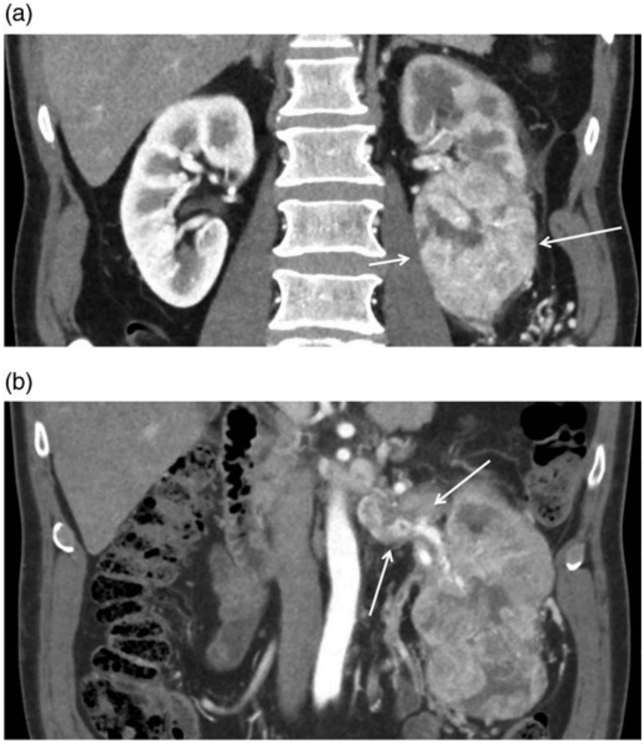

Figure 12.11 (a) Contrast-enhanced abdominal CT. The right kidney is normal. The left kidney is expanded by a large enhancing mass (arrows), which partially extends out of the lower pole. (b) In the same patient, the left kidney enhances less than the right kidney because tumor is growing into the left renal vein (arrows), obstructing venous drainage of the kidney. This decreases vascular flow through the kidney, delaying the uptake of contrast into the renal parenchyma.

small (under 4 cm) renal masses, a "watch and wait" approach may be elected, which often includes ongoing surveillance using contrast-enhanced CT or MRI.

Fluorodeoxyglucose positron emission tomography (^{18}F-FDG-PET, usually performed with CT and thus known as ^{18}F-FDG-PET/CT) is a well-known tool in oncologic imaging (see Chapter 15). FDG is a marker for metabolic activity, which is generally higher in tumors than in normal tissue. Regions of increased uptake are localized on PET/CT; although not perfectly specific, these hypermetabolic foci often represent tumor. The utility of ^{18}F-FDG-PET/CT for RCC and other renal tumors is unfortunately relatively limited. The kidneys concentrate and excrete ^{18}F-FDG into the urine and functional kidneys therefore have baseline high levels of ^{18}F-FDG uptake, limiting assessment for hypermetabolic tumors on this background [15]. A few investigations into alternate PET tracers for evaluation of RCC patients have been published and these may increase the practical applicability of PET in the future [16].

12.3.5 Renal Transplants

Renal transplants offer potential cure for patients with end-stage renal failure. Renal transplants are becoming increasingly common among the general population. While expertise in the implantation, monitoring, and management of renal transplants is increasing, complications still afflict up to 8% of patients [17]. US with Doppler assessment is the preeminent tool for evaluation of renal transplants. Transplant kidneys are usually more easily visualized than native kidneys as they lie more superficial in the abdomen and require less sound-wave penetration than deeper native kidneys. US may be used to assess the transplant parenchyma, vascular supply, and collecting system (Figure 12.12). Nuclear medicine scintigraphy with ^{99m}Tc-DTPA or ^{99m}Tc-MAG3 renography (see Chapter 4) may be elected for assessment of transplant function among certain patients but generally remains a second-line test in North America [18]. If a patient in renal failure is fortunate enough to find someone willing to act as a living renal donor, most renal transplant centers have a “Living Renal Donor” CT or MRI protocol for the donor to assess the vascular anatomy and to ensure that the intended transplant kidney is safe for transplant.

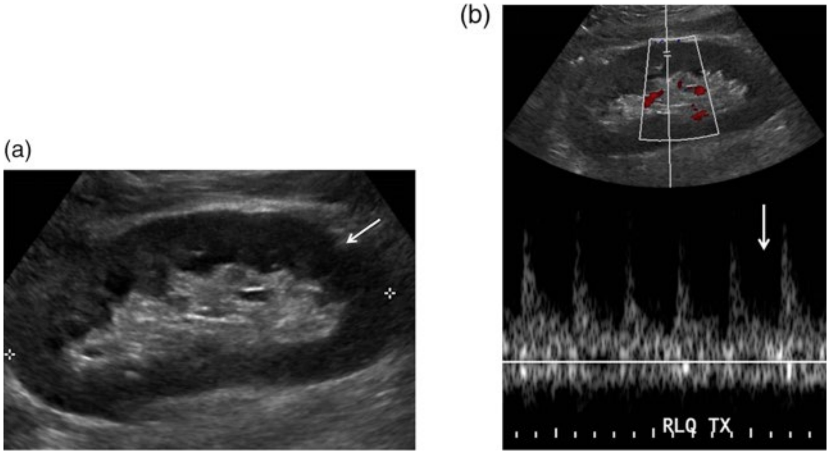

Figure 12.12 (a) Normal right lower quadrant transplant kidney on ultrasound. Normal parenchymal echotexture (arrow). (b) Doppler pulse wave ultrasound demonstrating normal vascularity of the right lower quadrant transplant kidney. A normal arterial waveform (ultrasound trace at the bottom of image) is obtained from parenchymal branch arteries (arrow). The resistive index, a vascular parameter used as a measure of blood flow in the kidney, is calculated from this waveform as 0.68, which is within the normal range. (*See insert for color representation of the figure.*)

12.3.6 Renal Function and Dysfunction

Renal dysfunction is a final common pathway in multiple disease processes, which may culminate in end-stage renal failure. Diagnosing the presence of renal failure may be straightforward but determining the underlying etiology is often challenging. Medical students learn a common approach to renal failure, which classifies the underlying cause as "Pre-renal, Renal or Post-renal" [19]. US is an appropriate tool to confirm or exclude a post-renal (obstructive) cause by assessing for hydronephrosis, the presence of which implies collecting system obstruction [20]. Nuclear medicine scintigraphy is a means of assessing renal function [11]. Discussion of the complex renal functional pathways is beyond the scope of a single chapter, but briefly, the kidneys are vigorously perfused with the majority of blood entering the renal glomeruli, where various products are filtered out of the blood and into the collecting system. The filtered products then pass through the renal tubules, where fluid and electrolyte balances are maintained by homeostatic alteration of reabsorption and secretion rates of water and electrolytes. The end-product, urine, is then excreted into the intrarenal collecting system before passing into the ureters and bladder. Important markers of renal function are therefore:

Renal plasma flow (RPF) – the amount of blood that reaches the kidneys. This is distinct from *Effective renal plasma flow* (ERPF), which reflects the amount of blood delivered to the kidneys AND extracted from the blood plasma.

Glomerular filtration rate (GFR) – the rate at which the glomeruli filter products from the blood.

Parenchymal transit time – the time elapsed between filtration and excretion.

These markers can be evaluated directly or indirectly by several nuclear medicine studies, which are sometimes described as "radionuclide scintigraphy." These involve the administration of radiopharmaceuticals that follow physiologic pathways such as renal excretion (see Chapter 4) with the distribution of the radiotracer detected by a gamma camera and the pathway function inferred based on the normal or abnormal distribution. Common radiotracers for renal radionuclide scintigraphy include ^{99m}Tc-DTPA (^{99m}Tc-diethylenetriaminepentaacetic acid), ^{99m}Tc-MAG3 (^{99m}Tc-mertiatide), and ^{99m}Tc-DMSA (^{99m}Tc-dimercaptosuccinic acid; ^{99m}Tc-succimer). ^{99m}Tc-DTPA and ^{99m}Tc-MAG3 allow "dynamic" renal imaging as these radiotracers sequentially move through perfusion, filtration, transit, and excretion from the kidneys (Figure 12.13). These radiotracers serve as a marker of renal blood flow and collecting system

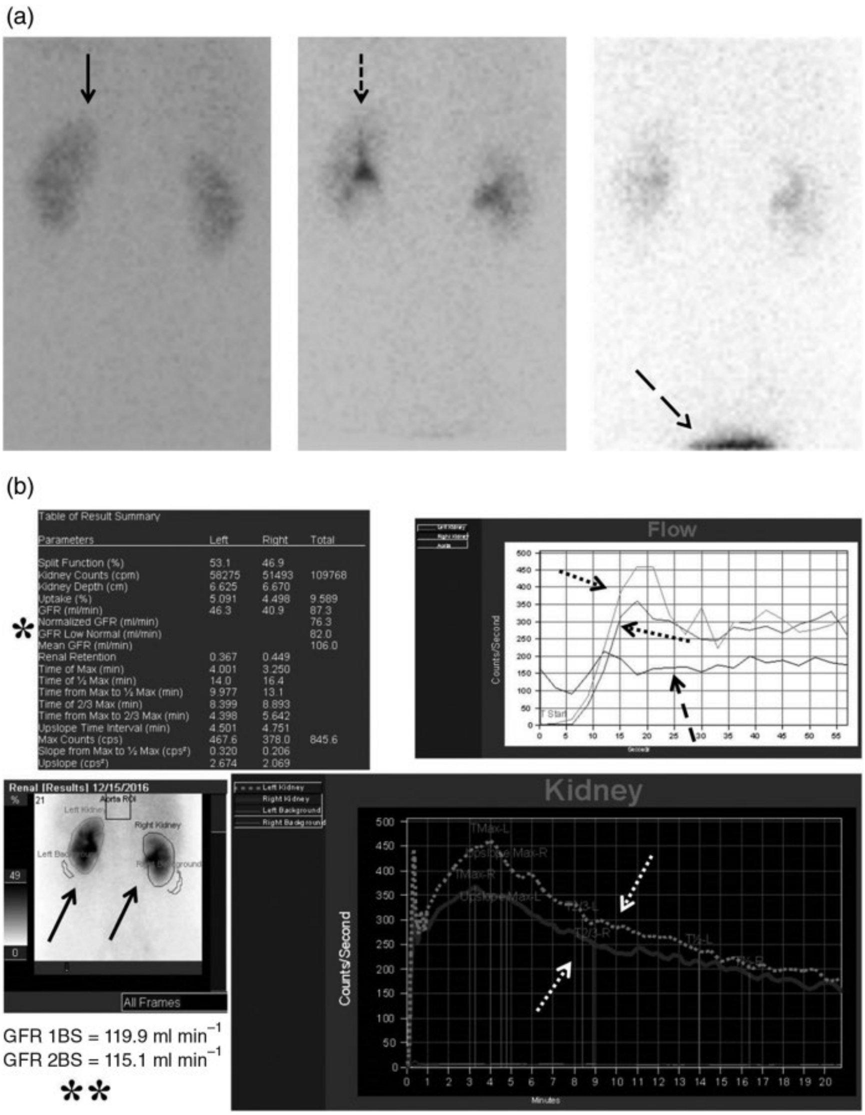

(a)
(b)
*
Renal [Results] 12/15/2016
Aorta ROI
Left Kidney
Right Kidney
Left Background
Right Background
All Frames
Flow
Left Kidney
Right Kidney
Aorta
Counts/Second
Seconds
T Start
Kidney
Left Kidney
Right Kidney
Left Background
Right Background
TMax-L
Upslope Max-R
TMax-R
Upslope Max-L
T2/3-L
T2/3-R
T½-L
T½-R
Counts/Second
Minutes
**

Table of Result Summary

Parameters	Left	Right	Total
Split Function (%)	53.1	46.9	
Kidney Counts (cpm)	58275	51493	109768
Kidney Depth (cm)	6.625	6.670	
Uptake (%)	5.091	4.498	9.589
GFR (ml/min)	46.3	40.9	87.3
Normalized GFR (ml/min)			76.3
GFR Low Normal (ml/min)			82.0
Mean GFR (ml/min)			106.0
Renal Retention	0.367	0.449	
Time of Max (min)	4.001	3.250	
Time of ½ Max (min)	14.0	16.4	
Time from Max to ½ Max (min)	9.977	13.1	
Time of 2/3 Max (min)	8.399	8.893	
Time from Max to 2/3 Max (min)	4.398	5.642	
Upslope Time Interval (min)	4.501	4.751	
Max Counts (cps)	467.6	378.0	845.6
Slope from Max to ½ Max (cps²)	0.320	0.206	
Upslope (cps²)	2.674	2.069	

GFR 1BS = 119.9 ml min^{-1}
GFR 2BS = 115.1 ml min^{-1}

Figure 12.13 (a) ^{99m}Tc-DTPA renal scintigraphy. SPECT images from a healthy 40-year-old patient after injection of ^{99m}Tc-DTPA radiotracer. Images were acquired at one, two, and five minutes postinjection of radiotracer and demonstrate uptake in the kidneys bilaterally at one minute (arrow), clearance into the bilateral collecting systems at two minutes (dotted arrow), and excretion into the bladder at five minutes (dashed arrow). (b) Normal quantitative results from renal scintigraphy. Renal function parameters are summarized for each kidney to determine the physiologic parameter of glomerular filtration rate (GFR). Regions of interest (ROI) are drawn around each kidney and radiotracer counts are obtained from the bilateral ROI (arrows). The "Flow" chart plots the tracer counts obtained from each region-of-interest (ROI; black dotted arrows) as a function of time during the first minute following tracer injection, and also plots the counts from the aorta during the first minute for comparison of the counts in the blood pool (dashed arrow). The "Kidney" chart plots the tracer counts obtained from each ROI (white dotted arrows) as a function of time for the 20 minutes following tracer injection. The quantitative results are summarized in a table (*) and are used to calculate the GFR (**).

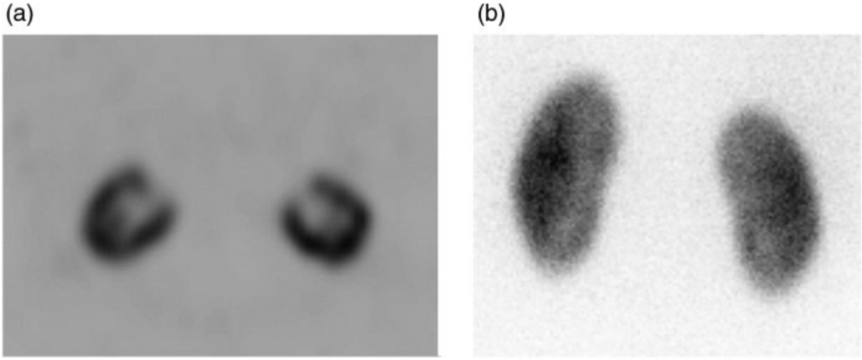

Figure 12.14 Normal renal ^{99m}Tc-DMSA nuclear medicine scintigraphic study. (a) Transaxial and (b) coronal SPECT images of the bilateral kidneys following ^{99m}Tc-DMSA administration, obtained three minutes postinjection. There is normal symmetric radiotracer uptake and excretion bilaterally.

outflow. ^{99m}Tc-DTPA is filtered by the glomeruli and so acts as a marker of glomerular filtration function. ^{99m}Tc-MAG3 is mainly cleared by secretion by the renal tubules, with only a small proportion filtered through the glomeruli. ^{99m}Tc-MAG3 undergoes more efficient extraction from blood plasma and so is the preferred agent for functional renal assessment, serving as a marker of ERPF [21]. ^{99m}Tc-DMSA is used for "static" renal morphology imaging since it binds to the renal cortex. By binding to the functional cortex, ^{99m}Tc-DMSA demarcates the volume of functional renal parenchyma and so serves as a marker of relative renal function or parenchymal loss [11] (Figure 12.14). Renal function is a very complex concept and imaging techniques such as CT or US, which offer only an anatomic assessment, may not provide sufficient information to aid further diagnosis and patient management. Radionuclide scintigraphy is currently the major technique allowing functional assessment but findings on these exams must always be correlated with the clinical history and patient status. Provision of a careful and comprehensive history and clearly outlining the clinical question of concern will aid in selecting the appropriate examination and ensuring a clinically relevant report.

12.3.7 Ureteric Neoplasms

CT and MRI are now the most common medical imaging modalities applied to ureteric assessment. Classically, intravenous urography (IVU) or retrograde urography (RU) allowed assessment of the ureters and bladder with fluoroscopy, but the improving speed and resolution of CT and MRI, and their ability to depict other findings outside the collecting system, which are not evident on IVU/RU, has limited the use of these older techniques to very specific indications.

CTU is a CT protocol dedicated to assessment of the renal and ureteric collecting system. The aim is to fill the collecting system with contrast, thereby better delineating any lesions as "filling defects" against the background contrast-filled collecting system. CTU is usually the initial study elected when a ureteric abnormality is suspected. US may serve as a screening test for collecting system obstruction but most of the ureter is obscured in many adult patients on US, limiting its use for detailed ureteric assessment. CTU techniques have been extensively researched and described and multiple authors and institutions have certain procedural preferences. In general, CTU protocols involve a three- or four-phase CT examination comprising an unenhanced phase, which will delineate radiodense renal calculi and other calcifications, followed by one or more contrast-enhanced phases targeted to assessment of the renal parenchyma, and ending by a delayed acquisition once contrast has passed into the collecting systems, which will outline any collecting system lesions or other obstructions (Figure 12.15). Contrast enhancement allows better delineation of enhancing (vascular) renal parenchyma from non-enhancing (avascular) collecting system. Contrast also helps to clarify abnormalities of the renal parenchyma, which can demonstrate variable degrees of contrast enhancement that are not appreciated on unenhanced examinations. Some centers may choose a two-phase examination (unenhanced followed by enhanced combined parenchymal-delayed phase) to decrease the associated radiation dose (two CT acquisitions rather than three) but the technical performance is more challenging as this requires a special technique known as the "split-bolus" technique. Regardless of the protocol elected, CTU allows a comprehensive assessment of the kidneys and ureters.

MRU may be used in selected patients or as a problem-solving tool following CTU. The principle is similar. MRU radiofrequency (RF) pulse sequences (see Chapter 5) are chosen to allow the best visualization of the collecting systems. In addition, a standard (enhanced or unenhanced) renal MRI using routine RF pulse sequences is performed simultaneously to assess for other abnormalities.

Most malignant ureteric tumors are TCC in histology. These also arise in the intrarenal collecting system and even more commonly in the bladder. Synchronous bilateral ureteric tumors are relatively common (up to 10%) and metachronous tumors (new primary tumors, which develop within a short time of the index [initial] lesion) have a similar incidence, occurring anywhere along the collecting system but especially within the bladder [22]. The classic presenting symptom is gross hematuria, which may prompt further investigations. These masses can be identified when highlighted with the specialized

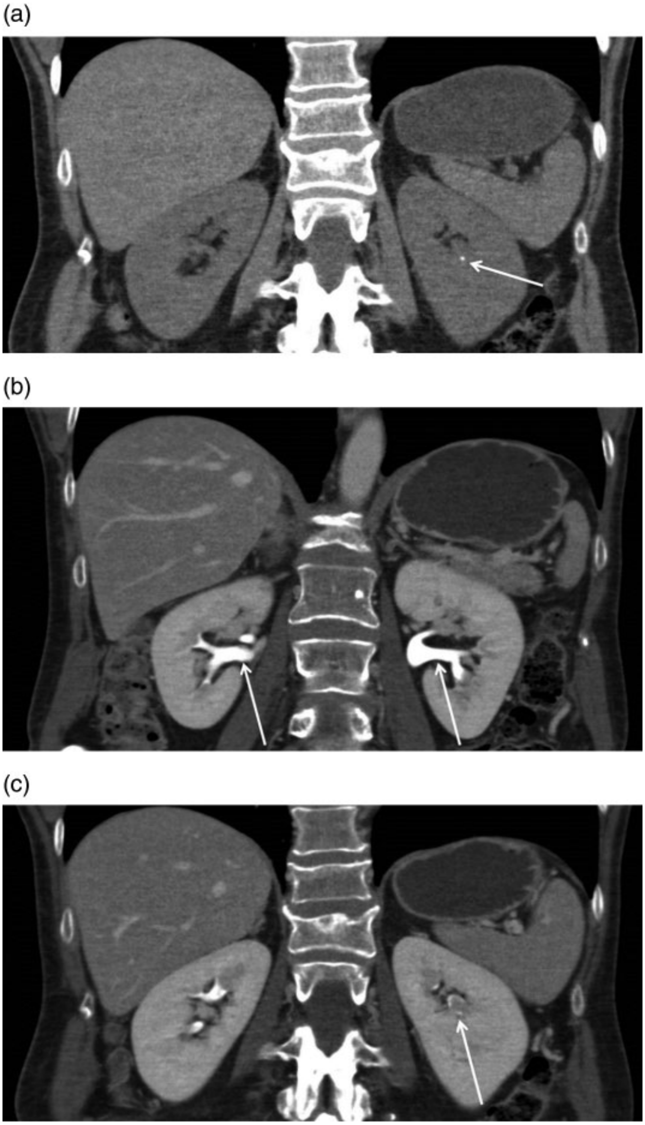

Figure 12.15 (a) A CT urogram was performed in this patient who presented with gross hematuria. The first unenhanced phase shows a tiny (3 mm) round hyperdense focus at the left renal equator (arrow) consistent with a small renal calculus. (b) Intravenous contrast has been injected into the patient following the "split-bolus" technique for CT urogram. The renal cortex enhances normally and dense contrast is present in the renal collecting systems bilaterally due to normal physiologic excretion (arrows). (c) More posterior CT image from the same patient. Some renal calyces, the peripheral components of the renal collecting system, remain incompletely opacified. These are not dilated and no obstructing lesion is present to suggest that non-opacification relates to mechanical obstruction of the flow of contrast by a lesion. Incomplete opacification therefore probably merely represents ongoing excretion as all contrast has not yet been cleared by the kidneys into the collecting systems. The small calculus in the left kidney is still identified, outlined by collecting system fluid surrounded by high-density contrast (arrow).

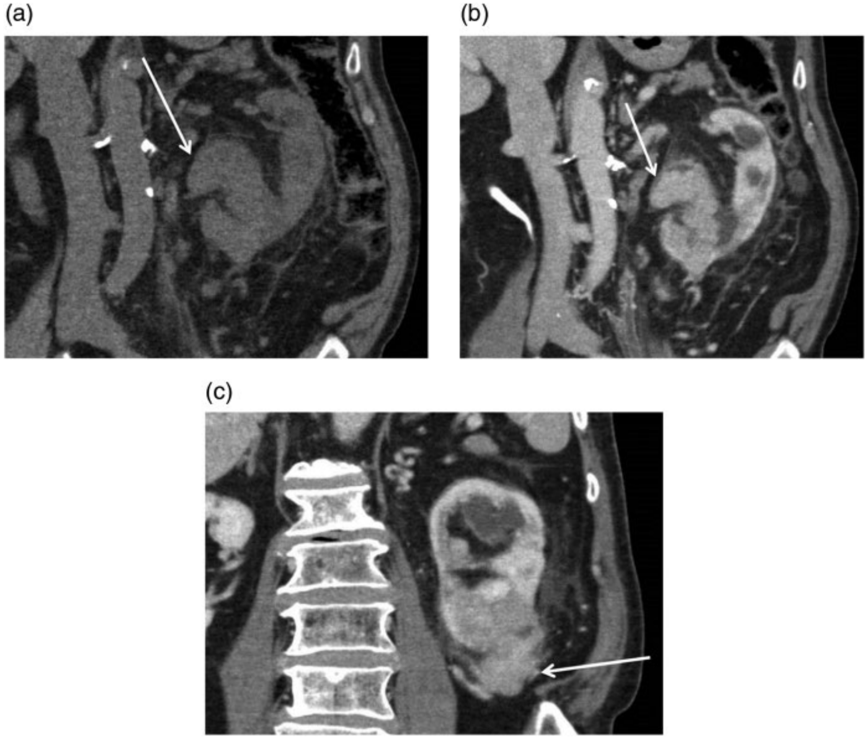

Figure 12.16 (a) Hyperdense solid tissue expands the left renal pelvis on this unenhanced CT (arrow), and there is no visualization of normal collecting system fluid. (b) The hyperdense solid tissue at the renal pelvis enhances after contrast administration consistent with enhancing tumor (arrow). (c) A different image from the same CT demonstrates that tumor also extends outside the kidney (arrow). Note also left upper pole hydronephrosis (retention of fluid in the kidney) caused by renal pelvis obstruction by the tumor.

CTU or MRU technique (Figure 12.16). Other relevant intra-abdominal findings will often also be revealed with these techniques.

Ureteric metastases are rare. These may be suspected when patients with a known malignancy present with increasing collecting system obstruction. Such lesions are also well-characterized with CTU/MRU. Ureters may also be invaded by adjacent abdominal neoplastic deposits with similar obstructive effect. Nonneoplastic abdominal or pelvic lesions may cause ureteric obstruction as well [22]. Classic obstructing lesions include retroperitoneal fibrosis and severe pelvic endometriosis. Clinical presentations include pain and decreasing renal function. If initial investigations lead to suspicion of collecting system obstruction, CTU or MRU will also clarify the level of ureteric involvement in such cases.

12.4 Bladder and Urethra

12.4.1 Bladder Cancer

The bladder is the most common site of urothelial malignancy [23]. Bladder cancer is more common among males and is associated with several known risk factors, including cigarette smoking, exposure to aromatic amines, and cyclophosphamide therapy [24]. The classic presenting symptom is painless hematuria (blood in the urine). Patients usually undergo a series of investigations for this concerning symptom, comprising CTU (less commonly MRU) as discussed in the prior section for evaluation of the "upper urinary tracts," and cystoscopy for evaluation of the bladder. Standard CTU protocols may not provide optimal bladder assessment as complete bladder distention may not be achieved. Cystoscopy is performed by urologic surgeons and allows direct visualization of the bladder via a cystoscope, but also provides an opportunity for biopsy when any suspicious lesions are identified. CTU protocols can be modified to optimize bladder assessment, and CT cystoscopy (filling the bladder with contrast via a catheter to achieve complete distension, outlining any lesions) is also an option. However, "optical" cystoscopy is often preferred due to the ability to simultaneously visually diagnose and manually sample any concerning lesions.

When bladder cancer has been confirmed, several management options are possible. At this point, medical imaging plays a major role in patient management. If not already completed, CTU (or less commonly, MRU) is appropriate. Due to the relatively high risk of synchronous (coexisting) urothelial carcinoma, the upper urinary tracts should be assessed prior to definitive management to ensure that no additional neoplastic lesions are present. Distant staging can be completed with CT chest/abdomen/pelvis at this time. The best examination (Figure 12.17) for assessing local bladder involvement to direct surgical planning or radiation therapy is contrast-enhanced bladder MRI [25]. US of the bladder allows visualization of large masses but sensitivity for detection of smaller masses is more limited and CT is still required for complete systemic staging after bladder tumors are diagnosed. Bladder tumors, like renal tumors, are not optimally visualized on ^{18}F-FDG-PET/CT due to high radiotracer activity in the urinary collecting system. Following diagnosis and management, contrast-enhanced CT (preferably but not necessarily CTU) is recommended for ongoing surveillance of patients with bladder cancer.

12.4.2 Lower Urinary Tract Trauma

Bladder injuries are frequently associated with pelvic fractures and may be secondary to blunt or penetrating pelvic trauma. A bladder injury is suspected when a patient with pelvic trauma presents with hematuria or if the

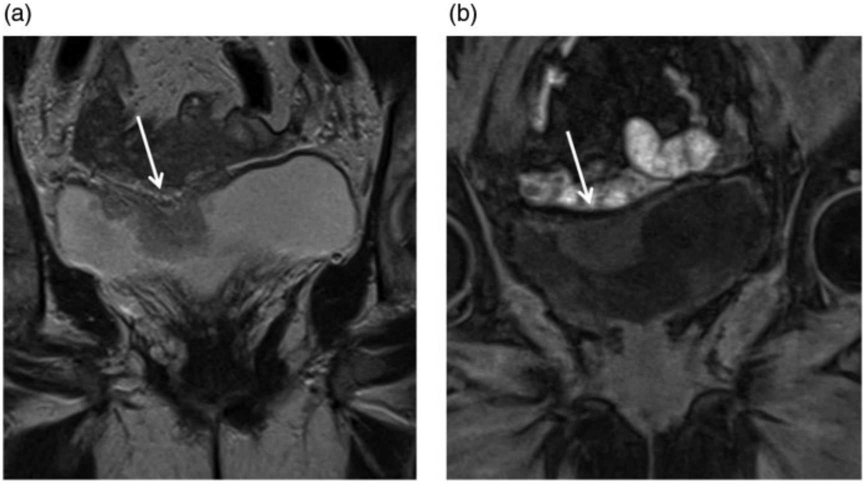

Figure 12.17 (a) Coronal T2-weighted and (b) fat-saturated T1-weighted MRI images demonstrate a large mass outlined by fluid at the bladder dome (arrow).

mechanism of trauma is severe enough that fractures are possible [26]. The traumatized bladder will rupture with fluid leaking into the peritoneal cavity, extraperitoneal space, or both (Figure 12.18). A CT cystogram is appropriate for patients with pelvic fractures and penetrating pelvic trauma when bladder injury is suspected [27]. The CT cystogram is performed after the bladder has been well distended with iodinated contrast, which is achieved via a Foley catheter. A Foley catheter should never be placed into the bladder unless urethral integrity has been documented [27]. Clinical features that indicate urethral injury include the presence of blood at the urethral opening onto the skin, perineal or penile hematoma, and straddle injury mechanism, for example, an impact injury of the groin from a bicycle crossbar [26]. Penetrating injury with trans-urethral trajectory is also suspicious for urethral trauma. Urethral injuries are much more common in male patients due to the longer male urethra. Retrograde urethrography, instillation of the urethra with contrast under fluoroscopy, is required to confirm an intact urethra before proceeding to place a Foley catheter for CT cystogram. On a standard CT cystogram, contrast outside the injured bladder is easily identified and confirms bladder rupture. MRI and US are rarely performed in the setting of acute trauma. Due to high rates of stricture following surgical repair, repeat retrograde urethrograms and/or urine flow dynamic studies are suggested for at least one year following the injury [26].

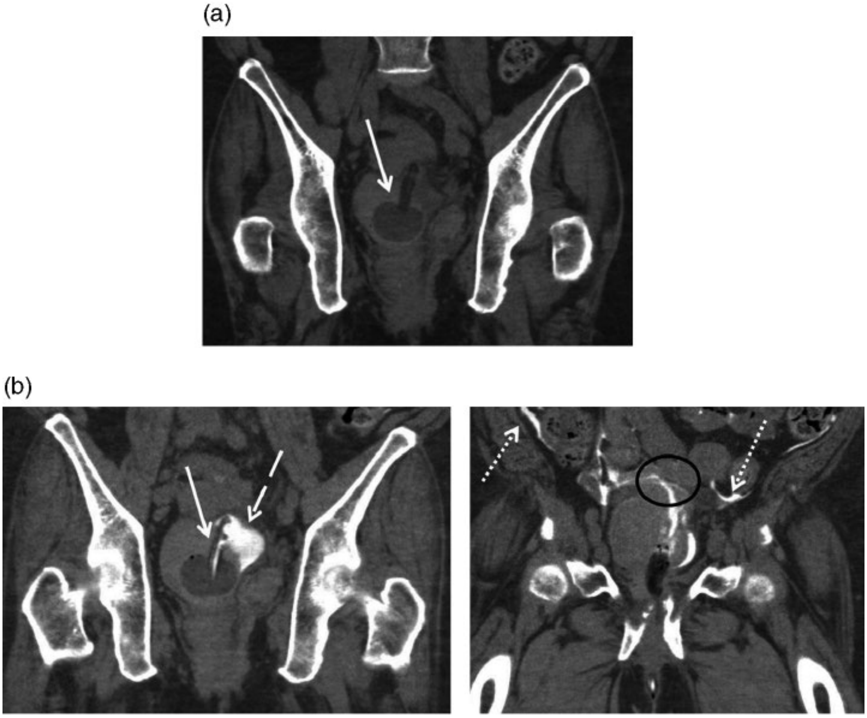

Figure 12.18 CT cystogram performed to check for bladder perforation in this patient with pelvic trauma. (a) A Foley catheter has been placed into the bladder on this unenhanced CT (arrow). (b) High-density CT contrast is then injected into the bladder through the Foley catheter (solid arrow), starting to fill the bladder (dashed arrow) and spilling into the pelvis (dotted arrows), through a defect in the bladder dome (circled) diagnostic of a bladder perforation.

12.5 Testicles

12.5.1 Testicular Cancer

Testicular cancer is the most common non-hematologic malignancy among males 15–49 years of age [28]. This cancer is more common in Caucasian populations. The incidence has increased over the last century. Most patients present with a painless palpable testicular mass while ~10% of patients will have a painful mass. About 20% of patients have metastatic adenopathy or other metastatic disease at presentation. Scrotal US is the first-line imaging evaluation of a suspected testicular mass following history and physical examination [28] (Figure 12.19). Correlation with tumor markers is also standard. After a suspicious scrotal mass is identified, staging of the chest, abdomen, and pelvis is

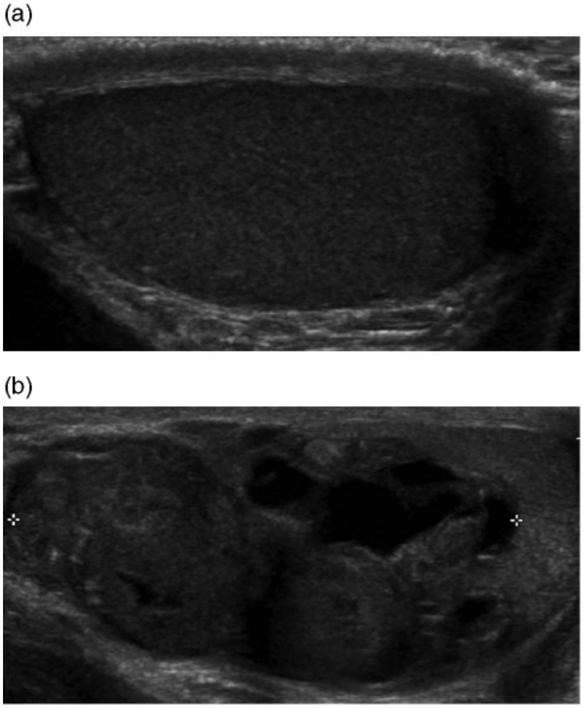

Figure 12.19 (a) Scrotal ultrasound of a normal right testicle. (b) Scrotal ultrasound in the same patient showing an abnormal contralateral left testicle, nearly completely replaced by a large heterogeneous mass (outlined by cross-hairs).

completed with contrast-enhanced CT. Patients then proceed to orchiectomy (surgical removal of the testicle). MRI is only occasionally performed as a problem-solving tool at diagnosis and is not currently used for staging. Testicular microlithiasis describes a condition diagnosed on scrotal US when multiple tiny testicular calculi (microliths) are found in the bilateral testicles. The significance of this finding is controversial since although this condition has been associated with testicular cancer, the association is not universally confirmed. A current guideline suggests that these patients do not require ongoing US screening and that US evaluation should be based on symptoms [29].

12.5.2 Testicular Pain

Testicular pain has a broad differential diagnosis. In the setting of acute trauma, the underlying etiology is clear. Other causes of testicular pain

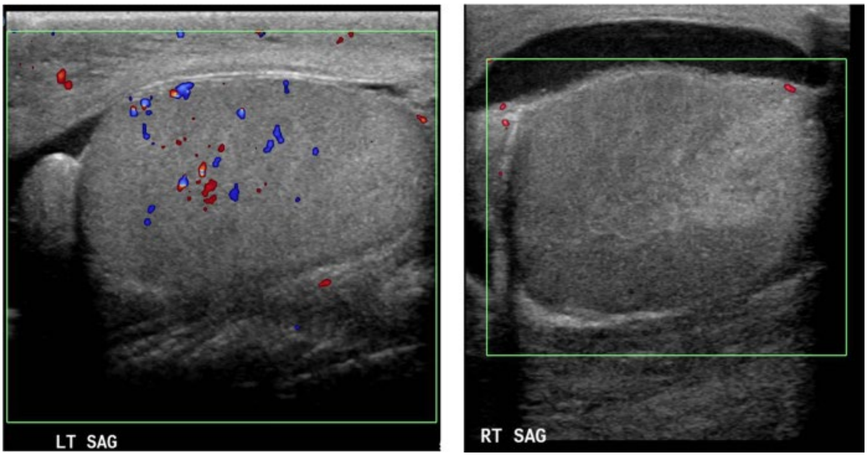

Figure 12.20 Scrotal Doppler ultrasound of the testicles. Normal blood flow, shown as colored foci on the ultrasound images, is easily identified in the normal left testicle (LT SAG). Flow is not revealed in the right testicle (RT SAG), consistent with testicular torsion. The vascular pedicle supplying the right testicle has torted (twisted), impairing flow into the right testicle. The torted cord is not shown on these images. (*See insert for color representation of the figure*.)

may be more difficult to diagnose clinically. A careful history and physical examination are very important for the diagnostic workup of testicular pain [30]. If the onset of pain is very acute and severe, testicular torsion may be suspected. This is an emergency diagnosis as failure to rapidly detort the testicle may lead to testicular ischemia and infarction, which carries implications for future fertility. Management is usually surgical. Infection of the testicle (orchitis) or epididymis (epididymitis) may also be acutely painful and these conditions often occur together (epididymo-orchitis). Cases are usually managed with supportive care or antibiotic therapy. In younger boys, torsion of the appendix testis, a small normal developmental remnant soft-tissue appendage of the testicle, is also relatively common. These three conditions account for at least 85% of cases of acute scrotal pain [30]. US is the imaging modality of choice for evaluation of the testicles in the setting of acute testicular pain [31]. A grayscale evaluation is performed for evaluation of testicular and epididymal morphology. Color Doppler evaluation is also required to confirm the presence of testicular blood flow, which will be absent in testicular torsion (Figure 12.20) but increased with acute inflammation (epididymo-orchitis).

12.6 Prostate

The prostate gland plays a role in the male fertility pathway. Unfortunately, this gland is also prone to the development of cancer. Prostate cancer is the most common cancer in males. Screening programs have been proposed, generally based on the measurement of serum prostate-specific antigen (PSA) levels. Screening with PSA is, however, not universally accepted due to concerns regarding the non-specificity of this marker and the increased identification of non-clinically significant cancers. Reference to local practice guidelines is suggested when considering screening. Regardless of screening investigations elected, the workup of suspected prostate cancer is more clear. An abnormally elevated PSA level will often prompt prostate biopsy to assess for an underlying prostate cancer. Diagnostic trans-rectal ultrasound (TRUS, see Figure 12.21) may also be performed as a screening evaluation for prostate cancer and positive results may prompt biopsy. Targeted (if a lesion has been identified) or nontargeted (random) biopsy is often performed under US guidance. US, however, has limited sensitivity and specificity for the detection of prostate cancer and it has been estimated that only up to 60% of prostate cancers are detectable on prostate US [32].

Prostate MRI has been the subject of extensive research and is now the primary diagnostic modality for prostate cancer (Figure 12.22). Prostate MRI examinations are multi-parametric, comprising multiple anatomic and functional RF pulse sequences [32]. Standardization of assessment and reporting is an additional goal. The Prostate Imaging Reporting and Data System (PiRADS) [33] has been developed for use when reporting prostate MRI and will ideally allow improved standardization between centers. Following prostate lesion identification and characterization on MRI, biopsy under US may be targeted to the lesion, improving yield; MRI-guided biopsies are also performed in some centers. Prostate cancer local staging can be completed on MRI as well. New treatment paradigms are also evolving given the enhanced information available on prostate MRI compared to US. Serial MRI examinations may be performed as a component of active surveillance in prostate cancer patients in whom surgery is not completed. MRI can also be used in planning prostate radiotherapy or other focal therapies, for example, cryoablation or high-intensity focused US (HIFU). MRI is also the modality of choice for assessing prostate cancer recurrence in postsurgical patients [32]. This technique continues to evolve but will likely continue to play a major role in the imaging assessment of prostate cancer.

Nuclear medicine imaging (scintigraphy), particularly a total body bone scan using ^{99m}Tc-medronate (see Chapter 4), is often obtained during prostate cancer staging since this examination highlights osseous metastases of prostate cancer. Staging of other metastatic disease is performed with diagnostic contrast-enhanced CT. Besides bone, lymph nodes are often involved

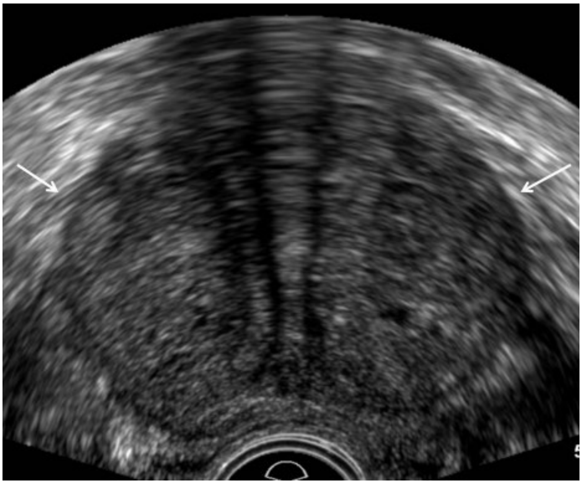

Figure 12.21 Transrectal ultrasound performed for assessment of the prostate gland. The prostate is enlarged (arrows outline the prostate gland).

Figure 12.22 Normal prostate MRI. The anatomy of the prostate gland (outlined by arrows) is more clearly delineated on prostate MRI than on transrectal ultrasound. This improves the sensitivity of lesion detection.

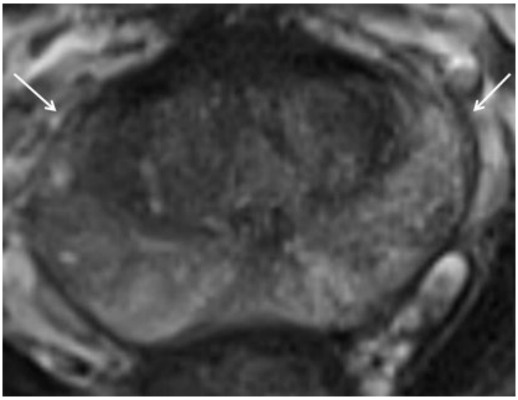

by metastatic deposits. Unfortunately, neither scintigraphy nor CT allows sufficiently detailed assessment of the prostate gland to obviate the need for MRI or US for local prostate assessment. More recently, PET/CT using the radiotracer ^{18}F sodium fluoride (Na^{18}F) has been proposed as an alternate technique for assessment of osseous metastases. ^{11}C choline PET/CT is an additional newer technique generally applied to assessment for recurrent disease posttreatment. Other PET radiotracers targeting prostate-specific membrane antigen (PSMA) have been shown to sensitively detect metastatic prostate cancer and may play a role in the diagnostic workup and for assessing recurrence and treatment efficacy in the future (see Chapter 15) [32].

12.7 Female Genitourinary Tract

The female GU tract comprises the uterus, vagina, bilateral ovaries, perineum, and associated soft-tissue structures. These organs are essential for the propagation of life but are also subject to a variety of abnormalities. Clinical diagnosis may be difficult due to difficult physical examination of these organs and imaging is often elected during workup. Several common problems will be presented from a symptom-based approach.

12.7.1 Abnormal Vaginal Bleeding

Abnormal vaginal (or abnormal uterine) bleeding may be a concerning symptom for women irrespective of age, but should be considered from a diagnostic perspective based on the patient's menopausal status. The differential diagnosis and treatment may be markedly different depending on premenopausal or postmenopausal status and this needs to be clarified before any further investigations are completed. Among premenopausal patients with abnormal vaginal bleeding, symptoms may relate to heavy bleeding during regular menstrual periods (menorrhagia), bleeding between regular menstrual cycles (metrorrhagia), or both (menometrorrhagia). Statistically, anovulatory bleeding (bleeding at a noncyclic time following absence of ovulation during the menstrual cycle) is the most common etiology of abnormal vaginal bleeding in this group [34]. However, various endometrial lesions are also associated with bleeding and may present in this age group. Lesions may be benign, for example, leiomyomas (fibroids) and endometrial or cervical polyps, but premalignant polyps as well as endometrial carcinoma are also possible. Diagnostic imaging is consequently important for further evaluation of these patients. Pelvic and transvaginal US is the most appropriate first-line investigation [34, 35]. Based on the results of this study, further assessment with a sonohysterogram may be recommended by the reporting radiologist. During a sonohysterogram, a catheter is placed into the cervix and sterile saline is instilled into the endometrial cavity. This examination is usually completed after a lesion is possibly identified in the region of the endometrium but is not well-visualized or fully characterized; distending the cavity with fluid will outline an endometrial-centered lesion and help to delineate its origin (Figure 12.23). If the diagnosis remains unclear, or if further workup is required, a pelvic contrast-enhanced MRI is generally the next best test. Gynecologic consultation may also be considered as endometrial biopsy may be elected in these patients based on clinical features in addition to imaging evaluation [36].

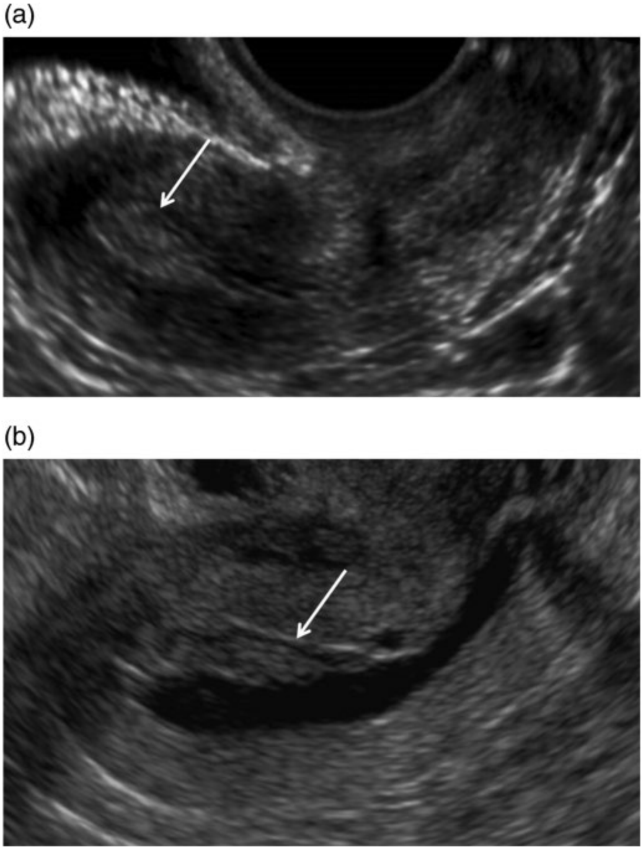

Figure 12.23 (a) Routine transvaginal ultrasound with the uterus in the sagittal plane. The endometrium is thickened near the fundus (arrow) in this patient with abnormal postmenopausal bleeding, but it is difficult to know whether this represents a focal mass lesion in this region. (b) Sonohysterogram is performed, with fluid instilled into the endometrial canal. As the cavity is distended, fluid outlines a small endometrial mass at the fundus (arrow), which is the cause of the focal endometrial thickening. This mass is a benign endometrial polyp.

12.7.2 Endometrial Cancer

Endometrial cancer is diagnosed after a positive endometrial biopsy. Biopsy is often performed based on the results of a previous US, but may be performed based on symptoms in the absence of prior imaging evaluation. Among postmenopausal women with abnormal vaginal bleeding, endometrial carcinoma is the primary diagnostic concern, although several other

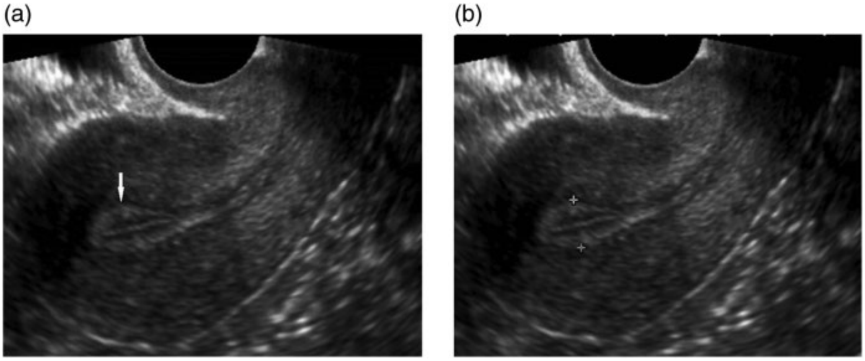

Figure 12.24 (a) Transvaginal ultrasound of the female pelvis demonstrates the endometrium in the central uterus (arrow). (b) Cross-hair calipers delineate the thickness of the endometrium, here 0.9 cm, which is normal in this premenopausal patient. This endometrial thickness would be abnormal in a postmenopausal patient with abnormal uterine bleeding.

conditions may account for abnormal bleeding in this population, including endometrial hyperplasia, polyps, and vaginal atrophy.

Endometrial cancer is the most common gynecologic malignancy and is more common in postmenopausal women [34]. Over 90% of patients with endometrial carcinoma will experience abnormal vaginal bleeding. Pelvic and transvaginal US is also the most appropriate first-line investigation in these patients and a key aim is to define the endometrial thickness (Figure 12.24). Endometrial cancer is very unlikely (<1%) when the endometrium is <5 mm thick. In a postmenopausal patient symptomatic with abnormal vaginal bleeding, endometrial thickness >5 mm is considered abnormal and needs to prompt a referral for endometrial biopsy. When endometrial thickness >5 mm is detected in a postmenopausal patient who is not experiencing abnormal vaginal bleeding, the recommendations are less clear. A current Canadian guideline suggests performing endometrial biopsy in this population when endometrial thickness is >11 mm [37]. Some hormone replacement therapy regimens used for treatment of menopause-related symptoms are associated with an increased risk of endometrial cancer [38]. Standardized guidelines for endometrial thickness in these patients also have not been established and gynecologic consultation is probably of value to determine further management when endometrial thickening is detected on US. Women on tamoxifen therapy for breast cancer tend to develop endometrial thickening and are also at increased risk of developing endometrial cancer. Standardized screening with US in these patients is not currently recommended [37], but transvaginal US is suggested if abnormal uterine bleeding develops. Endometrial biopsy may then be considered based on the standard recommendations for symptomatic women.

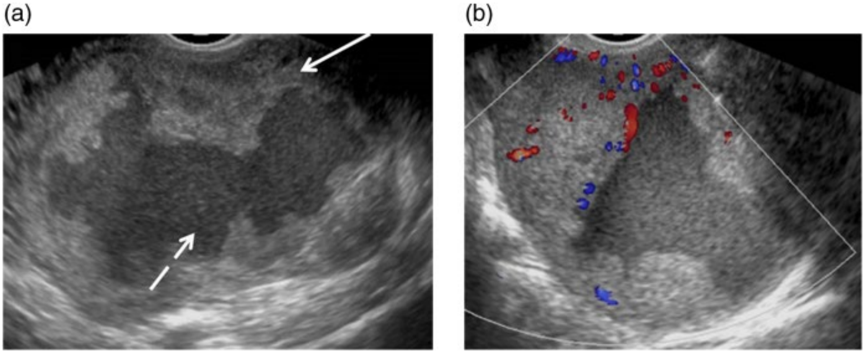

Figure 12.25 (a) Transvaginal ultrasound of the female pelvis demonstrates a very large endometrial mass with solid (arrow) and cystic (dashed arrow) components. The cystic component is complicated by low-level internal echoes (scattered brighter foci), which suggest complex proteinaceous/hemorrhagic rather than simple fluid. (b) Vascular flow is identified in the solid components when Doppler ultrasound is performed (color foci). This endometrial mass demonstrating internal vascularity is consistent with a large endometrial cancer. (*See insert for color representation of the figure*.)

Once endometrial cancer has been diagnosed on US (Figure 12.25), in North America, contrast-enhanced pelvic MRI is generally suggested for optimal local staging [39]. In other areas, or in certain clinical circumstances, US alone may be elected for endometrial cancer assessment based on local gynecologic oncology practices. CT does not play a role in assessment of the endometrium. Contrast-enhanced CT chest/abdomen/pelvis is, however, considered appropriate for evaluation of pelvic and retroperitoneal lymph node enlargement and other distant metastatic disease [40].

12.7.3 Cervical Cancer

In North America, cervical cancer is the third-most common gynecologic malignancy. Rates have decreased over recent decades, attributed to widespread screening with the Papanicolaou (“pap”) smear, allowing detection of earlier, less invasive cancers. Delineation of local extension is suboptimal on US. Contrast-enhanced pelvic MRI is the most appropriate first-line investigation following histologic diagnosis of cervical cancer [41] (Figure 12.26). MRI allows local neoplastic staging which directs clinical management, as the decision of surgical management depends on local cancer extent [42]. MRI can demonstrate enlargement of pelvic lymph nodes (adenopathy), but is not used for assessment of retroperitoneal nodes or other more distant metastatic disease. ^{18}FDG-PET/CT is recommended for optimal metastatic staging. Routine contrast-enhanced CT chest/abdomen/pelvis is also appropriate [41].

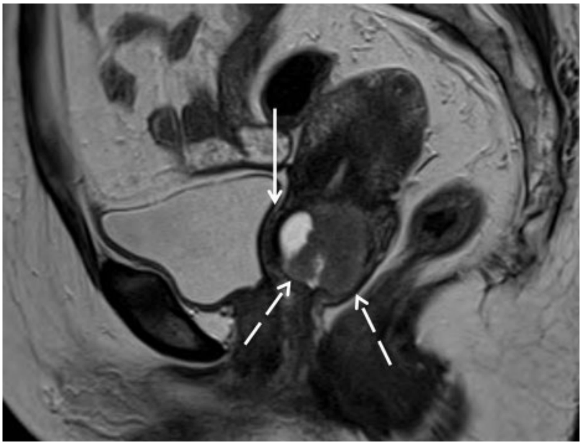

Figure 12.26 T2-weighted MRI of the pelvis in the sagittal plane. The anterior wall of the cervix is normal (solid arrow). The posterior wall demonstrates invasion by a large cervical tumor, which also grows into the cervical canal (dashed arrows).

12.7.4 Adnexal Masses and Ovarian Cancer

The space between the pelvic sidewall and the uterus on each side is the adnexa. Adnexal masses may be suspected on clinical history or following pelvic examination. Correlation with clinical history and pregnancy status is required. The current discussion applies to nonpregnant patients (please refer to later sections regarding imaging in pregnant women). When an adnexal mass is suspected, the most appropriate first investigation is pelvic and transvaginal US [43]. If an adnexal lesion is identified, every attempt should be made to clarify intraovarian vs. extra-ovarian location, as this discrimination determines the differential diagnosis. Doppler blood flow imaging (see Chapter 6) should also be applied to any lesion identified on US to confirm the absence of internal vascularity (Figure 12.27). Generally, a follow-up US will be recommended for an indeterminate lesion. Further evaluation with contrast-enhanced pelvic MRI may be required if intra vs. extra-ovarian location cannot be determined for a concerning lesion identified on US. If a lesion is obviously suspicious for malignancy, MRI or surgical referral may be suggested. If a lesion enlarges or develops other suspicious features on a follow-up US, contrast-enhanced pelvic MRI or surgical referral is then also usually appropriate [43]. In addition, if an adnexal lesion is very large (over 7 cm in maximal dimension), MRI is also often recommended as a lesion of this size may remain incompletely characterized on US [44].

Ovarian cancer is considered the most lethal gynecologic malignancy [45]. Unfortunately, ovarian cancer is rarely diagnosed at the localized disease stage and patients more often present with metastatic disease. Although routine

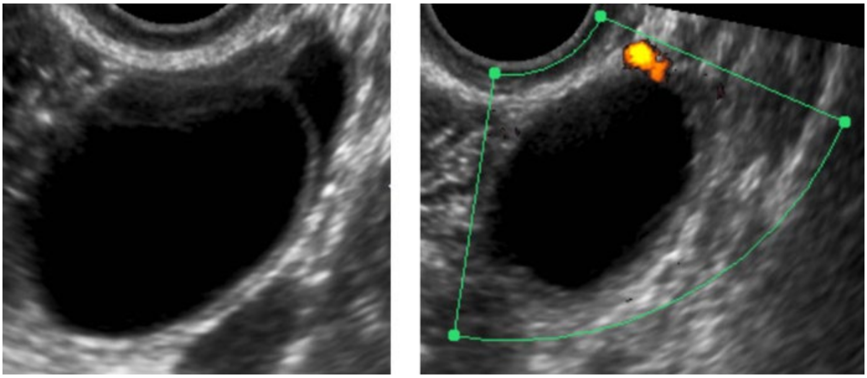

Figure 12.27 Normal premenopausal ovary on ultrasound. Grayscale ultrasound reveals a large cyst, which is a normal dominant follicle (a normal physiologic ovarian structure, which evolves with the menstrual cycle) in premenopausal women. This has no solid component or internal vascularity when Doppler ultrasound is performed, but vascular flow is present outside the lesion in the normal ovarian parenchymal tissue. (*See insert for color representation of the figure.*)

screening for ovarian cancer has been proposed with a variety of different tools (for example, US and serum Ca-125 levels), no marker has met the criteria for a successful screening tool and routine screening for ovarian cancer among women of average risk is consequently not recommended. Among women with known genetic risk factors for ovarian cancer, including BRCA1 and BRCA2 genes, and Lynch syndrome, routine screening with US may be considered starting at age 30–35 following individual patient discussion [45]. Following a diagnosis of ovarian cancer (Figure 12.28), CT chest/abdomen/pelvis is appropriate for full staging [46].

12.7.5 Acute Pelvic Pain

Acute pelvic pain in a premenopausal patient is a common presenting symptom and may be secondary to a variety of underlying causes. Etiologies include obstetric, gynecologic, and non-gynecologic sources. Consequently, it is of paramount importance to determine whether the patient is pregnant or not. This is determined by a positive β-hCG level. All patients in this clinical setting should undergo serum β-hCG measurement as part of the clinical assessment before proceeding to imaging. A positive serum β-hGC level confirms pregnancy and raises the possibility of an ectopic pregnancy, which may be life-threatening. Pelvic/transvaginal US is an appropriate investigation for acute pelvic pain in both pregnant and nonpregnant patients and again, the differential diagnosis in pregnant patients includes ectopic pregnancy. Additional diagnostic considerations include ovarian torsion, ovarian cysts, other adnexal

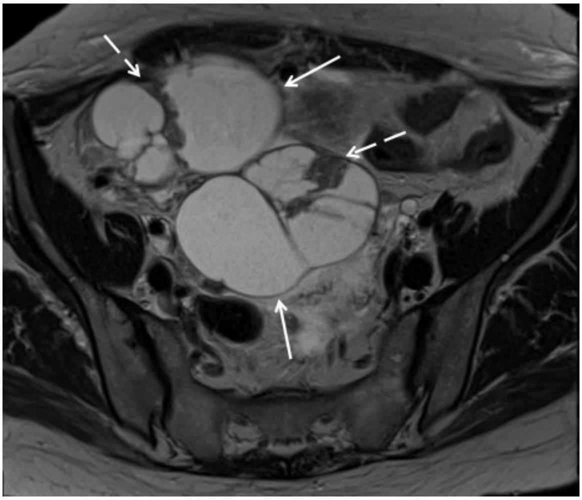

Figure 12.28 T2-weighted MR image of the pelvis demonstrating two pelvic masses, both with mixed cystic (solid arrows) and solid (dashed arrows) components consistent with bilateral ovarian carcinoma.

masses, and pelvic inflammatory disease with or without tubo-ovarian abscess. Non-gynecologic abnormalities including appendicitis and diverticulitis may also present with pelvic pain [47]. If US does not yield a diagnosis, contrast-enhanced CT abdomen/pelvis may be appropriate if non-gynecologic causes of pelvic pain are clinically suspected [48]. If further clarification of an adnexal abnormality is required in a nonpregnant patient, contrast-enhanced pelvic MRI may be appropriate in the correct clinical setting. In a pregnant patient with pelvic pain and nondiagnostic US, unenhanced pelvic MRI generally serves as the major follow-up examination, as CT with the attendant ionizing radiation is relatively contraindicated in the setting of pregnancy [48].

12.7.6 Pregnancy – First Trimester

Early pregnancy is confirmed upon documentation of a positive serum β-hCG level. Among pregnant patients presenting with concerning gynecologic symptoms, namely pelvic pain or vaginal bleeding, the most appropriate first investigation is pelvic and transvaginal US [49]. The location of the pregnancy, intrauterine or ectopic, must be determined (Figure 12.29). This determination is not possible at a very early gestational age as the early gestational sac may be too small to visualize with US. If the pregnancy cannot be accurately localized with US, it is deemed a "pregnancy of unknown location" and serial serum β-hCG level measurement and a repeat US (follow-up interval variable depending on clinical circumstances) are recommended [50].

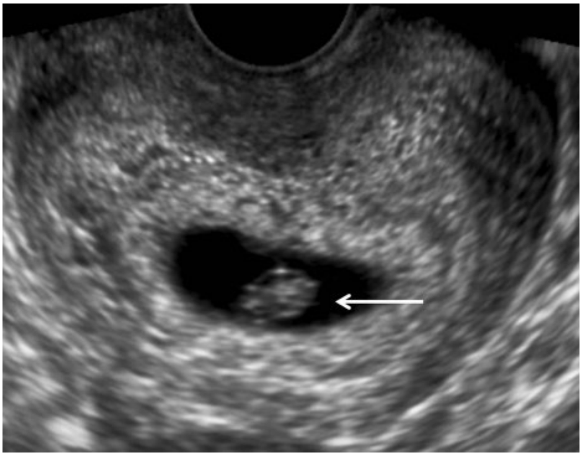

Figure 12.29 Transvaginal ultrasound demonstrating an intrauterine pregnancy. The uterus contains a tiny first trimester embryo (arrow) surrounded by a fluid-filled gestational sac.

12.7.7 Obstetrical Evaluation

Assessment of the fetus in utero is generally best achieved with US. Trans-Abdominal US is often sufficient for diagnostic purposes; transvaginal US may be required in certain circumstances for improved visualization of the fetus and gravid (pregnant) uterus. Obstetrical US performance is to some extent determined by local practice parameters. In North America, however, US is a component of routine prenatal screening in the first trimester and forms the basis of fetal anatomic evaluation in the second trimester. First-trimester screening is performed to determine the risk of fetal aneuploidy [51]. Other anomalies may also be detected, but the primary aim is to screen for aneuploidy (chromosomal abnormality). The routine first-trimester screening protocol may vary slightly by location but generally comprises the measurement of maternal serum biochemical markers and US assessment of fetal nuchal translucency. Nuchal translucency describes a space behind the embryonic neck which is visible on US in an early embryo. Nuchal translucency measurements have been correlated with aneuploidy risk. Based on combined results, the risk of aneuploidy is calculated and if high, may prompt further evaluation with amniocentesis. The assessment of fetal nuchal translucency is governed by a rigorous measurement system [52] and sonographers performing nuchal translucency US may complete a certificate course offered through the Fetal Medicine Foundation for certification of competence, the maintenance of which requires an annual audit.

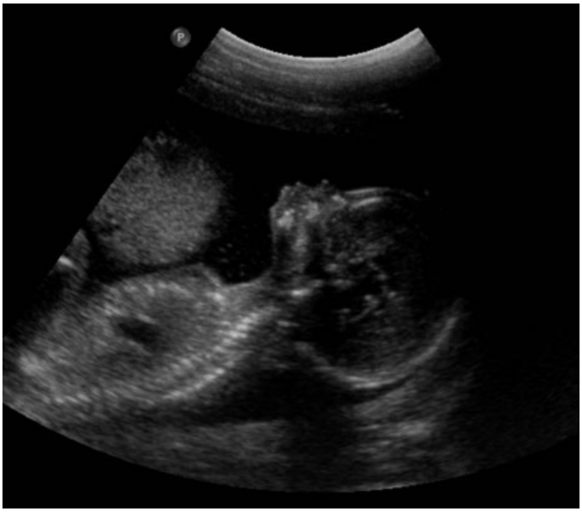

Figure 12.30 Routine prenatal anatomic ultrasound demonstrating the fetal head, chest, and upper abdomen.

Fetal anatomic evaluation in the second trimester is performed at 18–20 weeks gestational age (Figure 12.30). Fetal anomalies and "soft markers" of fetal aneuploidy may be revealed during these examinations. Approximately 1 in 28 couples will have a child with some form of congenital anomaly (birth defect). Some of these are lethal [53]. The routine sonographic evaluation in pregnancy was developed and implemented for the detection of medically relevant anomalies. In some regions, additional commercially-driven non-indicated US have become popular among expectant parents. Reference to local practice guidelines is suggested for referring practitioners to ensure that their patients receive the appropriate examination at the appropriate time. Follow-up US may be required following an initial anatomic survey if fetal structures remain incompletely visualized or if a fetal anomaly is questioned. Fetal echocardiography may also be performed at dedicated pediatric cardiac subspecialty centers if a fetal cardiac anomaly is suspected. Fetal MRI may be applied as a problem-solving tool if an anomaly is suspected on US but cannot be optimally characterized.

12.7.8 Pregnancy – Second and Third Trimester

US also serves as the major diagnostic imaging tool for pregnancies in the second and third trimester. In general, routine US in the third trimester is not appropriate in a low-risk routine pregnancy in an otherwise healthy mother [54].

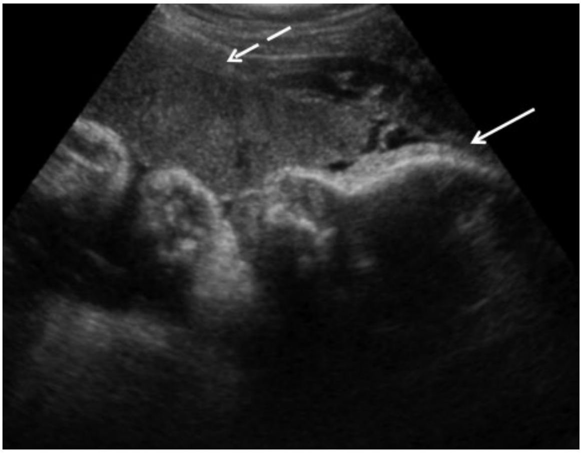

Figure 12.31 Normal fetal third trimester ultrasound. The fetus now occupies most of the uterus (solid arrow indicates fetal head in profile). The placenta (dashed arrow) is normal.

However, US provides valuable information on fetal health and growth and routine surveillance may be indicated based on high-risk fetal, maternal, or obstetrical features. Early identification of abnormal fetal growth or placental insufficiency (which may result in fetal asphyxia) allows early referral to obstetrical specialty centers for further management. The biophysical profile (BPP) is a standardized US assessment comprising evaluation of fetal breathing, movements, tone, and amniotic fluid volume (Figure 12.31). Doppler interrogation of the umbilical and uterine arteries provides relevant information regarding placental insufficiency and is often completed during the BPP. Doppler evaluation of the fetal middle cerebral artery provides additional supporting evidence for fetal vascular compromise and is occasionally performed when placental insufficiency is suspected [54]. The BPP may be correlated with a nonstress test for fetal cardiac rhythm assessment. Serial follow-up US examinations may be needed depending on clinical features.

The placenta is an important component of any pregnancy and placental assessment is a component of routine prenatal obstetric evaluation. Placental anomalies besides vascular insufficiency include abnormal position (too close or even overlying the internal cervical os, the opening of the cervix), abnormal invasion (of the underlying myometrium or even uterine serosa), or masses. Placental location <2 cm distant from the internal cervical os is termed "low-lying" placenta while placenta covering the internal os is placenta previa, which may be partial or complete [55]. These are not uncommon findings at anatomic US assessment in the second trimester; follow-up is suggested in the third trimester, as placenta position relative to the cervix may evolve with changing gestational age. Identification of a persistently abnormally positioned placenta allows appropriate obstetrical planning. Abnormal placental invasion is diagnosed when a normal rim of decidual reaction, the interface between the placenta and maternal myometrium, is absent around the placenta, with placental tissue extending to the uterine endometrium–myometrium junction (placenta accreta), into myometrium (placenta increta), or through the myometrium into uterine serosa (placenta percreta) [55]. Abnormal placental invasion may cause catastrophic maternal hemorrhage at the time of delivery. This spectrum of abnormal placentation may be a challenging diagnosis on US. When suspected, further evaluation with MRI may be recommended in an attempt to improve delineation of the degree of invasion [55]. The presence of these abnormalities also warrants referral for management at a specialized obstetrical center. Additional placental lesions include placental origin (trophoblastic) and more rare non-trophoblastic neoplasms and more acute placental abnormalities such as placental abruption (the separation of the placenta from the underlying myometrium) or trauma. US remains the first-line investigation when these abnormalities are suspected, with further evaluation with MRI when clinically indicated [56].

12.8 Pediatric Genitourinary Tract

12.8.1 Congenital Anomalies

Congenital renal anomalies, in North America, are often diagnosed on routine prenatal obstetrical US [57]. These include renal agenesis (failure to form one or both kidneys), renal ectopia (abnormal kidney location), and renal fusion. The anomalous kidney is at increased risk of infection, obstruction, and calculus formation. Ongoing sonographic surveillance may be elected throughout childhood. Congenital anomalies of the genitalia are rare and may be detected on prenatal US or on neonatal clinical inspection [58]. Some anomalies of the female genital tract, which generally arise due to anomalous development of structures derived from the embryonic Mullerian duct, may not present until adulthood when patients present with concerns regarding fertility. Any or all of the uterus, cervix, or vagina may be duplicated or absent in the spectrum of Mullerian duct anomalies. These are associated with renal anomalies and abdominal US should always be performed when a Mullerian duct abnormality is identified to check for associated renal abnormalities. Abnormalities of the male genitalia are usually identified on physical examination. These are also associated with additional renal and systemic anomalies, so complete abdominal US is also recommended for full diagnostic assessment [59]. Complex anomalies of the embryonic urogenital sinus, the embryonic progenitor of the bladder and genital organs, may be associated with a variety of syndromes.

Additional anomalies may also be complex and specialist referral may be required. Regardless, initial assessment is usually completed with US as well. In males, testicular assessment is a relatively common indication for neonatal US. The testicles may remain undescended at birth (contained within the abdomen) and US is performed to confirm the location outside the scrotum. Most descend into the scrotum by 3 months of age [60]. Persistent undescended testicles may be associated with infertility and carry a higher risk of testicular cancer.

12.8.2 Cystic Renal Disease

Cystic renal disease may also be identified on prenatal US, or may be detected on US completed in childhood [58]. Autosomal dominant and autosomal recessive polycystic kidney disease have a genetic association, as do a few more rare renal cystic diseases. Multicystic dysplastic kidney is a nonheritable condition involving replacement of part or all of the renal parenchyma by multiple cysts, probably secondary to severe congenital collecting system obstruction or abnormal development of the collecting system (Figure 12.32). The involved kidney is nonfunctional. This condition is usually diagnosed on prenatal US as well. Further radiologic evaluation should generally be individualized for each patient and performed to answer specific clinical questions [61].

12.8.3 Renal Masses

A few renal tumors are unfortunately prevalent among children. Wilm’s tumor is the most common overall [62]. Angiomyolipomas are prevalent among

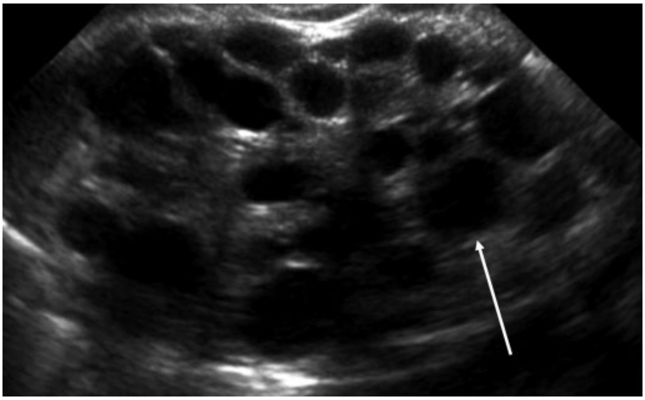

Figure 12.32 Multicystic dysplastic kidney disease. This neonatal left kidney is almost completely replaced by multiple cysts of varying sizes (arrow delineating one of the larger cysts).

children with tuberous sclerosis, a syndrome with multiple possible manifestations. Clinical presentation varies with patient age and tumor type. Very young infants may present with palpable abdominal masses while older children may express abdominal pain. The initial evaluation when a renal mass is suspected in a child should be an abdominal US. If a mass is detected, CT or MRI may be elected for further staging or surgical planning [58].

12.8.4 Urinary Tract Infections

UTI are relatively common in children, occurring more often in girls than in boys. Acute pyelonephritis has been labeled the most common severe childhood bacterial infection [63]. The incidence of febrile infection is highest in infants. In older children, UTI are usually non-febrile but if accompanied by fever are associated with an increased risk of renal infectious involvement. Pediatric renal infection may result in renal scarring and collecting system abnormalities including strictures. Imaging assessment for children with UTI remains somewhat controversial. Although many congenital anomalies are associated with an increased risk of infection, anomalies are rare in the general pediatric population and many are diagnosed on prenatal US. On first presentation of a child with UTI, US is considered appropriate in order to confirm the absence of any underlying anatomic anomaly [64]. US is not sensitive for the detection of renal involvement by pyelonephritis or scarring, and also will not accurately demonstrate vesicoureteral reflux (VUR). VUR occurs when bladder contents reflux retrograde through the ureterovesical junctions into the ureters. The refluxate may remain contained within the pelvic ureter or may reflux fully into the renal collecting system. If the bladder contents are infected, VUR predisposes the patient to renal infection if reflux occurs to the level of the kidneys, and therefore increases the risk of later renal scarring. VUR can easily be identified using “Voiding Cystourethrography” (VCUG). With this technique, the bladder is filled with contrast and the flow of contrast is observed under fluoroscopy as the child then voids. Contrast-enhanced urine refluxes into the ureter if the child has VUR (Figure 12.33). This technique will outline the urinary tract and so allows more detailed assessment of associated anatomic abnormalities. “Radionuclide Cystography” (RNC) is a nuclear medicine examination, which may also be used to assess for VUR. The bladder is filled with radiolabeled fluid and a gamma camera records radiotracer distribution out of the bladder. This technique will identify VUR if the tracer migrates into the ureters but does not provide anatomic details due to the low spatial resolution of gamma scintigraphy. As RNC has a lower radiation dose than VCUG, it may be used to screen for VUR. VCUG is generally recommended if a febrile UTI has certain atypical features or if the child has recurrent febrile UTI [63]. The use of VCUG for uncomplicated first infections is more controversial and often not considered appropriate [64]. A renal scintigraphy nuclear medicine

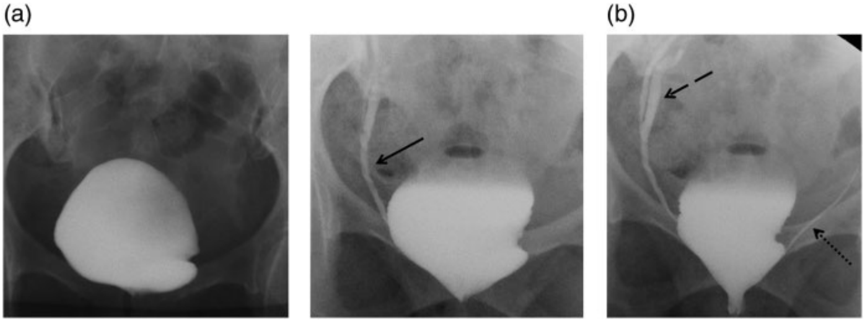

Figure 12.33 (a) Voiding cystourethrogram in an adolescent female. The bladder is filled with high-density contrast (left panel). As the bladder fills, spontaneous vesicoureteral reflux into the right ureter opacifies the ureter with contrast (arrow; right panel). (b) Contrast continues to reflux into the right ureter, revealing a duplicated ureter more proximally (dashed arrow). Ureteral duplication is one of the congenital genitourinary anomalies. Contrast now also refluxes into the left ureter (dotted arrow).

study using ^{99m}Tc-DMSA as a radiotracer may show pyelonephritis in the acute phase as the radiotracer will not distribute into the inflamed regions of the kidney, and will also show residual renal scarring after acute infection has resolved, as the radiolabeled tracer will not distribute into the scarred nonfunctional parts of the previously infected kidney. ^{99m}Tc-DMSA scans are generally considered more appropriate to check for renal scarring as a complication of prior febrile UTI [64].

12.8.5 Assessing Pediatric Genitalia

Children are subject to acute and more chronic abnormalities of the genital organs in addition to the congenital anomalies discussed previously. For example, children may suffer from ovarian or testicular torsion or testicular trauma. Unfortunately, younger children are often unable to accurately describe or localize their pain and careful clinical evaluation is required to elucidate the source of the acute episode. Abdominopelvic US is an appropriate first imaging test when genital or other pelvic abnormalities are suspected in children [65]. Neoplasms of the pelvic organs and genitalia can also develop in children. In boys, scrotal tumors can often be detected by physical examination. In girls, ovarian and uterine neoplasms may remain occult until quite large. US is usually the first imaging test ordered in children when a pelvic mass is suspected. MRI may then be ordered for further lesion characterization. Depending on the patient and tumor type, CT may be relevant for systemic staging.

12.9 Summary

Imaging of the GU tract requires a range of modalities, which have evolved to allow comprehensive assessment of the kidneys, urinary collecting system, other pelvic organs, and genitalia. Medical imaging contributes to accurate diagnosis in patients of all ages with a huge array of GU tract abnormalities. The use of image-guided therapy in treatment of these abnormalities is beyond the scope of the current chapter, but these therapies also often have a major beneficial impact on patient care. All medical imaging modalities are subject to ongoing refinement and improvement, and will hopefully continue to offer ever-more clinically relevant and patient-friendly contributions to medical diagnosis and treatment.

References

1 Kirkali, Z., Rasooly, R., Star, R.A., and Rodgers, G.P. (2015). Urinary stone disease: progress, status, and needs. *Urology* 86: 653.

2 Smith-Bindman, R., Aubin, C., Bailitz, J. et al. (2014). Ultrasonography versus computed tomography for suspected nephrolithiasis. *N. Engl. J. Med.* 371: 1100–1110.

3 Moreno, C.C., Beland, M.D., Goldfarb, S.C. et al. (2015). *ACR Appropriateness Criteria: Acute Onset Flank Pain – Suspicion of Stone Disease (Urolithiasis)* [Revised]. Reston, VA: American College of Radiology.

4 Moran, C.P. and Courtney, A.E. (2016). Managing acute and chronic renal stone disease. *Practitioner* 260: 17–20.

5 Grigoryan, L., Trautner, B.W., and Gupta, K. (2014). Diagnosis and management of urinary tract infections in the outpatient setting; a review. *JAMA* 312: 1677–1684.

6 Lazarus, E., Allen, B.C., Blaufox, D. et al. (2014). *ACR Appropriateness Criteria: Recurrent Lower Urinary Tract Infections in Women*. Reston, VA: American College of Radiology.

7 Nikolaidis, P., Casalino, D.D., Remer, E.M. et al. (2012). *ACR Appropriateness Criteria: Acute Pyelonephritis*. Reston, VA: American College of Radiology.

8 Craig, W.D., Wagner, B.J., and Travis, M.D. (2008). Pyelonephritis: radiologic-pathologic review. *Radiographics* 28: 277.

9 Sag, A.A., Inal, I., Okcuoglu, J. et al. (2016). Atherosclerotic renal artery stenosis in the post-CORAL era part 1: the renal penumbra concept and next-generation functional diagnostic imaging. *J. Am. Soc. Hypertens.* 10: 360–367.

10 Harvin, H.J., Casalino, D.D., Remer, E.M. et al. (2012). *ACR Appropriateness Criteria: Renovascular Hypertension*. Reston, VA: American College of Radiology.

11 Keramida, G., James, J.M., Prescott, M.C., and Peters, A.M. (2015). Pitfalls and limitations of radionuclide renal imaging in adults. *Semin. Nucl. Med.* 45: 428–439.

12 O'Connor, S.D., Silverman, S.G., Ip, I.K. et al. (2013). Simple cyst-appearing renal masses at unenhanced CT: can they be presumed to be benign? *Radiology* 269: 793–800.

13 Schieda, N., Kielar, A.Z., Al Dandan, O. et al. (2015). Ten uncommon and unusual variants of renal angiomyolipoma (AML): radiologic–pathologic correlation. *Clin. Radiol.* 70: 206–220.

14 Heilbrun, M.E., Remer, E.M., Casalino, D.D. et al. (2015). ACR appropriateness criteria indeterminate renal mass. *J. Am. Coll. Radiol.* 12: 333.

15 Takahashi, M., Kume, H., Koyama, K. et al. (2015). Preoperative evaluation of renal cell carcinoma by using 18-F FDG-PET/CT. *Clin. Nucl. Med.* 40: 936–940.

16 Middendorp, M., Maute, L., Sauter, B. et al. (2010). Initial experience with 18F-fluoroethylcholine PET/CT in staging and monitoring therapy response of advanced renal cell carcinoma. *Ann. Nucl. Med.* 24: 441–446.

17 Akbar, S.A., Jafri, S.Z., Amendola, M.A. et al. (2005). Complications of renal transplantation. *Radiographics* 25: 1335–1356.

18 Taffel, M.T., Nikolaidis, P., Beland, M.D. et al. (2016). *ACR Appropriateness Criteria; Clinical Condition: Renal Transplant Dysfunction* [Revised]. Reston, VA: American College of Radiology.

19 Agrawal, M. and Swartz, R. (2000). Acute renal failure. *Am. Fam. Physician* 61: 2077–2088.

20 Remer, E.M., Papanicolaou, N., Casalino, D.D. et al. (2013). *ACR Appropriateness Criteria: Renal Failure.* Reston, VA: American College of Radiology.

21 Taylor, A.T. (2014). Radionuclides in nephrourology, part 1: radiopharmaceuticals, quality control, and quantitative indices. *J. Nucl. Med.* 55: 608.

22 Moosavi, B., Fasih, N., Virmani, V., and Kielar, A. (2016). Beyond ureterolithiasis: gamut of abnormalities affecting the ureter. *Clin. Imaging* 40: 678–690.

23 Malayeri, A., Pattanayak, P., and Apolo, A. (2015). Imaging muscle-invasive and metastatic urothelial carcinoma. *Curr. Opin. Urol.* 25: 441–448.

24 Sanli, O., Dobruch, J., Knowles, M.A. et al. (2017). Bladder cancer. *Nat. Rev. Dis. Primers* 3: 17022.

25 Leyendecker, J.R., Clingan, M.J., Remer, E.M. et al. (2012). *ACR Appropriateness Criteria: Pretreatment Staging of Invasive Bladder Cancer.* Reston, VA: American College of Radiology.

26 Bryk, D.J. and Zhao, L.C. (2016). Guideline of guidelines: a review of urological trauma guidelines. *BJU Int.* 117: 226–234.

27 Lockhart, M.E., Remer, E.M., Leyendecker, J.R. et al. (2013). *ACR Appropriateness Criteria: Suspected Lower Urinary Tract Trauma* [Revision]. Reston, VA: American College of Radiology.

28 Kreydin, E.I., Barrisford, G.W., Feldman, A.S., and Preston, M.A. (2013). Testicular cancer: what the radiologist needs to know. *Am. J. Roentgenol.* 200: 1215–1225.

29 Winter, T.C., Kim, B., Lowrance, W.T., and Middleton, W.D. (2016). Testicular microlithiasis: what should you recommend? *Am. J. Roentgenol.* 206: 1164–1169.

30 Jefferies, M.T., Cox, A.C., Gupta, A., and Proctor, A. (2015). The management of acute testicular pain in children and adolescents. *BMJ* 350 (1563): h1563.

31 Mirochnik, B., Bhargava, P., Dighe, M.K., and Kanth, N. (2012). Ultrasound evaluation of scrotal pathology. *Radiol. Clin. North Am.* 50: 317–332.

32 Marko, J., Gould, C.F., Bonavia, G.H., and Wolfman, D.J. (2016). State-of-the-art imaging of prostate cancer. *Urol. Oncol.* 34: 134–146.

33 Vargas, H., Hötker, A., Goldman, D. et al. (2016). Updated prostate imaging reporting and data system (PIRADS v2) recommendations for the detection of clinically significant prostate cancer using multiparametric MRI: critical evaluation using whole-mount pathology as standard of reference. *Eur. Radiol.* 26: 1606–1612.

34 Khati, N.J., Glanc, P., Bhosale, P.R. et al. (2014). *ACR Appropriateness Criteria; Abnormal Vaginal Bleeding.* Reston, VA: American College of Radiology.

35 Bennett, G.L., Andreotti, R.F., Lee, S.I. et al. (2011). ACR appropriateness criteria® on abnormal vaginal bleeding. *J. Am. Coll. Radiol.* 8: 460–468.

36 Singh, S., Best, C., Dunn, S. et al. (2013). Abnormal uterine bleeding in pre-menopausal women. *J. Obstet. Gynaecol. Can.* 35: 473.

37 Wolfman, W., Leyland, N., Heywood, M. et al. (2010). Asymptomatic endometrial thickening. *J. Obstet. Gynaecol. Can.* 32: 990–999.

38 Burke, W.M., Orr, J., Leitao, M. et al. (2014). Endometrial cancer: a review and current management strategies: part II. *Gynecol. Oncol.* 393–402.

39 Epstein, E. and Blomqvist, L. (2014). Imaging in endometrial cancer. *Best Pract. Res. Clin. Obstet. Gynaecol.* 721–739.

40 Lee, J.H., Dubinsky, T., Andreotti, R.F. et al. (2011). ACR appropriateness criteria® pretreatment evaluation and follow-up of endometrial cancer of the uterus. *Ultrasound Q.* 27: 139.

41 Siegel, C.L., Andreotti, R.F., Cardenes, H.R. et al. (2012). ACR appropriateness criteria® pretreatment planning of invasive cancer of the cervix. *J. Am. Coll. Radiol.* 9: 395–402.

42 Devine, C., Gardner, C., Sagebiel, T., and Bhosale, P. (2015). Magnetic resonance imaging in the diagnosis, staging, and surveillance of cervical carcinoma. *Semin. Ultrasound CT MR* 36: 361–368.

43 Harris, R.D., Javitt, M.C., Glanc, P. et al. (2013). ACR appropriateness criteria® clinically suspected adnexal mass. *Ultrasound Q.* 29: 79.

44 Levine, D., Brown, D.L., Andreotti, R.F. et al. (2010). Management of asymptomatic ovarian and other adnexal cysts imaged at US. Society of Radiologists in Ultrasound consensus conference statement. *Ultrasound Q.* 26: 121–131.

45 Smith, R.A., Andrews, K., Brooks, D. et al. (2016). Cancer screening in the United States, 2016: a review of current American Cancer Society guidelines and current issues in cancer screening. *CA Cancer J. Clin.* 66: 95–114.

46 Mitchell, D.G., Javitt, M.C., Glanc, P. et al. (2013). ACR appropriateness criteria staging and follow-up of ovarian cancer. *J. Am. Coll. Radiol.* 10: 822.

47 Donaldson, C.K. (2015). Acute gynecologic disorders. *Radiol. Clin. North Am.* 53: 1293–1307.

48 Bhosale, P., Javitt, M., Atri, M. et al. (2016). ACR appropriateness criteria® acute pelvic pain in the reproductive age group. *Ultrasound Q.* 32: 108–115.

49 Lane, B., Wong-You-Cheong, J., Javitt, M. et al. (2013). ACR appropriateness criteria® first trimester bleeding. *Ultrasound Q.* 29: 91–96.

50 Doubilet, P.M., Benson, C.B., Bourne, T. et al. (2013). Diagnostic criteria for nonviable pregnancy early in the first trimester. *N. Engl. J. Med.* 369: 1443.

51 Rao, R. and Platt, L.D. (2016). Ultrasound screening: status of markers and efficacy of screening for structural abnormalities. *Semin. Perinatol.* 40: 67–78.

52 Pandya, P.P., Santiago, C., Snijders, R.J., and Nicolaides, K.H. (1995). First trimester fetal nuchal translucency. *Curr. Opin. Obstet. Gynecol.* 7: 95–102.

53 Hill, L.M. (2013). Timing of ultrasound in pregnancy – how often? At what intervals? *Semin. Perinatol.* 37: 327.

54 Simpson, L., Khati, N.J., Deshmukh, S.P. et al. (2016). ACR appropriateness criteria assessment of fetal well-being. *J. Am. Coll. Radiol.* 13: 1483–1493.

55 Azour, L., Besa, C., Lewis, S. et al. (2016). The gravid uterus: MR imaging and reporting of abnormal placentation. *Abdom. Radiol.* 41: 2411–2423.

56 Elsayes, K.M., Trout, A.T., Friedkin, A.M. et al. (2009). Imaging of the placenta: a multimodality pictorial review. *Radiographics* 29: 1371–1391.

57 Dias, T., Sairam, S., and Kumarasiri, S. (2014). Ultrasound diagnosis of fetal renal abnormalities. *Best Pract. Res. Clin. Obstet. Gynaecol.* 28: 403–415.

58 Muller, L.O. (2014). Ultrasound of the paediatric urogenital tract. *Eur. J. Radiol.* 83: 1538.

59 Servaes, S. and Epelman, M. (2013). The current state of imaging pediatric genitourinary anomalies and abnormalities. *Curr. Probl. Diagn. Radiol.* 42: 1–12.

60 Jhaveri, K.S., Mazrani, W., Chawla, T.P. et al. (2010). The role of cross-sectional imaging in male infertility: a pictorial review. *Can. Assoc. Radiol. J.* 61: 144–155.

61 Cardona-Grau, D. and Kogan, B.A. (2015). Update on multicystic dysplastic kidney. *Curr. Urol. Rep.* 16: 1–5.

62 Malkan, A.D., Loh, A., Bahrami, A. et al. (2015). An approach to renal masses in pediatrics. *Pediatrics* 135: 142.

63 Montini, G., Tullus, K., and Hewitt, I. (2011). Febrile urinary tract infections in children. *N. Engl. J. Med.* 365: 239–250.

64 Karmazyn, B., Brian, D., Coley, M. et al. (2016). *Appropriateness Criteria: Urinary Tract Infection – Child* [Revised]. Reston, VA: American College of Radiology.

65 Stranzinger, E. and Strouse, P.J. (2008). Ultrasound of the pediatric female pelvis. *Semin. Ultrasound CT MR* 29: 98–113.

Dr. Laila Alshafai

Dr. Laila Alshafai is an Assistant Professor in the Department of Medical Imaging at the University of Toronto. She obtained her medical degree at King Faisal University in Dammam, Saudi Arabia. She completed residency training in medical imaging at McGill University, Montreal, Canada. Dr. Alshafai completed a post-residency fellowship in neuroradiology at the University of Toronto. She is a staff neuroradiologist at Mount Sinai Hospital and at the University Health Network in Toronto.

Dr. Eugene Yu

Dr. Eugene Yu is an Associate Professor in the Departments of Medical Imaging and Otolaryngology – Head and Neck Surgery, University of Toronto. He obtained his medical degree and completed residency training in medical imaging at the University of Toronto. Dr. Yu completed a post-residency fellowship in neuroradiology at the University of Toronto. He is the Site Director for both the Neuroradiology Fellowship at the Princess Margaret Cancer Centre and is the lead in head and neck radiology at the University Health Network in Toronto. He is a member of the American Society of Head and Neck Radiology, the North American Skull Base Society; associate member of the American Head and Neck Society; and current president of the Eastern Neuroradiological Society (2017–2018).

Medical Imaging for Health Professionals: Technologies and Clinical Applications, First Edition.
Edited by Raymond M. Reilly.
© 2019 John Wiley & Sons, Inc. Published 2019 by John Wiley & Sons, Inc.

Dr. Sylvain Houle

Dr. Sylvain Houle is Director of the Centre for Addiction and Mental Health (CAMH) Research Imaging Centre and Preclinical Research and Associate Professor, Department of Psychiatry of the University of Toronto. He has a background in physics, electrical and computing engineering, and a specialty in nuclear medicine. Over the last 25 years he has led a multidisciplinary team of researchers in the application of Positron Emission Tomography (PET) to the investigation of mental disorders, addiction, and their treatment. His research work encompasses the development of new PET technology, particularly new PET radiotracers.

13

Imaging of the Head, Neck, Spine, and Brain

Laila Alshafai, Eugene Yu, and Sylvain Houle

13.1 Introduction

This chapter will discuss the appropriate imaging tests that are used to evaluate diseases of the brain, spine, and extracranial head and neck. For additional reading see Refs. [1–4]. This chapter does not cover pediatric imaging. Traditionally, computed tomography (CT) was thought of as an initial screening modality to guide further imaging (MRI or nuclear medicine) for patients with neurological symptoms. However, with recent technological advancements, in certain circumstances, CT may exceed or provide more accurate information than other modalities such as MRI. Also, CT has the advantage of "time" over MRI as it can provide imaging results in a matter of a few minutes compared to 20–60 minutes it may take with MRI. Also, MRI has many common contraindications such as the presence of pacemakers (see Chapter 5) and some patients experience claustrophobia. The one major concern for CT is iodinated intravenous contrast injection, which can result in acute renal failure if the renal function (GFR) is low or may cause varying degrees of allergic reactions (including anaphylaxis) (see Chapter 2). Therefore, to avoid or limit these complications, along with the requisition, radiologists will ask for a screening form to be filled out and in some instances, the radiologist will convert the case from CT to MRI or vice versa, depending on the patient. Metallic hardware (e.g. dental braces and aneurysmal clips) degrades the images of both CT and MRI, but there are advances in techniques to decrease the effect of these artifacts. Some of these techniques include dual energy for CT and using a spin-echo sequence instead of gradient sequence in MRI or using the multiacquisition variable resonance image combination (MARVIC). Also, another factor in choosing between CT and MRI is the availability and properties of each technology. Some institutions have better CT or MRI systems and this could result

Medical Imaging for Health Professionals: Technologies and Clinical Applications, First Edition.
Edited by Raymond M. Reilly.
© 2019 John Wiley & Sons, Inc. Published 2019 by John Wiley & Sons, Inc.

in some variations in the quality of the studies. In CT, the thinner the slice thickness, the higher the resolution but also the higher the radiation dose to the patient. Thin-slice CT is used to visualize fine anatomy such as the temporal bones or in cases of acute stroke, to detect a vessel occlusion. Intravenous contrast injection (see Chapter 2) improves the quality of the images, especially if the clinical question involves blood vessels, brain parenchyma, or conditions that involve the soft tissues of the neck. CT cannot assess the spinal canal for cord atrophy, cord tumor, epidural collections, or hematomas. However, if MRI (which is the gold standard to assess for these conditions) is contraindicated, the radiologist will try to improve the detection ability of CT by performing a myelogram CT (which requires a fluoroscopy-guided lumbar puncture with injection of contrast into the intrathecal space prior to the CT acquisition) to assess the canal for stenosis or other conditions. For abscesses in or around the spine, intravenous contrast can better delineate the pathology. Acute epidural hematoma in the spine can be seen on unenhanced CT but the test is not sensitive (i.e. if it is not seen, the radiologist cannot confidently exclude it). In general, in urgent situations, CT is the initial imaging modality.

13.2 Imaging the Skull and Brain

13.2.1 Trauma

CT without contrast is the ideal first test to assess for skull fractures, traumatic intracranial hemorrhage (Figures 13.1 and 13.2), related herniation, or obstructive hydrocephalus. Intravenous contrast injection is requested in case there is concern for vascular injury to the vessels (especially neck vessels). CT can also simultaneously assess the spine for fracture. If a CT of the head is relatively normal but there remains a high clinical suspicion of disease, then MRI can be considered to assess for diffuse axonal injury (DAI), which are traumatic shear lesions in closed brain injury (Figure 13.3).

13.2.2 Vascular Imaging

A CT angiogram (CTA) is a CT obtained after intravenous injection of iodinated contrast material, which enhances the vessels of a selected body segment (e.g. head and neck). These vessels will be hyperdense (white). The CT can be timed to be acquired in the arterial phase (arteriogram) or venous phase (venogram). Filling defects such as clots will appear as black areas within the vessel lumen. If the filling defect (embolus) is completely occluding the lumen, no contrast will be seen distal to the embolus. In cases of acute stroke, CT without contrast of the head followed by CTA of the head and neck in arterial phase is done to assess for the infarct, potential origin of the thromboembolic event

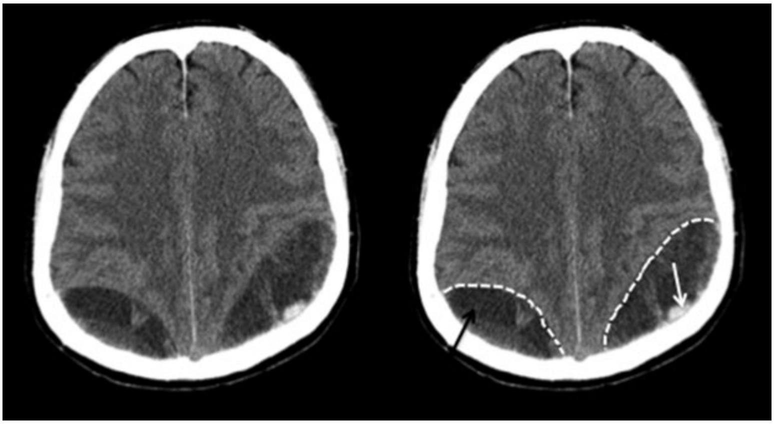

Figure 13.1 Epidural hematomas. Axial CT of the brain without contrast in the soft-tissue window. There are bilateral biconvex extra-axial blood collections in the parietal regions (shown by dashed lines) consistent with epidural hematomas. No associated fractures were evident. This was a 27-year-old male with known leukemia (leukemic patients often have altered coagulation status and are at risk for spontaneous bleeding). The densities are mixed in keeping with acute (hyperdense shown by white arrow) on chronic (hypodense shown by black arrow) hemorrhage.

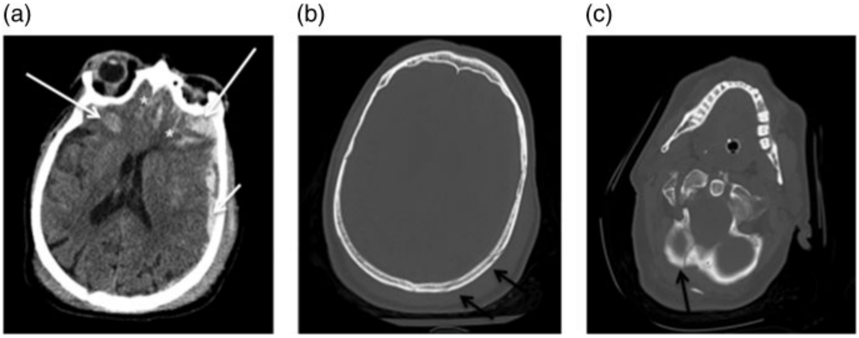

Figure 13.2 Victim of trauma with acute hemorrhagic lesions and fractures. (a) Axial CT of the brain without contrast in the soft-tissue window. There are multiple acute hemorrhagic parenchymal contusions in the frontal lobes (shown by long white arrows). There is a thin acute subdural hematoma in the left temporal region (shown by short white arrow). There are scattered foci of acute subarachnoid hemorrhage (shown by *). (b) and (c) Axial CT of the brain without contrast in the bone window. There are acute undisplaced fractures involving the left parietal and right occipital calvarium (shown by short black arrows).

and the location of the thromboembolic clot intracranially (Figure 13.4). In institutions where interventional neuroradiologists offer thrombectomy, the CTA component usually has an additional venous phase to assess for complete or partial occlusion of flow at the location of the clot. Post-processed perfusion

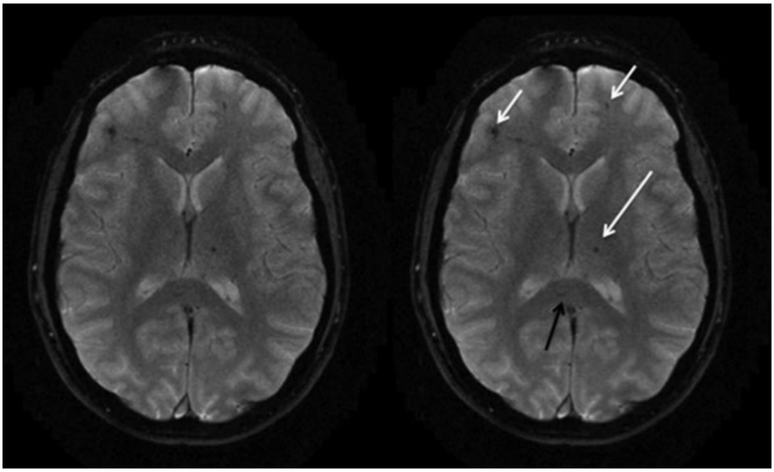

Figure 13.3 Diffuse axonal injury (DAI). Axial T2 gradient sequence demonstrating multiple scattered tiny foci of susceptibility artifact (hemorrhage) located in the cortical–subcortical white matter of the frontal lobes (shown by white short arrows), right side of the splenium of the corpus callosum (shown by short black arrow), and the left thalamus (shown by long white arrow). The patient had history of significant head trauma. These are in keeping with DAI.

maps are provided after the study. The perfusion maps are obtained through a computer software program where the information from the CTA is displaced in color codes, which reflect different information. The main maps used are mean transit time (MTT), cerebral blood flow (CBF), and cerebral blood volume (CBV). CTA are used in an attempt to differentiate between the infarct and penumbra, which is the area at risk to infarct, but can be saved by treatment (opening the occluded artery by thrombolytic therapy [tPA] or directly removing the clot through embolectomy in catheter angiography). Hemorrhagic transformation and mass effect are the two main reasons for close follow-up with CT without contrast post treatment. Hemorrhagic transformation is thought to happen due to preserved collateral blood flow or reperfusion from thrombolytic therapy in weak vessels. It is more frequent in the latter. In regard to mass effect, as the brain has fixed space/volume, any extra tissue (e.g. bleeding) will result in shifting of structures (herniation) and this will cause global ischemia (brain death) and hydrocephalus.

MRI plays a role if it is difficult to detect the acute infarcts on the unenhanced CT. A diffusion-weighted sequence is capable of detecting infarcts as early as three hours after the vascular event and this sequence remains positive for acute/subacute infarcts up to 7–10 days. Magnetic resonance angiography (MRA) is usually performed for problem-solving situations, e.g. in cases of dissections of the neck arteries. Dissections result from intimal injury (e.g. deep

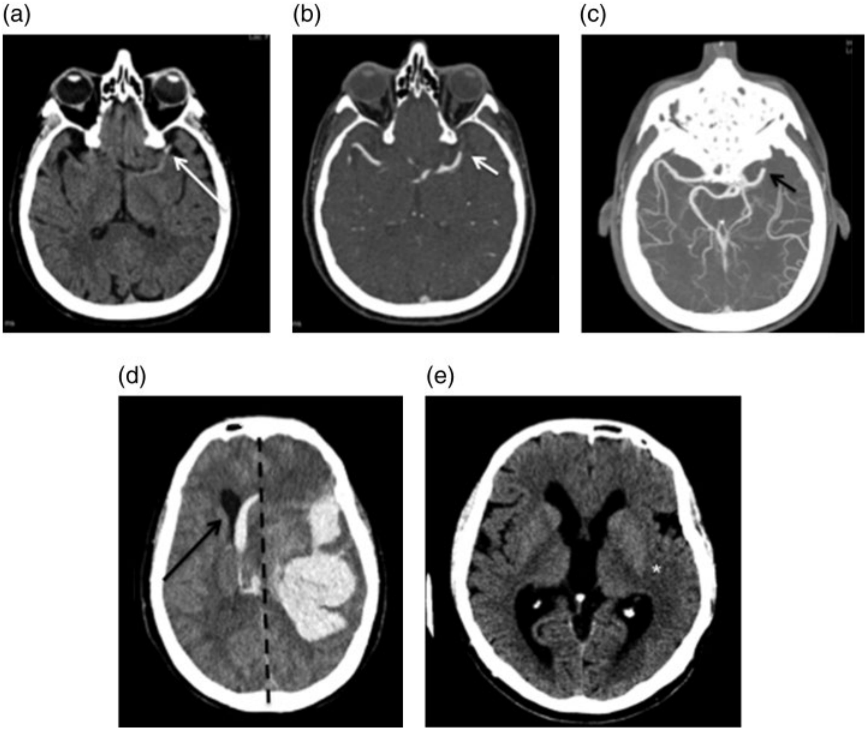

Figure 13.4 Acute stroke with hyperdense clot sign. (a) Axial CT of the brain without contrast in the soft-tissue window. There is focal hyperdensity in the left middle cerebral artery/MCA (shown by long white arrow) in keeping with a "hyperdense clot sign" reflecting the acute embolus. (b) The clot sign corresponds to a filling defect on the axial CTA (shown by short white arrow). (c) On the axial maximal intensity projection (MIP) reformats (post-processed image by computer software), it is easier to detect the filling defects (shown by short black arrow). (d) Follow-up axial CT without contrast after thrombectomy and tPA treatment showing acute hemorrhagic transformation of the left MCA territory infarct with mass effect; midline shift (shown by dashed black line), and obstructive hydrocephalus (shown by long black arrow). (e) Axial CT in the soft-tissue window of a different patient showing the acute infarct in the left MCA territory as loss of gray white matter differentiation in the posterior insular ribbon (shown by *).

atherosclerotic plaques or trauma). This diseased intima separates from the remainder of the vessel wall and projects into the lumen resulting in narrowing, occlusion, and turbulence of blood flow. The latter will result in clot formation. Dissections can be of indeterminate age on CT (acute and chronic dissections can look similar on CT). Axial T1 and T2 fast saturated sequences on MRI can detect acute mural hematoma (clot that builds up between the separated intima and media of the vessel contributing to vessel lumen narrowing), which will demonstrate high signal intensity in comparison to old mural

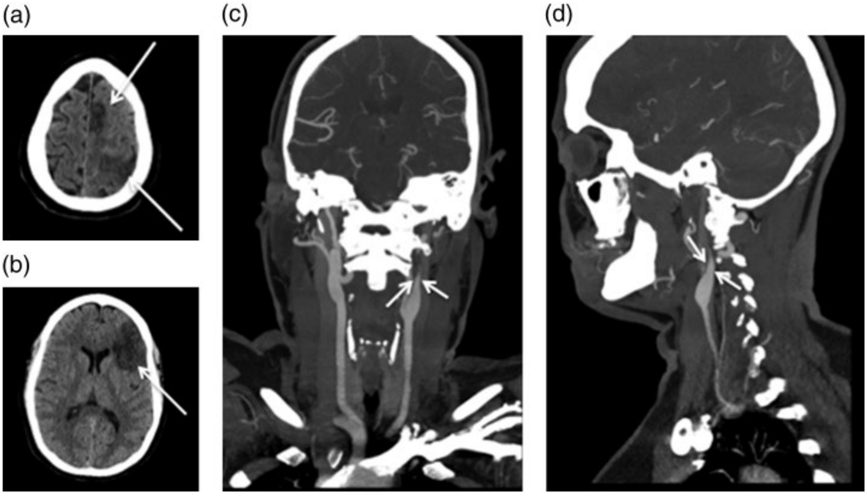

Figure 13.5 Acute dissection of the left cervical internal carotid artery. (a) and (b) Axial CT of the brain without contrast in the soft-tissue window. There are multiple peripheral wedge-shaped hypodensities with loss of the gray white matter differentiation in the left frontal and parietal lobes in keeping with acute infarcts in the left anterior circulation territory (ACA and MCA territories) (shown by long white arrows). The distribution is in keeping with a thromboembolic phenomenon. (c) and (d) Coronal and sagittal MIP reformats of CTA of the head and neck, respectively, demonstrate flame-shaped narrowing of the left cervical internal carotid artery just distal to its origin (shown by short white arrows) and non-filling of the distal course in keeping with acute dissection.

hematomas. In cases of multifocal intracranial vessel narrowing, a vessel wall study (high-resolution MRI sequences before and after contrast on a 3 Tesla system) can differentiate atherosclerotic disease from reversible cerebral vasoconstrictive syndrome (RCVS) from vasculitis, since the latter will show enhancement. RCVS will normalize after treatment.

In cases of suspected ruptured intracranial aneurysms, unenhanced CT of the head followed by CTA of the head and neck is performed. Acute subarachnoid hemorrhage will be seen and if imaged soon after the rupture, this finding will be most concentrated close to the ruptured aneurysm. The CTA is usually successful in detecting the ruptured aneurysm (Figures 13.5 and 13.6). Imaging may be complicated if the patient has multiple aneurysms or if there is a large clot compressing the aneurysm. A catheter angiogram usually follows (after a positive or negative CTA) for diagnosis and potential treatment. CTA of the neck is included in the study to give the interventionist an idea about the condition of the neck vessels (tortuosity, stenosis, underlying collagen vascular disease, dissection, etc.) to enable an efficient procedure (Figure 13.7). It is important to note that follow-up imaging will depend on the treatment. If coiling is used (coiling is one of the methods used during catheter angiography to occlude the aneurysm

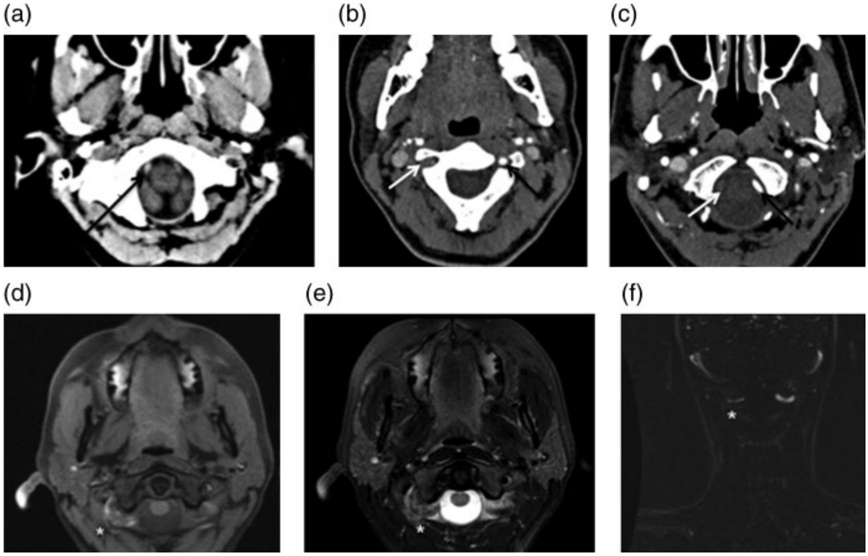

Figure 13.6 Acute dissection of the right vertebral artery. (a) Axial CT of the brain without contrast in the soft-tissue window at the level of foramen magnum demonstrating the acute thrombus in the V4 segment (shown by long black arrow). (b) and (c) Axial CTA demonstrating near-complete occlusion of the distal cervical segment within the C2 foramen transversarium and the V4 segments, respectively (shown by short white arrows). This is compared to normal vascular enhancement in the left vertebral artery (shown by short black arrows). (d) Axial fat-saturated T1 MR sequence at the level of foramen magnum demonstrating tram track-like hyperintensity in the junction of the distal cervical-V4 segment of the right vertebral artery (*) in keeping with acute mural hematoma (i.e. blood is in the walls of the artery). MRI gives more details about the dissection. (e) Corresponding axial T2 fat-saturated sequence demonstrating narrowing of the lumen of the artery (shown by *). (f) Coronal MRA of the head and neck arteries after gadolinium injection demonstrating narrowing of the caliber of the right vertebral artery (*).

lumen), MR/MRA is used, as the artifact related to the coil significantly distorts the CT image but not the MRI, depending on the sequences used. If surgical clipping is used, MRI is not feasible, as all the sequences will be significantly distorted. CT would be more informative although somewhat distorted. There are other causes of acute subarachnoid hemorrhage and other locations of intracranial hemorrhage (e.g. arteriovenous malformation, dural arteriovenous fistula, etc.), which are not discussed in this chapter.

If acute venous thrombosis is suspected, both CT and MRI with contrast in venogram phase are considered equally diagnostic. In most cases, CT would be obtained faster than MRI. CT is a faster and generally more readily available test. Both modalities would include a CT without contrast to detect the acute clot in the venous system. Venous congestion or hemorrhage and venogram phase will detect the clot (extent and location; Figure 13.8).

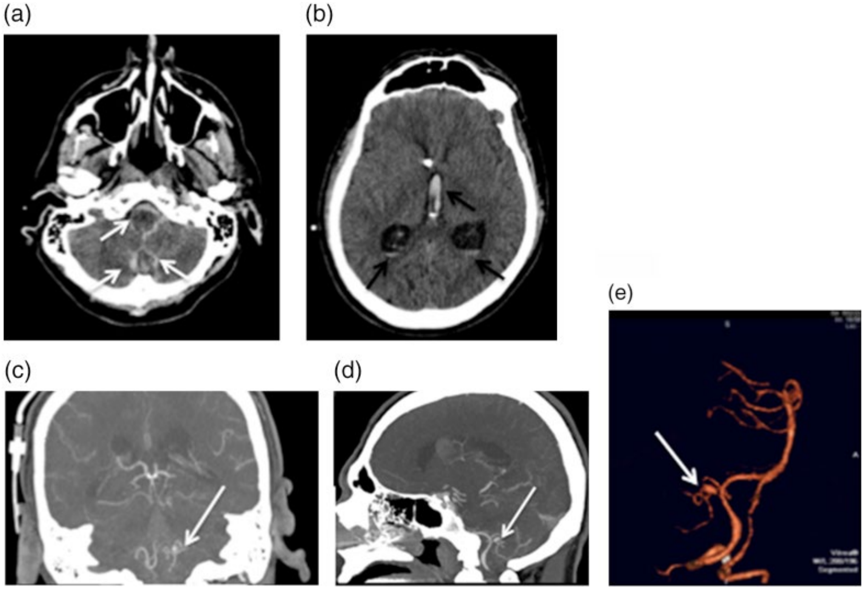

Figure 13.7 Ruptured intracranial aneurysm with acute subarachnoid hemorrhage. (a) and (b) Axial CT of the brain without contrast in the soft-tissue window demonstrating acute subarachnoid hemorrhage in the subarachnoid space (shown by short white arrows) with intraventricular extension (shown by short black arrows). (c) and (d) Coronal and sagittal maximum intensity projection (MIP) reformats of CTA, respectively, demonstrating a ruptured aneurysm from the left posterior inferior cerebellar artery/PICA (shown by long white arrows). (e) 3D reformats demonstrates the aneurysm (shown by long white arrow).

13.2.3 Tumor Imaging

If the patient history is unclear and the clinician needs to rule out multiple etiologies including tumor, unenhanced CT is an ideal initial examination. For example, if the history is headache, CT can detect extracranial causes for headache (e.g. sinusitis, temporomandibular joint pathology, etc.) or detect an intracranial mass, which could be further characterized on CT or MRI with contrast. Sometimes, no explanation of headache can be found on CT or MRI (Figure 13.9). If the patient is known for controlled/treated non-CNS malignancy and presents with new/changing pattern of headaches or neurological symptoms without focal neurological deficits (e.g. vertigo), CT with contrast is sufficient as the initial step in imaging as these patients are usually booked for routine MRI examinations. However, leptomeningeal or microparenchymal metastases can be missed on CT with contrast. Therefore, MRI with contrast is the gold standard for excluding intracranial metastases. In our institution we suggest initially requesting CT without or with contrast (the latter if highly concerned for metastases) and if negative, the patient can still be scheduled for MRI. If the patient is on chemotherapy and staging/restaging is required, MRI

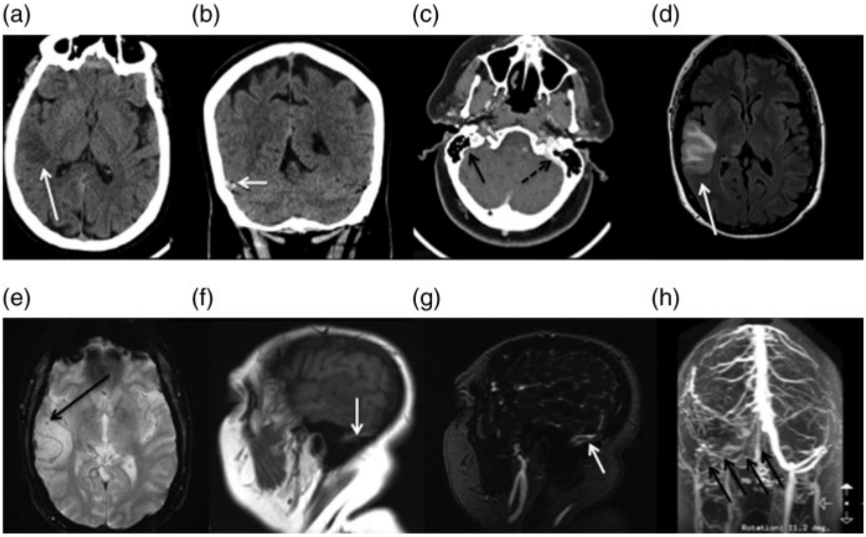

Figure 13.8 Acute thrombosis of the cortical and major dural venous sinuses with acute venous infarct. (a) Axial CT of the brain without contrast in the soft-tissue window demonstrating peripheral wedge-shaped hypodensity in the right temporal lobe without loss of the gray white matter differentiation in keeping with vasogenic edema (shown by long white arrow). (b) Coronal reformat of CT demonstrating a tubular hyperdensity in the extra-axial space (shown by short white arrow) in keeping with acute clot in a cortical vein (vein of Labbe). (c) Axial CT venogram demonstrating non-filling of the right sigmoid sinus (shown by short black arrow) compared to normal filling of the left side (shown by short black dashed arrow). (d) Axial T2 FLAIR sequence re-demonstrating the vasogenic edema with clear gray matter differentiation (shown by white long arrow). There is swelling of the overlying cortex (the patient presented with seizures). (e) Axial gradient sequence demonstrating tiny focus of blooming in keeping with microhemorrhage (shown by long black arrow). (f) Sagittal T1 sequence demonstrating hyperintense horizontally oriented tubular structure (shown by short white arrow) in keeping with acute thrombus in the right transverse-sigmoid sinuses. (g) Sagittal contrast-enhanced MRV demonstrating the corresponding filling defect (shown by short white arrow). (h) Coronal mean intensity projection (MIP) reformats of the MRV demonstrating the extent of the acute thrombosis, which also involves the proximal right transverse sinus and the torcular herophili (shown by short black arrows).

is usually done on a more urgent basis even if the suspicion for metastases is low or the patient is asymptomatic as the presence of intracranial metastases affects the eligibility of the patient to continue in the treatment regimen.

13.2.4 Infection Imaging

In cases of suspected meningitis/encephalitis, unenhanced CT is usually normal but necessary to perform to clear the patient for a lumbar puncture or rule out complications such as hydrocephalus, acute venous thrombosis, extra-axial

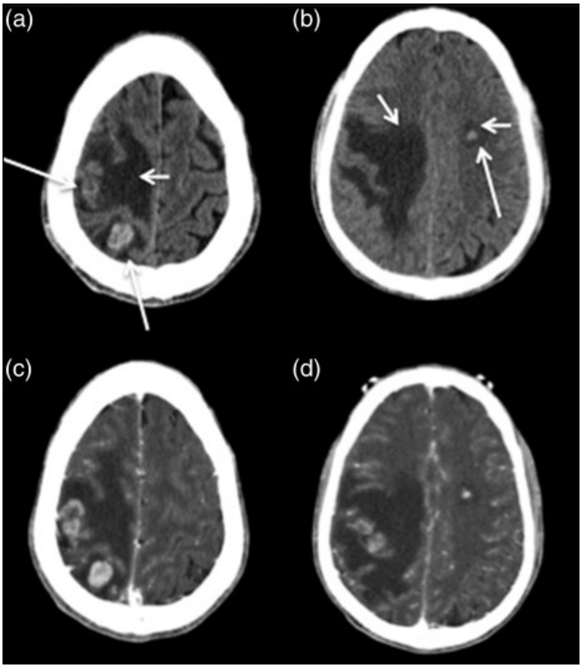

Figure 13.9 Multiple parenchymal metastases. (a) and (b) Axial CT of the brain without contrast in the soft-tissue window at the vertex demonstrating multiple intrinsically hyperdense (hemorrhagic or calcified) lesions (shown by long white arrows) in the parenchyma with significant associated vasogenic edema (shown by short white arrows) and sulcal effacement (mass effect). Patient had primary soft tissue malignancy. In this case the hyperdensity was related to hemorrhagic lesions. (c) and (d) Axial CT of the brain following intravenous contrast injection in the soft-tissue window at the same levels. The lesions demonstrate minimal enhancement.

collections (extra fluid that accumulates outside the brain parenchyma, which results in mass effect on it), or deep infarcts. If there is herniation, a lumbar puncture is contraindicated as it will cause further herniation by decreasing the intracranial pressure. Meningitis (pus in the subarachnoid space) may or may not be seen as hyperdensity in the sulci and basal cisterns (normal spaces that surround the brain parenchyma and contain CSF). The sensitivity of detection is increased by administering contrast on CT and further increased on MRI without contrast and even further increased with MRI contrast (Figure 13.10). Encephalitis will be seen on CT or MRI as cortical swelling with enhancement (Figure 13.11). It will demonstrate diffusion restriction on MRI (diffusion restriction will be shown as bright signal indicating certain acute pathology). Abscess will demonstrate a ring-enhancing lesion on contrast-enhanced CT and MRI (Figure 13.12). The common differential diagnosis to

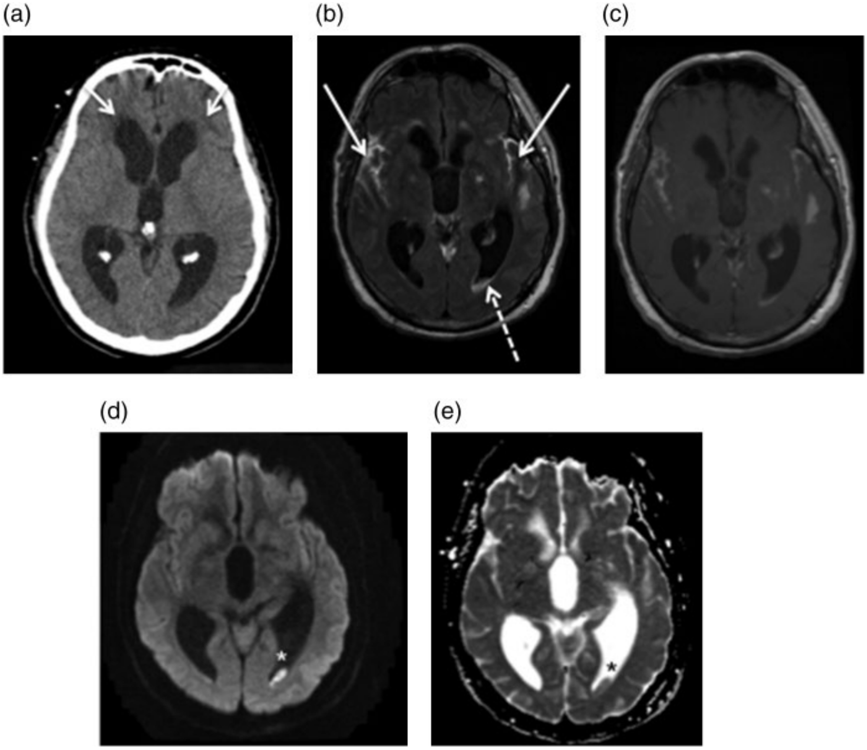

Figure 13.10 Acute meningitis with ventriculitis. (a) Axial CT of the brain without contrast in the soft-tissue window demonstrating moderate dilatation of the third and lateral ventricles (fourth ventricle is also dilated but not shown) with effacement of the sulci in keeping with communicating hydrocephalus. There is mild patchy periventricular hypodensities in keeping with transependymal CSF permeation (extravasation of CSF into the parenchyma) (shown by short white arrows) in keeping with active hydrocephalus. (b) Axial T2 FLAIR sequence demonstrating sulcal hyperintensity (shown by long white arrows) and intraventricular hyperintensity (occipital horns of the lateral ventricles, more obvious on the left side) (shown by long dashed white arrow) in keeping with purulent material. (c) Axial T1 post-gadolinium sequence showing enhancement in the same areas. (d) and (e) Axial DWI and ADC maps, respectively, showing diffusion restriction of the purulent material in the ventricles (i.e. high signal on DWI and low signal on ADC) (shown by *).

rule out is solitary cystic/necrotic metastasis or primary brain tumor (glioblastoma multiforme [GBM]). The diffusion-weighted sequence will differentiate an abscess from the other two entities as there will be central diffusion restriction. There are atypical cases that are more complicated and beyond the scope of this book. If there are multiple intracranial lesions, the main consideration is metastases until proven otherwise. Also, ventriculitis/ependymitis (when infection reaches the lining of the ventricles) can be present.

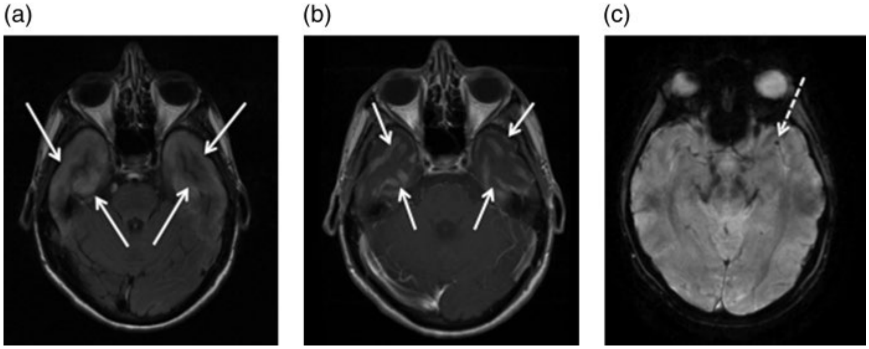

Figure 13.11 Acute encephalitis. (a) Axial T2 FLAIR MR sequence at the level of the middle cranial fossa demonstrating diffuse swelling with increased signal intensity of the cortex of the temporal lobes (shown by long white arrows) bilaterally in a symmetric fashion. (b) Axial T1 post-gadolinium sequence demonstrating diffuse enhancement of the abnormal cortex (shown by short white arrows). (c) Axial gradient sequence demonstrating tiny foci of susceptibility artifacts in keeping with micro-hemorrhage (shown by long dashed white arrow). Differential considerations include an antibody-mediated encephalitis versus a viral encephalitis such as herpes simplex virus (HSV). Less likely considerations include mitochondrial disorders and toxic causes (such as ethylene glycol). This patient had limbic (autoimmune) encephalitis. The patient did not receive steroids but has improved on intravenous immunoglobulins (IVIG).

13.2.5 Imaging Inflammatory/Metabolic Lesions

These conditions are beyond the scope of this book but multiple sclerosis is a common demyelinating disease and can be detected by imaging. CT is not sensitive for detecting white matter lesions but could be positive in cases of acute and large lesions or in chronic severe stage. MRI is the modality of choice. The FLAIR T2 sequence and spin-echo T2 sequences are the most important MRI sequences in detecting these lesions (Figure 13.13). Active lesions will show enhancement and can show diffusion restriction. If screening is the indication, contrast is not normally administered unless requested by a neurologist with a specific question, such as complications related to treatment, usually immunosuppressive therapy, resulting in progressive multifocal leukoencephalopathy (PML).

13.2.6 Imaging Dementia

MRI (and CT) will show the chronic findings of dementia, which is disproportionate cortical atrophy of particular lobes depending on the exact entity. Sometimes the pattern of atrophy is not typical and difficult to determine. Alzheimer's dementia typically results in symmetric bilateral atrophy of the temporal lobes (Figure 13.14). For further discussion on imaging dementia, see Section 13.5 and also Chapter 15.

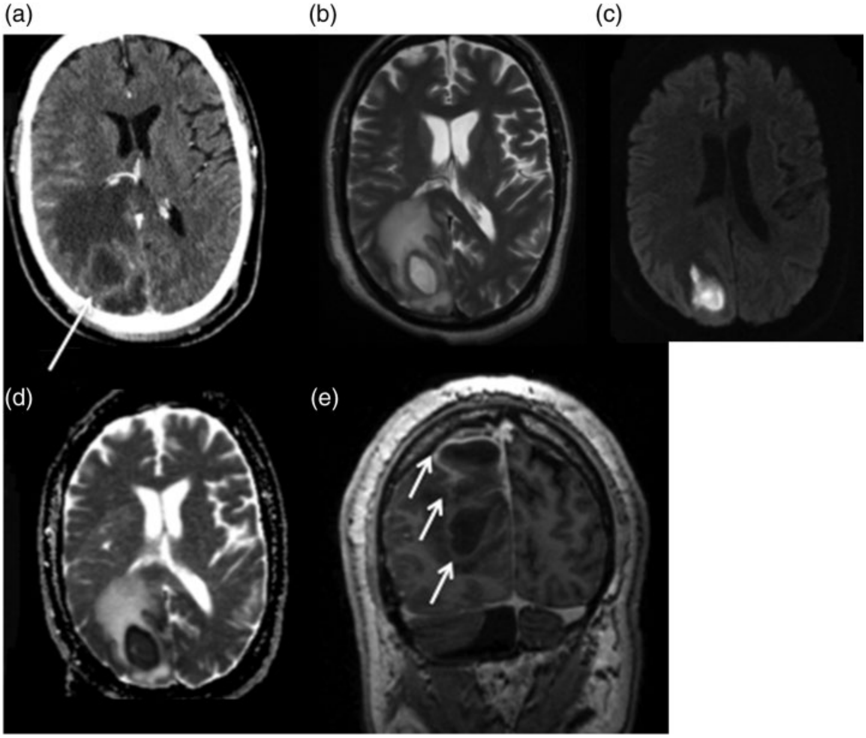

Figure 13.12 Intra-parenchymal abscess. (a) Axial CT of the brain following intravenous contrast injection in the soft-tissue window demonstrating a ring-enhancing lesion (shown by long white arrow) with marked perilesional vasogenic edema and mass effect. (b) Axial T2 sequence demonstrating a lesion with peripheral isointense rim and central liquefaction. (c) and (d) Axial DWI and ADC maps, respectively, demonstrating diffusion restriction. (e) Coronal T1 post-gadolinium reformatted sequences demonstrating rim enhancement of the lesion and the larger vertical extent (shown by short white arrows). This abscess was drained and grew Streptococcus G.

13.3 Imaging the Spine

13.3.1 Trauma

Unenhanced CT is the initial most appropriate study to image trauma to the spine. Unless vascular injury or other parts of the body are suspected to be injured, then contrast is typically not administered. Spine images could be reconstructed from a CT of the chest, abdomen, and pelvis instead of exposing the patient again to radiation. Particularly in the cervical spine, if ligamentous injury, acute epidural hematoma, or cord contusion/transection (complete cord tear) are to be ruled out, then MRI is the modality of choice. A T2

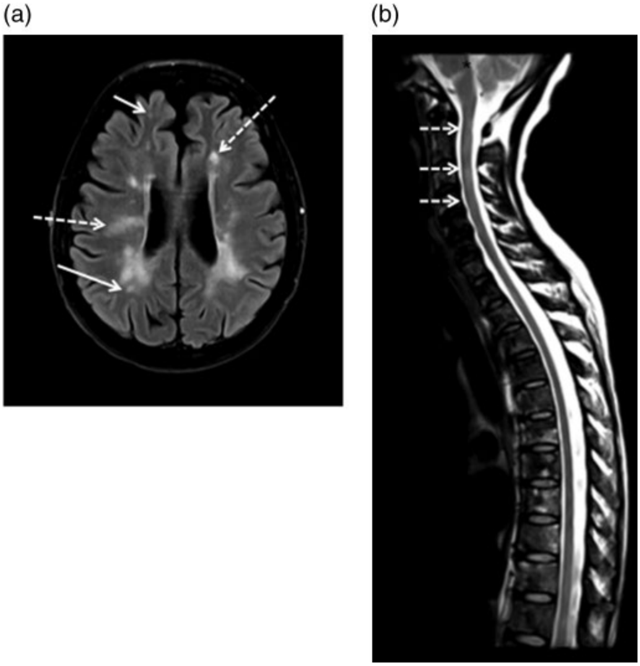

Figure 13.13 Multiple sclerosis (MS). (a) Axial T2 Flair sequence of the brain demonstrating multiple peripendicular callosal-septal hyperintense lesions in the deep white matter (shown by long white arrow), subcortical white matter (shown by short white arrow), and periventricular white matter compatible with so-called "Dawsons fingers" (shown by long dashed white arrows). (b) Sagittal T2 sequence of the cervical and thoracic spine demonstrating multiple patchy hyperintense lesions (shown by short dashed white arrows). There are also lesions in the posterior fossa, e.g. in the pons (shown by black *).

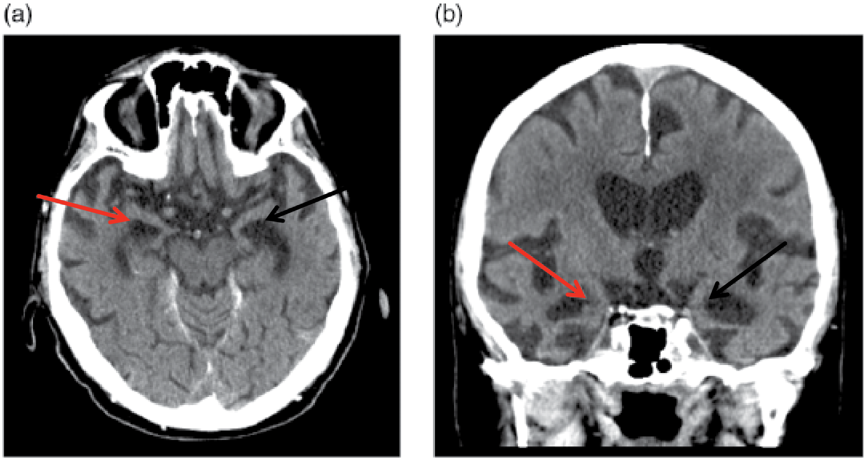

Figure 13.14 Alzheimer's dementia. (a) Axial CT of the brain without contrast in the soft-tissue window. (b) Coronal reformat. Bilateral medial temporal cortical atrophy involving the hippocampi (shown by long white arrows) disproportionate to the degree of atrophy of the reminder of the cerebral parenchyma.

fat-saturated sequence is sensitive for detecting ligamentous injury. Acute epidural hematoma or cord injury can be assessed on conventional T1 and T2 sequences (Figure 13.15).

13.3.2 Vascular Imaging

Traumatic injury was discussed previously. Acute arterial infarction of the cord is rare but can be seen in cases of dissecting or treated abdominal aortic aneurysm, among others. Dural arteriovenous fistula (Figure 13.16) is not an uncommon cause of acute back pain and neurologic deficits. Time-resolved MRA with contrast is usually performed followed by a catheter angiogram for further diagnosis and treatment.

13.3.3 Tumor Imaging

Bony metastases or a primary bone neoplasm in the spine can be assessed on unenhanced CT for extent and extra-osseous soft-tissue component. Involvement of the neural foramina or central canal can be assessed on CT. MRI is the most sensitive modality for detecting bone marrow metastases. It is also better for the assessment of the central canal and adds information regarding cord or cauda equina compression (mass effect from tumor on the cord results in local ischemia and tissue death [paralysis] in comparison to CT [Figure 13.17]). Cord neoplasia (primary or less commonly secondary) is best assessed on MRI. The imaging features include signal abnormality and expansion of the cord. Enhancement, hemorrhagic, or cystic components will depend on tumor pathology (Figure 13.18). Secondary syrinx (dilatation of CSF inside a small canal through the center of the cord [similar to the concept of hydrocephalus in the brain]) can be seen related to mass effect. The differential diagnosis depends on the extent of the lesion, which could include demyelinating, ischemic, or granulomatous processes among other etiologies.

13.3.4 Infection Imaging

For osteomyelitis and diskitis, both CT and MRI are diagnostic. CT without contrast will demonstrate the erosive changes in the endplates and reduction of the disc height. Infection can also involve the facet joints. The addition of contrast will better depict adjacent phlegmon or abscess formation in the prevertebral, paraspinal, or epidural spaces. Phlegmon is infectious material that has not yet liquefied and cannot be drained. When it liquefies it becomes an abscess. MRI will demonstrate bone marrow edema, T2 hyperintensity in the disc space and enhancement in these regions, and better assess for extension to the epidural space and cord or cauda equina compression (Figure 13.19). Imaging after treatment or in chronic stages will show progressive sclerosis.

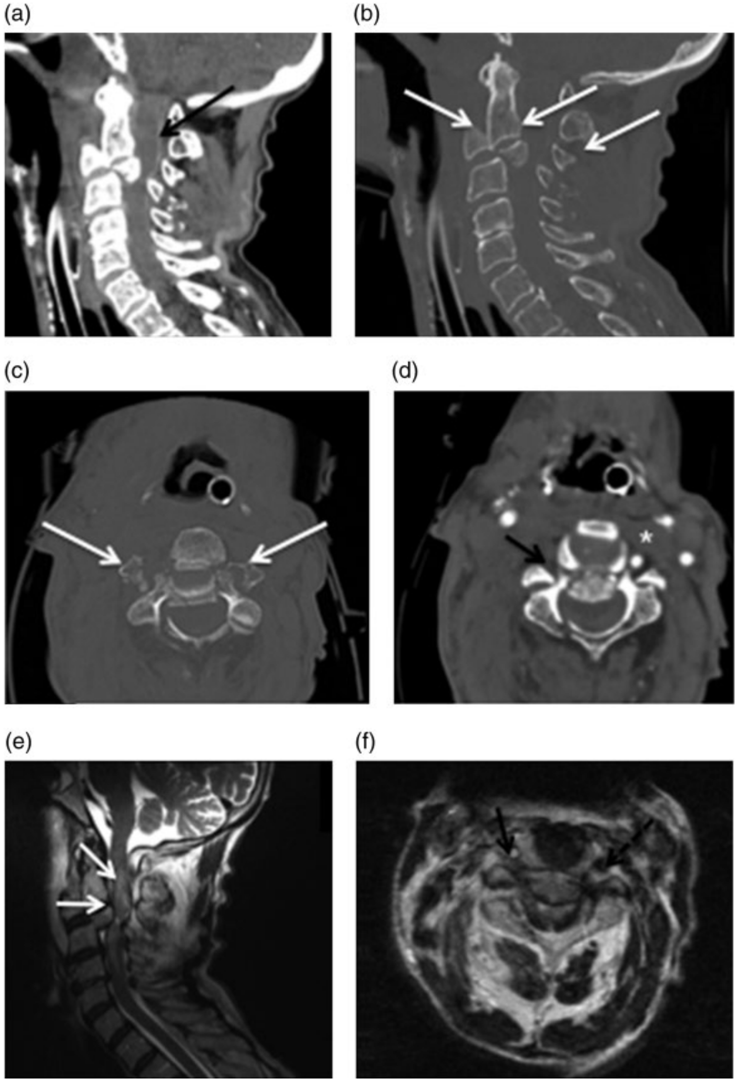

Figure 13.15 Acute fractures, dislocations with cord injury, and right vertebral arterial dissection. (a) Sagittal reformats of CT of the cervical spine without contrast in the soft-tissue window. (b) Sagittal reformats in the bone window. There is acute transverse fracture and dislocation through the C3 vertebral body (shown by long white arrows) with posterior and inferior displacement of the superior fragment into the central canal resulting in severe narrowing. There is thin linear hyperdensity posteriorly (shown by long black arrow in (a)) above the level of the fracture in keeping with acute epidural hematoma. (c) Axial CT in the bone window at the level of the fractures. There are fractures through foramina transversaria at C2–3 level (shown by long white arrows). (d) Axial CT angiogram at the same level demonstrating the absence of contrast enhancement in the right vertebral artery (shown by short black arrow) in keeping with dissection compared to the normal left side (shown by *). (e) Sagittal T2 MR sequence of the cervical spine demonstrates severe central canal narrowing and hyperintensity within the cord (shown by short white arrows) in keeping with cord edema/contusion. (f) Axial T2 MR sequence at the level of C2–3 foramina transversaria demonstrating loss of the normal flow void in the right vertebral artery (shown by short black arrow) in keeping with dissection compared to the normal left side (shown by short black dashed arrow).

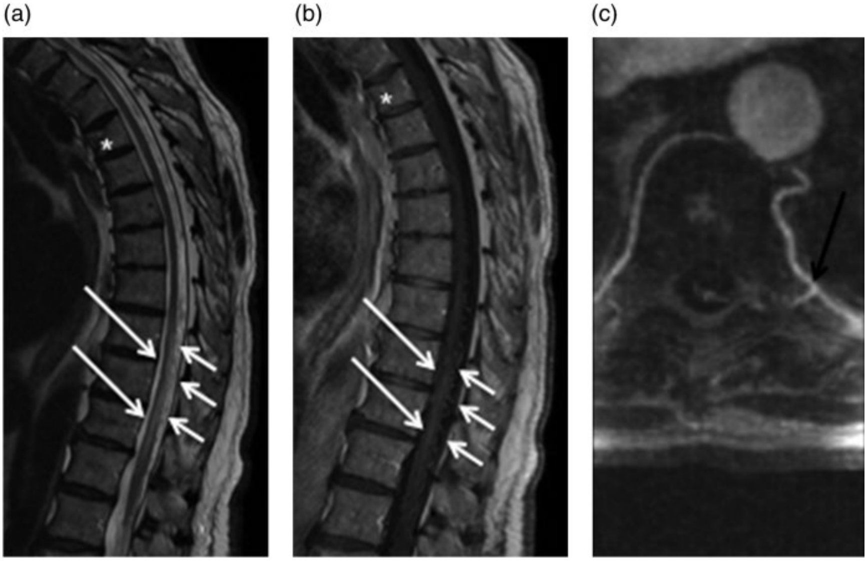

Figure 13.16 Spinal dural AVF. (a) Sagittal T2 MR sequence of the thoracic spine. There is extensive intra-medullary hyperintensity in the thoracic cord extending from T9 to the conus medullaris (shown by long white arrows) indicating venous congestion/edema and numerous dorsal serpiginous dark flow voids (shown by short white arrows) in keeping with dilated perimedullary veins. (b) Sagittal T1 post-gadolinium MR sequence. There is mild patchy enhancement of the cord (shown by long white arrows) and enhancement of the dorsal perimedullary veins (shown by short white arrows). (c) Axial MIP reformats of contrast-enhanced MRA at the level of arteriovenous fistula. There is an early draining vein seen anastomosing with the left radicular artery inferior to the pedicle at T8 (shown by long black arrow). Incidentally, there is a remote minor compression fracture of the superior endplate of T4 likely related to osteoporosis (shown by *) seen on (a) and (b).

Complications of diskitis/osteomyelitis include neural elements compression and pathologic fractures.

13.3.5 Imaging Inflammatory/Metabolic Conditions

A prototypical inflammatory process of the bony spine is the seronegative inflammatory spondylitis called ankylosing spondylitis. After screening plain radiographs, a whole spine MRI usually follows for either more sensitive screening or diagnosis, which will demonstrate the diffuse syndesmophytes (calcifications/heterotopic ossifications of the thickened anterior spinal ligament), squaring of the vertebral bodies, acute inflammatory changes as T2-weighted MRI hyperintensity involving the anterior corners of the vertebral bodies (Romanus lesions) or the disc spaces (Andersson lesions), and erosive changes in the sacroiliac joints. In the chronic stages, radiographs or CT will

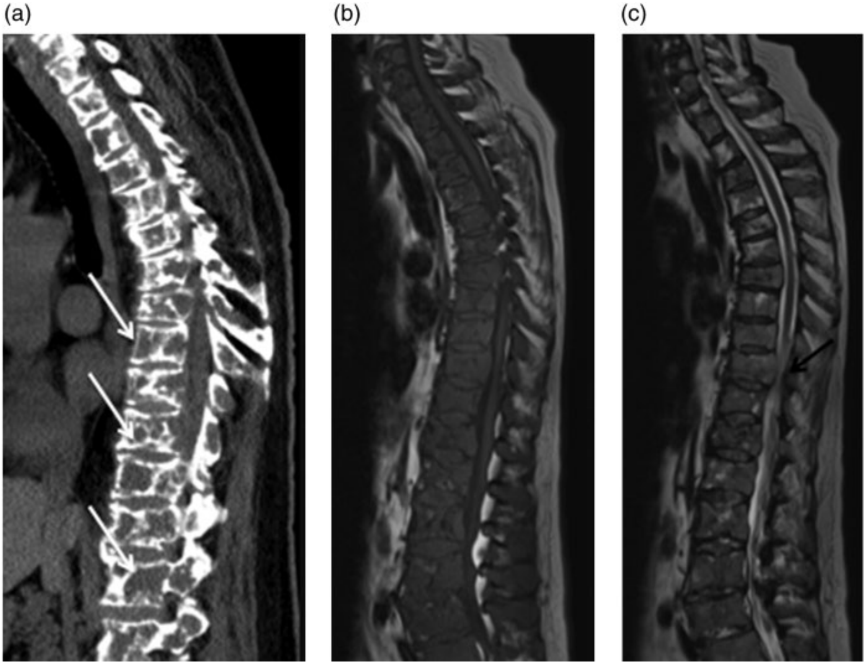

Figure 13.17 Abnormal bone marrow on CT and MRI in a case of multiple lytic bony metastases from breast cancer. (a) Sagittal reformat of CT of the chest and abdomen without contrast in the soft-tissue window. There are multiple lytic (destructive) bone marrow lesions (some are shown by long white arrows). (b) Sagittal T1 and (c) sagittal T2 MRI sequences without contrast demonstrates more extensive metastatic bony disease with diffuse infiltration of the bone marrow and epidural extension at some levels with cord compression at the T0 level (shown by short black arrow).

demonstrate bamboo spine (caused by diffuse syndesmophytic ankylosis, i.e. the spine looks like bamboo due to calcifications along the edges of the vertebrae [syndesmophytes]), shiny corners of vertebral bodies (sclerotic Romanus lesions), diffuse or multilevel ankylosis. The main complication is pathological fractures predominantly through the disc spaces after minor hyperextension injury and potentially cord or cauda equina compression (Figure 13.20). Inflammatory conditions of the cord are beyond the scope of this chapter, but MRI is the modality of choice to assess these conditions. Demyelinating processes can be seen as multifocal hyperintense cord lesions on T2-weighted MRI with or without enhancement in multiple sclerosis, or larger lesions (transverse myelitis) in cases of neuromyelitis optica (Devic's disease). This is a demyelinating disease with specific affinity to the optic nerves, deep brain structures, and spinal cord. Transverse myelitis is an umbrella term that

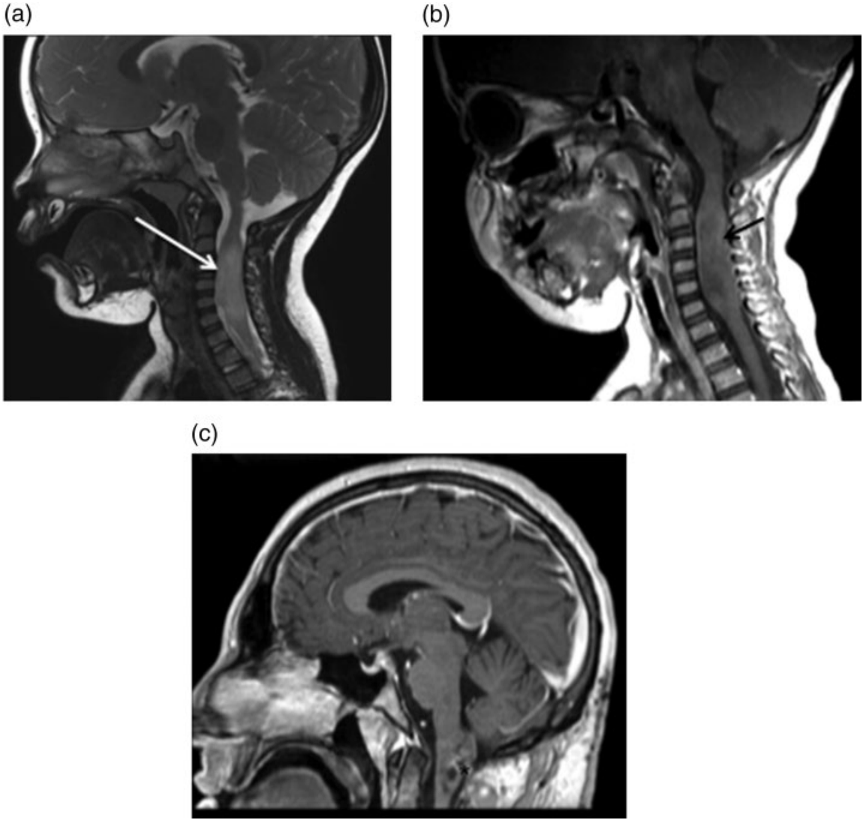

Figure 13.18 Cord astrocytoma. (a and b) Sagittal T2 and T1 MR sequence post-gadolinium sequences, respectively, in a child demonstrating a long segment of cord expansion with T2 hyperintensity (shown by long white arrow) and mild patchy enhancement (shown by short black arrow). (c) A sagittal T1 MR post-gadolinium sequence of the brain of a different patient, young adult with cervical-medullary juvenile pilocytic astrocytoma demonstrating cystic change (shown by black *).

includes multiple etiologies such as viral myelitis, vasculitis, etc. (Figure 13.21). With regard to metabolic conditions, one entity of note is vitamin B_{12} deficiency that results in accumulation of methylmalonic acid, which is believed to cause myelin toxicity resulting in dorsolateral cord demyelination. This is captured on MRI as diffuse increased signal on T2-weighted sequences and potential enhancement and the imaging picture is called subacute combined degeneration of the spinal cord.

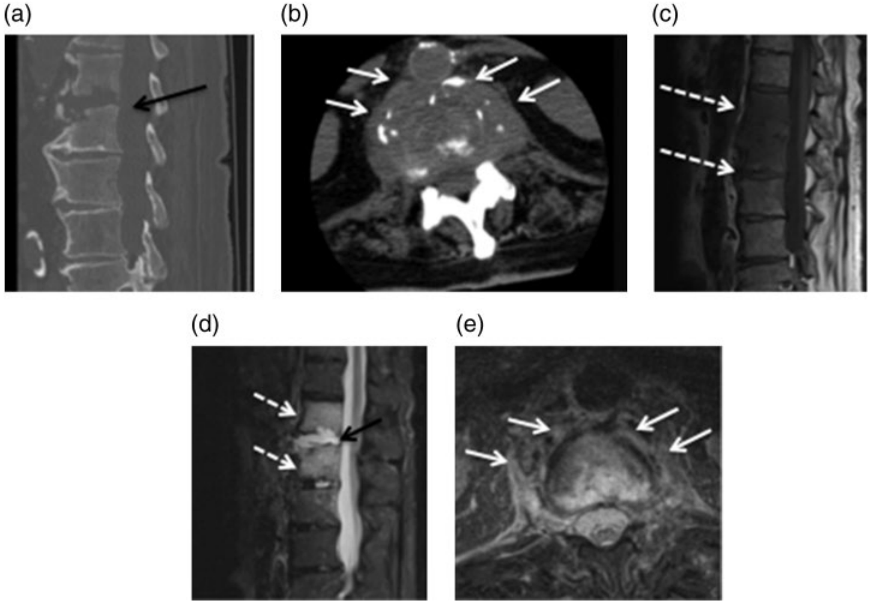

Figure 13.19 Acute osteomyelitis/diskitis. (a) Sagittal reformat of CT of the lumbar spine without contrast in the bone window demonstrating a destructive process centered at the T12–L1 disc level (shown by long black arrow). (b) Axial CT at T12–L1 disc level in the soft-tissue window demonstrating thin ill-defined soft tissue in the prevertebral and paraspinal spaces (shown by short white arrows) in keeping with phlegmon (inflammatory process). (c). Sagittal T1 sequence. (d) Sagittal T2 fat-saturated sequence. There is bone marrow edema involving the T12 and L1 vertebral bodies as demonstrated by marked diffuse T1 hypointensity (shown by long dashed white arrows) and T2 hyperintensity (shown by short dashed white arrows), respectively, reflecting acute osteomyelitis. These affected portions of the bone will demonstrate enhancement following contrast (not shown). This process surrounds marked T2 hyperintensity in the intervening disc (diskitis) shown by short black arrow. This affected disk will also demonstrate enhancement (not shown). (e) Axial T2 fat-saturated sequence at T12–L1 re-demonstrating prevertebral and paraspinal phlegmon formation (shown by short white arrows).

13.4 Imaging the Head and Neck

13.4.1 Trauma

In cases of fractures, unenhanced CT is the appropriate modality. When it involves the orbits, particularly the medial wall or floor, herniation of the medial or inferior recti muscles, the radiologist will examine these for potential entrapment, i.e. when there are fractures, the contents of the orbits protrude through the fracture (e.g. fat and muscles) and become entrapped. In orbital floor fractures, documentation is made of involvement of the infraorbital

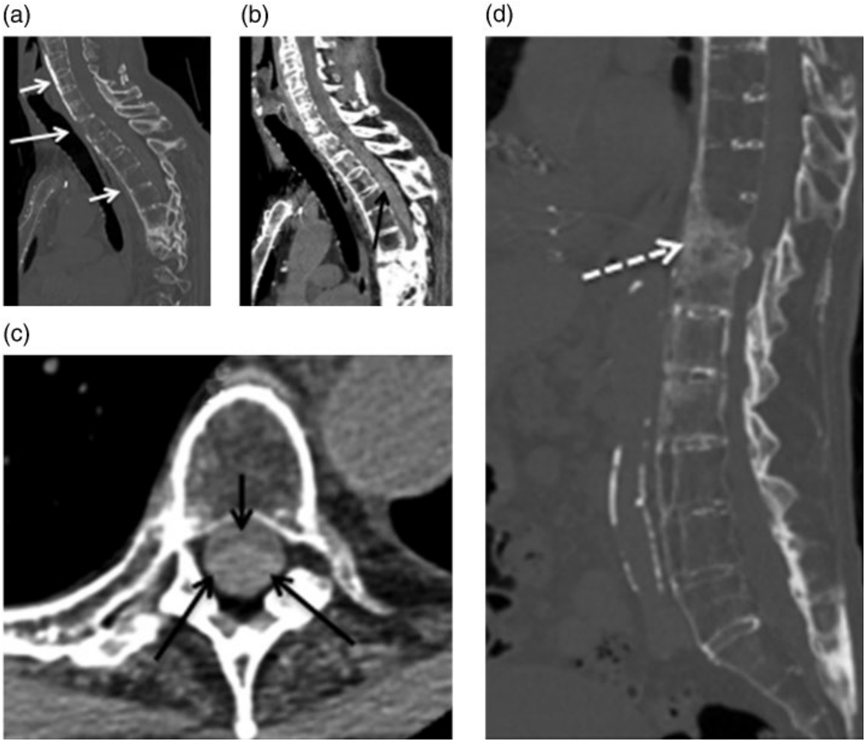

Figure 13.20 Ankylosing spondylitis with hyperextension fractures. (a) Sagittal reformat of CT of the cervicothoracic spine without contrast in the bone window. (b) In the soft-tissue window. (c) Axial CT in the soft-tissue window at the upper thoracic level. (d) Sagittal reformats of CT of the thoracolumbar spine. There is an acute horizontal fracture line through the C6/7 disc space with distraction (shown by long white arrow). There is syndesmophyte formation (shown by short white arrows). There is hyperdensity posteriorly in the central canal (shown by long black arrows) in keeping with acute epidural hematoma with anterior displacement and compression of the cord (shown by short black arrow). Old, healed hyperextension fracture at T11/12 (shown by long white dashed arrow).

foramen (Figure 13.22). A potential complication is traumatic carotid cavernous fistula. A fistula is an abnormal communication between an artery and vein, which requires urgent intervention (surgical or catheter-guided intervention). In mandibular fractures, involvement of the temporomandibular joint or the infra-alveolar canal should be determined (the trigeminal nerve branch runs in this canal and if there is a fracture, this nerve can be injured). Laryngeal cartilage fractures are rare but could be seen particularly in strangulation (Figure 13.23). Temporal bone fractures can be complex and may include injury of the inner ear structures (otic capsule, ossicular dislocation), facial nerve canal injury, or venous thrombosis of the internal jugular vein/sigmoid sinus among others.

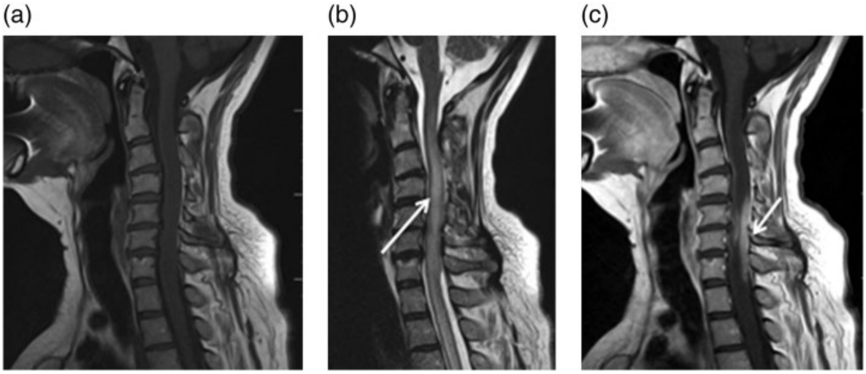

Figure 13.21 Transverse myelitis. (a) Sagittal T1, (b) sagittal T2, and (c) sagittal T1 post-gadolinium MR sequences of the cervical spine. There is a long segment of intramedullary T2 hyperintensity (shown by long white arrow) and patchy enhancement posteriorly (shown by short white arrow). This patient had neuro-sarcoidosis.

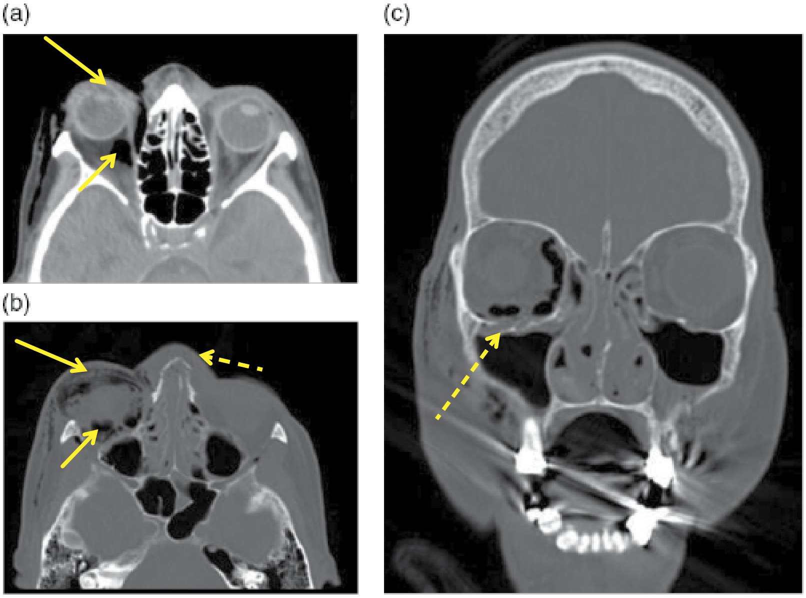

Figure 13.22 Acute orbital trauma. (a) Axial CT of the facial bones without contrast in the soft-tissue window, (b) bone window, and (c) coronal reformat in the bone window. There is acute soft tissue injury with emphysema centered in the right orbit involving the preseptal space (shown by long white arrows) and postseptal space (shown by short white arrows) with mild proptosis (bulge of the globe). There are comminuted fractures of the right orbital floor (shown by long white dashed arrow in panel c) and nasal bones (white dashed arrow in panel b). The patient had right zygomaticomaxillary complex (ZMC), right Le Fort I, and right naso-orbitoethmoid fractures (not all shown).

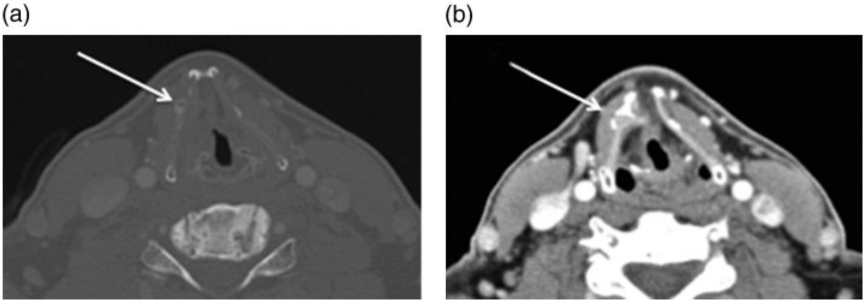

Figure 13.23 Laryngeal trauma. Axial CT of the neck following intravenous contrast injection at the level of the supraglottic larynx in the bone window (a) and in the soft-tissue window (b). There is an oblique fracture line in the right lamina of the thyroid cartilage (shown by long white arrows). There is sclerosis of the fracture edges indicating healing/ subacute age.

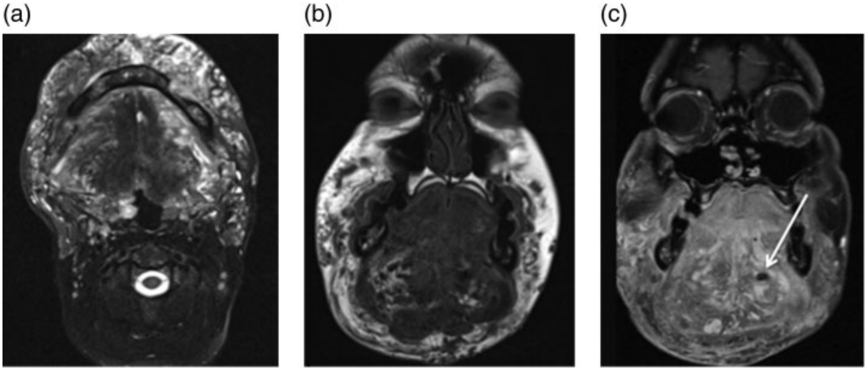

Figure 13.24 Venolymphatic malformation. (a) Axial fat-saturated T2 MR sequence on the neck at the level of the oral cavity, (b) coronal T1 sequence, and (c) coronal fat-saturated T1 post-gadolinium sequence. There is a diffuse trans-spatial process involving the face and deep spaces of the suprahyoid neck demonstrating enhancement and T2 hyperintensity. There is a focus of marked T1 hypointensity in the left floor of mouth in keeping with a phlebolith (calcification in a vein) (shown by long white arrow), this focus is calcified on CT (not shown).

13.4.2 Vascular Imaging

The main pathology imaged are vascular malformations, particularly slow flow lesions (venous components), mixed types (venolymphatic malformations) (Figure 13.24), or purely lymphatic. Regardless of the location, phleboliths (stones) and enhancement of the veins are findings of the venous components. The presence of a nonenhancing component that is similar to water density indicates lymphatic component. These lesions are commonly trans-spatial (do not respect boundaries and cross-multiple spaces) and may get superinfected. Both CT and MRI can be performed, usually with contrast. Ultrasound can also be performed for superficial lesions.

13.4.3 Tumor Imaging

Neoplasia of the aerodigestive mucosa is usually imaged with contrast-enhanced CT. There are many challenges as dental-related treatment can result in significant artifacts, which limit the evaluation of the oral cavity and oropharynx. Approaches to overcome these limitations are to perform additional angled views through these areas or perform MRI. Due to breathing and motion artifacts, MRI is suboptimal in evaluating the hypopharynx, larynx, and trachea and CT is the preferred modality. Laryngeal involvement by tumor remains difficult to image by CT but usually if there is a suspicion, MRI can be performed for potential further characterization. Metastatic lymphadenopathy is best assessed on CT. Lymph nodes are assessed for their size (in general, >1 cm in maximum axial dimension with some exceptions), morphology (rounded instead of oval shape, loss of the fatty hilum, cystic or necrotic change [Figure 13.25]), and extracapsular extension, which is identified by irregular margins or infiltration of adjacent structures. Encasement of the common or internal carotid arteries by

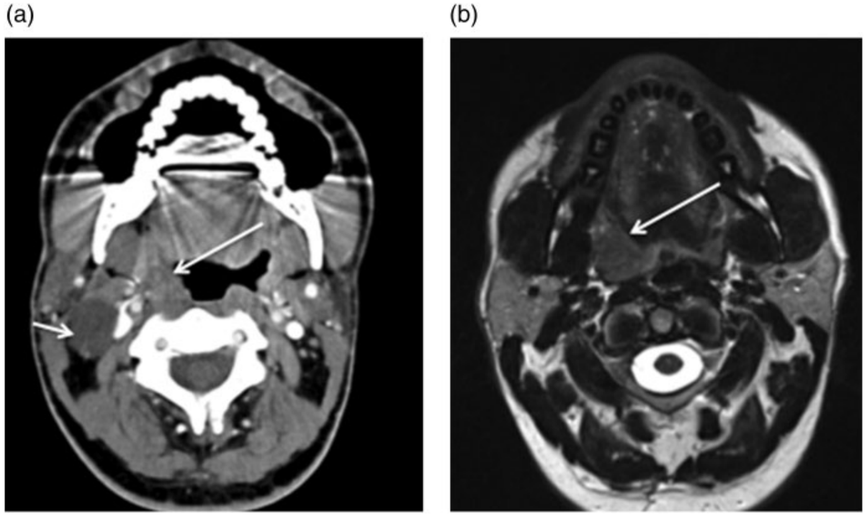

Figure 13.25 Tonsillar cancer. (a) Axial CT of the neck following intravenous contrast injection in the soft-tissue window at the level of the oropharynx. There is a bulky right tonsillar mass (shown by long white arrow) and an ipsilateral cystic/necrotic level 2a enlarged node (shown by short white arrow). (b) Axial T2 sequence at the same level demonstrating the right tonsillar mass (shown by long white arrow).

more than 270° by tumor or nodes deems the case nonsurgical while venous invasion does not. Soft-tissue tumors are not discussed in this chapter. MRI with contrast is indicated to evaluate for perineural spread, which can be suspected by proximity to the skull base foramina (particularly in cases of nasopharyngeal cancer) or by the tumor pathology, which has high propensity for perineural spread (like lymphoma or adenoid cystic cancer). Orbital and salivary gland tumors are best imaged on MRI with contrast.

13.4.4 Infection Imaging

The main reason for imaging the neck in cases of acute neck infections is to evaluate the airways and look for drainable abscesses. Contrast CT is the modality of choice. Common indications are tonsillar/peritonsillar infections (Figure 13.26), dental-related infections, and foreign bodies impeded within or around the aerodigestive mucosa. Bone necrosis related to osteomyelitis or necrosis postradiation is also evaluated on CT. In the acute stages of osteomyelitis, there will be cortical erosions, lytic process, bone fragments, air pockets in the bone, sinus tracts, periosteal reaction, and adjacent inflammatory changes in the soft tissue, which can include abscess (Figure 13.27). In the treated, subacute, or chronic stages, bone sclerosis (more bone formation resulting in whiter bones) will be seen.

13.4.5 Imaging Inflammatory Conditions

Inflammatory conditions of the salivary glands (parotids, submandibular, sublingual, and lacrimal glands) and thyroid gland are usually assessed on ultrasound due to their superficial location. Inflammation of the salivary glands can

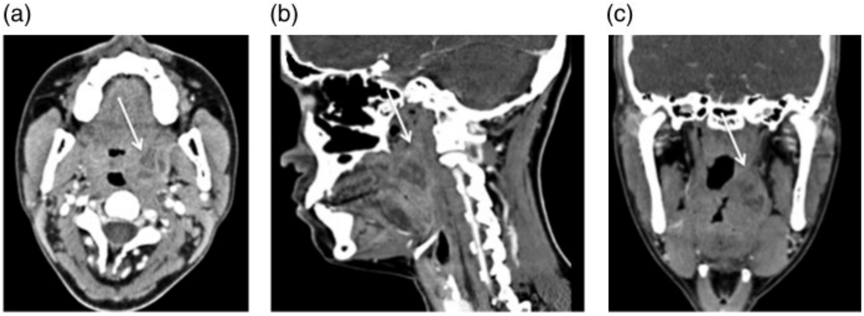

Figure 13.26 Tonsillar abscess. (a) Axial CT of the neck following intravenous contrast injection in the soft-tissue window at the level of the oropharynx. There is a multiseptated peripherally enhancing fluid collection in the left tonsillar/peritonsillar fossa (shown by long white arrows). There is slight narrowing of the oropharyngeal airway. (b) Sagittal reformat and (c) coronal reformat, both demonstrating the vertical extent of the abscess.

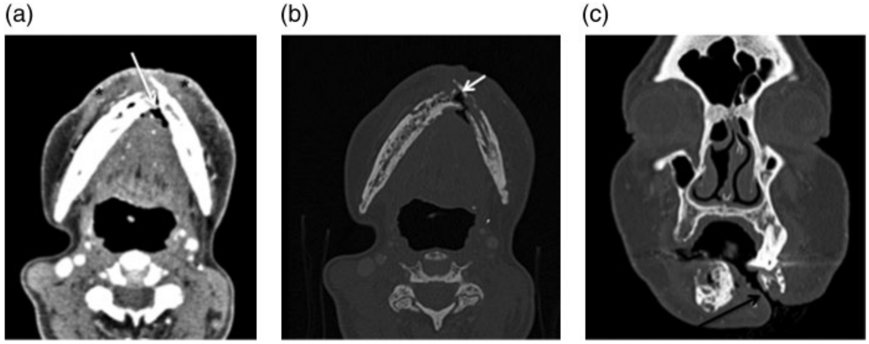

Figure 13.27 Osteonecrosis. (a) Axial CT of the neck following intravenous contrast injection at the level of the mandible in the soft-tissue window, (b) Bone window and (c) coronal reformat in the bone window. There is a destructive erosive process with fragmentation involving the mandible. There are small air bubbles in the bone marrow (shown by long white arrow) and pathological fracture (shown by short white arrow). There is mild diffuse soft tissue thickening and enhancement in the overlying mucosa (shown by black *). There is a fistulous tract in the left parasymphyseal region (shown by long black arrow). This patient had a tongue squamous cell carcinoma treated with radiotherapy. The destructive bony process is osteoradionecrosis with potential superimposed acute osteomyelitis.

be imaged on CT or MRI but MRI is the most sensitive modality. Ultrasound is useful as it will guide for potential biopsy. CT is useful if an obstructing stone in the ducts of the parotids, submandibular, sublingual glands is suspected. The inflammation could be related to viral or autoimmune conditions and usually bilateral and symmetric. In the acute stages, the glands will show enlargement and diffuse heterogeneous increased enhancement on the CT images. In chronic stages, the glands will shrink in size and will demonstrate decreased enhancement.

13.5 PET and SPECT Neuroimaging

Over the last three decades, radionuclide imaging with PET and SPECT has contributed to our understanding of the brain chemical and physiological processes in health, their alteration with aging, and their disruption in neurological and psychiatric disorders. The first steps in mapping brain function with radionuclide techniques were taken in the 1970s when Lassen and his colleagues demonstrated focal increases in the brain cortical blood flow (rCBF) in response to mental and motor tasks [5]. Mapping of the brain function to specific cortical regions originated with the postmortem work of Paul Broca in 1861 and was vividly demonstrated by direct electrical stimulation of the cortex of awake surgical patients by the neurosurgeon Wilder Penfield. Lassen offered a noninvasive method to extend our knowledge of the brain functional anatomy. His technique used an array of radiation detectors that recorded the gamma photons from the cerebral cortex following injection of the gamma emitter xenon-133 in a saline solution. While his team was carrying out their historical experiments, a new three-dimensional radionuclide imaging technique using molecules labeled with short-lived positron emitters was being perfected. This new technique, positron emission tomography (PET; see Chapter 3), allowed extension of Lassen's method to regions deep within the brain. PET initially used water radiolabeled with the short-lived positron emitter oxygen-15 ($H_2{}^{15}O$) as the blood flow radiotracer. The two-minute half-life of oxygen-15 allows the acquisition of several perfusion scans in one PET imaging session where the brain response to a mental, sensory, or motor tasks is compared to a baseline condition. These studies are known as *brain activation* studies because the brain regions that respond to these tasks become metabolically more active and need more oxygen and glucose resulting in increased blood flow and metabolism to those parts of the brain. While these activation studies provided a powerful tool to investigate brain function, they were hindered by the need to have a cyclotron on site to produce the oxygen-15 (see Chapter 4) and by the radiation dose to the subjects. Today, activation studies are performed with MRI using blood oxygenation level dependent (BOLD) contrast imaging, which do not have the constraints of a cyclotron and radiation dose (see Chapter 5).

Another breakthrough in radionuclide imaging of the brain occurred in 1978 when Tatsuo Ido and Al Wolf at the Brookhaven National Laboratory successfully synthesized the metabolic radiotracer [fluorine-18]fluorodeoxyglucose, ^{18}F-FDG (see Chapter 4). This radiotracer allowed the transfer of Sokolov's autoradiographic metabolic studies, with the beta emitter [carbon-14]-2-deoxy-D-glucose (^{14}C-2DG), to noninvasive metabolic studies of the living human brain. Since activation of a brain region not only increases blood flow but also the rate of glucose consumption to meet the additional energy needs of these brain cells, ^{18}F-FDG offers another way to probe the brain response to external stimuli either physiological or pharmacological. Furthermore, in neurodegenerative diseases such as dementia or Alzheimer's Disease, the destruction of brain cells reduces the metabolic needs of the affected brain regions resulting in lower uptake of ^{18}F-FDG. PET studies have revealed patterns of reduced ^{18}F-FDG update that are specific to certain disorders allowing the radiologist to distinguish among clinical entities with similar symptoms such as Alzheimer's Disease and dementia.

The assessment of altered regional metabolism is a very useful tool to gain a better understanding of brain disorders but it does not provide information about the underlying neurochemical alterations responsible for altered ^{18}F-FDG uptake. The latter information can only be obtained with chemical probes that target specific neurochemical or physiological processes. Dopamine became the early target of PET neurochemical studies because of its central role in schizophrenia, addiction, and Parkinson's Disease. Postmortem studies had suggested that the density of dopamine receptors might be elevated in schizophrenia. However, the PET studies were inconclusive likely due to confounding factors in the postmortem studies, such as prior drug treatment, and by major differences in the biological behavior of the dopamine radiotracers. While the hope of finding of diagnostic biomarker for schizophrenia faded, the dopamine radiotracers developed for PET imaging of the brain helped to demonstrate that patients suffering from psychosis have a hypersensitive dopamine system that is more susceptible to the dopamine-releasing effects of stress and of illicit drugs [6]. In addition, it provided new insights on the mechanism of antipsychotic drugs that target primarily the dopamine receptor. *Occupancy studies* measure the binding of a radiotracer to a receptor or enzyme before and after administering a drug that targets the same site (Figures 13.28 and 13.29). A dose occupancy curve can be constructed using a range of administered doses for the drug. With antipsychotics, an optimal therapeutic window was identified for the drug dose. Doses below that window were generally not clinically effective while doses above it were associated with more frequent serious extrapyramidal symptoms (such as muscle spasms and jerky movements). The findings also indicated that a low dose of antipsychotic was enough to achieve the desired receptor occupancy and led to new guidelines for the

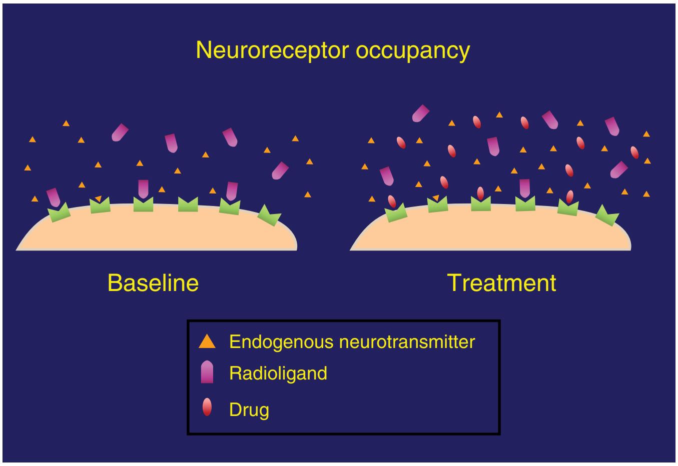

Figure 13.28 Neuroreceptor occupancy. A baseline scan is obtained where the radiotracer occupies the receptor sites that are not occupied by the endogenous neurotransmitter. When a therapeutic drug is administered, it occupies some of the receptor sites. If the scan is repeated during treatment, there are now less free receptor sites to which the radioligand can bind. By measuring the difference in the number of occupied sites by the radioligand, the percent occupancy of the receptor sites by the drug can be determined.

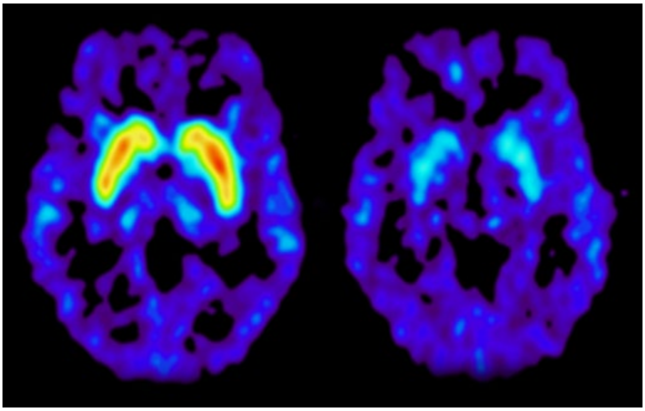

Figure 13.29 Occupancy of dopamine D2 receptors by an antipsychotic drug measured with ^{11}C-raclopride. The scan on the left is before treatment and the one on the right during treatment. The bright area in the center of the brain is the striatum where there are high densities of the dopamine D2 receptors. (*See insert for color representation of the figure.*)

treatment of patients experiencing a first episode of psychosis. Subsequent research with second-generation antipsychotic suggested that only intermittent dopamine receptor blockade might be necessary for an effective response [6]. Current work is underway to determine if alteration in dosage is required in the elderly population.

Parkinson's Disease is characterized by severe dopaminergic dysfunction and different aspects of its neurochemical pathology can be explored with ligands specific to subcomponents of the dopaminergic synapse: dopamine turnover with 6-^{18}F-fluoro-levodopa; the dopamine transporter with a variety of PET and SPECT radiotracers; the vesicular monoamine transporter type 2 (VMAT2) with ^{11}C-DTBZ; and the striatal postsynaptic dopamine D2 receptors with ^{11}C-raclopride and the extrastriatal receptors with higher affinity ligands such as ^{11}C-FLB-457 [7]. Radionuclide imaging has a limited role in the diagnostic workup of individuals suspected of Parkinson's Disease but had a major impact in studying the progression of the disease, evaluating various therapies aimed at compensating for the loss of dopamine production and investigating the cognitive and behavioral complications of the disease including dementia, pathological gambling, and other compulsive behaviors.

Dopamine is also the major component of the brain reward system. Disruption of the brain circuits associated with reward and impulsivity lead to drug addiction and related behaviors [8]. PET has been used to elucidate both short- and long-term neurochemical changes induced by drug of abuse, alcohol and nicotine, understand what triggers an addictive behavior, and devise novel therapeutic interventions targeted to specific addictions.

The main neurochemical dysfunction in affection disorders, such as depression, is the loss of intrasynaptic monoamines. Imaging studies have shown that particular symptoms of depression and their intensity are associated with disruption of the serotonin (mood symptoms) or dopamine system (motor symptoms). The most commonly prescribed antidepressant medications are selective serotonin reuptake inhibitors (SSRIs) that prevent the reuptake of synaptic serotonin by the dopamine transporter, thus raising extracellular serotonin. The effective dose of SSRIs had been established through large clinical trials involving escalating the administered SSRI dose until clinical improvement were observed. However, the relative occupancy of the transporter site by the drugs had never been determined. A PET radioligand, ^{11}C-DASB, was developed to measure the serotonin transporter occupancy by SSRIs. Studies with this radiotracer revealed that several different SSRIs all had an occupancy of 80% at their respective clinically effective dose even though they had markedly different affinities for the serotonin transporter [9]. This important result provided a target occupancy for new SSRIs that can be evaluated first with PET to determine what dose should be used for subsequent clinical trials or not be pursued any further because adequate occupancy could not be achieved. Because a receptor occupancy vs. dose can be rapidly determined in a small group of subjects, occupancy studies have become an important tool in the development of new drugs.

The early research in radiotracers for brain imaging was mainly directed to the transporter and various components of the dopamine and serotonin neurotransmitter because of their importance in schizophrenia, depression, and addiction. More recently, radionuclide imaging of the brain has targeted other neurochemical systems: other receptors, enzymes, various types of proteins involved in pathological processes, and intracellular signaling systems. Imaging microglial activation in neuroinflammation and quantifying the abnormal accumulation of β-amyloid and tau proteins in neurodegenerative disease such as Alzheimer's Disease have been the focus of intense PET research.

The formation of extracellular β-amyloid plaques in the brain has been one of two pathological hallmarks, Alzheimer's Disease. Most current therapeutic approaches attempt to stop and reduce the formation of these plaques and PET amyloid has been widely used to assess the efficacy of these treatments (see Chapter 15, Figure 15.6). Alzheimer's other major pathological hallmark is the formation of intracellular neurofibrillary tangles (NFT) made up of abnormally modified tau proteins. The current thinking is that these abnormal tau proteins are in fact more relevant to the pathology of Alzheimer's Disease and that their distribution patterns in the brain might help differentiate between different neurodegenerative diseases.

The definition of the psychiatric disorders is based almost entirely on clinical observation rather than on the underlying brain neurochemical and physiological processes. Consequently, it is not surprising that radionuclide imaging has not been useful as a diagnostic tool for psychiatry. Rather, PET imaging has contributed to identify specific brain dysfunctions such as increased levels of monoamine oxidase A (MAO-A) in postpartum depression, variation in levels of the serotonin transporter binding in seasonal affective disorders, and neuroinflammation in depression. These findings can potentially lead to new treatments. It can also explain how non-pharmacological treatments, such as cognitive behavioral therapy and transcranial magnetic stimulation (TMS), actually alter brain processes.

In theory, radiolabeled molecules could target any of the hundreds of different chemicals present in the brain. In practice, only a much smaller subset of these molecules can be labeled with a positron emitter for PET or single photon gamma emitter for SPECT (see Chapter 3). Their molecular structure might not be suitable for radiolabeling, a radiosynthetic path might not exist, the radiotracer may not cross the blood brain barrier, or the brain uptake might be too slow to allow imaging before the radiolabel decays. In some instances, magnetic resonance spectroscopy (MRS) provides an alternate method to quantify those molecules unsuitable for radionuclide imaging (see Chapter 5).

Genetic variations can alter how psychiatric disorders manifest themselves. PET neuroimaging studies are now routinely combined with a genetic profile of the genes associated with the disorder being investigated [10] in order to correlate clinical findings, imaging, and genetic findings. Furthermore, genetic polymorphism exists in some of the radiotracer brain targets. In some instances, the polymorphism affects the binding of the radioligand resulting in individuals that exhibit high binding and others low binding that prevent imaging of the target.

13.6 Summary

After completing this chapter, the reader should be able to understand the appropriate imaging modality for common neurologic conditions and be able to better understand the radiologic reports. Over the last three decades, PET and SPECT imaging of the brain have provided scientists and clinicians with increasingly sophisticated methods to unravel the neurochemical and physiological processes of psychiatric, addiction, and neurodegenerative disorders with the hope of identifying individuals at risk and discovering new therapeutic approaches.

References

1 Osborn, A. (2016). *Diagnostic Imaging: Brain*, 3e. Salt Lake City, UT: Amirsys.
2 Nadgir, R. and Yousem, D. (2016). *The Requisites: Neuroradiology*, 4e. Philadelphia, PA: Elsevier.

3 Som, P.M. and Curtin, H.D. (2011). *Head and Neck Imaging*, 5e. St Louis: Mosby.

4 Harnsberger, R. (2016). *Diagnostic Imaging: Head and Neck*, 2e. Salt Lake City, UT: Amirsys.

5 Lassen, N.A., Ingvar, D.H., and Skinhøj, E. (1978). Brain function and blood flow. *Sci. Am.* 239: 62–71.

6 Zipursky, R.B., Meyer, J.H., and Verhoeff, N.P. (2007). PET and SPECT imaging in psychiatric disorders. *Can. J. Psychiatry* 52: 146–157.

7 Stoessl, A.J., Lehericy, S., and Strafella, A.P. (2014). Imaging insights into basal ganglia function, Parkinson's disease, and dystonia. *Lancet* 384: 532–544.

8 Parvaz, M.A., Alia-Klein, N., Woicik, P.A., and Volkow, N.D. (2011). Goldstein RZ neuroimaging for drug addiction and related behaviors. *Rev. Neurosci.* 22: 609–624.

9 Meyer, J.H., Wilson, A.A., Sagrati, S. et al. (2004). Serotonin transporter occupancy of five selective serotonin reuptake inhibitors at different doses: an ^{11}C-DASB positron emission tomography study. *Am. J. Psychiatry* 161: 826–835.

10 Bigos, K.L., Hariri, A.R., and Weinberger, D.R. (eds.) (2016). *Neuroimaging Genetics: Principles and Practices*. New York: Oxford University Press.

Dr. Rakesh Mohankumar

Dr. Rakesh Mohankumar is an Assistant Professor of Medical Imaging at the University of Toronto. He is a Staff Musculoskeletal Radiologist at the Toronto Joint Department of Medical Imaging (Sinai Health System, University Health Network and Women's College Hospital). He undertook his Radiology residency in Manchester, UK and completed a fellowship in Musculoskeletal Imaging at the University of Toronto. His clinical expertise includes all facets of Musculoskeletal Imaging as well as ultrasound and intervention. His main fields of research include imaging of bone and soft-tissue sarcomas, comparative effectiveness, functional imaging, and biomarkers.

Dr. Ali Naraghi

Dr. Ali Naraghi is a staff radiologist in the Division of Musculoskeletal Radiology at the Toronto Joint Department of Medical Imaging at the University Health Network, Mount Sinai Hospital and Women's College Hospitals at the University of Toronto. He received his medical degree from the University of London, UK and undertook his residency at St. Bartholomew's Hospital, London. He completed his fellowship training in musculoskeletal radiology at the University of Toronto. Dr. Naraghi is an Assistant Professor at the University of Toronto. His academic interests include advanced imaging of inflammatory arthritis, imaging of peripheral nerves, and imaging of sports injuries.

Medical Imaging for Health Professionals: Technologies and Clinical Applications, First Edition.
Edited by Raymond M. Reilly.
© 2019 John Wiley & Sons, Inc. Published 2019 by John Wiley & Sons, Inc.

14

Musculoskeletal Imaging

Rakesh Mohankumar and Ali Naraghi

14.1 Introduction

Musculoskeletal imaging has advanced leaps and bounds from the time Roentgen utilized X-rays to obtain a plain radiograph in 1895. While plain radiographs still play a very important role in musculoskeletal imaging, technological innovations and utilization of other imaging modalities such as computed tomography (CT), magnetic resonance imaging (MRI), and ultrasound (US) have made multimodality imaging an integral part of the diagnostic pathway. In this chapter, the modalities commonly used in musculoskeletal imaging, including plain radiographs (X-rays), CT, MRI, and US will be outlined. The applications of the above modalities in the diagnosis and management of traumatic injuries, infection, arthritis, and tumors will also be discussed.

14.2 Plain Radiography (X-rays)

Despite the advances in imaging modalities and technology, plain radiographs still play an important role in the diagnosis and management of musculoskeletal disorders. For the vast majority of indications, plain radiographs are still the initial imaging modality. This is true particularly in the imaging of trauma. Plain radiography is the most economical of all imaging modalities. It is widely available and reproducible. Although plain radiography is excellent at assessment of bones and joints, it provides limited assessment of the soft tissues. There is also radiation exposure associated with plain radiography. While radiographic imaging of the extremities is only associated with a low radiation dose, radiographs of the axial skeleton and pelvis can result in higher radiation exposure, particularly to sensitive organs. Plain radiography is a two-dimensional depiction of

Medical Imaging for Health Professionals: Technologies and Clinical Applications, First Edition.
Edited by Raymond M. Reilly.
© 2019 John Wiley & Sons, Inc. Published 2019 by John Wiley & Sons, Inc.

three-dimensional structures and as such, evaluation of complex areas such as the foot, pelvis, and spine can be suboptimal. At these sites, further imaging may be necessary to assess for occult pathologies or to further evaluate abnormalities identified on plain radiography.

At least two orthogonal views are obtained in order to allow better detection and characterization of abnormalities (Figure 14.1). At certain sites additional views are commonly acquired to better evaluate the complex three-dimensional structures. These include the wrist, elbow, ankle, and foot. This is particularly true in the case of trauma, where pathology can be missed on a single projection. Standing radiographs are of value in assessment of arthritis of the weight-bearing joints, particularly, the knee, ankle, and foot. This will provide a better assessment of the degree of joint space loss, compared to non-weight-bearing views. Similarly, stress views may help elicit findings that may be absent on neutral or standard views. This is true in the case of a suspected scapholunate ligament injury (ligament between the scaphoid and lunate bones of the wrist) (Figure 14.2). Plain radiographs can be negative in neutral (relaxed) position,

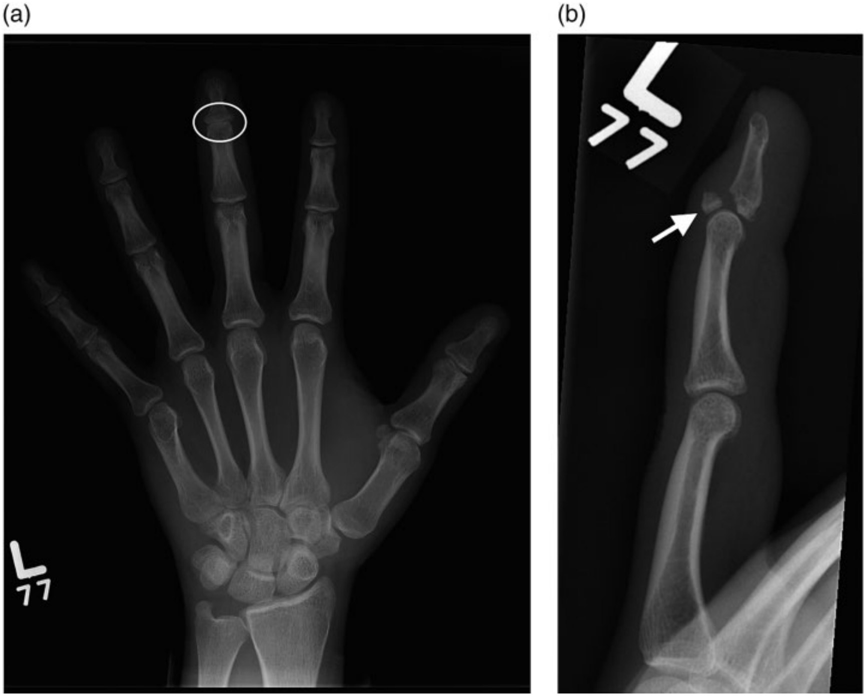

Figure 14.1 Importance of orthogonal views. Lateral view of the finger (b) demonstrates a fracture involving the distal phalanx (mallet fracture, arrow), which cannot be clearly identified (circle) in the frontal projection (a).

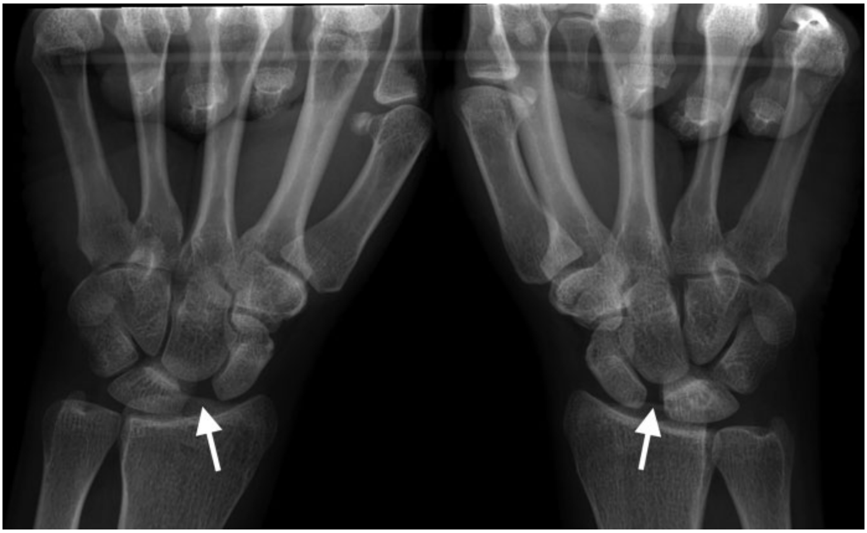

Figure 14.2 Stress radiographs of the wrist performed with the patient gripping on pencils between their fingers. This accentuates the widening of the distance between the scaphoid and lunate (arrows) in comparison with the distances between the other carpal bones in keeping with scapholunate ligament injury.

however, the widening of the joint space can be apparent in stress views, by asking the patient to clench their fist or grab a pencil in the palm of their hand. Similarly, assessment of acromioclavicular joint instability (joint between the acromion and the clavicle at the shoulder) can be assessed with the patient holding a weight in their hand, which can accentuate the instability. In the spine, segmental motion between vertebral bodies can be assessed with flexion and extension views, which is useful in assessment of alignment instability of the vertebrae. Plain radiography is the mainstay of imaging in trauma to confirm a clinical diagnosis of a fracture or dislocation. In addition, the pattern of injury identified on plain radiographs can help assist the clinician with determining a management plan. The role of plain radiographs in trauma will be further discussed in the subsequent section on trauma.

While assessment of soft tissues is limited with plain radiographs, valuable information can be obtained by evaluation of soft tissues. The presence of soft-tissue swelling adjacent to the site of injury may be secondary to a hematoma or an underlying fracture and highlight the area of injury. Joint effusions can be confirmed or excluded in joints such as the elbow, knee, and ankle, which can be a useful ancillary finding in the setting of trauma and internal derangement of joints. This is particularly true in the elbow joint (Figure 14.3), where radial head fractures are often radiographically

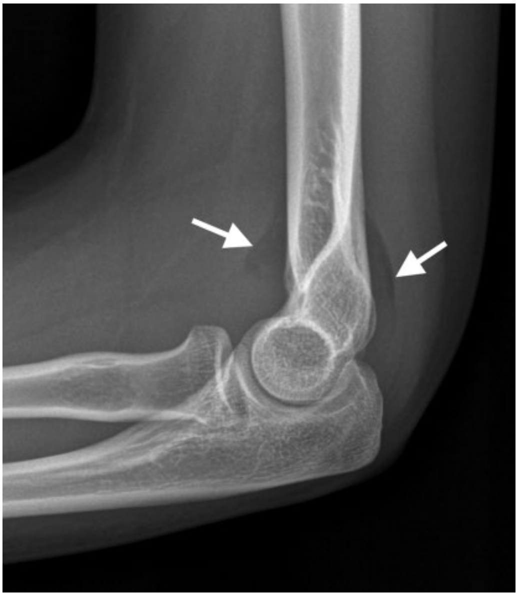

Figure 14.3 Elbow joint effusion demonstrated by elevation of the anterior and posterior fat pads (arrows) is highly suggestive of an intra-articular fracture, in the context of trauma.

occult on the initial radiographs. However, the presence of a joint effusion as demonstrated by elevation of anterior and posterior fat pads provides a high index of suspicion for an underlying fracture. In addition, soft-tissue ulcers and soft-tissue gas can be seen in infection. Radio-opaque foreign bodies are best evaluated with plain radiographs in the first instance. Assessment of soft-tissue mineralization is also useful in conditions like scleroderma, myositis ossificans (mineralization within muscles following trauma), and soft-tissue neoplasms.

Plain radiographs are also the mainstay in assessment of orthopedic hardware as metal-related artifacts are less of an issue than with CT and MRI. As such, plain radiographs are used for assessment of arthroplasties, fractures managed with open reduction and internal fixation or external fixation, and spinal surgery. Complications such as hardware fracture and loosening can be evaluated with plain radiographs but select cases may require further cross-sectional evaluation. Moreover, due to the lack of soft-tissue visualization, adjacent soft-tissue pathology such as abscesses may require CT or MRI assessment. Imaging of metal is also used for exclusion of metal debris in the orbits of the eyes prior to MRI. According to the American College of Radiology (ACR), all patients who have a history of orbit trauma with a potential ferromagnetic foreign body for which they sought medical attention should have their orbits cleared with radiographs.

14.3 Computed Tomography

With the advent of MRI, the utilization of CT in musculoskeletal imaging has declined. This is particularly true in the case of soft-tissue pathology. Despite this, CT is still a valuable tool in the diagnosis of musculoskeletal pathologies, particularly those affecting osseous structures. CT demonstrates exquisite bony detail. CT is complimentary and is often the second-line investigation for assessment of complex or intra-articular fractures. This will include fractures around the shoulder, elbow, wrist, and the spine. In the lower limb, acetabular (hip) fractures and their configuration is best evaluated by CT as the complex anatomy and overlapping structures provide less adequate visualization with plain radiographs. Complex intra-articular knee and ankle fractures can also be assessed with CT (Figure 14.4). These will provide better information regarding the fracture pattern and can act as a surgical roadmap for the clinician. Of particular importance are mid-foot fractures, particularly around the bases of the long bones of the foot (metatarsals). The small fractures between the bases of the metatarsals and the small bones of the foot (tarsometatarsal joints) are often not readily visible on plain radiographs but are indicative of a severe injury (Lisfranc fracture/dislocation). CT is also useful for assessment of nontraumatic pathologies like arthritis. Arthritis of the complex joints of the hind foot and mid foot, where there are many overlapping structures, is better assessed with CT than plain radiographs. Soft-tissue assessment with CT is inferior to the excellent soft-tissue visualization possible with US and MRI.

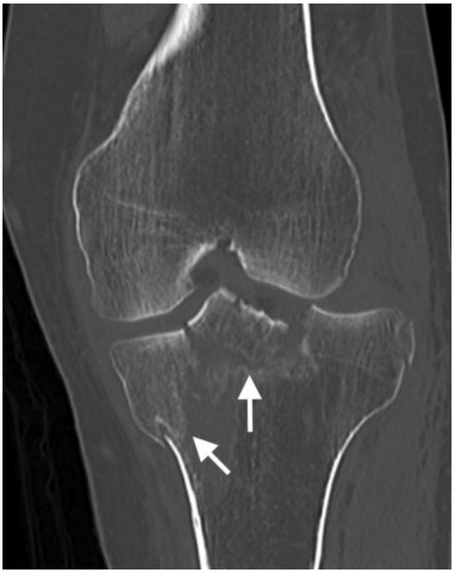

Figure 14.4 Coronal images from a knee CT demonstrate fractures of the tibial plateau (arrows) as well as the degree of a step at the articular surface of the tibial plateau.

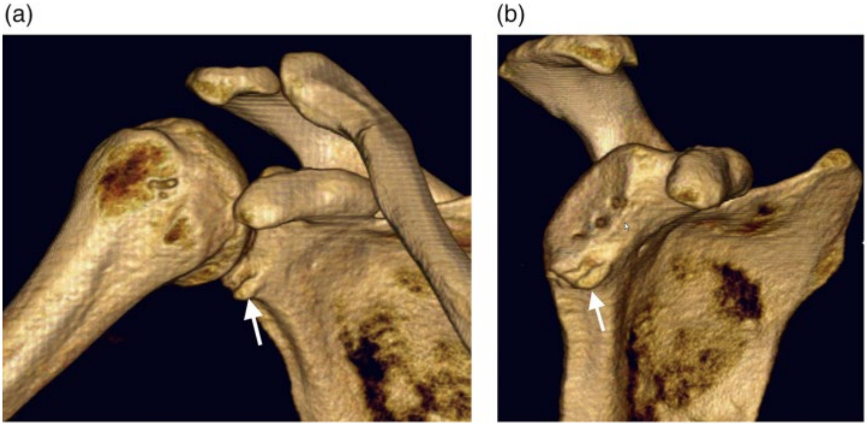

Figure 14.5 Three-dimensional reconstructions from a CT scan of the shoulder (a), and with humeral head digitally removed (b) in a patient with history of recurrent dislocation and prior stabilization surgery demonstrates a fracture of the anteroinferior glenoid (bony Bankart) (arrow).

However, characterization of soft-tissue mineralization can be performed with CT, in certain situations. These include assessment of myositis ossificans or synovial osteochondromatosis (numerous mineralized bodies within joints).

Recent advances in multi-planar reconstruction have enabled surgeons to best visualize bony detail in three dimensions, around complex joints. Image subtraction can be performed around joints to exclude overlapping osseous structures and give a better view of the abnormality (Figure 14.5). This is useful in assessment of Bankart fractures in the shoulder (fracture of the glenoid often associated with anterior dislocation of the shoulder) and assessment of the shape of the femur at the hip joint, which may predispose to arthritis. Evaluation and assessment of complications of orthopedic hardware such as malpositioning, hardware fracture, and loosening is readily available with CT and can be further optimized with special image reconstruction techniques.

One of the technological advances in CT, in the last decade, has been the advent of dual-energy CT. Simultaneous image acquisition is performed by the scanner, using two different energy X-ray beams (e.g. 80 and 140 kVp). Due to the physical properties of different materials and tissues within the body, the X-ray absorption of various tissues is different for the two energy beams. Post-processing and reconstruction algorithms can create images to account for the different materials, and hence can be used to identify pathology that could not be visualized with a single-energy source CT. Increasing numbers of applications have been introduced in musculoskeletal imaging using dual-energy CT. Assessment of gouty deposits using dual-energy CT has gained popularity in recent years. It is also useful in confirming soft-tissue masses as gouty tophi in

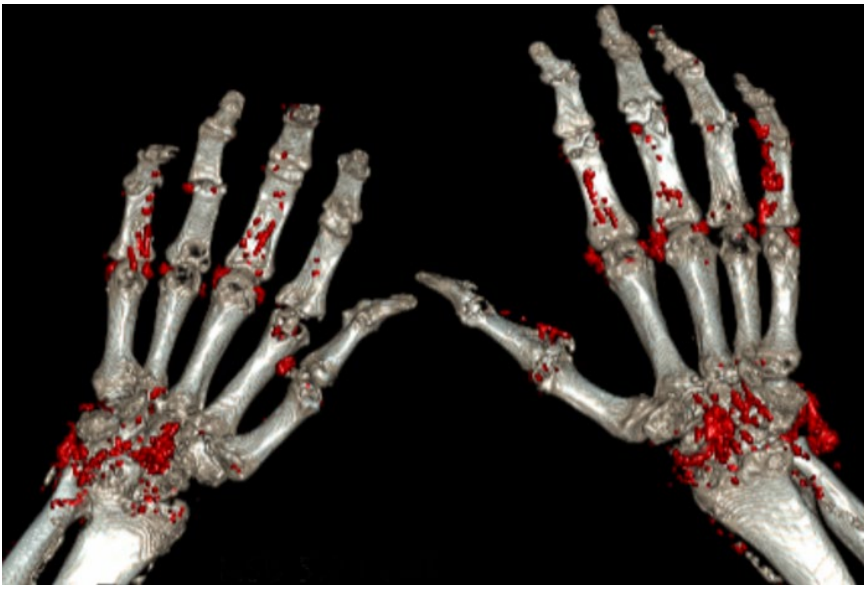

Figure 14.6 Three-dimensional reconstruction from a dual energy CT (DECT) in a patient with gouty arthropathy. The red colors represent deposits of monosodium urate crystals adjacent to the joints of the hands and wrists detected by DECT based on the differences in the physical properties of the different tissues. (*See insert for color representation of the figure.*)

suspected cases, without the need for a biopsy (Figure 14.6). Other utilities of dual-energy CT include assessment of bone marrow edema in trauma, which was only possible previously with MRI, and improving visualization around orthopedic metal hardware.

One has to be aware of the radiation implications associated with CT. A plain radiograph is almost always necessary prior to CT, and often information obtained from plain radiographs may negate the need for a CT scan. If the primary area of concern is within the soft tissues, an US or MRI may be considered. In case of patients who have frequent CT scans (CT abdomen and pelvis, for example), one should enquire if the musculoskeletal question can be answered from the most recent CT. Similar to US, CT can be used in guiding aspiration, injection, or biopsies. CT can be used for biopsy of bone lesions to assess for primary or metastatic bone lesions (Figure 14.7). Soft-tissue masses not accessible by US can also be biopsied by using CT guidance. Though fluoroscopy (real-time moving X-ray image) is routinely used for injection or aspiration of joints, CT can be used in difficult situations due to multiplanar imaging capability.

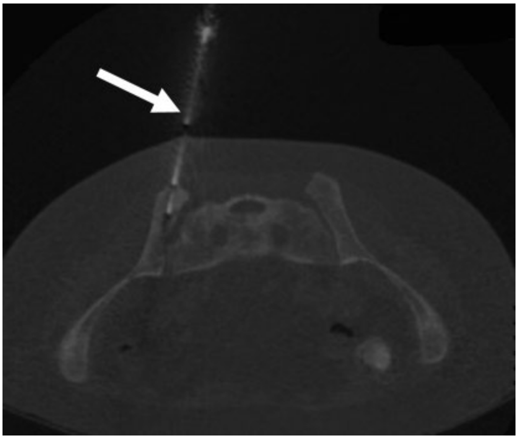

Figure 14.7 Image capture from a CT biopsy demonstrating a bone biopsy needle (arrow) in position within the posterior ilium to biopsy the abnormal bone marrow.

14.4 Magnetic Resonance Imaging

MRI is one of the more commonly used imaging modalities in musculoskeletal imaging, second only to plain radiography, owing to its excellent soft-tissue evaluation, multiplanar capabilities, and the lack of ionizing radiation. MRI is most commonly employed for imaging of joints, and the knee is the most commonly imaged joint. The high specificity and sensitivity of MRI in the diagnosis of meniscal and cruciate ligament tears makes it a valuable tool for assessment of post-traumatic knees (Figure 14.8). MRI is also the most accurate noninvasive means of assessing articular cartilage. In addition, MRI is also unparalleled in assessment of bone marrow. Assessment of bone marrow pathologies such as post-traumatic contusion, marrow edema, pathologic marrow infiltration, avascular necrosis, and osteomyelitis are best evaluated with MRI. Similar to the knee, assessment of the shoulder is very commonly obtained with MRI. MRI is useful for assessment of the rotator cuff, labrum (rim of fibrocartilage around the edge of the glenoid, which deepens the glenoid and stabilizes the shoulder joint), and articular cartilage (Figure 14.9). MRI arthrography, a technique in which intra-articular contrast (gadolinium) is injected and MR images are acquired subsequently, improves visualization of the labrum and articular cartilage in cases of shoulder instability but is semi-invasive. MRI of the elbow is performed for assessment of osteochondral injuries and collateral ligament and tendon injuries. MRI of the wrist and hand can be performed for assessment of ligamentous injuries or to exclude radiographically occult fractures. MRI of the hip is performed for assessment of the labrum and articular cartilage, as well as evaluation of the muscles and tendons around the hip joint. MRI of the foot and ankle is useful for assessment of osteochondral injuries, tendons, and ligaments, as well as assessment of arthropathy.

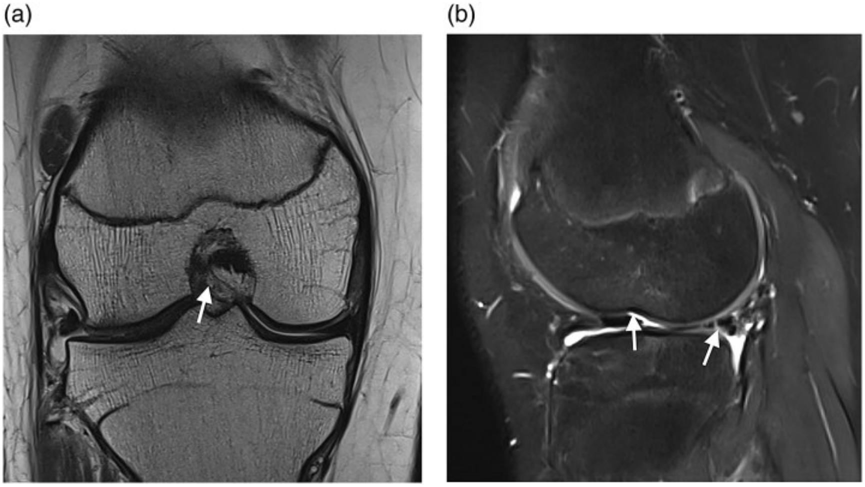

Figure 14.8 Coronal MRI image (a) demonstrates a complete anterior cruciate ligament (ACL) tear with non-visualization of ACL at its expected location (arrow). Sagittal T2 fat-suppressed MRI (b) demonstrates associated complex tear (arrows) of lateral meniscus and focal traumatic depression of the femur.

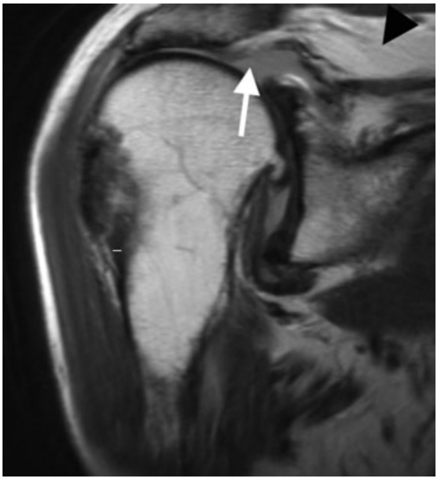

Figure 14.9 MRI of the shoulder demonstrates a complete tear of the rotator cuff (supraspinatus) tendon, which has retracted (arrow). The muscle fibers are atrophic and fatty due to the chronic nature of this injury (black arrowhead).

In addition to joints, due to the excellent soft-tissue resolution, MRI is useful for assessment of muscles and tendons. Muscle injuries can be accurately diagnosed and quantified with MRI (Figure 14.10). MRI can also be used for diagnosis and localization of myopathies and to identify an appropriate site for muscle biopsy. Bone and soft-tissue mass assessment is best performed with

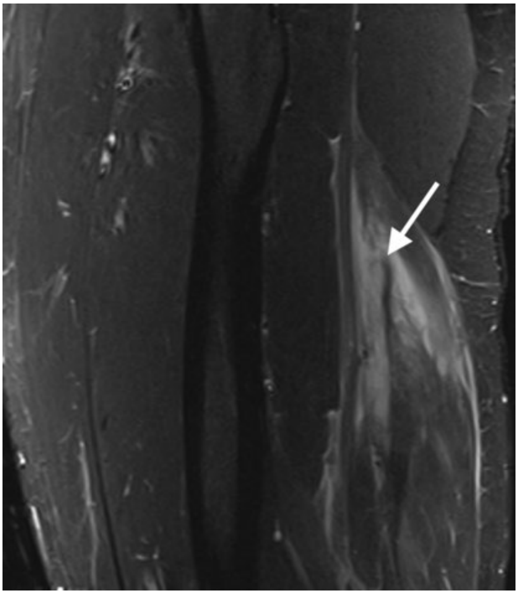

Figure 14.10 Sagittal T2 fat-suppressed MRI of the thigh demonstrates edema and tendon discontinuity within the biceps femoris muscle belly (arrow), in keeping with a high-grade tear.

MRI. MRI appearances can provide accurate diagnosis of many soft-tissue masses like lipoma, hemangioma, hematoma, fibromatosis, and cystic lesions like ganglion cysts (fluid outpouchings from joints). Local staging of bone and soft-tissue masses are best performed with MRI. This information is a valuable tool for the surgeon in management of musculoskeletal tumors. Furthermore, MRI is valuable in posttreatment follow-up and can identify recurrence before it is manifested clinically.

Implanted orthopedic hardware such as arthroplasties, plates and screws, or intramedullary rods are not a contraindication for MRI but can result in artifacts obscuring adjacent anatomy. New metal artifact reduction radiofrequency sequences (see Chapter 5) are useful to reduce artifacts from metal around hardware. This has been used to image around arthroplasty, extremity, and spinal instrumentation.

14.5 Ultrasound

US has been a prominent modality for investigation of musculoskeletal pathologies, and has been increasing in utilization over the years. Recent reports suggest over 300% increase in the use of musculoskeletal US in the last decade. US

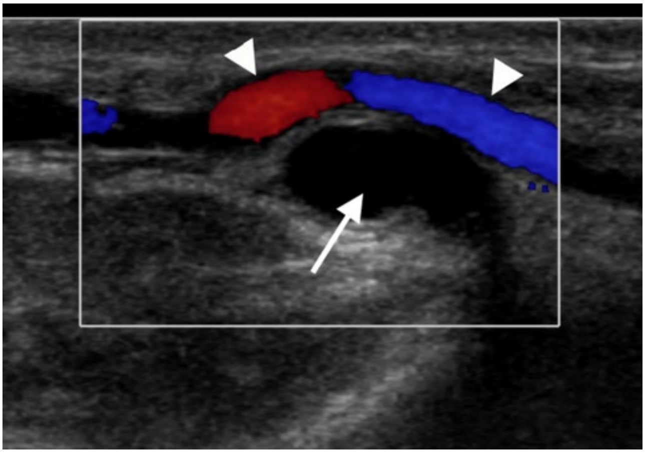

Figure 14.11 Static Doppler ultrasound image of a mass at the wrist demonstrates a well-defined anechoic (no internal echos) mass (arrow) next to the radial artery (arrowheads), with no vascular flow within it. This appearance is consistent with a ganglion cyst, an outpouching of fluid from the joint. (*See insert for color representation of the figure.*)

has many advantages over MRI or CT in assessment of soft tissues. There are no contraindications to US, there is no patient apprehension concerning claustrophobia, and there is no ionizing radiation. US can be safely used to image patients with pacemakers and other implantable devices. Metal-related artifacts with CT and MRI can be problematic despite image optimization techniques and US is an excellent alternative for soft-tissue assessment around such implants. The spatial resolution of US is superior to that of standard MRI techniques for evaluation of soft tissues. Using the standard high-frequency probes used in musculoskeletal US (7–10 MHz), a resolution of 0.5 mm can be achieved (Figure 14.11). This is useful for assessment of smaller structures like nerves and finger tendons. Soft-tissue calcification can be detected on US before being evident on radiography or MRI.

US is also useful in dynamic assessment of tendons, ligaments, and joints. For example, assessment of subacromial impingement (catching of the rotator cuff tendons under the acromion on elevation of the arm) can be performed under US with direct visualization of the rotator cuff impingement, while this is not possible with MRI. Other instances of utility of dynamic assessment with US includes ankle tendon subluxation (tendons moving away from their normal anatomical position), ulnar nerve dislocation at the elbow, iliotibial band friction syndrome (iliotibial band rubbing against the distal femur on flexion and extension of the knee) at the knee, and assessment of tendon integrity where partial thickness tears are clinically suspected. Patient interaction is a great advantage of US examination. The patient can direct you to the site of symptoms like pain or clicking. Comparison of an identified pathology with the contralateral side can also be readily performed.

Doppler US (see Chapter 6) is of value in assessment of inflammatory changes at the site of pathology. It can be used to assess for active inflammatory change in synovitis in patients with inflammatory arthropathy. This can be used for serial examinations to assess for response to treatment. Assessment of active inflammatory change in tendons can be useful to the clinician to direct appropriate management. Doppler US can also be used to evaluate vascularity of soft-tissue masses. US also allows for real-time guidance during diagnostic and therapeutic interventions. Joint and bursal injections can be performed with greater accuracy compared to blind technique. Aspiration and injection of cysts, ganglia, abscesses, and joint effusions can be performed with US as can soft-tissue biopsies.

The shoulder is one of the most commonly imaged joints with US. US is an excellent tool for assessment of rotator cuff tendons. According to the Society of Radiologists in Ultrasound, US should be the primary imaging modality for suspected rotator cuff disease. An MRI is only recommended as a problem-solving tool for equivocal cases, or if additional labral or articular pathology is suspected. Collateral ligaments of the elbow can be assessed with US. US offers the advantage of dynamically assessing the collateral ligaments, particularly the ulnar collateral ligament, to diagnose ligament laxity (abnormal stretching of ligaments in case of incomplete tears). Joint effusion and synovitis at the elbow joint can also be assessed with US. US of the knee is a common requisition seen in clinical practice. Like the hip, the knee is a large joint, and US is only useful for assessment of peripheral structures. US is excellent for assessment of quadriceps and patellar tendon pathologies, and for assessment of the medial and lateral collateral ligaments. Only the peripheral margins of the menisci are visualized with US, and while peripheral tears can be visualized on US, a comprehensive assessment of the menisci is best performed with MRI. Cruciate ligaments cannot be reliably assessed with US. The ankle ligaments and tendons can be visualized with US and assessment of ligamentous laxity can be performed dynamically. Assessment of joints of the hands and wrist and feet can be performed for diagnosis and follow-up.

14.6 Applications of Musculoskeletal Imaging

14.6.1 Trauma

Imaging plays a vital role in assessment of musculoskeletal trauma. Imaging is essential for the diagnosis and management of the majority of musculoskeletal injuries. Injuries to the musculoskeletal system can range from trivial to life threatening. The choice of imaging modality depends on the type of injury, clinical diagnosis as well as availability of the imaging modality. Clinicians also need to consider the emergent, urgent, or elective imaging following trauma. Plain radiographs are often the initial and only imaging modality necessary for diagnosis of trauma. In addition to identification of a fracture, plain radiographs provide important information regarding the plane of fracture, the degree of bone fragmentation (comminution), the degree and direction of displacement, and involvement of the articular surface. CT and MRI are useful in assessment of soft tissues, and CT is widely used as a second-line investigation in musculoskeletal trauma as outlined above. MRI is useful for assessment of internal derangement of joints, assessment of stress fractures, muscle, and tendon injuries. US is also a useful modality in the setting of trauma, particularly for diagnosis of muscle and tendon injuries.

With regard to the upper extremity, shoulder dislocations can be visualized on antero-posterior (AP) and/or lateral view of the shoulder joint (Figure 14.12). However, an axial or modified axial (Velpeau) view may be necessary in certain cases to exclude a dislocation. CT scan is a useful adjunct in assessment of complex upper limb fractures. Occult fractures of the wrist and hand (scaphoid, distal radius) can be readily identifiable with CT (Figure 14.13). MRI has a higher sensitivity than radiographs and even CT for occult fractures. This can often be beneficial from a patient management point of view, but should be balanced with the availability and cost of MRI at the institution. Ganglion cysts, tendon tears, and collateral ligament injuries can be assessed with US. MRI is also useful for assessment of above, as well as intrinsic ligament injuries of the hand and wrist.

Occult fractures of the hip require cross-sectional imaging. While CT is most readily available, recent guidelines from UK (NICE) and USA (ACR) suggest MRI as the imaging modality for diagnosis of occult hip fractures. The majority of patients with a clinical question of occult hip fracture are elderly and osteoporotic, and false-negative CTs can be encountered with non-displaced fractures. MRI with visualization of bone marrow edema secondary to a fracture is highly sensitive and specific for diagnosis of occult fractures (Figure 14.14). Following trauma, US is predominantly used for evaluation of suspected isolated muscle and tendon injuries such as Achilles tendon tears and calf muscle injuries. It is of limited value following traumatic joint injuries. MRI is excellent in assessment of internal derangement of joint, and can assess ligament, cartilage, and fibrocartilaginous injuries such as tears of the meniscus at the knee and the fibrocartilaginous labrum at the hip and shoulder tears.

In summary, plain radiographs are most often the initial modality of imaging in musculoskeletal trauma. CT is useful for diagnosis of occult fractures and for characterization of complex fractures. MRI is invaluable for assessment of soft-tissue pathology, including internal joint derangement, muscle and tendon injuries, and also for diagnosis of occult fractures not identified by other modalities.

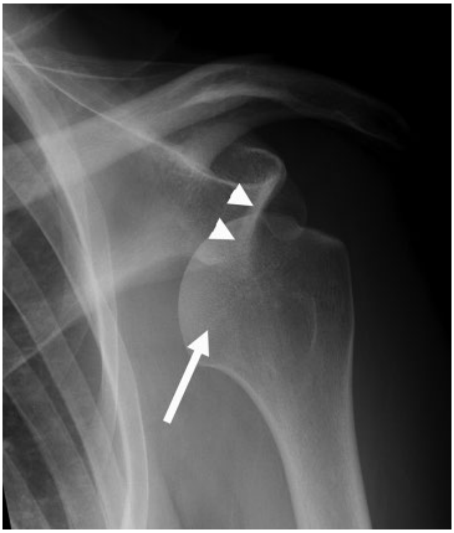

Figure 14.12 Antero-posterior (AP) view of the left shoulder obtained following trauma demonstrates an anterior and inferior dislocation of the humeral head (arrow), which is superimposed onto the inferior glenoid (arrowheads).

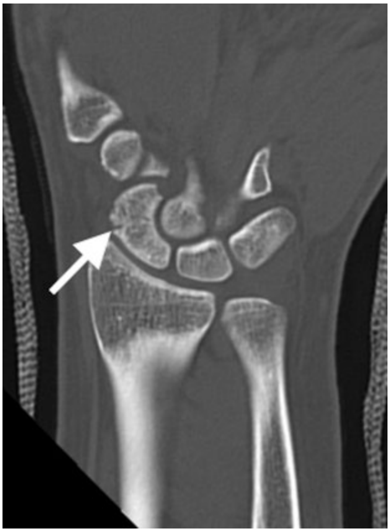

Figure 14.13 Coronal reformatted CT image of the wrist demonstrates a transverse lucency (darker area) of the waist of the scaphoid (arrow), in keeping with a fracture.

14.6.2 Infection

Imaging plays a crucial role in diagnosis and management of musculoskeletal infections. Often the clinical picture is unclear and imaging is essential to provide a diagnosis, assess the extent of bone, joint and soft-tissue involvement, and to localize abnormalities, which require diagnostic or therapeutic intervention. Cellulitis is often a clinical diagnosis and further imaging is not

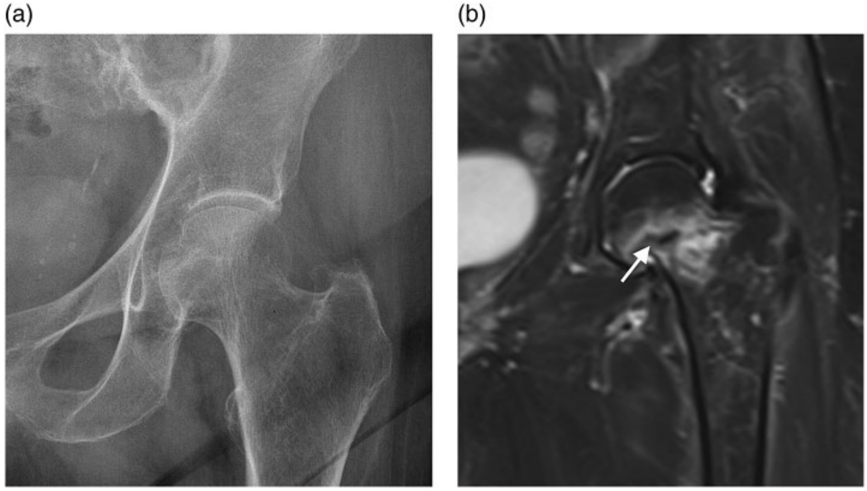

Figure 14.14 Antero-posterior (AP) radiograph of the left hip (a) following trauma shows no evidence of a fracture. Coronal T2-weighted fat-suppressed MRI of the hip (b) obtained due to inability to bear weight shows edema of the left femoral neck and associated low signal fracture line (arrow), in keeping with a non-displaced fracture.

essential for management. However, imaging can be considered to rule out an underlying soft-tissue abscess, or if clinical features suggest underlying osteomyelitis or septic arthritis. US is excellent for evaluation of soft tissues to assess for hematomas or abscesses. Aspiration or drainage of collections can also be performed using US guidance. Assessment of deeper collections may require cross-sectional imaging. While CT can be used to identify the presence of intramuscular and deep collections, MRI is excellent at quantifying the extent of a collection as well as involvement of the adjacent structures. Evaluation of soft tissues for gas in plain radiographs and CT is very important to exclude infection with a gas-forming organism.

Radiographs can demonstrate the characteristic findings of acute osteomyelitis. These include periosteal reaction, bony erosion and bone loss, and localized demineralization (Figure 14.15). More advanced cases can demonstrate a bone abscess (Brodie's abscess), and chronic cases can demonstrate sclerosis and cortical thickening. However, plain radiographs can appear normal in the early stage of acute osteomyelitis. Plain radiographs can also underestimate the extent of the osteomyelitis. CT can also be negative in early cases of osteomyelitis. MRI and bone scans are the most sensitive modalities for evaluation of osteomyelitis (Figure 14.16). MRI can demonstrate marrow and cortical edema before plain radiographic and CT findings becoming evident. In addition, adjacent ulceration, soft-tissue inflammatory changes, sinus tracts, and abscesses can be identified (Figure 14.17). Depending on availability, if plain radiographs

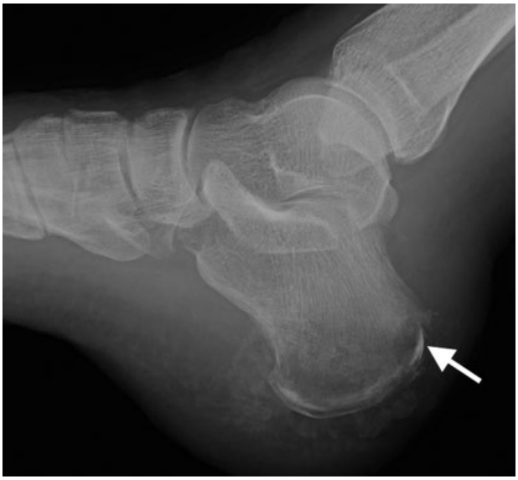

Figure 14.15 Lateral radiograph of the foot demonstrating cortical destruction of the posterior calcaneum (arrow) with an overlying ulcer in a diabetic patient, consistent with osteomyelitis.

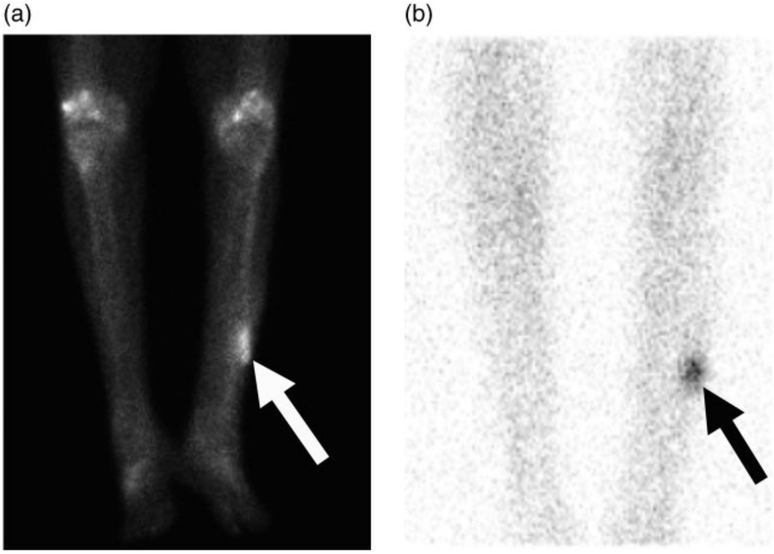

Figure 14.16 Anterior view of technetium-99m delayed bone scan of the lower legs (a) shows an area of increased uptake within the left tibia (arrow). Anterior view of indium-111 labeled white blood cell scan (b) also shows increased uptake in the same region (arrow) consistent with osteomyelitis.

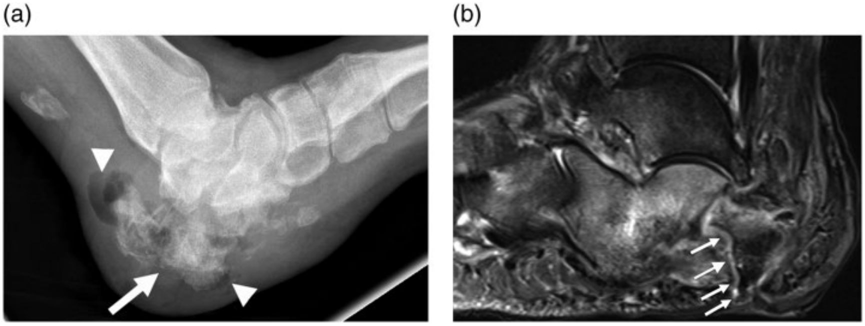

Figure 14.17 Radiograph (a) of the calcaneum demonstrates bone loss and bony destruction (arrow), with soft-tissue gas (arrowheads) consistent with osteomyelitis. Sagittal T2-weighted MRI (b) demonstrates a sinus tract extending into a pathological fracture of the calcaneum (arrows). There is extensive high signal bone marrow edema throughout the calcaneus in this patient with osteomyelitis.

are negative or equivocal in a patient with osteomyelitis and if further imaging is indicated clinically, MRI is often the modality of choice. Conversely, if there are findings of acute osteomyelitis on plain radiographs, further imaging with CT or MRI is not necessary for diagnosis. In certain clinical situations, cross-sectional imaging can be performed, in order to assist the surgeon with the extent of osteomyelitis for preoperative planning and to monitor treatment.

Plain radiographs are not sensitive in assessment of septic arthritis. US can be performed to assess for joint effusion. While the absence of a joint effusion has a high negative predictive value for septic arthritis, the presence of a joint effusion does not add value. Joint effusion can be seen in inflammatory and traumatic conditions or may be reactive in nature. MRI can provide more information on synovitis and adjacent soft tissue and bone marrow inflammatory changes in septic arthritis, but these findings can overlap with inflammatory arthropathies. If septic arthritis is clinically questioned, a joint aspiration should be performed for diagnosis. This can be performed under US or fluoroscopic guidance.

14.6.3 Arthritis

Peripheral arthritis is one of the most common musculoskeletal conditions and has been identified as the leading cause of disability in the United States. With an increase in life expectancy, arthritis poses a huge financial burden on society due to costs associated with health-care interventions as well as loss in productivity and employment. Arthritis can be broadly divided into inflammatory, depositional, and noninflammatory arthritis. Inflammatory arthritis consists of conditions such as rheumatoid arthritis, juvenile idiopathic arthritis

(JIA), septic arthritis, and seronegative arthritis consisting of psoriatic arthritis, ankylosing spondylitis, and reactive arthritis. Depositional and crystal-induced arthritis include gout and calcium pyrophosphate depositional disease (CPDD) and amyloid arthropathy. Noninflammatory arthritis consists of primary osteoarthritis, with no identifiable cause, or secondary osteoarthritis secondary to a preexisting abnormality such as prior trauma, an underlying inflammatory arthritis, avascular necrosis, or developmental dysplasia of the hip. Inflammatory joint pain is classically associated with pain, which is worse after rest or in the morning, morning stiffness, and pain at night whereas noninflammatory arthritis is often worse at the end of the day and after use. The hallmark of the inflammatory arthritis is the presence of synovitis, which, if unchecked, can produce destructive changes at the involved joints.

The distribution of the joint involvement can provide clues to the type of arthritis. Primary osteoarthritis primarily affects the proximal (PIP) and distal (DIP) interphalangeal joints of the hand, the scaphotrapeziotrapezoidal (STT), and first carpometacarpal joints as well as the hips and knees. Rheumatoid arthritis typically has a bilateral symmetrical distribution affecting the metacarpophalangeal (MCP), metatarsophalangeal (MTP), PIP joints, and the wrists. In chronic cases medium and large joint involvement may also be encountered. Ankylosing spondylitis primarily affects the spine and sacroiliac joints and large joints such as the hips. Psoriatic arthritis can have a variable distribution. It may primarily involve the DIP joints. It may have a distribution similar to rheumatoid arthritis or may present with an asymmetric arthritis, which may affect a single digit. It may result in a destructive form of arthritis known as arthritis mutilans or may predominantly involve the spine and sacroiliac joints similar to that seen in ankylosing spondylitis. Psoriatic arthritis and ankylosing spondylitis, due to their predilection for the axial skeleton, are often referred to as axial spondyloarthropathies. CPPD typically affects the wrists, second and third MCP joints, and the knees while gout often presents with an asymmetric arthropathy with predilection for the first MTPs, the wrists, and carpometacarpal and tarsometatarsal joints. Septic arthritis typically presents with an acute monoarthritis often accompanied by systemic symptoms.

The role of imaging in assessment of arthritis has evolved with improvements in medical and surgical management of patients. Imaging, together with clinical and laboratory features, is used to diagnose the type of arthritis, assess the degree of joint damage, evaluate the presence of active disease, gauge treatment response, and predict prognosis. Radiographs have been the mainstay of imaging evaluation of patients with arthritis and remain an integral part of patient evaluation. Radiographs are useful for diagnosing the type of arthritis and, in particular, distinguishing between inflammatory and noninflammatory arthritis. In general, radiographic features of inflammatory arthritis include erosions, uniform joint space loss, soft-tissue swelling, and in some cases periarticular osteopenia. However, there is some variability in the radiographic

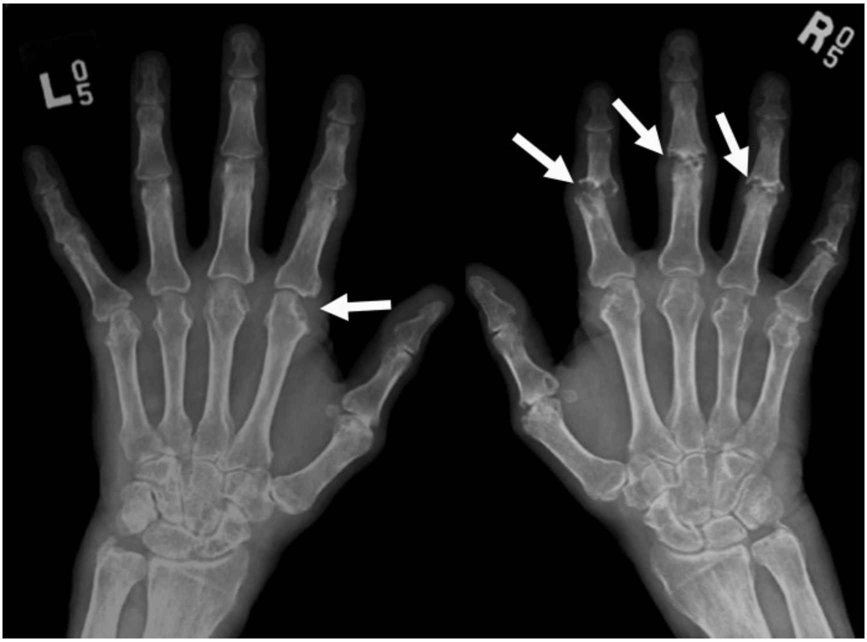

Figure 14.18 Bilateral hand radiographs in a patient with rheumatoid arthritis demonstrating erosive changes of the metacarpophalangeal (MCP) and proximal interphalangeal joints (PIP) joints (arrows).

appearances of the different types of inflammatory arthritis. In contrast noninflammatory arthritis demonstrate non-uniform joint space loss, sclerosis of the subchondral bone, osteophyte (bone spur) formation, subchondral cysts, and a lack of periarticular osteopenia (loss of bone density around the affected joints) and erosions. The earliest radiographic manifestations of rheumatoid arthritis are soft-tissue swelling and periarticular osteopenia. Soft-tissue swelling is best appreciated adjacent to the distal ulna at the wrist and at the MCP and PIP joints of the hand. Earliest sites of erosive disease include the ulnar styloids, the radial aspect of the second and third MCP joints and the lateral aspects of the fifth metatarsal heads (Figure 14.18). With more chronic disease joint space loss may be evident. In late-stage disease, bony ankylosis may be seen at the wrists.

Psoriatic arthritis affecting the peripheral joints may also produce erosions similar to those seen in rheumatoid arthritis but affecting the DIP joints far more commonly than in rheumatoid arthritis. In contrast to rheumatoid arthritis, periarticular bone density is preserved until late in the disease process. Additionally, periosteal new bone formation may be visualized particularly adjacent to areas of erosive disease, at the radial and ulnar styloids, and at

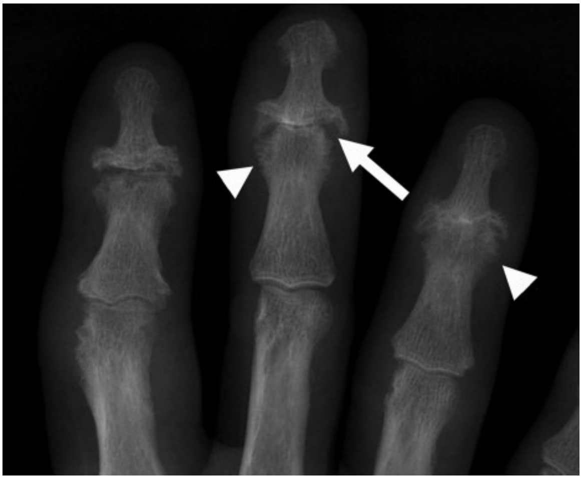

Figure 14.19 Radiograph of the distal interphalangeal joints (DIP) in a patient with psoriatic arthritis demonstrating erosive change (arrow) with adjacent proliferative new bone formation (arrowheads).

the carpal bones (Figure 14.19). Ankylosis in psoriatic arthritis may affect any of the joints in the hands and feet. New bone formation may also be evident at tendon and ligamentous insertions (enthesitis).

Ankylosing spondylitis most commonly involves the spine and sacroiliac joints. Radiographic features of ankylosing spondylitis include squaring of vertebral bodies (areas of new bone formation resulting in loss of concavity to the anterior wall of vertebral bodies), erosions and sclerosis at the corners of vertebral bodies (Romanus lesions), syndesmophyte formation (ossification along the outer fibers of the of the intervertebral discs), ossification of the ligaments between the spinous processes of the vertebrae (dagger sign), and ankylosis across the facet joints, costovertebral (articulation between the posterior ribs and vertebrae) joints, and across the disc spaces (Figure 14.20). Sacroiliac joint involvement is manifested by subchondral sclerosis (increased density of bone immediately adjacent to joint), erosive disease and eventually ankylosis. Similar sacroiliac joint involvement may be seen in psoriatic arthritis, reactive arthritis, and arthritis associated with inflammatory bowel disease.

Erosive disease may also be seen in gout and septic arthritis. Radiographically, gout is distinguished from inflammatory arthritis by erosions with overhanging edges, joint spaces that are preserved until late in the disease process and calcified tophi. Radiographic features of gout are usually only evident after many years. Septic arthritis, on the other hand, tends to be characterized by rapidly destructive changes and often profound periarticular osteopenia.

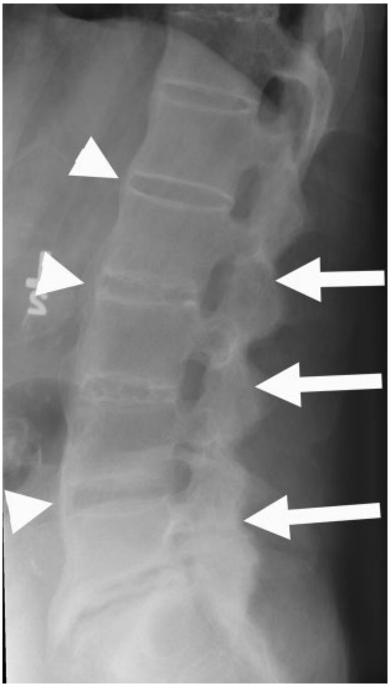

Figure 14.20 Lateral radiograph of the lumbar spine in a patient with ankylosing spondylitis demonstrating bridging bony spurs (syndesmophytes) (arrowheads) and fusion of the facet joints (arrows).

With the advent of newer disease modifying antirheumatic drugs (DMARDs) and biologic agents such as infliximab, etanercept, and adalimumab, there has been a paradigm shift in management of patients with inflammatory arthritis. There is strong evidence that significant joint damage occurs early in the course of RA and therefore modern treatment strategies in rheumatoid arthritis emphasize aggressive early treatment with disease-modifying agents to arrest inflammation and prevent radiographic progression, joint damage, and functional disability. This has led to the utilization of more advanced imaging methods for detection of early inflammatory arthritis and to assess treatment response (Figure 14.21).

Doppler US given its wide availability and excellent soft-tissue resolution has been increasingly used in evaluation of patients with inflammatory arthritis, particularly in those with involvement of small- and medium-sized joints. Gray scale US is able to evaluate the

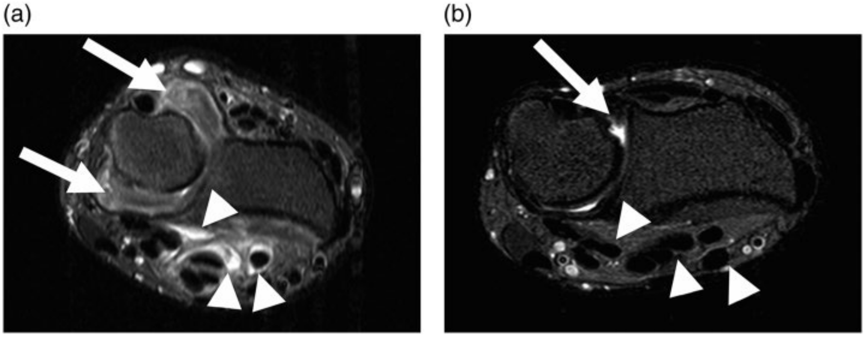

Figure 14.21 Axial T2-weighted fat-suppressed MR image through the distal radioulnar joint at the wrist (a) in a patient with rheumatoid arthritis shows marked distension of the joint capsule with synovitis (arrows). There is also high signal intensity (bright) fluid (arrowheads) surrounding the tendons along the palmar aspect of the wrist in keeping with inflammatory tendon changes and tenosynovitis. Axial T2-weighted fat-suppressed MR image in the same patient following one year of biologic treatment (b) shows resolution of the synovitis (arrow) and tenosynovitis (arrowheads).

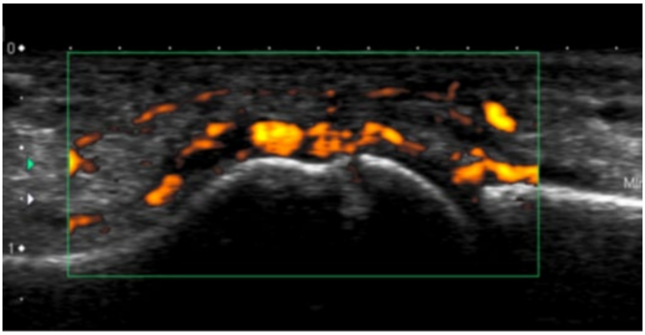

Figure 14.22 Longitudinal power Doppler US image of the metatarsophalangeal (MTP) joint in a patient with rheumatoid arthritis demonstrates extensive intra-articular and periarticular vascularity (red–yellow color) in keeping with active synovitis. (*See insert for color representation of the figure.*)

presence of synovial thickening and to distinguish this from joint effusions, a distinction that can pose challenges clinically. Effusions are characterized by anechoic (no echo) fluid, which is compressible, whereas synovitis is characterized by hypoechoic (low echo) tissue, which is only mildly compressible and may exhibit increased vascularity (Figure 14.22). In addition, US can distinguish between intra-articular inflammatory changes from those occurring in para-articular locations such as tendon sheaths. This can be important when considering systemic treatment as opposed to localized treatment with corticosteroid. Power Doppler US demonstrates greater sensitivity than clinical examination in detection of active synovitis and US has been used to demonstrate subclinical synovitis in patients judged to be in remission clinically. As such, US can be used to evaluate for synovitis at presentation before radiographic features of joint damage are evident and also to assess treatment response. Cases of active synovitis are characterized by increased vascularity within the synovium.

MRI has also been extensively studied in evaluation of patients with different forms of arthritis. MRI has the ability to comprehensively evaluate all components of a joint including the synovium, articular cartilage, subchondral bone, and ligamentous structures. Assessment of peripheral joints in patients with inflammatory arthritis demonstrates erosions before they are radiographically evident, shows active synovitis with gadolinium enhancement, which may not be clinically evident, and detects bone marrow edema (Figure 14.23). MRI may be used at presentation in inflammatory arthritis to confirm the diagnosis in equivocal cases, to assess the degree of inflammatory change, and to detect erosions. At follow-up, similar to US, MRI may be used to assess treatment response and detect subclinical synovitis, but, in addition, is more sensitive for progression of erosive disease in comparison with X-rays. MRI also has the added advantage of being able to evaluate the spine and sacroiliac joints

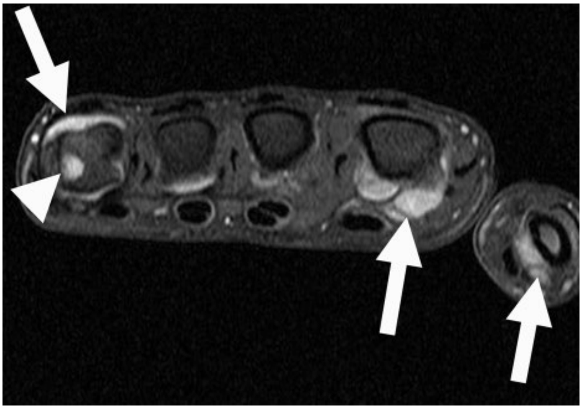

Figure 14.23 Axial T1-weighted fat-suppressed MRI of the hand following intravenous gadolinium demonstrates enhancing synovitis at multiple joints (arrows) as well as an erosion in the fifth metacarpal head (arrowhead).

for inflammatory changes in patients with axial spondyloarthropathies (inflammatory arthritis affecting the spine). Inflammatory changes in the spine are manifested by areas of osseous high T2 signal intensity on fat-suppressed fluid-sensitive images (Figure 14.24). These are commonly seen within the corners of the vertebral bodies, at the vertebral endplates, at the costovertebral junctions in the thoracic spine, and at sites of ligamentous attachments. In the

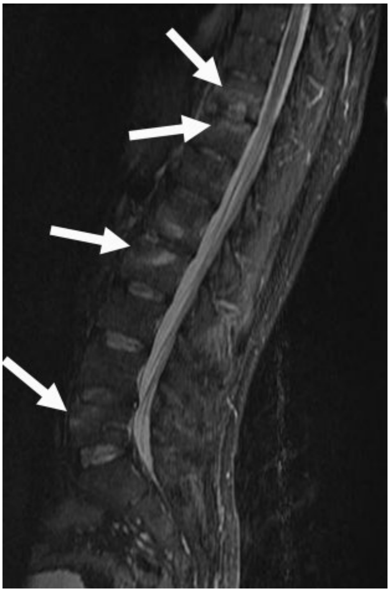

Figure 14.24 Sagittal T2-weighted fat-suppressed MRI of the lumbar spine in a patient with ankylosing spondylitis shows multiple areas of inflammatory change manifested as high signal intensity (arrows) at the corners of the vertebral bodies and at the vertebral endplates.

sacroiliac joints, inflammatory changes consist of subchondral bone marrow edema and erosions. However, it is important to bear in mind that endplate and sacroiliac joint bone marrow edema are not specific for inflammatory changes and may also be encountered with degenerative change.

MRI is also extensively used in evaluation of osteoarthritis in all joints. This is because MRI is the most accurate noninvasive method of directly visualizing the articular cartilage. Radiographs only allow for indirect assessment of cartilage loss by evaluating joint space loss. As such, discrepancies may arise due to a variety of factors such as radiographic technique, if weight-bearing views are not obtained or if the chondral loss is focal rather than diffuse. A variety of radiofrequency pulse sequences (see Chapter 5) have been used to directly visualize articular cartilage defects. Clinical pulse sequences for assessment of articular cartilage include intermediate and T2-weighted pulse sequences, as well as T1 spoiled gradient-recalled echo (SPGR), which shows better delineation of the articular cartilage. In addition, there are numerous pulse sequences used to assess various components of articular cartilage but these are predominantly used for research purposes. Another advantage of MRI in assessment of patients with osteoarthritis is direct visualization of meniscal or labral tears and ligamentous injuries, which may predispose to and result in progression of osteoarthritis.

14.6.4 Musculoskeletal Tumors

Musculoskeletal tumors comprise benign and malignant bone and soft-tissue tumors. It is important to bear in mind that of musculoskeletal tumors, benign lesions far outnumber malignant lesions. The majority of benign osseous lesions are encountered incidentally either on plain radiographs being performed for other reasons such as trauma and joint pain or on more advanced examinations such as CT and MRI of the chest, abdomen, or the spine. Soft-tissue tumors may also be encountered incidentally but are more commonly detected during investigation of a palpable mass. Overall, of the malignant osseous tumors, metastatic disease and multiple myeloma are the most common, particularly in the older population. In the younger population, primary malignant tumors and sarcoma represent a larger proportion of osseous tumors.

Imaging plays an important role in the detection, characterization, staging, and treatment monitoring of musculoskeletal tumors. The modalities used in investigation of musculoskeletal tumors vary depending on the origin of the tumor with regard to soft tissues, bone, and joints. Osseous tumors are often investigated initially by plain radiographs and depending on the radiographic features further characterization and staging may be undertaken by a combination of MRI, CT, and bone scans. Initial investigation of soft-tissue tumors is partly dependent on local availability of different modalities. Musculoskeletal US is often the initial modality used in many cases with CT and MRI used in select cases to further evaluate more complex or indeterminate lesions or for staging. For the remainder of this section we will review an approach to investigation of osseous and soft-tissue musculoskeletal tumors and the role of the different modalities.

Plain radiographs are usually the initial investigation in the majority of osseous tumors. As well as detection of osseous tumors, plain radiographs can be helpful in stratifying tumors as aggressive or nonaggressive. Radiographic features that are helpful in making this distinction include lesion margins and zone of transition (how sharply the lesion is marginated), the status of the overlying cortex, and periosteal reaction. Other features that are helpful in formulating a differential diagnosis include the age of the patient, multiplicity of lesions, location of the lesion within the bone, the tumor matrix, and osseous expansion. The age of the patient is a critical determinant of formulating a differential diagnosis. For instance, within the first two decades of life the most common primary malignant tumors of bone are osteosarcomas and Ewing sarcoma, whereas after the fifth decade, multiple myeloma and chondrosarcoma are the most common primary tumors.

Multiplicity of lesions is also helpful in narrowing the differential diagnosis. The differential diagnosis for multiple benign bone lesions includes enchondromas, osteochondromas, fibrous dysplasia, Langerhans cell histiocytosis, hemangiomas, Brown tumors in the setting of primary hyperparathyroidism, or renal bone disease and infection. Multiple malignant lesions are typically due to metastases, multiple myeloma, and lymphoma. The location of a lesion within the bone is also an important consideration in the differential diagnosis. The differential diagnosis for epiphyseal lesions includes subchondral cysts or ganglions, chondroblastoma (Figure 14.25), giant cell tumors, Langerhans cell histiocytosis, and infection. Diaphyseal lesions include Ewing sarcoma, myeloma, lymphoma, metastases, and fibrous dysplasia. Metaphyseal lesions include enchondromas, solitary bone cysts, aneurysmal bone cysts, chondromyxoid fibromas, non-ossifying fibroma, and chondrosarcomas. Many of the epiphyseal and diaphyseal lesions may also demonstrate metaphyseal (epiphysis: ends of long bones, diaphysis: middle of long bones, metaphysis: the part of bone between the epiphysis and diaphysis) involvement. The location of the lesions within the axial plane of the bone can also provide clues to the nature of the lesion. Most lesions such as enchondromas, fibrous dysplasia, simple bone cysts, osteosarcomas, Ewing sarcoma, and chondrosarcoma have their epicenter centrally within the medullary cavity. Eccentric lesions include aneurysmal bone cyst, giant cell tumor, enchondroma, chondromyxoid fibroma, and osteosarcoma. Subcortical or intracortical lesion location may be encountered with non-ossifying fibromas, osteoid osteoma, Brodie's abscess (abscess within bone secondary to osteomyelitis), and Brown tumors (lucent bone lesions seen in hyperparathyroidism), whereas a juxtacortical or surface location can be seen with juxtacortical chondroma or chondrosarcoma, parosteal osteosarcoma, aneurysmal bone cysts, and osteochondromas.

Figure 14.25 Coronal T2-weighted fat-suppressed MRI of the left shoulder in a patient with chondroblastoma shows an epiphyseal lesion (arrow) with surrounding bone marrow edema (arrowheads).

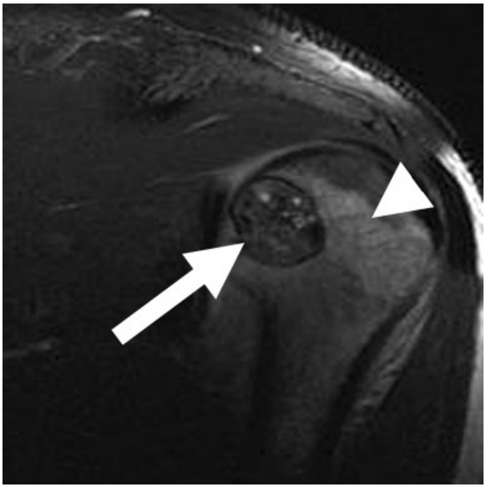

One of the most important radiographic features in determining the biological activity of an osseous lesion is the lesion margin (Figure 14.26). Well-defined geographic lesions with a thin sclerotic margin suggest a nonaggressive indolent lesion such as a simple bone cyst, chondroblastoma, chondromyxoid fibroma, non-ossifying fibroma, or fibrous dysplasia. Well-defined geographic lesions without surrounding sclerosis are also commonly benign in nature and include bone cysts, giant cell tumor, chondroblastoma, enchondroma, and fibrous dysplasia. However, metastases and multiple myeloma can also exhibit this radiographic pattern. Lesions with an ill-defined moth eaten or permeative border, whereby the lesions margin cannot be easily distinguished from adjacent normal bone, have a more aggressive biological activity and include Ewing sarcoma, osteosarcoma, chondrosarcoma, multiple myeloma, metastases, and acute osteomyelitis. Cortical erosions and destruction with extra-osseous soft-tissue extension is reflective of an aggressive lesion. Depending on the degree of osseous destruction, the transition zone and the relationship of the lesion to the X-ray beam, some osseous tumors may be occult on radiographs, requiring more advanced imaging methods for detection.

The periosteal reaction overlying a lesion can also be a clue to the biological activity of a lesion (Figure 14.27). Nonaggressive lesions may have a solid periosteal reaction, whereas discontinuous, interrupted, or speculated periosteal reactions resulting in a Codman triangle (interrupted elevated periosteal reaction at the edge of tumor), a laminated “onion skin” appearance, or a speculated “hair-on-end” or “sunburst” appearance often reflect aggressive biological behavior and may be seen with osteosarcoma, Ewing sarcoma, or osteomyelitis. Matrix mineralization on radiographs may be seen with osteoid or chondroid lesions. The presence of rings and arcs or stippled calcification is suggestive of a chondroid lesion including enchondroma, chondroblastoma,

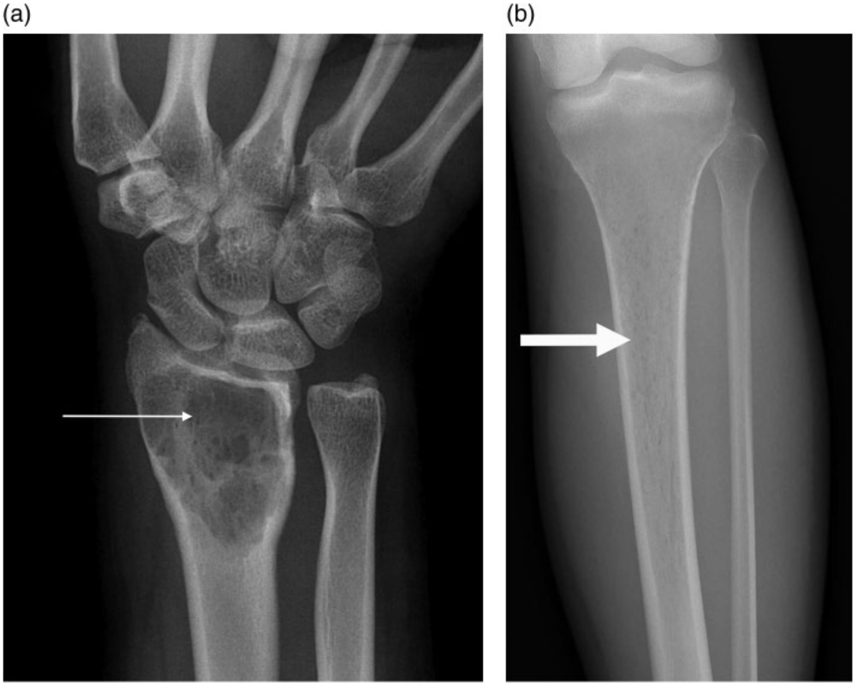

Figure 14.26 Wrist radiograph (a) in a patient with giant cell tumor of the distal radius shows a well-defined geographic lesion without a sclerotic margin adjacent to the wrist joint (arrow). Antero-posterior (AP) radiograph of the lower leg (b) in a patient with Ewing sarcoma shows a lesion without definable borders consistent with a permeative lytic lesion (arrow) in keeping with an aggressive lesion.

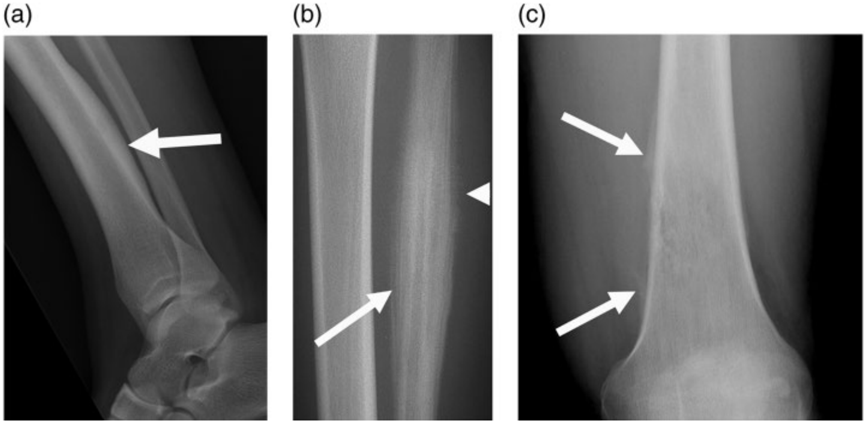

Figure 14.27 Different types of periosteal reaction. Lateral view of the ankle (a) demonstrates nonaggressive periosteal and cortical thickening of the tibia (arrow) in a patient with an osteoid osteoma. Antero-posterior (AP) view of the fibula (b) shows an aggressive periosteal reaction consisting of an "onion skin" appearance (arrow) and hair on end appearance (arrowhead). AP view of the knee (c) in a patient with osteosarcoma shows an interrupted periosteal reaction (Codman's triangle) (arrows).

chondromyxoid fibroma, or chondrosarcoma. Denser cloud like mineralization may be seen with osteoid lesions such as osteosarcoma.

MRI is useful for detection of radiographically occult lesions, lesion characterization, and staging. Radiofrequency pulse sequences routinely utilized for assessment of osseous tumors include T1 and fluid-sensitive fat-suppressed sequences. Gadolinium enhancement may be useful in selected cases. MRI is more sensitive than plain radiographs and CT for detection of musculoskeletal tumors. MRI features can also be useful for narrowing the differential diagnosis. A lesion with fluid signal intensity and no internal enhancement (lack of increased signal on T1-weighted images following gadolinium contrast administration) following gadolinium administration is in keeping a bone cyst. Multiple fluid–fluid levels within a lesion are seen with primary and secondary aneurysmal bone cysts. Lobulated intramedullary high T2 signal intensity lesions are suggestive of a chondroid lesion. Giant cell tumors, in comparison to many musculoskeletal neoplasms, have a relatively low T2 signal intensity. Lesions with high T1 signal intensity are suggestive of an intra-osseous lipoma or hemangioma. Lesions with pronounced surrounding edema and high T2 signal intensity (Figure 14.25) include osteoid osteoma, osteoblastoma, chondroblastoma, giant cell tumor, Langerhans cell histiocytosis, Brodie's abscess, or a pathological fracture. MRI is used in staging of osseous neoplasms. Features evaluated in staging of osseous tumors include intramedullary extent of tumor, cortical destruction and extra-osseous extension, intra-articular extension, and neurovascular involvement as demonstrated by loss of fat planes between the tumor and neurovascular structures on T1 images (Figure 14.28). CT may be used in addition to MRI for staging purposes to evaluate the status of the overlying cortex and the subchondral bone owing to the better spatial resolution of CT in comparison with MRI. Radionuclide bone scans are very sensitive for detection of osseous neoplasms but, in general, lack specificity. The advantage of bone scans over other imaging modalities includes the ability to image the whole skeleton. As such, radionuclide bone scans are used for detection of metastatic disease and detection of radiographically occult lesions (Figure 14.29).

Regarding soft-tissue tumors, the vast majority are benign in nature. The most common benign lesions are ganglia, lipomas, nodular fasciitis, neurogenic tumors such as schwannomas and neurofibromas, angiomatous lesions such as hemangiomas and vascular malformations, fibromatosis, and giant cell tumors of the tendon sheath. The most common malignant primary neoplasms of the soft tissues include undifferentiated pleomorphic sarcoma (previously referred to as malignant fibrous histiocytoma), liposarcoma, spindle cell sarcoma not otherwise specified, leiomyosarcoma, synovial sarcoma, and malignant peripheral nerve sheath tumor. The mainstay of imaging of soft-tissue tumors consists of MRI and US. In general, plain radiographs are not as helpful as in the setting of bone tumors. The presence of mineralization within a soft-tissue lesion on X-rays and CT can be helpful in narrowing the

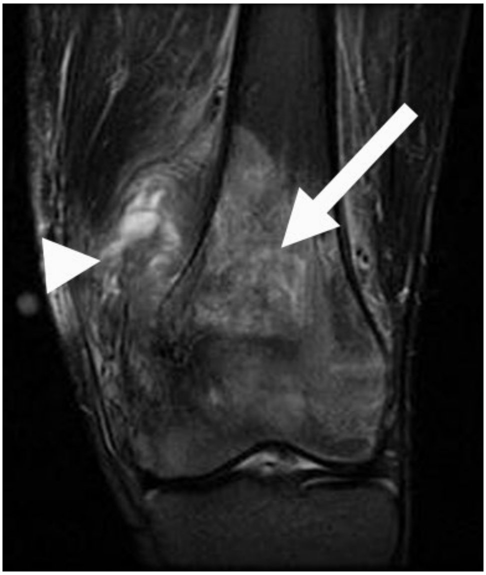

Figure 14.28 Coronal T2-weighted fat-suppressed MRI of the knee in a patient with osteosarcoma demonstrates extensive intramedullary disease (arrow) as well as an extra-osseous soft-tissue mass (arrowhead).

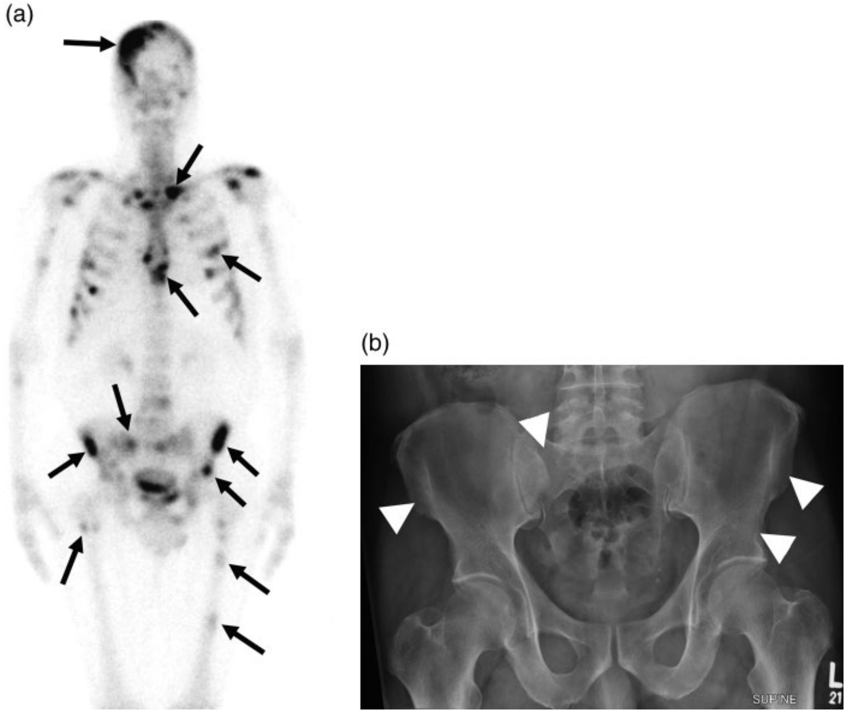

Figure 14.29 Delayed anterior view of technetium-99m bone scan (a) in a patient with lung cancer shows diffuse areas of uptake throughout the skeleton (some of which have been highlighted with arrows) consistent with widespread metastases. Antero-posterior (AP) radiograph of the pelvis (b) in the same patient following the bone scan shows no definite abnormality in the corresponding areas (some highlighted with arrows), i.e. radiographically occult lesions.

differential diagnosis. The presence of ring-like calcification may reflect phleboliths (small ring-like calcifications within vascular channels), which may be encountered in vascular lesions such as vascular malformations. Calcification can also be encountered in malignant lesions such as synovial sarcoma. Amorphous calcification or ossification may be seen with soft-tissue osteosarcomas. These typically demonstrate central mineralization with ill-defined margins and a peripheral unossified soft-tissue component. This is in contrast to myositis ossificans, a post-traumatic lesion that can be mistaken for a soft-tissue osteosarcoma. Myositis ossificans in contrast to osteosarcoma demonstrates more mature bone peripherally within the lesion with more immature mineralization centrally. This zonal pattern is best appreciated on CT. Calcification may also be evident in tumor-like masses such as gout.

Other than detection and characterization of soft-tissue mineralization, CT is otherwise of relatively limited utility. In the absence of access to MRI or when a contraindication to MRI exists, CT may be used to assess lesion location, size, and proximity to neurovascular structures. CT is an excellent modality, however, to better define the degree of cortical bone involvement in cases where the mass abuts and invades adjacent osseous structures. US is an excellent modality in distinguishing cystic from solid lesions. Cystic lesions such as ganglia and bursae are classically anechoic (no echo) with posterior acoustic enhancement and a lack of flow on power Doppler (Figure 14.11). Complex cystic lesions may exhibit some internal echogenicity but power Doppler often remains negative in the absence of inflammatory change or infection. US can also be used to assess lesion vascularity and compressibility, features that may be helpful in assessment of vascular malformations and hemangiomas.

MRI is the modality of choice in assessment of soft-tissue tumors for the purposes of lesion characterization and staging. As opposed to bone tumors, whereby lesion margin reflects biological behavior, many malignant soft-tissue neoplasms have a well-defined margin. There are no absolute indicators of a malignant soft-tissue neoplasm but a mass larger than 5 cm, a rapidly growing mass, a mass deep to the deep fascia, or one fixed to the fascia should raise concern for a malignant lesion. However, there is significant overlap between benign and malignant lesions with regard to some of these features. MRI characteristics of the mass can suggest help narrow the differential diagnosis. For instance, a subcutaneous lesion most commonly represents lipoma. Other benign subcutaneous lesions would include nodular fasciitis, skin appendage tumors, and angiomatous tumors, whereas malignant subcutaneous lesions include unspecified pleomorphic sarcoma and dermatofibrosarcoma protuberans (a skin-based soft-tissue sarcoma). Most malignant lesions tend to be intramuscular or intermuscular in nature, whereas intra-articular masses are rarely malignant. Lesion signal intensity on MRI can also be a helpful feature in lesion characterization. Benign and low-grade lipomatous neoplasms are of diffusely high T1 signal intensity and of low T2 signal intensity on T2

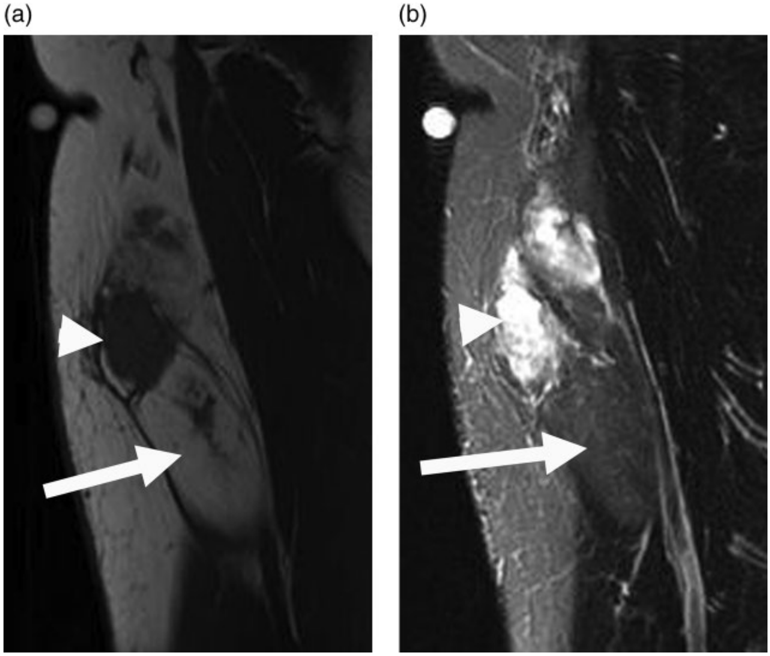

Figure 14.30 Sagittal T1 (a) and T2-weighted fat-suppressed MRI of the thigh (b) in a patient with dedifferentiated liposarcoma shows areas of high T1 and low T2 signal (arrows) consistent with a fatty tumor. However, there are areas that show low T1 and high T2 signal (arrowheads) reflecting the de-differentiated component.

fat-suppressed images. Nodular areas of high T2 signal intensity within a lipomatous lesion may reflect malignancy but can also be seen following trauma and fat necrosis (Figure 14.30). Lesions with very high T2 signal intensity, similar to fluid signal intensity, may reflect a ganglion, myxoid tumors containing gelatinous tissue such as myxoid liposarcoma or intramuscular myxoma, a cystic nerve sheath tumor, or a hemorrhagic tumor such as synovial sarcoma. Use of intravenous gadolinium is advantageous in distinguishing a non-enhancing ganglion from a high T2 signal solid tumor, which typically shows variable internal enhancement (Figure 14.31). Low T2 signal intensity lesions may be seen with calcified masses, lesions with hemosiderin staining as a result of hemorrhage such as pigment villonodular synovitis and giant cell tumors of the tendons sheath, fibrous lesions such as fibromatosis, or tumor like lesions such as amyloid. Similar to bone tumors, a major role of MRI is in pretreatment staging as this is one of the most important considerations in planning treatment and surgery. Important factor to consider and highlight include the compartment involved, trans-fascial spread to adjacent compartments, osseous involvement, and relationship to neurovascular structures.

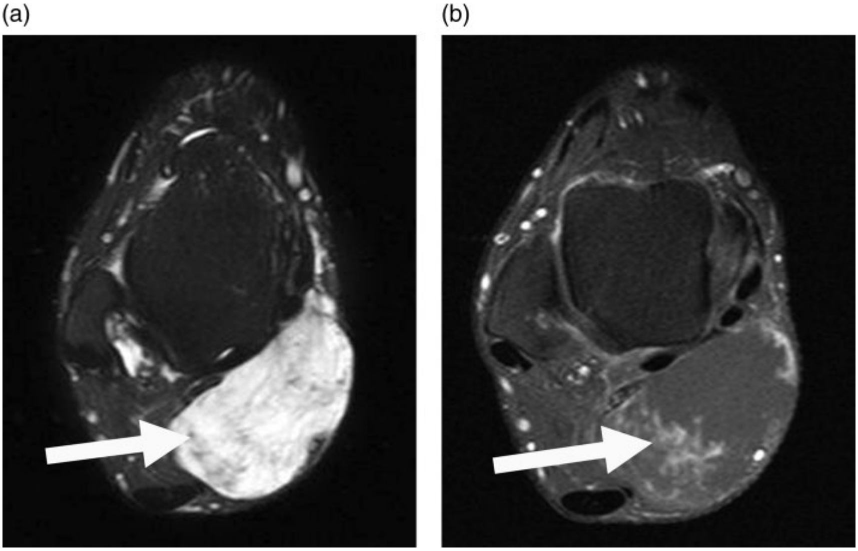

Figure 14.31 Axial T2-weighted fat-suppressed MRI of the ankle demonstrates a high T2 signal intensity mass posteromedially (a) (arrow). Axial T1 fat-suppressed MRI following administration of intravenous gadolinium shows heterogeneous internal enhancement (arrow) in this patient with a myxoid liposarcoma (b).

14.7 Summary

Musculoskeletal imaging utilizes multiple imaging modalities to explore various imaging pathologies. In this chapter, we have discussed the main imaging modalities used in musculoskeletal imaging, and have also discussed the use of various modalities in the commonly encountered clinical situations. The judicious use of the appropriate imaging modality is essential to achieve a high diagnostic accuracy. It is always prudent to ask the help of the radiologist if there are any concerns regarding the clinical situation and the imaging pathway to the considered.

Additional Reading

Amrami, K.K. (2012). Imaging of the seronegative spondyloarthropathies. *Radiol. Clin. North Am.* 50 (4): 841–854.

Bancroft, L.W., Pettis, C., and Wasyliw, C. (2013). Imaging of benign soft tissue tumors. *Semin. Musculoskelet. Radiol.* 17 (2): 156–167.

Blankenbaker, D.G. and Davis, K.W. (2016). *Diagnostic Imaging: Musculoskeletal Trauma*, 2e. Philadelphia: Elsevier.

Brower, A.C. and Flemming, D.J. (2012). *Arthritis in Black and White: Expert Consult*. Philadelphia: Elsevier.

Kransdorf, M.J. and Bridges, M.D. (2013). Current developments and recent advances in musculoskeletal tumor imaging. *Semin. Musculoskelet. Radiol.* 17 (2): 145–155.

Manaster, B.J. (2013). Soft-tissue masses: optimal imaging protocol and reporting. *AJR Am. J. Roentgenol.* 201 (3): 505–514.

Manaster, B.J. (2016). *Diagnostic imaging: musculoskeletal non-traumatic disease*, 2e. Philadelphia: Elsevier.

Rogers, L.F. and West, O.C. (2014). *Imaging of Skeletal Trauma*, 4e. Philadelphia: Elsevier.

Soldatos, T., Pezeshk, P., Ezzati, F. et al. (2016). Cross-sectional imaging of adult crystal and inflammatory arthropathies. *Skeletal Radiol.* 45 (9): 1173–1191.

Dr. Ur Metser

Dr. Ur Metser is the Division Head of Molecular Imaging and a staff radiologist at the Toronto Joint Department of Medical Imaging (University Health Network, Mount Sinai Hospital and Women's College Hospital) and a Professor of Radiology, Department of Medical Imaging at the University of Toronto. He is also the clinical lead in the core of Radiochemistry and Nanotechnology at the Techna Institute and chairs the Ontario Provincial Positron Emission Tomography Steering Committee at Cancer Care Ontario, responsible for the evidence-based introduction of PET in Ontario. He graduated from the Faculty of Medicine at the Technion (Haifa) and completed his residency training at the Sourasky Medical Center (affiliate of Tel Aviv University) and fellowship programs in abdominal imaging at the University of Toronto, and PET imaging at McMaster University. After serving as a staff radiologist at the Departments of Radiology and Nuclear Medicine in Tel-Aviv, he joined the Joint Department of Medical Imaging in the Divisions of Abdominal Imaging and Molecular Imaging. He is a fellow of the Royal College of Physicians (Canada) and an active member in multiple international professional societies including the Radiological Society of North America, American Roentgen Ray Society, and Society of Nuclear Medicine. Dr. Metser has published over 90 manuscripts in peer-reviewed journals, as well as multiple review articles, book chapters, and practice guidelines. His main clinical and research interests focus on novel molecular imaging probes, hybrid imaging (PET/CT and PET/MR) for tumor detection, and characterization and assessment of response to therapy with functional imaging.

Dr. Noam Tau

Dr. Noam Tau is a clinical/research fellow in molecular and abdominal imaging in the Joint Department of Medical Imaging at the University of Toronto. His interests include novel radiopharmaceuticals, data mining, automatic diagnostic tools, and the general advancing of medical science. Dr. Tau believes that the future is in the hidden data within images, and his vision is to exploit these data for the benefit of patients.

Medical Imaging for Health Professionals: Technologies and Clinical Applications, First Edition.
Edited by Raymond M. Reilly.
© 2019 John Wiley & Sons, Inc. Published 2019 by John Wiley & Sons, Inc.

Dr. Amit Singnurkar

Dr. Amit Singnurkar is an Associate Professor of Radiology and Medicine at McMaster University in Hamilton, Ontario, Canada. He is a nuclear medicine and molecular imaging specialist. He is currently the nuclear medicine lead at the Hamilton General Hospital and St. Joseph's Health Care, Hamilton and is the program lead for cardiac PET. Dr. Singnurkar's main interest is in policy development to ensure the provision of appropriate and high-quality imaging tied to improved health outcomes. His other interests include translational research of novel radiotracers and imaging techniques primarily in the fields of oncology, cardiology, and neurology.

15

Molecular Imaging with Positron Emission Tomography

Ur Metser, Noam Tau, and Amit Singnurkar

15.1 Introduction

Molecular imaging refers to the "visualization, characterization and measurement of biological processes at the molecular and cellular levels in humans and other living systems" [1]. Clinically, molecular imaging directly or indirectly monitors and spatially records the occurrence of molecular or cellular processes for biochemical, biologic, diagnostic, or therapeutic applications. This is achieved with the use of a labeled probe that interacts with a target and is detected externally. The probe–target interaction may be through targeted binding, accumulation of a probe in the cell, or less commonly, the probe may be activated by a cellular molecule, usually an enzyme. Unlike morphological imaging techniques like CT or MRI, molecular imaging identifies processes intrinsic to metabolism, gene expression, or cell signaling. A major catalyst for the adoption of current clinical molecular imaging applications has been the rapid progress in understanding of molecular mechanisms of disease along with imaging technology advances [2]. In recent years, positron emission tomography (PET) has become an indispensable clinical tool for many indications in oncology, cardiology, and neurology, and is one of the most commonly used molecular imaging techniques clinically. One of the major limitations of PET is low anatomical resolution. The combination of PET with a morphological imaging modality, CT or MR, in modern integrated PET/CT or PET/MR scanners (see Chapter 3) became technically possible in the past 15 years. Combined PET/CT or PET/MR images compensate for this limitation of PET, enabling accurate anatomical localization of a metabolic event. With the data from CT or the exquisite tissue contrast of MR, specificity may also improve in integrated PET/CT or PET/MR examinations [3].

Medical Imaging for Health Professionals: Technologies and Clinical Applications, First Edition.
Edited by Raymond M. Reilly.
© 2019 John Wiley & Sons, Inc. Published 2019 by John Wiley & Sons, Inc.

15.2 PET Probes Including ^{18}F-FDG

PET probes may utilize various probe–target interactions. Probes that undergo targeted binding bind to their target with high affinity and for sufficient time to enable measurement of the probe–target interaction. For example, ^{68}Ga-DOTATATE (GDT), a radiolabeled somatostatin analog, can bind to tumors that exhibit somatostatin receptors (SSTRs), not only enabling detection of the tumor but also revealing the degree of receptor expression in these tumors. Receptor expression may also be exploited for therapeutic purposes, as the same receptors may be used to bind radioisotopes that emit forms of radiation that can impact the viability or proliferation of tumor cells (e.g. β-particles) [4]. Other probes, including ^{18}F-2-fluorodeoxyglucose (^{18}F-FDG; see Chapter 4), the most commonly used radiopharmaceutical in PET, accumulate within cells. ^{18}F-FDG is a glucose analog that is taken into cells by glucose transporters. Once in the cell, ^{18}F-FDG may undergo phosphorylation by the enzyme hexokinase. After phosphorylation, FDG is effectively trapped within the cell, as it cannot cross the cell membrane again or continue through the glycolytic pathway. The amount of ^{18}F-FDG within tissues can be measured as a marker of glucose uptake and glycolysis. Increased glucose metabolism is seen in certain disease processes, such as many malignant tumors or inflammation due to overexpression of glucose transporters, and higher levels of hexokinase. This enables imaging of these processes with ^{18}F-FDG PET [5].

15.2.1 ^{18}F-FDG PET/CT Protocol

^{18}F-FDG PET/CT is performed after appropriate patient preparation including fasting for at least six hours prior to the examination. The scan is performed ~60 minutes (range, 50–90) after intravenous administration of ^{18}F-FDG, at a dose of ~5 MBq kg^{-1} body weight, up to 550 MBq. Initially, a noncontrast low-dose CT (130 kVp; 105 mAs) is obtained for the scan field from the skull base to the upper thighs. Immediately after completion of CT, a PET scan of the same area is obtained using 2D or 3D mode (typical parameters would include three minutes per bed position for a total of five to seven bed positions per patient). Interpretation of integrated PET/CT improves overall diagnostic accuracy as compared to interpretation of PET and CT acquired separately. This is mostly due to improved lesion localization and improved specificity when incorporating morphological parameters on CT [3, 6].

15.2.2 Technical Considerations in Performing and Interpreting PET

Interpretation of a PET scan needs to be done with an understanding of the normal biodistribution of the imaging probe (Figure 15.1), and the

Figure 15.1 Normal biodistribution of ^{18}F-FDG: maximum intensity projection image shows high-level uptake of ^{18}F-FDG in the gray matter of the brain, variable uptake in the myocardium and gastrointestinal tract, and low-to-moderate uptake in the liver and spleen. ^{18}F-FDG is excreted through the kidneys and therefore the renal collecting system, ureters, and bladder often show high uptake of the radiopharmaceutical.

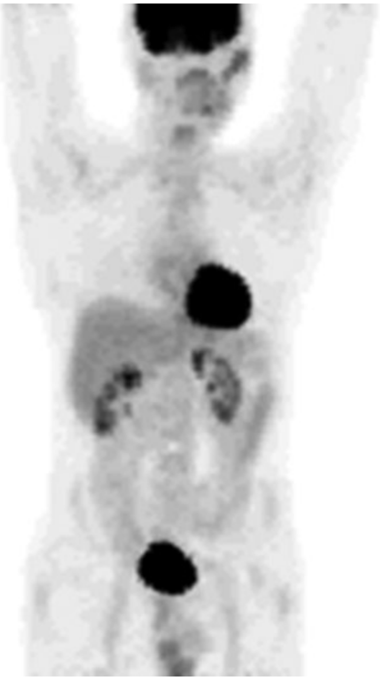

physiological and iatrogenic processes, which may affect the distribution of the radiopharmaceutical. For example, if ^{18}F-FDG PET is performed with significantly elevated serum glucose (as may be seen in poorly controlled diabetes), the endogenous glucose will "compete" with ^{18}F-FDG in normal tissues and hypermetabolic tissues, limiting the ability of PET to detect hypermetabolic lesions. Patients are often requested to refrain from strenuous physical activity prior to ^{18}F-FDG PET as this may result in redistribution of the radiopharmaceutical to skeletal muscles. Furthermore, therapy given to the patient needs to be taken into account when scheduling a PET scan. For instance, if the examination is performed immediately after radiotherapy, increased ^{18}F-FDG uptake within the tumor may be due to residual viable tumor or alternatively due to radiation-induced inflammation. In order to avoid potential false-positive results yet allowing further therapeutic intervention if incomplete response has been achieved with radiotherapy, it is suggested to wait for a period of 9–12 weeks after radiotherapy prior to performing PET [7]. Similarly, false-positive results may be encountered in the immediate postoperative period due to inflammatory changes, with or without infection, and it is usually recommended to wait at least six weeks after surgery prior to obtaining a PET scan.

15.3 ^{18}F-FDG PET in Oncology

^{18}F-FDG PET/CT has become pivotal in the diagnosis and management of many malignancies. Although a full review of the role of PET in oncology is beyond the scope of this chapter, the evidence to support the utilization of PET for a few of the more common malignancies including lung cancer, lymphoma, and gastrointestinal malignancies will be reviewed.

15.3.1 ^{18}F-FDG-PET/CT in the Management of Lung Cancer

A large part of a modern-day practice of PET oncology is spent in the evaluation of lung cancer. ^{18}F-FDG-PET can be used for initial diagnosis, staging, treatment planning, and follow-up for recurrent tumor after completion of initial therapy. This is possible because most lung malignancies demonstrate high metabolic activity and are readily detectable on PET imaging. Notable exceptions include adenocarcinoma in situ and pulmonary carcinoid tumors. Additional limitations include differentiation between concurrent inflammatory processes such as sarcoidosis, or concurrent lung infection. Despite these known challenges, ^{18}F-FDG-PET has permanently changed the management of lung cancer and is firmly in the management algorithm for these patients, since it has been shown to change management decisions in 33–42% of patients [8, 9].

^{18}F-FDG-PET has been shown to be of great clinical utility in the characterization of solitary pulmonary nodules (SPN). ^{18}F-FDG-PET has high sensitivity (92%) for malignancy in SPN and thus can be used to exclude these patients from further invasive testing and redirection to a surveillance approach [10, 11]. A major limitation of ^{18}F-FDG-PET in the evaluation of SPN is in the detection of adenocarcinoma in situ with a sensitivity of ~20% [12]. ^{18}F-FDG-PET is most useful in patients with an intermediate clinical probability for malignancy and can be considered as the initial test for evaluation before CT-guided biopsy [13].

The primary role of ^{18}F-FDG-PET in lung cancer staging has become to increase the accuracy of nodal staging and evaluation for distant metastases. Mediastinal staging is limited by a lower positive predictive value but has high negative predictive value (67 and 95%, respectively) [14]. Low positive predictive value is related to false-positive uptake arising from inflammatory or infection sources, requiring confirmation of nodal disease with invasive nodal staging techniques. Invasive nodal staging in the context of negative FDG-PET in patients with small peripheral tumors can be excluded in clinically N0 disease (no spread to nearby lymph nodes) but is required in clinically N1 or N2 disease (spread to lymph nodes located within the lungs, hilum, or mediastinum on the same side as the primary tumor) [15].

^{18}F-FDG-PET has proven exceptionally effective in preventing futile thoracotomies and redirecting patients to other treatment pathways involving radiation therapy or systemic therapy (Figure 15.2). In a randomized study of 189 patients, in patients staged with ^{18}F-FDG-PET, the rate of future thoracotomies was significantly lower compared to conventional staging; however, with no significant observed change in survival [16]. Another randomized trial, which added cranial imaging, showed similar findings, noting also that ^{18}F-FDG-PET may inappropriately upstage disease in a small number of patients [17]. Similarly, ^{18}F-FDG-PET changes management in those planned to undergo curative-intent radiation and chemotherapy [18].

The management questions in today's practice are slowly changing with an increased understanding that M1 disease (spread to the contralateral lung, pleura, pleural fluid, pericardial fluid, or distant lymph nodes or organs) does not behave homogeneously and can be reclassified into prognostic subcategories [19]. The opportunity to use enhanced surgical approaches, new biologic therapies, and planning of complex radiation therapy fields is also spurring development of new approaches for these patients. This is placing an even greater emphasis on accurate whole-body staging. In large part, this realization has come about as a consequence of advanced staging capabilities with modalities such as PET. Evidence to support these new approaches is still lacking but

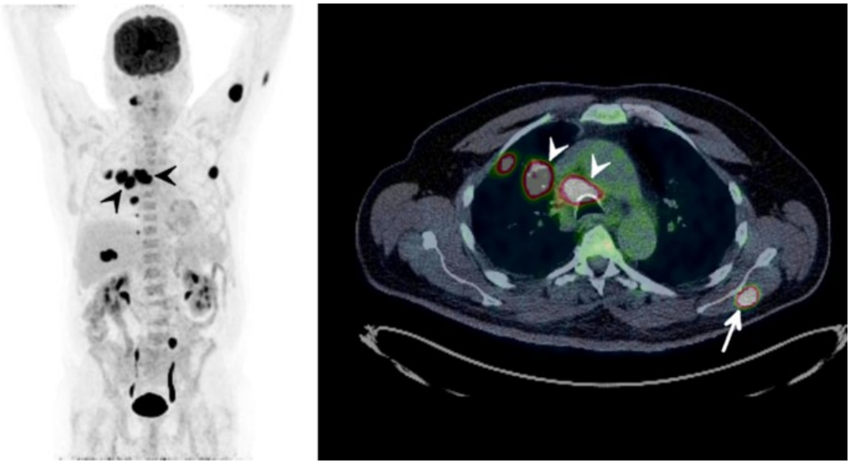

Figure 15.2 A 63-year-old man with biopsy-proven non-small cell lung cancer, thought to be stage IIIA on CT (limited to the chest). The patient was planned to receive chemoradiotherapy with curative intent. ^{18}F-FDG-PET/CT performed subsequently showed metabolically active lung tumor with metastatic nodes in the right lung hilum and mediastinum (arrowheads). Further, PET showed unsuspected multiple metastases to skeletal muscle (see deposit in muscle superficial to left scapula; arrow in transaxial image). (*See insert for color representation of the figure.*)

^{18}F-FDG-PET will likely play a key role in better understanding the nuances in the treatment of stage IV disease [20].

^{18}F-FDG-PET is also useful in the setting of localized disease with the proliferation of alternative modalities to surgery such as radiofrequency ablation (RFA) or stereotactic body radiation therapy (SBRT). ^{18}F-FDG-PET is a key tool for excluding nodal and distant metastases when treatment is being considered with SBRT [21]. Planning of radiation treatment, particularly when region definition becomes difficult in areas of atelectasis (complete or partial collapse of the lung), is enhanced by the definition of metabolic tumor volumes and is increasingly being used by radiation oncologists. This leads to change in treatment volume in up to 60% of patients and reduction in interobserver variability compared to standard tumor delineation [22].

With increased consideration and use of RFA of lung tumors and metastases, ^{18}F-FDG-PET is becoming more critical for excluding metastatic spread prior to therapy and for evaluation of incomplete ablation or recurrent tumor. RFA presents a unique problem as the treated mass persists or is larger after completion of therapy [23]. Standard imaging with CT is therefore limited in ensuring complete treatment and for diagnosing tumor recurrence. ^{18}F-FDG-PET has been shown to be an effective modality both to document incomplete tumor ablation and predict tumor recurrence [24–26].

Detection of recurrent tumor is an important consideration in the management of lung cancer patients, not just after RFA, but also after treatment with chemotherapy, radiation, or surgery. ^{18}F-FDG-PET is useful in the evaluation of patients with suspected or known recurrence both to confirm local disease and to evaluate disease extent [27]. It follows from the performance of ^{18}F-FDG-PET at the diagnosis and staging portion of the patient journey that restaging with ^{18}F-FDG-PET at the time of suspected recurrence would direct patients to the appropriate therapeutic pathway. However, the overall impact on survival based on currently available therapies, even with enhanced PET staging data, is not completely certain at this time.

Currently, PET prognostic information is not widely used to estimate prognosis and to change management decisions beyond standard anatomic PET staging data. Multiple small studies have shown the ability of metabolic activity measured by ^{18}F-FDG-PET to prognosticate lung cancer patients, the results of which have been encapsulated in systematic reviews and meta-analyses performed by the European lung cancer working party for the International Association for the Study of Lung Cancer (IASLC) staging project [28, 29]. In their latest study in 2010, they analyzed 21 studies in total, which showed that patients with high standard uptake values (SUV), a quantitative measure of tumor uptake on PET images, have a worse prognosis than those with low SUV values with an overall hazard rate ratio of 2.08 comparing low and high SUV patients divided by the median SUV value in each individual study.

15.3.2 Role of ^{18}F-FDG PET in Lymphoma

15.3.2.1 Staging

Lymphomas are one of the most common malignancies in humans, with more than 80 000 new cases diagnosed in the United States in 2016. There are over 50 subtypes of lymphoma according to the World Health Organization International Classification of Disease [30]. Lymphomas are broadly classified into Hodgkin's and non-Hodgkin's lymphoma (HL and NHL, respectively), with NHL being approximately nine times more prevalent than HL. The various subtypes of lymphoma have different clinical and histologic features with indolent, aggressive, or very aggressive disorders. Although the incidence has been gradually rising in the past several decades, the overall outcome of patients with lymphoma has improved due to improvement in clinical management [31]. Therapy of lymphoma is based on the type of lymphoma, stage of disease, baseline prognostic factors, and the patient's comorbidities [32]. Therefore, accurate staging of disease is crucial for selection of appropriate treatment strategies.

Staging and therapy response assessment has traditionally been performed with CT, given its widespread availability. Recently, international guidelines (also known as the "Lugano classification") have incorporated PET/CT in the staging of lymphoma. The Lugano classification for staging and response assessment of HL and NHL was developed following workshops at the International Conference on Malignant Lymphoma in Lugano, Switzerland and was published in the *Journal of Clinical Oncology* in 2014 [33]. ^{18}F-FDG-PET/CT was recommended for the initial staging of all FDG-avid lymphomas. These include aggressive NHL, HL, and some of the indolent lymphomas [34]. ^{18}F-FDG PET/CT was noted to be more accurate than CT for staging of HL and NHL, especially in the detection of extranodal disease, with upstaging occurring more commonly than downstaging resulting in management change in some patients [33, 35].

Follicular lymphoma is the most common indolent lymphoma and second-most common form of NHL, accounting for up to one quarter of adult NHL. It has a variable course, usually indolent, with some patients experiencing a complete response (CR), while others may undergo transformation to an aggressive subtype or recur. Nearly a quarter of cases may spontaneously regress [36]. Treatment varies depending on the stage and clinical presentation. Although patients with advanced stage disease (stages III–IV) who are asymptomatic are usually managed with watchful waiting, durable remissions have been attained in approximately one-third of patients with early-stage disease treated with involved field radiotherapy alone [37]. PET has an emerging role in more accurately staging of patients with follicular lymphoma and more appropriately identifying patients who may benefit from radiotherapy [38].

There is mounting evidence in recent years that in patients with aggressive lymphoma, ^{18}F-FDG-PET/CT impacts disease stage in a significant proportion of patients and therefore may impact the routine workup of these patients at baseline and patient management. There are several clinical trials comparing ^{18}F-FDG-PET/CT to conventional CT in the staging of aggressive lymphoma [39–41]. Raanani et al. reported the impact of ^{18}F-FDG-PET/CT on 103 patients (NHL, $n = 68$; HL, $n = 35$) and showed that the impact of PET/CT was primarily for patients with presumed limited stage disease per conventional staging. In their cohort, ^{18}F-FDG-PET/CT resulted in upstaging and downstaging of 31% and 1% of patients with NHL, and 32 and 15% of patients with HL, respectively [41]. A recent prospective study by Barrington et al. comparing CT to ^{18}F-FDG-PET/CT in staging of 1171 patients with advanced HL ("Response Adapted Therapy in Advanced Hodgkin Lymphoma"; RATHL trial) has shown that PET results in upstaging of 14% and downstaging of 6% of advanced HL patients. Upstaging was often due to identification of extranodal disease in the bone marrow, lung, or multiple sites [42]. A further study assessing 454 patients with newly diagnosed early-stage HL with ^{18}F-FDG-PET/CT has shown that bone marrow biopsy can be safely omitted from routine workup, as it did not alter the risk assessment or treatment strategy of these patients [43].

There is sufficient evidence to show a significant impact of ^{18}F-FDG-PET/CT to the workup and management of patients with aggressive lymphoma. Although the Lugano classification recommends PET/CT for staging of FDG-avid lymphomas, a diagnostic contrast-enhanced CT examination should still be included at initial stage to optimize anatomic assessment and to better delineate lymphadenopathy from surrounding structures for the purpose of radiotherapy planning. This may be challenging with the routine low radiation dose non-enhanced CT performed routinely for ^{18}F-FDG PET/CT [33].

15.3.2.2 Therapy Response Assessment

Confirmation of CR at the end of therapy is crucial for management of patients with potentially curable aggressive lymphomas. Traditionally, this has been done with CT. However, for many patients residual masses are present at the end of therapy, and many of these represent scar tissue or fibrosis, especially when significant response (decrease >75% on CT) has been documented. ^{18}F-FDG-PET/CT-based therapy response assessment criteria have a high negative predictive value, 95–100% for HL and 80–100% for aggressive NHL [35]. Residual masses at the end of therapy are assessed on a 5-point scale on PET called the Deauville score (Table 15.1). Mediastinal blood pool activity (intensity of ^{18}F-FDG uptake within the large mediastinal vessels) and normal metabolic activity in the liver, usually higher than mediastinal blood pool, are used as reference points. At the end of therapy, a Deauville score of 1–3 is considered negative for residual disease (Figure 15.3), whereas a score of 4 or 5 is considered positive [35]. As there is variability in the reported positive predictive value of ^{18}F-FDG-PET/CT, especially for NHL, and given the implications

Table 15.1 Deauville scoring criteria for assessing treatment response in lymphoma by PET/CT.

Score 1	No uptake
Score 2	Uptake ≤ mediastinum
Score 3	Uptake > mediastinum but ≤ liver
Score 4	Uptake moderately > liver
Score 5	Uptake markedly > liver and/or new lesions
Score *X*	New areas of uptake unlikely to be related to lymphoma

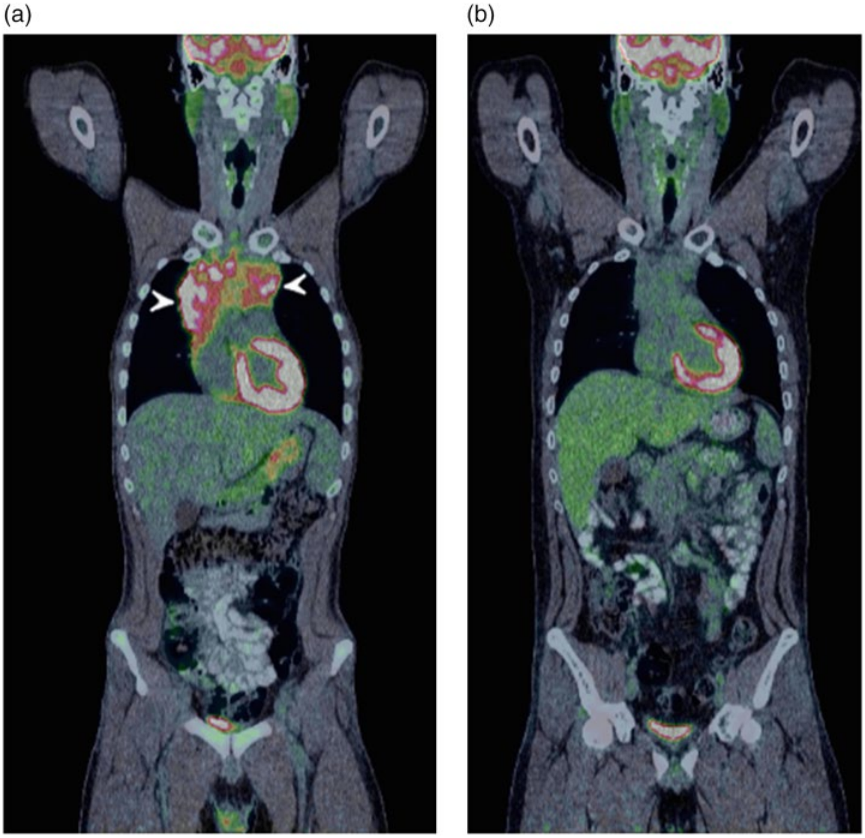

Figure 15.3 A 28-year-old man with Hodgkin's lymphoma. PET performed at baseline and three weeks after completion of chemotherapy shows a bulky metabolically active mediastinal mass at baseline (arrowheads) (a), which decreased in size after therapy (b). The residual mass seen on CT is no longer metabolically active with uptake similar to mediastinal blood pool (Deauville score, 2), confirming complete metabolic response. (*See insert for color representation of the figure*.)

to patient management, if further treatment is being considered (such as salvage chemotherapy, stem cell transplant), histological confirmation is strongly advised. In cases, where biopsy is not feasible, follow-up PET may confirm residual disease, if it documents progression.

^{18}F-FDG-PET/CT can also be used early during the course of therapy to confirm adequate response. Interim PET performed after two or three cycles of chemotherapy offers insight into the chemosensitivity of the tumor. A negative interim PET in HL has been shown to indicate favorable response at the end of therapy. Recently, it has been shown that for patients with advanced-stage HL, PET can be used to tailor management with de-escalation of therapy in patients showing favorable response. In these patients, the omission of bleomycin from the therapeutic regimen decreased pulmonary toxicity without significantly altering outcome. Patients who show continuing abnormal metabolic activity on interim PET received escalated therapy [44].

In summary, ^{18}F-FDG-PET/CT is an important tool in the staging and response assessment of patients with aggressive lymphoma, including risk-adapted management in patients with HL. PET/CT enables more appropriate selection of patients with indolent lymphoma for curative intent radiotherapy.

15.3.3 ^{18}F-FDG PET/CT in Gastrointestinal Malignancies

^{18}F-FDG PET/CT has a role in the staging and/or restaging of patients with gastrointestinal malignancies. In this section the role of PET in the staging of patients with esophageal cancer is discussed and the indications for PET in patients with colorectal cancer (CRC) are reviewed.

15.3.3.1 ^{18}F-FDG-PET/CT in Esophageal Cancer

It is estimated that nearly 17 000 new cases of esophageal cancer were diagnosed in the United States alone in 2016. Esophageal cancer carries an overall poor prognosis with a five-year survival rate of only 18.4% [45]. The main reason for the poor prognosis is that esophageal cancer is diagnosed late as it is often asymptomatic in its early stages with local spread, or spread to local lymph nodes or distant sites at the time of diagnosis. Curative therapy can be offered when the disease is still localized. Current management for patients with esophageal cancer can include upfront surgery, surgery after neoadjuvant chemoradiotherapy, or chemoradiation therapy alone. Each of these treatment modalities is associated with significant morbidity and a risk of complications including death in <5% of patients [46]. Therefore, accurate staging of the disease at baseline and identification of patients who may benefit from curative intent therapy is crucial to ensure that patients that harbor distant metastases and would not benefit from aggressive therapies are spared the associated risks and complications. Traditionally, esophageal cancer is staged locally by endoscopy and endoscopic ultrasound (EUS). These methods enable determination of the local extent of tumor including depth of invasion into or through the esophageal wall, and with the aid of fine needle aspiration EUS may also aid in assessing involvement of regional lymph nodes [47]. The overall accuracy of EUS in accurately determining the depth of invasion is ~85% and has a sensitivity of 70–80% in identifying regional nodal metastases [48]. Although CT may identify the invasion of tumor into adjacent structures, it does not have the contrast resolution to differentiate superficial from deep invasion into the esophageal wall and its sensitivity in identifying lymph node metastases is also limited.

Despite high specificity, the detection of distant metastases with CT has been shown to be limited, with an overall sensitivity of ~52%. A systematic review has shown that ^{18}F-FDG-PET has a higher overall sensitivity of >70% [49]. A recent prospective multicenter registry of ^{18}F-FDG-PET in the initial staging of patients with potentially resectable esophageal cancer including 491 patients has shown that PET may lead to clinically important changes in stage in 24% of patients, mostly due to upstaging. These changes resulted in differences in actual patient management and patients with higher stage on PET also had a significantly shorter survival [50]. Four hundred ninety-one patients who received a ^{18}F-FDG-PET/CT scan for staging of potentially resectable esophageal cancer were included in the study cohort. PET/CT led to clinically important changes in stage for a total of 188 patients (24.0%): 107 patients (21.8%) were upstaged and 11 patients (2.2%) were downstaged. The results of PET/CT were associated with differences in actual management. At the six-month follow-up, use of surgery was greater in patients without non-regional metastatic disease (i.e. those who had metastases limited to nodes in the vicinity of the tumor), compared to those with non-regional lymph node metastases (25%, $p < 0.001$) or distant metastases (71.3%, $p < 0.001$), based on PET/CT.

The overall cohort had a median survival of 603 days, and higher stage of disease on PET/CT (i.e. M stage) was associated with shorter survival ($p < 0.001$). The impact on stage in nearly one in four patients and the downstream implications of stage migration on clinical management of these patients make ^{18}F-FDG-PET/CT an important clinical tool in the workup of patients with potentially resectable esophageal cancer.

The role of surgery after chemoradiotherapy in patients with esophageal cancer is uncertain. There are two randomized trials that showed no survival benefit for patients with squamous cell carcinoma of the esophagus treated with surgery after neoadjuvant therapy. Furthermore, the overall survival of patients receiving chemoradiotherapy alone is similar to that which has been reported for patients undergoing chemoradiotherapy followed by surgery, ranging from 25 to 40% [51, 52]. Although chemoradiotherapy can downstage locally advanced tumors and result in improved local control of disease, it is associated with an increase in surgery-associated complications and mortality. A recent study showed that overall >30% of patients receiving chemoradiotherapy achieve CR to therapy on ^{18}F-FDG-PET (PET-CR). PET-CR predicted improved outcome for patients undergoing chemoradiotherapy (two-year survival rate of 71% compared to only 11%), but not for patients undergoing surgery after chemoradiotherapy, likely because FDG-PET residual disease was resected. For patients undergoing chemoradiotherapy, on multivariate analysis, PET-CR was the strongest prognostic independent variable on survival. These findings suggest a further significant role for PET in selecting patients for surgery after chemoradiotherapy, as patients who achieve a PET-CR may not benefit from added resection [53], although this needs to be validated in prospective trials.

15.3.3.2 ^{18}F-FDG-PET/CT in Colorectal Cancer

Increased screening with colonoscopy, which enables histological diagnosis of malignancy and resection of premalignant polyps, and advances in systemic therapy have resulted in an annual 3% decline in mortality from CRC over the past decade. Nonetheless, CRC remains the second leading cause of cancer death in the United States [54]. When diagnosed, CRC is usually staged with CT. CT can delineate local tumor extent, and identify regional nodal and distant metastases. For rectal cancer, MRI of the pelvis is commonly performed in addition to CT, to better assess the local extent of tumor into the bowel wall, its distance from the fascia surrounding the rectum, and invasion of adjacent structures. All of these parameters may impact patient management as they may determine whether the patient would benefit from upfront surgery or would need neoadjuvant chemoradiotherapy. In locally advanced tumors, neoadjuvant therapy may downstage the tumor, thereby increasing the likelihood of negative surgical margins and decreasing the probability of local recurrence after surgery [55].

There is currently little evidence to justify routine use of ^{18}F-FDG-PET/CT in the initial staging of patients with CRC that have no distant metastases on CT [56]. However, PET may be valuable for imaging of hepatic and extrahepatic metastases in patients with metastatic CRC being considered for curative resection. When limited metastases exist, aggressive local therapy, including surgical resection, RFA, SBRT, or a combination of these, is often considered. Current data suggest that in well-selected patients, survivals of up to 30–50% at 5–10 years can be achieved.

For patients with hepatic metastases, hepatic resection remains the only potential curative therapy with a reported five-year survival rate of ~50% [57]. Although in recent years, surgical resection alone or in combination with other ablative therapies is being performed for more extensive metastatic disease, the presence of peritoneal metastases, retroperitoneal lymph node metastases, or unresectable extrahepatic metastases, such as to bone, are generally considered contraindications for surgery. Recurrence rates after resection of more than four liver metastases are high and recurrence rates approach 100% after resection of both liver and extrahepatic metastases, although long-term disease control may be achieved [58]. Therefore, appropriate patient selection for resection of limited hepatic and/or extrahepatic metastases is paramount.

There are conflicting results from two randomized trials evaluating the role of ^{18}F-FDG-PET/CT in selecting patients with metastatic CRC to the liver for surgery. The first trial, by Ruers et al. included patients who underwent upfront surgery and showed that PET may prevent unnecessary surgery in one of six patients [59]. A further randomized trial by Moulton et al. [60] showed a relatively infrequent change in surgical management with PET (8%). The differences may be explained by the study population selected for inclusion in the two trials and the differences in definitions in resectable hepatic disease. In the Ruers trial, liver resection was limited to four metastases, whereas in the latter randomized trial, patients with more extensive hepatic metastases were included, as long as these were felt to be fully resectable in one or more surgical procedures. Furthermore, the latter trial included a significant proportion of patients who had received chemotherapy prior to undergoing PET. A recent analysis of a cohort of patients from the latter trial has estimated that when evaluating only patients who were chemotherapy-naïve, PET may have prevented futile surgery in nearly 15% of the cohort, similar to the results of the Ruers trial. This may be explained by the effect that current chemotherapy regimens in CRC may have on the metabolic activity of metastatic sites and thus on their detectability with PET. Patients who undergo chemotherapy within several weeks prior to PET may have decreased sensitivity in identifying additional sites of metastases [61]. This highlights the importance of understanding the need to optimize timing of metabolic imaging tests such as ^{18}F-FDG-PET to a patient's therapy schedule. In patients with metastatic colon cancer, PET may best be utilized prior to administration of chemotherapy, or at an interval of several weeks after completion of therapy.

^{18}F-FDG-PET/CT also has a proven role in the detection of recurrent disease after primary therapy, especially in patients who have elevated serum tumor markers such as carcinoembryonic antigen (CEA). CEA may be used to detect tumor recurrence even when asymptomatic. However, elevated CEA alone without identification of the site of metastatic disease does not justify therapy for presumed metastatic disease [62]. Therefore, early identification of sites of tumor recurrence is clinically relevant. Identification of recurrence is important even when sites of disease recurrence are not amenable to surgical resection, as a survival benefit has been shown for systemic therapy compared to supportive care [63]. ^{18}F-FDG-PET/CT is superior to conventional imaging in identifying recurrent CRC in patients with rising CEA levels [64–67], with a higher sensitivity and specificity than multidetector CT: 98.1 and 75% versus 66.7 and 62.5%, respectively [65]. ^{18}F-FDG-PET/CT may be better to identify patients who may be candidates for salvage surgical resection of tumor recurrence or metastases versus those who may benefit from systemic therapy.

15.3.4 ^{18}F-FDG-PET/CT in Head and Neck Cancers

Head and neck malignancies, most commonly squamous cell carcinoma, present several challenges, including most prominently identifying occult primary malignancies with biopsy confirmed lymph node metastases, and accurate staging. Also, the demographics and behavior of this malignancy have changed, now with increased incidence in women due to higher rates of smoking, and incidence in a younger patient population through exposure to human papilloma virus (HPV) [68, 69]. ^{18}F-FDG-PET is well suited for the management of this disease and can have a major impact on patient outcomes. Approximately 5–10% of head and neck malignancies present as cervical lymph node metastases associated with unknown primary sites, which are eventually proven to be squamous cell cancer in ~75% of cases [70, 71]. The primary sites remain occult after standard investigation with physical exam, endoscopy, contrast CT, and MRI. ^{18}F-FDG-PET has been shown to identify 24.5% of these occult tumors [72]. The detection rate increased to 44.2% if performed prior to panendoscopy (visual examination of the pharynx, larynx, upper trachea, and esophagus) [73, 74]. Identification on PET allows targeted evaluation on endoscopy and improved diagnostic yield on biopsy.

PET is able to increase the accuracy of staging of patients, mainly through improved nodal staging and assessment of distant metastatic deposits. Nodal staging is not reliant on size or morphologic criteria as on CT and MRI, but rather guided by metabolic activity. Compared to standard CT and MRI, PET has the same positive predictive value of 73%, and a higher negative predictive value of 80% compared to 71% on standard imaging when assessed on a per-patient basis [75]. Additional studies have shown an ~21% reclassification rate from negative neck evaluation by conventional radiologic examinations to positive disease [76].

A limitation of ^{18}F-FDG-PET is in the evaluation of patients with stage N0 disease (no spread to nearby lymph nodes). This is most likely attributable to a high rate of false-positive findings due to physiologic uptake and metabolic activity related to inflammatory lymph nodes [77]. PET is also limited in the assessment of micrometastases as PET resolution is best suited for the evaluation of lesions larger than 7–8 mm [78].

As for other head and neck malignancies, ^{18}F-FDG-PET provides a clear diagnostic advantage over standard imaging modalities for the determination of distant metastatic spread. The performance of PET is most pronounced in patients with nasopharyngeal malignancies, which tend to present with distant metastases more frequently [79]. A meta-analysis by Shen and colleagues showed a pooled sensitivity and specificity for distant metastases of 87 and 96%, respectively [80]. When compared to whole body 3 T MRI in oro- and hypopharyngeal malignancies, PET showed a higher negative predictive value (93 vs. 96%) and similar positive predictive values (80 vs. 79%) [81].

Head and neck malignancies tend to have a higher rate of synchronous malignancies (two or more malignancies detected simultaneously that are histologically distinct), mainly of the aero-digestive tract (for example, esophagus, lungs), that result in changes in diagnostic and management considerations in many patients. Approximately 10% of these patients are diagnosed with synchronous malignancies [82]. The main advantages of ^{18}F-FDG-PET in this scenario are the relative high conspicuity (high uptake of tracer within the lesion relative to background activity) of these lesions due to their increased metabolic activity and the fact that standard field of view in PET spans the entire aero-digestive tract. Taken together, for head and neck cancers in general, Xu and colleagues, in a separate meta-analysis, showed a pooled sensitivity and specificity of 89 and 95%, respectively, in the diagnosis of distant metastases and synchronous malignancies [83].

In those patients with head and neck cancers who exhibit a CR to chemoradiotherapy, ~10% develop recurrent disease [84, 85]. ^{18}F-FDG-PET is well suited for the surveillance of individuals in this patient population. In a multicenter randomized controlled study of 564 patients in the United Kingdom, patients in the PET-guided surveillance arm had similar survival to those individuals with planned neck dissections after chemoradiotherapy. Patients in the former group also underwent significantly fewer procedures [86].

^{18}F-FDG-PET is also used to assess patients suspected of recurrent papillary or follicular thyroid cancer based on biochemical markers, specifically rising levels of thyroglobulin or thyroglobulin antibody during surveillance after ablative radioiodine therapy. When suspected of recurrence, patients are typically first imaged with ^{131}I (radioiodine). PET is most useful when no recurrence is detected on radioiodine imaging. The rationale behind this is that as tumors become less differentiated and therefore less able to concentrate iodine, they become more aggressive and metabolically active resulting in greater glucose metabolism [87]. PET can also be used to provide prognostic information and to guide therapy [88].

15.4 ^{18}F-FDG PET in Non-Oncology Indications

In the following section the role of PET for non-oncology indications is reviewed. Some of these, like myocardial viability assessment, have been routinely incorporated into clinical use in many jurisdictions, while others are largely still under evaluation.

15.4.1 Cardiac PET

The mainstay of cardiac PET imaging is myocardial perfusion imaging (MPI). This technique is used in the investigation of patients to diagnose myocardial ischemia, assess for myocardial injury, monitor stent and graft function, and to risk stratify patients (see Chapter 7). A frequent query when performing MPI is to evaluate those patients presenting with anginal symptoms and multiple cardiac risk factors, who have an abnormal ECG stress test. MPI allows more efficient resource utilization by identifying those patients who would benefit from more invasive treatment with percutaneous intervention (cardiac catheterization and stent implantation) or coronary artery bypass grafting [89].

The most frequently used radiotracer for cardiac PET imaging today is a generator-derived radionuclide, rubidium-82 chloride (^{82}Rb) (see Chapter 4). Investigations to date have noted a significant clinical advantage of PET MPI over SPECT MPI, which employs ^{99m}Tc-sestamibi, ^{99m}Tc-tetrofosmin, or ^{201}Tl [90]. PET is more effective than SPECT in diagnosing significant flow-limiting disease as seen on coronary angiography. When a significant flow-limiting stenosis is defined as 70% of vessel diameter, the sensitivity, specificity, and accuracy of PET compared to SPECT in a matched population is 87, 93, and 89% versus 82, 73, and 79%, respectively [91].

Pooled estimates of sensitivity, specificity, and accuracy of detecting angiographically significant disease across several studies are 90, 89, and 90% [92]. This is attributable to higher sensitivity of the PET camera, greater myocardial extraction efficiency of ^{82}Rb compared to the ^{99m}Tc MPI agents, and lower susceptibility of the studies to attenuation artifacts caused by overlying tissues. An added benefit is the lower radiation absorbed dose to the patient in the order of two to three times less dose (5 mSv) than a standard SPECT MPI study (10–15 mSv).

The ability of PET MPI to risk stratify patients is further enhanced by the ability to perform coronary flow reserve (CFR). CFR is especially useful in the setting of balanced three-vessel ischemia. CFR is defined as absolute coronary blood flow with pharmacologic stress divided by flow under resting conditions. A normal patient typically experiences a flow increase of three- to fivefold from baseline rest conditions. Aberrant CFR is an indication of ischemia either in the epicardial or microvascular circulation. Therefore, it is particularly useful in the setting of nonobstructive epicardial coronary artery disease (<50% stenosis in the left main artery or <70% stenosis in the other major vessels) or diffuse coronary atherosclerosis on anatomic imaging to confirm the presence of microvascular disease.

The use of CFR measurements has a significant impact on prognosis. At different levels of reversible ischemia seen on MPI, CFR can further sub-stratify these patients into more accurate risk categories. For example, patients typically considered low risk on the basis of a normal perfusion study can be further stratified into lower risk patients with an annualized mortality rate of 0.1–3.6% in the highest risk stratum [93]. Accurate determination of ischemic load, including at the level of the microvasculature can result in more accurate medical treatment strategies via disease-modifying drugs.

Cardiac PET when performed with ^{18}F-FDG (^{18}F-FDG-PET) has been shown to be an effective modality in determining cardiac viability in patients with severe ischemic cardiomyopathy being considered for revascularization [94]. Although no definitive prospective randomized trials exist to date, this has become routine clinical practice because of the demonstrated relationship between viability testing including the determination of degree of hibernating myocardium, and clinical outcomes [95]. It is the most sensitive modality for detecting viable myocardium with a pooled analysis of 24 studies showing a sensitivity of 92% and specificity of 63% [96]. It offers significant advantages over standard modalities including dobutamine echocardiography and SPECT ^{201}Tl imaging and is complementary to MRI.

The most recent area of PET imaging growth in cardiology is for the diagnosis of cardiac sarcoidosis. An apparent increase in the prevalence of cardiac sarcoidosis over the last 20 years has resulted from better diagnostic and imaging techniques [97]. ^{18}F-FDG PET has helped show that the incidence of this disease has been greatly underestimated. This fits well with autopsy data that indicate that cardiac sarcoidosis is present in up to 25% of patients diagnosed with sarcoidosis [98, 99]. It is useful in the clinical setting of new conduction abnormalities in young patients (<60 years), abnormal screening test in patients with extra-cardiac sarcoidosis, idiopathic sustained ventricular tachycardia, or to monitor treatment effect with immunosuppressant drugs or steroids.

15.4.2 Neurological Applications of PET

PET imaging provides detailed information regarding brain function and neurotransmitter receptor protein distribution depending on the agent used (see also Chapter 13). PET is able to provide additional information when no discernible or defining abnormality is visible with MRI or other structural imaging modalities. PET is most useful in cases where clinicians face a complex differential diagnosis due to overlapping symptomology between neurodegenerative syndromes or in many cases overlapping disease processes. Outcomes research supporting the use of PET is currently limited.

The most accepted scenario for imaging with ^{18}F-FDG-PET is in patients assessed by a dementia specialist who have also had standard structural brain imaging whose diagnosis remains uncertain preventing adequate clinical management [100]. Although limited by study heterogeneity, results from a meta-analysis of 15 studies between 1989 and 2003 show a sensitivity and specificity of 86 and 86%, respectively, for Alzheimer's disease (AD) with more recent work from 2011 showing a sensitivity and specificity of 90 and 89%, respectively [101, 102]. Commonly assessed dementia syndromes assessed with the technique besides AD are frontotemporal dementia (FTD), dementia with Lewy Bodies (DLB), and Parkinson's dementia (PD). Management varies for these disorders and PET can help in making more informed clinical decisions. ^{18}F-FDG-PET is also useful for assessing patients with primary progressive aphasias (inability to understand or generate language), which are often prodromal syndromes for AD and FTD [103].

More recent work has shifted from looking at metabolic abnormalities to more specific biomarkers. Dementing syndromes can be defined by specific histopathologic characteristics, of which the most understood and studied are amyloid plaque, tubulin associated protein (tau), and Lewy Bodies (LB). Amyloid (Aβ) plaque is a marker of neurodegeneration, which is present in patients with AD and also those patients with predementia or mild cognitive impairment who are at risk for developing AD. There are three amyloid imaging agents, Amyvid (^{18}F-florbetapir), Visamyl (^{18}F-flutemetamol; Figure 15.4), and Neuraceq (^{18}F-florbetaben), that are US FDA approved and available for clinical use. An important caveat is that Aβ plaque can be present in normal individuals and in those with DLB and PD, so correlation with clinical symptoms is important [104, 105].

^{18}F-FDG-PET is an important addition to the existing clinical tools and imaging modalities available to localize epileptogenic foci prior to curative surgical resection in both adult and pediatric patients with medically intractable epilepsy. Initial workup for epilepsy is performed with neuropsychologic testing, surface EEG, and MRI. When these results are concordant, the patient can then undergo curative surgical therapy with a high success rate. Disconcordance of findings necessitates further workup with intracranial EEG. Imaging with

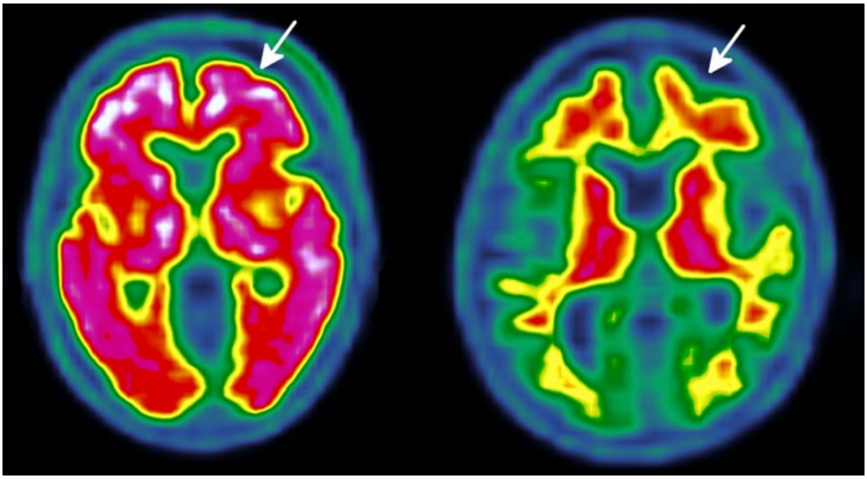

Figure 15.4 Fused ^{18}F-Flutemetamol (Vizamyl) PET/CT image of the brain from two separate patients for evaluation of dementia. On the right is a negative scan, showing normal tracer uptake in white matter with low-level uptake in the frontal cerebral cortex (arrow). In contrast, on the left is a positive scan, showing high-level uptake in the frontal cerebral cortex (arrow), suggestive of abnormal amyloid deposition. (*See insert for color representation of the figure.*)

PET presents an additional opportunity to localize the epileptogenic focus noninvasively by assessing changes in brain metabolism [106]. ^{18}F-FDG-PET is performed during the interictal state and has a sensitivity of 85–90% in temporal lobe epilepsy and is lower for extratemporal epilepsy (45–92%) [106]. A meta-analysis of PET for epileptogenic focus localization showed that the predictive value for ipsilateral PET hypometabolism was 86% for good outcomes, 80% in those with normal MRI, and 72% in those with normal EEG [107]. Importantly, it was also shown that there is no additional value of ^{18}F-FDG-PET in those with epileptogenic foci localized with ictal scalp EEG and MRI. Finally, PET findings influence the clinical decision-making in 53–71% of adult patients and 51–95% of pediatric patients [108].

15.4.3 ^{18}F-FDG-PET in Infectious and Inflammatory Disorders

Use of ^{18}F-FDG-PET/CT for imaging inflammatory and infectious causes has seen a rise in recent years. Initially, it was noted that inflammatory cells associated with a tumor have high levels of metabolic activity, and in fact may even possess higher ^{18}F-FDG avidity than the tumor cells themselves [109]. Later studies have shown that inflammatory and infectious conditions may have high ^{18}F-FDG avidity, even when there is no underlying malignant disease. This fact allowed for ^{18}F-FDG-PET/CT to become a helpful tool in diagnosing and monitoring these conditions. In this section, a few examples of ^{18}F-FDG-PET/CT utilization in inflammatory and infectious diseases are discussed, including in the diagnosis and monitoring of disease activity in sarcoidosis, assessment of patients with fever of unknown origin (FUO), and infected implanted medical devices.

15.4.3.1 Sarcoidosis

Sarcoidosis is a multisystem inflammatory disease with an unknown etiology, most common in African–American and northern European individuals. The disease mostly involves the lungs and hilar and mediastinal lymph nodes, but is not restricted to the chest. Sarcoidosis may also involve the kidneys, skin, eyes, central nervous system, myocardium, and in fact almost any organ. ^{18}F-FDG-PET/CT is used in systemic sarcoidosis to determine the level of disease activity, assess response to therapy, and to evaluate organ involvement. ^{18}F-FDG-PET/CT can also be used for patients with a suspected sarcoidosis, in order to identify a suitable target for biopsy to confirm the disease [110].

One of the most feared, and potentially fatal, sites of disease involvement is the heart, affecting up to 25% of sarcoidosis patients [99, 111, 112]. This may present as heart failure or various electrical conduction problems, including ventricular arrhythmias. Therefore, cardiac involvement in sarcoidosis needs to be diagnosed and treated as early as possible, as cardiac involvement is reversible when treated early and aggressively. In fact, when faced with a young

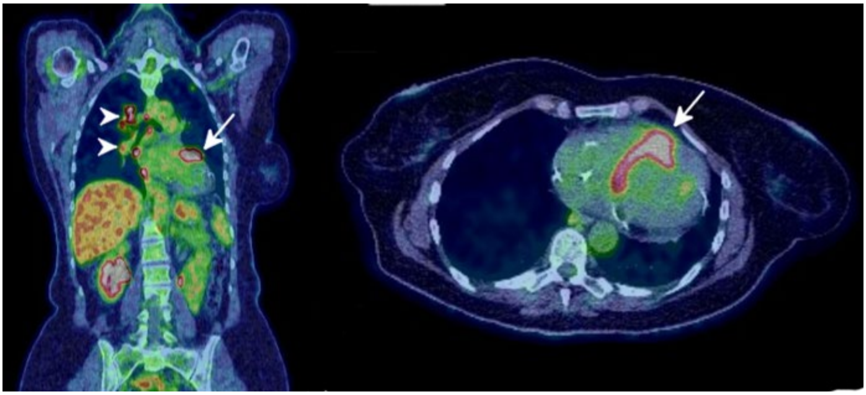

Figure 15.5 Evaluation of arrhythmia. PET shows focal abnormal FDG uptake in the myocardium (arrow). Also note, focal increased FDG uptake in hilar and mediastinal lymph nodes (arrowheads), in a typical distribution for sarcoidosis. (*See insert for color representation of the figure.*)

patient who has new and unexplainable arrhythmia, cardiac involvement of a yet undiagnosed sarcoidosis should be a considered. Although FDG uptake in the myocardium is not specific for sarcoidosis (and may be seen in other inflammatory conditions), in the appropriate clinical setting, ^{18}F-FDG-PET/CT can be used to confirm or refute sarcoid involvement of the myocardium (Figure 15.5).

The main challenge in detecting cardiac sarcoidosis is the unpredictable nature of physiological ^{18}F-FDG uptake of cardiac muscle. To bypass this issue, patients are put on a high-fat and low-carbohydrate diet before the ^{18}F-FDG-PET/CT scan. This eliminates the normal physiologic cardiac uptake of ^{18}F-FDG, and uptake is seen only in areas of disease involvement, which increases the confidence in diagnosing cardiac sarcoidosis. After appropriate medical therapy is administered (such as steroids), the same imaging protocol can be again used for therapy response assessment. Until recently, ^{18}F-FDG-PET/CT has not been used as a standard method for diagnosing cardiac sarcoidosis, or for therapy response assessment, and cardiac MRI has been commonly used. Given recently introduced evidence on the high overall accuracy of PET for this indication, this paradigm is shifting with increased utilization of PET in many centers.

15.4.3.2 Fever of Unknown Origin

FUO is defined as fever of 38.3 °C (101 °F) or higher for three or more weeks, in an otherwise healthy immunocompetent patient, or as fever in an immunocompetent patient after one week of hospital workup [113]. Many underlying conditions can result in FUO, including infections, tumors, and inflammatory conditions. To qualify as "FUO," the search for a "potentially diagnostic clue" (PDC) should not be able to locate the reason for fever after using standard investigation methods [114]. These methods include a thorough physical exam, obtaining a complete history and blood tests. When all these fail to find a PDC, CT of the chest and abdomen is used to try and find a likely cause for fever.

A meta-analysis published by Takeuchi et al. in 2016 gathered previously published studies, with overall assessment of 2058 patients presenting with FUO [115]. These patients underwent various imaging studies, including ^{67}Ga scintigraphy, radiolabeled white blood cells scan, PET, and PET/CT. Calculated overall, ^{18}F-FDG-PET and ^{18}F-FDG-PET/CT both have a sensitivity of 76–86% for finding the culprit, significantly higher than ^{67}Ga scintigraphy or radiolabeled white blood cells scan (60 and 30%, respectively). When taking into account both sensitivity and specificity, ^{18}F-FDG-PET/CT had a diagnostic yield (ability to accurately locate a disease focus) of ~60%, much higher than all other modalities. ^{18}F-FDG-PET/CT is limited in identifying an etiology for FUO in patient populations with low incidence of infectious and neoplastic diseases. Although these are often FDG-avid, the most common causes of a negative ^{18}F-FDG-PET/CT in FUO were adult-onset Still's disease, polymyalgia rheumatica (inflammatory diseases of various etiologies), and tuberculosis. Due to its overall high sensitivity and specificity, ^{18}F-FDG-PET/CT has become an additional clinical tool in the workup of patients with FUO.

15.4.3.3 Infected Implanted Medical Devices

Infection of implantable medical devices, such as prosthetic heart valves, pacemaker leads and subcutaneous generator pocket, vascular grafts, and central catheters, cause high rates of morbidity and mortality to patients. If diagnosed early and accurately, long-term antibiotic treatment or device removal can dramatically improve patient outcomes. Standard investigation methods, including echocardiogram for suspected infected cardiac devices, blood cultures, and physical exam, have a low yield in this setting and alternate diagnostic methods have been explored.

Several studies using ^{18}F-FDG-PET/CT have shown a very high sensitivity and specificity (>90%) in diagnosing infected medical devices. Additionally, the negative predictive value was also shown to be high (>85%), making the confidence level in the results of ^{18}F-FDG-PET/CT high [116–119]. Interestingly, an association with malignancies has been found for certain bacteria identified in blood cultures. A common example is *bovis group streptococci*, which may be related to gastrointestinal malignancies. These malignancies are usually undiagnosed until such an infection occurs, and ^{18}F-FDG-PET/CT can help identifying both the infected medical device and the associated underlying malignancy. Although it has yet to become part of the standard investigational protocol, prospective studies are being conducted and show great promise in ^{18}F-FDG-PET/CT becoming an important adjunct in the diagnosis of infected implantable medical devices.

15.5 Overview of Other PET Radiopharmaceuticals

Carbon, nitrogen, and oxygen are common elements in molecules, and thus, positron-emitting radionuclides of these elements (e.g. ^{11}C, ^{13}N, and ^{15}O) are attractive for synthesis of radiolabeled imaging probes. The disadvantage of ^{11}C, ^{13}N, and ^{15}O labeled compounds is the very short half-life of these radionuclides. For ^{15}O, with a half-life of two minutes, only very simple imaging probes can be synthesized (e.g. ^{15}O water) and the agent must be directly transferred via a pneumatic tube from the cyclotron to the PET suite. There is similarly little time for radiopharmaceutical synthesis when using ^{13}N, with a 10 minutes half-life, and thus again only simple radiopharmaceuticals are produced (e.g. ^{13}N ammonia). ^{11}C has a 20 minutes half-life, which is long enough to synthesize more complex radiopharmaceuticals and has been used clinically for many radiotracers in research, but usually requires an onsite cyclotron. Some radionuclides, such as Gallium-68 (^{68}Ga; half-life of 68 minutes), are produced with a generator rather than a cyclotron (see Chapter 4). Nonetheless, the vast majority of PET radiopharmaceuticals currently used are cyclotron-produced. With a half-life of 110 minutes, enabling complex syntheses and transportation from a cyclotron to remote PET facilities, ^{18}F has become the most widely used radionuclide in clinical practice.

As described earlier in this chapter, by far the most common PET radiopharmaceutical currently in clinical use is ^{18}F-FDG, a glucose analog. The first FDA-approved PET radiopharmaceutical was ^{18}F-sodium fluoride (Na^{18}F), a bone-imaging agent. Na^{18}F has a biodistribution similar to ^{99m}Tc-bisphosphonates (e.g. ^{99m}Tc-medronate), but is more sensitive for detecting bone lesions due to the greater sensitivity of PET compared to SPECT (see Chapter 3). After intravenous injection, Na^{18}F is rapidly removed from the plasma and either binds to bone or is excreted through the kidneys. Na^{18}F PET is sensitive for the detection of both osteolytic (destructive) and osteoblastic (sclerotic) bone lesions. Its specificity is increased when interpreted in conjunction with CT data, obtained at the time of PET/CT [120]. Other more commonly investigated PET radiopharmaceuticals include probes that target: membrane synthesis (e.g. ^{11}C or ^{18}F-labeled choline) [121], hypoxia (e.g. ^{18}F-Fluoromisonidazole [^{18}FMISO] or ^{18}F-fluoroazomycin arabinoside [^{18}FAZA]) [122], protein synthesis (e.g. ^{11}C-methionine or 3,4-dihydroxy-^{18}F-6-fluoro-L-phenylalanine [^{18}FDOPA]) [123], DNA replication (e.g. ^{18}F-Fluorothymidine [^{18}FLT]) [124], blood perfusion (e.g. ^{82}Rb [125] or ammonia [i.e. $^{13}NH_3$]), and various probes targeting cell surface receptors such as ^{68}Ga-DOTA-octreotate (GDT) for

SSTRs [126], or ^{68}Ga-PSMA HBED-CC ligands targeting prostate-specific membrane antigen (PSMA) [127].

In the following sections, the utility of selected PET radiopharmaceuticals that have been evaluated, or are in clinical use for assessment of myocardial perfusion, proliferation, and hypoxia are discussed. We also review the current evidence for the use of GDT for neuroendocrine tumors (NETs) and ^{68}Ga-PSMA ligands in the imaging of prostate cancer.

15.5.1 Other PET Agents for Myocardial Perfusion Imaging

Short-lived MPI agents until recently were limited to research applications and available only in tertiary care hospitals with radiopharmaceutical research facilities. The main barrier to more widespread use of these radiotracers are their short physical half-lives, 2.1 minutes for ^{15}O-H_2O, 10.0 minutes for ^{13}N-NH_3, and 1.2 minutes for ^{82}RbCl [128]. This necessitates the presence of an on-site cyclotron or in the case of ^{82}RbCl, radionuclide generators, both expensive propositions. Short half-lives also preclude exercise stress testing, which to date is preferred over pharmacologic stress testing due to the additional physiologic and prognostic information derived from the former. Use scenarios for these radiotracers are directly affected by their physical characteristics. ^{15}O-H_2O is distinguished by the fact that it has a 100% extraction fraction into myocardial tissue [129]. This means that any reduction in myocardial blood flow is directly proportional to and quantified by its myocardial uptake. ^{13}N-NH_3 has an extraction fraction of ~80%, which makes it less accurate than ^{15}O-H_2O in quantifying blood flow [130]. Its longer half-life, however, can enable exercise stress testing under research conditions but is not practical for routine clinical use. The recent success of ^{82}RbCl is predicated on the fact that it is generator-derived. This allows a continuous supply of radiotracer for four to six weeks and moreover, it is produced by the generator to dose patients every 10 minutes [92]. Although it has the lowest extraction fraction of the PET agents (50–65%), PET with ^{82}Rb has better diagnostic performance in comparison to SPECT with ^{99m}Tc MPI agents, which is the mainstay of cardiac perfusion imaging today [91]. The practicality of ^{82}Rb in comparison to the other currently available PET radiotracers, in addition to its superior performance and lower radiation dose compared to the current standard have resulted in a proliferation of its clinical use as described earlier in this chapter.

15.5.2 Agents for Imaging Tumor Proliferation

^{18}F-Fluorothymidine (^{18}F-FLT) is an analog of the nucleoside thymidine, but the 3′-fluorine atom prevents ^{18}F-FLT from completely following the biochemical pathway of thymidine. After active transport into cells, ^{18}F-FLT is a substrate for thymidine kinase I (TK1) and is phosphorylated but is not incorporated into DNA. Once phosphorylated, ^{18}F-FLT cannot exit the cell and is retained. The accumulation of ^{18}F-FLT within cells is thought to be proportional to TK1 activity. ^{18}F-FLT-PET therefore indirectly enables noninvasive, in vivo assessment of cell proliferation [131]. A correlation has been shown between Ki-67 immunohistochemistry, which measures proliferation in pathology specimens and ^{18}F-FLT uptake in certain malignancies including brain, lung, and breast cancer [132]. ^{18}F-FLT PET may aid in assessing response to systemic therapy, radiotherapy, and concurrent chemoradiotherapy. Furthermore, if validated, ^{18}F-FLT-PET has the potential to contribute to drug development by enabling early assessment of the effectiveness of drugs in the early phases of clinical trials. Persistent abnormal ^{18}F-FLT uptake at tumor sites would imply that an anti-cancer drug either did not reach its target or was ineffective in inhibiting tumor growth. A further advantage of PET in this instance is its ability to noninvasively demonstrate heterogeneity in cell proliferation within a tumor or at various tumor sites, which would not be feasible with random tumor sampling to assess proliferation ex vivo using Ki-67 or other indices.

Numerous studies have evaluated ^{18}F-FLT-PET and ^{18}F-FDG-PET for assessing the response to systemic therapy in cancer patients with variable results. Of clinical concern is data showing that at times changes in both ^{18}F-FLT- and ^{18}F-FDG-PET fail to accurately predict final outcome from therapy [133]. There may be many variables affecting radiotracer uptake after initiating a systemic therapy, including the type and location of tumor, biologic alterations induced by the specific drug being used, timing of the examination in relation to drug delivery, or a combination of these. For example, for patients with NHL treated with standard R-CHOP regimen (cyclophosphamide, doxorubicin, vincristine, and prednisolone with rituximab), lower mean SUVmean values on ^{18}F-FLT PET before initiation of therapy correlated with a higher rate of CR [134]. Similarly, a study on patients with non-small cell lung cancer treated with the tyrosine kinase inhibitor (TKI) erlotinib showed that lower maximum SUVmax values in the tumor on ^{18}F-FLT-PET at baseline proved to be a prognostic indicator and correlated with response to treatment and prolonged survival [135]. Decreased ^{18}F-FLT uptake within a tumor on sequential scans before and after initiation of therapy can predict response to therapy, presumably due to a decrease in proliferation rate and demand for thymidine as a response to systemic therapy. As an example, a study by Contractor et al. assessing the response of 20 patients with breast cancer to therapy with docetaxel has shown that the decrease in ^{18}F-FLT uptake on PET was significantly different for responders than nonresponders [136]. Therapies that interfere with endogenous thymidine synthesis (such as 5-fluorouracil used in CRC) may increase TK1 activity and if ^{18}F-FLT-PET is performed, a "flare" phenomenon may be observed, with an inverse correlation between the degree of the flare and therapy outcome [137].

The ability of ^{18}F-FLT-PET to predict response to radiotherapy is variable. A correlation has been shown between decreased ^{18}F-FLT uptake in the tumor and radiotherapy outcome in patients with head and neck cancer with changes in FLT preceding decrease in tumor volume [138], but no correlation has been found between ^{18}F-FLT uptake in non-small cell lung cancer and therapy response, the development of local recurrence or metastases or survival [139]. The results of the latter trial may have been hampered by radiation-induced pneumonitis, which confounded quantitation of tumor response.

In general, the results of initial trials suggest that ^{18}F-FLT-PET may be used as a biomarker for early response to systemic therapy, radiotherapy, or chemoradiotherapy. For many tumor types, a correlation between ^{18}F-FLT uptake and progression-free survival (PFS) is demonstrated although this correlation is less consistent when assessing overall patient survival (OS). It remains to be determined whether ^{18}F-FLT-PET can impact outcome in patients when used to tailor therapy for tumor subvolumes with higher proliferation index on PET.

15.5.3 Agents for Tumor Receptor Imaging

15.5.3.1 ^{68}Ga-DOTATATE

The most promising PET radiotracers for the evaluation of NETs include GDT, ^{68}Ga-DOTANOC, and ^{68}Ga-DOTATOC, which are somatostatin analogs labeled with the generator-produced and short-lived positron-emitter, ^{68}Ga (half-life = 68 minutes). These agents behave similarly, exploiting the overexpression of SSTRs in neuroendocrine malignancies, and demonstrate essentially equivalent diagnostic performance [130, 140]. As a family of SSTR-imaging radiotracers (GDx), they are superior to ^{18}F-FDOPA and ^{18}F-FDG [141]. They also offer logistical advantages given their technically more facile production since they can be prepared from a radiopharmaceutical kit (see Chapter 4) and as mentioned, ^{68}Ga is prepared from the ^{68}Ge/^{68}Ga generator providing a reliable and continuous source of the radionuclide.

GDx tracers result in more accurate diagnosis and staging when compared to accepted standards for evaluation of patients with NETs. In a prospective study of 131 patients, PET with GDT was compared to SPECT/CT with ^{111}In-pentetreotide, which also probes SSTRs, and CT for the detection of gastero-entero-pancreatic tumors [142]. There was a significant difference between imaging modalities for lesion detection with 95.1% of lesions detected with GDT, 45.3% with CT, and 30.9% with ^{111}In-pentetreotide. This led to a change in management in 32.8% of patients due to additional lesions detected with GDT, compared to CT and ^{111}In-pentreotide. However, outcome data proving the impact of these management changes are unfortunately lacking to date.

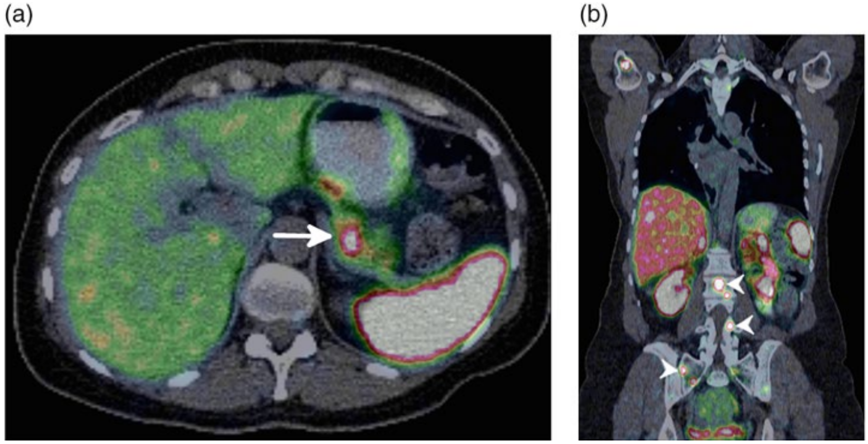

Figure 15.6 A 56-year-old woman after resection of a small bowel neuroendocrine tumor, with lung metastasis. Restaging ^{68}Ga-DOTATATE-PET/CT was performed prior to treatment with peptide receptor radionuclide therapy (PRRT). On PET, there is clear evidence for ^{68}Ga-DOTATATE avid disease in her pancreas (arrow) (a) and skeleton (arrowheads) (b). As most of her known metastases show high ^{68}Ga-DOTATATE uptake, the patient was found eligible for PRRT. (*See insert for color representation of the figure*.)

A growing array of therapeutic options is available for the treatment of NETs and GDx tracers are emerging as critical tools in directing patients to appropriate therapies. Briefly, therapeutic pathways for patients with NETs include surgery, treatment with somatostatin analogs (e.g. octreotide), biologically targeted therapy (e.g. everolimus), chemotherapy, and peptide receptor radionuclide therapy (PRRT) (e.g. ^{177}Lu-DOTATE, ^{90}Y-DOTATOC) (Figure 15.6). GDx tracers provide a valuable tool to select the appropriate treatment strategy for these patients, specifically altering surgical strategies or selection of the most appropriate systemic approaches [143–145].

GDx-PET has resulted in the largest and growing current clinical implementation to date of a concept known as "*theranostics*." Tumors that accumulate GDT are more highly differentiated, i.e. express SSTR and are therefore suitable targets for ^{177}Lu-DOTATATE therapy [146]. GDT uptake correlates with tumor grade and has been shown to decrease from G1 to G3 (well differentiated to poorly differentiated) tumors [147]. If the tumor is targeted by this radiotracer, it follows that the patient would respond favorably to treatment with ^{177}Lu-DOTATATE [146]. The pharmaceutical (or drug delivery mechanism) is the same as the diagnostic agent (GDT) with the radioactive moiety exchanged to transform the agent from a diagnostic agent with radiation suitable only for imaging, to a therapeutic agent that emits beta radiation, which enables therapy. This represents a significant advancement from using SPECT radiotracers such as ^{111}In-pentreotide only to identify neuroendocrine malignancies suitable for treatment with somatostatin drug analogs.

15.5.3.2 Imaging PSMA in Prostate Cancer

Prostate cancer is one of the most common types of cancer worldwide, and is the second to third most common cause of cancer-related mortality in men, after lung and CRC [148]. Although prostate cancer is prevalent, and can be found in 30–40% of men at age 60, the risk of clinically evident or fatal prostate cancer is low, <10%. Over two-thirds of men diagnosed with prostate cancer present with disease localized to the prostate gland with low prostatic-specific antigen (PSA) levels and low-grade cancer (low "Gleason score"). As treatment choice is highly dependent on disease stage, whether at presentation or at time of recurrence, diagnostic studies are critical to properly select patients for the appropriate treatment, and therefore improving their disease-free and overall survival rates.

When disease is localized to the prostate, it can be treated with several modalities, including surgical radical prostatectomy or radiotherapy. Careful consideration should be given to proper patient selection for this curative-intent therapy, as these treatments have been shown to be effective only when disease is localized. To date, the standard method of staging patients presenting with prostate cancer includes MR of the prostate, for detection and local staging of the tumor, and CT of the abdomen and bone scan, for detection of lymph node and distant metastases. It is estimated that using these methods, up to 40% of patients thought to have disease confined to the prostate harbor metastases, especially lymph node metastases. This fact may explain the fact that up to a third of patients treated for a presumed localized disease, later develop recurrence, identified by early increase in PSA levels on serial tests after initial treatment ("biochemical recurrence"). Although this may be due to local disease recurrence, some of these may be due to lymph node or distant metastases overlooked at initial staging using conventional workup algorithms. If a biochemical recurrence occurs, restaging the patient's disease is performed using the same conventional methods, i.e. MR of the pelvis to detect local tumor recurrence and CT abdomen and bone scan to identify lymph node or distant metastases. As in initial staging, these standard imaging modalities have low sensitivity for identifying disease beyond the prostate bed. This may result in inappropriate patient management.

In an attempt to improve the low diagnostic accuracy of conventional imaging, studies have examined the use of PET for prostate cancer patients. These were performed using both ^{18}F-FDG and more recently ^{18}F-choline-based radiotracers (see Chapter 4). These show better accuracy than standard radiological imaging methods, but still have limited sensitivity and specificity for local recurrence, lymph node, and distant metastases. The limitations of all these methods resulted in a search for a new, more accurate radiotracer for imaging prostate cancer.

PSMA is a transmembrane protein expressed on the surface of prostate cancer cells, whether located in the prostate gland or in metastatic sites. PSMA expression in cancer cells is significantly elevated as the grade and stage of prostate cancer increases, and even to a higher degree in cancers that did not respond well to previous androgen-targeted treatments ("castrate-resistant"), with up to a 100-fold increase. Owing to this fact, PSMA has become a promising target for molecular imaging in these patients. Imaging is performed using a radio-labeled PSMA inhibitor (such as ^{68}Ga-PSMA of ^{18}F-DCFPyL), which binds with high affinity to PSMA. Studies using these PSMA tracers for prostate cancer were performed, both in the initial staging of prostate cancer patients, and in first or second disease recurrence. Overall, these studies clearly show that in both scenarios, PSMA-PET has better accuracy in locating sites of disease, both when combined with CT or with MRI [127, 149–152].

When PSMA imaging is used for initial staging of patients with high-risk disease (tumors that extend beyond the prostate or that have a high Gleason score, or patients with serum PSA >20 ng ml^{-1}), PSMA-PET was found to have a detection rate of 40–80% for extra-prostatic spread of disease (lymph node or distant metastases). It was also shown that the higher the presenting PSA levels at disease diagnosis, the better PSMA can accurately stage the patient's disease. For patients suspected to have recurrent disease, imaging using PSMA is able to locate foci of recurrence, whether located in the surgical prostatic bed, in lymph nodes, or distant metastases, in 50–75% of patients. As is the case with initial staging, PSMA has better detection rates when PSA levels are higher, but may be positive in cases of low PSA, when conventional imaging workup and ^{18}F-choline PET are negative. Overall, PSMA PET has a high specificity, exceeding 85%, for identifying disease sites in the initial staging of high-risk prostate cancer or at time of biochemical recurrence; and is markedly more accurate than standard imaging methods or PET performed with ^{18}F-FDG or ^{18}F-Choline [153]. With the emerging data on the value of PSMA-PET in prostate cancer patients, and especially if impact on patient outcome is proven, PSMA-based imaging may be incorporated into routine clinical practice facilitating accurate and personalized patient care.

15.5.4 Imaging Tumor Hypoxia

Hypoxia occurs in the development of solid tumors, in areas where the consumption of oxygen outpaces the delivery from the vascular system. It is a negative prognostic factor in many tumors, and predictive of metastatic spread and poor responsiveness to both chemotherapy and radiotherapy [154–157]. Hypoxia may diminish the effectiveness of radiotherapy since radiation depends on the formation of oxygen-free radicals to inflict DNA damage, resulting in tumor resistance. Hypoxia-induced resistance to chemotherapy is multifactorial, and includes decreased drug activity with reduced oxygen or pH changes, reduced tumor cell proliferation, induction of prosurvival gene expression, and difficulty in drug diffusion from the vasculature [154]. For example, in CRC, it has been shown that increasing transcription factor hypoxia inducible factor 1α (HIF-1α) activity reduces the efficacy of 5-fluorouoracil, the backbone of chemotherapy in CRC and a radiosensitizer in the context of chemoradiotherapy [155]. HIF-1α has been associated with poor prognosis in certain tumors. It has been suggested that hypoxic regions may provide a protective niche for cancer stem-like cells, preventing their eradication with chemotherapy and/or radiotherapy and providing a permissive environment for tumor recurrence [157]. Data from preclinical xenograft models in CRC, glioblastoma, and cervical cancers indicate that hypoxic areas are associated with increased numbers of cancer stem-like cells and worse prognosis tumors. Hence there is a rationale for the identification of hypoxic rectal cancers, for both prognostication, and for stratification of response to chemotherapy.

Measurement of hypoxia in tumors may be direct (e.g. use of a polarographic needle electrode inserted into a tumor), or indirect (e.g. blood oxygen level-dependent [BOLD] MRI). In recent years, there has been a growing interest in the development of imaging agents for PET to noninvasively assess tumor hypoxia. The advantages of PET in imaging of tumor hypoxia include the ability of PET to evaluate the entire tumor, overcoming the limitations of direct assessment, which include sampling error and tumor heterogeneity with variable presence of hypoxia throughout the tumor. PET can also be repeated over time to demonstrate changes in hypoxia within the tumor, before and after therapy. PET of tumor hypoxia uses hypoxia-sensitive imaging radiotracers, usually nitroimidazoles, labeled with a positron emitter (such as ^{18}F or ^{64}Cu). These radiotracers undergo chemical reduction under hypoxic conditions, which causes them to bind to macromolecules in hypoxic cells (see Chapter 4) thereby enabling spatial localization of the distribution of hypoxia within the tumor [158–161]. They are not reduced and exported from normal cells, thus providing good demarcation between hypoxic and normoxic tissues. Examples of nitroimidazoles used in PET include ^{18}F-fluoromisonidazole (^{18}F-FMISO), ^{18}F-EF5, ^{18}F-fluoroazomycin arabinoside (^{18}F-FAZA), and ^{64}Cu(II)-diacetyl-bis(N^4-methylthiosemicarbazone) (^{64}Cu-ATSM). Pretreatment PET imaging of tumor hypoxia in patients with head and neck cancer (^{18}F-FMISO) or cervix cancer (^{64}Cu-ATSM) has been shown to correlate with clinical outcome following radiotherapy [161, 162]. A recent study evaluating sequential ^{18}F-FAZA PET scans in patients with head and neck cancers has shown that ^{18}F-FAZA-PET can delineate hypoxic volumes and therefore may be used to individualize radiation therapy by escalating the dose to hypoxic regions within the tumor [163]. However, changes in hypoxia during treatment may necessitate repeated scans, which is termed “adaptive radiotherapy.”

15.6 Multimodal Imaging – PET/CT Versus PET/MR

15.6.1 Technical Challenges in PET/MR

In recent years, technological advances have enabled the integration of PET and MRI into a single imaging system to exploit the high sensitivity of PET for molecular imaging with the exquisite anatomical spatial resolution of MRI. The development of these multimodal PET-MRI systems required solutions to the technical problems of integrating a PET detector ring along with its electronics within a strong magnetic field without significant interference. In particular, the photomultiplier tubes (PMTs) in a PET detector are especially sensitive to the magnetic field (see Chapter 3). Different approaches have been used to solve this problem. One relatively simple approach was to place the MRI and modified PET components in tandem, much like the configuration of a PET-CT scanner. While this obviates the need to develop a new PET-MRI compatible system, it does not allow simultaneous acquisition of data that necessitates longer scan times (as PET and MRI data are obtained separately) and results in a much larger physical footprint for the scanner. These limitations have been resolved in the recently introduced integrated PET-MRI scanners [164].

The technical obstacle that had to be addressed in the development of an integrated PET-MRI system included the development of MRI-compatible PET detectors that are not sensitive to magnetic fields and readout electronics. Most PET detectors used clinically have been based on an array of inorganic scintillation crystals optically coupled to PMTs, which enable determination of the position, energy, and time of a 511 keV photon incident on the crystals resulting from the positron decay [165]. However, standard PMTs are highly sensitive to magnetic fields. To resolve this problem, robust MRI-compatible solid-state photodetectors such as avalanche photodiodes or silicon photomultipliers have been developed. Silicon photomultipliers feature high sensitivity and fast coincidence timing resolution enabling time-of-flight (TOF) reconstruction (see Chapter 3). This enables more precise localization of the positron event, leading to improved image quality with a better signal-to-noise ratio. There are also negative effects of insertion of a PET detector ring into the MRI gantry, which include electromagnetic interference by the PET detector and electronics. The presence of PET hardware within the gradient coil would result in gradient imperfections, which would degrade imaging spatial resolution, scan time, and image homogeneity. This problem was addressed by removing as much of the PET electronics out of the gantry and into an equipment room, routing of cabling through radiofrequency (RF) filters, and covering of the PET detector modules with copper foil to shield RF noise. Studies have shown that this configuration results in equivalent RF noise whether the PET detectors are powered on or off [166].

Although integrated PET-MR scanners are clinically available, adoption of PET-MRI into clinical use is dependent on identification of clinical indications where PET-MRI would be advantageous over PET-CT, and especially where simultaneous acquisition of PET and MRI data results in clinically pertinent information not available on separate acquisition of PET and MRI. In the following section the current clinical evidence in the literature for the use of PET-MRI is discussed.

15.6.2 Current Status of Clinical PET/MRI

PET/MRI is a promising technology that may change diagnosis and management in oncology patients. PET/MRI can offer some advantages over PET/CT. Although not expected to replace PET/CT, which is the mainstay in current oncologic molecular imaging, PET/MRI can offer advantages in scenarios where staging can be enhanced by the increased contrast resolution of MRI such as in head and neck structures, or in the pelvis. It also excels in local staging, which can potentially result in "one-stop" staging exams when certain technical limitations, discussed above, are overcome and the costs of this technology decline to a level that is fiscally feasible.

In the limited studies available to date, PET/MRI has shown similar diagnostic performance as PET/CT in malignancies of the head and neck, and thorax. Specifically, in head and neck cancer, no significant difference has been shown in diagnostic performance when comparing PET/CT to PET/MRI in local tumor staging and diagnosis of recurrence [167, 168]. Similarly for thyroid cancer, no significant difference has been found in detecting local relapse, or lymph node and bone metastases, with a lower detection rate for lung metastases [169]. In lung cancer, PET/MRI offers no significant advantage for detecting lymph node metastases or determining resectability [170]. In a study population with resectable esophageal cancer, there was no significant difference between PET/MRI and PET/CT in detecting lymph node metastases [171].

PET/MRI is more effective than PET/CT in defining the local extent of disease in patients with breast cancer while having equal performance when detecting lymph node metastases [172]. In another study, PET/MRI detected more bone metastases with a sensitivity of 96.3 versus 85.2% for PET/CT resulting in management changes [173]. PET/MRI also excels in detecting liver metastases [174]. Studies so far have shown similar performance when comparing PET/MRI and PET/CT in detecting recurrent female pelvic malignancies, especially cervical and uterine cancer [175, 176].

Based on the early evidence to date, PET/MRI appears to be comparable to PET/CT and in some specific use scenarios, superior. PET/MRI excels at local tumor characterization and is comparable when assessing nodal and distant metastatic disease. However, given the scarcity of data, as well as heterogeneity of the imaging protocols and study methodologies, the role of PET/MRI in clinical practice remains to be defined. Well-designed prospective cohort or randomized controlled trials evaluating the impact of PET/MRI on predefined clinical outcomes such as management changes and survival are necessary. In an increasing fiscally challenging health care environment, cost-effectiveness analyses are vital to justify the increased cost of PET/MRI examinations, specifically comparing integrated PET/MRI with the current standard practice of obtaining PET/CT and site-specific MRI on separate visits.

15.7 Summary

Over the past two decades, PET imaging has been incorporated into routine clinical practice for many oncology indications as well as a few cardiovascular and neurologic applications. The vast majority of clinical PET examinations performed are with ^{18}F-FDG, a glucose analog, but there is an increasing use of other probes to assess perfusion, proliferation, hypoxia, or expression of receptors. In the coming decades, we will likely see an increase in the use of PET using novel probes to assess for the presence of specific features of a disease process, clinically and in research. These unique molecular imaging techniques may improve individualized therapy planning and may result in improved therapy outcome.

References

1 Thakur, M. and Lentle, B.C. (2005). Report of a summit on molecular imaging. *Radiology* 236: 753–755.

2 Townsend, D.W., Carney, J.P., Yap, J.T., and Hall, N.C. (2004). PET/CT today and tomorrow. *J. Nucl. Med.* 45 (Suppl 1): 4S–14S.

3 Metser, U., Miller, E., Lerman, H., and Even-Sapir, E. (2007). Benign nonphysiologic lesions with increased ^{18}F-FDG uptake on PET/CT: characterization and incidence. *AJR Am. J. Roentgenol.* 189: 1203–1210.

4 Sainz-Esteban, A., Prasad, V., Schuchardt, C. et al. (2012). Comparison of sequential planar ^{177}Lu-DOTA-TATE dosimetry scans with ^{68}Ga-DOTA-TATE PET/CT images in patients with metastasized neuroendocrine tumours undergoing peptide receptor radionuclide therapy. *Eur. J. Nucl. Med. Mol. Imaging* 39: 501–511.

5 Pauwels, E.K., Ribeiro, M.J., Stoot, J.H. et al. (1998). FDG accumulation and tumor biology. *Nucl. Med. Biol.* 25: 317–322.

6 Bar-Shalom, R., Yefremov, N., Guralnik, L. et al. (2003). Clinical performance of PET/CT in evaluation of cancer: additional value for diagnostic imaging and patient management. *J. Nucl. Med.* 44: 1200–1209.

7 Martin, R.C., Fulham, M., Shannon, K.F. et al. (2009). Accuracy of positron emission tomography in the evaluation of patients treated with chemoradiotherapy for mucosal head and neck cancer. *Head Neck* 31: 244–250.

8 Gregory, D.L., Hicks, R.J., Hogg, A. et al. (2012). Effect of PET/CT on management of patients with non-small cell lung cancer: results of a prospective study with 5-year survival data. *J. Nucl. Med.* 53: 1007–1015.

9 Hillner, B.E., Siegel, B.A., Hanna, L. et al. (2012). Impact of ^{18}F-FDG PET used after initial treatment of cancer: comparison of the National Oncologic PET Registry 2006 and 2009 cohorts. *J. Nucl. Med.* 53: 831–837.

10 Fletcher, J.W., Kymes, S.M., Gould, M. et al. (2008). A comparison of the diagnostic accuracy of ^{18}F-FDG PET and CT in the characterization of solitary pulmonary nodules. *J. Nucl. Med.* 49: 179–185.

11 Lowe, V.J., Fletcher, J.W., Gobar, L. et al. (1998). Prospective investigation of positron emission tomography in lung nodules. *J. Clin. Oncol.* 16: 1075–1084.

12 Nomori, H., Watanabe, K., Ohtsuka, T. et al. (2004). Evaluation of F-18 fluorodeoxyglucose (FDG) PET scanning for pulmonary nodules less than 3 cm in diameter, with special reference to the CT images. *Lung Cancer* 45: 19–27.

13 Ost, D.E. and Gould, M.K. (2012). Decision making in patients with pulmonary nodules. *Am. J. Respir. Crit. Care Med.* 185: 363–372.

14 Darling, G., Maziak, D., Inculet, R. et al. (2009). PET-CT compared to invasive mediastinal staging in non-small cell lung cancer (NSCLC). *J. Clin. Oncol.* 27: 7575.

15 Darling, G.E., Maziak, D.E., Inculet, R.I. et al. (2011). Positron emission tomography-computed tomography compared with invasive mediastinal staging in non-small cell lung cancer: results of mediastinal staging in the early lung positron emission tomography trial. *J. Thorac. Oncol.* 6: 1367–1372.

16 Fischer, B., Lassen, U., Mortensen, J. et al. (2009). Preoperative staging of lung cancer with combined PET-CT. *N. Engl. J. Med.* 361: 32–39.

17 Maziak, D.E., Darling, G.E., Inculet, R.I. et al. (2009). Positron emission tomography in staging early lung cancer: a randomized trial. *Ann. Intern. Med.* 151: 221–228. W-248.

18 MacManus, M.P., Hicks, R.J., Matthews, J.P. et al. (2001). High rate of detection of unsuspected distant metastases by PET in apparent stage III non-small-cell lung cancer: implications for radical radiation therapy. *Int. J. Radiat. Oncol. Biol. Phys.* 50: 287–293.

19 Goldstraw, P., Chansky, K., Crowley, J. et al. (2016). The IASLC lung cancer staging project: proposals for revision of the TNM stage groupings in the forthcoming (eighth) edition of the TNM classification for lung cancer. *J. Thorac. Oncol.* 11: 39–51.

20 Novoa, N.M., Varela, G., and Jimenez, M.F. (2016). Surgical management of oligometastatic non-small cell lung cancer. *J. Thorac. Dis.* 8: S895–S900.

21 Grills, I.S., Mangona, V., Welsh, R. et al. (2009). Outcomes after stereotactic lung radiotherapy or wedge resection for stage I non-small cell lung cancer (NSCLC). *J. Clin. Oncol.* 27: 7516.

22 Xu, Y., Ma, S., Yu, D. et al. (2009). FDG-PET/CT imaging for staging and definition of tumor volumes in radiation treatment planning in non-small cell lung cancer. *J. Clin. Oncol.* 27: 7574.

23 Ambrogi, M.C., Lucchi, M., Dini, P. et al. (2006). Percutaneous radiofrequency ablation of lung tumours: results in the mid-term. *Eur. J. Cardiothorac. Surg.* 30: 177–183.

24 Singnurkar, A., Solomon, S.B., Gonen, M. et al. (2010). ^{18}F-FDG PET/CT for the prediction and detection of local recurrence after radiofrequency ablation of malignant lung lesions. *J. Clin. Oncol.* 51: 1833–1840.

25 Higuchi, M., Honjo, H., Shigihara, T. et al. (2014). A phase II study of radiofrequency ablation therapy for thoracic malignancies with evaluation by FDG-PET. *J. Cancer Res. Clin. Oncol.* 140: 1957–1963.

26 Alafate, A., Shinya, T., Okumura, Y. et al. (2013). The maximum standardized uptake value is more reliable than size measurement in early follow-up to evaluate potential pulmonary malignancies following radiofrequency ablation. *Acta Med. Okayama* 67: 105–112.

27 Jimenez-Bonilla, J.F., Quirce, R., Martinez-Rodriguez, I. et al. (2013). Diagnosis of recurrence and assessment of post-recurrence survival in patients with extracranial non-small cell lung cancer evaluated by ^{18}F-FDG PET/CT. *Lung Cancer* 81: 71–76.

28 Paesmans, M., Berghmans, T., Dusart, M. et al. (2010). Primary tumor standardized uptake value measured on fluorodeoxyglucose positron emission tomography is of prognostic value for survival in non-small cell lung cancer: update of a systematic review and meta-analysis by the European Lung Cancer Working Party for the International Association for the Study of Lung Cancer Staging Project. *J. Thorac. Oncol.* 5: 612–619.

29 Berghmans, T., Dusart, M., Paesmans, M. et al. (2008). Primary tumor standardized uptake value (SUVmax) measured on fluorodeoxyglucose positron emission tomography (FDG-PET) is of prognostic value for survival in non-small cell lung cancer (NSCLC): a systematic review and meta-analysis (MA) by the European Lung Cancer Working Party for the IASLC Lung Cancer Staging Project. *J. Thorac. Oncol.* 3: 6–12.

30 Campo, E., Swerdlow, S.H., Harris, N.L. et al. (2011). The 2008 WHO classification of lymphoid neoplasms and beyond: evolving concepts and practical applications. *Blood* 117: 5019–5032.

31 Issa, D.E., van de Schans, S.A.M., Chamuleau, M.E.D. et al. (2015). Trends in incidence, treatment and survival of aggressive B-cell lymphoma in the Netherlands 1989–2010. *Haematologica* 100: 525–533.

32 Hasenclever, D., Diehl, V., Armitage, J. et al. (1998). A prognostic score for advanced Hodgkin's disease. International Prognostic Factors Project on Advanced Hodgkin's Disease. *N. Engl. J. Med.* 339: 1506–1514.

33 Cheson, B.D., Fisher, R.I., Barrington, S.F. et al. (2014). Recommendations for initial evaluation, staging, and response assessment of Hodgkin and non-Hodgkin lymphoma: the Lugano classification. *J. Clin. Oncol.* 32: 3059–3068.

34 Weiler-Sagie, M., Bushelev, O., Epelbaum, R. et al. (2010). ^{18}F-FDG avidity in lymphoma readdressed: a study of 766 patients. *J. Nucl. Med.* 51: 25–30.

35 Barrington, S.F., Mikhaeel, N.G., Kostakoglu, L. et al. (2014). Role of imaging in the staging and response assessment of lymphoma: Consensus of the International Conference on Malignant Lymphomas Imaging Working Group. *J. Clin. Oncol.* 32: 3048–3058.

36 Horning, S.J. and Rosenberg, S.A. (1984). The natural history of initially untreated low-grade non-Hodgkin's lymphomas. *N. Engl. J. Med.* 311: 1471–1475.

37 Guadagnolo, B.A., Li, S., Neuberg, D. et al. (2006). Long-term outcome and mortality trends in early-stage, grade 1–2 follicular lymphoma treated with radiation therapy. *Int. J. Radiat. Oncol. Biol. Phys.* 64: 928–934.

38 Metser, U., Hussey, D., and Murphy, G. (2014). Impact of ^{18}F-FDG PET/CT on the staging and management of follicular lymphoma. *Br. J. Radiol.* 87: 20140360.

39 Hutchings, M., Loft, A., Hansen, M. et al. (2006). Position emission tomography with or without computed tomography in the primary staging of Hodgkin's lymphoma. *Haematologica* 91: 482–489.

40 Rigacci, L., Vitolo, U., Nassi, L. et al. (2007). Positron emission tomography in the staging of patients with Hodgkin's lymphoma: a prospective multicentric study by the Intergruppo Italiano Linfomi. *Ann. Hematol.* 86: 897–903.

41 Raanani, P., Shasha, Y., Perry, C. et al. (2006). Is CT scan still necessary for staging in Hodgkin and non-Hodgkin lymphoma patients in the PET/CT era? *Ann. Oncol.* 17: 117–122.

42 Barrington, S.F., Kirkwood, A.A., Franceschetto, A. et al. (2016). PET-CT for staging and early response: results from the Response-Adapted Therapy in Advanced Hodgkin Lymphoma study. *Blood* 127: 1531–1538.

43 El-Galaly, T.C., d'Amore, F., Mylam, K.J. et al. (2012). Routine bone marrow biopsy has little or no therapeutic consequence for positron emission tomography/computed tomography-staged treatment-naïve patients with Hodgkin lymphoma. *J. Clin. Oncol.* 30: 4508–4514.

44 Johnson, P., Federico, M., Kirkwood, A. et al. (2016). Adapted treatment guided by interim PET-CT scan in advanced Hodgkin's lymphoma. *N. Engl. J. Med.* 374: 2419–2429.

45 https://seer.cancer.gov/statfacts/html/esoph.html (accessed 29 August 2018).

46 Karl, R.C., Schreiber, R., Boulware, D. et al. (2000). Factors affecting morbidity, mortality and survival in patients undergoing Ivor Lewis esophagogastrectomy. *Ann. Surg.* 231: 635–643.

47 Reed, C.E., Mishra, G., Sahai, A.V. et al. (1999). Esophageal cancer staging: improved accuracy by endoscopic ultrasound of celiac lymph nodes. *Ann. Thorac. Surg.* 67: 319–322.

48 Romagnuolo, J., Scott, J., Hawes, R.H. et al. (2002). Helical CT versus EUS with fine needle aspiration for celiac nodal assessment in patients with esophageal cancer. *Gastrointest. Endosc.* 55: 648–654.

49 van Vliet, E.P., Heijenbrok-Kal, M.H., Hunink, M.G. et al. (2008). Staging investigations for oesophageal cancer: a meta-analysis. *Br. J. Cancer* 98: 547–557.

50 You, J.J., Wong, R.K., Darling, G. et al. (2013). Clinical utility of ^{18}F-fluorodeoxyglucose positron emission tomography/computed tomography in the staging of patients with potentially resectable esophageal cancer. *J. Thorac. Oncol.* 8: 1563–1569.

51 Bedenne, L., Michel, P., Bouche, O. et al. (2007). Chemoradiation followed by surgery compared with chemoradiation alone in squamous cancer of the esophagus: FFCD 9102. *J. Clin. Oncol.* 25: 1160–1168.

52 Stahl, M., Stuschke, M., Lehmann, N. et al. (2005). Chemoradiation with and without surgery in patients with locally advanced squamous cell carcinoma of the esophagus. *J. Clin. Oncol.* 23: 2310–2317.

53 Monjazeb, A.M., Riedlinger, G., Aklilu, M. et al. (2010). Outcomes of patients with esophageal cancer staged with [^{18} F]fluorodeoxyglucose positron emission tomography (FDG-PET): can postchemoradiotherapy FDG-PET predict the utility of resection? *J. Clin. Oncol.* 28: 4714–4721.

54 Siegel, R., Naishadham, D., and Jemal, A. (2013). Cancer statistics, 2013. *CA Cancer J. Clin.* 63: 11–30.

55 MERCURY Study Group (2007). Extramural depth of tumor invasion at thin-section MR in patients with rectal cancer: results of the MERCURY study. *Radiology* 243: 132–139.

56 Brush, J., Boyd, K., Chappell, F. et al. (2011). The value of FDG positron emission tomography/computerized tomography (PET/CT) in pre-operative staging of colorectal cancer: a systematic review and economic evaluation. *Health Technol. Assess.* 15: 1–192. iii–iv.

57 House, M.G., Ito, H., Gönen, M. et al. (2010). Survival after hepatic resection for metastatic colorectal cancer: trends in outcomes for 1,600 patients during two decades at a single institution. *J. Am. Coll. Surg.* 210: 744–752. 752-755.

58 Altendorf-Hofmann, A. and Scheele, J. (2003). A critical review of the major indicators of prognosis after resection of hepatic metastases from colorectal carcinoma. *Surg. Oncol. Clin. N. Am.* 12: 165–192.

59 Ruers, T.J., Wiering, B., van der Sijp, J.R. et al. (2009). Improved selection of patients for hepatic surgery of colorectal liver metastases with ^{18}F-FDG PET: a randomized study. *J. Nucl. Med.* 50: 1036–1041.

60 Moulton, C.A., Gu, C.S., Law, C.H. et al. (2014). Effect of PET before liver resection on surgical management for colorectal adenocarcinoma metastases: a randomized clinical trial. *JAMA* 311: 1863–1869.

61 Metser, U., Halankar, J., Langer, D. et al. (2017). Effect of chemotherapy on the impact of FDG-PET/CT in selection of patients for surgical resection of colorectal liver metastases: single center analysis of PET-CAM randomized trial. *Ann. Nucl. Med.* 31 (2): 153–162.

62 Locker, G.Y., Hamilton, S., Harris, J. et al. (2006). ASCO 2006 update of recommendations for the use of tumor markers in gastrointestinal cancer. *J. Clin. Oncol.* 24: 5313–5327.

63 Cohen, A.M., Minsky, B.D., and Schilsky, R.L. (1993). Colon cancer. In: *Cancer: Principles and Practice of Oncology*, 4e (ed. V.T. DeVita Jr., S. Hellman and S.A. Rosenberg), 929–977. Philadelphia, PA: Lippincott.

64 Kitajima, K., Murakami, K., Yamasaki, E. et al. (2009). Performance of integrated FDG PET/contrast-enhanced CT in the diagnosis of recurrent colorectal cancer: comparison with integrated FDG PET/non-contrast-enhanced CT and enhanced CT. *Eur. J. Nucl. Med. Mol. Imaging* 36: 1388–1396.

65 Metser, U., You, J., McSweeney, S. et al. (2010). Assessment of tumor recurrence in patients with colorectal cancer and elevated carcinoembryonic antigen level: FDG PET/CT versus contrast-enhanced 64-MDCT of the chest and abdomen. *AJR Am. J. Roentgenol.* 194: 766–771.

66 Lee, J.H., Park, S.G., Jee, K.N. et al. (2010). Performance of FDG PET/CT in postoperative colorectal cancer patients with a suspected recurrence and a normal CEA level. *Nucl. Med. Commun.* 31: 576–582.

67 Kyoto, Y., Momose, M., Kondo, C. et al. (2010). Ability of ^{18}F-FDG PET/CT to diagnose recurrent colorectal cancer in patients with elevated CEA concentrations. *Ann. Nucl. Med.* 24: 395–401.

68 Krabbe, C.A., Balink, H., Roodenburg, J.L. et al. (2011). Performance of ^{18}F-FDG PET/contrast-enhanced CT in the staging of squamous cell carcinoma of the oral cavity and oropharynx. *Int. J. Oral Maxillofac. Surg.* 40: 1263–1270.

69 Tahari, A.K., Alluri, K.C., Quon, H. et al. (2014). FDG PET/CT imaging of oropharyngeal squamous cell carcinoma: characteristics of human papillomavirus-positive and -negative tumors. *Clin. Nucl. Med.* 39: 225–231.

70 Guntinas-Lichius, O., Peter Klussmann, J., Dinh, S. et al. (2006). Diagnostic work-up and outcome of cervical metastases from an unknown primary. *Acta Otolaryngol.* 126: 536–544.

71 Pavlidis, N., Briasoulis, E., Hainsworth, J. et al. (2003). Diagnostic and therapeutic management of cancer of an unknown primary. *Eur. J. Cancer* 39: 1990–2005.

72 Rusthoven, K.E., Koshy, M., and Paulino, A.C. (2004). The role of fluorodeoxyglucose positron emission tomography in cervical lymph node metastases from an unknown primary tumor. *Cancer* 101: 2641–2649.

73 Johansen, J., Petersen, H., Godballe, C. et al. (2011). FDG-PET/CT for detection of the unknown primary head and neck tumor. *Q. J. Nucl. Med. Mol. Imaging* 55: 500–508.

74 Waltonen, J.D., Ozer, E., Hall, N.C. et al. (2009). Metastatic carcinoma of the neck of unknown primary origin: evolution and efficacy of the modern workup. *Arch. Otolaryngol. Head Neck Surg.* 135: 1024–1029.

75 Roh, J.L., Park, J.P., Kim, J.S. et al. (2014). ^{18}F fluorodeoxyglucose PET/CT in head and neck squamous cell carcinoma with negative neck palpation findings: a prospective study. *Radiology* 271: 153–161.

76 Nguyen, A., Luginbuhl, A., Cognetti, D. et al. (2014). Effectiveness of PET/CT in the preoperative evaluation of neck disease. *Laryngoscope* 124: 159–164.

77 Piao, Y., Bold, B., Tayier, A. et al. (2009). Evaluation of 18F-FDG PET/CT for diagnosing cervical nodal metastases in patients with oral cavity or oropharynx carcinoma. *Oral Surg. Oral Med. Oral Pathol. Oral Radiol. Endod.* 108: 933–938.

78 Kovacs, A.F., Dobert, N., Gaa, J. et al. (2004). Positron emission tomography in combination with sentinel node biopsy reduces the rate of elective neck dissections in the treatment of oral and oropharyngeal cancer. *J. Clin. Oncol.* 22: 3973–3980.

79 Ahmad, A. and Stefani, S. (1986). Distant metastases of nasopharyngeal carcinoma: a study of 256 male patients. *J. Surg. Oncol.* 33: 194–197.

80 Shen, G., Zhang, W., Jia, Z. et al. (2014). Meta-analysis of diagnostic value of ^{18}F-FDG PET or PET/CT for detecting lymph node and distant metastases in patients with nasopharyngeal carcinoma. *Br. J. Radiol.* 87: 20140296.

81 Chan, S.C., Wang, H.M., Yen, T.C. et al. (2011). ^{18}F-FDG PET/CT and 3.0-T whole-body MRI for the detection of distant metastases and second primary tumours in patients with untreated oropharyngeal/hypopharyngeal carcinoma: a comparative study. *Eur. J. Nucl. Med. Mol. Imaging* 38: 1607–1619.

82 Krabbe, C.A., Pruim, J., Dijkstra, P.U. et al. (2009). ^{18}F-FDG PET as a routine posttreatment surveillance tool in oral and oropharyngeal squamous cell carcinoma: a prospective study. *J. Nucl. Med.* 50: 1940–1947.

83 Xu, G.Z., Guan, D.J., and He, Z.Y. (2011). ^{18}FDG-PET/CT for detecting distant metastases and second primary cancers in patients with head and neck cancer. A meta-analysis. *Oral. Oncol.* 47: 560–565.

84 Hanna, E., Alexiou, M., Morgan, J. et al. (2004). Intensive chemoradiotherapy as a primary treatment for organ preservation in patients with advanced cancer of the head and neck: efficacy, toxic effects, and limitations. *Arch. Otolaryngol. Head Neck Surg.* 130: 861–867.

85 Liauw, S.L., Mancuso, A.A., Amdur, R.J. et al. (2006). Postradiotherapy neck dissection for lymph node-positive head and neck cancer: the use of computed tomography to manage the neck. *J. Clin. Oncol.* 24: 1421–1427.

86 Mehanna, H., Wong, W.L., McConkey, C.C. et al. (2016). PET-CT surveillance versus neck dissection in advanced head and neck cancer. *N. Engl. J. Med.* 374: 1444–1454.

87 Al-Nahhas, A., Khan, S., Gogbashian, A. et al. (2008). Review: ^{18}F-FDG PET in the diagnosis and follow-up of thyroid malignancy. *In Vivo* 22: 109–114.

88 Robbins, R.J., Wan, Q., Grewal, R.K. et al. (2006). Real-time prognosis for metastatic thyroid carcinoma based on 2-[^{18}F] fluoro-2-deoxy-D-glucose-positron emission tomography scanning. *J. Clin. Endocrinol. Metab.* 91: 498–505.

89 Merhige, M.E., Breen, W.J., Shelton, V. et al. (2007). Impact of myocardial perfusion imaging with PET and ^{82}Rb on downstream invasive procedure utilization, costs, and outcomes in coronary disease management. *J. Nucl. Med.* 48: 1069–1076.

90 Mc Ardle, B.A., Dowsley, T.F., deKemp, R.A. et al. (2012). Does rubidium-82 PET have superior accuracy to SPECT perfusion imaging for the diagnosis of obstructive coronary disease?: a systematic review and meta-analysis. *J. Am. Coll. Cardiol.* 60: 1828–1837.

91 Bateman, T.M., Heller, G.V., McGhie, A.I. et al. (2006). Diagnostic accuracy of rest/stress ECG-gated Rb-82 myocardial perfusion PET: comparison with ECG-gated Tc-99m sestamibi SPECT. *J. Nucl. Cardiol.* 13: 24–33.

92 Di Carli, M.F., Dorbala, S., Meserve, J. et al. (2007). Clinical myocardial perfusion PET/CT. *J. Nucl. Med.* 48: 783–793.

93 Murthy, V.L., Naya, M., Foster, C.R. et al. (2011). Improved cardiac risk assessment with noninvasive measures of coronary flow reserve. *Circulation* 124: 2215–2224.

94 Lim, S.P., Mc Ardle, B.A., Beanlands, R.S. et al. (2014). Myocardial viability: it is still alive. *Semin. Nucl. Med.* 44: 358–374.

95 Beanlands, R.S., Nichol, G., Huszti, E. et al. (2007). F-18-fluorodeoxyglucose positron emission tomography imaging-assisted management of patients with severe left ventricular dysfunction and suspected coronary disease: a randomized, controlled trial (PARR-2). *J. Am. Coll. Cardiol.* 50: 2002–2012.

96 Schinkel, A.F., Bax, J.J., Poldermans, D. et al. (2007). Hibernating myocardium: diagnosis and patient outcomes. *Curr. Probl. Cardiol.* 32: 375–410.

97 Birnie, D.H., Nery, P.B., Ha, A.C. et al. (2016). Cardiac sarcoidosis. *J. Am. Coll. Cardiol.* 68: 411–421.

98 Iwai, K., Tachibana, T., Takemura, T. et al. (1993). Pathological studies on sarcoidosis autopsy. I. Epidemiological features of 320 cases in Japan. *Acta Pathol. Jpn.* 43: 372–376.

99 Perry, A. and Vuitch, F. (1995). Causes of death in patients with sarcoidosis: a morphologic study of 38 autopsies with clinicopathologic correlations. *Arch. Pathol. Lab. Med.* 119: 167–172.

100 Gauthier, S., Patterson, C., Chertkow, H. et al. (2012). Recommendations of the 4th Canadian consensus conference on the diagnosis and treatment of dementia (CCCDTD4). *Can. Geriatr. J.* 15: 120–126.

101 Patwardhan, M.B., McCrory, D.C., Matchar, D.B. et al. (2004). Alzheimer disease: operating characteristics of PET – a meta-analysis. *Radiology* 231: 73–80.

102 Bloudek, L.M., Spackman, D.E., Blankenburg, M. et al. (2011). Review and meta-analysis of biomarkers and diagnostic imaging in Alzheimer's disease. *J. Alzheimers Dis.* 26: 627–645.

103 Cerami, C., Dodich, A., Greco, L. et al. (2017). The role of single-subject brain metabolic patterns in the early differential diagnosis of primary progressive aphasias and in prediction of progression to dementia. *J. Alzheimers Dis.* 55: 183–197.

104 Frey, K.A. and Petrou, M. (2015). Imaging amyloidopathy in Parkinson disease and parkinsonian dementia syndromes. *Clin. Transl. Imaging* 3: 57–64.

105 Ossenkoppele, R., Jansen, W.J., Rabinovici, G.D. et al. (2015). Prevalence of amyloid PET positivity in dementia syndromes: a meta-analysis. *JAMA* 313: 1939–1949.

106 Ergun, E.L., Saygi, S., Yalnizoglu, D. et al. (2016). SPECT-PET in epilepsy and clinical approach in evaluation. *Semin. Nucl. Med.* 46: 294–307.

107 Wallach, P.M., O'Donnell, L.R., Leibowitz, A.I. et al. (1991). Symptomatic adult polycystic liver disease in a young woman. *J. Fla. Med. Assoc.* 78: 637–640.

108 Burneo, J.G., Poon, R., Kellett, S., and Snead, O. (2015). The utility of positron emission tomography in epilepsy. *Can. J. Neurol. Sci.* 42: 360–371.

109 Kubota, R., Yamada, S., Kubota, K. et al. (1992). Intratumoral distribution of fluorine-18-fluorodeoxyglucose in vivo: high accumulation in macrophages and granulation tissues studied by microautoradiography. *J. Nucl. Med.* 33: 1972–1980.

110 Treglia, G., Taralli, S., and Giordano, A. (2011). Emerging role of whole-body ^{18}F-fluorodeoxyglucose positron emission tomography as a marker of disease activity in patients with sarcoidosis: a systematic review. *Sarcoidosis Vasc. Diffuse Lung Dis.* 28: 87–94.

111 Youssef, G., Leung, E., Mylonas, I. et al. (2012). The use of ^{18}F-FDG PET in the diagnosis of cardiac sarcoidosis: a systematic review and metaanalysis including the Ontario experience. *J. Nucl. Med.* 53: 241–248.

112 Valeyre, D., Prasse, A., Nunes, H. et al. (2014). Sarcoidosis. *Lancet* 383: 1155–1167.

113 Bleeker-Rovers, C.P. and van der Meer, J.W.M. (2015). Fever of unknown origin. In: *Harrison's Principles of Internal Medicine*, 19e (ed. A. Fauci, S. Hauser, D. Longo, et al.), 135–142. New York: McGraw Hill.

114 Bleeker-Rovers, C.P., Vos, F.J., Mudde, A.H. et al. (2007). A prospective multi-centre study of the value of FDG-PET as part of a structured diagnostic protocol in patients with fever of unknown origin. *Eur. J. Nucl. Med. Mol. Imaging* 34: 694–703.

115 Takeuchi, M., Dahabreh, I.J., Nihashi, T. et al. (2016). Nuclear imaging for classic fever of unknown origin: meta-analysis. *J. Nucl. Med.* 57: 1913–1919.

116 Granados, U., Fuster, D., Pericas, J.M. et al. (2016). Diagnostic accuracy of ^{18}F-FDG PET/CT in infective endocarditis and implantable cardiac electronic device infection: a cross-sectional study. *J. Nucl. Med.* 57: 1726–1732.

117 Sah, B.R., Husmann, L., Mayer, D. et al. (2015). Diagnostic performance of ^{18}F-FDG-PET/CT in vascular graft infections. *Eur. J. Vasc. Endovasc. Surg.* 49: 455–464.

118 Tokuda, Y., Oshima, H., Araki, Y. et al. (2013). Detection of thoracic aortic prosthetic graft infection with 18F-fluorodeoxyglucose positron emission tomography/computed tomography. *Eur. J. Cardiothorac. Surg.* 43: 1183–1187.

119 Ahmed, F.Z., James, J., Cunnington, C. et al. (2015). Early diagnosis of cardiac implantable electronic device generator pocket infection using ^{18}F-FDG-PET/CT. *Eur. Heart J. Cardiovasc. Imaging* 16: 521–530.

120 Even-Sapir, E., Metser, U., Mishani, E. et al. (2006). The detection of bone metastases in patient with high-risk prostate cancer: ^{99}mTc-MDP planar bone scintigraphy, single- and -field-of view SPECT, ^{18}F-fluoride PET, and ^{18}F-fluoride PET/CT. *J. Nucl. Med.* 47: 287–297.

121 Jackowski, S. (1994). Coordination of membrane phospholipid synthesis with the cell cycle. *J. Biol. Chem.* 269: 3858–3867.

122 Postema, E.J., McEwan, A.J., Riauka, T.A. et al. (2009). Initial results of hypoxia imaging using 1-alpha-D: -(5-deoxy-5-[^{18}F]-fluoroarabinofuranosyl)-2-nitroimidazole (18F-FAZA). *Eur. J. Nucl. Med. Mol. Imaging* 36: 1565–1573.

123 Luxen, A., Guillaume, M., Melega, W.P. et al. (1992). Production of 6-[^{18}F] fluoro-L-dopa and its metabolism in vivo – a critical review. *Int. J. Rad. Appl. Instrum. B* 19: 149–158.

124 Vesselle, H., Grierson, J., Muzi, M. et al. (2002). In vivo validation of 30 deoxy-30-[$^{(18)}$F]fluorothymidine ([(18)F]FLT) as a proliferation imaging tracer in humans: correlation of [$^{(18)}$F]FLT uptake by positron emission tomography with PET radiochemistry and radiopharmacy 29 Ki-67 immunohistochemistry and flow cytometry in human lung tumors. *Clin. Cancer Res.* 8: 3315–3323.

125 El Fakhri, G., Kardan, A., Sitek, A. et al. (2009). Reproducibility and accuracy of quantitative myocardial blood flow assessment with ^{82}Rb PET: comparison with ^{13}N-ammonia PET. *J. Nucl. Med.* 50: 1062–1071.

126 Deppen, S.A., Blume, J., Bobbey, A.J. et al. (2016). ^{68}Ga-DOTATATE compared with 111In-DTPA-octreotide and conventional imaging for pulmonary and gastroenteropancreatic neuroendocrine tumors: a systematic review and meta-analysis. *J. Nucl. Med.* 57: 872–878.

127 Eiber, M., Maurer, T., Souvatzoglou, M. et al. (2015). Evaluation of hybrid ^{68}Ga-PSMA ligand PET/CT in 248 patients with biochemical recurrence after radical prostatectomy. *J. Nucl. Med.* 56: 668–674.

128 Heo, R., Nakazato, R., Kalra, D. et al. (2014). Noninvasive imaging in coronary artery disease. *Semin. Nucl. Med.* 44: 398–409.

129 Bol, A., Melin, J.A., Vanoverschelde, J.L. et al. (1993). Direct comparison of [^{13}N]ammonia and [^{15}O]water estimates of perfusion with quantification of regional myocardial blood flow by microspheres. *Circulation* 87: 512–525.

130 Johnbeck, C.B., Knigge, U., and Kjaer, A. (2014). PET tracers for somatostatin receptor imaging of neuroendocrine tumors: current status and review of the literature. *Future Oncol.* 10: 2259–2277.

131 Shields, A.F., Grierson, J.R., Dohmen, B.M. et al. (1998). Imaging proliferation in vivo with [18F]FLT and positron emission tomography. *Nat. Med.* 4 (11): 1334–1336.

132 Chalkidou, A., Landau, D.B., Odell, E.W. et al. (2012). Correlation between Ki-67 immunohistochemistry and ^{18}F-fluorothymidine uptake in patients with cancer: a systematic review and meta-analysis. *Eur. J. Cancer* 48: 3499–3513.

133 Jensen, M.M. and Kjaer, A. (2015). Monitoring of anti-cancer treatment with ^{18}F-FDG and ^{18}F-FLT PET: a comprehensive review of pre-clinical studies. *Am. J. Nucl. Med. Mol. Imaging* 12: 431–456.

134 Herrmann, K., Buck, A.K., Schuster, T. et al. (2011). Predictive value of initial ^{18}F-FLT uptake in patients with aggressive non-Hodgkin lymphoma receiving R-CHOP treatment. *J. Nucl. Med.* 52: 690–696.

135 Scheffler, M., Zander, T., Nogova, L. et al. (2013). Prognostic impact of [^{18}F] fluorothymidine and [^{18}F]fluoro-D-glucose baseline uptakes in patients with lung cancer treated first-line with erlotinib. *PLoS One* 8: e53081.

136 Contractor, K.B., Kenny, L.M., Stebbing, J. et al. (2011). [^{18}F]-3′deoxy-3′-fluorothymidine positron emission tomography and breast cancer response to docetaxel. *Clin. Cancer Res.* 17: 7664–7672.

137 Hong, Y.S., Kim, H.O., Kim, K.P. et al. (2013). 39-Deoxy-39-^{18}F-fluorothymidine PET for the early prediction of response to leucovorin, 5-fluorouracil, and oxaliplatin therapy in patients with metastatic colorectal cancer. *J. Nucl. Med.* 54: 1209–1216.

138 Menda, Y., Boles Ponto, L.L., Dornfeld, K.J. et al. (2009). Kinetic analysis of 3′-deoxy-3′-(^{18})F-fluorothymidine ((18)F-FLT) in head and neck cancer patients before and early after initiation of chemoradiation therapy. *J. Nucl. Med.* 50: 1028–1035.

139 Saga, T., Koizumi, M., Inubushi, M. et al. (2011). PET/CT with 3′-deoxy-3′-[^{18}F]fluorothymidine for lung cancer patients receiving carbon-ion radiotherapy. *Nucl. Med. Commun.* 32: 348–355.

140 Virgolini, I., Ambrosini, V., Bomanji, J.B. et al. (2010). Procedure guidelines for PET/CT tumour imaging with ^{68}Ga-DOTA-conjugated peptides: ^{68}Ga-DOTA-TOC, ^{68}Ga-DOTA-NOC, ^{68}Ga-DOTA-TATE. *Eur. J. Nucl. Med. Mol. Imaging* 37: 2004–2010.

141 Janssen, I., Blanchet, E.M., Adams, K. et al. (2015). Superiority of [^{68}Ga]-DOTATATE PET/CT to other functional imaging modalities in the localization of SDHB-associated metastatic pheochromocytoma and paraganglioma. *Clin. Cancer Res.* 21: 3888–3895.

142 Sadowski, S.M., Neychev, V., Millo, C. et al. (2016). Prospective study of ^{68}Ga-DOTATATE positron emission tomography/computed tomography for detecting gastro-entero-pancreatic neuroendocrine tumors and unknown primary sites. *J. Clin. Oncol.* 34: 588–596.

143 Prasad, V., Steffen, I.G., Pavel, M. et al. (2015). Somatostatin receptor PET/CT in restaging of typical and atypical lung carcinoids. *EJNMMI Res.* 5: 53.

144 Cives, M., Soares, H.P., and Strosberg, J. (2016). Will clinical heterogeneity of neuroendocrine tumors impact their management in the future? Lessons from recent trials. *Curr. Opin. Oncol.* 28: 359–366.

145 Singh, S., Asa, S.L., Dey, C. et al. (2016). Diagnosis and management of gastrointestinal neuroendocrine tumors: an evidence-based Canadian consensus. *Cancer Treat. Rev.* 47: 32–45.

146 Campana, D., Ambrosini, V., Pezzilli, R. et al. (2010). Standardized uptake values of ^{68}Ga-DOTANOC PET: a promising prognostic tool in neuroendocrine tumors. *J. Nucl. Med.* 51: 353–359.

147 Kloppel, G. (2011). Classification and pathology of gastroenteropancreatic neuroendocrine neoplasms. *Endocr. Relat. Cancer* 18 (Suppl 1): S1–S16.

148 Parkin, D.M., Ferlay, J., Curado, M.P. et al. (2010). Fifty years of cancer incidence: CI5 I–IX. *Int. J. Cancer* 127: 2918–2927.

149 Afshar-Oromieh, A., Avtzi, E., Giesel, F.L. et al. (2015). The diagnostic value of PET/CT imaging with the ^{68}Ga-labelled PSMA ligand HBED-CC in the diagnosis of recurrent prostate cancer. *Eur. J. Nucl. Med. Mol. Imaging* 42: 197–209.

150 Ceci, F., Uprimny, C., Nilica, B. et al. (2015). ^{68}Ga-PSMA PET/CT for restaging recurrent prostate cancer: which factors are associated with PET/CT detection rate? *Eur. J. Nucl. Med. Mol. Imaging* 42: 1284–1294.

151 Eyben, F.E., Picchio, M., Eyben, R. et al. (2016). ^{68}Ga-labelled prostate-specific membrane antigen ligand positron emission tomography/computed tomography for prostate cancer: a systematic review and meta-analysis. *Eur. Urol. Focus* pii: S2405-4569(16)30160-2. doi: 10.1016/j.euf.2016.11.002.

152 Perera, M., Papa, N., Christidis, D. et al. (2016). Sensitivity, specificity, and predictors of positive 68Ga-prostate-specific membrane antigen positron emission tomography in advanced prostate cancer: a systematic review and meta-analysis. *Eur. Urol.* 70 (6): 926–937.

153 Afshar-Oromieh, A., Haberkorn, U., Eder, M. et al. (2012). [^{68}Ga]-labelled PSMA ligand as superior PET tracer for the diagnosis of prostate cancer: comparison with 18F-FECH. *Eur. J. Nucl. Med. Mol. Imaging* 39: 1085–1086.

154 Bristow, R.G. and Hill, R.P. (2008). Hypoxia and metabolism. Hypoxia, DNA repair and genetic instability. *Nat. Rev. Cancer* 8: 180–192.

155 Ravizza, R., Molteni, R., Gariboldi, M.B. et al. (2009). Effect of HIF-1 modulation on the response of two- and three-dimensional cultures of human colon cancer cells to 5-fluorouracil. *Eur. J. Cancer* 45: 890–898.

156 Mao, Q., Zhang, Y., Fu, X. et al. (2013). A tumor hypoxic niche protects human colon cancer stem cells from chemotherapy. *J. Cancer Res. Clin. Oncol.* 39: 211–222.

157 Saigusa, S., Tanaka, K., Toiyama, Y. et al. (2011). Clinical significance of CD133 and hypoxia inducible factor-1α gene expression in rectal cancer after preoperative chemoradiotherapy. *Clin. Oncol. (R. Coll. Radiol.)* 23: 323–332.

158 Krohn, K.A., Link, J.M., and Mason, R.P. (2008). Molecular imaging of hypoxia. *J. Nucl. Med.* 49 (Suppl 2): 129S–148S.

159 Lee, S.T. and Scott, A.M. (2007). Hypoxia positron emission tomography imaging with ^{18}F-fluoromisonidazole. *Semin. Nucl. Med.* 37: 451–461.

160 Thorwarth, D., Eschmann, S.M., Paulsen, F., and Alber, M. (2005). A kinetic model for dynamic [^{18}F]-Fmiso PET data to analyse tumour hypoxia. *Phys. Med. Biol.* 50: 2209–2224.

161 Thorwarth, D., Eschmann, S.M., Scheiderbauer, J. et al. (2005). Kinetic analysis of dynamic ^{18}F-fluoromisonidazole PET correlates with radiation treatment outcome in head-and-neck cancer. *BMC Cancer* 5: 152.

162 Dehdashti, F., Grigsby, P.W., Lewis, J.S. et al. (2008). Assessing tumor hypoxia in cervical cancer by PET with ^{60}Cu-labeled diacetyl-bis(N^4-methylthiosemicarbazone). *J. Nucl. Med.* 49: 201–205.

163 Servagi-Vernat, S., Differding, S., Hanin, F.X. et al. (2014). A prospective clinical study of ^{18}F-FAZA PET-CT hypoxia imaging in head and neck squamous cell carcinoma before and during radiation therapy. *Eur. J. Nucl. Med. Mol. Imaging* 41: 1544–1552.

164 Vandenberghe, S. and Marsden, P.K. (2015). PET-MRI: a review of challenges and solutions in the development of integrated multimodality imaging. *Phys. Med. Biol.* 60: R115–R154.

165 Muzic, R.F. and DiFilippo, F.P. (2014). PET/MRI – technical review. *Semin. Roentgenol.* 49: 242–254.

166 Delso, G., Furst, S., Jakoby, B. et al. (2011). Performance measurements of the Siemens mMR integrated whole-body PET/MR scanner. *J. Nucl. Med.* 52: 1914–1922.

167 Kubiessa, K., Purz, S., Gawlitza, M. et al. (2014). Initial clinical results of simultaneous ^{18}F-FDG PET/MRI in comparison to ^{18}F-FDG PET/CT in patients with head and neck cancer. *Eur. J. Nucl. Med. Mol. Imaging* 41: 639–648.

168 Schaarschmidt, B.M., Heusch, P., Buchbender, C. et al. (2016). Locoregional tumour evaluation of squamous cell carcinoma in the head and neck area: a comparison between MRI, PET/CT and integrated PET/MRI. *Eur. J. Nucl. Med. Mol. Imaging* 43: 92–102.

169 Vrachimis, A., Burg, M.C., Wenning, C. et al. (2016). [^{18}F]FDG PET/CT outperforms [(18)F]FDG PET/MRI in differentiated thyroid cancer. *Eur. J. Nucl. Med. Mol. Imaging* 43: 212–220.

170 Fraioli, F., Screaton, N.J., Janes, S.M. et al. (2015). Non-small-cell lung cancer resectability: diagnostic value of PET/MR. *Eur. J. Nucl. Med. Mol. Imaging* 42: 49–55.

171 Paspulati, R.M., Partovi, S., Herrmann, K.A. et al. (2015). Comparison of hybrid FDG PET/MRI compared with PET/CT in colorectal cancer staging and restaging: a pilot study. *Abdom. Imaging* 40: 1415–1425.

172 Grueneisen, J., Nagarajah, J., Buchbender, C. et al. (2015). Positron emission tomography/magnetic resonance imaging for local tumor staging in patients with primary breast cancer: a comparison with positron emission tomography/computed tomography and magnetic resonance imaging. *Invest. Radiol.* 50: 505–513.

173 Catalano, O.A., Nicolai, E., Rosen, B.R. et al. (2015). Comparison of CE-FDG-PET/CT with CE-FDG-PET/MR in the evaluation of osseous metastases in breast cancer patients. *Br. J. Cancer* 112: 1452–1460.

174 Melsaether, A.N., Raad, R.A., Pujara, A.C. et al. (2016). Comparison of whole-body ^{18}F FDG PET/MR imaging and whole-body ^{18}F FDG PET/CT in terms of lesion detection and radiation dose in patients with breast cancer. *Radiology* 281: 193–202.

175 Beiderwellen, K., Grueneisen, J., Ruhlmann, V. et al. (2015). [^{18}F]FDG PET/MRI vs. PET/CT for whole-body staging in patients with recurrent malignancies of the female pelvis: initial results. *Eur. J. Nucl. Med. Mol. Imaging* 42: 56–65.

176 Grueneisen, J., Schaarschmidt, B.M., Heubner, M. et al. (2015). Implementation of FAST-PET/MRI for whole-body staging of female patients with recurrent pelvic malignancies: a comparison to PET/CT. *Eur. J. Radiol.* 84: 2097–2102.

Index

a

abdominal imaging
  acute peritoneal pathologies
    ascites 268–269
    hemoperitoneum 267–268
    peritoneal carcinomatosis 269–270
    pneumoperitoneum 266–267
  bile ducts 304–306
  biliary tract 300–301
  colorectal adenocarcinoma 282, 285–287
  diffuse hepatic disease 289–292
  focal hepatic disease (*see* focal hepatic disease)
  gallbladder 301–304
  GI/digestive tract
    appendicitis 277–278
    bowel obstruction 271–274
    diverticulitis 274–277
  hepatic system 287, 289
  inflammatory bowel disease (*see* inflammatory bowel disease)
  pancreas
    acute pancreatitis 306–308
    chronic pancreatitis 310
    pancreatic ductal adenocarcinoma 311–313
    pancreatic neoplasms 310–311
    pancreatic trauma 309
  peritoneum/mesentery 265–266
  spleen/lymph nodes 313–316
  surgical sieve 265
abnormal vaginal bleeding 350, 351
absolute percentage of washout (APW) 250, 251
acoustic impedance 109
acute abdomen 277
acute appendicitis 277, 278
acute cecal diverticulitis 276
acute cholecystitis 302–304
acute diverticulitis 274–276
acute encephalitis 380, 382
acute large bowel obstruction 274, 275
acute orbital trauma 390–392
acute osteomyelitis 418
acute pancreatitis 306–308
acute pelvic pain 355–356
acute peritoneal pathology
  ascites 268–269
  hemoperitoneum 267–268
  peritoneal carcinomatosis 269–270
  pneumoperitoneum 266–267
acute pulmonary embolism 170
acute surgical abdomen 271

Medical Imaging for Health Professionals: Technologies and Clinical Applications, First Edition.
Edited by Raymond M. Reilly.
© 2019 John Wiley & Sons, Inc. Published 2019 by John Wiley & Sons, Inc.

adalimumab 424
adnexal masses 354–356
adrenal glands 249–250
adrenal myelolipoma 253
adrenocortical adenoma 250–252
adrenocortical carcinoma (ACC) 252–253
aerodigestive mucosa 394
aerodigestive tract 240, 453
aggressive lymphoma 445–446
Alzheimer's dementia 382, 384
Alzheimer's disease (AD) 455, 456
American Association for the Surgery of Trauma (AAST) classification system 315
American College of Radiology (ACR) 328, 407
American Thyroid Association in 2015 240
amyloid arthropathy 421
Anger camera 31–32
angiomyolipomas 333, 361
angiotensin converting enzyme (ACE)-inhibitor 332
angular momentum 88
ankylosing spondylitis 387, 388, 391, 421, 423
ankylosis 423
antipsychotics 398
appendicitis 277–278
appendicolith 277
arthritis 408
  ankylosing spondylitis 423
  biologic agents 424
  depositional and crystal-induced 421
  Doppler US 424–425
  gout and septic 423
  inflammatory 420–421, 424
  MRI 425–427
  noninflammatory 421, 422
  psoriatic 422
  radiographs 421
ascites 268–269
asthma 166
autoimmune hypothyroidism 237
autoimmune thyroiditis 234

b

balanced steady-state free precession (b-SSFP) technique 118
bamboo spine 388
barium enteroclysis 279
benign osseous lesions 427
Bethesda System for Reporting Thyroid Cytopathology 241
bilateral multifocal post-viral *Streptococcus* pneumonia 159–160
bile ducts
  biliary dilation 304–305
  neoplasms 305–306
biliary tract 300–301
biophysical profile (BPP) 359
BI-RADS assessment category 209, 214, 215
bismuth germinate (BGO) 28
black/dark-blood sequences 118
bladder cancer 343, 344
bladder injury 343–344
blood oxygenation level dependent (BOLD) 397
body contouring 38
bone imaging, radiopharmaceuticals 77–79
bone loss 418
bony erosion 418
bowel ischemia 273
bowel obstruction 271–274
brain activation 397
brain/CNS imaging
  ^{11}C-flumazenil 72, 74
  ^{11}C-methylspiperone 72–73
  ^{11}C-raclopride 72–73
  ^{18}F-fluorodeoxyglucose 70
  ^{18}F-fluorodopa 72–73

  ^{23}I-iodobenzamide 72–73
  ^{123}I-iomazenil 74
  ^{111}In-diethylenetriaminepentaacetic acid 74
  ^{13}N ammonia 72
  ^{15}O water 72
  radiopharmaceuticals used 70–71
  ^{99m}Tc-ethyl cysteinate dimer 72
  ^{99m}Tc-hexamethylpropylene amine oxime 70, 72
brain cortical blood flow (rCBF) 396
brain imaging
  dementia 382, 384
  infection imaging 379–383
  inflammatory/metabolic lesions 382
  PET and SPECT 396–401
  trauma 372–373
  tumor imaging 378–379
  vascular imaging 372–379
BRCA1 and BRCA2 genes 355
breast cancer
  anatomy 189–191
  benign *vs.* malignant imaging features 203–205
  BI-RADS assessment categories 209, 214, 215
  breast masses 203, 206–213
  breast tomosynthesis 197
  contrast-enhanced spectral mammography 202–203
  extramammary staging 219–220
  high-risk screening 188–189
  image-guided breast intervention 209, 212, 216–219
  image review and mammography views 192–193
  imaging techniques 191
  lymphoscintigraphy 220
  mammographic BI-RADS lexicon 196
  mammography system 191
  MRI 198–202
  normal mammogram 193–195
  PEM and breast-specific gamma camera imaging 202
  risk factors for 186–187
  screening in average risk women 188
  screening *vs.* diagnostic mammogram 195
  ultrasound BI-RADS lexicon 198–199
  ultrasound technique 198
breast imaging *see also* breast cancer
breast lymphoscintigraphy 220
breast masses
  axillary masses 207, 212
  breast asymmetries 207, 209, 213
  breast calcifications 207, 212, 213
  circumscribed solid masses 203, 207, 208
  cystic breast masses 207, 210
  fat-containing breast masses 203, 206
  malignant masses 207, 211
breast MRI 198–202
breast MRI BI-RADS 201–202
breast-specific gamma camera imaging 202
breast-specific gamma imaging/molecular breast imaging (BSGI/MBI) 202
breast tomosynthesis 197
Bremsstrahlung X-rays 11–13
bright-blood sequences 118
bronchiectasis 165–166
bronchopneumonia 158
brown tumors 428

C

calcium pyrophosphate depositional disease (CPDD) 421
calculi 328

cancer
  bladder 343, 344
  breast (*see* breast cancer)
  cervical 353, 354
  colorectal 450–451
  endometrial 351–353
  esophageal 448–450
  lung (*see* lung cancer)
  ovarian 354–356
  pancreatic 312, 314
  prostate 465–466
  testicles 345–346
  thyroid 240–244
  tonsillar 395
Colorectal cancer (CRC) 284, 450–451, 467
carcinoembryonic antigen (CEA) 451
carcinoid tumors 258–259
cardiac imaging
  cardiovascular MRI techniques 117–129
  echocardiography 129–133
  ^{18}F-2-fluorodeoxyglucose 60, 63
  ^{123}I-metaiodobenzylguanidine 60, 63
  MUGA scans 58
  ^{13}N ammonia 62
  nuclear cardiology 133–140
  ^{15}O water 62
  ^{82}Rb rubidium chloride 62
  ^{99m}Tc-labeled red blood cells 58
  ^{99m}Tc red blood cells 62–63
  ^{99m}Tc-sestamibi 58–60
  ^{99m}Tc-tetrofosmin 58–61
  ^{201}Tl thallous chloride 61
cardiac PET imaging 453–455
cardiac sarcoidosis 458
Cardiolite 134
cardiovascular MRI (CMR) techniques 117–118
  cardiac anatomy 118–119
  cardiac function 118–121
  imaging modalities 126–129
  myocardial tissue characterization 119–120, 122–125
  myocardial viability 124–125
  prognostic value of LGE imaging 125–127
cavernous hemangioma 293, 294
^{11}C choline PET/CT 349
cecal diverticulitis 274, 276
CECT *see* contrast-enhanced CT (CECT)
cellulitis 417
centrilobular emphysema 163–164
cerebral blood flow (CBF) 374
cerebral blood volume (CBV) 374
cervical cancer 353, 354
^{11}C-flumazenil 72, 74
characteristic X-rays 11–13
charge-coupled devices (CCD) 16
chemoradiotherapy 449
chest CT 155–157
chest radiograph 146–148
chest X-ray 15–16
  airways 148–151
  chest wall 155
  colorectal cancer 285
  diaphragm 155
  heart 154–155
  mediastinum 154
  pleural space 152–153
  pulmonary hila 149, 152
  radiographic density and pulmonary markings 152–153
cholangiocarcinoma 305
choledocholithiasis 301, 303
cholelithiasis 301–302
chronic bronchitis 164–165
chronic obstructive pulmonary disease (COPD)
  asthma 166
  bronchiectasis 165–166
  chronic bronchitis 164–165
  emphysema 163–164
chronic pancreatitis 310

^{11}C-methylspiperone 72–73
cognitive behavioral therapy 401
cold nodules 230, 232, 233
collimator design 34–35
colonoscopy 284
colorectal adenocarcinoma
  imaging 285–288
  screening 282, 284–285
colorectal cancer 450–451
colorectal liver metastases 297, 298
colorectal screening program 284
color flow Doppler US 112
computed tomography (CT) imaging
  adrenal lesions 250
  appendicitis 277, 278
  ascites 269
  attenuation of an X-ray beam 16
  bile duct dilation 304, 305
  biliary tract 300
  biopsy of bone lesions 410, 411
  bone marrow metastases 385, 388
  of brain 373, 375
  carcinoid tumors 258–259
  colorectal cancer 286
  cone beam 17–18
  contrast agents 21–23
  Crohn's disease 279
  cysts 294, 295
  dementia 382, 384
  diffuse hepatic fat/steatosis 289, 290
  diverticulitis 274
  encephalitis 379, 380, 382
  fan beam 17
  focal splenic masses 316
  gallstones 301
  GU tract 326
  HCC 299, 300
  headache 378
  hemangioma 293, 294
  hemoperitoneum 268
  hepatic system 287
  image acquisition 18–20
  image reconstruction 20–21
  lymph nodes 316
  musculoskeletal disorders 408–411
  occult fractures 416
  osteomyelitis 385
  pancreatic necrosis 308
  PanNET 255, 257, 258
  polyps 303
  renal and ureteric collecting system 340
  SBO 272, 273
  spine trauma 383, 385
  ureteric assessment 339
cone beam CT 17–18
congenital anomalies 360–361
contrast agents (CA) 21–23, 112–113
contrast-enhanced CT (CECT)
  acute cholecystitis 302, 303
  acute diverticulitis 274, 276
  acute pancreatitis 307
  aerodigestive mucosa 394
  chronic pancreatitis 310, 311
  hepatic abscesses 292, 293
  hypervascular liver metastases 296, 298
  LBO 273–275
  pancreatic adenocarcinoma 312, 313
  pancreatic trauma 309
  pelvis 345, 346
  splenic trauma 315
  ulcerative colitis 281, 283
contrast-enhanced spectral mammography (CESM) 202–203
COPD *see* chronic obstructive pulmonary disease (COPD)
cord astrocytoma 389
cord neoplasia 385
coronary flow reserve (CFR) 454
coronary reserve 135
^{11}C-raclopride 72–73
Crohn's disease (CD) 279–280

crystal-induced arthritis 421
CT *see* computed tomography (CT) imaging
CT angiogram (CTA)
  head and neck 372, 376
  renal arteries 332, 333
CT colonography (CTC) 284, 285
CT cystogram 344, 345
CT urography (CTU) 343
CTU urogram 340–342
culprit diverticulum 274
cumulative radioactivity 6
curative therapy 448
cyclotron production 50–53
cystic renal disease 361
cystic tumors 311
cystoscopy 343
cysts 294–295

d

Deauville score 446, 447
Definity® 112, 113
dementia 382, 384
dementia with Lewy Bodies (DLB) 455, 456
dementing syndromes 456
demyelinating processes 388
depositional arthritis 421
depression 400
de Quervain thyroiditis 234
diffuse axonal injury (DAI) 372, 374
diffuse hepatic disease
  fatty infiltration 289–290
  hepatic cirrhosis 290–292
diffuse syndesmophytes 387
digital breast tomosynthesis (DBT) 197
disease modifying antirheumatic drugs (DMARDs) 424
diskitis 385, 387, 390
distal interphalangeal joints (DIP) 423
diverticulitis 274–277
dopamine 397, 399
Doppler US 111–112
  arthritis 424–425
  synovitis 415
dose-related acute effects 5
double duct sign 311
dual-energy CT (DECT) 408, 409

e

early gadolinium enhancement (EGE) 120
echocardiography
  cardiac chambers 130–133
  cardiac valves 133
  M-mode and two-dimensional cardiac imaging 129–130
  pericardial disease and the great vessels 133
  two-dimensional and color Doppler 129, 131
echogenic septa 237
effective dose 4
effective renal plasma flow (ERPF) 337
elbow joint effusion 406, 407
electromagnetic radiation 3
embryonic Mullerian duct 360
emphysema 163–164
encephalitis 379, 380, 382
endocrine gland
  adrenal glands 249–250
  adrenal medulla 253–255
  mass lesions, adrenal cortex
    ACC 252–253
    adrenal myelolipoma 253
    adrenocortical adenoma 250–252
  neuroendocrine diseases (*see* neuroendocrine diseases)
  parathyroid glands (PTGs)
    altered production of 244–245
    4D CT imaging 248
    parathyroid adenoma 246–247

    parathyroid carcinoma 248
    parathyroid hyperplasia 247
    primary hyperparathyroidism 245
    secondary and tertiary hyperparathyroidism 248–249
  thyroid
    cancer 240–244
    hormone diseases 227–240
    thyroid gland 225–227
endometrial cancer 351–353
endometrial hyperplasia 352
endoscopic retrograde cholangiopancreatography (ERCP) 302, 308
endoscopic ultrasound (EUS)
  esophageal cancer 448
  pancreatic cancer 312
entriculitis/ependymitis 381
equivalent dose 4
erosive disease 423
esophageal cancer 448–450
etanercept 424
EUS *see* endoscopic ultrasound (EUS)
Ewing sarcoma 429
extramammary staging 219–220
extrapyramidal symptoms 398
exudative ascites 268–269

f
fan beam CT 17
^{18}F-and ^{11}C-choline 66–67
fatty infiltration 289–290
fecal occult blood test (FOBT) 284
female genitourinary tract
  abnormal vaginal bleeding 350, 351
  acute pelvic pain 355–356
  adnexal masses 354–356
  cervical cancer 353, 354
  endometrial cancer 351–353
  obstetrical evaluation 357–358
  ovarian cancer 354–356
  pregnancy
    first trimester 356, 357
    second and third trimester 358–360
fetal anatomic evaluation 358
Fever of Unknown Origin (FUO) 458–459
^{18}F-FAZA PET scans 467
^{18}F-FDG PET/CT
  colorectal cancer 287
  lymph nodes 316
  in non-oncology indications
    cardiac PET imaging 453–455
    in infectious and inflammatory disorders 457–460
    neurological applications of 455–457
  in oncology
    gastrointestinal malignancies 448–451
    head and neck cancers 452–453
    lung cancer management 442–444
    lymphoma 445–448
  pancreatic cancer 312, 314
  peritoneal carcinomatosis 270
^{18}F-FLT-PET 463
1-(5-^{18}F-fluoro-5-deoxy-α–D-arabinofuranosyl)–2–nitroimidazole (^{18}F-FAZA) 66–67
^{18}F-fluorodeoxyglucose (^{18}F-FDG) 64, 66, 70
^{18}F-2-fluorodeoxyglucose (^{18}F-FDG) 60, 440
^{18}F-2-fluorodeoxyglucose (^{18}F-FDG) PET/CT 178, 180
^{18}F-fluorodopa (^{18}F-FDOPA) 72–73
^{18}F-fluoroethyltyrosine (^{18}F-FET) 66–67
6-^{18}F-fluoro-levodopa 399
^{18}F-fluoro-L-thymidine (^{18}F-FLT) 64
^{18}F-fluorothymidine (18F-FLT) 461–462

^{18}F-flutemetamol 456
filtered backprojection 38
FLAIR T2 sequence 382
"flare" phenomenon 462
Fleischner sign 170
flip angle 90–91
fluorine-18 (^{18}F) 50
fluorine-18-labeled fluorodeoxyglucose (^{18}F-FDG) 134
  Alzheimer's Disease and dementia 397
  glucose transporters 440
  interpretation of 440–441
  phosphorylation 440
fluoroscopic contrast enema imaging 275
fluoroscopy 279
focal hepatic disease
  cavernous hemangioma 293, 294
  cysts 294–295
  FNH 295–296
  HCC 299, 300
  hepatic abscess 292, 293
focal nodular hyperplasia (FNH) 295–297
focal splenic masses 315
Focussed Assessment with Sonography in Trauma (FAST) scan 267
follicular lymphoma 445
frequency encoding 97
frontotemporal dementia (FTD) 455
^{18}F sodium fluoride (Na^{18}F) 79, 349, 460

g

gadolinium (Gd^{3+}) 102–104
gadolinium-based contrast agents (GBCA) 119
gadolinium orthosilicate (GSO) 28
gadolinium sulfide (Gd_2O_2S) scintillator 15
^{68}Ga-DOTANOC 463–465
^{68}Ga-DOTATATE (GDT) 440
^{68}Ga-DOTATOC/DOTATATE 67–68
^{67}Ga gallium citrate 69, 83
gallbladder
  acute cholecystitis 302, 303
  cholelithiasis 301–302
  neoplasms 302–304
gallstone pancreatitis 306
gallstones 301
gamma camera
  Anger camera 31–32
  collimator designs 34–35
  image acquisition, display, and analysis 34–37
  lead collimator 32
  principle of image formation 33
  Z-circuit signal 34
gastrointestinal malignancies
  colorectal cancer 450–451
  esophageal cancer 448–450
gastrointestinal (GI) tract
  acute and non-acute setting 270
  appendicitis 277–278
  bowel obstruction 271–274
  diverticulitis 274–277
gastrointestinal tract neuroendocrine tumors (GI-NET) 258
^{68}Ge/^{68}Ga and ^{82}Sr/^{82}Rb generator 56–57
generator production of radionuclide 52
  ^{68}Ge/^{68}Ga and ^{82}Sr/^{82}Rb generator 56–57
  ^{99}Mo/^{99m}Tc generator 54–56
  ^{99}Tc decay product 53
genitourinary (GU) tract system
  computed tomography 326
  female
    abnormal vaginal bleeding 350, 351
    acute pelvic pain 355–356
    adnexal masses and ovarian cancer 354–356
    cervical cancer 353, 354

    endometrial cancer 351–353
    obstetrical evaluation 357–358
    pregnancy (*see* pregnancy)
  magnetic resonance imaging 326, 327
  nuclear scintigraphy 326, 328
  pediatric 360–363
  ultrasound 321–326
Ghon focus 161
glomerular filtration rate (GFR) 337
gout 421
gradient coils 95, 99–100
granulomatous thyroiditis 234
Graves disease 228–233
Graves ophthalmopathy 236
gynecologic consultation 350

h

half-fourier acquisition single-shot turbo spin echo (HASTE) technique 118
Hampton's hump 170
hardware fracture 407
Hashimoto's thyroiditis 237
head imaging 390 *see also* neck imaging
hemangioma 293, 294
hemithyroidectomy 240
hemoperitoneum 267–268
hepatic abscess 292, 293
hepatic cirrhosis 290–292
hepatic system 287, 289
hepatobiliary imaging 76–77
hepatobiliary iminodiacetic acid 302
hepatocellular carcinoma (HCC) 299, 300
high-intensity focused US (HIFU) 348
Hodgkin's lymphoma 445–447
hot nodule 230, 232
Hounsfield Units (HU) 18–19
hyperfunctional multinodular goiter 228
hyperfunctional thyroid adenoma 228
hypertension 332
hyperthyroidism 227
hypertrophic cardiomyopathy (HCM) 122–123
hypervascular liver metastases 296, 298
hypokinetic 135
hypoparathyroidism 244
hypoxia 466–467

i

^{123}I-and ^{131}I sodium iodide 46, 68–69, 81–82
^{123}I-iodobenzamide (^{123}I-IBZM) 72–73
^{123}I-iomazenil 74
image acquisition
  computed tomography 18–20
  and display modes 110
image-guided breast intervention 209, 212, 216–219
image reconstruction 20–21
imaging infection/inflammation 83–84
^{123}I-metaiodobenzylguanidine (^{123}I-MIBG) 60, 63, 67–68
^{111}In-capromab pendetide 69–70
incidentaloma 250
^{111}In-diethylenetriaminepentaacetic acid (^{111}In-DTPA) 74
infectious diseases
  FUO 458–459
  infected implanted medical devices 459–460
  sarcoidosis 457–458
inflammatory arthritis 420, 424
inflammatory bowel disease
  Crohn's disease 279–280
  ulcerative colitis 280–283
inflammatory diseases
  FUO 458–459
  infected implanted medical devices 459–460
  sarcoidosis 457–458

infliximab 424
influenza viral pneumonia 159, 161
^{111}In-ibritumomab tiuxetan 69
^{111}In-or ^{99m}Tc-labeled leukocytes (^{111}In-or ^{99m}Tc-WBC) 83–84
^{111}In-pentetreotide 67–68, 259
International Association for the Study of Lung Cancer (IASLC) 444
intra-parenchymal abscess 380, 383
intrathoracic goiter 240
intravenous (i.v.) iodinated contrast 239
intravenous urography (IVU) 339
iodinated contrast agents (CA) 21
ionic-iodinated CA 22
ionizing *vs.* nonionizing radiation 3–4
isotopically pure ^{18}O water 51

j

Jod–Basedow phenomenon 239
juvenile idiopathic arthritis (JIA) 420–421

k

kidneys and collecting systems
  renal function and dysfunction 337–339
  renal infection and inflammation 329–331
  renal lesions 333–336
  renal transplants 336
  renal vascular anomalies 332–334
  ureteric neoplasms 339–342
  urinary tract calculi 328–329
Kidneys, Ureters, and Bladder (KUB) radiographs 329, 330
K-space and image formation 97

l

large bowel obstruction (LBO) 271–274
Larmor frequency 90
laryngeal cartilage fractures 391, 393
Lassen's method 397
late gadolinium enhancement (LGE) imaging 119, 122, 124
Late iodine enhancement 129
lipid rich 250
Liver MRI 287
"Living Renal Donor" 336
lobar pneumonia 158–159
longitudinal relaxation 92
low energy all-purpose (LEAP) collimator 34
lower urinary tract trauma 343–345
"low lying" placenta 359
Lugano classification 445
lung cancer 176–177
  chest CT 178–179
  chest radiography 177–178
  ^{18}F-2-fluorodeoxyglucose (^{18}F-FDG) PET/CT 178, 180
  small cell/non-small cell 177
  tumor node metastasis 177
lung imaging
  chest radiograph 146–148
  chronic obstructive pulmonary disease 163–166
  lung cancer 176–180
  normal findings in a chest CT 155–157
  normal findings in a chest X-ray 148–155
  pleural effusion 167–168
  pneumonia 158–161
  pneumothorax 169–170
  pulmonary embolism 170–173
  radiopharmaceuticals 79–80
  solitary pulmonary nodule 172, 174–176
  tuberculosis 159, 161–162
lutetium silicate (LSO) 28
lutetium yttrium oxyorthosilicate (LYSO) 28
lymphadenopathy 316

lymphoma
  staging 445–446
  therapy response assessment 446–448
Lynch syndrome 355

m

magnetic moment 88
magnetic resonance imaging (MRI)
  acute infarcts 374
  acute mural hematoma 375
  adrenal lesions 250
  angular momentum 88
  ankle 434, 435
  appendix 277
  arthritis 425–427
  ascites 269
  bile duct dilation 304, 305
  biliary tract 301
  bone marrow metastases 385, 388
  breast cancer 198–202
  carcinoid tumors 258–259
  colorectal cancer 285, 286
  components 98–99
  computer and image storage system 100
  contrast agents 102–104
  Crohn's disease 279, 280
  dementia 382, 384
  diffuse hepatic fat/steatosis 289, 290
  encephalitis 379, 380, 382
  FNH 296, 297
  focal splenic masses 316
  gallstones 301–302
  gradient coils 99–100
  GU tract 326, 327
  hemangioma 293, 294
  hepatic system 287
  K-space and image formation 97
  lymph nodes 316
  magnetic moment 88
  magnetic resonance signal 91–92
  musculoskeletal imaging 411–413
  net magnetization vector 88
  orbital and salivary gland 395
  osteomyelitis 385
  PanNET 255, 257, 258
  peritoneal carcinomatosis 270
  polyps 303
  precession 88–90
  prostate cancer 348
  resonance and phase 90–91
  RF coils 99–100
  RF pulse sequences 92–94
  safety considerations 100–101
  signal encoding using magnetic gradients 95–98
  superconducting magnet 99
  T1-and T2-times 94
  T1-and T2-weighted MRI 94–96
  thigh 434
  ureteric assessment 339
mammographic BI-RADS lexicon 196
mammography
  breast tomosynthesis 197
  craniocaudal views 192–193
  mammographic BI-RADS lexicon 196
  mediolateral oblique view 192–193
  normal mammogram 193–195
  screening *vs.* diagnostic mammogram 195
  system 23–24, 191
  tomosynthesis 25
Marine–Lenhart Syndrome 230, 236
matrix mineralization 429
mean transit time (MTT) 374
medical cyclotron 50
medical imaging
  procedures in Canada 2–3
  procedures involving ionizing *vs.* nonionizing radiation 3–4
  radiation doses and increased use 8
  radiation doses estimation 5–8

Medical Internal Radiation Dose (MIRD) 5
medical ultrasound imaging system 109–110
meningitis 379, 380
mesenteric hematoma 267, 268
mesorectal lymph node assessment 287
metacarpophalangeal (MCP) 421, 422
metastatic lymphadenopathy 394
metatarsophalangeal (MTP) 421
microbubble contrast-enhanced US 112–113, 296
M-mode and two-dimensional cardiac imaging 129–130
modern multiple detector CT (MDCT) systems 19
^{99}Mo/^{99m}Tc generator 54–56
monoamine oxidase A (MAO-A) 401
MR angiogram (MRA) 332
MR cholangiopancreatography (MRCP) 300
MR-guided vacuum-assisted core biopsy 218
MRI *see* magnetic resonance imaging (MRI)
MR urography (MRU) 330–331, 340, 342
multichannel analyzer (MCA) 30
multicystic dysplastic kidney disease 361
multi-gated cardiac acquisitions (MUGA) scans 134, 139–140
multimodality imaging 41–42
multinodular goiter 232, 239
multiple sclerosis (MS) 382, 384
musculoskeletal imaging
  arthritis (*see* Arthritis)
  computed tomography 408–411
  infection 417–420
  MRI 411–413
  plain radiography (X-rays) 404–407
  trauma 415–418
  tumors 427–435
  ultrasound 413–415
myocardial ischemia 453
myocardial perfusion imaging (MPI) 133
  anginal symptoms 454
  multiple cardiac risk factors 454
  myocardial ischemia 453
myocardial tissue characterization 119–120, 122–125
myositis ossificans 408

n

NaI(Tl) scintillation crystals 28
^{13}N ammonia ($^{13}NH_3$) 62, 72
neck imaging
  acute neck infections 395
  inflammatory conditions 395–396
  trauma 390, 392, 393
  tumor 394–395
  vascular imaging 393–394
neoplasms 302–306
Nephrogenic Systemic Fibrosis (NSF) 326
nephroureterolithiasis 328–329
net magnetization vector (NMV) 88
neurodegenerative diseases 397
neuroendocrine diseases
  carcinoid tumors 258–259
  PanNET 255, 257, 258
neuroendocrine tumors (NETs) 463–465
neurofibrillary tangles (NFT) 400
neuroreceptor occupancy 398
nodular Graves disease 230
noncompressible appendix 277
non-enhanced CT 250
non-gallstone pancreatitis 306
non-Hodgkin's lymphoma (NHL) 445
noninflammatory arthritis 421, 422
nonionic CA 22
nonischemic cardiomyopathy 122

non-mass like enhancement (NMLE) 201–202
non-stochastic effects 5
Nuchal translucency measurements 357
nuclear cardiology
  MUGA scan 139–140
  myocardial perfusion imaging 133–138
  PET myocardial viability imaging 136, 138
nuclear medicine imaging 301
  biliary tract 301
  Crohn's disease 279
  gamma camera 31–37
  multimodality imaging 41–42
  positron emission tomography 38–41
  scintillation detectors 28–31
  single photon emission computed tomography 37–38

o
occult fractures 416
occupancy studies 398, 399
omental cake 270
optical cystoscopy 343
Optison® 112
osseous tumors 427
osteoarthritis 427
osteomyelitis 385, 387, 390, 417, 429
osteonecrosis 395, 396
ovarian cancer 354–356
ovarian teratoma 235–236
^{15}O water ($H_2{}^{15}O$) 62, 72

p
painless thyroiditis 234
pancreas
  acute pancreatitis 306–308
  chronic pancreatitis 310
  pancreatic ductal adenocarcinoma 311–313
  pancreatic neoplasms 310–311
  pancreatic trauma 309
pancreatic ductal adenocarcinoma 311–313
pancreatic neoplasms 310–311
pancreatic neuroendocrine tumors (PanNET) 255, 257, 258
pancreatic trauma 309
paragangliomas 255, 256
parathyroid adenoma 246–247
parathyroid carcinoma 248
parathyroid gland imaging agents 82
parathyroid glands (PTGs)
  altered production of 244–245
  4D CT Imaging 248
  parathyroid adenoma 246–247
  parathyroid carcinoma 248
  parathyroid hyperplasia 247
  primary hyperparathyroidism 245
  secondary and tertiary hyperparathyroidism 248–249
parathyroid hyperplasia 247
parathyroid imaging 80–82
parenchymal transit time 337
Parkinson's dementia (PD) 455, 456
Parkinson's disease 399
pediatric genitourinary tract
  congenital anomalies 360–361
  cystic renal disease 361
  genital organs 363
  renal masses 361–362
  UTI 362–363
periosteal reaction 418, 429, 430
peripheral arthritis 420
peritoneal carcinomatosis 269–270
peritoneum/mesentery 265–266
PET *see* positron emission tomography (PET)
PET/CT
  colorectal cancer 287, 288
  functional and molecular imaging 41–42
PET/MR 41–42

PET myocardial viability imaging 136, 138
phantoms 5
phase encoding 97
pheochromocytoma 253–255
photomultiplier tubes (PMTs) 468
placenta 359–360
plain film X-ray
  ascites 269
  chronic pancreatitis 310
  colorectal cancer 285
  Crohn's disease 279
  GI tract 270
  LBO 273–275
  musculoskeletal disorders 404–407
  osseous tumors 428
  pneumoperitoneum 266, 267
  SBO 272
  ulcerative colitis 281
pleural effusion 167–168
Plummer disease 230
plunging goiter 240
Pneumocystis jirovecii pneumonia 159–160
pneumonia 158–161
pneumoperitoneum 266–267
pneumothorax 169–170
polyps 302–303, 352
positron emission mammography (PEM) 202
positron emission tomography (PET)
  brain 396–401
  decay of a positron-emitting radionuclide 38–39
  design 40
  ^{18}F-FDG
    glucose transporters 440
    interpretation of 440–441
    phosphorylation 440
  ^{18}F-FDG PET/CT in oncology
    gastrointestinal malignancies 448–451
    head and neck cancers 452–453
    lung cancer management 442–444
    in lymphoma 445–448
  18F-FDG PET in non-oncology indications
    cardiac PET imaging 453–455
    in infectious and inflammatory disorders 457–460
    neurological applications of 455–457
  511 keV γ–photons 39
  PET/CT *vs.* PET/MR
    current clinical evidence 469–470
    technical challenges in 468–469
  radiopharmaceutical
    agents for tumor receptor imaging 463–466
    disadvantage of 460
    ^{68}Ga-DOTATATE 463–465
    hypoxia 466–467
    myocardial perfusion 461
    Na^{18}F 460
    prostate cancer 465–466
    tumor proliferation 461–463
  scintillation crystals 38–39
  time-of-flight 40–41
postmenopausal women 351–352
postprimary reactivation tuberculosis 162
potentially diagnostic clue (PDC) 459
precession 88–90
pregnancy
  first trimester 356, 357
  second and third trimester 358–360
pre-surgical wire localization and specimen imaging 218–219
primary hyperparathyroidism 245
primary hypothyroidism 237, 238
primary osteoarthritis 421
Primovist™ 296
probe–target interaction 440

progression-free survival (PFS) 463
progressive multifocal leukoencephalopathy (PML) 382
prostate cancer 465–466
prostate gland 348–349
Prostate Imaging Reporting and Data System (PiRADS) 348
prostate MRI 348, 349
prostate-specific membrane antigen (PSMA) 349, 465–466
prostatic-specific antigen (PSA) 348, 465
pseudocysts 310
pseudodiaphragmatic contour 167
psoriatic arthritis 421, 422
psychiatric disorders 400
PTGs *see* parathyroid glands (PTGs)
pulmonary embolism (PE) 170–173
pulmonary sarcoidosis 122–123
pulmonary tuberculosis (TB) 159, 161–162
pulse-echo mode 110

r

radiation doses
  estimation 5–8
  and increased use of medical imaging 8
radioactive iodine (RAI) treatment
  of hyperthyroidism 236–237
  of thyroid cancer 243–244
radioactive iodine uptake (RAIU) 228–230
radiofrequency ablation (RFA) 444
radiofrequency (RF) coils 99–100
radiofrequency pulse sequences 431
radiographs 15–16
  acute osteomyelitis 418
  DIP 423
radionuclide bone scans 431
"Radionuclide Cystography" (RNC) 362
radionuclide imaging
  of brain 397
  liver 289
  used for PET 28–29
  used for SPECT 28–29
radionuclide production
  cyclotron production 50–53
  generator production 52–57
  longer-lived parent radionuclide 47
  reactor production 48–50
  short-lived daughter radionuclide 47
radionuclide scintigraphy 339
radionuclide ventriculography (RVG) scans 35, 134
radiopaque markers 218
radiopharmaceuticals 46–47, 70–71
  agents for tumor receptor imaging 463–466
  bone imaging 77–79
  for bone imaging 77–79
  for brain/CNS imaging 70–74
  for cardiac imaging 58–63
  disadvantage of 460
  ^{68}Ga-DOTATATE 463–465
  for hepatobiliary imaging 76–77
  hypoxia 466–467
  for imaging infection/inflammation 83–84
  for lung imaging 79–80
  myocardial perfusion 461
  Na^{18}F 460
  preparation and supply 57–58
  prostate cancer 465–466
  for renal imaging 74–76
  therapeutic 84
  for thyroid/parathyroid imaging 80–82
  for tumor imaging 63–70
  tumor proliferation 461–463
rapid iodine turnover 230
^{82}Rb rubidium chloride 62
reactive arthritis 421

reactor production, radionuclide 48–50
rebound phenomenon 234
red blood cells (RBCs) 293
relative percentage of washout (RPW) 250, 251
renal artery stenosis (RAS) 332
renal cell carcinoma (RCC) 333
renal imaging
  ^{99m}Tc-diethylenetriaminepentaacetic acid 74–75
  ^{99m}Tc-dimercaptosuccinic acid 75–76
  ^{99m}Tc-glucoheptonate 75–76
  ^{99m}Tc-mercaptoacetylglycine 75–76
renal lesions 333–336
renal masses 361–362
renal plasma flow (RPF) 337
renal transplants 336
renal vascular anomalies 332–334
renovascular hypertension 332
resonance 90
retrograde urography (RU) 339
reversible cerebral vasoconstrictive syndrome (RCVS) 376
rheumatoid arthritis 420, 421
right upper quadrant (RUQ) 302
Roentgen, Wilhelm Conrad 11–12
rubidium-82 (^{82}Rb) 134
rubidium-82 chloride (^{82}Rb) 454
ruptured intracranial aneurysms 376, 378

S

sacroiliac joint involvement 423
sarcoidosis 456–457
scapholunate ligament injury 405
scaphotrapeziotrapezoidal (STT) 421
scintigraphy
  genitourinary (GU) tract system 326, 328
  thyroid 228, 230–232
scintillation detectors
  amplification and analysis of the electronic signal 30–31
  conversion of light to an electronic signal 30–31
  properties of solid scintillators 28
  radionuclides used for PET imaging 28–29
  radionuclides used for SPECT imaging 28–29
screening *vs.* diagnostic mammogram 195
scrotal ultrasound 345, 346
secondary hypothyroidism 238
secondary syrinx 385
selective serotonin reuptake inhibitors (SSRIs) 400
sentinel clot sign 268
sentinel lymph node mapping 220
septic arthritis 417, 421, 423
sequential axial acquisition mode 19
seronegative arthritis 421
single photon emission computed tomography (SPECT) 37–38
  brain 396–401
skull 372 *see also* brain imaging
small bowel followthrough (SBFT) 279, 280
small bowel obstruction (SBO) 271, 272
soft-tissue mineralization 408
solid malignant neoplasms 310–311
solitary pulmonary nodules (SPN) 172, 174–176, 442
SPECT/CT 41–42
spinal dural AVF 385, 387
spin-echo sequence 92
spin-echo T2 sequences 382
spine imaging
  infection 385, 387, 390
  inflammatory/metabolic conditions 387, 389, 391, 392
  trauma 383, 385, 386

  tumor 385, 388, 389
  vascular 385, 387
spin lattice relaxation 92
spin-spin relaxation 92
spleen/lymph nodes
  lymphadenopathy 316
  splenic trauma 313, 315
  splenomegaly/splenic masses 315–316
splenomegaly/splenic masses 315–316
"splitbolus" technique 340
spoiled gradient-recalled echo (SPGR) 427
SSTR-imaging radiotracers (GDx) 463–464
standard uptake values (SUV) 444
steady-state free precession (SSFP) MRI images 119
stenosis 135
stereotactic body radiation therapy (SBRT) 444
stereotactic-vacuum-assisted core needle biopsy 217
stochastic effects 5
Streptococcus bovis group 460
subacute lymphocytic thyroiditis 234–235
superconducting magnet 99
surgical sieve 265
symptomatic gallstone disease 302
synovial osteochondromatosis 408

t
^{99m}Tc aerosols 80
^{99m}Tc-bicisate 72
^{99m}Tc-bisphosphonate 78–79
^{99}Tc decay product 53
^{99m}Tc-diethylenetriaminepentaacetic acid (^{99m}Tc-DTPA) 74–75
^{99m}Tc-dimercaptosuccinic acid (^{99m}Tc-DMSA) 75–76
^{99m}Tc-DMSA 363
^{99m}Tc-DTPA renal scintigraphy 337, 338
^{99m}Tc-ethyl cysteinate dimer (^{99m}Tc-ECD) 72
^{99m}Tc-exametazime 70, 72
^{99m}Tc-glucoheptonate 75–76
^{99m}Tc-hexamethylpropylene amine oxime (^{99m}Tc-HMPAO) 70, 72
^{99m}Tc iminodiacetic acid (^{99m}Tc-IDA) derivatives 77–78
^{99m}Tc-labeled red blood cells 132
^{99m}Tc-macroaggregated albumin (^{99m}Tc-MAA) 79–80
^{99m}Tc-MAG3 339
^{99m}Tc-medronate 348
^{99m}Tc-mercaptoacetylglycine (^{99m}Tc-MAG$_3$) 75–76
^{99m}Tc-mertiatide 75–76
^{99m}Tc pertechnetate 46, 234
^{99m}Tc red blood cells 62–63
^{99m}Tc-sestamibi 58–60, 134
^{99m}Tc sodium pertechnetate (^{99m}TcO4^{-}) 82
^{99m}Tc-succimer 75–76
^{99m}Tc-sulesomab Fab' 84
^{99m}Tc sulfur colloid 77, 296
^{99m}Tc-Technegas 80
^{99m}Tc-tetrofosmin 58–61, 134
Technetium-99m (^{99m}Tc)-labeled compounds 134
testicles
  cancer 345–346
  pain 346–347
testicular cancer 345–346
testicular microlithiasis 346
thallium-201 (^{201}Tl) 134
therapeutic radiopharmaceuticals 84
thin film transistor (TFT) 24
thrombolytic therapy (tPA) 374
thumb printing in ulcerative colitis 281, 282
thymidine kinase I (TK1) 461

thyroid
  cancer
    Bethesda System for Reporting Thyroid Cytopathology 241
    FNA biopsy 240, 241
    metastasis 241–243
    RAI 243–244
    subtypes 240
  glands 225–227
  hormone diseases
    decreased production of 237
    granulomatous thyroiditis 234
    Graves disease 229–233
    hyperfunctional “toxic” thyroid adenoma 230
    increased production of 227–229
    iodinated contrast 239
    mass lesions in the thyroid gland 239
    multinodular goiter 232
    primary hypothyroidism 237, 238
    RAI treatment of hyperthyroidism 236–237
    secondary hypothyroidism 238
    struma ovarii 235–236
    subacute lymphocytic thyroiditis 234–235
  radiopharmaceuticals 80–82
thyroid imaging agents 82
thyroid inferno 230
thyroid inflammation 228
thyroiditis 228
thyroid releasing hormone (TRH) 227
thyroid scintigraphy 228, 230–232
thyroid stimulating hormone (TSH) 227
thyroid-stimulating immunoglobulin (TSI) 229
thyrotoxicosis 227
time-of-flight (TOF) PET 40–41
^{201}Tl thallous chloride 61
tomosynthesis 25
tonsillar cancer 395
total mesorectal excision (TME) 285
transcranial magnetic stimulation (TMS) 401
transitional cell carcinoma (TCC) 333, 340
trans-rectal ultrasound (TRUS) 287, 348, 349
transudative ascites 268
transvaginal ultrasound
  female pelvis 352, 353
  intrauterine pregnancy 357
  uterus 351
transverse decay 92
transverse myelitis 388, 392
tuberculosis 159, 161–162
tumor imaging 63–64
  ^{18}F-and ^{11}C-choline 66–67
  ^{18}F-FAZA 66–67
  ^{18}F-fluorodeoxyglucose 64, 66
  ^{18}F-fluoroethyltyrosine 66–67
  ^{18}F-fluoro-L-thymidine 64
  ^{67}Ga gallium citrate 69
  ^{123}I and ^{131}I sodium iodide 68–69
  ^{123}I-metaiodobenzylguanidine 67–68
  ^{111}In-capromab pendetide 69–70
  ^{111}In-ibritumomab tiuxetan 69
  ^{111}In-pentetreotide 67–68
tyrosine kinase inhibitor (TKI) 462

u

ulcerative colitis 280–283
ultrasound BI-RADS lexicon 198–199
ultrasound-guided core needle biopsy 216
ultrasound-guided needle aspiration 216–217
ultrasound (US) imaging
  acoustic impedance 109
  acute cholecystitis 302, 303

  acute pancreatitis 306, 307
  appendicitis 277, 278
  ascites 269
  audible range 107
  bile duct dilation 304, 305
  biliary tract 300
  breast cancer 197–199
  contrast agents 112–113
  Crohn's disease 279
  cysts 294, 295
  diffuse hepatic fat/steatosis 289, 290
  diverticulitis 274
  Doppler US 111–112
  endometrial cancer 353
  focal splenic masses 316
  gallstones 301, 303
  Graves disease 230–232
  GU tract 321–326
  HCC 299
  hepatic cirrhosis 291
  hepatic system 287
  image acquisition and display modes 110
  infrasound range 107–108
  joint effusion 420
  lymph nodes 316
  medical ultrasound imaging system 109–110
  musculoskeletal imaging 413–415
  pregnancy 358–359
  premenopausal ovary 354, 355
  range of sound frequencies 107–108
  reflection of a high-frequency sound wave 107–108
  relative intensity 107
  thyroid lobe 238
  transducer 108–111
  transplant kidney 336
  ultrasound transducer 107–108
  UTI 362
ureteric neoplasms 339–342
urethral injuries 344
urinary tract calculi 328–329
urinary tract infections (UTI) 362–363
US imaging *see* ultrasound (US) imaging
US transducer 107–111

V

vaginal atrophy 352
vaginal bleeding 350, 351
vasodilator stress myocardial perfusion imaging 124–125
venolymphatic malformation 393
ventilation-perfusion (V/Q) lung scintigraphy 171–173
vesicoureteral reflux (VUR) 362
vesicular monoamine transporter type 2 (VMAT2) 399
Vialmix® 113
"Voiding Cystourethrography" (VCUG) 362

W

Westermark sign 170
Wilm's tumor 361
Wolff–Chaikoff effect 239
World Health Organization International Classification of Disease 445
wrist radiograph 429, 430

X

X-ray machine 14–15
X-rays
  Bremsstrahlung 11–13
  characteristic 11–13
  X-ray machine 14–15
  X-ray tube 13–14
X-ray tube 13–14

Z

Zollinger–Ellison syndrome 255

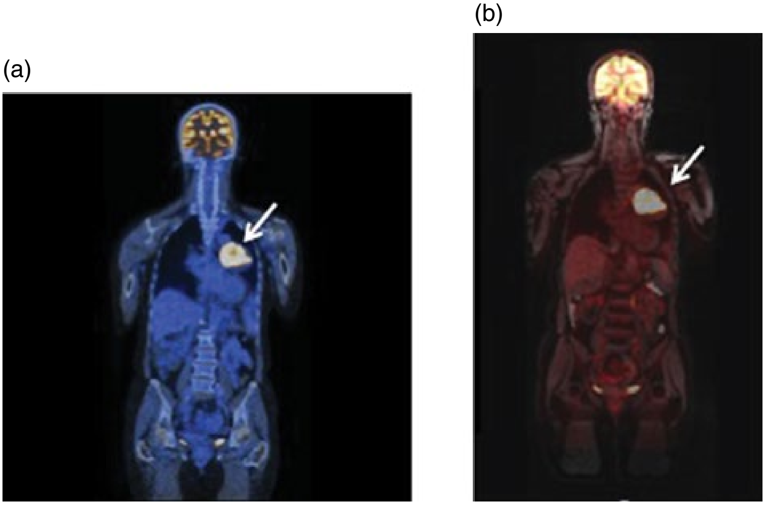

PET/CT

PET/MR

Figure 3.8 (a) PET/CT combines functional and molecular imaging obtained by PET with the high spatial resolution anatomical imaging provided by CT. A whole-body CT image was co-registered with the PET image obtained with ^{18}F-2-fluorodeoxyglucose (^{18}F-FDG) in a patient with lung cancer (arrow) to provide a multimodality PET/CT image. (b) PET/MR similarly combines PET with high spatial resolution MR images. A whole-body PET image obtained with ^{18}F-FDG was co-registered with the MR image of a patient with lung cancer (arrow) to provide a multimodality PET/MR image. *Source:* Images provided by Dr. Patrick Veit-Haibach, Joint Department of Medical Imaging, University Health Network, Toronto, Canada.

Medical Imaging for Health Professionals: Technologies and Clinical Applications, First Edition.
Edited by Raymond M. Reilly.
© 2019 John Wiley & Sons, Inc. Published 2019 by John Wiley & Sons, Inc.

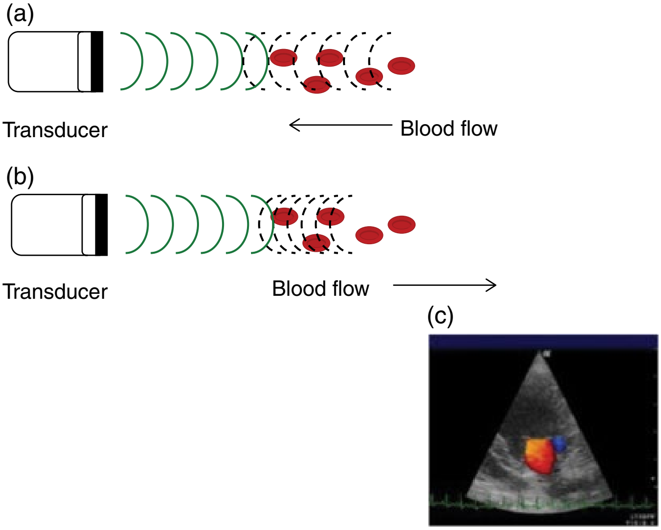

Figure 6.5 Doppler ultrasound is a technique to visualize blood flow. (a) The incident ultrasound wave created by the transducer (green solid lines) is reflected off the surface of red blood cells. If the blood is moving away from the transducer, the frequency of the reflected sound wave (black broken lines) decreases due to expansion of the wave. (b) If the blood is moving toward the transducer, the reflected sound wave is compressed, resulting in an increase in frequency. (c) Doppler ultrasound is often used to image blood flow in the heart (echocardiogram) to assess valve function. *Source:* Panel (c). Obtained from https://en.wikipedia.org/wiki/Doppler_echocardiography.

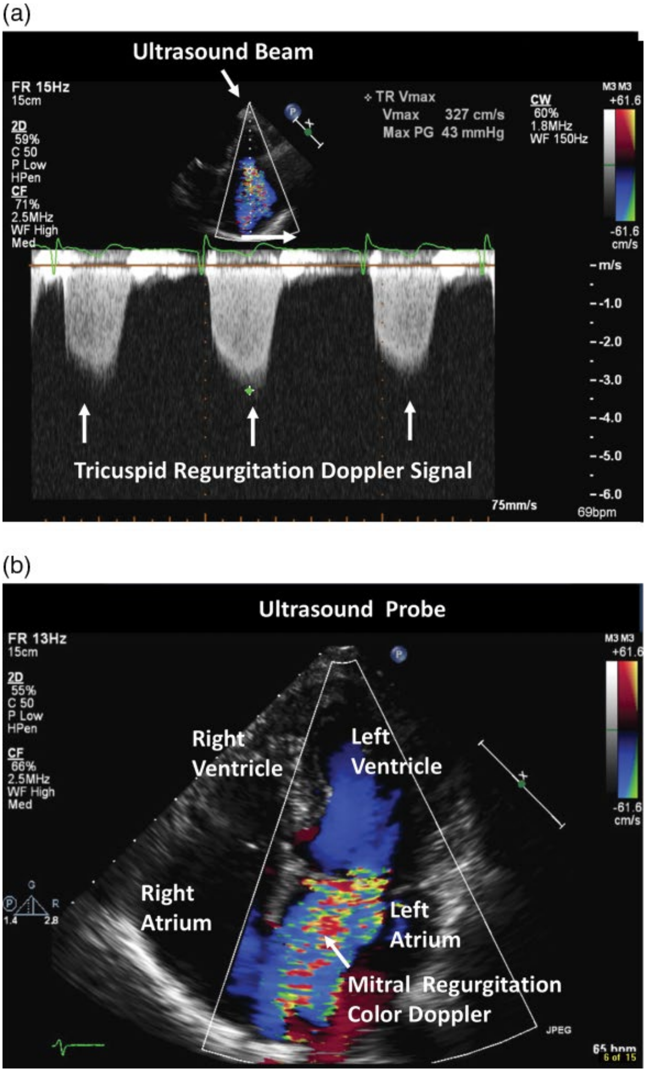
(a)
Ultrasound Beam
FR 15Hz
15cm
2D
59%
C 50
P Low
HPen
CF
71%
2.5MHz
WF High
Med
TR Vmax
Vmax 327 cm/s
Max PG 43 mmHg
CW
60%
1.8MHz
WF 150Hz
M3 M3
+61.6
-61.6
cm/s
m/s
-1.0
-2.0
-3.0
-4.0
-5.0
-6.0
Tricuspid Regurgitation Doppler Signal
75mm/s
69bpm
(b)
Ultrasound Probe
FR 13Hz
15cm
2D
55%
C 50
P Low
HPen
CF
66%
2.5MHz
WF High
Med
M3 M3
+61.6
-61.6
cm/s
Right Ventricle
Left Ventricle
Right Atrium
Left Atrium
Mitral Regurgitation Color Doppler
JPEG
65 bpm
6 of 15

Figure 7.15 Two-dimensional and color Doppler. (a) Doppler signal from the tricuspid valve across time; the velocity of the regurgitant jet is measured and used to estimate the right ventricular systolic pressure. (b) Color Doppler showing systolic blue flow with shades of green within the left atrium due to a turbulent jet of mitral regurgitation.

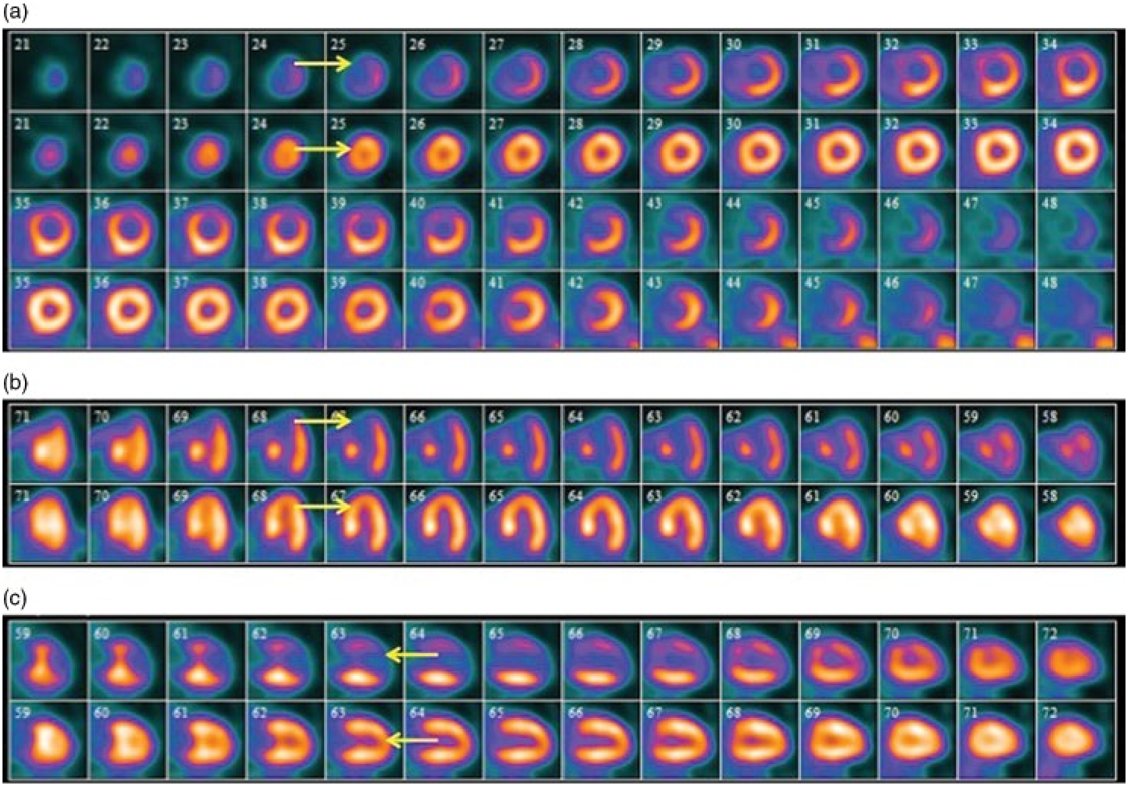
(a)
21 22 23 24 25 26 27 28 29 30 31 32 33 34
21 22 23 24 25 26 27 28 29 30 31 32 33 34
35 36 37 38 39 40 41 42 43 44 45 46 47 48
35 36 37 38 39 40 41 42 43 44 45 46 47 48
(b)
71 70 69 68 67 66 65 64 63 62 61 60 59 58
71 70 69 68 67 66 65 64 63 62 61 60 59 58
(c)
59 60 61 62 63 64 65 66 67 68 69 70 71 72
59 60 61 62 63 64 65 66 67 68 69 70 71 72

Figure 7.17 Perfusion images of the heart showing ischemia. (a) Short-axis projection images of the heart after stress (top and third row) compared with rest (second and bottom row) show reduced perfusion following stress that is not seen at rest suggesting ischemia (arrows). (b) Horizontal long-axis images of the heart after stress (top row) compared with rest (bottom row) also show ischemia (arrows). (c) Vertical long-axis images of the heart after stress (top row) compared with rest (bottom row) also show ischemia (arrows).

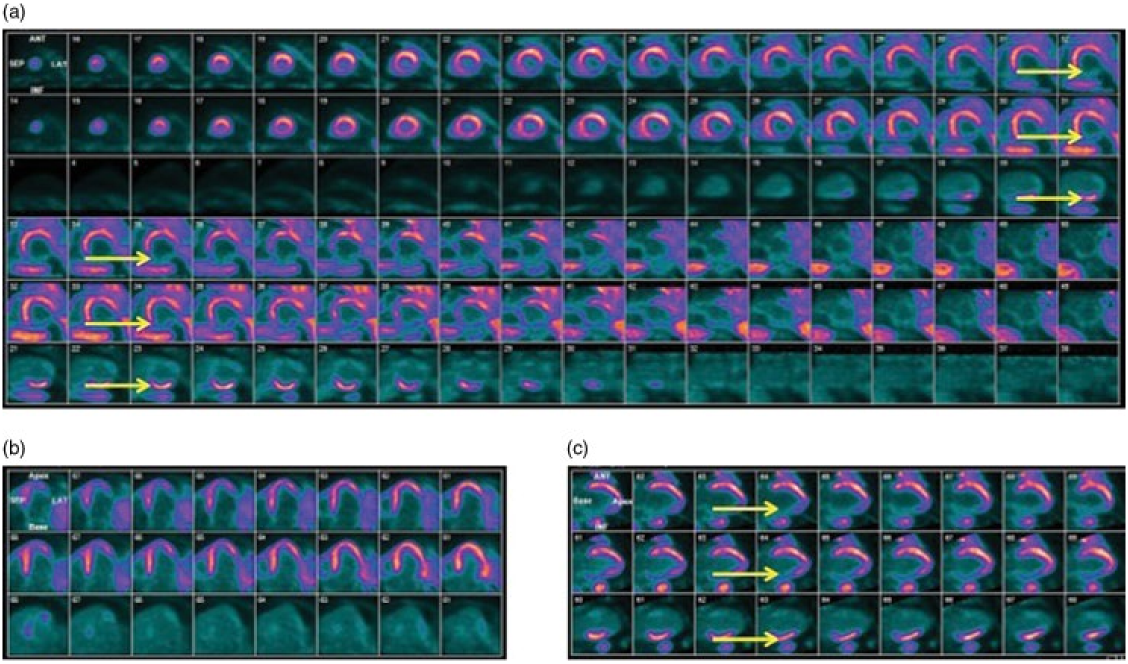

Figure 7.18 Perfusion and viability images of the heart showing hibernating myocardium. (a) Short-axis perfusion images of the heart after stress (top and fourth row) and after rest (second and fifth row) as well as viability images (third and bottom row) are shown. (b) Horizontal long-axis images of the heart after stress (top row) and after rest (middle row) as well as viability images (bottom row) are shown. (c) Vertical long-axis images of the heart after stress (top row) and after rest (middle row) and viability images (bottom row) are shown. The area of reduced perfusion in the inferior wall seen on stress/rest images (arrows) has mismatched increased glucose metabolism (arrows) and is alive, i.e. hibernating. The segments other than the inferior wall on ^{18}F-FDG images that do not show ^{18}F-FDG uptake can sometimes be due to intense glucose avidity of the hibernating segment resulting in apparent lack of uptake in the normal segments. Radiotracer uptake is seen in the lungs as well as below the diaphragm in this patient with heart failure. *With acknowledgement to Dr. Sharmila Dorbala at Brigham and Women's Hospital.*

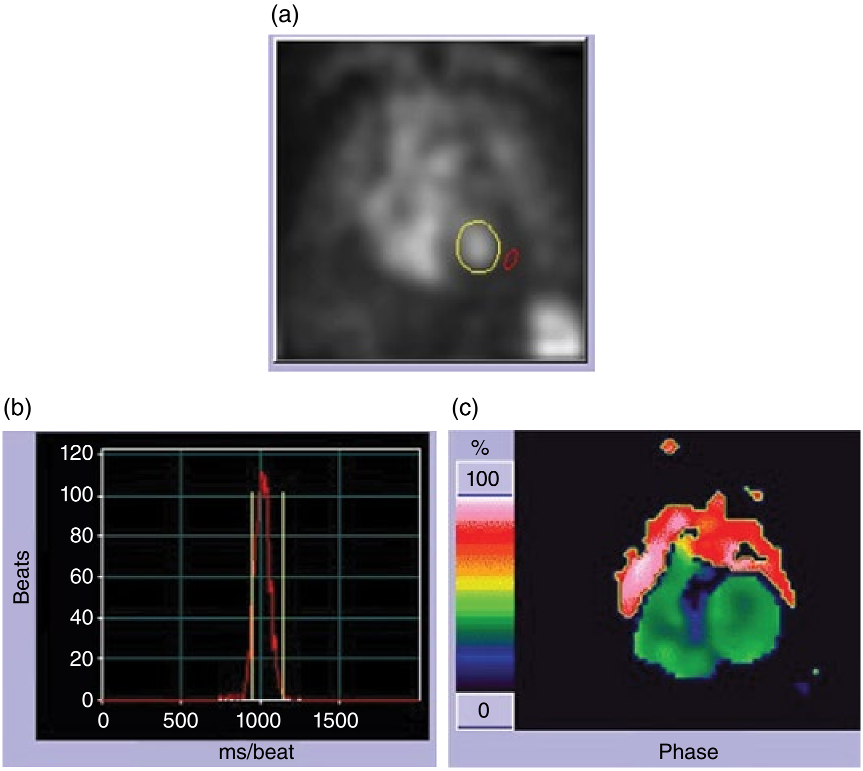

Figure 7.19 Images from a MUGA scan in a patient with LVEF of 65%. (a) An image of the heart with a region of interest drawn over the left ventricle (yellow circle) and background (red circle) so that the amount of radioactivity within the left ventricular cavity may be estimated during the cardiac cycle. (b) Graph showing all of the cardiac beats were at the same rate, indicating that the cardiac rhythm was regular during the study. (c) A "phase" image of the heart, showing that the atria (red) and ventricles (green) had uniform contraction (were uniform in color throughout) and that the atrial contraction was at a different time from the ventricular contraction, as would be expected in a normal heart.

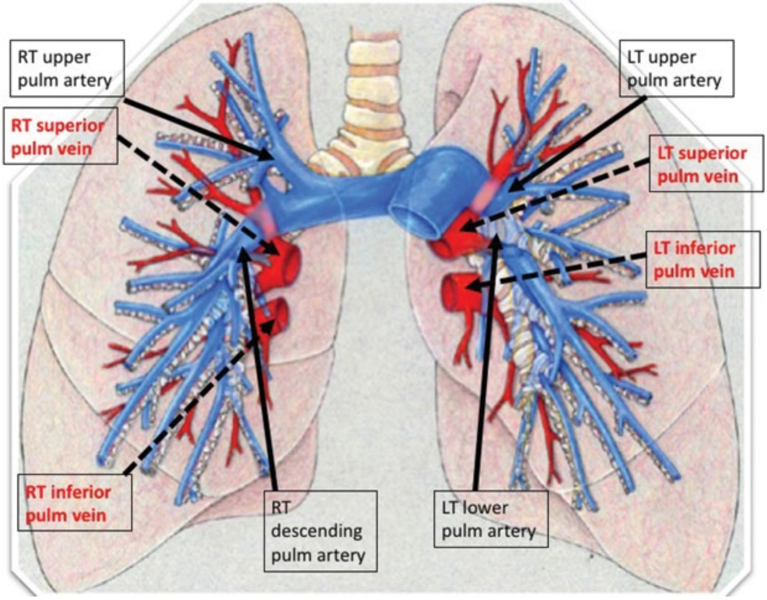
RT upper pulm artery
RT superior pulm vein
LT upper pulm artery
LT superior pulm vein
LT inferior pulm vein
RT inferior pulm vein
RT descending pulm artery
LT lower pulm artery

Figure 8.6 Diagrammatic presentation of the anatomy of the pulmonary arteries and veins.

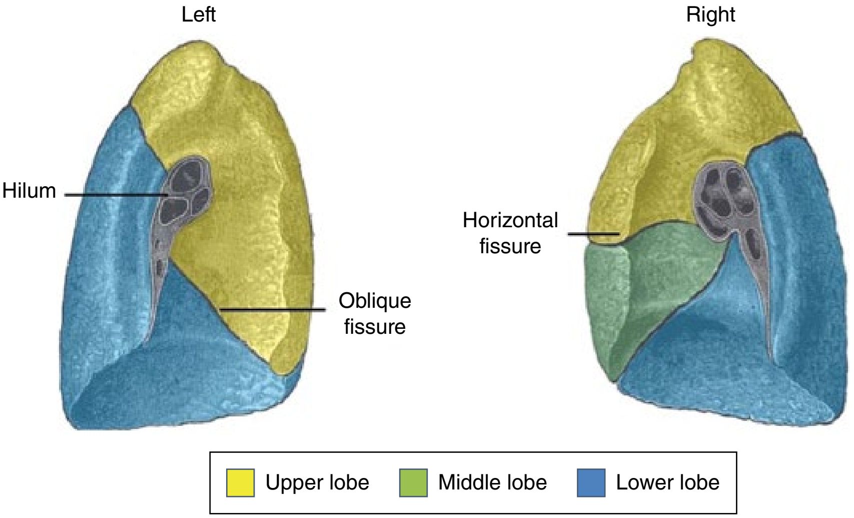
Left
Right
Hilum
Horizontal fissure
Oblique fissure
🟨 Upper lobe
🟩 Middle lobe
🟦 Lower lobe

Figure 8.8 Diagrammatic presentation of the horizontal fissure (right lung) and bilateral oblique fissures separating the different lobes in the right and left lungs. *Source:* From http://teachmeanatomy.info/thorax/organs/lungs.

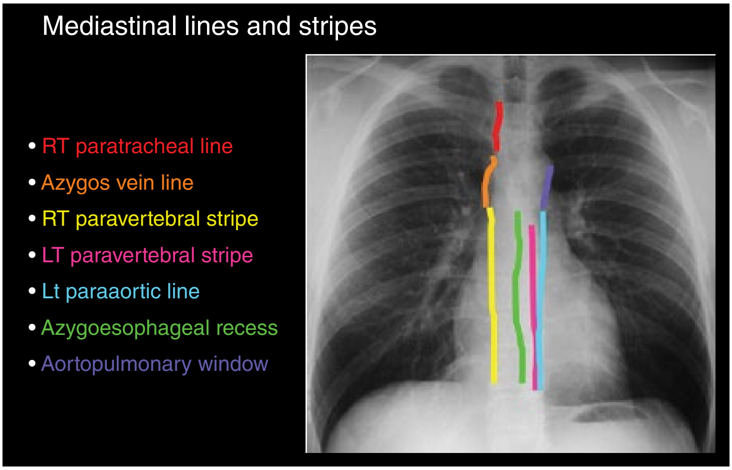

Mediastinal lines and stripes

- RT paratracheal line
- Azygos vein line
- RT paravertebral stripe
- LT paravertebral stripe
- Lt paraaortic line
- Azygoesophageal recess
- Aortopulmonary window

Figure 8.10 Mediastinal lines and stripes.

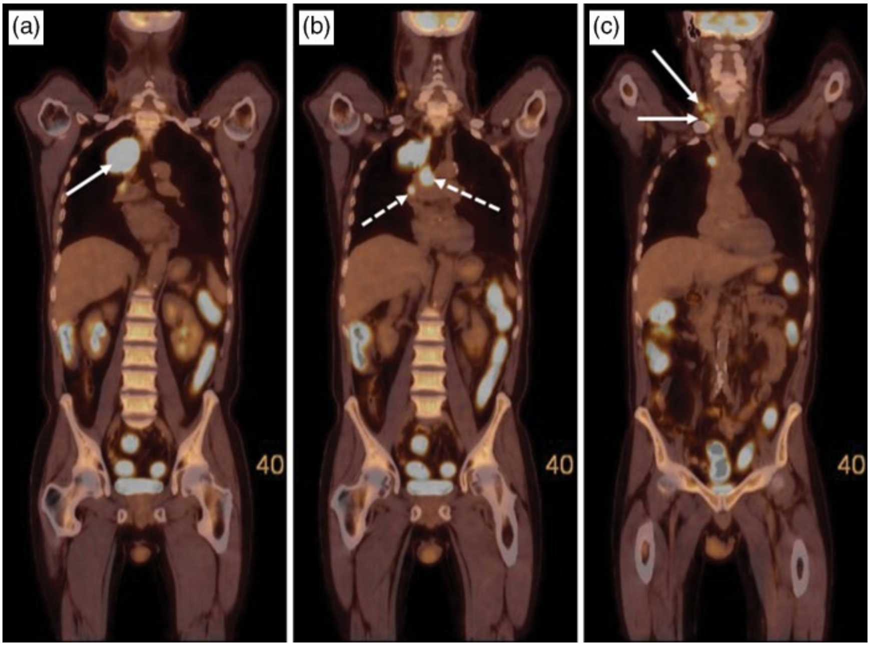

Figure 8.30 ^{18}F-2-fluorodeoxyglucose (^{18}F-FDG) PET/CT in a 72-year-old male for staging of lung cancer. FDG-avid right upper lobe mass (solid white arrow) is consistent with the known diagnosis of lung cancer (a). FDG-avid right hilar and right mediastinal (white dotted arrows in panel b) and right lower cervical and supraclavicular (white arrows in panel c) lymph nodes are consistent with metastatic nodal disease. No other distant metastatic disease is noted. The stage according to the PET/CT findings is IIIB (any T [size of tumor or invasion of chest wall or mediastinal structures], N3 [infiltration of supraclavicular nodes], and M0 [no distant metastases found]).

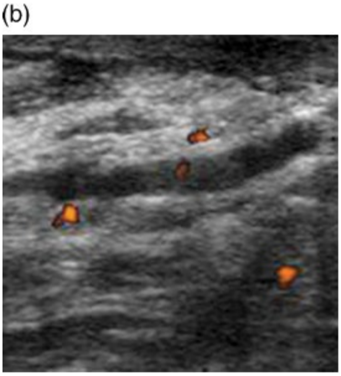

Figure 9.18 Circumscribed solid masses. (b) Intraductal papillomas are benign tumors arising from the lactiferous ducts. These lesions commonly present with bloody, serosanguinous (blood – tinged serous fluid), or serous nipple discharge in women aged 30–50 years. Intraductal papillomas are often subareolar round/oval, circumscribed/irregular masses. Ultrasound appearances are that of an isoechoic (similar intensity as surrounding tissue) solid mass with internal vascularity on color Doppler imaging (bright orange areas), often with an accompanying duct dilated with fluid. On galactography (duct imaging performed by introducing contrast dye into the duct prior to mammography), intraductal papillomas often produce intraductal filling defects.

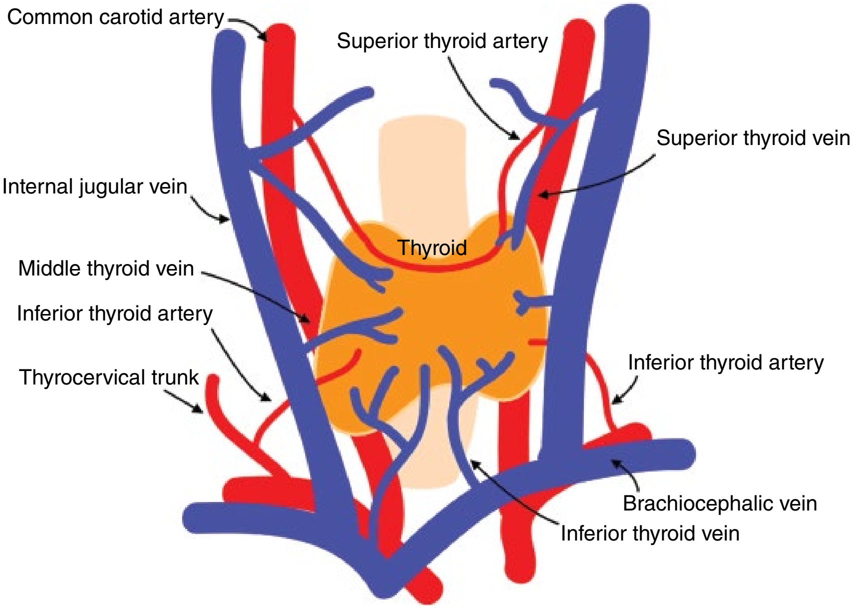
Common carotid artery
Superior thyroid artery
Superior thyroid vein
Internal jugular vein
Thyroid
Middle thyroid vein
Inferior thyroid artery
Thyrocervical trunk
Inferior thyroid artery
Brachiocephalic vein
Inferior thyroid vein

Figure 10.1 Arterial and venous supply of the thyroid gland.

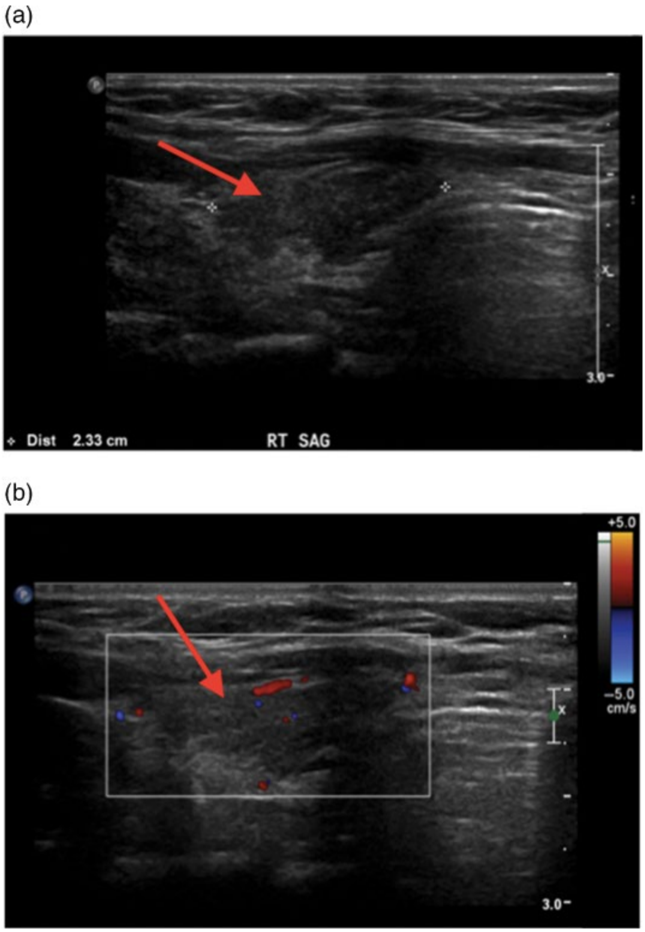
(a)
Dist 2.33 cm
RT SAG
3.0
(b)
+5.0
−5.0
cm/s
3.0

Figure 10.10 Sagittal ultrasound images through the right thyroid lobe (arrows) demonstrate atrophy of the lobe and diffuse hypoechoic parenchyma (a) with reduced internal vascularity on color Doppler assessment (b), in keeping with end-stage atrophy seen with chronic Hashimoto's thyroiditis.

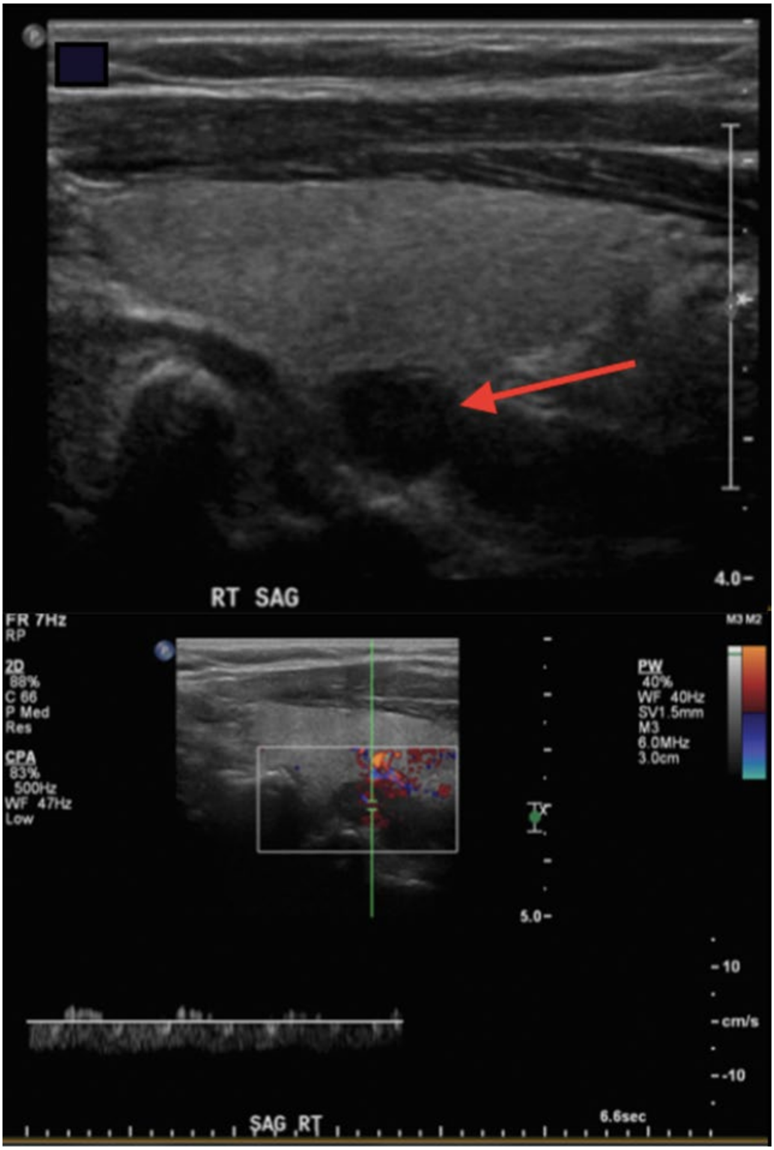
4.0
RT SAG
FR 7Hz
RP
2D
88%
C 66
P Med
Res
CPA
83%
500Hz
WF 47Hz
Low
M3 M2
PW
40%
WF 40Hz
SV1.5mm
M3
6.0MHz
3.0cm
5.0
10
cm/s
-10
SAG RT
6.6sec

Figure 10.14 Selected ultrasound images from right neck of the same patient as in Figure 10.13 above demonstrates a hypoechoic vascular mass deep to the mid to lower pole of the right thyroid lobe (arrow). This is the typical ultrasound appearance of a parathyroid adenoma.

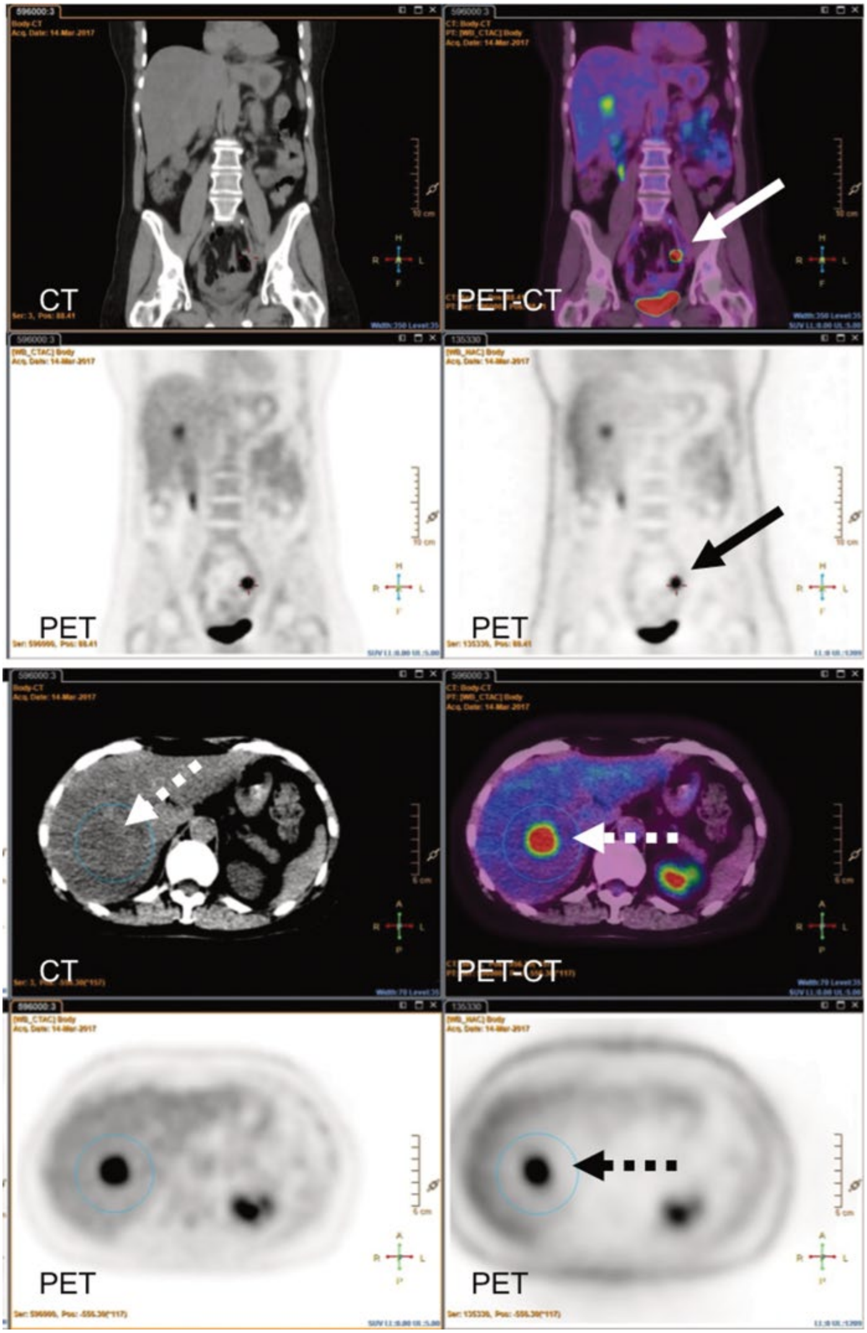

Figure 11.17 Colorectal cancer with synchronous liver metastasis on ^{18}F-FDG PET/CT. Top two image rows (Coronal CT only, PET-CT [fused], and PET only imaging): A hypermetabolic mass is seen in the left pelvis (solid arrow) corresponding to a primary sigmoid cancer. Bottom two image rows (Axial CT only, PET-CT [fused], and PET only imaging): A hypermetabolic lesion is seen in the right lobe of the liver (dashed arrow), consistent with synchronous metastasis. Of note, the liver metastasis is partially imaged on the coronal set of imaging on the PET-CT (fused) and PET only images.

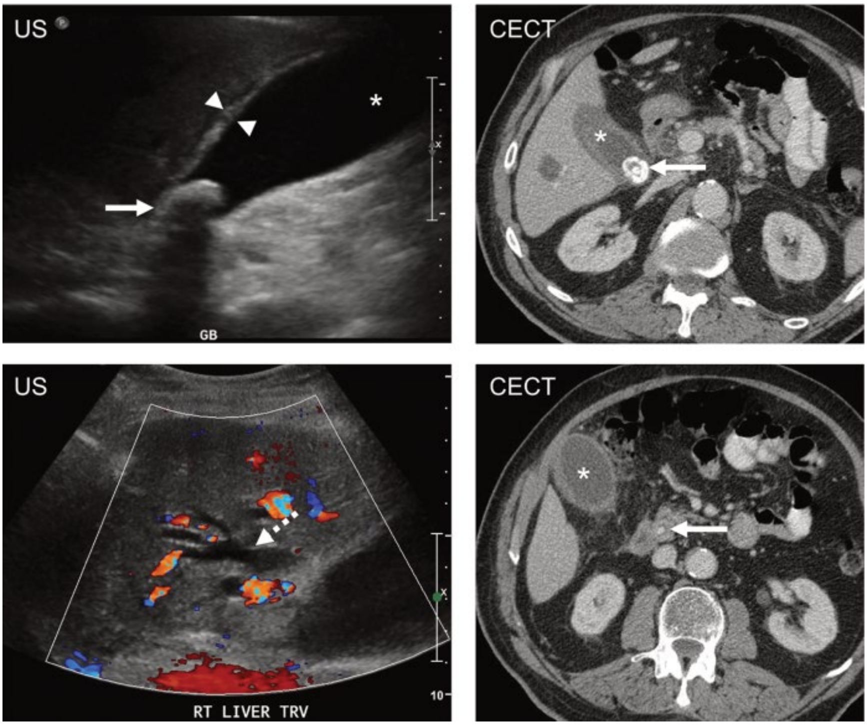

Figure 11.27 Acute cholecystitis and choledocholithiasis (i.e. stones in the common bile duct) – US and contrast-enhanced CT (CECT). US imaging (top left) shows a dilated gallbladder (*) with a dominant calculus (gallstone) at the gallbladder neck (solid arrow) showing classic shadowing below the stone. Note gallbladder wall thickening with surrounding trace fluid (arrow heads). Hepatic US imaging (bottom left) shows dilated intrahepatic bile ducts (dashed arrow). CECT (top right) shows same laminated stone in the gallbladder (solid arrow) within a thick-walled, inflamed gallbladder (*), consistent with acute cholecystitis. A small obstructing stone is noted at the distal common bile duct (bottom right image; solid white arrow), likely the cause of bile duct dilation and gallbladder inflammation.

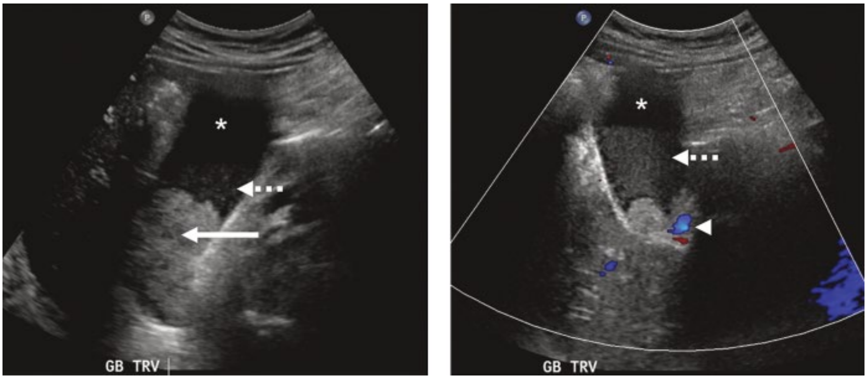

Figure 11.29 Gallbladder cancer – US. Left image: Focal soft-tissue mass located at the gallbladder neck (solid white arrow) causing mild distension of the gallbladder (*) and layering sludge above the tumor (white dashed arrow). Right image: Color Doppler US imaging shows focal vascularity within the soft-tissue component, allowing differentiation from dense sludge.

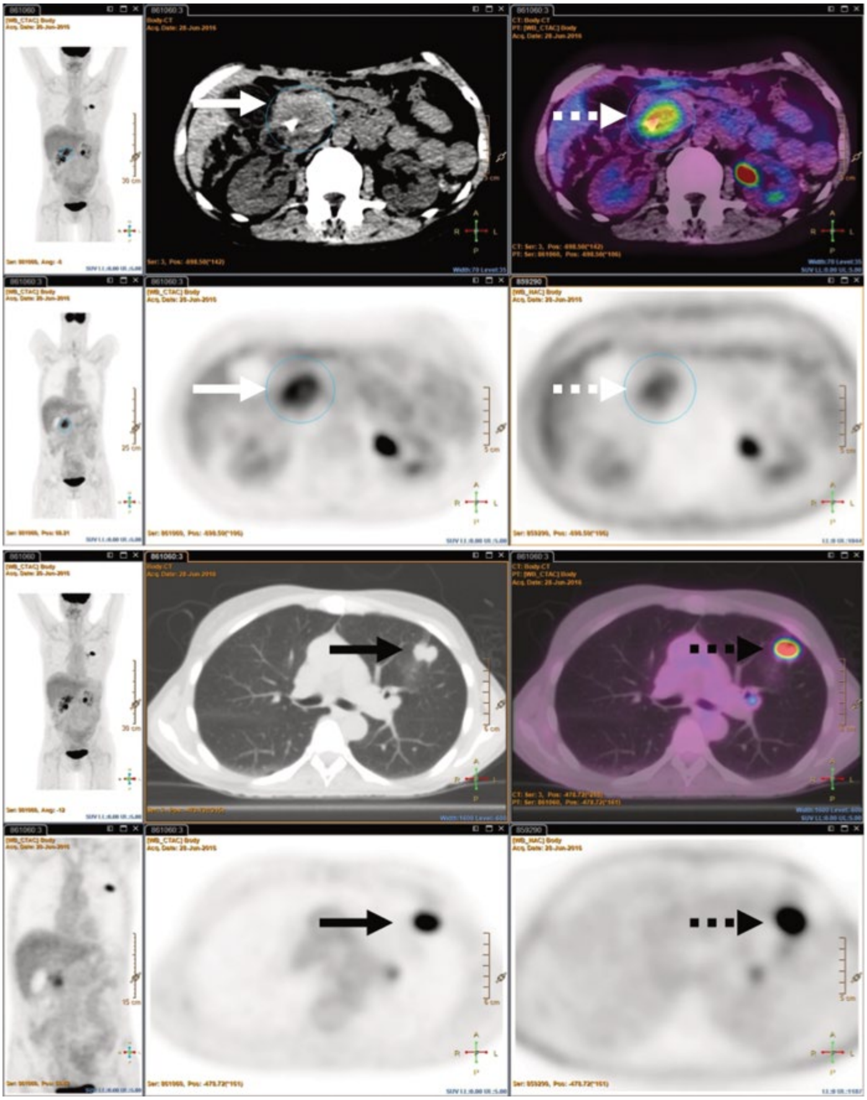

Figure 11.34 Pancreatic cancer on PET-CT. Top two rows of images represent the PET/CT and PET only images of the abdomen: A mass is seen within the pancreatic head (white solid arrow) on CT that demonstrates hypermetabolic activity (white dashed arrow), which was proven to be a pancreatic neuroendocrine tumor. Bottom two rows of images represent the PET/CT and PET only images of the chest: A hypermetabolic pulmonary metastasis is also seen in the left lung, both on CT (solid black arrow) and PET (black dashed arrow).

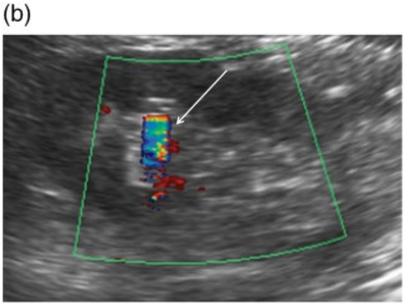

Figure 12.4 (b) The echogenic focus shows "twinkle" artifact when color Doppler ultrasound (US) is applied (arrow), which suggests that the structure is mineralized, like most renal calculi.

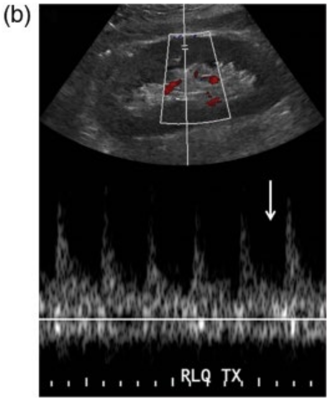

Figure 12.12 (b) Doppler pulse wave ultrasound demonstrating normal vascularity of the right lower quadrant transplant kidney. A normal arterial waveform (ultrasound trace at the bottom of image) is obtained from parenchymal branch arteries (arrow). The resistive index, a vascular parameter used as a measure of blood flow in the kidney, is calculated from this waveform as 0.68, which is within the normal range.

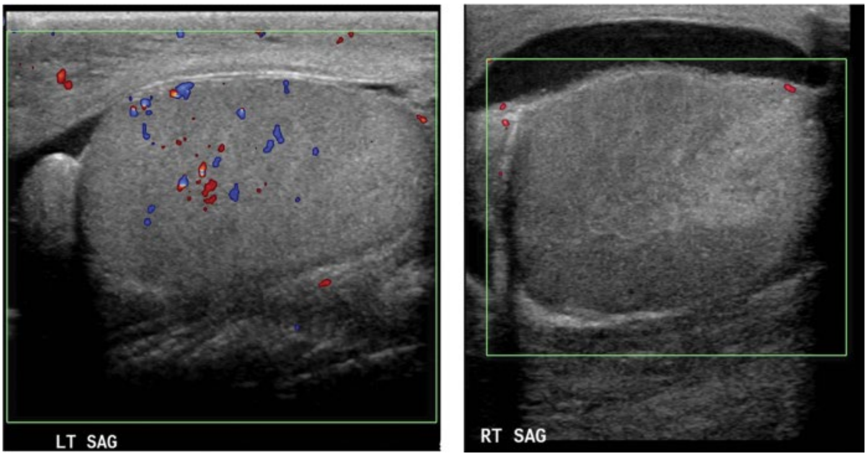

Figure 12.20 Scrotal Doppler ultrasound of the testicles. Normal blood flow, shown as colored foci on the ultrasound images, is easily identified in the normal left testicle (LT SAG). Flow is not revealed in the right testicle (RT SAG), consistent with testicular torsion. The vascular pedicle supplying the right testicle has torted (twisted), impairing flow into the right testicle. The torted cord is not shown on these images.

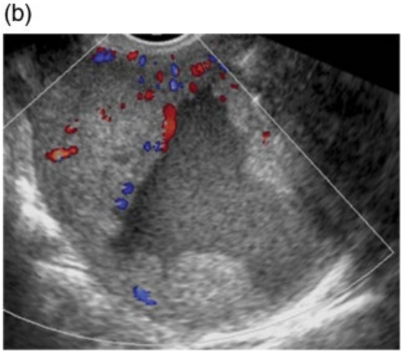

Figure 12.25 (b) Vascular flow is identified in the solid components when Doppler ultrasound is performed (color foci). This endometrial mass demonstrating internal vascularity is consistent with a large endometrial cancer.

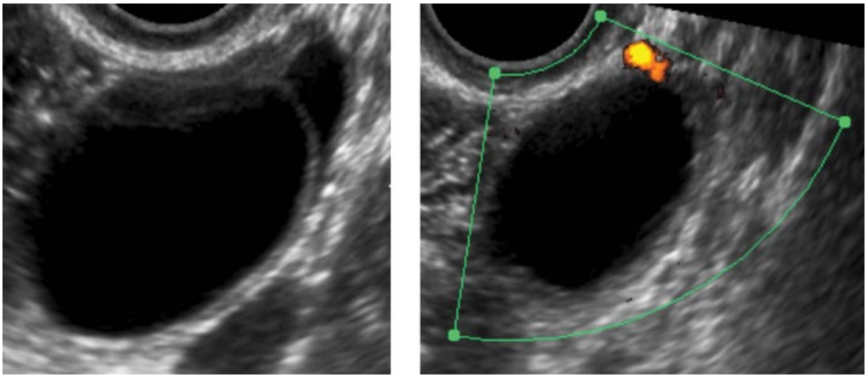

Figure 12.27 Normal premenopausal ovary on ultrasound. Grayscale ultrasound reveals a large cyst, which is a normal dominant follicle (a normal physiologic ovarian structure, which evolves with the menstrual cycle) in premenopausal women. This has no solid component or internal vascularity when Doppler ultrasound is performed, but vascular flow is present outside the lesion in the normal ovarian parenchymal tissue.

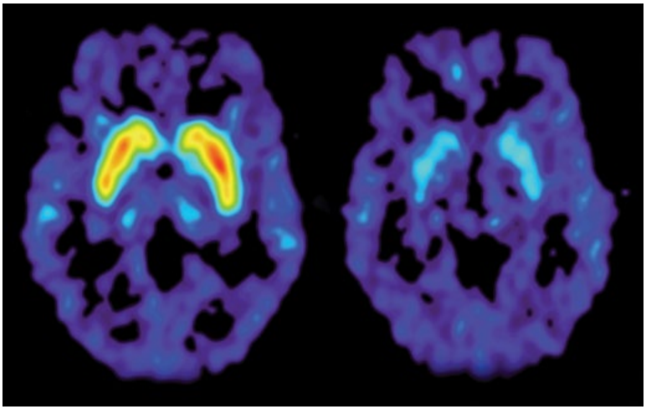

Figure 13.29 Occupancy of dopamine D2 receptors by an antipsychotic drug measured with ^{11}C-raclopride. The scan on the left is before treatment and the one on the right during treatment. The bright area in the center of the brain is the striatum where there are high densities of the dopamine D2 receptors.

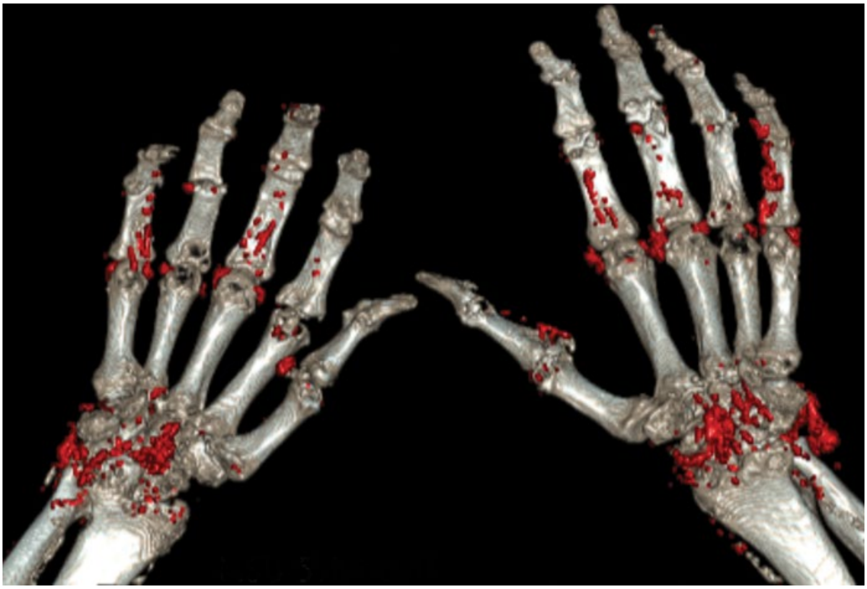

Figure 14.6 Three-dimensional reconstruction from a dual energy CT (DECT) in a patient with gouty arthropathy. The red colors represent deposits of monosodium urate crystals adjacent to the joints of the hands and wrists detected by DECT based on the differences in the physical properties of the different tissues.

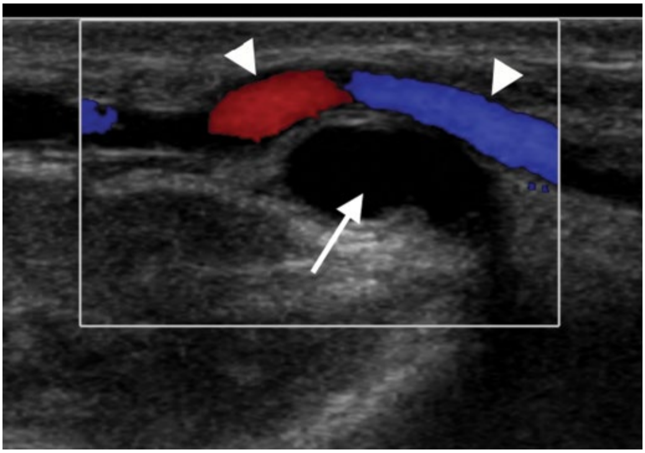

Figure 14.11 Static Doppler ultrasound image of a mass at the wrist demonstrates a well-defined anechoic (no internal echos) mass (arrow) next to the radial artery (arrowheads), with no vascular flow within it. This appearance is consistent with a ganglion cyst, an outpouching of fluid from the joint.

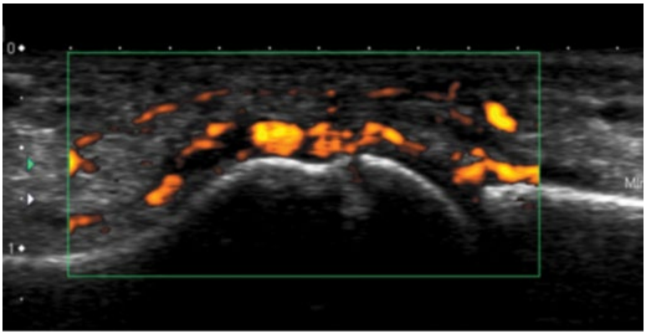

Figure 14.22 Longitudinal power Doppler US image of the metatarsophalangeal (MTP) joint in a patient with rheumatoid arthritis demonstrates extensive intra-articular and periarticular vascularity (red–yellow color) in keeping with active synovitis.

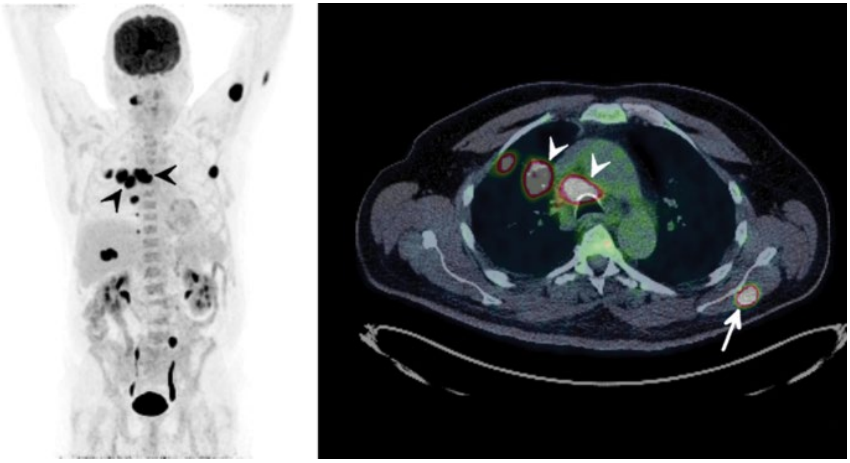

Figure 15.2 A 63-year-old man with biopsy-proven non-small cell lung cancer, thought to be stage IIIA on CT (limited to the chest). The patient was planned to receive chemoradiotherapy with curative intent. ^{18}F-FDG-PET/CT performed subsequently showed metabolically active lung tumor with metastatic nodes in the right lung hilum and mediastinum (arrowheads). Further, PET showed unsuspected multiple metastases to skeletal muscle (see deposit in muscle superficial to left scapula; arrow in transaxial image).

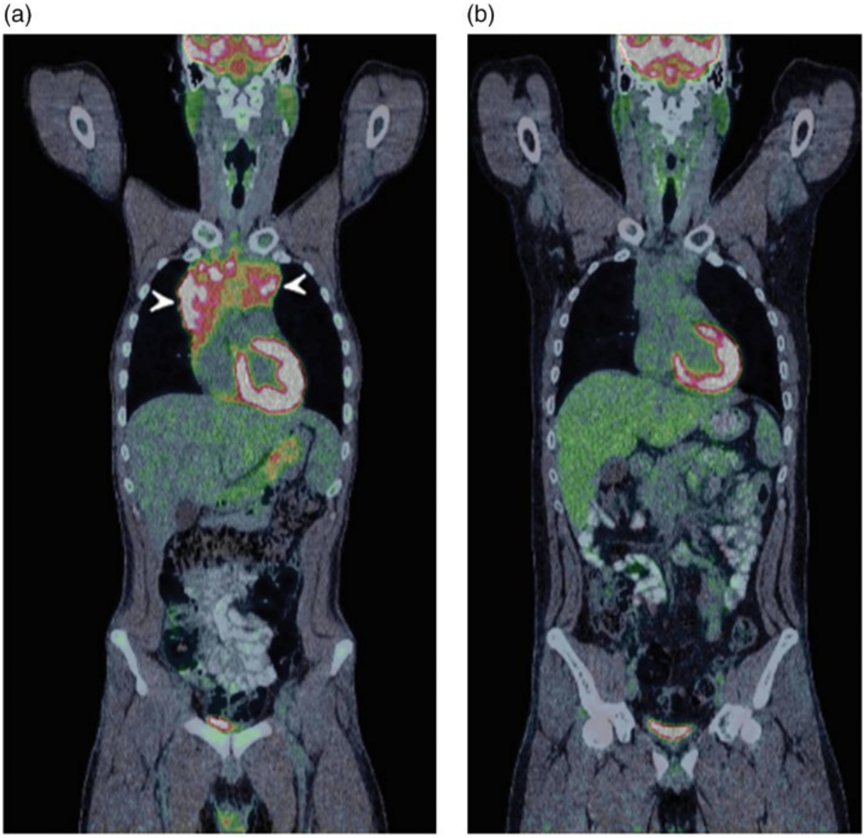

Figure 15.3 A 28-year-old man with Hodgkin's lymphoma. PET performed at baseline and three weeks after completion of chemotherapy shows a bulky metabolically active mediastinal mass at baseline (arrowheads) (a), which decreased in size after therapy (b). The residual mass seen on CT is no longer metabolically active with uptake similar to mediastinal blood pool (Deauville score, 2), confirming complete metabolic response.

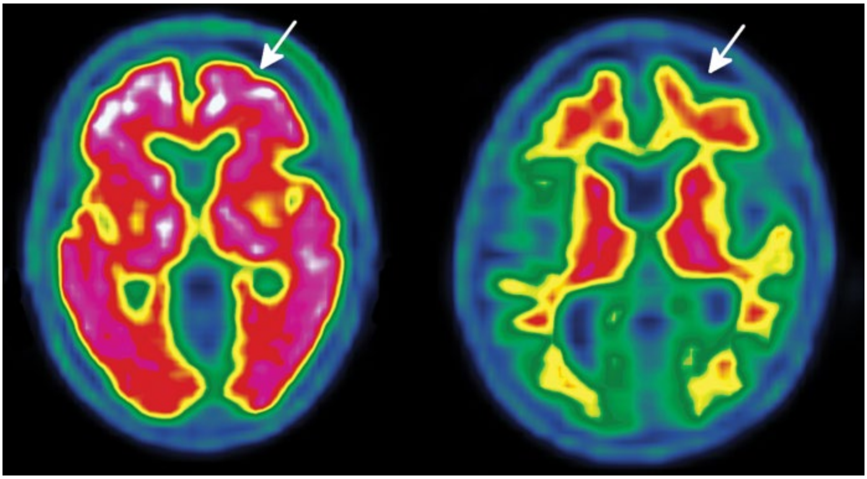

Figure 15.4 Fused ^{18}F-Flutemetamol (Vizamyl) PET/CT image of the brain from two separate patients for evaluation of dementia. On the right is a negative scan, showing normal tracer uptake in white matter with low-level uptake in the frontal cerebral cortex (arrow). In contrast, on the left is a positive scan, showing high-level uptake in the frontal cerebral cortex (arrow), suggestive of abnormal amyloid deposition.

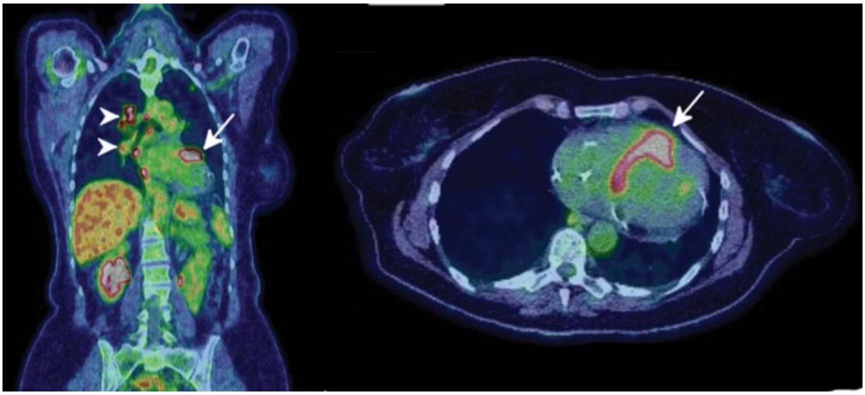

Figure 15.5 Evaluation of arrhythmia. PET shows focal abnormal FDG uptake in the myocardium (arrow). Also note, focal increased FDG uptake in hilar and mediastinal lymph nodes (arrowheads), in a typical distribution for sarcoidosis.

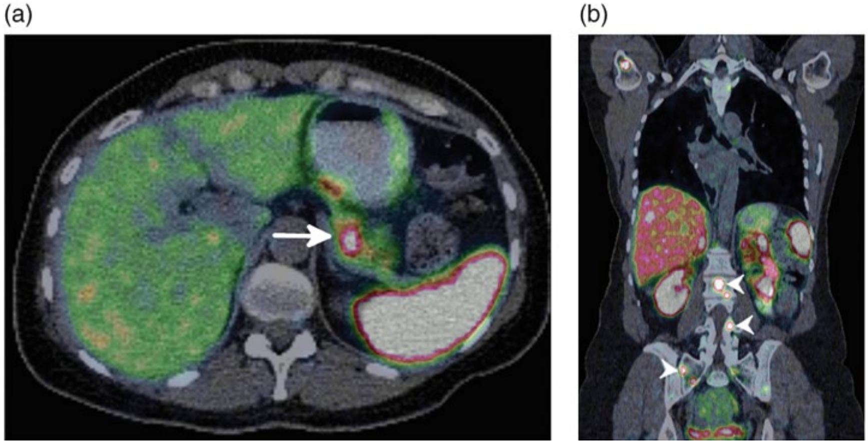

Figure 15.6 A 56-year-old woman after resection of a small bowel neuroendocrine tumor, with lung metastasis. Restaging ^{68}Ga-DOTATATE-PET/CT was performed prior to treatment with peptide receptor radionuclide therapy (PRRT). On PET, there is clear evidence for ^{68}Ga-DOTATATE avid disease in her pancreas (arrow) (a) and skeleton (arrowheads) (b). As most of her known metastases show high ^{68}Ga-DOTATATE uptake, the patient was found eligible for PRRT.